

Realistic Large-Break LOCA Evaluation Methodology Using the Automated Statistical Treatment of Uncertainty Method (ASTRUM)

Authors:

M. E. Nissley, C. Frepoli,
K. Ohkawa, K. Muftuoglu

Manager:

J. P. Sechrist



ABSTRACT

Westinghouse has developed and licensed a best-estimate large-break loss-of-coolant accident (LOCA) methodology for 3- and 4-loop designs (1996), and later extended the methodology to 2-loop upper plenum injection plants (1999). The licensed methodology uses a response surface technique for the uncertainty treatment. In this method, uncertainty contributors are ranged individually and in combination to determine the expected peak cladding temperature (PCT) response. Later, these results are combined to generate an overall PCT uncertainty distribution. An additional uncertainty exists since PCT response to any one parameter or group of parameters is not independent from other contributors. This additional uncertainty, resulting from a linear combination assumption, is quantified by applying a superposition correction. This correction factor is based on a series of calculations in which parameters from each of the uncertainty categories are varied simultaneously.

In this report, an alternative uncertainty methodology is developed. This methodology replaces the response surface technique with a statistical sampling method. In this technique, the uncertainty parameters are simultaneously sampled for each case. The necessary number of cases to calculate the 95th percentile PCT are determined based on well-established statistical theory. One of the advantages of this method is that the complexity of making accident simulation runs is reduced by increased automation. The uncertainty contributors in both methodologies are primarily the same, and no changes are being made to the approved uncertainties and their distribution functions. However, the new technique eliminates the additional uncertainty step coming from superposition assumption. The new method is called the Automated Statistical Treatment of Uncertainty Method (ASTRUM).

This report documents a road map to the methodology, patterned after the Code Scaling, Applicability, and Uncertainty (CSAU) methodology. The thermal-hydraulic computational tool used in ASTRUM is WCOBRA/TRAC MOD7A. The models and correlations used in the code are also documented here. The sections describing the models and correlations are taken from the approved topical report with minimal revisions. Application to a 4-loop Westinghouse plant is given as a demonstration of ASTRUM, following the technical bases of the methodology changes. Also included in the report are the technical justification for applying the methodology to Combustion Engineering designs, and regression testing of WCOBRA/TRAC MOD7A with changes made since its approval.

ACKNOWLEDGMENTS

The Westinghouse best-estimate LOCA methodology was originally developed based on contributions from many people. The methodology presented in this report relies on the existing methodology to a large extent. We would like to recognize, in particular, the significant contributions of Mike Young, Dr. Steve Bajorek, Dr. Larry Hochreiter, Mitch Nissley, Dr. Katsu Ohkawa, Dr. Kenji Takeuchi, Sonny Nguyen, and Sue Dederer in the development of the currently licensed codes and methods.

Development of the methodology presented here has been a true team effort. Significant effort went into preparation of the tools and the computer programs used in the analysis. The authors would like to acknowledge the support of John Besspiata and Aaron Everhard in preparing, validating, and documenting the computer programs. The support of Dave Scherf for technical help and of Sharen Saunders for document preparation is deeply appreciated. The overall support provided by Regina Null is gratefully acknowledged.

Editor Susan Iverson helped greatly in bettering our final product. Her help and dedication is acknowledged.

Preparation of this report placed stringent demands on Technical and Online Publishing Services, headed by Pat Cheripka. The talents and patience of Carla Hamilton, Lynn Flora, Martina Funk, Rose Prutz, and Sherry Palm are truly appreciated.

We would like to acknowledge the technical advice, guidance, and review by Bob Perdue, Mike Young, Bob Kemper, Bob McFetridge, Jeff Petzold, and Sonny Nguyen.

Finally, the overall support provided by the LOCA Integrated Services group (led by Jim Sechrist) is gratefully acknowledged.

TABLE OF CONTENTS

<u>Section</u>	<u>Title</u>	<u>Page</u>
	ABSTRACT	iii
	ACKNOWLEDGMENTS	v
	LIST OF TABLES	xix
	LIST OF FIGURES	xxiii
	ACRONYMS	xxxvii
	NOMENCLATURE	xli
 1	 ROADMAP OF ASTRUM	 1-1
1-1	BACKGROUND	1-1
1-2	RELATIONSHIP OF ASTRUM TO EXISTING METHODOLOGY	1-1
1-2-1	Step 1: Scenario Specification	1-1
1-2-2	Step 2: Nuclear Power Plant Selection	1-3
1-2-3	Step 3: Phenomena Identification and Ranking	1-3
1-2-3-1	Fuel Rod	1-3
1-2-3-2	Core	1-4
1-2-3-3	Upper Plenum	1-6
1-2-3-4	Hot Leg	1-7
1-2-3-5	Pressurizer	1-7
1-2-3-6	Steam Generators	1-8
1-2-3-7	Pump	1-8
1-2-3-8	Cold Leg/Accumulator	1-8
1-2-3-9	Downcomer	1-9
1-2-3-10	Lower Plenum	1-10
1-2-3-11	Break	1-10
1-2-3-12	Loop	1-10
1-2-4	Step 4: Frozen Code Selection	1-11
1-2-5	Step 5: Provide Complete Documentation	1-12
1-2-6	Step 6: Code Applicability Determination	1-13
1-2-7	Step 7: Establishment of Assessment Matrix	1-13
1-2-8	Step 8: Define Nodalization	1-13
1-2-9	Step 9: Determine Code and Experiment Accuracy	1-13
1-2-10	Step 10: Determine Effect of Scale	1-14
1-2-11	Step 11: Determine Effect of Reactor Input Parameters and State	1-15
1-2-12	Step 12: Perform NPP Sensitivity Calculations	1-16
1-2-13	Step 13: Combine Biases and Uncertainties	1-17
1-2-14	Step 14: Calculate Total Uncertainty	1-17

TABLE OF CONTENTS (Cont'd)

<u>Section</u>	<u>Title</u>	<u>Page</u>
1-3	ORGANIZATION OF THE REPORT	1-17
1-4	REFERENCES	1-19
2	<u>WCOBRA/TRAC CONSERVATION EQUATIONS</u>	2-1
2-1	INTRODUCTION	2-1
2-2	VESSEL COMPONENT CONSERVATION EQUATIONS (MODEL BASIS)	2-1
2-2-1	Three-Field Equation Formulation	2-2
2-2-2	Vessel Component Three-Field Conservation Equations	2-3
2-2-2-1	Conservation of Mass	2-6
2-2-2-2	Conservation of Momentum	2-7
2-2-2-3	Conservation of Energy	2-7
2-2-3	Cartesian Coordinate Representation	2-8
2-2-4	Subchannel Coordinate Formulation	2-11
2-2-5	Comparison of Cartesian and Subchannel Formulations	2-14
2-3	VESSEL COMPONENT COMPUTATIONAL CELL STRUCTURE (MODEL AS CODED)	2-15
2-3-1	Introduction	2-15
2-3-2	Vessel Component Computational Mesh	2-16
2-3-3	Vessel Component Finite-Difference Equations	2-17
2-3-3-1	Conservation of Mass Equations	2-17
2-3-3-2	Conservation of Momentum Equations	2-19
2-3-3-3	Conservation of Energy Equations	2-27
2-3-4	Source, Viscous, and Turbulence Terms	2-29
2-3-4-1	Mass, Energy, and Momentum Source Terms	2-29
2-3-4-2	Boundary Condition Source Terms	2-33
2-3-4-3	Turbulent Shear Stress Tensors and Heat Flux Vectors	2-34
2-4	CONSERVATION EQUATIONS FOR ONE-DIMENSIONAL COMPONENTS (MODEL BASIS)	2-40
2-4-1	Introduction	2-40
2-4-2	Conservation of Mixture Mass	2-41
2-4-3	Conservation of Mixture Momentum	2-43
2-4-4	Vapor and Mixture Energy Conservation Equations	2-43
2-4-5	Closure of the Conservation Equations	2-45
2-5	ONE-DIMENSIONAL COMPONENT COMPUTATIONAL CELL STRUCTURE (MODEL AS CODED)	2-46
2-5-1	Introduction	2-46

TABLE OF CONTENTS (Cont'd)

<u>Section</u>	<u>Title</u>	<u>Page</u>
2-5-2	One-Dimensional Component Computational Mesh	2-46
2-5-3	One-Dimensional Component Finite Difference Formulation	2-47
2-5-3-1	Semi-Implicit Formulation	2-48
2-5-3-2	Fully Implicit Formulation	2-51
2-6	NUMERICAL SOLUTION METHOD	2-53
2-6-1	Introduction	2-53
2-6-2	Vessel Component Numerical Solution	2-53
2-6-2-1	Solution of the Momentum Equations	2-54
2-6-2-2	Linearization of the Mass and Energy Equations	2-55
2-6-2-3	Solution of the System Pressure Matrix	2-58
2-6-2-4	Cells Connected to One-Dimensional Components	2-59
2-6-3	One-Dimensional Component Numerical Solution	2-60
2-6-3-1	Solution of Momentum Equations	2-60
2-6-3-2	Solution of Mass and Energy Equations	2-61
2-6-3-3	Component Boundary Conditions	2-63
2-6-3-4	Fully Implicit One-Dimensional Components	2-64
2-6-4	Network Matrix Equation	2-65
2-6-5	WCOBRA/TRAC Solution Routines	2-69
2-6-5-1	Transient Calculation Routines	2-69
2-6-5-2	Sequence of Outer Iteration Calculations	2-71
2-7	TIMESTEP SIZE AND CONVERGENCE CRITERIA	2-73
2-7-1	Introduction	2-73
2-7-2	Coded Convergence Criteria	2-73
2-7-3	Timestep Size Control	2-74
2-7-4	Numerical Stability	2-75
2-8	REFERENCES	2-76
2-9	RAI LISTING	2-76
3	WCOBRA/TRAC FLOW REGIME MAPS AND INTERFACIAL AREA	3-1
3-1	INTRODUCTION	3-1
3-2	VESSEL COMPONENT NORMAL WALL FLOW REGIMES	3-1
3-2-1	Introduction	3-1
3-2-2	Small Bubble Regime	3-3
3-2-3	Small to Large Bubble Regime	3-6
3-2-4	Churn-Turbulent Flow Regime	3-10
3-2-5	Film/Drop Flow Regime	3-11

TABLE OF CONTENTS (Cont'd)

<u>Section</u>	<u>Title</u>	<u>Page</u>
3-3	VESSEL COMPONENT HOT WALL FLOW REGIMES	3-13
3-3-1	Introduction	3-13
3-3-2	Inverted Annular Flow Regime	3-13
3-3-3	Inverted Liquid Slug Flow Regime	3-14
3-3-4	Dispersed Droplet Flow Regime	3-16
3-3-5	Falling Film Regime	3-16
3-3-6	Top Deluge Flow Regime	3-17
3-3-7	Interfacial Area Transport Equation	3-18
3-4	ONE-DIMENSIONAL COMPONENT FLOW REGIMES	3-20
3-4-1	Introduction	3-20
3-4-2	Bubbly Flow Regime	3-21
3-4-3	Slug Flow Regime	3-23
3-4-4	Churn Flow Regime	3-24
3-4-5	Annular-Mist Flow Regime	3-26
3-5	REFERENCES	3-28
3-6	RAI LISTING	3-29
4	WCOBRA/TRAC MOMENTUM TRANSFER MODELS	4-1
4.1	INTRODUCTION	4-1
4-2	VESSEL COMPONENT WALL SHEAR MODELS	4-2
4-3	VESSEL COMPONENT FORM LOSS	4-10
4-4	VESSEL COMPONENT INTERFACIAL SHEAR MODELS	4-13
4-4-1	Small Bubble Flow Regime Interfacial Drag	4-15
4-4-2	Small-to-Large Bubble Flow Regime Interfacial Drag	4-21
4-4-3	Churn-Turbulent Flow Regime Interfacial Drag	4-24
4-4-4	Film/Drop Flow Regime	4-25
4-4-5	Inverted Annular Flow Regime	4-29
4-4-6	Inverted Liquid Slug Regime	4-30
4-4-7	Dispersed Droplet Flow Regime	4-32
4-4-8	Falling Film Flow Regime	4-34
4-4-9	Top Deluge Flow Regime	4-35
4-5	VESSEL COMPONENT INTERCELL DRAG	4-37
4-6	VESSEL COMPONENT ENTRAINMENT AND DE-ENTRAINMENT MODELS	4-39
4-6-1	Introduction	4-39
4-6-2	Entrainment in Film Flow	4-39

TABLE OF CONTENTS (Cont'd)

<u>Section</u>	<u>Title</u>	<u>Page</u>
4-6-3	Entrainment During Bottom Reflood	4-44
4-6-4	Entrainment During Top Down Reflood	4-50
4-6-5	Spacer Grid Droplet Breakup Model	4-57
4-6-6	De-entrainment in Film Flow	4-63
4-6-7	Crossflow De-entrainment	4-65
4-6-8	De-entrainment at Area Changes	4-67
4-6-9	De-entrainment at Solid Surfaces and Liquid Pools	4-69
4-7	ONE-DIMENSIONAL COMPONENT MOMENTUM TRANSFER	
	MODELS	4-69
4-7-1	Introduction	4-69
4-7-2	Annular Flow Friction Factor Model	4-70
4-7-3	Relative Velocity Models	4-74
4-7-4	One-Dimensional Component Form Loss	4-78
4-8	CRITICAL FLOW MODEL	4-84
4-8-1	Natural Choking Approach (TRAC-PD2)	4-84
4-8-2	Critical Flow Model (TRAC-PF1)	4-85
4-8-3	Post Critical Flow Model	4-94
4-9	REFERENCES	4-96
4-10	RAI LISTING	4-100
5	WCOBRA/TRAC INTERFACIAL HEAT AND MASS TRANSFER MODELS	5-1
5-1	INTRODUCTION	5-1
5-2	VESSEL COMPONENT INTERFACIAL HEAT AND MASS	
	TRANSFER MODELS	5-1
5-2-1	Small Bubble Regime	5-1
5-2-2	Small to Large Bubble Regime	5-5
5-2-3	Churn-Turbulent Regime	5-7
5-2-4	Film/Drop Regime	5-11
5-2-5	Inverted Annular Regime	5-13
5-2-6	Inverted Liquid Slug Regime	5-15
5-2-7	Dispersed Droplet Flow Regime	5-17
5-2-8	Falling Film Regime	5-19
5-2-9	Top Deluge Flow Regime	5-21
5-2-10	Effect of Grid Spacers on Interfacial Heat Transfer	5-22
5-2-11	Effect of Noncondensables	5-24
5-2-12	Vessel Component Interfacial Mass Transfer	5-27

TABLE OF CONTENTS (Cont'd)

<u>Section</u>	<u>Title</u>	<u>Page</u>
5-3	ONE-DIMENSIONAL COMPONENT INTERFACIAL HEAT AND MASS TRANSFER MODELS	5-32
5-3-1	Bubbly Flow Regime	5-32
5-3-2	Slug Flow Regime	5-35
5-3-3	Churn Flow Regime	5-37
5-3-4	Annular-Mist Flow Regime	5-39
5-3-5	Effect of Noncondensables	5-41
5-3-6	One-Dimensional Component Interfacial Mass Transfer	5-42
5-4	REFERENCES	5-44
5-5	RAI LISTING	5-46
6	<u>WCOBRA/TRAC WALL HEAT TRANSFER MODELS</u>	6-1
6-1	INTRODUCTION	6-1
6-2	VESSEL COMPONENT WALL HEAT TRANSFER MODELS	6-1
6-2-1	Convection to Single-Phase Vapor	6-2
6-2-2	Convection to Single-Phase Liquid	6-5
6-2-3	Saturated and Subcooled Nucleate Boiling	6-7
6-2-4	Critical Heat Flux and Wall Temperature at CHF	6-16
6-2-5	Transition Boiling	6-20
6-2-6	Minimum Film Boiling Wall Temperature	6-25
6-2-7	Inverted Annular Film Boiling	6-27
6-2-8	Dispersed Flow Film Boiling	6-31
6-2-9	Thermal Radiation Heat Transfer	6-36
6-2-10	Grid Rewet Model	6-42
6-2-11	Wall to Fluid Heat Transfer	6-44
6-3	One-Dimensional Component Wall Heat Transfer	6-47
6-3-1	Single-Phase Liquid Natural Convection	6-48
6-3-2	Single-Phase Liquid Forced Convection	6-50
6-3-3	Nucleate Boiling	6-51
6-3-4	Critical Heat Flux	6-54
6-3-5	Transition Boiling	6-56
6-3-6	Minimum Film Boiling Temperature	6-59
6-3-7	Film Boiling Heat Transfer	6-61
6-3-8	Convection to Single-Phase Vapor	6-64
6-3-9	Heat Transfer to Two-Phase Mixtures	6-65
6-3-10	Condensation Heat Transfer	6-68
6-3-11	Wall to Fluid Heat Transfer	6-70

TABLE OF CONTENTS (Cont'd)

<u>Section</u>	<u>Title</u>	<u>Page</u>
6-4	Heat Flux Splitting in <u>W</u> COBRA/TRAC	6-71
6-4-1	Single-Phase Liquid Forced Convection	6-73
6-4-2	Saturated Nucleate Boiling	6-74
6-4-3	Subcooled Nucleate Boiling	6-74
6-4-4	Transition Boiling	6-75
6-4-5	Inverted Annular Film Boiling (IAFB)	6-75
6-4-6	Inverted Annular Dispersed Flow Film Boiling (IADF) and Dispersed Droplet Film Boiling	6-76
6-5	References	6-77
6-6	RAI Listing	6-81
7	<u>W</u> COBRA/TRAC MODELS FOR HEATED AND UNHEATED STRUCTURES	7-1
7-1	INTRODUCTION	7-1
7-2	CONDUCTOR GEOMETRIES MODELLED IN THE VESSEL	7-1
7-2-1	Conduction Equation	7-3
7-2-2	Calculation of Thermal Conductance	7-6
7-3	FUEL ROD MODELLING	7-10
7-3-1	Fuel Rod Quench Front Model	7-10
7-3-2	Pellet-Cladding Gap Conductance Model	7-11
7-4	FUEL ROD DEFORMATION MODEL	7-16
7-4-1	Deformation Mechanisms	7-17
7-4-2	Effects of Fuel Rod Deformation on Core Thermal-Hydraulics	7-30
7-5	CLADDING REACTION MODEL	7-33
7-6	UNHEATED CONDUCTOR MODELLING	7-37
7-7	CONDUCTOR MODELLING IN ONE-DIMENSIONAL COMPONENTS	7-38
7-8	SCALING CONSIDERATIONS	7-39
7-9	CONCLUSIONS	7-40
7-10	REFERENCES	7-41
7-11	RAI LISTING	7-43
8	<u>W</u> COBRA/TRAC REACTOR KINETICS AND DECAY HEAT MODELS	8-1
8-1	INTRODUCTION	8-1
8-2	DECAY HEAT SOURCE	8-1
8-3	FISSION HEAT	8-4
8-4	ACTINIDE DECAY HEAT SOURCE	8-6
8-5	SPACE DEPENDENT HEAT SOURCE MODEL	8-8

TABLE OF CONTENTS (Cont'd)

<u>Section</u>	<u>Title</u>	<u>Page</u>
8-6	ENERGY DEPOSITION MODELLING	8-12
8-6-1	Introduction	8-12
8-6-2	Generalized Energy Deposition Model	8-14
8-7	DECAY HEAT UNCERTAINTY EVALUATION	8-21
8-8	REACTOR POINT KINETICS VALIDATION	8-21
8-9	JUSTIFICATION OF SIMPLIFICATIONS AND ASSUMPTIONS	8-22
8-9-1	Actinide Decay Power	8-22
8-9-2	WCOBRA/TRAC Fission Energy Accounting	8-22
8-9-3	Decay Heat Absorption Effects	8-23
8-10	GENERALIZED ENERGY DEPOSITION MODEL (GEDM) VALIDATION	8-23
8-11	INTERFACE BETWEEN NEUTRONICS AND THERMAL-HYDRAULICS MODELS	8-24
8-12	REACTOR KINETICS, DECAY HEAT, AND INTERFACE MODELS AS CODED	8-24
8-13	REACTOR KINETICS, DECAY HEAT, AND INTERFACE MODELS SCALING CONSIDERATIONS	8-25
8-14	CONCLUSIONS	8-25
8-15	REFERENCES	8-25
8-16	RAI LISTING	8-26
9	WCOBRA/TRAC ONE-DIMENSIONAL COMPONENT MODELS	9-1
9-1	INTRODUCTION	9-1
9-2	PIPE COMPONENT	9-1
9-3	TEE COMPONENT	9-2
9-4	PUMP COMPONENT	9-3
9-5	STEAM GENERATOR COMPONENT (STGEN)	9-9
9-6	PRESSURIZER COMPONENT (PRIZER)	9-10
9-7	VALVE COMPONENT	9-11
9-8	ACCUMULATOR COMPONENT (ACCUM)	9-11
9-9	BREAK AND FILL COMPONENTS	9-15
9-10	REFERENCES	9-16
9-11	RAI LISTING	9-17
10	THERMOPHYSICAL PROPERTIES	10-1
10-1	INTRODUCTION	10-1

TABLE OF CONTENTS (Cont'd)

<u>Section</u>	<u>Title</u>	<u>Page</u>
10-2	THERMOPHYSICAL PROPERTIES OF WATER	10-1
10-2-1	Vessel Component Water Properties	10-1
10-2-1-1	Saturated Fluid Properties	10-1
10-2-1-2	Properties of Superheated Vapor	10-3
10-2-1-3	Subcooled Liquid Properties	10-6
10-2-2	One-Dimensional Component Water Properties	10-7
10-2-2-1	Saturated Fluid Properties	10-7
10-2-2-2	Properties of Superheated Vapor	10-11
10-2-2-3	Subcooled Vapor Properties	10-16
10-2-2-4	Subcooled Liquid Properties	10-18
10-2-2-5	Transport Properties	10-22
10-3	THERMOPHYSICAL PROPERTIES OF AIR	10-27
10-3-1	Vessel Component	10-27
10-3-2	One-Dimensional Components	10-28
10-4	THERMAL PROPERTIES OF NUCLEAR FUEL ROD MATERIALS	10-30
10-4-1	Uranium Dioxide	10-30
10-4-2	Zircaloy-4	10-31
10-4-3	ZIRLO™	10-32
10-4-4	Fuel Rod Gas Mixtures	10-34
10-5	THERMAL PROPERTIES OF STRUCTURAL MATERIALS	10-35
10-5-1	Vessel Component Structural Material Properties	10-35
10-5-2	One-Dimensional Component Structural Material Properties	10-36
10-6	CONCLUSIONS	10-38
10-7	REFERENCES	10-39
11	SENSITIVITY AND UNCERTAINTY ANALYSIS (CSAU ELEMENT 3)	11-1
11-1	TECHNICAL BASIS FOR REVISED UNCERTAINTY METHODOLOGY	11-1
11-1-1	Statistical Sampling Approach	11-1
11-1-2	Application of the Statistical Method	11-6
11-2	TECHNICAL BASIS FOR ADDITIONAL PARAMETERS CONSIDERED IN UNCERTAINTY ANALYSIS	11-7
11-2-1	Break Type and Size	11-7
11-2-1-1	Modeling of DECLG Breaks	11-7
11-2-1-2	Modeling of Split Breaks	11-8
11-2-1-3	Compliance to NUREG 1.157 on Break Type and Size	11-10
11-2-1-4	Conclusions	11-11

TABLE OF CONTENTS (Cont'd)

<u>Section</u>	<u>Title</u>	<u>Page</u>
11-2-2	Time in Cycle	11-11
11-2-2-1	Burnup Effects on Stored Energy and Peak Cladding Temperature	11-11
11-2-2-2	Burnup Treatment in ASTRUM	11-11
11-3	NPP SENSITIVITY CALCULATIONS WITH ASTRUM (CSAU STEP 12)	11-12
11-3-1	Confirmatory Calculations	11-13
11-3-2	NPP Uncertainty Calculations	11-14
11-4	DETERMINATION OF COMBINED BIAS AND UNCERTAINTY (CSAU STEP 13)	11-14
11-4-1	Fuel Rod	11-14
11-4-2	Core	11-15
11-4-3	Upper Plenum	11-16
11-4-4	Hot Leg	11-17
11-4-5	Pressurizer	11-17
11-4-6	Steam Generator	11-17
11-4-7	Pump	11-17
11-4-8	Cold Leg/Accumulator	11-17
11-4-9	Downcomer	11-18
11-4-10	Lower Plenum	11-19
11-4-11	Break	11-19
11-4-12	Loop	11-20
11-5	DETERMINATION OF TOTAL UNCERTAINTY (CSAU STEP 14)	11-20
11-6	APPLICATION TO OTHER 10CFR50.46 ACCEPTANCE CRITERIA	11-20
11-6-1	Local Oxidation	11-20
11-6-2	Core-Wide Oxidation	11-21
11-7	REFERENCES	11-21
12	EXAMPLE PWR APPLICATION	12-1
12-1	INTRODUCTION	12-1
12-2	SAMPLE PWR PLANT DESCRIPTION AND NODALIZATION	12-2
12-3	REFERENCE TRANSIENT AND ALLOWABLE PLANT OPERATING CONDITIONS	12-8
12-3-1	Plant Physical Description	12-8
12-3-2	Plant Initial Operating Conditions: Reactor Power	12-9
12-3-3	Plant Initial Operating Conditions: Fluid Conditions	12-10
12-3-4	Accident Boundary Conditions	12-11

TABLE OF CONTENTS (Cont'd)

<u>Section</u>	<u>Title</u>	<u>Page</u>
	12-3-5 Plant Operating Range	12-12
	12-3-6 Confirm Reference Case Limiting Assumptions	12-12
12-4	REFERENCE TRANSIENT ANALYSIS	12-12
	12-4-1 Steady-State Calculation	12-13
	12-4-2 Transient Calculation	12-15
	12-4-3 Reference Transient Results	12-15
12-5	DEVELOPMENT OF RUN MATRIX	12-16
12-6	ASTRUM RESULTS AND DETERMINATION OF THE 95/95 PCT VALUE ...	12-16
12-7	OTHER 10CFR50.46 CRITERIA	12-19
12.8	REFERENCES	12-19
13	METHODOLOGY SUMMARY	13-1
13-1	COMPLIANCE WITH 10CFR50.46	13-1
13-2	COMPLIANCE WITH REGULATORY GUIDE 1.157	13-1
	13-2-1 Regulatory Position 1, "Best-Estimate Calculations"	13-2
	13-2-2 Regulatory Position 2, "Considerations for Thermal-Hydraulic Best-Estimate Codes"	13-3
	13-2-3 Regulatory Position 3, "Best-Estimate Code Features"	13-4
	13-2-4 Regulatory Position 4, "Estimation of Overall Computational Uncertainty"	13-27
13-3	EFFECT OF REVISED UNCERTAINTY METHODOLOGY ON PRIOR SER REQUIREMENTS	13-31
	13-3-1 WCAP-12945-P-A SER Requirements	13-32
	13-3-2 WCAP-14449-P-A SER Requirements	13-36
13-4	REFERENCES	13-37
APPENDIX A EXTENSION OF ASTRUM TO COMBUSTION ENGINEERING DESIGNS		A-1
APPENDIX B VALIDATION OF WCOBRA/TRAC MOD7A REVISION 6		B-1

LIST OF TABLES

<u>Table No.</u>	<u>Title</u>	<u>Page</u>
Table 1-1	PIRT for Large-Break LOCA	1-20
Table 1-2	Blowdown/Refill Assessment for WCOBRA/TRAC	1-24
Table 1-3	Refill/Reflood Assessment for WCOBRA/TRAC	1-25
Table 1-4	Blowdown Phenomena Assessment Matrix	1-26
Table 1-5	Refill Phenomena Assessment Matrix	1-27
Table 1-6	Reflood Phenomena Assessment Matrix	1-28
Table 1-7	Uncertainty Distributions for Global Models	1-29
Table 1-8	Uncertainty Distributions for Local Models	1-30
Table 1-9	Burst Strain Summary	1-31
Table 1-10	Power-Related Parameters Considered in Uncertainty Methodology	1-32
Table 1-11	Initial and Boundary Conditions Considered in Uncertainty Methodology	1-33
Table 1-12	Changes in Sections 2 through 10	1-34
Table 2-1	Timestep Size Reduction Limits	2-78
Table 2-2	Code Backup Limits	2-79
Table 4-1	Sudden Contraction	4-102
Table 4-2	Sudden Expansion	4-102
Table 4-3	Combination	4-103
Table 4-4	Comparison of Thom's Slip Ratios and Ishii C_o and Modified C_o	4-103
Table 4-5	Comparisons of TRAC Predicted Expansion Pressure Loss to Test Data	4-104
Table 4-6	Comparisons of Abrupt Contraction Loss Coefficients	4-104
Table 4-7	Comparison of Predicted Contraction Pressure Loss to Test Data	4-105
Table 4-8	Comparison of Normalized Contraction Pressure Loss with Test Data	4-105
Table 4-9	Comparison of TRAC Predicted Loss With Test Data for Combined Contraction and Expansion	4-105
Table 6-1	One-Dimensional Component Heat Transfer Regimes	6-84
Table 7-1	Cladding Thermal Expansion Correlations	7-44
Table 7-2	Cladding Correlations for Modulus of Elasticity (E) and Shear Modulus (G)	7-45
Table 7-3	Creep Correlation Coefficients for Westinghouse Zircaloy-4 Cladding	7-46
Table 7-4	Creep Correlation Coefficients for Westinghouse ZIRLO™ Cladding	7-47
Table 7-5	Creep Correlation Coefficients for Sandvik (NRU) Cladding	7-48
Table 8-1	ANSI/ANS 5.1-1979 Decay Heat Standard Data for U-235 Thermal Fission	8-27
Table 8-2	ANSI/ANS 5.1-1979 Decay Heat Model Comparison for Infinite Radiation of U-235	8-30
Table 8-3	ANSI/ANS 5.1-1971 Decay Heat Standard Data for U-235 Thermal Fission	8-31
Table 8-4	ANSI/ANS 5.1-1971 Decay Heat Standard for U-235 Thermal Fission	8-32
Table 8-5	Typical Normalized Interaction Frequency Fit Data	8-33

LIST OF TABLES (Cont'd)

<u>Table No.</u>	<u>Title</u>	<u>Page</u>
Table 8-6	Actinide Heat Source Data	8-33
Table 8-7	Typical Radiation Source Timing, Strength, and Range	8-34
Table 8-8	Typical Values for Redistribution Fraction Values	8-34
Table 8-9	Neutron Heating Transfer Model	8-35
Table 8-10	Gamma Photon Energy Spectrum	8-36
Table 8-11	BUGLE-80 Gamma Kerma Data	8-37
Table 8-12	Typical 15x15 GEDM Gamma Transfer Matrix	8-38
Table 8-13	[.....] ^{a,c}	8-39
Table 8-14	Decay Group Uncertainty Factors Per One Sigma (%)	8-40
Table 8-15	Point Reactor Kinetics Validation	8-41
Table 8-16	Actinide Isotope Nuclear Data	8-42
Table 8-17	Prompt Fission Energy Release Data	8-43
Table 8-18	[.....] ^{a,c}	8-44
Table 9-1	The Four Segments of Pump Homologous Curves	9-18
Table 9-2	Pump Control Input Parameter	9-19
Table 9-3	Valve Control Options	9-20
Table 10-1	Constants for Saturated Liquid Enthalpy	10-40
Table 10-2	Constants for Saturated Vapor Enthalpy	10-40
Table 10-3	Vessel Component Saturated Water Thermal Properties	10-41
Table 10-4	Superheated Vapor Temperature Constants	10-45
Table 10-5	Subcooled Water Density Constants	10-46
Table 10-6	Saturated Steam Internal Energy Constants	10-46
Table 10-7	Saturated Steam Enthalpy Constants	10-46
Table 10-8	Saturated Liquid Internal Energy Constants	10-47
Table 10-9	Constants for Specific Heat	10-47
Table 10-10	Liquid Viscosity Constants	10-48
Table 10-11	Vapor Viscosity Constants	10-49
Table 10-12	Liquid and Vapor Thermal Conductivity Constants	10-49
Table 10-13	Surface Tension Constants	10-49
Table 10-14	Constants for Specific Heat of Air	10-50
Table 10-15	Constants for Viscosity of Air	10-50
Table 10-16	Specific Heat of Zircaloy-4	10-51
Table 10-17	Chemical Composition of ZIRLO™ and Zircaloy-4 Alloys	10-52
Table 10-18	Specific Heat of ZIRLO™ Alloy	10-52
Table 11-1	Break Spectrum Results (WCOBRA/TRAC MOD7)	11-23
Table 11-2	Effect of Changing Marviken Model Pipe Flow Area on Predicted Flowrate	11-24
Table 11-3	Summary of Sampling Strategy for Break Type, Size, and CD	11-25

LIST OF TABLES (Cont'd)

<u>Table No.</u>	<u>Title</u>	<u>Page</u>
Table 11-4	Burnup Effects on Peak Cladding Temperature	11-26
Table 11-5	Physical Models and Plant Parameters Included in the Uncertainty Analysis	11-26
Table 11-6	Generic Rod Power Census Used for Core-Wide Oxidation Assessment	11-27
Table 12-1	Channel Descriptions for <u>W</u> COBRA/TRAC IP2 Vessel Model	12-21
Table 12-2	Gap Connections for <u>W</u> COBRA/TRAC IP2 Vessel Model	12-25
Table 12-3	Reference Values and Plant Operating Range-IP2	12-26
Table 12-4	Reference, Nominal, and Range Values for Plant Initial Operating Conditions	12-29
Table 12-5	Reference Case Confirmatory Studies	12-30
Table 12-6	Criteria for Acceptable Steady-State	12-31
Table 12-7	Values of the Sampled Parameters for the Top 9 Most Limiting Cases	12-32
Table 12-8	Summary of Statistical Variables in HOTSPOT	12-34
Table 12-9	Results from the Parametric Study	12-34
Table A-1	Combustion Engineering and Westinghouse PIRT for Large-Break LOCA	A-7
Table A-2	Critical Flow Model Assessment	A-12
Table A-3	Typical Conditions in a PWR During Blowdown	A-13
Table A-4	Blowdown Heat Transfer Test Conditions	A-14
Table A-5	Code Validation Test Range of Conditions	A-15
Table A-6	Typical Conditions in a PWR During Reflood	A-16
Table A-7	Reflood Heat Transfer Test Conditions	A-17
Table A-8	Reflood Separate Effects Test Range of Conditions	A-18
Table A-9	ECC Bypass/CCFL Model Assessment	A-19
Table A-10	Condensation Model Assessment	A-20
Table B-1	Changes and Errors Reported Since Approval of <u>W</u> COBRA/TRAC MOD7A Revision 1	B-22

LIST OF FIGURES

<u>Figure No.</u>	<u>Title</u>	<u>Page</u>
Figure 1-1	Code Scaling, Applicability, and Uncertainty Evaluation Methodology (Boyack et al., 1989)	1-38
Figure 1-2	Cumulative Distribution Function for Critical Flow Multipliers	1-39
Figure 1-3	Cumulative Distribution Function for Blowdown Cooling Heat Transfer Multipliers	1-40
Figure 1-4	Cumulative Distribution Function for Refill Heat Transfer Multipliers	1-41
Figure 1-5	Cumulative Distribution Function for Reflood Heat Transfer Multipliers	1-42
Figure 1-6	Typical Power Shape Used for Reference Transient	1-43
Figure 2-1	Control Volume for Cartesian Coordinates	2-80
Figure 2-2	Basic Mesh Cell	2-81
Figure 2-3	Variable Mesh Cell	2-82
Figure 2-4	Mesh Cell for Vertical Velocities	2-83
Figure 2-5	Mesh Cell for Transverse Velocities	2-84
Figure 2-6	Vertical Stresses Acting on a Vertical Momentum Cell	2-85
Figure 2-7	Velocity Gradient for Point A	2-86
Figure 2-8	One-Dimensional Computational Cell Structure	2-87
Figure 2-9	Sample Model of a Thermal-Hydraulic Network	2-88
Figure 2-10	Numerical Solution Routines	2-89
Figure 2-11	WCOBRA/TRAC Prepass Calculation Routines	2-90
Figure 2-12	WCOBRA/TRAC Outer Iteration Routines	2-91
Figure 2-13	WCOBRA/TRAC Routines for Post Pass Calculations	2-92
Figure 2-14	Effect of Numerical Damping on Transient Value of y	2-93
Figure 3-1	Normal Wall Flow Regimes	3-31
Figure 3-2	Normal Wall Flow Regime Selection Logic	3-32
Figure 3-3	Effect of Scale on Vertical Upflow Flow Regime Transitions Predicted by Taitel, Bornea, and Dukler (1980)	3-33
Figure 3-4	Effect of Scale on Vertical Upflow Flow Regime Transitions Predicted by WCOBRA/TRAC	3-34
Figure 3-5	Small to Large Bubble Regime - Formation of Large Bubbles	3-35
Figure 3-6	Vessel Component Hot Wall Flow Regimes	3-36
Figure 3-7	Hot Wall Flow Regime Selection Logic	3-37
Figure 3-8	One-Dimensional Component Flow Regime Map	3-38
Figure 3-9	One-Dimensional Component Churn Flow Ramping Factor	3-39
Figure 4-1	One-Dimensional Vessel Channel with Area Change	4-106
Figure 4-2	Bubble Drag Coefficients (Ishii and Chawla, 1979)	4-107

LIST OF FIGURES (Cont'd)

<u>Figure No.</u>	<u>Title</u>	<u>Page</u>
Figure 4-3	Effect of Ramps On Interfacial Friction Factor. (a) Small Bubble Regime, (b) Large Bubble Regime	4-108
Figure 4-4	Interfacial Friction Factor for Smooth Films (Wallis, 1969)	4-109
Figure 4-5	Hanstock and Hanratty (1976) Film Flow Interfacial Shear	4-110
Figure 4-6a	Comparison of Droplet Data Range and Droplet Size Limits in WCOBRA/TRAC at 40 psia	4-111
Figure 4-6b	Comparison of Droplet Data Range and Droplet Size Limits in WCOBRA/TRAC at 20 psia	4-112
Figure 4-7	Impingement of a Droplet on a Grid Spacer (a) Shattering Process (b) Definition of Droplet Offset Parameter	4-113
Figure 4-7c	Leading Edge of a Wetted Grid; Effect of Vapor Velocity	4-114
Figure 4-8	The Relationship of Droplet Diameter Ratio Versus Droplet Weber Number	4-115
Figure 4-9	Comparison of CQD Equation 4-186 with Data from Whalley (1973)	4-116
Figure 4-10	Comparison of TRAC-PD2 Two-Phase Multiplier to Collier et al. (1972) Data, Case 1	4-117
Figure 4-11	Comparison of TRAC-PD2 Two-Phase Multiplier to Collier et al. (1972) Data, Case 2	4-118
Figure 4-12	Comparison of TRAC-PD2 Two-Phase Multiplier to Collier et al. (1972) Data, Case 3	4-119
Figure 4-13	Comparison of TRAC-PD2 Two-Phase Multiplier to Collier et al. (1972) Data, Case 4	4-120
Figure 4-14	Sudden Expansion in 1-D Component	4-121
Figure 4-15	Sudden Contraction in 1-D Component	4-121
Figure 4-16	Contraction and Expansion in 1-D Component	4-122
Figure 4-17	1-D / Vessel Junction	4-123
Figure 4-18	Broken Cold Leg Nozzle Junction to Vessel	4-124
Figure 4-19	Pipe for Revised Critical Flow Model	4-125
Figure 5-1	Description of Interfacial Heat Transfer	5-48
Figure 5-2	Large Void Fraction Gradient Ramp for Subcooled Liquid Interfacial Area	5-49
Figure 5-3	Comparison of the Theofanous (1979) Interfacial Heat Transfer Correlation to Others (Liles et al., 1988)	5-50
Figure 6-1	Boiling Curve	6-85
Figure 6-2	Heat Transfer Regime Selection Logic for Vessel Component	6-86
Figure 6-3	Heat Transfer Regime Map for Vessel Component	6-87
Figure 6-4	Heat Transfer Coefficient for Single-Phase Vapor	6-88

LIST OF FIGURES (Cont'd)

<u>Figure No.</u>	<u>Title</u>	<u>Page</u>
Figure 6-5	Chen Correlation Convective Multiplier F_{CHEN}	6-89
Figure 6-6	Chen Boiling Suppression Factor S_{CHEN}	6-90
Figure 6-7	Droplet Contact Effectiveness (as coded) at Atmospheric Pressure	6-91
Figure 6-8	Droplet Contact Effectiveness (as coded) at High Pressure	6-92
Figure 6-9	Transition Boiling (Model 2) Ramp F_z	6-93
Figure 6-10	Film Boiling Model Components	6-94
Figure 6-11	Enhancement of Convective Heat Transfer Due to Droplets	6-95
Figure 6-12	Effect of Spacer Grids on Convective Heat Transfer	6-96
Figure 6-13	One-Dimensional Component Heat Transfer Regime Selection	6-97
Figure 6-14	Biasi CHF Correlation Switch Over Quality	6-98
Figure 6-15	One-Dimensional Component Heat Transfer Regime Selection Process at High Void and Quality	6-99
Figure 6-16	Heat Flux Paths for Nucleate Boiling	6-100
Figure 6-17	Heat Flux Paths for Transition Boiling and Dispersed Flow Film Boiling	6-101
Figure 6-18	Heat Flux Paths for Film Boiling	6-102
Figure 7-1	Nuclear Fuel Rod Geometry	7-49
Figure 7-2	Heater Rod Geometry	7-49
Figure 7-3	Tube and Wall Conductor Geometries	7-50
Figure 7-4	Control Volume for Heat Balance	7-50
Figure 7-5	Noding for Fuel Rod Conduction Model	7-51
Figure 7-6	Conductance Between Nodes	7-51
Figure 7-7	Steady-State Temperature Distribution in a Flat Plate with No Internal Heat Generation	7-52
Figure 7-8	Steady-State Temperature Distribution in a Hollow Cylinder with No Internal Heat Generation	7-52
Figure 7-9	Typical Heat Transfer Noding Scheme	7-53
Figure 7-10	Examples of Heat Transfer Node Insertion	7-54
Figure 7-11	Cladding Temperature Profile with Fine Mesh Renoding	7-55
Figure 7-12	Surface Heat Flux Profile with Fine Mesh Renoding	7-55
Figure 7-13	Temperature Jump Distances for an Ideal Gap	7-56
Figure 7-14	Instantaneous Creep Rates for Westinghouse Zircaloy-4 Cladding	7-57
Figure 7-15	Instantaneous Creep Rates for Westinghouse ZIRLO™ Cladding	7-58
Figure 7-16	Instantaneous Creep Rates for Sandvik (NRU) Cladding	7-59
Figure 7-17	Heatup Rate Scenarios	7-60
Figure 7-18	Circumferential Strain Following Rupture - Zircaloy-4 Cladding	7-61
Figure 7-19	Burst Temperature Correlation - Westinghouse ZIRLO™ Cladding	7-62

LIST OF FIGURES (Cont'd)

<u>Figure No.</u>	<u>Title</u>	<u>Page</u>
Figure 7-20	Circumferential Strain Following Rupture - Westinghouse ZIRLO™ Cladding	7-63
Figure 7-21	Rod Strain at Burst Elevation	7-64
Figure 7-22	Flow Area Reduction Due to Blockage - Zircaloy-4 Cladding	7-65
Figure 7-23	Flow Area Reduction Due to Blockage - ZIRLO™ Cladding	7-66
Figure 7-24	Application of Blockage Factor Following Hot Assembly Rod Burst	7-67
Figure 7-25	Geometry for One-Dimensional Component Conductor	7-68
Figure 8-1	U-235 Fission Fraction	8-45
Figure 8-2	Pu-239 Fission Fraction	8-46
Figure 8-3	U-238 Fission Fraction	8-47
Figure 8-4	Calculated Normalized Macroscopic Cross Sections versus Core Average Water Density	8-48
Figure 8-5	$\bar{\beta}$ vs. Burnup at Various Enrichments	8-49
Figure 8-6	Prompt Neutron Lifetime	8-50
Figure 8-7	Prompt Energy Release	8-51
Figure 8-8	Total Energy Release	8-52
Figure 8-9	Delayed Group I Lambda	8-53
Figure 8-10	Delayed Group II Lambda	8-54
Figure 8-11	Delayed Group III Lambda	8-55
Figure 8-12	Delayed Group IV Lambda	8-56
Figure 8-13	Delayed Group V Lambda	8-57
Figure 8-14	Delayed Group VI Lambda	8-58
Figure 8-15	U-238 Capture/Fission Ratio as a Function of Initial Enrichment and Burnup	8-59
Figure 8-16	15x15 Material Composition Assignment Layout	8-60
Figure 8-17	15x15 Core Balance Fixed Source Distribution	8-61
Figure 8-18	15x15 Hot Assembly Fixed Source Distribution	8-62
Figure 8-19	15x15 Hot Rod Fixed Source Distribution	8-63
Figure 8-20	Gamma Kerma Cross Section Energy Dependence	8-64
Figure 8-21	Typical Heat Flux Deposition Fractions versus Coolant Density	8-65
Figure 8-22	Typical Heat Flux Deposition Fractions versus Coolant Density	8-66
Figure 8-23	Percent Fit Deviations for U-235 ANSI/ANS 5.1 - 1979 Plus Two Sigma	8-67
Figure 8-24	Percent Fit Deviations for Pu-239 ANSI/ANS 5.1 - 1979 Plus Two Sigma	8-68
Figure 8-25	Percent Fit Deviations for U-238 ANSI/ANS 5.1 - 1979 Plus Two Sigma	8-69
Figure 8-26	U-235 ANSI/ANS 5.1 - 1979 Decay Heat Standard vs. Fitted Results	8-70
Figure 8-27	Pu-239 ANSI/ANS 5.1 - 1979 Decay Heat Standard vs. Fitted Results	8-71
Figure 8-28	U-238 ANSI/ANS 5.1 - 1979 Decay Heat Standard vs. Fitted Results	8-72

LIST OF FIGURES (Cont'd)

<u>Figure No.</u>	<u>Title</u>	<u>Page</u>
Figure 8-29	Time Dependent Reactor Period for + 0.003 ΔK Reactivity Insertion versus Time After Insertion	8-73
Figure 8-30	Time Dependent Reactor Period for + 0.0015 ΔK Reactivity Insertion versus Time After Insertion	8-74
Figure 8-31	Time Dependent Reactor Period for - 0.030 ΔK Reactivity Insertion versus Time After Insertion	8-75
Figure 8-32	Total Actinide Decay Power versus Burnup and Initial Enrichment	8-76
Figure 8-33	Actinide Decay Power versus Burnup and Initial Enrichment	8-77
Figure 8-34	Capture Correction versus Burnup and Initial Enrichment	8-78
Figure 8-35	WCOBRA/TRAC Calculation Block Diagram	8-79
Figure 9-1	PIPE Component Noding	9-22
Figure 9-2	TEE Component Noding	9-23
Figure 9-3	PUMP Noding Diagram	9-24
Figure 9-4	93A Pump Single-Phase Homologous Head Curves	9-25
Figure 9-5	93A Pump Two-Phase Homologous Head Curves	9-26
Figure 9-6	93A Pump Single-Phase Homologous Torque Curves	9-27
Figure 9-7	93A Pump Two-Phase Homologous Torque Curves	9-28
Figure 9-8	Steam Generator Noding Diagram	9-29
Figure 9-9	Pressurizer (PRIZER) Component Noding	9-30
Figure 9-10	VALVE Component Noding	9-31
Figure 9-11	Accumulator Noding Diagram	9-32
Figure 9-12	Condensation Suppression Region for Accumulator/Nitrogen Model	9-33
Figure 9-13	Pressure Boundary Condition Using BREAK Component	9-34
Figure 9-14	Velocity Boundary Condition Using FILL Component	9-34
Figure 10-1	WCOBRA/TRAC Vessel Component Saturated Liquid Enthalpy Function	10-53
Figure 10-2	WCOBRA/TRAC Vessel Component Saturated Vapor Enthalpy Function	10-54
Figure 10-3	WCOBRA/TRAC Vessel Component Saturation Temperature	10-55
Figure 10-4	WCOBRA/TRAC Vessel Component Saturated Liquid Density	10-56
Figure 10-5	WCOBRA/TRAC Vessel Component Saturated Vapor Density	10-57
Figure 10-6	WCOBRA/TRAC Vessel Component Saturated Liquid Viscosity	10-58
Figure 10-7	WCOBRA/TRAC Vessel Component Saturated Vapor Viscosity	10-59
Figure 10-8	WCOBRA/TRAC Vessel Component Saturated Liquid and Vapor Conductivity Thermal Conductivity	10-60
Figure 10-9	WCOBRA/TRAC Vessel Component Saturated Liquid Specific Heat	10-61
Figure 10-10	WCOBRA/TRAC Vessel Component Saturated Vapor Specific Heat	10-62
Figure 10-11	WCOBRA/TRAC Vessel Component Saturated Liquid Surface Tension	10-63

LIST OF FIGURES (Cont'd)

<u>Figure No.</u>	<u>Title</u>	<u>Page</u>
Figure 10-12	<u>W</u> COBRA/TRAC Vessel Component Superheated Vapor Enthalpy	10-64
Figure 10-13	<u>W</u> COBRA/TRAC Vessel Component Superheated Vapor Temperature	10-65
Figure 10-14	<u>W</u> COBRA/TRAC Vessel Component Superheated Vapor Density	10-66
Figure 10-15	<u>W</u> COBRA/TRAC Vessel Component Superheated Vapor Thermal Conductivity ..	10-67
Figure 10-16	<u>W</u> COBRA/TRAC Vessel Component Superheated Vapor Viscosity	10-68
Figure 10-17	<u>W</u> COBRA/TRAC 1-D Component Saturation Pressure	10-69
Figure 10-18	<u>W</u> COBRA/TRAC 1-D Component Saturated Vapor Density	10-70
Figure 10-19	<u>W</u> COBRA/TRAC 1-D Component Saturated Liquid Density	10-71
Figure 10-20	<u>W</u> COBRA/TRAC 1-D Component Saturated Vapor Enthalpy	10-72
Figure 10-21	<u>W</u> COBRA/TRAC 1-D Component Saturated Liquid Enthalpy	10-73
Figure 10-22	<u>W</u> COBRA/TRAC 1-D Component Saturated Vapor Specific Heat	10-74
Figure 10-23	<u>W</u> COBRA/TRAC 1-D Component Saturated Liquid Specific Heat	10-75
Figure 10-24	<u>W</u> COBRA/TRAC 1-D Component Saturated Vapor Viscosity	10-76
Figure 10-25	<u>W</u> COBRA/TRAC 1-D Component Saturated Liquid Viscosity	10-77
Figure 10-26	<u>W</u> COBRA/TRAC 1-D Component Saturated Vapor Thermal Conductivity	10-78
Figure 10-27	<u>W</u> COBRA/TRAC 1-D Component Saturated Liquid Thermal Conductivity	10-79
Figure 10-28	<u>W</u> COBRA/TRAC 1-D Component Surface Tension	10-80
Figure 10-29	<u>W</u> COBRA/TRAC UO ₂ Thermal Conductivity (95% of Theoretical Density)	10-81
Figure 10-30	<u>W</u> COBRA/TRAC UO ₂ Specific Heat	10-82
Figure 10-31	<u>W</u> COBRA/TRAC Zircaloy-4 Thermal Conductivity	10-83
Figure 10-32	<u>W</u> COBRA/TRAC Zircaloy-4 Specific Heat	10-84
Figure 10-33	Comparison of ZIRLO™ and Zircaloy-4 Specific Heat	10-85
Figure 10-34	<u>W</u> COBRA/TRAC 1-D Component 304 Stainless Steel Thermal Conductivity	10-86
Figure 10-35	<u>W</u> COBRA/TRAC 1-D Component 304 and 316 Stainless Steel Specific Heat	10-87
Figure 10-36	<u>W</u> COBRA/TRAC 1-D Component 316 Stainless Steel Thermal Conductivity	10-88
Figure 10-37	<u>W</u> COBRA/TRAC 1-D Component 347 Stainless Steel Thermal Conductivity	10-89
Figure 10-38	<u>W</u> COBRA/TRAC 1-D Component 347 Stainless Steel Specific Heat	10-90
Figure 10-39	<u>W</u> COBRA/TRAC 1-D Component Carbon Steel Thermal Conductivity	10-91
Figure 10-40	<u>W</u> COBRA/TRAC 1-D Carbon Steel Specific Heat	10-92
Figure 10-41	<u>W</u> COBRA/TRAC 1-D Component Inconel 600 Thermal Conductivity	10-93
Figure 10-42	<u>W</u> COBRA/TRAC 1-D Component Inconel 600 Specific Heat	10-94
Figure 11-1	Split vs. DECLG for 3- and 4-Loop PWRs	11-28
Figure 11-2	DECLG Break Noding Scheme	11-29
Figure 11-3	Guillotine Break Noding Used in <u>W</u> COBRA/TRAC	11-30
Figure 11-4	Split Cold-Leg Break Noding Scheme	11-31

LIST OF FIGURES (Cont'd)

<u>Figure No.</u>	<u>Title</u>	<u>Page</u>
Figure 11-5	Split Break Noding Used in <u>W</u> COBRA/TRAC	11-32
Figure 11-6	Assemblies Included in the Peripheral (Low-Power) Assembly Channel for 2-Loop Plants	11-33
Figure 11-7	Assemblies Included in the Peripheral (Low-Power) Assembly Channel for 3-Loop Plants	11-34
Figure 11-8	Assemblies Included in the Peripheral (Low-Power) Assembly Channel for 4-Loop Plants	11-35
Figure 11-9	Quench Time Predictions for CCTF Gravity Reflood Tests	11-36
Figure 11-10	Quench Time Predictions for SCTF Gravity Reflood Test	11-37
Figure 12-1	IP2 Vessel Profile	12-35
Figure 12-2	Vessel Component Elevations	12-36
Figure 12-3	Front View of Sections 1 and 2	12-37
Figure 12-4	Top View of Lower Dome and Channel Divisions in Section 1	12-38
Figure 12-5	IP2 Vessel Noding (Vertical View)	12-39
Figure 12-6	IP2 Vessel Sections 1 to 3 (Horizontal View)	12-40
Figure 12-7	IP2 Vessel Sections 4 to 6 (Horizontal View)	12-41
Figure 12-8	IP2 Vessel Sections 7 to 9 (Horizontal View)	12-42
Figure 12-9	Upper Plenum Internal Distribution	12-43
Figure 12-10	Vertical View of Open Hole, Support Column, Free-Standing Mixer, and Guide Tube in Upper Plenum	12-44
Figure 12-11	IP2 <u>W</u> COBRA/TRAC Model Vessel/Loop Layout (Steady-State)	12-45
Figure 12-12	Power Shape 10	12-46
Figure 12-13	Broken Colde Leg 1-D Components Arrangement for DECLG Break	12-47
Figure 12-14	Broken Cold Leg 1-D Components Arrangement for Split Break	12-48
Figure 12-15	Reference Transient: Peak Cladding Temperature	12-49
Figure 12-16	PCT and Cladding Temperature at Limiting Locations	12-50
Figure 12-17	Reference Transient: Core Pressure	12-51
Figure 12-18	Reference Transient: Lower Plenum Collapsed Liquid Level	12-52
Figure 12-19	Reference Transient: Downcomer Collapsed Liquid Level	12-53
Figure 12-20	Reference Transient: Core Collapsed Liquid Level	12-54
Figure 12-21	Reference Transient: Vessel Fluid Mass	12-55
Figure 12-22	PCT for the Limiting Case and Reference Case	12-56
Figure 12-23	PCT for the Most Limiting Transients	12-57
Figure 12-24	Effect of FQ	12-58
Figure 12-25	Effect of KN	12-59
Figure 12-26	Effect of CD	12-60

LIST OF FIGURES (Cont'd)

<u>Figure No.</u>	<u>Title</u>	<u>Page</u>
Figure 12-27	Effect of Burnup	12-61
Figure 12-28	Effect of Break Area for the Reference Split Break	12-62
Figure 12-29	Final PCT vs. (CD x A)	12-63
Figure 12-30	Final PCT vs. FQ	12-64
Figure 12-31	Final PCT vs. FQ for Most Limiting Cases	12-65
Figure 12-32	Final PCT vs. KN	12-66
Figure 12-33	Final PCT vs. KN for Most-Limiting Cases	12-67
Figure 12-34	Final PCT vs. Burnup	12-68
Figure 12-35	Final PCT vs. Burnup for Most-Limiting Cases	12-69
Figure 12-36	Local Oxidation vs. PCT	12-70
Figure B-1	FLECHT-SEASET Test 31805 Rod Temperature at 48-inch Elevation (Revision 0)	B-24
Figure B-2	FLECHT-SEASET Test 31805 Rod Temperature at 48-inch Elevation (Revision 6)	B-24
Figure B-3	FLECHT-SEASET Test 31805 Rod Temperature at 78-inch Elevation (Revision 0)	B-25
Figure B-4	FLECHT-SEASET Test 31805 Rod Temperature at 78-inch Elevation (Revision 6)	B-25
Figure B-5	FLECHT-SEASET Test 31805 Rod Temperature at 120-inch Elevation (Revision 0)	B-26
Figure B-6	FLECHT-SEASET Test 31805 Rod Temperature at 120-inch Elevation (Revision 6)	B-26
Figure B-7	FLECHT-SEASET Test 31701 Rod Temperature at 48-inch Elevation (Revision 0)	B-27
Figure B-8	FLECHT-SEASET Test 31701 Rod Temperature at 48-inch Elevation (Revision 6)	B-27
Figure B-9	FLECHT-SEASET Test 31701 Rod Temperature at 78-inch Elevation (Revision 0)	B-27
Figure B-10	FLECHT-SEASET Test 31701 Rod Temperature at 78-inch Elevation (Revision 6)	B-28
Figure B-11	FLECHT-SEASET Test 31701 Rod Temperature at 120-inch Elevation (Revision 0)	B-29
Figure B-12	FLECHT-SEASET Test 31701 Rod Temperature at 120-inch Elevation (Revision 6)	B-29
Figure B-13	FLECHT Test 05132 Rod Temperature at 48-inch Elevation (Revision 0)	B-30
Figure B-14	FLECHT Test 05132 Rod Temperature at 48-inch Elevation (Revision 6)	B-30

LIST OF FIGURES (Cont'd)

<u>Figure No.</u>	<u>Title</u>	<u>Page</u>
Figure B-15	FLECHT Test 05132 Rod Temperature at 78-inch Elevation (Revision 0)	B-31
Figure B-16	FLECHT Test 05132 Rod Temperature at 78-inch Elevation (Revision 6)	B-31
Figure B-17	FLECHT Test 05132 Rod Temperature at 120-inch Elevation (Revision 0)	B-32
Figure B-18	FLECHT Test 05132 Rod Temperature at 120-inch Elevation (Revision 6)	B-32
Figure B-19	FLECHT Test 13812 Rod Temperature at 48-inch Elevation (Revision 0)	B-33
Figure B-20	FLECHT Test 13812 Rod Temperature at 48-inch Elevation (Revision 6)	B-33
Figure B-21	FLECHT Test 13812 Rod Temperature at 72-inch Elevation (Revision 0)	B-34
Figure B-22	FLECHT Test 13812 Rod Temperature at 72-inch Elevation (Revision 6)	B-34
Figure B-23	FLECHT Test 13812 Rod Temperature at 132-inch Elevation (Revision 0)	B-35
Figure B-24	FLECHT Test 13812 Rod Temperature at 132-inch Elevation (Revision 6)	B-35
Figure B-25	WCOBRA/TRAC MOD7A Rev. 0 vs. Experiment Comparison: G-2 Reflood Test 550 Rod Temperatures at 82-inch Elevation	B-36
Figure B-26	WCOBRA/TRAC MOD7A Rev. 6 Prediction of G-2 Reflood Test 550 Rod Temperatures at 82-inch Elevation	B-36
Figure B-27	WCOBRA/TRAC MOD7A Rev. 0 vs. Experiment Comparison: G-2 Reflood Test 550 Rod Temperatures at 94-inch Elevation	B-37
Figure B-28	WCOBRA/TRAC MOD7A Rev. 6 Prediction of G-2 Reflood Test 550 Rod Temperatures at 94-inch Elevation	B-37
Figure B-29	WCOBRA/TRAC MOD7A Rev. 0 vs. Experiment Comparison: G-2 Reflood Test 550 Rod Temperatures at 111-inch Elevation	B-38
Figure B-30	WCOBRA/TRAC MOD7A Rev. 6 Prediction of G-2 Reflood Test 550 Rod Temperatures at 111-inch Elevation	B-38
Figure B-31a	Predicted (Component 810) and Measured (PE-PC-001) Pressure, Test L2- 2 with MOD7A Rev. 0	B-39
Figure B-31b	Predicted (Component 810) and Measured (PE-PC-001) Pressure, Test L2- 2 with MOD7A Rev. 6	B-40
Figure B-32a	Predicted (Component 900) and Measured (FR-BL-216) Mass Flowrate in Broken Hot Leg, Test L2-2 with MOD7A Rev. 0	B-41
Figure B-32b	Predicted (Component 900) and Measured (FR-BL-216) Mass Flowrate in Broken Hot Leg, Test L2-2 with MOD7A Rev. 6	B-42
Figure B-33a	Predicted (Component 950) and Measured (FR-BL-116) Mass Flowrate in Broken Cold Leg, Test L2-2 with MOD7A Rev. 0	B-43
Figure B-33b	Predicted (Component 950) and Measured (FR-BL-116) Mass Flowrate in Broken Cold Leg, Test L2-2 with MOD7A Rev. 6	B-44
Figure B-34a	Predicted (Component 300) and Measured (FT-P129-27) Mass Flowrate in Intact Hot Leg, Test L2-2 with MOD7A Rev. 0	B-45

LIST OF FIGURES (Cont'd)

<u>Figure No.</u>	<u>Title</u>	<u>Page</u>
Figure B-34b	Predicted (Component 300) and Measured (FT-P129-27) Mass Flowrate in Intact Hot Leg, Test L2-2 with MOD7A Rev. 6	B-46
Figure B-35a	Predicted (Component 840) and Measured (FT-P120-36) Volumetric Flowrate in Accumulator, Test L2-2 with MOD7A Rev. 0	B-47
Figure B-35b	Predicted (Component 840) and Measured (FT-P120-36) Volumetric Flowrate in Accumulator, Test L2-2 with MOD7A Rev. 6	B-48
Figure B-36a	Predicted (2.87 ft) and Measured (TE-5F4-030) Cladding Temperature in the Hot Channel, Test L2-2 with MOD7A Rev. 0	B-49
Figure B-36b	Predicted (2.87 ft) and Measured (TE-5F4-030) Cladding Temperature in the Hot Channel, Test L2-2 with MOD7A Rev. 6	B-50
Figure B-37	Revised Broken Cold Leg Modeling	B-51
Figure B-38	SCTF Run 619 Cladding Temperature at 6.25 ft for Channel 5 (Rod 2) MOD7A vs. Data Comparison	B-52
Figure B-39	SCTF Run 619 Cladding Temperature at 6.25 ft for Channel 5-(Rod 2): MOD7A Rev. 6 vs. Data Comparison	B-53
Figure B-40	SCTF Run 619 Cladding Temperature at 8.35 ft for Channel 5-(Rod 2) MOD7A vs. Data Comparison	B-54
Figure B-41	SCTF Run 619 Cladding Temperature at 8.35 ft for Channel 5-(Rod 2) MOD7A Rev. 6 vs. Data Comparison	B-55
Figure B-42	SCTF Run 619 Cladding Temperature at 9.76 ft for Channel 5-(Rod 2) MOD7A vs. Data Comparison	B-56
Figure B-43	SCTF Run 619 Cladding Temperature at 9.76 ft for Channel 5-(Rod 2) MOD7A Rev. 6 vs. Data Comparison	B-57
Figure B-44	SCTF Run 619 Liquid Level in Core: MOD7A vs. Data Comparison	B-58
Figure B-45	SCTF Run 619 Liquid Level in Core: MOD7A Rev. 6 vs. Data Comparison	B-59
Figure B-46	SCTF Run 619 Liquid Level in Inner Global Region of Upper Plenum: MOD7A vs. Data Comparison	B-60
Figure B-47	SCTF Run 619 Liquid Level in Inner Global Region of Upper Plenum: MOD7A Rev. 6 vs. Data Comparison	B-61
Figure B-48	CCTF Run 62 Cladding Temperature at 6.0 ft: MOD7A Rev. 0 vs. Data Comparison	B-62
Figure B-49	CCTF Run 62 Cladding Temperature at 6.0 ft: MOD7A Rev. 6 vs. Data Comparison	B-63
Figure B-50	CCTF Run 62 Cladding Temperature at 8.0 ft: MOD7A Rev. 0 vs. Data Comparison	B-64
Figure B-51	CCTF Run 62 Cladding Temperature at 8.0 ft: MOD7A Rev. 6 vs. Data Comparison	B-65

LIST OF FIGURES (Cont'd)

<u>Figure No.</u>	<u>Title</u>	<u>Page</u>
Figure B-52	CCTF Run 62 Cladding Temperature at 10.0 ft: MOD7A Rev. 0 vs. Data Comparison	B-66
Figure B-53	CCTF Run 62 Cladding Temperature at 10.0 ft: MOD7A Rev. 6 vs. Data Comparison	B-67
Figure B-54	CCTF Run 62 Vapor Temperature at 6.0 ft for Channel 9	B-68
Figure B-55	CCTF Run 62 Vapor Temperature at 6.0 ft: MOD7A Rev. 6 vs. Data Comparison	B-69
Figure B-56	CCTF Run 62 Liquid Level in Core	B-70
Figure B-57	CCTF Run 62 Liquid Level in Core: MOD7A Rev. 6 vs. Data Comparison	B-71
Figure B-58	CCTF Run 62 Liquid Level in Upper Plenum	B-72
Figure B-59	CCTF Run 62 Liquid Level in Upper Plenum: MOD7A Rev. 6 vs. Data Comparison	B-73
Figure B-60	CCTF Run 62 Pressure Difference Across Intact Loop	B-74
Figure B-61	CCTF Run 62 Pressure Difference Across Intact Loop: MOD7A Rev. 6 vs. Data Comparison	B-75
Figure B-62	CCTF Run 62 Pressure Difference Across Broken Loop	B-76
Figure B-63	CCTF Run 62 Pressure Difference Across Broken Loop: MOD7A Rev. 6 vs. Data Comparison	B-77
Figure B-64	Axial Heater Rod Temperature Profile at 10 Seconds of Transient for Test 3.03.6AR: MOD7A Rev. 0 vs. Data Comparison	B-78
Figure B-65	Axial Heater Rod Temperature Profile at 10 Seconds of Transient for Test 3.03.6AR: MOD7A Rev. 6 vs. Data Comparison	B-79
Figure B-66	Transient Heater Rod Temperature at 95 inches for Test 3.03.6AR, Nominal Inlet Flow Conditions: WCOBRA/TRAC MOD7A Rev. 0 vs. Data Comparison ..	B-80
Figure B-67	Transient Heater Rod Temperature at 96-inch Elevation: WCOBRA/TRAC MOD7A Rev. 6 vs. Data Comparison	B-80
Figure B-68	Transient Heater Rod Temperature at 118-(Near Level F) inches for Test 3.03.6AR, Nominal Inlet Flow: MOD7A Rev. 0 vs. Data Comparison	B-81
Figure B-69	ORNL Test 3.03.6AR Cladding Temperature Comparison at 118-inch Elevation: MOD7A Rev. 6 vs. Data Comparison	B-81
Figure B-70	Transient Heater Rod Temperature at 143 inches for Test 3.03.6AR, Nominal Inlet Flow: MOD7A Rev. 0 vs. Data Comparison	B-82
Figure B-71	ORNL Test 3.03.6AR Cladding Temperature Comparison at 143-inch Elevation: MOD7A Rev. 6 vs. Data Comparison	B-82
Figure B-72	G-2 Refill Test 760 Cladding Temperature Time History Comparison (12.3-inch Elevation): MOD7A Rev. 0 vs. Data	B-83

LIST OF FIGURES (Cont'd)

<u>Figure No.</u>	<u>Title</u>	<u>Page</u>
Figure B-73	G-2 Refill Test 760 Cladding Temperature Comparison at 12.3-inch Elevation: MOD7A Rev. 6 vs. Data	B-83
Figure B-74	G-2 Refill Test 760 Cladding Temperature Time History Comparison (28.7-inch Elevation) MOD7A Rev. 0 vs. Data	B-84
Figure B-75	G-2 Refill Test 760 Cladding Temperature Comparison at 28.7-inch Elevation: MOD7A Rev. 6 vs. Data	B-84
Figure B-76	G-2 Refill Test 760 Cladding Temperature Time History Comparison (45.1-inch Elevation) MOD7A Rev. 0 vs. Data	B-85
Figure B-77	G-2 Refill Test 760 Cladding Temperature Comparison at 45.1-inch Elevation: MOD7A Rev. 6 vs. Data	B-85
Figure B-78	G-2 Refill Test 760 Cladding Temperature Time History Comparison (82.0-inch Elevation) MOD7A Rev. 0 vs. Data	B-86
Figure B-79	G-2 Refill Test 760 Cladding Temperature Comparison at 82.0-inch Elevation: MOD7A Rev. 6 vs. Data	B-86
Figure B-80	G-2 Refill Test 760 Cladding Temperature Time History Comparison (118.9-inch Elevation) MOD7A Rev. 0 vs. Data	B-87
Figure B-81	G-2 Refill Test 760 Cladding Temperature Comparison at 118.9-inch Elevation: MOD7A Rev. 6 vs. Data	B-87
Figure B-82	G-2 Refill Test 760 Axial Cladding Temperature Comparison (Time = 50 Seconds) MOD7A Rev. 0 vs. Data	B-88
Figure B-83	G-2 Refill Test 760 Axial Cladding Temperature at 50 Seconds, MOD7A Rev. 6 Results	B-88
Figure B-84a	Measured Absolute Pressure in the Upper Plenum and Downcomer, Test 6 - Run 131	B-89
Figure B-84b	Predicted Absolute Pressure in the Upper Plenum and Downcomer, Test 6 - Run 131 with MOD7A	B-89
Figure B-84c	Predicted Absolute Pressure in the Upper Plenum and Downcomer, Test 6 -Run 131 with MOD7A Rev. 6	B-90
Figure B-85a	Measured Downcomer Fluid Temperature at Level 21, Test 6 - Run 131	B-91
Figure B-85b	Predicted Mixture Enthalpy at Level 21, Test 6 - Run 131 with MOD7A	B-91
Figure B-85c	Predicted Mixture Enthalpy at Level 21, Test 6 - Run 131 with MOD7A Rev. 6 ..	B-92
Figure B-86a	Measured Downcomer Fluid Temperature at Level 01, Test 6 - Run 131	B-93
Figure B-86b	Predicted Downcomer Mixture Enthalpy at Level 01, Test 6 - Run 131 with MOD7A	B-93
Figure B-86c	Predicted Downcomer Mixture Enthalpy at Level 01, Test 6 - Run 131 with MOD7A Rev. 6	B-94

LIST OF FIGURES (Cont'd)

<u>Figure No.</u>	<u>Title</u>	<u>Page</u>
Figure B-87a	Predicted Liquid Flow at Bottom of Downcomer in Intact Side (Channels 8 and 9), Test 6 - Run 131 with MOD7A	B-95
Figure B-87b	Predicted Liquid Flow at Bottom of Downcomer in Intact Side (Channels 8 and 9), Test 6 - Run 131 with MOD7A Rev. 6	B-96
Figure B-88a	Predicted Liquid Flow at Bottom of Downcomer in Broken Side (Channels 10 and 11), Test 6 - Run 131 with MOD7A	B-97
Figure B-88b	Predicted Liquid Flow at Bottom of Downcomer in Broken Side (Channels 10 and 11), Test 6 - Run 131 with MOD7A Rev. 6	B-98
Figure B-89a	Measured Differential Pressure Between Upper Plenum and Downcomer, Test 6 - Run 131	B-99
Figure B-89b	Predicted Differential Pressure Between Upper Plenum and Downcomer, Test 6 - Run 131 with MOD7A	B-99
Figure B-89c	Predicted Differential Pressure Between Upper Plenum and Downcomer, Test 6 - Run 131 with MOD7A Rev. 6	B-100
Figure B-90a	Measured Axial Differential Pressure in Downcomer, Test 6 - Run 131	B-101
Figure B-90b	Predicted Axial Differential Pressure in Downcomer, Test 6 - Run 131 with MOD7A	B-101
Figure B-90c	Predicted Axial Differential Pressure in Downcomer, Test 6 - Run 131 with MOD7A Rev. 6	B-102
Figure B-91a	Measured Axial Differential Pressure in Downcomer, Test 6 - Run 131	B-103
Figure B-91b	Predicted Axial Differential Pressure in Downcomer, Test 6 - Run 131 with MOD7A	B-103
Figure B-91c	Predicted Axial Differential Pressure in Downcomer, Test 6 - Run 131 with MOD7A Rev. 6	B-104
Figure B-92a	Measured Azimuthal Differential Pressure in Downcomer at Level 06, Test 6 - Run 131	B-105
Figure B-92b	Predicted Transverse Differential Pressure in Downcomer at Level 06, Test 6 - Run 131 with MOD7A	B-105
Figure B-92c	Predicted Transverse Differential Pressure in Downcomer at Level 06, Test 6 - Run 131 with MOD7A Rev. 6	B-106
Figure B-93a	Measured Azimuthal Differential Pressure in Downcomer at Level 22, Test 6 - Run 131	B-107
Figure B-93b	Predicted Transverse Differential Pressure in Downcomer at Level 22, Test 6 - Run 131 with MOD7A	B-107
Figure B-93c	Predicted Transverse Differential Pressure in Downcomer at Level 22, Test 6 - Run 131 with MOD7A Rev. 6	B-108
Figure B-94a	Estimated Water Level in UPTF Vessel, Test 6 - Run 131	B-109

LIST OF FIGURES (Cont'd)

<u>Figure No.</u>	<u>Title</u>	<u>Page</u>
Figure B-94b	Predicted Water Level in UPTF Vessel, Test 6 - Run 131 with MOD7A	B-109
Figure B-94c	Predicted Water Level in UPTF Vessel, Test 6 - Run 131 with MOD7A Rev. 6 . .	B-110
Figure B-95a	Estimated Downcomer Water Levels (Referenced to 3495 mm Elevation), Test 6 - Run 131	B-111
Figure B-95b	Predicted Downcomer Water Levels (Referenced to 1180 mm Elevation), Test 6 - Run 131 with MOD7A	B-111
Figure B-95c	Predicted Downcomer Water Levels (Referenced to 1180 mm Elevation), Test 6 - Run 131 with MOD7A Rev. 6	B-112
Figure B-96	GE CCFL Test No. 60. Liquid Drain Rate as a Function of Steam Injection Rate: MOD7A Revision 1 vs. Data Comparison	B-113
Figure B-97	GE CCFL Test No. 60. Liquid Drain Rate as a Function of Steam Injection Rate: MOD7A Revision 6 vs. Data Comparison	B-114
Figure B-98	GE CCFL Test No. 69. Liquid Drain Rate as a Function of Steam Injection Rate: MOD7A Revision 1 vs. Data Comparison	B-115
Figure B-99	GE CCFL Test No. 69. Liquid Drain Rate as a Function of Steam Injection Rate: MOD7A Revision 6 vs. Data Comparison	B-116
Figure B-100	GE CCFL Test 60. Prediction vs. Bankoff Flooding Correlations: MOD7A Revision 1 vs. Test Data Comparison	B-117
Figure B-101	GE CCFL Test 60. Flooding Relationship Comparison: MOD7A Revision 6 vs. Data	B-118
Figure B-102	GE CCFL Test 69. MOD7A Revision 1 Prediction vs. Bankoff Flooding Correlations and Test Data	B-119
Figure B-103	GE. CCFL Test 69. Flooding Relationship Comparison: MOD7A Revision 6 vs. Data	B-120

ACRONYMS

ANS	American Nuclear Society
ANSI	American National Standards Institute
APWR	advanced pressurized water reactor
ASME	American Society of Mechanical Engineers
ASTRUM	Automated Statistical Treatment of Uncertainty Method
B&W	Babcock and Wilcox
BCL	broken cold leg
BE	best estimate
BELOCA	best-estimate loss-of-coolant accident
BMFT	Bundesministerium fuer Forschung und Technologie (Germany's Federal Ministry for Research and Technology)
BOCREC	beginning of core recovery
BOL	beginning of life
BWR	boiling water reactor
CCF	counter-current flow
CCFL	counter-current flow limitation
CCTF	cylindrical core test facility
CD	discharge coefficient
CE	Combustion Engineering
CEGB	Central Electricity Generating Board
CFR	Code of Federal Regulations
CHF	critical heat flux
CL	cold leg
CQD	Code Qualification Document
CSAU	code scaling, applicability, and uncertainty
CT	churn-turbulent
CV	calculated value
DECLG	double-ended cold-leg guillotine
DFFB	dispersed droplet film flow boiling
DNB	departure from nucleate boiling
DV	desired value
ECC	emergency core cooling
ECCS	emergency core cooling system
EM	evaluation model

ACRONYMS (Cont'd)

EOB	end of bypass
EPRI	Electric Power Research Institute
FD	film drop
FEBA	flooding experiments with blocked array
FM	free-standing mixer
FQ	peaking factor
GE	General Electric
GEDM	generalized energy deposition model
GT	guide tube
HA	hot assembly
HFP	hot full power
HHSI	high-head safety injection
HL	hot leg
HPI	high-pressure injection
HT	heat transfer
HTC	heat transfer coefficient
ICL	intact cold leg
IADF	inverted annular dispersed flow
IAFB	inverted annular film boiling
IP2	Indian Point Unit 2
JAERI	Japan Atomic Energy Research Institute
KWU	Kraftwerk Union
LBLOCA	large-break loss-of-coolant accident
L/D	length over diameter
LFR	low flooding rate
LHSI	low-head safety injection
LOCA	loss-of-coolant accident
LOFT	loss-of-fluid test
LP	low power
LWR	light water reactor

ACRONYMS (Cont'd)

MTC	moderator temperature coefficient
NBS	National Bureau of Standards
NPP	nuclear power plant
NRC	Nuclear Regulatory Commission
NRU	National Research Universal
OFA	optimized fuel assembly
OH	open hole
ORNL	Oak Ridge National Laboratory
PCT	peak cladding temperature
PF	packing fraction
PIRT	Phenomena Identification Ranking Table
PV	parameter value
PWR	pressurized water reactor
RAI	request for additional information
RCS	reactor coolant system
RFL	reflood peak location
RG	Regulatory Guide
SB	small bubble
SC	support column
SCNB	subcooled nucleate boiling
SCTF	slab core test facility
SER	Safety Evaluation Report
SG	steam generator
SGTP	steam generator tube plugging
SI	safety injection
SIS	safety injection system
SL	surge line
SLB	small to large bubble
SPL	single-phase liquid
SPV	single-phase vapor
SQN	Sequoyah
SSE	safe shutdown earthquake

ACRONYMS (Cont'd)

T/C	thermocouple
TER	Technical Evaluation Report
THTF	Thermal-Hydraulic Test Facility
UCLA	University of California at Los Angeles
UCP	upper core plate
UHI	upper head injection
UPI	upper plenum injection
UPTF	upper plenum test facility
VRA	North Anna Unit 1
1-D	one-dimensional
3-D	three-dimensional

COMMONLY USED NOMENCLATURE

a	sonic velocity	G_Z	transverse mass flux
a_r	grid blockage ratio	h	heat transfer coefficient
a_v	vapor absorption coefficient	h	normalized pump head (Ch. 9)
a_t	liquid absorption coefficient	h_i	interfacial heat transfer coefficient
A	area	H	enthalpy
A_X	axial flow area	H_{fg}	enthalpy of vaporization
A_z	lateral flow area	H_m	Meyer hardness
A_w	wall heat transfer area	I	grid rewet index (Ch. 5,6)
A_I	intercell friction area	I	pump moment of inertia (Ch. 9)
A_i	interfacial area	k	thermal conductivity
B	mass transfer number	K	loss coefficient (Ch. 2,4)
C_O	slip distribution parameter	K	conductance (Ch. 7)
C_D	drag coefficient	K_{ix}	vertical interfacial drag coefficient
C_p	specific heat at constant pressure	K_{iz}	transverse interfacial drag coefficient
C_v	specific heat at constant volume	K_{wx}	vertical wall drag coefficient
D	diameter	K_{wz}	transverse wall drag coefficient
D_h	hydraulic diameter	K_X	axial flow form loss coefficient
\underline{D}	deformation tensor	K_Z	transverse flow form loss coefficient
e	specific energy	L	length
f_w	wall friction factor	L_g	gap width
f_i	interfacial friction factor	L_g^o	orthogonal gap width
f	theoretical density fraction (Ch. 7)	L_b	mean beam length
F	ramping function	ℓ_m	momentum mixing length
\underline{F}	turbulence anisotropy tensor	ℓ_H	energy mixing length
F	gray body factor (Ch. 6)	\dot{m}	mass flowrate
F_{CHEN}	Chen convective boiling multiplier	M	momentum (Ch. 2)
\mathcal{F}	force	M	molecular weight (Ch. 7)
g	gravitational acceleration	M	pump head multiplier (Ch. 9)
g_c	gravitational conversion constant	n	mole fraction
\underline{g}	gravitational acceleration vector	N	number density
G	mass flux	N	pump torque multiplier (Ch. 9)
G_X	axial mass flux	N_μ	viscosity number
		P	pressure

σ	surface tension	fb	film boiling
σ	stress (Ch. 2, 7)	fr	flow regime
$\underline{\underline{g}}$	fluid-fluid stress tensor	$fric$	friction loss
σ_{SB}	Stephan-Boltzmann constant	$form$	form loss
τ	shear stress	FC	forced convection
$\underline{\underline{\tau}}$	viscous drag force	FD	film/drop flow regime
τ_i	interfacial drag force	FF	falling film flow regime
v	specific volume	g	saturated vapor
v	normalized pump volumetric flow	gas	gas
χ	Martinelli-Nelson factor	gv	grid to vapor
ψ_a	absorption efficiency	Gr	Grashof number
Ω	source term	h	hydraulic
ω	specific speed	$Henry$	Henry correlation
<u>Subscripts</u>		i	interfacial
am	annular-mist flow regime	IVA	inverted annular flow regime
ACC	accumulator	IVS	inverted liquid slug flow regime
b	bubble	k	phase k
br	bubble rise	ℓ	liquid field
$bubbly$	bubbly flow regime	liq	liquid
$Brom$	Bromley correlation	LB	large bubble
$crit$	critical	lfc	laminar forced convection
cwv	convection wall-vapor	lnc	laminar natural convection
$CHEN$	Chen correlation	m	mixture
CHF	critical heat flux	MIN	minimum film boiling point
$churn$	churn flow regime	nc	natural convection
CT	churn-turbulent flow regime	N	normalized
d	drop	NB	nucleate boiling
$dcht$	direct contact heat transfer	o	orifice
DD	dispersed droplet flow regime	p	pipe
DE	de-entrainment	QF	quench front
$dffb$	dispersed flow film boiling	r	relative
$DFFB$	dispersed flow film boiling	r	radial (Ch. 7)
e	entrained field	rwe	radiation wall-entrained field
E	entrainment	rwg	radiation wall to grid
f	saturated liquid	rwl	radiation wall-liquid field
		rwv	radiation wall-vapor field
		s	drop formation
		sat	saturation

<i>slug</i>	slug flow regime
<i>S</i>	slug
<i>SB</i>	small bubble flow regime
<i>SCL</i>	subcooled liquid
<i>SCNB</i>	subcooled nucleate boiling
<i>SCV</i>	subcooled vapor
<i>SHL</i>	superheated liquid
<i>SHV</i>	superheated vapor
<i>SLB</i>	small to large bubble flow regime
<i>SPL</i>	single-phase liquid
<i>SPV</i>	single-phase vapor
<i>sup</i>	suppression
<i>TB</i>	transition boiling
<i>TD</i>	top deluge flow regime
<i>tnc</i>	turbulent natural convection
<i>TQ</i>	top quench
<i>UO₂</i>	uranium dioxide
<i>v</i>	vapor field
<i>vap</i>	vapor
<i>ve</i>	between vapor and entrained fields
<i>vℓ</i>	between vapor and liquid fields
<i>w</i>	wall
<i>wb</i>	wall to fluid as latent heat
<i>wℓ</i>	wall to liquid
<i>wv</i>	wall to vapor
<i>x</i>	vertical direction, Cartesian coordinates
<i>X</i>	vertical direction, subchannel coordinates
<i>X</i>	axial direction, 1-D components
<i>y</i>	transverse direction, Cartesian coordinates
<i>z</i>	transverse direction, Cartesian coordinates
<i>Z</i>	transverse direction, subchannel coordinates
<i>Zr</i>	Zirconium
<i>2φ</i>	two-phase
<i>Γ</i>	phase change

Superscripts

<i>i</i>	interfacial surface average
<i>n</i>	old time value
<i>\bar{n}</i>	donor cell old time value
<i>T</i>	turbulent
<i>t</i>	transpose
<i>''</i>	per unit area
<i>'''</i>	per unit volume

1 ROADMAP OF ASTRUM

1-1 BACKGROUND

Westinghouse's previously approved best-estimate large-break loss-of-coolant-accident (LBLOCA) methodology is described in WCAP-12945-P-A (Bajorek et al., 1998) for Westinghouse designed 3- and 4-loop plants with emergency core cooling system (ECCS) injection into the cold legs. The methodology is described in WCAP-14449-P-A (Dederer et al., 1999) for Westinghouse designed 2-loop plants with upper plenum injection (UPI). Both methodologies were patterned after the Code Scaling, Applicability, and Uncertainty (CSAU) methodology developed under the guidance of the US Nuclear Regulatory Commission (NRC) (Boyack et al., 1989). They are virtually identical, with the exception of the physical phenomena that are ranged as part of the uncertainty methodology. More specifically, the ranging of condensation in the downcomer, performed as part of the 3- and 4-loop plant uncertainty methodology, is replaced by ranging of interfacial drag and condensation in the regions of the vessel that control the upper plenum drain distribution in 2-loop plants. In the remainder of this section, the previously approved methodology will be referred to as the Code Qualification Document (CQD) methodology.

The purpose of this report is to describe an improvement to the uncertainty methodology, hereafter referred to as the Automated Statistical Treatment of Uncertainty Method (ASTRUM). The differences between the ASTRUM and the CQD methodology are discussed below.

1-2 RELATIONSHIP OF ASTRUM TO EXISTING METHODOLOGY

The ASTRUM is also patterned after the CSAU methodology. The only significant difference from the CQD methodology is in the application of the uncertainty analysis to the pressurized water reactor (PWR) (Element 3 of the CSAU methodology). The following discussion compares ASTRUM with the CQD methodology, on a step-by-step basis using the CSAU framework, as shown in Figure 1-1. This discussion is applicable to both 3- and 4-loop cold-leg injection and 2-loop UPI applications.

1-2-1 Step 1: Scenario Specification

An LBLOCA is a hypothetical, design-basis accident that is considered in the sizing of ECCS components. The accident is initiated by an instantaneous rupture of a reactor coolant system (RCS) pipe. The break type considered is either a double-ended guillotine, defined as a complete severance of the pipe resulting in unimpeded flow from either end, or a split break, defined as a partial tear. Consistent with prior Westinghouse LBLOCA methodologies, the break sizes considered vary from 1 ft² up to 2 times the pipe area. A break in the cold-leg piping, between the reactor coolant pump and the reactor vessel inlet nozzle, has been concluded to be the most limiting location for a large break in PWRs. (See the response to RAI5-53 of WCAP-12945-P-A for information supporting this conclusion.)

An LBLOCA transient can be characterized by three distinct periods: blowdown, refill and reflood. The blowdown period extends from the initiation of the break until the primary side depressurizes sufficiently that emergency core cooling (ECC) water can start to penetrate the downcomer. The flow out of the break is high, but limited by critical flow phenomena. Boiling and flashing occur in the core as the flow reverses, shutting down the fission process. The hot fuel rods quickly exceed the critical heat flux, resulting in a sharp reduction in heat transfer to the coolant. The cladding temperature rises rapidly as the initial stored energy in the fuel pellets is transferred to the cladding.

Within the next several seconds, coolant in all regions of the vessel and loops begins to flash. The break flow becomes saturated, and is substantially reduced. This reduces the depressurization rate, and may also lead to a short period of positive core flow as the intact loop pumps continue to supply coolant to the vessel. Cladding temperatures may be reduced, and some portions of the core may rewet.

Two-phase conditions in the pumps reduce their effectiveness, and the core flow again reverses. Significant core cooling occurs as the fission process is, by now, completely shut down and the fuel rods are generating only decay heat.

At approximately 10 to 15 seconds after the break, the RCS pressure decreases to the point where accumulators begin injecting cold water into the cold legs. As this water flows into the downcomer, it is initially swept out of the vessel and into the broken cold leg by the continuing high flow of steam from the core.

Approximately 20 to 30 seconds after the break, the RCS has depressurized to a level approaching that of the containment, and refill begins. The ECCS water from the accumulators and the pumped safety injection penetrates the steam upflow in the downcomer, refilling the lower plenum within a few seconds. As the coolant enters the core, the reflooding process begins.

The flow into the core is oscillatory, as cold water rewets the hot fuel rods, generating steam. This steam, and the water it entrains, must pass through the vessel upper plenum, the broken loop hot leg, the steam generator, and the pump before it can be vented out the break. Entrained water that enters the steam generators is also vaporized, increasing the flow path resistance. Because of the relatively low flow during this time period, cladding temperatures continue to slowly increase until the water level in the core reaches several feet. After about two to four minutes, the cladding temperatures in the higher regions of the core begin to decrease due to heat transfer to the dispersed droplet flow. Eventually, the entire core rewets and enters the long-term cooling phase.

The scenario for a 2-loop plant with upper head injection (UHI) is the same through blowdown and refill. The low-head safety injection flow into the upper head begins during the refill period. Reflood is initiated by the intact loop accumulator, and then continues as the UPI water drains down the low-power peripheral regions of the core. The steam flow up the hotter internal regions of the core prevents downflow from the upper plenum, and cooling of the hot assemblies is by bottom-up reflood, as in 3- and 4-loop plants.

The LBLOCA scenario is independent of the uncertainty methodology used.

1-2-2 Step 2: Nuclear Power Plant Selection

ASTRUM and the CQD methodology were both designed to address an LBLOCA in the cold leg of a Westinghouse designed PWR. ASTRUM is also applicable to the LBLOCA analysis of Combustion Engineering designed PWRs. The justification for this conclusion is provided in Appendix A of this report.

1-2-3 Step 3: Phenomena Identification and Ranking

The Phenomena Identification and Ranking Table (PIRT) for all operating Westinghouse plant designs (3- and 4-loop plants with cold-leg ECCS injection, and UPI plants) is provided in Table 1-1. The development of the Westinghouse PIRT used the CSAU (Boyack et al., 1989) expert team ranking and phenomena as a starting point, and included additional information learned during the development of the Westinghouse best-estimate LBLOCA methodology. The Westinghouse 3- and 4-loop plants with cold-leg injection are treated as a single group. Differences between cold-leg and UPI designs that affect the PIRT are discussed below. (This discussion is taken from Section 2-4 of WCAP-14449-P-A. Table 1-1 is identical to Table 2-3 of that report.)

In our ranking of importance of the thermal-hydraulic phenomena, we did not rank anything below a value of "5." This ranking should not be interpreted to mean that those phenomena that were not ranked can be ignored or do not have to be simulated. The table is used to identify those phenomena that have the greatest influence on the calculated peak cladding temperature (PCT), and therefore require a thorough assessment.

The Westinghouse PIRT is presented using the same format from the CSAU, with the CSAU expert team ranking as a comparison guide. Westinghouse also retained the same definition of the LOCA periods as identified in the CSAU PIRT. The blowdown phase of the accident is from the accident initiation to the initiation of the accumulator injection into the intact loops (approximately 600 psia in Westinghouse 3- and 4-loop plants, and 700 psia in UPI). Refill is assumed to begin with accumulator injection and continue until the lower plenum is refilled and the bottom of the core is recovered. (Note that in the rest of this report, refill is assumed to begin when ECC bypass ends and the lower plenum begins to fill.) Reflood continues from the bottom of the core recovery and continues until the PCT has occurred and the cladding is cooling down. These definitions are different from the traditional definitions for the blowdown and refill periods (refill usually begins when ECC bypass ends). However, to remain consistent with the CSAU PIRT, the Westinghouse PIRT was adjusted accordingly.

1-2-3-1 Fuel Rod

The stored energy is most important (rank = 9) during blowdown since the resulting pellet temperature distribution undergoes a readjustment that determines the heatup of the cladding after departure from

nucleate boiling (DNB). The stored energy also reflects the power level at which the hot rod is operating before the initiation of the transient. In the Westinghouse analysis, items such as the gas gap conductance, fuel conductivity, effects of pellet radial power, or pellet cracking are considered as part of the initial stored energy used in the plant calculation. The stored energy effects diminish during refill but are still important since they represent the power history (peak kw/ft) of the hot rod.

The decay heat is ranked high during the reflood period (rank = 8), but ranked lower than the stored energy during blowdown. The rationale for the difference is the relative heatup rates of fuel rod cladding for the different periods. During blowdown, the cladding heatup rate is approximately 200°F/sec, whereas, during reflood, the adiabatic heatup rate is approximately 15°F/sec.

The cladding oxidation is important but is rated lower since the best-estimate calculations result in lower calculated PCTs, therefore reducing the oxidation contribution.

The gas conductance is important because it helps establish the initial stored energy. It is accounted for in the assumed value used for the pellet stored energy. [

]ac

1-2-3-2 Core

The importance of DNB is ranked high during blowdown because of the rapid cladding heatup that takes place after DNB has occurred. It is not a question of whether DNB will occur, but if DNB can be delayed for a fraction of a second so that more of the initial stored energy in the fuel can be removed, then the resulting cladding heatup will be less severe. The DNB is not ranked for the other periods since it is assumed that it has already occurred.

Post-critical heat flux (CHF) heat transfer is ranked high for both blowdown and the refill period. This is the main mechanism for heat removal from the cladding when it is at an elevated temperature.

Rewet is also ranked relatively high during blowdown. The CSAU ranked it as an "8," based on the LOFT experiments. However, most calculations of 3- and 4-loop plants indicate that the hot assembly will not rewet during blowdown. Typically, the low-power and average-power regions experience rewet. The possibility for rewet diminishes toward the end of the refill period since the reverse flow blowdown period ends as the vessel and system drain.

Reflood heat transfer is ranked high, consistent with the expert ranking.

The importance of three-dimensional flow during blowdown is a difference between the Westinghouse PIRT and the CSAU PIRT. More specifically, the importance of distinguishing between several channels of different geometries is recognized in the Westinghouse methodology. The hardware in the reactor upper plenum can affect the amount of flow the fuel assemblies receive during the blowdown downflow period when the flow is from the upper plenum and upper head into the core. The guide tube assemblies

have a direct flow communication path to the upper head. In some plants, there are free-standing mixers on the upper core plate that are solid cylinders approximately 13 inches high so that for the assembly to receive direct flow, the water must pool to a higher elevation. There may also be orifices on the upper core plate that reduce the flow area between the upper plenum and the core. These hardware and geometry effects have to be modeled to accurately predict the flow split for the different assemblies. There will be different flows entering the top of the core channels. When the CSAU was developed, the industry was just beginning to utilize low-leakage fuel management designs. The presence of a low-power zone on the edge of the core provides an easier flow bypass path from the upper plenum to the lower plenum. The low-power zone may be at powers that are sufficiently low for this channel to quench during blowdown such that, after quench, the steam generation will be low. As a result, the liquid in the upper plenum can more easily bypass the center regions of the core and drain down the low-power region. This effect must be modeled, or otherwise the flow through the center region of the core may be over estimated. The effect of channel geometry differences in the core is less pronounced during reflood since the liquid level moves up the core uniformly. However, radial power shapes in the core can lead to a thermal chimney effect with higher induced flows in the hot assembly. Three-loop, four-loop, and UPI plants have similar hardware and utilize low-leakage fuel management loading patterns.

The void generation and distribution are also ranked high during blowdown since this follows the multiple channel flow discussion above. Assemblies, such as the guide tube assemblies, will have a different void distribution since they are connected to the upper head as compared to an assembly that is beneath an orifice hole in the upper core plate. Also, the radial power distribution will generate a different radial void distribution during blowdown. [

] ^{a,c}

The entrainment and de-entrainment during reflood is important since it determines the amount of liquid flow at the PCT location during reflood. There is an overlap with this process and the broader definition of "reflood heat transfer" given above. We have separated the 2 since it is the entrainment that determines the level or magnitude of the heat transfer. The entrainment and de-entrainment phenomena are ranked as "8" for reflood stage.

Flow reversal and stagnation is an important parameter for the blowdown phase of the transient since it determines how much of the downflow will pass through the core versus how much of the flow will go to the broken loop. This parameter depends on the break size being analyzed, the flow path resistance, and the performance of the reactor coolant pumps. The major difference between a 3-loop plant and a 4-loop plant is the flow demand of the break relative to the pumping power of the available reactor coolant pumps, and the relative resistances from the core to the break versus the resistance of the broken loop. For a 3-loop plant, the transition to downflow would occur earlier since the break is the same size as in a 4-loop plant, and the RCS volume is smaller. Also, in the 3-loop plant, there is 1 less pump available to force positive flow through the core. Similarly, the transition to downflow for a UPI plant will be earlier than the 3- and 4-loop plants. For a 2-loop plant, the double-ended cold leg guillotine (DECLG)

results in earlier transition to downflow in the core, due to the relative size of the break in relation to the plant. With only 2 loops, 1 of them with a break, there is only 1 intact loop pump trying to force positive flow through the core, versus 2 or 3 pumps for the 3- and 4-loop plants, respectively. Thus, the pumping capability to resist the downflow force of the break is reduced by one-third to one-half for the 2-loop plants. This results in an earlier transition to downflow in the core immediately following the initiation of the transient. In addition, the 2-loop plant is smaller, resulting in a shorter blowdown period.

1-2-3-3 Upper Plenum

[

]ac

The other item in the PIRT that is of importance for the upper plenum is the entrainment/de-entrainment that occurs during refill and reflood. The entrainment and de-entrainment within the upper plenum structure during UPI flow during both refill and reflood stages are among the most important phenomena in an LBLOCA transient for UPI plants. The amount of entrainment/de-entrainment directly affects the amount of the UPI flow that is available for draining to the core. The effect of the flow pattern determines the lower plenum refill rate and core cooling. Our ranking of this phenomenon is of moderate importance for 3- and 4-loop plants, whereas the CSAU expert team ranked it higher. The CSAU expert team ranking matches our ranking for the UPI plants, where the entrainment/de-entrainment is more important due to the UPI.

The phase separation phenomenon is related to the entrainment and de-entrainment in the upper plenum. Usually, what is found is that the mass in the upper plenum will increase to a constant value as the liquid de-entrains on the upper plenum structures, and the liquid pools on the upper core plate (UCP) as a low void fraction mixture. The additional liquid is then swept into the steam generator lower plenums where the de-entrainment process starts again. As a result, less water is carried into the tubes and the best-estimate codes are less sensitive to the steam binding effects and the separation is ranked as a "6" for 3- and 4-loop plants.

For UPI plants, the phase separation is also related to entrainment and de-entrainment in the upper plenum. With UPI, deeper pooling of water on the UCP could occur. The best-estimate UPI calculations have sufficiently detailed nodding to account for a low-power core zone with lower steam upflow, such that the UPI water pooling on the UCP can drain into the core. The steam generated in the higher power zone is vented through the UCP, where the pooled liquid can be entrained and carried out the hot leg. The separation phenomenon is ranked as a "7" during the reflood period for UPI plants.

Subcooled or saturated counter-current flow (CCF) phenomenon at the UCP or top nozzle is of importance for the UPI plants. As discussed earlier, the core cooling and refill rate are dependent on the amount of UPI flow draining to the core and lower plenum. During the refill and reflood stages, the steam generated in the core tends to prevent the draining at the UCP and the top fuel nozzle regions where the flow area is restricted. The counter-current flow limit (CCFL) is therefore the controlling factor for the draining. The CCF phenomenon is ranked as an "8" during the refill stage and as a "9" during the reflood stage. The reason for a lower rank during the refill stage is that the steam generation in the core during the refill stage is less than that during the reflood stage.

Condensation phenomena in the upper plenum are important for UPI plants due to the large amount of subcooled ECCS water being injected into the upper plenum. Since this injection typically begins during the refill phase, when the upper plenum is full of steam generated by the core, the effects of condensation are given a high rank for refill and then again during reflood.

1-2-3-4 Hot Leg

The flow reversal is ranked as a medium parameter of importance during blowdown. The flow reversal is important but the role of the hot legs in the reversal is of lower importance because they do not contain significant mass inventory that can flow into the core.

The CSAU expert team ranked the entrainment/de-entrainment for the hot legs as very important for reflood. [

] ^{a,c}

1-2-3-5 Pressurizer

The high CSAU expert team ranking is, we believe, from the LOFT tests that indicated that the two-phase mixture from pressurizer draining could flow back into the vessel during the reverse flow period of blowdown. Since the loop that could have the break is unknown, sensitivity studies are performed to determine the most limiting loop for the pressurizer. The sensitivity studies reduce the importance of the pressurizer location as an uncertainty since the limiting location is used.

1-2-3-6 Steam Generators

The major effect of the steam generators is to increase the steam binding effects during reflood. The CSAU expert team ranked this item a "9," whereas Westinghouse has ranked it slightly lower. The basis for the lower ranking is that the best-estimate calculations will allow liquid de-entrainment in the reactor upper plenum and in the steam generator inlet plenums. Therefore, there is a delay in the liquid reaching the hot steam generators tubes, and less liquid is entrained into the tubes. These effects reduce the importance of this phenomenon.

1-2-3-7 Pump

The experts ranked the pump 2-phase performance as a "9," [

]^{ac}

1-2-3-8 Cold Leg/Accumulator

The condensation effects are the most important item for the accumulator behavior during the refill period for the 3- and 4-loop and UPI plants. Most of the ECC water is bypassed early in the refill period, but the condensation process at the top of the downcomer helps to induce downflow through the core, promoting cooling. The condensation effects are diminished during the reflood period as the accumulators end their injection and the lower flow pumped injection continues.

The effects of noncondensable gases are important during the reflood period when the accumulators empty and the nitrogen from the accumulators is released into the primary system. The CSAU expert team ranks this item as a "9." However, when the evaluation of the effects of the noncondensable gases were made in the CSAU report and subsequent reports, the effects on the PCT were found to be small ($(\Delta PCT)_{N_2} = 17.8^\circ F$; p. 69 of CSAU), which refers to the effects of dissolved nitrogen. The Westinghouse analysis also indicates that the effects of dissolved nitrogen is negligible (RAI1-134 of Bajorek et al., 1998).

The effect of nitrogen injection after the accumulators have emptied may be significant (Section 25-5-5-8 of Bajorek et al., 1998). This is reflected by ranking "Reflood Heat Transfer (HT)" as "9."

[

] ^{ac}

1-2-3-9 Downcomer

Entrainment and de-entrainment, as well as condensation, are components of the ECC bypass and downcomer penetration phenomena that are most important during the refill period when the accumulator water is flowing into the downcomer annulus. These phenomena are the same for 3- and 4-loop plants. As the transient progresses into the reflood phase, the importance of the phenomena decreases since the downflow is more easily predicted after the upflow of steam in the downcomer annulus has ended and the water penetrates more easily.

The counter-current, slug, and non-equilibrium flows are characteristic of the ECC bypass phenomena during the refill period and are the same for the 3- and 4-loop and UPI plants. Again, while the phenomena are the same, there are geometric differences. These phenomena end at the conclusion of the refill period when the lower plenum is filled and there is no longer any steam flow up the downcomer.

[

] ^{ac}

Liquid level oscillations are a gravity reflood phenomenon, which is a result of the heat released in the core and the corresponding pressure drop in the loops. This phenomenon is important during the reflood phase since it can influence the core heat transfer, resulting entrainment, and the effects of the downcomer driving head on the system response.

1-2-3-10 Lower Plenum

The lower plenum sweep-out effect for the original primary system water, during the refill period, is important since it determines the time and accumulated ECCS flow needed to refill the vessel and to recover the bottom of the core. The experts ranked this phenomenon as a "7," [

] ^{a,c}

The hot-wall effect for the lower plenum is important since the thick metal structures will give up their heat to the reflood liquid reducing its subcooling. As the subcooling decreases for the water that refloods the core, more of the core will remain in nucleate boiling and additional steam will be generated that must be vented through the loops. Therefore, this phenomenon is ranked higher in reflood.

1-2-3-11 Break

The critical flow at the break is a highly ranked phenomenon and is equally important for 3- and 4-loop and UPI designs. The calculations are ranged over the expected uncertainties in the critical flow to assess its effects on the plant response. The importance of the critical flow is higher during the early blowdown phase of the transient since it, along with the loop resistance differences, determines the core flow during blowdown. The importance decreases somewhat during refill as the flows through the vessel decrease and the system voids.

[

] ^{a,c}

1-2-3-12 Loop

The two-phase pump ΔP has already been discussed under the Subsection 1-2-3-7.

[

] ^{a,c}

[

]ac

The dominant phenomena identified by the PIRT process and the CQD methodology development have previously been grouped as follows, based on the physical processes involved:

- Critical flow
- Break path resistance
- Initial stored energy/fuel rod
- Core heat transfer
- Delivery and bypassing of the ECC
- Steam binding/entrainment
- Cold-leg/downcomer condensation
- Noncondensable gases/accumulator nitrogen
- Upper plenum drain distribution (UPI plants only)

The PIRT and the dominant phenomena determination are unaffected by the uncertainty methodology differences between ASTRUM and the CQD methodology.

1-2-4 Step 4: Frozen Code Selection

The CQD methodology was approved based on the frozen code version WCOBRA/TRAC MOD7A Revision 1. ASTRUM is based on the frozen code version WCOBRA/TRAC MOD7A Revision 6. The differences between these frozen versions include logic to facilitate the automation aspects of ASTRUM, user conveniences, and error corrections. These differences are described in Appendix B, which also includes the evaluations performed to ensure that the prior code assessments against experimental data remain valid.

The WCOBRA/TRAC code uses a two-fluid, three-field representation of flow in the vessel component. The three fields are a vapor field, a continuous liquid field, and an entrained liquid drop field. Each field uses a separate set of continuity, momentum, and energy equations with one exception. A common energy equation is used by the continuous liquid and the entrained liquid drop fields.

The one-dimensional components consist of all the major components in the primary system, such as pipes, pumps, valves, steam generators, and the pressurizer. The one-dimensional components are represented by a two-phase, five-equation, drift flux model. This formulation consists of two equations for the conservation of mass, two equations for the conservation of energy, and a single equation for the conservation of momentum. Closure for the field equations requires specification of the relative velocities, interfacial heat and mass transfer, and other thermodynamic and constitutive relationships.

1-2-5 Step 5: Provide Complete Documentation

The documentation of the original COBRA/TRAC computer code is contained in NUREG/CR-3046 (Thurgood et al., 1983). Documentation of the WCOBRA/TRAC MOD7A Rev. 1 code version, the code assessment against experimental data, and the uncertainty methodology for analyses of Westinghouse designed 3- and 4-loop plants with ECC injection into the cold legs is documented in WCAP-12945-P-A (Bajorek et al., 1998). That report is organized as follows:

- Volume 1 (Models and Correlations) includes a roadmap of the CQD methodology, the PIRT, and details of the WCOBRA/TRAC code (numerics and physical models).
- Volume 2 (Heat Transfer Model Validation) documents comparisons of WCOBRA/TRAC's heat transfer predictions with separate-effects test data.
- Volume 3 (Hydrodynamics, Components, and Integral Validation) documents code assessment using integral-effects test data, and assessments of specific phenomena, such as CCFL, condensation, and critical flow. Assessments of component models, such as the accumulator and reactor coolant pump, are also addressed. Appendix A to Volume 3 presents an investigation of the potential for compensating errors.
- Volume 4 (Assessment of Uncertainty) provides the scaling assessment and calculation of the overall code bias and uncertainty, and identifies additional sources of uncertainty such as plant operating conditions and analysis assumptions.
- Volume 5 (Quantification of Uncertainty) develops the overall uncertainty methodology including the treatment of each of the dominant contributors to uncertainty, and combination and propagation of uncertainties. Demonstration of compliance with the Code of Federal Regulations (CFR) 10 CFR 50.46 and Regulatory Guide 1.157 is also provided.

The CQD methodology for 2-loop plants with UPI is documented in WCAP-14449-P-A (Dederer et al., 1999). That report focuses on the aspects of the CSAU methodology that are affected by the different physical phenomena (such as, PIRT, nodalization, code assessment against experimental data, ranging of physical models, and compensating error assessment).

This report provides an alternate uncertainty methodology that can be used for PWRs with cold-leg ECC injection or UPI. The principal differences from the CQD methodology are in the application of CSAU Element 3, Sensitivity and Uncertainty Analysis. A description of the content and organization of this report is provided in Section 1-3.

1-2-6 Step 6: Code Applicability Determination

The WCOBRA/TRAC code was shown to be applicable for the specified accident scenario and Westinghouse designed plant types in WCAP-12945-P-A and WCAP-14449-P-A. There is no feature of ASTRUM that has any effect on those conclusions. Appendix A of this report justifies the applicability of WCOBRA/TRAC and ASTRUM to Combustion Engineering designed plants.

1-2-7 Step 7: Establishment of Assessment Matrix

The WCOBRA/TRAC assessment matrix was developed based on the phenomena that were highly ranked in the PIRT. Tables 1-2 and 1-3 summarize the main features of each test facility included in the assessment matrix, and indicate which physical processes were present in each test series. Tables 1-4 through 1-6 list all of the highly ranked phenomena from the PIRT, and indicate which tests examined those phenomena.

The use of ASTRUM has no effect on the selection of tests used to assess the code performance for highly ranked phenomena.

1-2-8 Step 8: Define Nodalization

A consistent noding philosophy was developed for the code validation against experimental data, and for nuclear power plant (NPP) calculations. Typical nodalization schemes for test facilities and PWRs are described in Section 20 of WCAP-12945-P-A (Bajorek et al., 1998) for 3- and 4-loop plants with ECCS injection into the cold legs, and in Section 3 of WCAP-14449-P-A (Dederer et al., 1999) for 2-loop plants with UPI. Section 12-1 of this report describes the nodalization for the 4-loop plant used to illustrate ASTRUM.

The use of ASTRUM has no effect on the nodalization used for experiment simulations, or for NPP calculations.

1-2-9 Step 9: Determine Code and Experiment Accuracy

The WCOBRA/TRAC models for the dominant LOCA phenomena identified by the PIRT process were assessed over the expected range of conditions in Volumes 2 and 3 of WCAP-12945-P-A (Bajorek et al., 1998), and in Section 4 of WCAP-14449-P-A (Dederer et al., 1999). Estimates were made of the bias and uncertainty for the highly ranked models and phenomena in Sections 25 and 3-4-1, respectively, of those reports. Estimates of the overall code bias and uncertainty, and of the experiment accuracy, were made in Section 19 of WCAP-12945-P-A, and shown to remain valid for 2-loop plants with UPI.

Minor changes have been made to the WCOBRA/TRAC code version used to define the biases and uncertainties accounted for in the CQD methodology. These changes were made to correct errors discovered since that code version was approved. Appendix B describes the code changes introduced in order to obtain the current frozen version, WCOBRA/TRAC MOD7A Rev. 6. A subset of the original code assessment cases has been reanalyzed with the current code version. As shown in Appendix B, the reanalysis results support the conclusion that the biases and uncertainties previously established for the highly ranked models and phenomena remain valid.

Tables 1-7 and 1-8 identify the uncertainty distributions that have been established for global models and local models, respectively. In the Westinghouse methodologies, global models are those thermal-hydraulic phenomena that affect the response of the entire RCS. The effects of global models are calculated using WCOBRA/TRAC. Local models are those that affect the response of the hot spot on the fuel rod. Their effects are calculated using HOTSPOT, a one-dimensional conduction code that uses boundary conditions calculated by WCOBRA/TRAC.

The use of ASTRUM has no effect on the biases and uncertainties established for global and local models.

1-2-10 Step 10: Determine Effect of Scale

Section 18 of WCAP-12945-P-A (Bajorek et al., 1998) evaluated the effect of using scaled-down experiments in some instances to assess highly ranked models and phenomena. Of particular interest were scale effects on ECC bypass and upper plenum de-entrainment experimental results, since full-scale data for those phenomena were not available at the time of the original CSAU study. Westinghouse used the full-scale Upper Plenum Test Facility (UPTF) data to examine scaling trends of these phenomena. Prediction of the Creare 1/5 scale bypass tests and UPTF Test 6 results indicated [

]^{a,c}. Comparison

of the Slab Core Test Facility (SCTF) and Cylindrical Core Test Facility (CCTF) upper plenum mass retention with that of UPTF Test 29B [

]^{a,c}. The effect of scale on heated rod bundle

PCT predictions was also examined. No scale effects were observed. Based on these evaluations, it was concluded that no additional uncertainty or bias is required as a result of using scaled experiments.

Scaling effects were also examined for 2-loop plants with UPI in Section 4-6 of WCAP-14449-P-A (Dederer et al., 1999). The scaling parameters of interest for UPI plants were recommended in NUREG/IA-0127 (Damerell and Simons, 1993) to be:

- Breakthrough flow area as percentage of core flow area
- Downflow rate as percentage of available water

- Net hot-leg water carryover rate as percentage of available water
- Collapsed liquid level/height to hot-leg centerline

Comparison of the CCTF Run 72, Run 76, and UPTF Test 20 predictions with the data indicated that WCOBRA/TRAC predicted the scaling trends of these parameters well. Based on these evaluations, it was concluded that no additional uncertainty or bias is required as a result of using scaled experiments to assess UPI phenomena.

The use of ASTRUM has no effect on the prior conclusions regarding the effect of scale.

1-2-11 Step 11: Determine Effect of Reactor Input Parameters and State

In the CQD methodology, the effect of reactor input parameters and reactor state at the time of the design-basis accident are accounted for by a combination of plant-specific confirmatory analyses and uncertainty analyses. The confirmatory analyses performed for each plant are as follows:

- [

J^{ac}

[

] ^{a,c}

In the CQD methodology, the plant parameters included in the uncertainty analysis are considered in separate categories. The first category addresses the power-related parameters shown in Table 1-10. Parameters in this category are analyzed using WCOBRA/TRAC, and response surfaces are developed based on the changes in PCT as a function of FQ, FdH, PBOT, and PMID. The second category addresses the other plant initial and boundary conditions shown in Table 1-11. These parameters are analyzed by performing [

] ^{a,c}

The ASTRUM considers the same plant parameters as shown in Tables 1-10 and 1-11. [

] ^{a,c}

1-2-12 Step 12: Perform NPP Sensitivity Calculations

The CQD methodology requires that 4 sets of NPP sensitivity calculations be performed in order to establish the total uncertainty. These 4 sets address the power-related parameters listed in Table 1-10, the initial and boundary condition parameters listed in Table 1-11, the thermal-hydraulic models listed in Tables 1-7 and 1-8, and the superposition correction run matrix. The superposition correction runs simultaneously vary uncertainties from each of the other 3 uncertainty components, and are used to establish the uncertainty corresponding to the assumption that those 3 components can be linearly combined.

In ASTRUM, [

] ^{a,c}

[
]ac

1-2-13 Step 13: Combine Biases and Uncertainties

The CQD methodology calculates the final PCT uncertainty distribution by a combination of response surface equations and Monte Carlo sampling. Details of the process used are discussed in Section 26-5-2 of WCAP-12945-P-A (Bajorek et al., 1998). Conservative biases resulting from phenomena that are conservatively predicted by WCOBRA/TRAC are ignored.

In ASTRUM, the 95th percentile PCT is established at 95-percent confidence using non-parametric order statistics. Details of the methods used are presented in Section 11 of this report. Conservative biases resulting from phenomena that are conservatively predicted by WCOBRA/TRAC are ignored.

1-2-14 Step 14: Calculate Total Uncertainty

Step 14 of the CSAU methodology has a provision to consider adding margin to the results of Step 13, if warranted due to limitations in the code or data base. There are no significant limitations in the code or data base that require the consideration of additional margin. The results of Step 13 are, therefore, considered to be the final results for both the CQD methodology and ASTRUM.

1-3 ORGANIZATION OF THE REPORT

Sections 2 through 10 describe the models and correlations used in WCOBRA/TRAC MOD7A Rev. 6. These sections are identical to Sections 2 through 10 of WCAP-12945-P-A (Bajorek, et al., 1998), with the exception of the text changes and error corrections marked with change bars. Table 1-12 provides a summary of the changes to Sections 2 through 10. Most of the changes are the addition of references to WCAP-12945-P-A.

A number of Requests for Additional Information (RAIs) regarding the models and correlations were issued during the review of WCAP-12945-P-A. Responses to those RAIs have been incorporated into the text of Sections 2 through 10, or are referenced by a superscripted number within brackets, e.g., ⁽¹⁾. At the end of each of these sections is a listing of the RAI number corresponding to the superscripted number within the brackets.

Section 2 describes the conservation equations and numerical methods used in WCOBRA/TRAC MOD7A Rev. 6. Flow regimes are described in Section 3, and the interfacial area for each regime is discussed. Section 4 provides information on momentum transfer, including the models and correlations used to determine interfacial shear, form loss and pressure drop, droplet breakup on structures, and entrainment/de-entrainment phenomena. The methods used to evaluate interfacial heat and mass transfer

are described in Section 5. The wall-to-fluid heat transfer models and correlations are discussed in Section 6, while the thermal-mechanical behavior of the structures used to model nuclear fuel rods and experimental fuel rod simulators is contained in Section 7.

All of the first 7 sections use a common nomenclature. Section 8 describes the kinetics model and decay heat models, and uses a separate nomenclature. Special component models, used to model equipment such as pumps, steam generators, and safety injection, are described in Section 9. Section 10 provides information on the calculation of the thermodynamic and transport properties of water and common fuel rod and RCS structural materials.

Sections 2 through 10 include 4 elements that appear as subheadings. "Model Basis" identifies the model or correlation and gives reference to its origin and technical basis. "Model as Coded" provides specific information on how the models and correlations are programmed in the code. Numerical ramps, limits, and approximations of the true correlation are identified where applicable. "Scaling Considerations" discusses the range of scale over which the models apply or identifies the assessments that were performed in order to demonstrate scale independence. The "Conclusions" section describes the applicability of the models for best-estimate LOCA calculations. Simulations that validate the models and correlations are identified.

Section 11 describes the ASTRUM methodology in detail, and is organized in accordance with CSAU Element 3. The technical basis for ASTRUM is presented, as well as the technical justification for several important changes in the uncertainty treatment for break type, split break size, and time in cycle. The method used to determine the 95th percentile PCT with 95-percent confidence is presented. The treatment of all medium- and high-ranked phenomena from the PIRT is summarized. The methods use to verify that the acceptance criteria for local oxidation and core-wide oxidation are met are also presented.

Section 12 provides a sample application of ASTRUM to a typical 4-loop Westinghouse designed PWR. Sensitivity studies performed to support the methodology are included.

Section 13 addresses the compliance of ASTRUM with 10 CFR 50.46 and Regulatory Guide 1.157. The effect of the revised uncertainty methodology on prior Safety Evaluation Report (SER) requirements and restrictions is also discussed.

There are two appendices to this report. Appendix A presents the justification for use of ASTRUM for Combustion Engineering designed PWRs. Appendix B discusses the coding changes made to evolve from WCOBRA/TRAC MOD7A Rev. 1 to Rev. 6.

1-4 REFERENCES

Bajorek, S. M., et al., 1998, "Code Qualification Document for Best Estimate LOCA Analysis," WCAP-12945-P-A, Volume 1, Revision 2, and Volumes 2 through 5, Revision 1, and WCAP-14747 (Non-Proprietary).

Boyack, B., et al., 1989, "Quantifying Reactor Safety Margins: Application of Code Scaling, Applicability, and Uncertainty (CSAU) Evaluation Methodology to a Large-Break, Loss-of-Coolant Accident," NUREG/CR-5249.

Damerell, P. S., and Simons, J. W., ed., 1993, "Reactor Safety Issues Resolved by the 2D/3D Program," NUREG/IA-0127.

Dederer, S. I., et al., 1999, "Application of Best Estimate Large Break LOCA Methodology to Westinghouse PWRs with Upper Plenum Injection," WCAP-14449-P-A, Revision 1, and WCAP-14450-NP-A, Revision 1 (Non-Proprietary).

Spier, E. M., et al., 1988, "Evaluation of Nuclear Hot Channel Factor Uncertainty," WCAP-7308-L-P-A.

Thurgood, M. J., et al., 1983, "COBRA/TRAC – A Thermal-Hydraulic Code for Transient Analysis of Nuclear Reactor Vessels and Primary Coolant Systems," NUREG/CR-3046.

USNRC, 1987, "Compendium of ECCS Research for Realistic LOCA Analysis," NUREG-1230.

[illegible]

Table 1-1
(cont.)

PIRT for Large-Break LOCA

[illegible]

Table 1-1
(cont.)

PIRT for Large-Break LOCA

[illegible]

Table 1-2 Blowdown/Refill Assessment for WCOBRA/TRAC								
Facilities Simulated			Processes Assessed					
SETs	Test Feature	No. Tests	Critical Flow	Break Resistance	Fuel Rod	Heat Transfer	ECC Bypass	Condensation
ORNL	Upflow blowdown cooling, 17x17	3				X		
G-1	Downflow blowdown cooling, 15x15	6				X		
G-2	Downflow blowdown cooling, 17x17	4				X		
G-2	Downflow refill cooling, 17x17	7				X		
Marviken	Critical flow	16	X					
WSWM	1/3-scale steam/water mixing	12						X
UPTF 8	Full-scale steam/water mixing	7						X
CREARE	1/15, 1/5-scale ECC bypass	7					X	X
UPTF 6	Full-scale ECC bypass	5		X			X	X
Various	In pile and out of pile nuclear tests				X			
IETs								
LOFT	Nuclear core, scaled PWR	4	X	X	X	X	X	X

Table 1-3 Refill/Reflood Assessment for WCOBRA/TRAC								
Facilities			Processes Evaluated					
SETs	Test Feature	No. Tests	Heat Transfer	Condensation	N2 Injection	Fuel Rod	Entrainment	UP Drain Dist.
G-2	Forced reflood, cosine power shape, 17x17, MVG	3	X				X	
FLECHT LFR	Forced reflood, cosine power shape, core entrainment, 15x15	3	X				X	
FLECHT Skewed	Forced reflood, skewed power shape, core entrainment, 15x15	5	X				X	
FLECHT SEASET	Forced reflood, cosine power shape, core entrainment, 17x17	5	X				X	
FEBA	Forced reflood, flat cosine, effect of grids	4	X				X	
NRU	Forced reflood, skewed power shape, nuclear rods, cladding rupture	2	X			X	X	
PBF	Cladding rupture, fuel relocation	4				X		
Achilles	Gravity reflood with nitrogen injection	1	X		X		X	
GE CCFL	Subcooled and saturated CCFL, rod bundle	5						X
UPTF 29B	Full-scale upper plenum, entrainment, de-entrainment	6					X	
UPTF 25	Full-scale downcomer entrainment	4					X	
UPTF 20	Full-scale upper plenum injection	3		X			X	X
IETs								
CCTF	Gravity reflood, loop flows, core and upper plenum entrainment	5	X	X			X	
SCTF	Forced and gravity reflood, radial power, core & upper plenum entrainment	5	X				X	
LOFT	Nuclear core, scaled PWR	4	X	X	X		X	
CCTF 72, 76	Gravity reflood, UPI	2	X	X			X	X

Table 1-4 Blowdown Phenomena Assessment Matrix											
I											
											JAC

Table 1-5 Refill Phenomena Assessment Matrix										
[
										J ^{a,c}

a. Specific to UPI

Re: Map of ASTRUM
i-Non-Sec1.wpd-052703

Table 1-7 Uncertainty Distributions for Global Models		
[
		$J^{a,c}$

- a. 3- and 4-loop
- b. 2-loop plants

Table 1-8 Uncertainty Distributions for Local Models

[illegible]
$$\}^{a,c}$$

Table 1-9 Burst Strain Summary			
			jac

Table 1-10 Power-Related Parameters Considered in Uncertainty Methodology		
[
		$J^{a,c}$

Table 1-11 Initial and Boundary Conditions Considered in Uncertainty Methodology	
[
] ^{a,c}

Table 1-12 Changes in Sections 2 through 10	
Page	Description of Change
2-28	Add missing subscript to α in final term
2-61	Correct equation number in text
2-73	Add reference to WCAP-12945-P-A
2-76, 2-77	Add reference to WCAP-12945-P-A. Change page numbers in RAI listing
2-88	Add 2' to side tube, consistent with text (p. 2-66)
3-5	Add reference to WCAP-12945-P-A
3-9	Add reference to WCAP-12945-P-A
3-10	Modify text to be specific to churn-turbulent flow regime
3-13	Add sentence clarifying that hot wall regime is only used for channels with heated structures
3-14	Add reference to WCAP-12945-P-A
3-15	Add reference to WCAP-12945-P-A
3-28	Add reference to WCAP-12945-P-A
3-29, 3-30	Change page numbers in RAI listing
4-2	Add reference to WCAP-12945-P-A
4-10	Add reference to WCAP-12945-P-A
4-13	Add reference to WCAP-12945-P-A
4-21	Add reference to WCAP-12945-P-A
4-23	Add reference to WCAP-12945-P-A
4-25	Add reference to WCAP-12945-P-A
4-30	Add reference to WCAP-12945-P-A
4-34	Add reference to WCAP-12945-P-A
4-36	Delete reference to Semiscale
4-37	Correct CCFL terminology
4-39	Add reference to WCAP-12945-P-A

Table 1-12 Changes in Sections 2 through 10 (cont.)	
Page	Description of Change
4-44	Add references to WCAP-12945-P-A and WCAP-14449-P-A. Clarify conclusions. Add sentence clarifying that bottom reflood entrainment is only used for channels with heated structures.
4-49	Add reference to WCAP-12945-P-A
4-51	Clarify application of orifice droplet breakup model
4-52	Correct text to be consistent with coding (downflow only)
4-53	Correct text to be consistent with coding (downflow only)
4-55	Correct text to be consistent with coding (downflow only)
4-56	Correct text to be consistent with coding (downflow only). Add references to WCAP-12945-P-A and WCAP-14449-P-A. Delete reference to Semiscale.
4-64	Add references to WCAP-12945-P-A and WCAP-14449-P-A. Clarify scaling trends.
4-67	Add references to WCAP-12945-P-A and WCAP-14449-P-A. Clarify conclusions.
4-73	Add reference to WCAP-12945-P-A. Delete reference to Semiscale.
4-77	Add reference to WCAP-12945-P-A
4-83	Add reference to WCAP-12945-P-A
4-86, 4-87	Change $L/D > 1.5$ to $L/D \geq 1.5$
4-90	Correct nomenclature
4-94	Add reference to WCAP-12945-P-A
4-97	Add references to WCAP-12945-P-A and WCAP-14449-P-A
4-100 to 4-102	Change page numbers in RAI listing
5-4	Add reference to WCAP-12945-P-A
5-7	Add reference to WCAP-12945-P-A
5-11	Add reference to WCAP-12945-P-A
5-12	Add reference to WCAP-12945-P-A
5-24	Correct ORNL test facility acronym

Table 1-12 Changes in Sections 2 through 10 (cont.)	
Page	Description of Change
5-27	Add reference to WCAP-12945-P-A
5-32	Add reference to WCAP-12945-P-A
5-41	Add reference to WCAP-12945-P-A
5-42	Add reference to WCAP-12945-P-A
5-44	Add reference to WCAP-12945-P-A
5-46, 5-47	Change page numbers in RAI listing
6-5	Add reference to WCAP-12945-P-A
6-18	Add sentence clarifying limits on CHF search
6-20	Add reference to WCAP-12945-P-A
6-25	Add reference to WCAP-12945-P-A. Add missing word, "occur"
6-27	Add reference to WCAP-12945-P-A. Delete reference to Semiscale.
6-33	Add text consistent with "Incorrect Wall Friction Factor for Convective Enhancement Term" discussion in Appendix B
6-35	Correct Equation 6-130 consistent with "Grid Heat Transfer Error" discussion in Appendix B
6-36	Delete reference to Semiscale
6-38	Clarify that equations are in units of (ft) ⁻¹
6-40, 6-41	Add "prime" to gray body factors to distinguish from earlier equations that didn't include Stefan-Boltzmann constant
6-45	Correct the sign for $\alpha > 0.999$
6-56	Correct the reference for Equation 6-206
6-70	Add reference to WCAP-12945-P-A. Correct discussion of tests used in model assessment.
6-77	Add reference to WCAP-12945-P-A
6-82, 6-83	Change page numbers in RAI listing
7-25	Add reference to WCAP-12945-P-A
7-29	Add reference to WCAP-12945-P-A

Table 1-12 **Changes in Sections 2 through 10**
(cont.)

Page	Description of Change
7-30	Add reference to WCAP-12945-P-A
7-31	Add reference to WCAP-12945-P-A
7-34	Add reference to WCAP-12945-P-A
7-35	Add reference to WCAP-12945-P-A
7-36	Add reference to WCAP-12945-P-A
7-41	Add reference to WCAP-12945-P-A
8-4 to 8-8, 8-11	Correct nomenclature for neutron velocity ($v \Rightarrow v$)
8-26	Change page numbers in RAI listing
9-13	Add reference to WCAP-12945-P-A
9-15	Add reference to WCAP-12945-P-A
9-16	Add reference to WCAP-12945-P-A
10-10	Correct nomenclature for derivative ($\partial T_{in} \Rightarrow dT_{in}$)

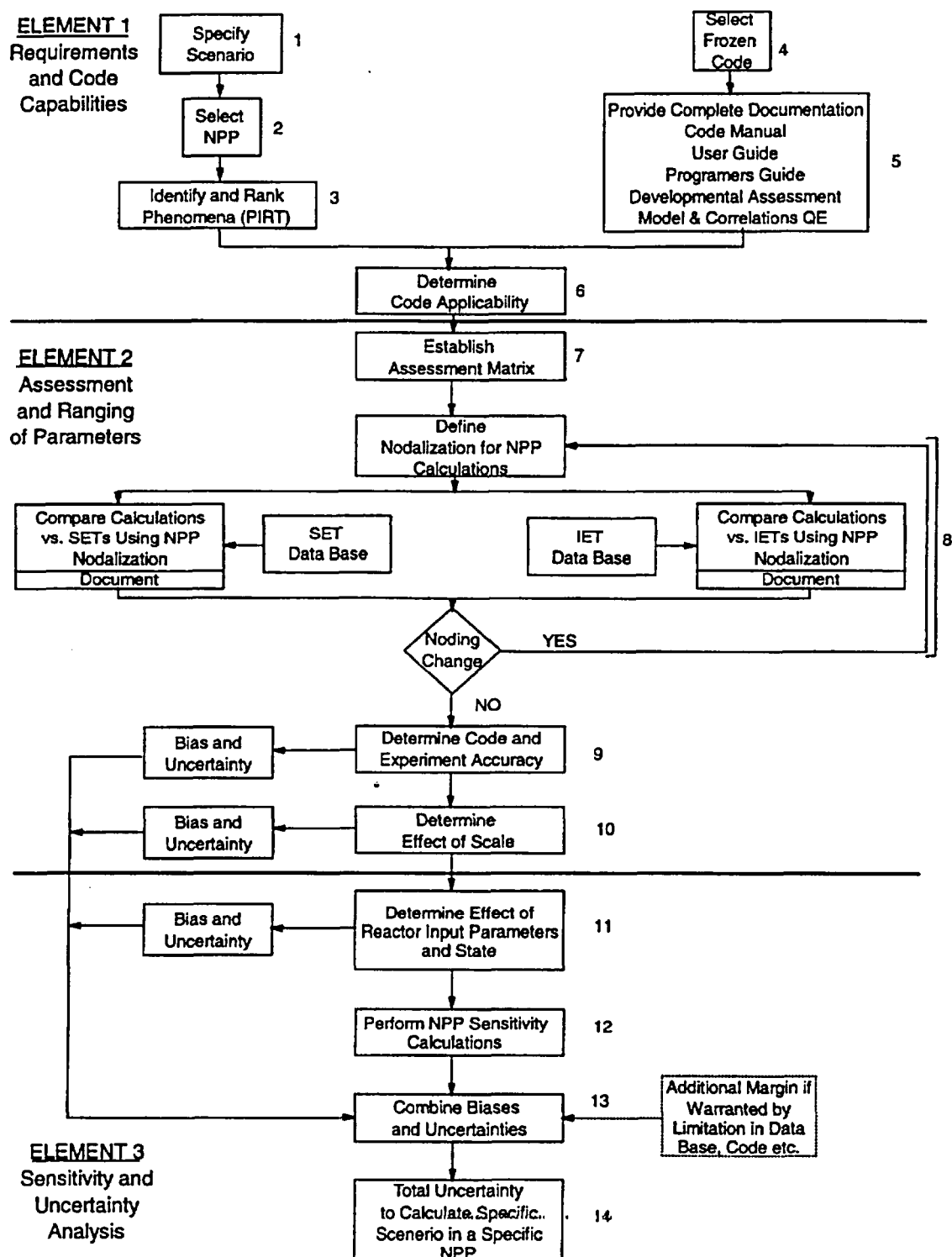


Figure 1-1. Code Scaling, Applicability, and Uncertainty Evaluation Methodology (Boyack et al., 1989)

a,c

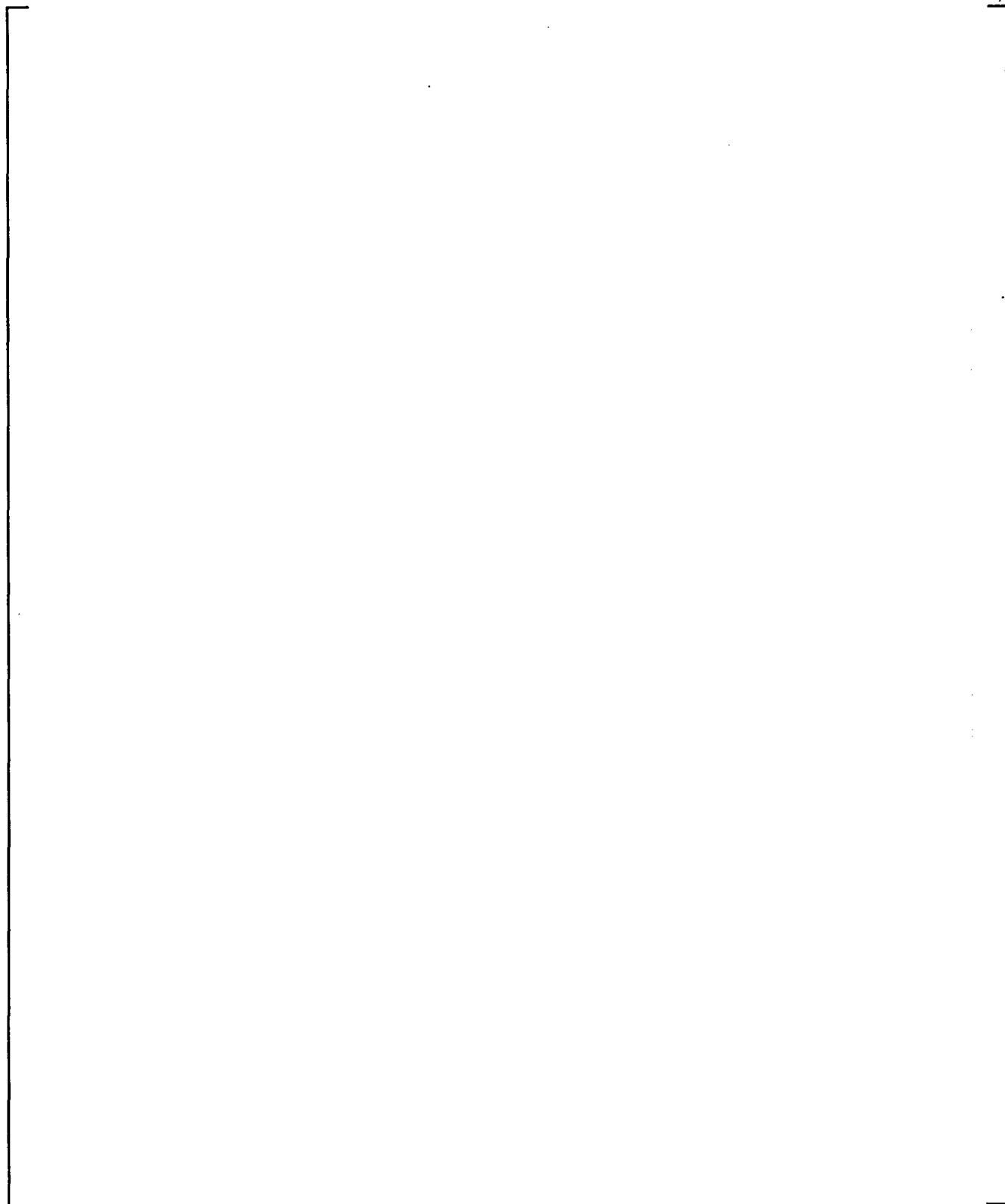


Figure 1-2. Cumulative Distribution Function for Critical Flow Multipliers

a,c

Figure 1-3. Cumulative Distribution Function for Blowdown Cooling Heat Transfer Multipliers

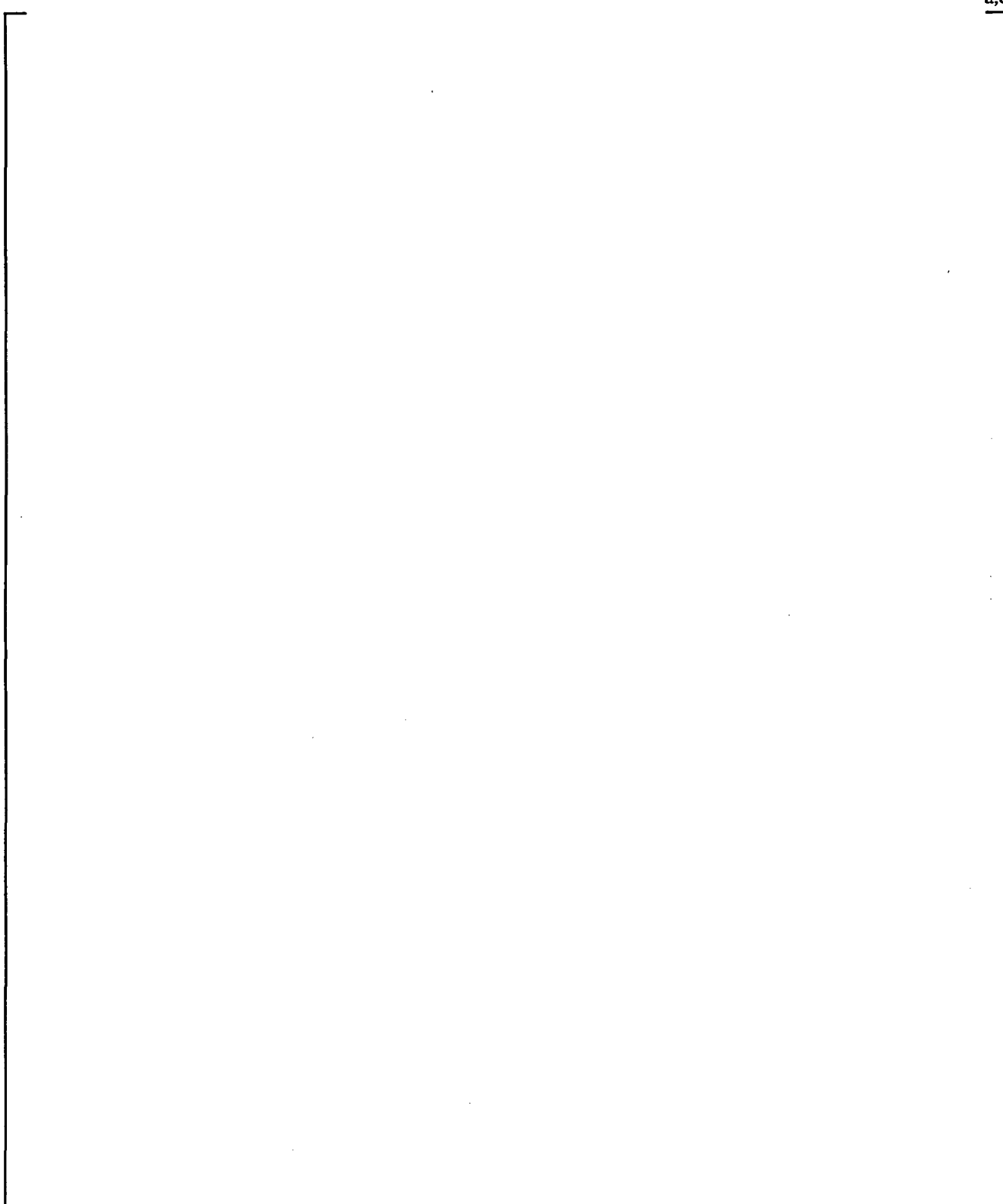


Figure 1-4. Cumulative Distribution Function for Refill Heat Transfer Multipliers

a,c

Figure 1-5. Cumulative Distribution Function for Reflood Heat Transfer Multipliers

a,c

Figure 1-6. Typical Power Shape Used for Reference Transient

2 WCOBRA/TRAC CONSERVATION EQUATIONS

2-1 INTRODUCTION

This chapter describes the WCOBRA/TRAC conservation equations and numerical solution methods for the vessel and one-dimensional components. The governing equations for the vessel and the one-dimensional components use different representations of two-phase flow and are discussed separately. Sections 2-2 and 2-3 describe the conservation equations and the three-dimensional computational cell structure used in the vessel component, while Sections 2-4 and 2-5 discuss the one-dimensional components. The numerical solution methods for the vessel component and the one-dimensional components are described in Section 2-6; Section 2-7 outlines the timestep size selection and convergence criteria.

WCOBRA/TRAC uses a two-fluid, three-field representation of flow in the vessel component. The three fields are a vapor field, a continuous liquid field and an entrained liquid drop field. Each field in the vessel uses a set of three dimensional continuity, momentum, and energy equations with one exception. A common energy equation is used by both the continuous liquid and the entrained liquid drop fields.

The one-dimensional components consist of all the major components in the primary system, such as pipes, pumps, valves, steam generators, and the pressurizer. The one-dimensional components are represented by a two-phase, five equation drift flux model. This formulation consists of two equations for the conservation of mass, two equations for the conservation of energy, and a single equation for the conservation of momentum. Closure for the field equations requires specification of the interphase relative velocities, interfacial heat and mass transfer, and other thermodynamic and constitutive relationships.

2-2 VESSEL COMPONENT CONSERVATION EQUATIONS (MODEL BASIS)

The two-fluid formulation used in the vessel component employs a separate set of conservation equations and constitutive relations for each phase. The effects of one phase on another are accounted for by the interaction terms appearing in the governing equations. The conservation equations have the same form for each phase; only the constitutive relations and physical properties differ. Note that although usually derived for a two-phase flow, the two-fluid formulation can be readily extended to multi-phase flow.

This section describes the development of the two-fluid, three-field conservation equations solved in the vessel component of WCOBRA/TRAC. The two-fluid phasic conservation equations are presented in Section 2-2-1 along with the physical assumptions necessary to obtain them. Expressions representing the three-field conservation equations are presented in Section 2-2-2. The Cartesian coordinate representation of the conservation equations is presented in Section 2-2-3 and in subchannel form in Section 2-2-4.

2-2-1 Three-Field Equation Formulation

The three-field formulation used in the vessel component of WCOBRA/TRAC is a straightforward extension of the two-fluid model. The fields included are vapor, continuous liquid, and entrained liquid. Dividing the liquid phase into two fields is the most convenient and physically reasonable way of handling flows where the liquid can appear in both film and droplet form. In such flows, the motion of the droplets can be quite different from the motion of the film, so a single set of average liquid phase equations cannot adequately describe the liquid flow or the interaction between liquid and vapor.

The average conservation equations used in the vessel module of WCOBRA/TRAC are derived following the methods of Ishii (1977). The average used is a simple Eulerian time average over a time interval (Δt), assumed to be long enough to smooth out the random fluctuations present in a multiphase flow, but short enough to preserve any global unsteadiness in the flow. The resulting average equations can be cast in either the mixture form or the two-fluid form. Because of its greater physical appeal and broader range of application, the two-fluid approach is used as the foundation for WCOBRA/TRAC.

The phasic conservation equations in their most general form describe the time-averaged behavior of phase k , which can be any phase in a multiphase flow. The averaging process used to obtain these equations is based on the work of Ishii (1977). A detailed description of this averaging process for the COBRA/TRAC code is presented in Appendix A of Thurgood et al. (1983), and is not repeated here. The generalized phasic conservation equations are as follows:

Conservation of Mass

$$\frac{\partial}{\partial t} (\alpha_k \rho_k) + \nabla \cdot (\alpha_k \rho_k \underline{U}_k) = \Gamma_k \quad (2-1)$$

Conservation of Momentum

$$\begin{aligned} \frac{\partial}{\partial t} (\alpha_k \rho_k \underline{U}_k) + \nabla \cdot (\alpha_k \rho_k \underline{U}_k \underline{U}_k) = & \alpha_k \rho_k \underline{g} - \alpha_k \nabla P \\ & + \nabla \cdot \left[\alpha_k \left(\underline{\tau}_k + \underline{\tau}_k^T \right) \right] + \underline{M}_k^T + \underline{M}_k^d \end{aligned} \quad (2-2)$$

Conservation of Energy

$$\begin{aligned} \frac{\partial}{\partial t} (\alpha_k \rho_k H_k) + \nabla \cdot (\alpha_k \rho_k H_k \underline{U}_k) = & - \nabla \cdot \left[\alpha_k \left(\underline{Q}_k + \underline{q}_k^T \right) \right] \\ & + \Gamma_k H_k^i + q_{ik}''' + \alpha_k \frac{\partial P}{\partial t} \end{aligned} \quad (2-3)$$

where the terms are defined as:

α_k	=	average k -phase void fraction
ρ_k	=	average k -phase density
\underline{U}_k	=	average k -phase velocity vector
Γ_k	=	average rate of mass transfer to phase k from the other phases
\underline{g}	=	acceleration of gravity vector
P	=	average pressure
$\underline{\tau}_k$	=	average k -phase viscous stress tensor (stress deviator)
$\underline{\tau}_k^T$	=	k -phase turbulent (Reynolds) stress tensor
\underline{M}_k^r	=	average supply of momentum to phase k due to mass transfer to phase k
\underline{M}_k^d	=	average drag force on phase k by the other phases
H_k	=	average k -phase enthalpy
H_k^i	=	saturation enthalpy of phase k
\underline{Q}_k	=	average k -phase conduction vector
\underline{q}_k^T	=	k -phase turbulent heat flux vector
q_{ik}'''	=	heat flow to k -phase

The generalized phasic conservation equations assume that:

1. Gravity is the only body force.
2. There is no volumetric heat generation in the fluid.
3. Radiation heat transfer is limited to wall to drop and wall to vapor.
4. The pressure is the same in all phases.
5. Internal dissipation can be neglected in the energy equation.

While the third and fourth assumptions simplify the conservation equations considerably, they do limit their applicability. For situations typical of those expected in large and small break loss-of-coolant accidents, these assumptions are justified.

2-2-2 Vessel Component Three-Field Conservation Equations

The WCOBRA/TRAC vessel component uses a three-field representation of a two-phase flow. The three-field conservation equation formulation uses three continuity equations, three momentum equations, and two energy equations. (The continuous liquid and the entrained liquid fields are assumed to be in thermal equilibrium, which eliminates the need for one of the energy equations.) The equations

for each field are obtained directly from Equations 2-1 through 2-3 by introducing the three-field notation and several simplifying assumptions.

The subscripts v , ℓ , and e refer to the vapor, continuous liquid, and entrained liquid fields, respectively. The three fields are coupled by the vapor generation and entrainment rate terms. The term Γ''' represents the average rate of vapor generation per unit volume. Since both liquid fields contribute to the vapor generation rate, Γ''' can be expressed as

$$\Gamma''' = \Gamma_t''' + \Gamma_e''' \quad (2-4)$$

If $\eta^{(11)}$ denotes the fraction of total vapor generation coming from the entrained liquid field, then $\Gamma_e''' = \eta \Gamma'''$ and $\Gamma_t''' = (1-\eta) \Gamma'''$.

In addition to phase change, the two liquid fields also exchange mass by entrainment. Let S''' represent the average net rate of entrainment per unit volume. With the definitions for S''' and η , the mass transfer terms can be written as:

$$\Gamma_v = \Gamma''' \quad (2-5)$$

$$\Gamma_t = -\Gamma_t''' - S''' = -(1-\eta) \Gamma''' - S''' \quad (2-6)$$

$$\Gamma_e = -\Gamma_e''' + S''' = -\eta \Gamma''' + S''' \quad (2-7)$$

The terms M_v^d , M_t^d , and M_e^d represent the momentum exchange at the interface. These interfacial momentum terms can be expressed as

$$M_v^d = -\tau_{i,v\ell}''' - \tau_{i,ve}''' \quad (2-8)$$

$$M_t^d = \tau_{i,v\ell}''' \quad (2-9)$$

$$M_e^d = \tau_{i,ve}''' \quad (2-10)$$

where:

$\tau_{i,v\ell}'''$ is the average drag force per unit volume by the vapor on the continuous liquid,

and

$\tau_{i,ve}'''$ is the average drag force per unit volume by the vapor on the entrained liquid.

The momentum exchange due to mass transfer between the three fields can be written as

$$M_v^{\Gamma} = (\Gamma_e''' U) - (\Gamma_i''' U) \quad (2-11)^{(1qq)}$$

$$M_i^{\Gamma} = -(\Gamma_i''' U) - (S''' U) \quad (2-12)^{(1qq)}$$

$$M_e^{\Gamma} = -(\Gamma_e''' U) + (S''' U) \quad (2-13)^{(1qq)}$$

Note also that the velocity associated with the mass transfer rate are the phase velocities of the source. If, for example, $\Gamma_i''' > 0$ (evaporation), $U = U_i$. Otherwise (condensation), $U = U_v$. In the following momentum equations, this convention will be used.

Note that M_v^{Γ} is due only to mass transfer from vapor generation, but M_i^{Γ} and M_e^{Γ} are due to both vapor generation and entrainment.

Three-Field Model Assumptions

The following assumptions are used to obtain the WCOBRA/TRAC vessel component three-field conservation equations, Equations 2-1 through 2-3:

1. The turbulent stresses and the turbulent heat flux of the entrained phase are neglected. Thus,

$$\begin{aligned} \underline{T}_e^T &= 0 \\ \underline{q}_e^T &= 0 \end{aligned} \quad (2-14)$$

2. Viscous stresses can be partitioned into wall shear and fluid-fluid shear, and fluid-fluid shear can be neglected in the entrained liquid phase. With this assumption,

$$\begin{aligned} \nabla \cdot (\alpha_e \underline{\tau}_e) &= \tau_{w,e}''' \\ \nabla \cdot (\alpha_v \underline{\tau}_v) &= \tau_{w,v}''' + \nabla \cdot (\alpha_v \underline{\sigma}_v) \\ \nabla \cdot (\alpha_i \underline{\tau}_i) &= \tau_{w,i}''' + \nabla \cdot (\alpha_i \underline{\sigma}_i) \end{aligned} \quad (2-15)$$

Forces exerted by the wall on the vapor, entrained liquid, and continuous liquid are $\tau_{w,v}'''$, $\tau_{w,e}'''$, and $\tau_{w,l}'''$, respectively.

The fluid-fluid viscous stress tensors are $\underline{\sigma}_v$ and $\underline{\sigma}_l$.

3. The conduction heat flux can be partitioned into a wall term and a fluid-fluid conduction term. The latter is assumed to be negligible in the entrained liquid. Thus,

$$\begin{aligned} -\nabla \cdot (\alpha_v Q_v) &= -\nabla \cdot (\alpha_v q_v) + Q_{wv}''' \\ -\nabla \cdot (\alpha_e Q_e + \alpha_l Q_l) &= -\nabla \cdot (\alpha_l q_l) + Q_{wl}''' \end{aligned} \quad (2-16)$$

Where Q_{wv}''' and Q_{wl}''' are the wall heat transfer rates per unit volume to the vapor and liquid, respectively; q_l is the fluid-fluid conduction vector for the continuous liquid; and q_v is the fluid-fluid conduction vector for the vapor.

4. All mass entering or leaving a phase interface is at saturation. Therefore,

$$\begin{aligned} H_v^i &= H_g \\ H_l^i &= H_f \end{aligned} \quad (2-17)$$

The three-field conservation equations used in the WCOBRA/TRAC vessel component are arrived at by substituting the definitions (2-5) through (2-13) and assumptions (2-14) through (2-17) into Equations 2-1, 2-2, and 2-3. The resulting expressions for conservation of mass, momentum, and energy are listed in Sections 2-2-2-1, 2-2-2-2, and 2-2-2-3.

2-2-2-1 Conservation of Mass

$$\frac{\partial}{\partial t} (\alpha_v \rho_v) + \nabla \cdot (\alpha_v \rho_v U_v) = \Gamma''' \quad (2-18)$$

$$\frac{\partial}{\partial t} (\alpha_l \rho_l) + \nabla \cdot (\alpha_l \rho_l U_l) = -\Gamma_l''' - S''' \quad (2-19)$$

$$\frac{\partial}{\partial t} (\alpha_e \rho_e) + \nabla \cdot (\alpha_e \rho_e U_e) = -\Gamma_e''' + S''' \quad (2-20)$$

2-2-2-2 Conservation of Momentum

Vapor Field

$$\begin{aligned} \frac{\partial}{\partial t} (\alpha_v \rho_v U_v) + \nabla \cdot (\alpha_v \rho_v U_v U_v) &= -\alpha_v \nabla P + \alpha_v \rho_v g \\ + \nabla \cdot [\alpha_v (\underline{g}_v + \underline{I}^T)] + \Gamma_{w,v}''' - \Gamma_{i,v}''' - \Gamma_{i,ve}''' + (\Gamma''' U) \end{aligned} \quad (2-21)^{(5)}$$

Continuous Liquid Field

$$\begin{aligned} \frac{\partial}{\partial t} (\alpha_l \rho_l U_l) + \nabla \cdot (\alpha_l \rho_l U_l U_l) &= -\alpha_l \nabla P + \alpha_l \rho_l g \\ + \nabla \cdot [\alpha_l (\underline{g}_l + \underline{I}^T)] + \Gamma_{w,l}''' + \Gamma_{i,l}''' - (\Gamma_l''' U) - (S''' U) \end{aligned} \quad (2-22)$$

Entrained Liquid Field

$$\begin{aligned} \frac{\partial}{\partial t} (\alpha_e \rho_e U_e) + \nabla \cdot (\alpha_e \rho_e U_e U_e) &= -\alpha_e \nabla P + \alpha_e \rho_e g \\ + \Gamma_{w,e}''' + \Gamma_{i,ve}''' - (\Gamma_e''' U) + (S''' U) \end{aligned} \quad (2-23)$$

2-2-2-3 Conservation of Energy

Vapor Field

$$\begin{aligned} \frac{\partial}{\partial t} (\alpha_v \rho_v H_v) + \nabla \cdot (\alpha_v \rho_v H_v U_v) &= -\nabla \cdot [\alpha_v (\underline{q}_v + \underline{q}_v^T)] \\ + \Gamma''' H_g + q_{iv}''' + Q_{wv}''' + \alpha_v \frac{\partial P}{\partial t} \end{aligned} \quad (2-24)^{(23)}$$

Liquid Fields

$$\begin{aligned} \frac{\partial}{\partial t} [(\alpha_l + \alpha_e) \rho_l H_l] + \nabla \cdot (\alpha_l \rho_l H_l U_l) + \nabla \cdot (\alpha_e \rho_e H_e U_e) \\ = -\nabla \cdot [\alpha_l (\underline{q}_l + \underline{q}_l^T)] - \Gamma''' H_f + q_{ir}''' + Q_{wl}''' + (\alpha_l + \alpha_e) \frac{\partial P}{\partial t} \end{aligned} \quad (2-25)^{(23)}$$

The use of a single energy equation for the combined continuous liquid and liquid droplet fields means that both fields are assumed to be at the same temperature. In regions where both liquid droplets and liquid films are present, this can be justified in view of the large rate of mass transfer between the two fields, which will tend to draw both to the same temperature.

2-2-3 Cartesian Coordinate Representation

The vessel component in WCOBRA/TRAC can be represented with either rectangular Cartesian coordinates or with a subchannel coordinate system. In geometries amenable to description by a Cartesian coordinate system, WCOBRA/TRAC allows a fully three-dimensional treatment. Let u , v , and w denote the x , y , and z components of velocity with x being the vertical coordinate. Figure 2-1 shows the control volume for a scalar mesh cell in the Cartesian coordinate system. The conservation equations in Cartesian form are as follows:

Conservation of Mass

Vapor Conservation of Mass:

$$\frac{\partial}{\partial t} (\alpha_v \rho_v) + \frac{\partial}{\partial x} (\alpha_v \rho_v u_v) + \frac{\partial}{\partial y} (\alpha_v \rho_v v_v) + \frac{\partial}{\partial z} (\alpha_v \rho_v w_v) = \Gamma''' \quad (2-26)$$

Continuous Liquid Conservation of Mass:

$$\frac{\partial}{\partial t} (\alpha_l \rho_l) + \frac{\partial}{\partial x} (\alpha_l \rho_l u_l) + \frac{\partial}{\partial y} (\alpha_l \rho_l v_l) + \frac{\partial}{\partial z} (\alpha_l \rho_l w_l) = -\Gamma_l''' - S''' \quad (2-27)$$

Entrained Liquid Conservation of Mass:

$$\frac{\partial}{\partial t} (\alpha_e \rho_e) + \frac{\partial}{\partial x} (\alpha_e \rho_e u_e) + \frac{\partial}{\partial y} (\alpha_e \rho_e v_e) + \frac{\partial}{\partial z} (\alpha_e \rho_e w_e) = -\Gamma_e''' + S''' \quad (2-28)$$

Conservation of Momentum

Vapor Conservation of Momentum:

(x -component)

$$\begin{aligned} \frac{\partial}{\partial t} (\alpha_v \rho_v u_v) + \frac{\partial}{\partial x} (\alpha_v \rho_v u_v u_v) + \frac{\partial}{\partial y} (\alpha_v \rho_v u_v v_v) + \frac{\partial}{\partial z} (\alpha_v \rho_v u_v w_v) = \\ -\alpha_v \frac{\partial P}{\partial x} - \alpha_v \rho_v g + \tau_{wx,v}''' - \tau_{ix,v}''' - \tau_{ix,ve}''' + \Gamma_l''' u_v \end{aligned} \quad (2-29)$$

(y-component)

$$\begin{aligned} \frac{\partial}{\partial t} (\alpha_v \rho_v v_v) + \frac{\partial}{\partial x} (\alpha_v \rho_v v_v u_v) + \frac{\partial}{\partial y} (\alpha_v \rho_v v_v v_v) + \frac{\partial}{\partial z} (\alpha_v \rho_v v_v w_v) = \\ -\alpha_v \frac{\partial P}{\partial y} + \tau_{wy,v}''' - \tau_{iy,v}''' - \tau_{iz,v}''' + \Gamma''' v_v \end{aligned} \quad (2-30)$$

(z-component)

$$\begin{aligned} \frac{\partial}{\partial t} (\alpha_v \rho_v w_v) + \frac{\partial}{\partial x} (\alpha_v \rho_v w_v u_v) + \frac{\partial}{\partial y} (\alpha_v \rho_v w_v v_v) + \frac{\partial}{\partial z} (\alpha_v \rho_v w_v w_v) = \\ -\alpha_v \frac{\partial P}{\partial z} + \tau_{wz,v}''' - \tau_{iz,v}''' - \tau_{ix,v}''' + \Gamma''' w_v \end{aligned} \quad (2-31)$$

Continuous Liquid Conservation of Momentum:

(x-component)

$$\begin{aligned} \frac{\partial}{\partial t} (\alpha_l \rho_l u_l) + \frac{\partial}{\partial x} (\alpha_l \rho_l u_l u_l) + \frac{\partial}{\partial y} (\alpha_l \rho_l u_l v_l) + \frac{\partial}{\partial z} (\alpha_l \rho_l u_l w_l) = \\ -\alpha_l \frac{\partial P}{\partial x} - \alpha_l \rho_l g + \tau_{wx,l}''' - \tau_{ix,l}''' + \Gamma''' u_l \end{aligned} \quad (2-32)$$

(y-component)

$$\begin{aligned} \frac{\partial}{\partial t} (\alpha_l \rho_l v_l) + \frac{\partial}{\partial x} (\alpha_l \rho_l v_l u_l) + \frac{\partial}{\partial y} (\alpha_l \rho_l v_l v_l) + \frac{\partial}{\partial z} (\alpha_l \rho_l v_l w_l) = \\ -\alpha_l \frac{\partial P}{\partial y} + \tau_{wy,l}''' - \tau_{iy,l}''' + \Gamma''' v_l \end{aligned} \quad (2-33)$$

(z-component)

$$\begin{aligned} \frac{\partial}{\partial t} (\alpha_l \rho_l w_l) + \frac{\partial}{\partial x} (\alpha_l \rho_l w_l u_l) + \frac{\partial}{\partial y} (\alpha_l \rho_l w_l v_l) + \frac{\partial}{\partial z} (\alpha_l \rho_l w_l w_l) = \\ -\alpha_l \frac{\partial P}{\partial z} + \tau_{wz,l}''' - \tau_{iz,l}''' + \Gamma''' w_l \end{aligned} \quad (2-34)$$

Entrained Liquid Conservation of Momentum:

(x-component)

$$\begin{aligned} \frac{\partial}{\partial t} (\alpha_e \rho_t u_e) + \frac{\partial}{\partial x} (\alpha_e \rho_t u_e u_e) + \frac{\partial}{\partial y} (\alpha_e \rho_t u_e v_e) + \frac{\partial}{\partial z} (\alpha_e \rho_t u_e w_e) = \\ -\alpha_e \frac{\partial P}{\partial x} - \alpha_e \rho_t g + \tau_{wx,e}''' - \tau_{ix,ve}''' + \Gamma_e''' u_e \end{aligned} \quad (2-35)$$

(y-component)

$$\begin{aligned} \frac{\partial}{\partial t} (\alpha_e \rho_t v_e) + \frac{\partial}{\partial x} (\alpha_e \rho_t v_e u_e) + \frac{\partial}{\partial y} (\alpha_e \rho_t v_e v_e) + \frac{\partial}{\partial z} (\alpha_e \rho_t v_e w_e) = \\ -\alpha_e \frac{\partial P}{\partial y} + \tau_{wy,e}''' - \tau_{iy,ve}''' + \Gamma_e''' v_e \end{aligned} \quad (2-36)$$

(z-component)

$$\begin{aligned} \frac{\partial}{\partial t} (\alpha_e \rho_t w_e) + \frac{\partial}{\partial x} (\alpha_e \rho_t w_e u_e) + \frac{\partial}{\partial y} (\alpha_e \rho_t w_e v_e) + \frac{\partial}{\partial z} (\alpha_e \rho_t w_e w_e) = \\ -\alpha_e \frac{\partial P}{\partial z} + \tau_{wz,e}''' - \tau_{iz,ve}''' + \Gamma_e''' w_e \end{aligned} \quad (2-37)$$

Vapor Conservation of Energy:

$$\begin{aligned} \frac{\partial}{\partial t} (\alpha_v \rho_v H_v) + \frac{\partial}{\partial x} (\alpha_v \rho_v H_v u_v) + \frac{\partial}{\partial y} (\alpha_v \rho_v H_v v_v) + \frac{\partial}{\partial z} (\alpha_v \rho_v H_v w_v) = \\ - \frac{\partial}{\partial x} [\alpha_v (q_v + q_v^T)_x] - \frac{\partial}{\partial y} [\alpha_v (q_v + q_v^T)_y] - \frac{\partial}{\partial z} [\alpha_v (q_v + q_v^T)_z] \\ + \Gamma''' H_g + q_{iv}''' + Q_{wv}''' + \alpha_v \frac{\partial P}{\partial t} \end{aligned} \quad (2-38)$$

Liquid Conservation of Energy:

$$\begin{aligned} \frac{\partial}{\partial t} [(\alpha_t + \alpha_e) \rho_t H_t] + \frac{\partial}{\partial x} (\alpha_t \rho_t H_t u_t) + \frac{\partial}{\partial x} (\alpha_e \rho_t H_t u_e) \\ + \frac{\partial}{\partial y} (\alpha_t \rho_t H_t v_t) + \frac{\partial}{\partial y} (\alpha_e \rho_t H_t v_e) + \frac{\partial}{\partial z} (\alpha_t \rho_t H_t w_t) + \frac{\partial}{\partial z} (\alpha_e \rho_t H_t w_e) = \\ - \frac{\partial}{\partial x} [\alpha_t (q_t + q_t^T)_x] - \frac{\partial}{\partial y} [\alpha_t (q_t + q_t^T)_y] - \frac{\partial}{\partial z} [\alpha_t (q_t + q_t^T)_z] \\ - \Gamma''' H_f + q_{it}''' + Q_{wt}''' + (\alpha_t + \alpha_e) \frac{\partial P}{\partial t} \end{aligned} \quad (2-39)$$

2-2-4 Subchannel Coordinate Formulation

Fixed transverse coordinates are not used in the subchannel formulation. Instead, all transverse or lateral flows are assumed to occur through "gaps." Thus, one transverse momentum equation applies to all gaps regardless of the gap orientation.⁽²⁴⁾ This reduces the number of component momentum equations to only two: vertical and transverse.

Because of its greater adaptability, the subchannel formulation is often selected over the Cartesian formulation when modelling complex or irregular geometries. The subchannel approach is typically used for rod bundle thermal-hydraulic analysis. The conservation equations used in the subchannel formulation are shown below. In the subchannel coordinate system, X is the axial coordinate and U is the velocity in that direction. The transverse (or lateral) direction is denoted by Z , and W is the velocity of the lateral flow.

Vapor Conservation of Mass:

$$\frac{\partial}{\partial t} (\alpha_v \rho_v A_x) + \frac{\partial}{\partial X} (\alpha_v \rho_v U_v A_x) - \sum_k (\alpha_v \rho_v W_{v,k} L_{g,k}) = \Gamma''' A_x \quad (2-40)$$

Continuous Liquid Conservation of Mass:

$$\frac{\partial}{\partial t} (\alpha_l \rho_l A_x) + \frac{\partial}{\partial X} (\alpha_l \rho_l U_l A_x) - \sum_k (\alpha_l \rho_l W_{l,k} L_{g,k}) = - (\Gamma_t''' + S''') A_x \quad (2-41)$$

Entrained Liquid Conservation of Mass:

$$\frac{\partial}{\partial t} (\alpha_e \rho_e A_x) + \frac{\partial}{\partial X} (\alpha_e \rho_e U_e A_x) - \sum_k (\alpha_e \rho_e W_{e,k} L_{g,k}) = - (\Gamma_e''' - S''') A_x \quad (2-42)$$

Vapor Conservation of Momentum:

(vertical momentum)

$$\begin{aligned} & \frac{\partial}{\partial t} (\alpha_v \rho_v U_v A_x) + \frac{\partial}{\partial X} (\alpha_v \rho_v U_v U_v A_x) - \sum_k (\alpha_v \rho_v U_v W_{v,k} L_{g,k}) / 2 \\ & = -\alpha_v A_x \frac{\partial P}{\partial X} - \alpha_v \rho_v A_x g + \tau_{wx,v}''' A_x - \tau_{ix,v}''' A_x - \tau_{ix,v} A_x + \Gamma''' U A_x \end{aligned} \quad (2-43)^{(1c)}$$

(transverse momentum)

$$\begin{aligned}
& \frac{\partial}{\partial t} (\alpha_v \rho_v W_v A_z) + \frac{\partial}{\partial Z} (\alpha_v \rho_v W_v W_v A_z) + \frac{\partial}{\partial X} (\alpha_v \rho_v W_v U_v A_z) \\
& - \frac{\Delta X}{\Delta Z} \sum_{k^o} (\alpha_v \rho_v W_v W_v^o L_g^o) / 2 \\
& = -\alpha_v A_z \frac{\partial P}{\partial Z} + \tau_{wz,v}''' A_z - \tau_{iz,v}''' A_z - \tau_{iz,ve}''' A_z + \Gamma''' W A_z
\end{aligned} \tag{2-44}^{(1c)}$$

Continuous Liquid Conservation of Momentum:

(vertical momentum)

$$\begin{aligned}
& \frac{\partial}{\partial t} (\alpha_t \rho_t U_t A_x) + \frac{\partial}{\partial X} (\alpha_t \rho_t U_t U_t A_x) - \sum_k (\alpha_t \rho_t U_t W_t L_g)_k / 2 \\
& = -\alpha_t A_x \frac{\partial P}{\partial X} - \alpha_t \rho_t A_x g + \tau_{wx,t}''' A_x + \tau_{ix,t}''' A_x + \Gamma_t''' U A_x + S''' U A_x
\end{aligned} \tag{2-45}^{(1c)}$$

(transverse momentum)

$$\begin{aligned}
& \frac{\partial}{\partial t} (\alpha_t \rho_t W_t A_z) + \frac{\partial}{\partial Z} (\alpha_t \rho_t W_t W_t A_z) + \frac{\partial}{\partial X} (\alpha_t \rho_t W_t U_t A_z) - \frac{\Delta X}{\Delta Z} \sum_{k^o} (\alpha_t \rho_t W_t W_t^o L_g^o) / 2 \\
& = -\alpha_t A_z \frac{\partial P}{\partial Z} + \tau_{wz,t}''' A_z + \tau_{iz,t}''' A_z + \Gamma_t''' W A_z + S''' W A_z
\end{aligned} \tag{2-46}^{(1c)}$$

Entrained Liquid Conservation of Momentum:

(vertical momentum)

$$\begin{aligned}
& \frac{\partial}{\partial t} (\alpha_e \rho_e U_e A_x) + \frac{\partial}{\partial X} (\alpha_e \rho_e U_e U_e A_x) - \sum_k (\alpha_e \rho_e U_e W_e L_g)_k / 2 \\
& = -\alpha_e A_x \frac{\partial P}{\partial X} - \alpha_e \rho_e A_x g + \tau_{wx,e}''' A_x + \tau_{ix,ve}''' A_x + \Gamma_e''' U A_x - S''' U A_x
\end{aligned} \tag{2-47}^{(1c)}$$

(transverse momentum)

$$\begin{aligned}
 & \frac{\partial}{\partial t} (\alpha_e \rho_t W_e A_z) + \frac{\partial}{\partial Z} (\alpha_e \rho_t W_e W_e A_z) + \frac{\partial}{\partial X} (\alpha_e \rho_t W_e U_e A_z) \\
 & - \frac{\Delta X}{\Delta Z} \sum_{k^o} (\alpha_e \rho_t W_e W_e^o L_g^o) / 2 \\
 & = -\alpha_e A_z \frac{\partial P}{\partial Z} + \tau_{wze}''' A_z + \tau_{izve}''' A_z + \Gamma_e''' U A_z - S''' U A_z
 \end{aligned} \tag{2-48}^{(1c)}$$

Vapor Conservation of Energy:

$$\begin{aligned}
 & \frac{\partial}{\partial t} (\alpha_v \rho_v H_v A_x) + \frac{\partial}{\partial X} (\alpha_v \rho_v H_v U_v A_x) - \sum_k (\alpha_v \rho_v H_v W_v L_{gk}) = \\
 & - \frac{\partial}{\partial X} [\alpha_v (q_v + q_v^T)_x A_x] + \Gamma''' H_g A_x + q_{iv}''' A_x + Q_{wv}''' A_x + \alpha_v \frac{\partial P}{\partial t} A_x
 \end{aligned} \tag{2-49}$$

Liquid Conservation of Energy:

$$\begin{aligned}
 & \frac{\partial}{\partial t} [(\alpha_t + \alpha_e) \rho_t H_t A_x] + \frac{\partial}{\partial X} (\alpha_t \rho_t H_t U_t A_x) + \frac{\partial}{\partial X} (\alpha_e \rho_t H_t U_e A_x) - \sum_k (\alpha_t \rho_t H_t W_t L_{gk}) \\
 & - \sum_k (\alpha_e \rho_t H_t W_e L_{gk}) = \\
 & \frac{\partial}{\partial X} [\alpha_t (q_t + q_t^T)_x A_x] - \Gamma''' H_f A_x + q_{it}''' A_x + Q_{wt}''' A_x + (\alpha_t + \alpha_e) \frac{\partial P}{\partial t} A_x
 \end{aligned} \tag{2-50}$$

The following notation has been used in the subchannel equations:

- U = vertical velocity
- W = transverse velocity
- W^o = orthogonal gap velocity
- A = axial flow area of subchannel
- A_z = transverse flow area of gap
- L_g = gap width
- L_g^o = orthogonal gap width
- X = axial coordinate
- Z = transverse coordinate
- Subscript k refers to gap k
- Subscript k^o refers to orthogonal gap $k^{o(2)}$

2-2-5 Comparison of Cartesian and Subchannel Formulations

The subchannel vertical momentum equations, Equations 2-43, 2-45, and 2-47, contain derivatives only with respect to X and t , and are already partially finite-differenced. The corresponding Cartesian component equations, Equations 2-29, 2-32, and 2-35, are still completely in differential form. To compare the two forms, the Cartesian equations must be put in a form compatible with the subchannel equations.

Consider a rectangular control volume with side lengths Δx , Δy , and Δz . Expressing Equation 2-29 in partially finite-differenced form for this control volume yields

$$\begin{aligned} & \frac{\partial}{\partial t} (\alpha_v \rho_v u_v) A_x + \frac{\partial}{\partial x} (\alpha_v \rho_v u_v u_v) A_x + \left[(\alpha_v \rho_v u_v v_v)_{y_o + \Delta y} - (\alpha_v \rho_v u_v v_v)_{y_o} \right] \Delta z \\ & \quad + \left[(\alpha_v \rho_v u_v w_v)_{z_o + \Delta z} - (\alpha_v \rho_v u_v w_v)_{z_o} \right] \Delta y \\ & = -\alpha_v \frac{\partial P}{\partial x} A_x - \alpha_v \rho_v g A_x + \tau_{wx,v}''' A_x - \tau_{ix,vl}''' A_x - \tau_{ix,ve}''' A_x + \Gamma''' u A_x \end{aligned} \quad (2-51)$$

The y - and z -direction vapor momentum equations can be treated in the same fashion. Equation 2-30 becomes

$$\begin{aligned} & \frac{\partial}{\partial t} (\alpha_v \rho_v v_v) A_y + \frac{\partial}{\partial y} (\alpha_v \rho_v v_v v_v) A_y + \left[(\alpha_v \rho_v v_v u_v)_{x_o + \Delta x} - (\alpha_v \rho_v v_v u_v)_{x_o} \right] \Delta z \\ & \quad + \left[(\alpha_v \rho_v v_v w_v)_{z_o + \Delta z} - (\alpha_v \rho_v v_v w_v)_{z_o} \right] \Delta x \\ & = -\alpha_v \frac{\partial P}{\partial y} A_y + \tau_{wy,v}''' A_y - \tau_{iy,vl}''' A_y - \tau_{iy,ve}''' A_y + \Gamma''' v A_y \end{aligned} \quad (2-52)$$

and Equation 2-31 becomes

$$\begin{aligned} & \frac{\partial}{\partial t} (\alpha_v \rho_v w_v) A_z + \frac{\partial}{\partial z} (\alpha_v \rho_v w_v w_v) A_z + \left[(\alpha_v \rho_v w_v u_v)_{x_o + \Delta x} - (\alpha_v \rho_v w_v u_v)_{x_o} \right] \Delta y \\ & \quad + \left[(\alpha_v \rho_v w_v v_v)_{y_o + \Delta y} - (\alpha_v \rho_v w_v v_v)_{y_o} \right] \Delta x \\ & = -\alpha_v \frac{\partial P}{\partial z} A_z + \tau_{wz,v}''' A_z - \tau_{iz,vl}''' A_z - \tau_{iz,ve}''' A_z + \Gamma''' w A_z \end{aligned} \quad (2-53)$$

The conditions for equivalency between the subchannel and Cartesian momentum equations can be demonstrated with the above equations. Assuming the subchannels are arranged in a rectangular array, equivalence requires

$$\begin{aligned}
 - \sum_k (\alpha_v \rho_v U_v W_v L_g) / 2 = & \left[(\alpha_v \rho_v u_v v_v)_{y_o + \Delta y} - (\alpha_v \rho_v u_v v_v)_{y_o} \right] \Delta z \\
 & + \left[(\alpha_v \rho_v u_v w_v)_{z_o + \Delta z} - (\alpha_v \rho_v u_v w_v)_{z_o} \right] \Delta y
 \end{aligned} \quad (2-54)$$

In addition, gaps with unit vectors in the y-direction must have

$$- \frac{\Delta x}{\Delta y} \sum_{k^o} (\alpha_v \rho_v W_v W_v^o L_g^o) / 2 = \left[(\alpha_v \rho_v v_v w_v)_{z_o + \Delta z} - (\alpha_v \rho_v v_v w_v)_{z_o} \right] \Delta x \quad (2-55)^{(3)}$$

while gaps with unit vectors in the z-direction must have

$$- \frac{\Delta x}{\Delta z} \sum_{k^o} (\alpha_v \rho_v W_v W_v^o L_g^o) / 2 = \left[(\alpha_v \rho_v w_v v_v)_{y_o + \Delta y} - (\alpha_v \rho_v w_v v_v)_{y_o} \right] \Delta x \quad (2-56)^{(3)}$$

The user selects by input either the three-dimensional Cartesian equations or the subchannel formulation. When the subchannel formulation is chosen, the second and fourth terms on the left side of the transverse momentum equation Equation 2-44 are neglected, yielding the historical form of the subchannel transverse momentum equation. The corresponding components of viscous and turbulent shear stresses are also neglected in the subchannel formulation.

2-3 VESSEL COMPONENT COMPUTATIONAL CELL STRUCTURE (MODEL AS CODED)

2-3-1 Introduction

The three-field conservation equations for multidimensional flow in the vessel component are presented in Section 2-2. Chapters 3-10 of this document provide a description of the physical models required for their closure. The finite-difference form of these equations will be presented here, and the term by term correspondence between the conservation equations and the finite-difference equations will be pointed out.

The finite-difference equations are written in a semi-implicit form using donor cell differencing for the convected quantities. Since a semi-implicit form is used, the timestep, Δt , is limited by the material Courant limit

$$\Delta t < \left| \frac{\Delta X}{U} \right| \quad (2-57)$$

where ΔX is the mesh spacing and U is the fluid velocity.

Section 2-7-3 provides a description of the WCOBRA/TRAC timestep size control and convergence criteria.

The finite-difference equations are written such that they may be solved on Cartesian coordinates or using the subchannel formulation in which some of the convective terms in the transverse momentum equations are neglected and idealistic assumptions are made concerning the shape of the transverse momentum control volumes.

The computational mesh and finite-difference equations are described using the generalized subchannel notations. These equations are equivalent to the three-dimensional Cartesian equations when the limiting assumptions of the subchannel formulation are not used and the mesh is arranged on a rectangular grid.

2-3-2 Vessel Component Computational Mesh

The equations are solved using a staggered-difference scheme where the velocities are obtained at the mesh cell faces and the state variables, such as pressure, density, enthalpy, and void fraction, are obtained at the cell center. The mesh cell is characterized by its axial cross-sectional area, A_x , its height, ΔX , and the width of its connection with adjacent mesh cells, L_g . The basic mesh cell is shown in Figure 2-2. The basic mesh cell may be used to model any one, two, or three-dimensional region. The dimensionality of the flow is dependent upon the number of faces on the cell that connect with adjacent mesh cells.

The size of a mesh cell used to model the flow field inside of a reactor vessel is generally quite large because the volume of the reactor vessel is very large and the cost of using a fine mesh in solving the two-fluid equations for the whole vessel would be prohibitive. However, many important flow paths and flow phenomena may be overlooked when a large mesh size is used in some areas of the vessel. This can be minimized by allowing a variable mesh size within the vessel. A finer mesh can be used in areas where a more detailed calculation of the flow field is required. The vessel component has been set up to allow such a variable mesh size. The variable mesh is formed by connecting two or more cells to any or all of the faces of a mesh cell, as illustrated in Figure 2-3. A single mesh cell with area A_1 is shown connected to four mesh cells above it with areas A_2 , A_3 , etc. These four mesh cells may connect through transverse connections L_2 , L_3 , etc., to allow transverse flow in that region, or they may not connect to each other forming one or more one-dimensional flow paths that connect to mesh cell 1.

The mesh cells shown in Figures 2-2 and 2-3 represent the mesh for the scalar continuity and energy equations. The momentum equations are solved on a staggered mesh where the momentum cell is centered on the scalar mesh cell boundary. The mesh cells for vertical and transverse velocities are shown in Figures 2-4 and 2-5, respectively.

The vertical velocities are subscripted with I and j , where I identifies the location of the mesh cell within the horizontal plane and j identifies its vertical location. The mesh cells for the scalar equations carry the same subscripts, but their mesh cell centers lie a distance $\Delta X/2$ below the mesh cell center for the correspondingly subscripted velocity and are denoted by the capital letter J in the discussion below.

Transverse velocities are subscripted with k and J where k identifies the location of the mesh cell in the horizontal plane and J identifies its vertical location. The node centers for the scalar equations and transverse momentum equations lie in the same horizontal plane.

The finite-difference equations are written using this subscripting convention based on the mesh as defined above.

2-3-3 Vessel Component Finite-Difference Equations

The finite-difference equations follow. Quantities that are evaluated at the old time carry the superscript n . Donor cell quantities that have the superscript \bar{n} are evaluated at the old time, and form the explicit portions of the equations. The new time values do not have superscripts. The corresponding term in the conservation equation for each term in the finite-difference equation is provided in the brackets below each equation, along with a verbal description of the term. The subscripts I and k are assumed to be obvious and are not shown.

2-3-3-1 Conservation of Mass Equations

Vapor Mass Equation:

$$\begin{aligned} \frac{[(\alpha_v \rho_v)_J - (\alpha_v \rho_v)_J^n]}{\Delta t} A_{c_J} = & \frac{\sum_{KB=1}^{NB} [(\alpha_v \rho_v)^{\bar{n}} U_{v_{j-1}} A_{m_{j-1}}]_{KB} - \sum_{KA=1}^{NA} [(\alpha_v \rho_v)^{\bar{n}} U_{v_j} A_{m_j}]_{KA}}{\Delta X_J} \\ & + \sum_{KL=1}^{NKK} L_{KL} [(\alpha_v \rho_v)^{\bar{n}} W_{v_L}]_J + \frac{\Gamma_J}{\Delta X_J} + \frac{S_{cv_J}}{\Delta X_J} \end{aligned} \quad (2-58)$$

Liquid Mass Equation:

$$\begin{aligned} \frac{[(\alpha_l \rho_l)_J - (\alpha_l \rho_l)_J^n]}{\Delta t} A_{c_J} = & \frac{\sum_{KB=1}^{NB} [(\alpha_l \rho_l)^{\bar{n}} U_{l_{j-1}} A_{m_{j-1}}]_{KB} - \sum_{KA=1}^{NA} [(\alpha_l \rho_l)^{\bar{n}} U_{l_j} A_{m_j}]_{KA}}{\Delta X_J} \\ & + \sum_{KL=1}^{NKK} L_{KL} [(\alpha_l \rho_l)^{\bar{n}} W_{l_L}]_J - \frac{(1-\eta) \Gamma_J}{\Delta X_J} - \frac{S_J^n}{\Delta X_J} + \frac{S_{\alpha_J}}{\Delta X_J} \end{aligned} \quad (2-59)$$

Entrained Liquid Mass Equation:

$$\begin{aligned} \frac{[(\alpha_e \rho_t)_J - (\alpha_e \rho_t)_J^n]}{\Delta t} A_{c_J} = & \frac{\sum_{KB=1}^{NB} [(\alpha_e \rho_t)^{\bar{n}} U_{e_{j-1}} A_{m_{j-1}}]_{KB} - \sum_{KA=1}^{NA} [(\alpha_e \rho_t)^{\bar{n}} U_{e_j} A_{m_j}]_{KA}}{\Delta X_J} \\ & + \sum_{KL=1}^{NKK} L_{KL} [(\alpha_e \rho_t)^{\bar{n}} W_{e_L}]_J - \frac{\eta \Gamma_J}{\Delta X_J} + \frac{S_J^n}{\Delta X_J} + \frac{S_{ce_J}}{\Delta X_J} \end{aligned} \quad (2-60)$$

$$\begin{aligned} \left[\begin{array}{c} \text{Rate of Change of Mass} \\ A \frac{\partial}{\partial t} (\alpha_k \rho_k) \end{array} \right] = & - \left[\begin{array}{c} \text{Rate of Mass Efflux in the} \\ \text{Vertical Direction} \\ \frac{\partial \alpha_k \rho_k U_{k_A}}{\partial X} \end{array} \right] \\ - \left[\begin{array}{c} \text{Rate of Mass Efflux in} \\ \text{the Transverse Direction} \\ \sum_{KL} (\alpha_k \rho_k W_k)_{KL} L_{KL} \end{array} \right] + & \left[\begin{array}{c} \text{Rate of Creation} \\ \text{of Vapor Mass Due} \\ \text{to Phase Change} \\ \Gamma_k \end{array} \right] + \left[\begin{array}{c} \text{Mass Efflux} \\ \text{Due to} \\ \text{Entrainment} \\ S' \end{array} \right] + \left[\begin{array}{c} \text{Phase} \\ \text{Source} \\ \text{term} \\ S_c \end{array} \right] \end{aligned}$$

The rate of mass efflux in the transverse direction is given as the sum of the mass entering the cell through all transverse connections to all of the faces. The total number of transverse connections to the cell is NKK. The rate of mass efflux in the vertical direction is given as the sum of the mass entering (or leaving) the cell through all vertical connections to the top and bottom of the cell. The total number of connections to the top of the cell is NA and the number of connections to the bottom of the cell is NB.

The velocity in each of the convection terms is taken to be the new time value, while the convected quantity, in this case $(\alpha_k \rho_k)^{\bar{n}}$, is taken at the old time. The mass creation term is evaluated at the new time. However, it consists of an implicit and explicit part. The rate of mass generation due to phase change, Γ_J , is given by

$$\Gamma_J = - \frac{(h_i A_i)_h^n (H_f - H_t)}{[C_{pl} (H_v - H_f)]^n} - \frac{(h_i A_i)_v^n (H_g - H_v)}{[C_{pv} (H_g - H_t)]^n} \quad (2-61)$$

The product of the interfacial area and heat transfer coefficient, the specific heats, and the heat of vaporization are all evaluated at the old time value and form the explicit portion of the mass creation term, while the enthalpies are evaluated at the new time value, forming the implicit portion. This term is also multiplied by the ratio $(1-\alpha_v)(1-\alpha_v^n)$ for vaporization or α_v/α_v^n for condensation. This is done to provide an implicit ramp that will cause the interfacial area to go to zero as all of the donor phase is depleted. An explicit ramp is also applied to the product $(h_i A_i)^n$ to cause it to go to zero as the volume fraction of the donor phase approaches zero. The entrainment rate is explicit and is also multiplied by implicit and explicit ramps that force it to zero as the donor liquid phase is depleted.⁽²⁶⁾

The last term in the equations is the phase mass source term and is evaluated at the new time. This term accounts for sources of vapor mass that are exterior to the vessel mesh. These sources includes one-dimensional component connections, mass injection boundary conditions, and pressure boundary conditions. These source terms will be defined in Section 2-3-4-1.

2-3-3-2 Conservation of Momentum Equations

Vertical Direction:

(Vapor Phase)

$$\begin{aligned}
 & \frac{[(\alpha_v \rho_v U_v)_j - (\alpha_v \rho_v U_v)_j^n] A_{m_j}}{\Delta t} = \sum_{KB=1}^{NB} \frac{[(\alpha_v \rho_v U_v)_j^n U_{v_j}^n]_{KB} A_{m_{KB}}}{\Delta X_j} \\
 & - \sum_{KA=1}^{NA} \frac{[(\alpha_v \rho_v U_v)_j^n U_{v_{j+1}}^n]_{KA} A_{m_{KA}}}{\Delta X_j} + \sum_{KLB=1}^{NKB} \frac{[(\alpha_v \rho_v U_v)_j^n W_{v_j}^n]_{LB} \frac{L_{KLB}}{2}}{\Delta X_j} \\
 & + \sum_{KLA=1}^{NKA} \frac{[(\alpha_v \rho_v U_v)_j^n W_{v_{j+1}}^n]_{KLA} \frac{L_{KLA}}{2}}{\Delta X_j} - (\alpha_v \rho_v)_j^n g A_{m_j} - \frac{(P_{j+1} - P_j)}{\Delta X_j} \alpha_{v_j}^n A_{m_j} \\
 & - K_{w,v_j} (2U_{v_j} - U_{v_j}^n) A_{m_j} - K_{i,v_e j} [2(U_v - U_t)_j - (U_v - U_t)_j^n] A_{m_j} \\
 & - K_{i,v_e j} [2(U_v - U_e)_j - (U_v - U_e)_j^n] A_{m_j} \\
 & - \frac{[\Gamma_C U_v^n - (1-\eta) \Gamma_E U_t^n - \eta \Gamma_E U_e^n]_j}{\Delta X_j} + \frac{S_{mv_j}}{\Delta X_j} + T_{v_j}^T
 \end{aligned} \tag{2-62}^{(1b,4,5,6)}$$

(Liquid Phase)

$$\begin{aligned}
& \frac{[(\alpha_t \rho_t U_t)_j - (\alpha_t \rho_t U_t)_j^n] A_{m_j}}{\Delta t} = \sum_{KB=1}^{NB} \frac{[(\alpha_t \rho_t U_t)^{\bar{n}} U_{t_j}^n]_{KB} A_{m_{KB}}}{\Delta X_j} \\
& - \sum_{KA=1}^{NA} \frac{[(\alpha_t \rho_t U_t)^{\bar{n}} U_{t,j+1}^n]_{KA} A_{m_{KA}}}{\Delta X_j} + \sum_{KLB=1}^{NKB} \frac{[(\alpha_t \rho_t U_t)^{\bar{n}} W_{t_j}^n]_{LB} \frac{L_{KLB}}{2}}{\Delta X_j} \\
& + \sum_{KLA=1}^{NKA} \frac{[(\alpha_t \rho_t U_t)^{\bar{n}} W_{t,j+1}^n]_{LA} \frac{L_{KLA}}{2}}{\Delta X_j} - (\alpha_t \rho_t)_j^n g A_{m_j} - \frac{(P_{j+1} - P_j)}{\Delta X_j} \alpha_{t_j}^n A_{m_j} \\
& - K_{w,t_j} (2U_{t_j} - U_{t_j}^n) A_{m_j} + K_{i,v,t_j} [2(U_v - U_{t_j}) - (U_v - U_{t_j})^n] A_{m_j} \\
& + \frac{(1-\eta) [\Gamma_C U_v^n - \Gamma_E U_{t_j}^n]_j}{\Delta X_j} + \frac{(S_D U_e^n - S_E U_{t_j}^n)_j}{\Delta X_j} + \frac{S_{m,t_j}^n}{\Delta X_j} + T_{t_j}^T
\end{aligned}$$

(2-63)^(1b,5,6)

(Entrained Liquid Phase)

$$\begin{aligned}
& \frac{[(\alpha_e \rho_t U_e)_j - (\alpha_e \rho_t U_e)_j^n] A_{m_j}}{\Delta t} = \frac{\sum_{KB=1}^{NB} [(\alpha_e \rho_t U_e)^{\bar{n}} U_{e_j}^n]_{KB} A_{m_{KB}}}{\Delta X_j} \\
& - \frac{\sum_{KA=1}^{NA} [(\alpha_e \rho_t U_e)^{\bar{n}} U_{e_{j+1}}^n]_{KA} A_{m_{KA}}}{\Delta X_j} + \sum_{KLB=1}^{NKB} [(\alpha_e \rho_t U_e)^{\bar{n}} W_{e_j}^n]_{LB} \frac{L_{KLB}}{2} \\
& + \sum_{KLA=1}^{NKA} [(\alpha_e \rho_t U_e)^{\bar{n}} W_{e_{j+1}}^n]_{LA} \frac{L_{KLA}}{2} - (\alpha_e \rho_t)_j^n A_{m_j} - \frac{(P_{j+1} - P_j)}{\Delta X_j} \alpha_{e_j}^n A_{m_j} \\
& - K_{w,e_j} (2U_{e_j} - U_{e_j}^n) A_{m_j} + K_{i,ve_j} [2(U_v - U_{e_j}) - (U_v - U_{e_j})^n] A_{m_j} \\
& + \frac{\eta [\Gamma_c U_v^n - \Gamma_e U_e^n]_j}{\Delta X_j} - \frac{(S_D U_e^n - S_E U_t^n)_j}{\Delta X_j} - \frac{S_{me_j}^n}{\Delta X_j}
\end{aligned} \tag{2-64}^{(1b,6)}$$

$$\left[\begin{array}{l} \text{Rate of Change} \\ \text{of Vertical} \\ \text{Momentum} \\ A \frac{\partial(\alpha_k \rho_k U_k)}{\partial t} \end{array} \right] = - \left[\begin{array}{l} \text{Rate of Efflux of Momentum at Bottom of Cell.} \\ \text{Rate of Efflux of Momentum at Top of Cell.} \\ A \frac{\partial}{\partial x} (\alpha_k \rho_k U_k U_k) \end{array} \right]^{(1a)}$$

$$+ \left[\begin{array}{l} \text{Rate of Efflux of Momentum in} \\ \text{the Transverse Direction} \\ \sum_{KL} (\alpha_k \rho_k U_k W_k)_{KL} L_{KL} \end{array} \right] - \left[\begin{array}{l} \text{Gravitational} \\ \text{Force} \\ \alpha_k \rho_k g \end{array} \right]$$

$$- \left[\begin{array}{l} \text{Pressure Gradient} \\ \text{Force} \\ \alpha_k \frac{\partial P}{\partial x} \end{array} \right] - \left[\begin{array}{l} \text{Wall Shear} \\ \tau_w \end{array} \right] + \left[\begin{array}{l} \text{Interfacial Shear} \\ \tau_{i,vl} + \tau_{i,ve} \end{array} \right]$$

$$+ \left[\begin{array}{c} \text{Momentum Exchange Due} \\ \text{to Mass Transfer} \\ \text{Between Fields} \\ \Gamma U_k + S U_k \end{array} \right] + \left[\begin{array}{c} \text{Momentum Source Term} \\ S_m \end{array} \right] + \left[\begin{array}{c} \text{Viscous and Turbulent} \\ \text{Shear Stress} \\ \nabla \cdot [\alpha_k (\sigma_k + T_k^T)] \end{array} \right]$$

The rate of momentum efflux in the vertical direction is given as the sum of the momentum entering (or leaving) the cell through all vertical connections. The total number of momentum mesh cells facing the top of the cell is NA and the total facing the bottom of the cell is NB. The rate of momentum efflux in the transverse direction is given as the sum of the momentum entering (or leaving) the cell through all transverse connections. The total number of transverse connections to the top half of the momentum cell is NKA. The total number of connections to the bottom half of the cell is NKB. To achieve stability with this semi-implicit formulation of the momentum equation, donor cell momentum, $(\alpha_k \rho_k u_k)^{\bar{a}}$, is convected by the velocities at the momentum cell face through the minimum area of the connections at the momentum cell face. That is, the flow area $A_{m_{KB}}$ is selected as the minimum of the flow area in momentum cell j and in the cell below, $j - 1$. Similarly, the flow area $A_{m_{KA}}$ is selected as the minimum of the flow area in cell j and the cell above it, $j + 1$.

A simple linear average between adjacent momentum cell velocities is taken to obtain the velocity at momentum cell faces since velocities are not computed at this location:

$$U_j = \frac{U_j + U_{j-1}}{2} \quad (2-65)$$

Likewise, linear averages are used to obtain other variables at a location where they are not defined.⁽²⁷⁾ The void fraction of the momentum cell is given as

$$\alpha_j = \frac{\alpha_j + \alpha_{j+1}}{2} \quad (2-66)$$

and the density is given as

$$\rho_j = \frac{\rho_j + \rho_{j+1}}{2} \quad (2-67)$$

Velocities are obtained from the flow computed by the mass flowrate, $(\alpha_k \rho_k U_k A_m)_j$, by dividing it by the momentum cell macroscopic density and momentum cell area

$$U_{k_j} = \frac{(\alpha_k \rho_k U_k A_m)_j}{(\alpha_k \rho_k A_m)_j} \quad (2-68)$$

The pressures in the pressure force term are taken at the new time, as are the velocities in the wall shear and interfacial shear terms. The shear terms have been weighted toward the new time velocity by differencing them in the form: $K(2U - U^n)$. All other terms and variables are computed using old time values. The donor phase momentum is convected during mass exchange between fields. The explicit viscous and turbulent shear stresses will be expanded in the next section.

Transverse Direction:

(Vapor Phase)

$$\begin{aligned}
 & \frac{\left[(\alpha_v \rho_v W_v) - (\alpha_v \rho_v W_v)^n \right]_J L_J \Delta X_J}{\Delta t} = \frac{\sum_{KL=1}^{NKJ} \left[(\alpha_v \rho_v W_v)^n_{v_{KL}} W_{v_{KL}}^n L_{KL} \right] \Delta X_J}{\Delta Z_J} \\
 & - \frac{\sum_{KL=1}^{NKJJ} \left[(\alpha_v \rho_v W_v)^n_{v_{KL}} W_{v_{KL}}^n L_{KL} \right] \Delta X_J}{\Delta Z_J} + \frac{\sum_{KL=1}^{NG} \left[(\alpha_v \rho_v W_v)^n_{v_{KL}} W_{v_{KL}}^{on} \frac{L_{KL}}{2} \right] \Delta X_J}{\Delta Z_J} \\
 & + \frac{\sum_{IB=1}^{NCB} \left[(\alpha_v \rho_v W_v)^n_{v_{IB}} U_{v_{IB}}^n A_{Z_{IB}} \right]}{\Delta Z_J} - \frac{\sum_{IA=1}^{NCA} \left[(\alpha_v \rho_v W_v)^n_{v_{IA}} U_{v_{IA}}^n A_{Z_{IA}} \right]}{\Delta Z_J} \\
 & - \frac{\alpha_{v_{II-JJ}}^n (P_{JJ} - P_{II}) L_J \Delta X_J}{\Delta Z_J} - K_{wZv_J} \left(2W_{v_J} - W_{v_J}^n \right) - K_{iZv_J} \left[2(W_v - W_t)_J - (W_v - W_t)_J^n \right] \\
 & - K_{iZve_J} \left[2(W_v - W_e)_J - (W_v - W_e)_J^n \right] - \frac{\left[\Gamma_C W_v^n - (1-\eta) \Gamma_E W_t^n - \eta \Gamma_E W_e^n \right]_J}{\Delta Z_J} + \frac{S_{mv_J}^n}{\Delta Z_J} + T_{v_J}^T
 \end{aligned} \tag{2-69}^{(1c,5)}$$

where:

$$A_{Z_{IB(A)}} = \left(\frac{L \Delta Z}{2} \right)_{IB(A)}$$

(Liquid Phase)

$$\begin{aligned}
& \frac{[(\alpha_i \rho_i W_i) - (\alpha_i \rho_i W_i)^n]_J L_J \Delta X_J}{\Delta t} = \frac{\sum_{KL=1}^{NKIJ} [(\alpha_i \rho_i W_i)_J^{\bar{n}} W_{iL}^n L_{KL}] \Delta X_J}{\Delta Z_J} \\
& - \frac{\sum_{KL=1}^{NKJJ} [(\alpha_i \rho_i W_i)_J^{\bar{n}} W_{iL}^n L_{KL}] \Delta X_J}{\Delta Z_J} + \frac{\sum_{KL=1}^{NG} [(\alpha_i \rho_i W_i)_J^{\bar{n}} W_{iL}^{on} \frac{L_{KL}}{2}] \Delta X_J}{\Delta Z_J} \\
& + \frac{\sum_{IB=1}^{NCB} [(\alpha_i \rho_i W_i)_J^{\bar{n}} U_{iB}^n A_{Z_{IB}}]}{\Delta Z_J} - \frac{\sum_{IA=1}^{NCA} [(\alpha_i \rho_i W_i)_J^{\bar{n}} U_{iA}^n A_{Z_{IA}}]}{\Delta Z_J} \\
& - \frac{\alpha_{iII-J}^n (P_{JJ} - P_{II}) L_J \Delta X_J}{\Delta Z_J} - K_{wZ,J} (2W_{iJ} - W_{vJ}^n) L_{KL} \Delta X_J \\
& + K_{iZ,v,J} [2(W_v - W_{iJ}) - (W_v - W_{iJ})^n] L_{KL} \Delta X_J \\
& - \frac{[(1-\eta) \Gamma_C W_v^n - (1-\eta) \Gamma_E W_{iJ}^n]}{\Delta Z_J} + \frac{S_D W_e^n - S_E W_{iJ}^n}{\Delta Z_J} + \frac{S_{mt,J}^n}{\Delta Z_J} + T_{iJ}^T
\end{aligned} \tag{2-70}^{(1c,5,7)}$$

(Entrained Liquid Phase)

$$\begin{aligned}
& \frac{\left[(\alpha_e \rho_t W_e) - (\alpha_e \rho_t W_e)^n \right]_J L_J \Delta X_J}{\Delta t} = \frac{\sum_{KL=1}^{NKIJ} \left[(\alpha_e \rho_t W_e)_J^{\bar{i}} W_{e_{KL}}^n L_{KL} \right] \Delta X_J}{\Delta Z_J} \\
& - \frac{\sum_{KL=1}^{NKIJ} \left[(\alpha_e \rho_t W_e)_J^{\bar{i}} W_{e_{KL}}^n L_{KL} \right] \Delta X_J}{\Delta Z_J} + \frac{\sum_{KL=1}^{NG} \left[(\alpha_e \rho_t W_e)_J^{\bar{i}} W_{e_{KL}}^{on} \frac{L_{KL}}{2} \right] \Delta X_J}{\Delta Z_J} \\
& + \frac{\sum_{IB=1}^{NCB} \left[(\alpha_e \rho_t W_e)_J^{\bar{i}} U_{e_{IB}}^n A_{Z_{IB}} \right]}{\Delta Z_J} - \frac{\sum_{IA=1}^{NCA} \left[(\alpha_e \rho_t W_e)_J^{\bar{i}} U_{e_{IA}}^n A_{Z_{IA}} \right]}{\Delta Z_J} \\
& - \frac{\alpha_{e_{II-J}}^n (P_{JJ} - P_{II}) L_J \Delta X_J}{\Delta Z_J} - K_{wZe_J} (2W_{e_J} - W_{e_J}^n) L_{KL} \Delta X_J \\
& + K_{iZve_J} \left[2(W_v - W_{e_J}) - (W_v - W_{e_J})^n \right] L_{KL} \Delta X_J \\
& + \frac{(\eta \Gamma_C W_v^n - \eta \Gamma_E W_e^n)_J}{\Delta Z_J} - \frac{S_D W_e^n - S_E W_t^n}{\Delta Z_J} + \frac{S_{me_J}^n}{\Delta Z_J Z_J} +
\end{aligned}
\tag{2-71}^{(1c,7)}$$

$$\begin{aligned}
& \left[\begin{array}{l} \text{Rate of Change} \\ \text{of Transverse} \\ \text{Momentum} \end{array} \right] = - \left[\begin{array}{l} \text{Rate of Transverse} \\ \text{Momentum Efflux} \\ \text{by Transverse Convection} \end{array} \right] + \left[\begin{array}{l} \text{Rate of Transverse} \\ \text{Momentum Efflux} \\ \text{by Orthogonal} \\ \text{Transverse Convection} \end{array} \right] \\
& \left[A_z \frac{\partial(\alpha_k \rho_k W_k)}{\partial t} \right] = - \left[\frac{\partial(\alpha_k \rho_k W_k W_k A_z)}{\partial Z} \right] + \left[\sum_{NK} (\alpha_k \rho_k W_k W_k^o L_g) \right] \\
& + \left[\begin{array}{l} \text{Rate of Transverse} \\ \text{Momentum} \\ \text{by Vertical Convection} \end{array} \right] - \left[\begin{array}{l} \text{Pressure Gradient}^{(1d)} \\ \text{Force} \end{array} \right] - \left[\begin{array}{l} \text{Transverse} \\ \text{Wall Shear} \end{array} \right] \\
& + \left[\frac{\partial}{\partial X} \alpha_k \rho_k W_k U_k A_z \right] - \left[\alpha_k A_z \frac{\partial P}{\partial Z} \right] - \left[\tau_{wz}''' A_z \right] \\
& + \left[\begin{array}{l} \text{Interfacial Drag Between} \\ \text{Vapor and Continuous Liquid} \end{array} \right] + \left[\begin{array}{l} \text{Interfacial Drag Between} \\ \text{Vapor and Drops} \end{array} \right] \\
& + \left[\tau_{iz,vt}''' A_z \right] + \left[\tau_{iz,ve}''' A_z \right] \\
& + \left[\begin{array}{l} \text{Transverse Momentum} \\ \text{Exchange Due to Mass} \\ \text{Transfer Between Fields} \end{array} \right]^{(4)} + \left[\begin{array}{l} \text{Transverse Momentum} \\ \text{Source Term} \end{array} \right] + \left[\begin{array}{l} \text{Viscous and Turbulent} \\ \text{Shear Stress} \end{array} \right] \\
& + \left[\Gamma W_k + S W_k \right] + \left[S_m \right] + \left[\nabla \cdot \left[\alpha_k \left(\underline{\underline{g}}_k + \underline{\underline{T}}_k^T \right) \right] \right]
\end{aligned}$$

As in the vertical momentum equations, the pressures in the pressure force term and the velocities in the wall and interfacial drag term are the new time values, while all other terms and variables are computed using old time values. The rate of the momentum efflux by transverse convection is given as the sum of the momentum entering (or leaving) the cell through all transverse connections. Momentum convected by transverse velocities (that are in the direction of the transverse velocity being solved for) is the sum of the momentum entering (or leaving) through mesh cell faces connected to the face of the mesh cell for which the momentum equation is being solved. NKII is the number of mesh cells facing the upstream face of the mesh cell and NKJJ is the number facing the downstream face of the mesh cell. Momentum convected out the sides of the mesh cell by velocities that are orthogonal to the velocity to be solved for, but lying in the same horizontal plane, is given by the sum of the momentum convected into (or out of) cells connected to the sides of the transverse momentum mesh cell. The number of cells connected to the mesh cell under consideration, whose velocities are orthogonal to its velocity, is given by NG. The momentum convected by vertical velocities through the top and bottom of the mesh cell is the sum of the momentum convected into (or out of) cells connected to the top and bottom of the mesh cell. This momentum depends on the number of cells connected to the top (NCA) and bottom (NCB) of the mesh cell.

A simple linear average is used to obtain velocities at mesh cell faces:

$$W_{L_{II}} = \frac{W_{J_{II}} + W_J}{2} \quad (2-72)$$

Linear averages also are used to obtain other variables at a location where they are not defined.

Velocities are obtained from the flows computed by transverse momentum equations. To obtain the velocities, the flows are divided by the momentum cell macroscopic density and transverse momentum flow area:

$$W_{k_J} = \frac{(\alpha_k \rho_k W_k L \Delta X)_J}{(\alpha_k \rho_k L \Delta X)_J} \quad (2-73)$$

Donor cell differencing is used for all convective terms and the donor phase momentum is convected in the mass transfer terms. The viscous and turbulent shear stresses are discussed in Section 2-3-4.

2-3-3-3 Conservation of Energy Equations

Vapor Energy Equation:

$$\begin{aligned} & \frac{[(\alpha_v \rho_v H_v)_J - (\alpha_v \rho_v H_v)_J^n] A_{c_J}}{\Delta t} = \\ & \frac{\sum_{KB=1}^{NB} [(\alpha_v \rho_v H_v)^i U_{v_{j-1}} A_{m_{j-1}}]_{KB} - \sum_{KA=1}^{NA} [(\alpha_v \rho_v H_v)^i U_{v_j} A_{m_j}]_{KA}}{\Delta X_J} \quad (2-74)^{(8,9,10)} \\ & + \sum_{KL=1}^{NKK} L_{KL} [(\alpha_v \rho_v H_v)^i W_{v_L}]_J + \frac{\Gamma_J H_{g_J}}{\Delta X_J} + \frac{q_{iv_J}}{\Delta X_J} + \frac{Q_{wv_J}^n}{\Delta X_J} + \frac{S_{ev}}{\Delta X_J} + \frac{Q_{wv_J}^{Tn}}{\Delta X_J} + \frac{\alpha_{v_J}^n (P - P^n)_J A_{c_J}}{\Delta t} \end{aligned}$$

Liquid Energy Equation:

$$\frac{\left\{ \left[(\alpha_t + \alpha_e) \rho_t H_t \right]_J - \left[(\alpha_e + \alpha_t) \rho_t H_t \right]_J^n \right\} A_{c_j}}{\Delta t} =$$

(2-75)^(8,9,10)

$$\begin{aligned} & \frac{1}{\Delta X_j} \left\{ \sum_{KB=1}^{NB} \left[(\alpha_t \rho_t H_t)^i U_{t_{j-1}} A_{m_{j-1}} + (\alpha_e \rho_t H_t)^i U_{e_{j-1}} A_{m_{j-1}} \right]_{KB} - \sum_{KA=1}^{NA} \left[(\alpha_t \rho_t H_t)^i U_{t_j} A_{m_j} \right. \right. \\ & \quad \left. \left. + (\alpha_e \rho_t H_t)^i U_{e_j} A_{m_j} \right]_{KA} \right\} + \sum_{KL=1}^{NKK} L_{KL} \left[(\alpha_t \rho_t H_t)^i W_{t_{KL}} + (\alpha_e \rho_t H_t)^i W_{e_{KL}} \right]_J \\ & - \frac{\Gamma_j H_{f_j}}{\Delta X_j} + \frac{q_{it_j}}{\Delta X_j} + \frac{Q_{wt_j}^n}{\Delta X_j} + \frac{S_{et}}{\Delta X_j} + \frac{Q_{wt_j}^{Tn}}{\Delta X_j} + \frac{\alpha_{t_j}^n (P - P^n)_j A_{c_j}}{\Delta t} \end{aligned}$$

$$\left[\begin{array}{c} \text{Rate of Change of Enthalpy} \\ A \frac{\partial}{\partial t} (\alpha_k \rho_k H_k) \end{array} \right] = - \left[\begin{array}{c} \text{Rate of Efflux of Enthalpy} \\ \text{in the Vertical Direction} \\ \frac{\partial}{\partial X} (A \alpha_k \rho_k H_k U_k) \end{array} \right]^{(1e)}$$

$$+ \left[\begin{array}{c} \text{Rate of Efflux of Enthalpy} \\ \text{in the Transverse Direction} \\ \sum_{KL} (\alpha_k \rho_k H_k W_k)_{KL} L_{KL} \end{array} \right] + \left[\begin{array}{c} \text{Energy Efflux Due To Mass} \\ \text{Transfer Between Fields} \\ \Gamma'_k H_k \end{array} \right]$$

$$+ \left[\begin{array}{c} \text{Interfacial Heat} \\ \text{Transfer} \\ q_i' \end{array} \right] + \left[\begin{array}{c} \text{Heat Addition} \\ \text{from Solid} \\ Q_w \end{array} \right] + \left[\begin{array}{c} \text{Fluid Convection} \\ \text{and Turbulent} \\ \text{Heat Flux} \\ \nabla \cdot \left[\alpha_k (q_k + q_k^T) \right] \end{array} \right]^{(1e)} + \left[\begin{array}{c} \text{Pressure} \\ \text{Derivative} \\ A \alpha_k \frac{\partial P}{\partial t} \end{array} \right]^{(1e)}$$

Again, the rate of energy efflux in the transverse direction is the sum of all transverse connections on all faces of the cell; the rate of energy efflux in the vertical direction is the sum of all connections to the top and bottom of the cell. New time velocities convect the donor cell $(\alpha_k \rho_k H_k)^i$, which is evaluated using old time values. New time enthalpies are convected in the phase change term. The interfacial heat transfer term, like the vapor generation term, has an implicit temperature difference and an explicit heat transfer

coefficient and interfacial area. The wall heat transfer is explicit. The energy source terms corresponding to the mass source terms will be defined in the next section. The fluid conduction and turbulent heat flux are explicit and will be expanded in Section 2-3-4.

2-3-4 Source, Viscous, and Turbulence Terms

Terms not fully expanded in the presentation of the finite-difference equations in Section 2-3-3 are presented in this section. These include the mass, energy, and momentum source terms, the viscous shear stress tensors, the turbulent shear stress tensors, the fluid conduction vector, and the turbulent heat flux vector.

2-3-4-1 Mass, Energy, and Momentum Source Terms

Two types of source terms are required for the mass, energy, and momentum finite-difference equations. The first type is associated with one-dimensional component connections to the vessel mesh, and the second type is associated with arbitrary boundary conditions that may be specified anywhere in the vessel mesh.

Vessel Connection Source Terms

The vessel connection energy and mass source terms have an implicit and an explicit term arising from the five-equation drift flux model used in the one-dimensional components. The mixture velocity, U_m , in the source terms is taken at the new time and represents the implicit portion of the source term. The donor cell quantities (denoted by the \tilde{n} superscript) and the relative velocity, U_r , are computed using currently known values and are therefore explicit. The donor cell is determined by the sign of the mixture and relative velocities, respectively. If flow is leaving the vessel, then vessel properties are used. If flow is entering the vessel, then properties in the one-dimensional component are used. The finite-difference form of the source terms is as follows:

Vapor Mass Source Term: [

$$]^{a,c} (2-76)^{(32)}$$

Liquid Mass Source Term: [

$$]^{a,c} (2-77)^{(11)}$$

Entrained Liquid Mass Source Term: [

] ^{a,c} (2-78)

Vapor Energy Source Term: [

] ^{a,c} (2-79)⁽¹²⁾

Liquid Energy Source Term: [

] ^{a,c} (2-80)⁽¹²⁾

The velocities are calculated at the junction between the vessel and the one-dimensional component. They are calculated using the five-equation drift flux model, hence the subscript *p* (for pipe), and are based on the flow area at the junction, A_{jun} .

Liquid flowing from a 1-D component to the vessel is apportioned between the continuous and dispersed fields in several different ways, depending on user specified options. These options are:

OPTION 1: [

] ^{a,c}.

OPTION 2: [

] ^{a,c}.

OPTION 3: [

] ^{a,c}.

Option 1 is used for all PWR and experimental validation calculations.

The momentum source terms for the vessel connections are somewhat more complex, as they depend on the orientation of the pipe connection. Both horizontal and vertical pipes may be connected to the vessel mesh. However, only one pipe connection is allowed per vessel mesh cell. In all cases it has been assumed that the pipe is normal to the face of the vessel mesh cell.⁽²⁹⁾ The momentum sources are as follows:

Transverse Momentum Convected Out a Vertical Loop

$$\Omega_{mv} = \begin{cases} - (\alpha_v \rho_v W_v)_J^i U_{vp} A_{jun} & \text{if flow is out of vessel } (U_{vp} \text{ positive}) \\ 0 & \text{if flow is into vessel } (U_{vp} \text{ negative}) \end{cases} \quad (2-81)^{(1f)}$$

$$\Omega_{mt} = \begin{cases} - (\alpha_t \rho_t W_t)_J^i U_{tp} A_{jun} & U_{tp} > 0 \\ 0 & U_{tp} < 0 \end{cases} \quad (2-82)^{(1f)}$$

$$\Omega_{me} = \begin{cases} - (\alpha_e \rho_e W_e)_J^i U_{ep} A_{jun} & U_{ep} > 0 \\ 0 & U_{ep} < 0 \end{cases} \quad (2-83)^{(1f)}$$

Transverse Momentum Convected by a Horizontal Loop

Normal of cell face is orthogonal to the pipe axis:⁽¹³⁾

$$\Omega_{mv} = \begin{cases} - (\alpha_v \rho_v W_v)_J^i W_{vj}^n L_g \Delta X & \text{if flow is out of vessel } (U_{vp} \text{ positive}) \\ 0 & \text{if flow is into vessel } (U_{vp} \text{ negative}) \end{cases} \quad (2-84)^{(1f)}$$

$$\Omega_{mt} = \begin{cases} - (\alpha_t \rho_t W_t)_J^i W_{tj}^n L_g \Delta X & U_{tp} > 0 \\ 0 & U_{tp} < 0 \end{cases} \quad (2-85)^{(1f)}$$

$$\Omega_{me} = \begin{cases} - (\alpha_e \rho_e W_e)_J^i W_{ej}^n L_g \Delta X & U_{ep} > 0 \\ 0 & U_{ep} < 0 \end{cases} \quad (2-86)^{(1f)}$$

Normal of cell face is parallel to the pipe axis:

$$\Omega_{mv} = (\alpha_v \rho_v W_v)^{\bar{n}} \left(\frac{W_{v_j} + U_{v_p}}{2} \right)^n A_z \quad (2-87)$$

$$\Omega_{ml} = (\alpha_l \rho_l W_l)^{\bar{n}} \left(\frac{W_{l_j} + U_{l_p}}{2} \right)^n A_z \quad (2-88)$$

$$\Omega_{me} = (\alpha_e \rho_e W_e)^{\bar{n}} \left(\frac{W_{e_j} + U_{e_p}}{2} \right)^n A_z \quad (2-89)$$

In the latter case, the donor cell quantity $(\alpha \rho W)^{\bar{n}}$ is computed using pipe variables, if the flow is into the vessel, or vessel variables, if the flow is out of the vessel. The area A_z , through which momentum is convected, is the minimum of the pipe flow area, A_{jun} , and the area of the vessel mesh cell face $L_g \Delta X$. The same logic holds for the following source term.

Vertical Momentum Convected Out a Vertical Loop

$$\Omega_{mv} = (\alpha_v \rho_v U_v)^{\bar{n}} \left(\frac{U_{v_j} + U_{v_p}}{2} \right)^n A_x \quad (2-90)$$

$$\Omega_{ml} = (\alpha_l \rho_l U_l)^{\bar{n}} \left(\frac{U_{l_j} + U_{l_p}}{2} \right)^n A_x \quad (2-91)$$

$$\Omega_{me} = (\alpha_e \rho_e U_e)^{\bar{n}} \left(\frac{U_{e_j} + U_{e_p}}{2} \right)^n A_x \quad (2-92)$$

Vertical Momentum Convected by a Horizontal Loop

$$\Omega_{mv} = \begin{cases} - (\alpha_v \rho_v U_v)_j^n U_{v_p}^n A_m & U_{v_p} > 0 \\ 0 & U_{v_p} < 0 \end{cases} \quad (2-93)$$

$$\Omega_{ml} = \begin{cases} -(\alpha_l \rho_l U_l)_j^n U_{lp}^n A_m & U_{lp} > 0 \\ 0 & U_{lp} < 0 \end{cases} \quad (2-94)$$

$$\Omega_{me} = \begin{cases} -(\alpha_e \rho_e U_e)_j^n U_{ep}^n A_m & U_{ep} > 0 \\ 0 & U_{ep} < 0 \end{cases} \quad (2-95)$$

The pipe velocities are computed as follows from the mixture and relative velocities used in the five-equation drift flux model:

$$U_{lp} = U_m - \frac{\alpha \rho_g}{\rho_m} U_r \quad (2-96)$$

$$U_{vp} = U_m + \frac{(1-\alpha) \rho_l}{\rho_m} U_r \quad (2-97)$$

The pipe velocity for the entrained liquid phase is always assumed to be equal to the liquid velocity in the pipe, since only two velocity fields (vapor and liquid) are available in the one-dimensional components.

2-3-4-2 Boundary Condition Source Terms

There are five basic types of boundary conditions that may be specified within the vessel mesh. The first type allows the user to specify the pressure and the mixture enthalpy in any cell. The normal momentum equations are then solved on the cell faces to obtain flows into or out of the cell. If the flow is out of the cell, properties specified within the cell are convected to surrounding cells. If the flow is into the cell, properties of surrounding cells are convected into the specified cell. However, since the properties of the cell are specified, the pressure, temperature, and void fractions do not change accordingly, so the pressure boundary condition can act as a mass, energy, and momentum sink, if flow is into the cell, or source, if flow is out of the cell.

The second type of boundary condition allows the user to specify the mixture enthalpy and the continuity mass flow rate at the top of the cell. It is assumed that all three phases have the same velocity at the cell face. No momentum solution is performed at the top of the cell for this case since the flow is specified. Otherwise, the boundary condition behaves in the same way as the first type of boundary condition, acting as a source (or sink) of mass, momentum, and energy, depending on the direction of flow.

The third type of boundary condition specifies the flow on any mesh cell face, and therefore does not produce any mass, momentum, or energy sources.

The fourth type of boundary condition allows the user to specify a mass and energy source in any computational cell without changing the computed fluid properties within the cell. Again, all three phases are assumed to travel at the mixture velocity, and the amount of flow is determined by the volume fraction of each phase specified in the boundary condition. Momentum of this source is added only if the flow is in the transverse direction and into the vessel mesh, or if flow is out of the mesh.

The fifth type of boundary condition is not used in any of the WCOBRA/TRAC test simulations or in a PWR analysis, but is described here for completeness. This final type of boundary condition allows the user to specify a pressure sink to be connected to any cell. A simple momentum equation is solved between the sink pressure and the cell pressure, and the resulting flow produces a mass, momentum, and energy sink if flow is out of the vessel, and a mass and energy source if the flow is into the vessel. The sink vapor momentum equation is as follows:

$$\begin{aligned}
 (\alpha_v \rho_v W_v A)_{SINK} &= (\alpha_v \rho_v v_v A)_{SINK}^n + \frac{\Delta t}{\Delta X} A_{SINK} (P_{SINK} - P_J)^n \\
 &- K_{w,v,SINK} U_{v,SINK}^n - K_{i,v} (U_v - U_i)_{SINK} - K_{i,v,e} (U_v - U_e)_{SINK}
 \end{aligned}
 \quad (2-98)$$

Transverse and vertical momentum is convected out of the vessel mesh by the sink velocity computed from the above equation in the same way that vessel/pipe connections convect momentum from the mesh. The same equations may be used to represent the sink momentum sources if the pipe velocity is replaced with the sink velocity in the source equations.

2-3-4-3 Turbulent Shear Stress Tensors and Heat Flux Vectors

The turbulent shear stress tensors and heat flux vectors are used only when the turbulence models in WCOBRA/TRAC are desired by the user. In the simulations of experiments and PWR analyses reported later in this document, the turbulence models are not used. For completeness, however, the turbulent shear stress and heat flux terms are described here. The viscous and turbulent shear stress tensors represented in the finite-difference equation given in Section 2-3-3 by T_{kj}^T are expanded in this section. This term represents the viscous and turbulent stress tensors, $\nabla \cdot [\alpha_k (\sigma_k + T_k^T)]$, of the partial differential equations. The viscous stress tensor may be written as:

$$\underline{\underline{\sigma}}_k = \begin{bmatrix} \sigma_{k_{xx}} & \sigma_{k_{xy}} & \sigma_{k_{xz}} \\ \sigma_{k_{yx}} & \sigma_{k_{yy}} & \sigma_{k_{yz}} \\ \sigma_{k_{zx}} & \sigma_{k_{zy}} & \sigma_{k_{zz}} \end{bmatrix}
 \quad (2-99)$$

The turbulent stress tensor \underline{T}_k^T may be written in a similar way. Further,

$$\begin{aligned}
 \nabla \cdot [\alpha_k (\underline{\sigma}_k + \underline{T}_k^T)] &= \left\{ \frac{\partial}{\partial x} [\alpha_k (\sigma_{k_{xx}} + T_{k_{xx}}^T)] + \frac{\partial}{\partial y} [\alpha_k (\sigma_{k_{yx}} + T_{k_{yx}}^T)] \right. \\
 &\quad + \frac{\partial}{\partial z} [\alpha_k (\sigma_{k_{zx}} + T_{k_{zx}}^T)] \left. \right\} i + \left\{ \frac{\partial}{\partial x} [\alpha_k (\sigma_{k_{xy}} + T_{k_{xy}}^T)] \right. \\
 &\quad + \frac{\partial}{\partial y} [\alpha_k (\sigma_{k_{yy}} + T_{k_{yy}}^T)] + \frac{\partial}{\partial z} [\alpha_k (\sigma_{k_{zy}} + T_{k_{zy}}^T)] \left. \right\} j \\
 &\quad + \left\{ \frac{\partial}{\partial x} [\alpha_k (\sigma_{k_{xz}} + T_{k_{xz}}^T)] + \frac{\partial}{\partial y} [\alpha_k (\sigma_{k_{yz}} + T_{k_{yz}}^T)] + \frac{\partial}{\partial z} [\alpha_k (\sigma_{k_{zz}} + T_{k_{zz}}^T)] \right\} k
 \end{aligned} \tag{2-100}$$

The coordinate system used is shown in Figure 2-1.

The first subscript on the shear stress denotes the face the stress is acting on; the second subscript denotes the direction the stress acts in. (For example, $\sigma_{k_{ij}}$ is the shear stress acting on face i in the j direction.)

The viscous and turbulent stresses are defined in terms of the bulk deformation tensor, \underline{D}_{k_B} , given by

$$\underline{D}_{k_B} = \frac{1}{2} [\nabla \underline{u} + (\nabla \underline{u})^t] \tag{2-101}$$

or

$$\underline{D}_{k_B} = \begin{pmatrix} \frac{\partial u}{\partial x} & \frac{1}{2} \left(\frac{\partial u}{\partial y} + \frac{\partial v}{\partial x} \right) & \frac{1}{2} \left(\frac{\partial u}{\partial z} + \frac{\partial w}{\partial x} \right) \\ \frac{1}{2} \left(\frac{\partial u}{\partial y} + \frac{\partial v}{\partial x} \right) & \frac{\partial v}{\partial y} & \frac{1}{2} \left(\frac{\partial v}{\partial z} + \frac{\partial w}{\partial y} \right) \\ \frac{1}{2} \left(\frac{\partial u}{\partial z} + \frac{\partial w}{\partial x} \right) & \frac{1}{2} \left(\frac{\partial v}{\partial z} + \frac{\partial w}{\partial y} \right) & \frac{\partial w}{\partial z} \end{pmatrix} \tag{2-102}$$

Eliminating the normal stresses such that the diagonal term is zero produces the deleted bulk deformation tensor $\underline{D}_{k_B}^*$.

Neglecting the viscous contribution to the normal stresses and eliminating the normal stress due to pressure already accounted for in the finite-difference equation leaves

$$\underline{\underline{\sigma}}_k = 2\mu \underline{\underline{D}}_{k_B}^* \quad (2-103)$$

Thus,

$$\sigma_{k_{xy}} = \sigma_{k_{yx}} = \mu \left(\frac{\partial u}{\partial y} + \frac{\partial v}{\partial x} \right) \quad (2-104)$$

$$\sigma_{k_{xz}} = \sigma_{k_{zx}} = \mu \left(\frac{\partial u}{\partial z} + \frac{\partial w}{\partial x} \right) \quad (2-105)$$

$$\sigma_{k_{yz}} = \sigma_{k_{zy}} = \mu \left(\frac{\partial v}{\partial z} + \frac{\partial w}{\partial y} \right) \quad (2-106)$$

The turbulent stress tensor is given by

$$\underline{\underline{T}}^T = -P_k^T \underline{\underline{E}}_k + 2\mu_k^T \underline{\underline{D}}_{k_B}^* \quad (2-107)$$

P^T is the turbulent pressure. $\underline{\underline{E}}$ is the anisotropy tensor which is assumed to be equal to the unit tensor in general. μ^T is the turbulent or "eddy" viscosity. The above tensor, $\underline{\underline{T}}^T$, may be written in matrix form as

$$\underline{\underline{T}}_k^T = \begin{bmatrix} -P_k^T F_{k_{xx}} & \mu_k^T \left(\frac{\partial u}{\partial y} + \frac{\partial v}{\partial x} \right) & \mu_k^T \left(\frac{\partial u}{\partial z} + \frac{\partial w}{\partial x} \right) \\ \mu_k^T \left(\frac{\partial u}{\partial y} + \frac{\partial v}{\partial x} \right) & -P_k^T F_{k_{yy}} & \mu_k^T \left(\frac{\partial v}{\partial z} + \frac{\partial w}{\partial y} \right) \\ \mu_k^T \left(\frac{\partial u}{\partial z} + \frac{\partial w}{\partial x} \right) & \mu_k^T \left(\frac{\partial v}{\partial z} + \frac{\partial w}{\partial y} \right) & -P_k^T F_{k_{zz}} \end{bmatrix} \quad (2-108)$$

The turbulent viscosity is given by

$$\mu_k^T = \rho_k \ell_m^2 \sqrt{2\underline{\underline{D}}_{k_B}^* : \underline{\underline{D}}_{k_B}^*} \quad (2-109)$$

and the turbulent pressure by

$$P_k^T = \rho_k \ell_m^2 \left(2\underline{\underline{D}}_{k_B}^* : \underline{\underline{D}}_{k_B}^* \right) \quad (2-110)$$

The double dot product of two second order tensors $\underline{\underline{A}}$ and $\underline{\underline{B}}$ is defined as

$$\underline{\underline{A}} : \underline{\underline{B}} = A_{ij} B_{ji} \quad (2-111)$$

In this case, this gives

$$2\underline{\underline{D}}_{k_B}^* : \underline{\underline{D}}_{k_B}^* = \left(\frac{\partial u}{\partial y} + \frac{\partial v}{\partial x} \right)^2 + \left(\frac{\partial u}{\partial z} + \frac{\partial w}{\partial x} \right)^2 + \left(\frac{\partial v}{\partial z} + \frac{\partial w}{\partial y} \right)^2 \quad (2-112)$$

Now that all of the terms for the viscous and turbulent shear stresses have been expanded, the finite-difference form of the terms can be presented. The total force resulting from viscous and turbulent shear stresses acting on a mesh cell may be obtained using the divergence theorem:

$$\mathcal{F} = \iiint_{vol} \nabla \cdot \left[\alpha_k \left(\underline{\underline{\sigma}}_k + \underline{\underline{T}}_k^T \right) \right] d^3x = \iint_{surface} \underline{n} \cdot \left[\alpha_k \left(\underline{\underline{\sigma}}_k + \underline{\underline{T}}_k^T \right) \right] ds \quad (2-113)$$

The finite-difference approximation for this total force is

$$\begin{aligned}
 \underline{\mathcal{F}} = & i \cdot \left\{ \alpha_k \left(\sigma_{k_{xx}} + T_{k_{xx}}^T \right) |_{+x} \Delta y \Delta z - \alpha_k \left(\sigma_{k_{xx}} + T_{k_{xx}}^T \right) |_{-x} \Delta y \Delta z \right. \\
 & + \alpha_k \left(\sigma_{k_{yx}} + T_{k_{yx}}^T \right) |_{+y} \Delta x \Delta z - \alpha_k \left(\sigma_{k_{yx}} + T_{k_{yx}}^T \right) |_{-y} \Delta x \Delta z \\
 & + \alpha_k \left(\sigma_{k_{zx}} + T_{k_{zx}}^T \right) |_{+z} \Delta x \Delta y - \alpha_k \left(\sigma_{k_{zx}} + T_{k_{zx}}^T \right) |_{-z} \Delta x \Delta y \left. \right\} \\
 & + j \cdot \left\{ \alpha_k \left(\sigma_{k_{xy}} + T_{k_{xy}}^T \right) |_{+x} \Delta y \Delta z - \alpha_k \left(\sigma_{k_{xy}} + T_{k_{xy}}^T \right) |_{-x} \Delta y \Delta z \right. \\
 & + \alpha_k \left(\sigma_{k_{yy}} + T_{k_{yy}}^T \right) |_{+y} \Delta x \Delta z - \alpha_k \left(\sigma_{k_{yy}} + T_{k_{yy}}^T \right) |_{-y} \Delta x \Delta z \\
 & + \alpha_k \left(\sigma_{k_{zy}} + T_{k_{zy}}^T \right) |_{+z} \Delta x \Delta y - \alpha_k \left(\sigma_{k_{zy}} + T_{k_{zy}}^T \right) |_{-z} \Delta x \Delta y \left. \right\} \\
 & + k \cdot \left\{ \alpha_k \left(\sigma_{k_{xz}} + T_{k_{xz}}^T \right) |_{+x} \Delta y \Delta z - \alpha_k \left(\sigma_{k_{xz}} + T_{k_{xz}}^T \right) |_{-x} \Delta y \Delta z \right. \\
 & + \alpha_k \left(\sigma_{k_{yz}} + T_{k_{yz}}^T \right) |_{+y} \Delta x \Delta z - \alpha_k \left(\sigma_{k_{yz}} + T_{k_{yz}}^T \right) |_{-y} \Delta x \Delta z \\
 & + \alpha_k \left(\sigma_{k_{zx}} + T_{k_{zx}}^T \right) |_{+z} \Delta y \Delta z - \alpha_k \left(\sigma_{k_{zx}} + T_{k_{zx}}^T \right) |_{-z} \Delta x \Delta y \left. \right\} \quad (2-114)
 \end{aligned}$$

The various stresses ($\sigma_{k_{xx}}, T_{k_{xx}}^T, \sigma_{k_{yx}}, T_{k_{yx}}^T$, etc.) must be evaluated on various surfaces of vertical and transverse momentum cells. For example, the stresses acting in the vertical direction on a vertical momentum cell are shown in Figure 2-6.

The velocity gradients are calculated by taking differences between adjacent cell velocities to obtain values for $\Delta u/\Delta x$ and $\Delta w/\Delta z$ on continuity cell edges. This is illustrated in Figure 2-7.

In this figure, the velocity gradient at point A is given by

$$\left(\frac{\partial u}{\partial z} + \frac{\partial w}{\partial x} \right)_A = \left(\frac{u_2 - u_1}{\Delta l} + \frac{w_2 - w_1}{\Delta x} \right) \quad (2-115)$$

The derivatives for the other edges (B, C, D, E, F, G, H, I, J, K, L) are computed in a similar fashion and the process is repeated for other cells. If a solid surface bounds the cell in the transverse direction, it is

assumed that the velocity gradient is zero at the wall. Velocity is assumed to be zero at the wall for solid surfaces that bound the cell in a vertical direction.

The derivative at the mass cell center is obtained by taking a four-point average of the derivatives on the cell edges.

$$\begin{aligned} \left(\frac{\partial u}{\partial z} + \frac{\partial w}{\partial x} \right)_{\text{cell center}} &= \frac{1}{4} \left\{ \left(\frac{\partial u}{\partial z} + \frac{\partial w}{\partial x} \right)_A + \left(\frac{\partial u}{\partial z} + \frac{\partial w}{\partial x} \right)_B \right. \\ &\quad \left. + \left(\frac{\partial u}{\partial z} + \frac{\partial w}{\partial x} \right)_C + \left(\frac{\partial u}{\partial z} + \frac{\partial w}{\partial x} \right)_D \right\} \end{aligned} \quad (2-116)$$

The same procedure is used to find

$$\left(\frac{\partial u}{\partial y} + \frac{\partial v}{\partial x} \right) \text{ and } \left(\frac{\partial v}{\partial z} + \frac{\partial w}{\partial x} \right)$$

at the mass cell center. The quantity $2\underline{D}_{k_B}^* : \underline{D}_{k_B}^*$ at the cell center is then calculated from Equation 2-112 using these averaged derivatives. The turbulent viscosity and turbulent pressure are then calculated at the cell center using Equations 2-109 and 2-110.

The shear stress acting on the sides of the momentum cell is computed from the appropriate velocity gradients calculated on that face, and the fluid properties at these locations are computed using a four-point average of the properties in the surrounding four mass cells.

The turbulent thermal diffusivity for the mass cell center is computed from the double dot product of the deformation tensor in the same manner as the turbulent viscosity was obtained using the expression

$$\epsilon_k^T = \ell_h \ell_m \sqrt{2\underline{D}_{k_B}^* : \underline{D}_{k_B}^*} \quad (2-117)$$

The sum of the conduction and turbulent heat flux between two mass cells is then computed from

$$\left(q_{k_j} + q_{k_j}^T \right) |_{+x} = - \rho_k \left(\epsilon_k + \epsilon_k^T \right) \frac{(H_{j+1} - H_{j-1})}{\Delta x_j} \quad (2-118)$$

The heat fluxes from all surrounding cells are summed up to give the net heat flux into cell J .

Since the viscous and turbulent shear stresses are computed explicitly, the timestep is limited by the criterion

$$\Delta t < \text{minimum} \left[\frac{1}{\frac{2(\mu + \mu^T)}{\rho \Delta x^2} + \frac{u}{\Delta x}} \right]_j \quad (2-119)$$

2-4 CONSERVATION EQUATIONS FOR ONE-DIMENSIONAL COMPONENTS (MODEL BASIS)

2-4-1 Introduction

WCOBRA/TRAC uses a two-phase five-equation drift-flux model in the one-dimensional components. The hydrodynamic formulation consists of two equations for the conservation of mass, two equations for the conservation of energy, and a single equation for the conservation of momentum of the two-phase mixture. Closure of the field equations requires specification of interphase relative velocity, thermodynamic functions, interphase heat and mass transfer, and other constitutive relationships.

Each of the field equations is described below in the context of a quasi-one-dimensional flow in a pipe of non-uniform cross-sectional area. The principal assumptions that permit the field equations to be easily integrated over the cross-sectional area are: no slip at the wall and small transverse pressure gradients. The latter assumption allows the individual phase density cross-sectional profiles to be assumed flat; thus, these densities represent their own averages.

The type of averaging used for a given variable depends on the nature of the physical quantity the variable is representing. A simple area average,

$$\langle F \rangle \equiv \frac{1}{A} \int_A F dA \quad (2-120)$$

is used for phase fractions and mixture density.

Phase-fraction-weighted averages are used for individual phase velocities and phase energies.

Vapor

$$\langle\langle F \rangle\rangle \equiv \frac{\langle \alpha F \rangle}{\langle \alpha \rangle} \quad (2-121)$$

Liquid

$$\langle\langle F \rangle\rangle \equiv \frac{\langle (1-\alpha) F \rangle}{\langle 1-\alpha \rangle} \quad (2-122)$$

The averaged mixture velocity, mixture internal energy and relative velocity are defined as follows:

$$\overline{U}_m \equiv \frac{\langle \rho_m U_m \rangle}{\langle \rho_m \rangle} \quad (2-123)$$

$$\overline{e}_m \equiv \frac{\langle \rho_m e_m \rangle}{\langle \rho_m \rangle} \quad (2-124)$$

$$\overline{U}_r \equiv \langle\langle U_v \rangle\rangle - \langle\langle U_l \rangle\rangle \quad (2-125)$$

The mathematics of averaging the two-phase conservation equations over a duct of arbitrary cross-section has been dealt with by Ishii (1977) and will not be reproduced here. In the following sections, variables with an underline are vector quantities, while variables with an overline are averaged scalar quantities (see above).^(1g)

2-4-2 Conservation of Mixture Mass

The conservation of mass is provided by a mixture continuity equation

$$\frac{\partial \rho_m}{\partial t} + \nabla \cdot (\rho_m \underline{U}_m) = 0 \quad (2-126)$$

and a vapor continuity equation

$$\frac{\partial}{\partial t} (\alpha \rho_v) + \nabla \cdot (\alpha \rho_v \underline{U}_m) + \nabla \cdot (\rho_f \underline{U}_r) = \Gamma \quad (2-127)$$

where:

$$\underline{U}_r = \underline{U}_v - \underline{U}_t \quad (2-128)$$

is the interphase relative velocity and

$$\rho_f = \frac{\alpha (1-\alpha) \rho_t \rho_v}{\rho_m} \quad (2-129)^{(14)}$$

Integrating the two continuity equations over the pipe cross-sectional area and introducing the appropriate averages gives

$$\frac{\partial \langle \rho_m \rangle}{\partial t} + \frac{1}{A} \frac{\partial}{\partial X} (A \langle \rho_m \rangle \bar{U}_m) = 0 \quad (2-130)$$

$$\frac{\partial}{\partial t} (\langle \alpha \rangle \rho_v) + \frac{1}{A} \frac{\partial}{\partial X} (A \langle \alpha \rangle \rho_v \bar{U}_m) + \frac{1}{A} \frac{\partial}{\partial X} (\bar{A} \bar{\rho}_f \bar{U}_r) = \langle \Gamma \rangle \quad (2-131)$$

where $\bar{\rho}_f$ is defined as:

$$\bar{\rho}_f = \frac{\langle \alpha \rangle (1 - \langle \alpha \rangle) \rho_t \rho_v}{\langle \rho_m \rangle} \quad (2-132)^{(14)}$$

Note that Equations 2-130 and 2-131 are not equivalent to the usual one-dimensional conservation equations.⁽¹⁸⁾ These equations correctly account for transverse flows arising from axial changes in the pipe cross-sectional area. These equations are derived with no simplifying assumptions except those previously noted.

2-4-3 Conservation of Mixture Momentum

The conservation of momentum is provided by a mixture momentum equation

$$\frac{\partial}{\partial t} (\rho_m \underline{U}_m) + \nabla \cdot (\rho_m \underline{U}_m \underline{U}_m) + \nabla \cdot (\rho_f \underline{U}_r \underline{U}_r) = -\nabla P - L_{fric} + \rho_m g \cos \theta \quad (2-133)$$

where L_{fric} represents the irreversible pressure losses due to wall friction and sudden cross-sectional area changes. The viscous diffusion terms have been neglected since these are expected to be relatively small. Averaging the three-dimensional equation over the pipe area and neglecting the momentum flux covariant derivative results in

$$\begin{aligned} \frac{\partial}{\partial t} (\langle \rho_m \rangle \bar{U}_m) + \frac{1}{A} \frac{\partial}{\partial X} (A \langle \rho_m \rangle \bar{U}_m^2) + \frac{1}{A} \frac{\partial}{\partial X} (A \bar{\rho}_f \bar{U}_r^2) = \\ - \frac{\partial P}{\partial X} - \langle L_{fric} \rangle + \langle \rho_m \rangle g \cos \theta \end{aligned} \quad (2-134)$$

For ducts of circular cross-section, an analysis of the magnitude of the covariant terms is provided by Ishii (1977). For circumstances of practical interest, the covariant terms are insignificant for annular flow and are proportional to $1.5 (C_o - 1)$ for the bubbly and churn flow regimes. Here C_o is the slip distribution parameter. Thus, the relative contribution of the momentum flux derivatives could be increased by 15 percent.⁽¹⁵⁾ In view of the large momentum losses and gains in the typical geometries to which Equation 2-134 is applied, it is concluded that the covariance terms are relatively insignificant.

2-4-4 Vapor and Mixture Energy Conservation Equations

The conservation of energy is provided by a mixture energy equation

$$\begin{aligned} \frac{\partial}{\partial t} (\rho_m e_m) + \nabla \cdot (\rho_m e_m \underline{U}_m) + \nabla \cdot (\rho_f (e_v - e_l) \underline{U}_r) = \\ - P \nabla \cdot \underline{U}_m - P \nabla \cdot \left(\rho_f \left(\frac{1}{\rho_v} - \frac{1}{\rho_l} \right) \underline{U}_r \right) + q_{wf}''' + q_{wv}''' \end{aligned} \quad (2-135)$$

and a vapor energy equation

$$\begin{aligned} \frac{\partial}{\partial t} (\alpha \rho_v e_v) + \nabla \cdot (\alpha \rho_v e_v \underline{U}_m) + \nabla \cdot (\rho_f e_v \underline{U}_r) = \\ - P \frac{\partial \alpha}{\partial t} - P \nabla \cdot (\alpha \underline{U}_m) - P \nabla \cdot \left(\frac{\rho_f}{\rho_v} \underline{U}_r \right) + q_{wv}''' + q_{iv}''' + \Gamma''' H_g \end{aligned} \quad (2-136)$$

In these equations q_{wv}''' and q_{iv}''' are the rates of heat deposited in the vapor and liquid from the wall, q_{iv}''' is the rate of heat across the phase interface and $\Gamma''' H_g$ represents the increase in energy due to vapor generation. All terms associated with viscous dissipation and surface tension energy have been neglected.

Integrating the mixture energy equation over the cross-sectional area of the pipe gives

$$\begin{aligned} \frac{\partial}{\partial t} (\langle \rho_m \rangle \bar{e}_m) + \frac{1}{A} \frac{\partial}{\partial X} [A \langle \rho_m \rangle \bar{e}_m \bar{U}_m] + \frac{1}{A} \frac{\partial}{\partial X} [A \bar{\rho}_f (\langle e_v \rangle - \langle e_l \rangle) \bar{U}_r] \\ = - \frac{P}{A} \frac{\partial}{\partial X} (A \bar{U}_m) - \frac{P}{A} \frac{\partial}{\partial X} \left(A \bar{\rho}_f \left(\frac{1}{\rho_v} - \frac{1}{\rho_l} \right) \bar{U}_r \right) + \langle q_{wv}''' \rangle + \langle q_{iv}''' \rangle \end{aligned} \quad (2-137a)^{(16)}$$

and

$$\begin{aligned} \frac{\partial}{\partial t} (\langle \alpha \rangle \rho_v e_v) + \frac{\partial}{\partial X} (\langle \alpha \rangle \rho_v e_v \bar{U}_m) + \frac{\partial}{\partial X} [\bar{\rho}_f \bar{U}_r e_v] + P \frac{\partial}{\partial X} (\langle \alpha \rangle \bar{U}_m) \\ + P \frac{\partial}{\partial X} \left(\frac{\bar{\rho}_f}{\rho_v} \bar{U}_r \right) = \langle q_{wv}''' \rangle + \langle q_{iv}''' \rangle - P \frac{\partial}{\partial t} \langle \alpha \rangle + \langle \Gamma''' H_g \rangle \end{aligned} \quad (2-137b)^{(17)}$$

In developing this averaged equation from Equation 2-133, the covariant derivatives have been neglected. The magnitude of these terms can be assessed by the deviation from unity of the energy flux distribution parameters; for the vapor phase

$$C_{ev} = \frac{\langle \alpha e_v U_v \rangle}{\langle \alpha \rangle \langle e_v \rangle \langle U_v \rangle} \quad (2-138)$$

and for the liquid phase

$$C_{et} = \frac{\langle (1-\alpha) e_t U_m \rangle}{(1-\langle \alpha \rangle) \langle e_t \rangle \langle U_m \rangle} \quad (2-139)$$

Physically these parameters represent the interaction between non-uniform cross-sectional profiles for the internal energy and the velocity. For saturated conditions these parameters are effectively unity. An analysis of these parameters for circular ducts by Ishii (1977) indicates that their importance is only significant for highly non-equilibrium flows; however under these circumstances other terms will dominate in the energy equation, and thus they may still be ignored. Thus, $C_{ew} = C_{et} = 1$.

2-4-5 Closure of the Conservation Equations

The closure of Equations 2-130, 2-131, 2-134, and 2-137 is obtained with the thermodynamic relations as described in Section 10, and the specification of the relative velocity, interfacial heat and mass transfers, wall heat transfer, and wall friction. As discussed in Section 4, the effects of both local and profile slip are accounted for in the specification of the averaged relative velocity U_r .

The phase change rate is evaluated from a simple thermal energy jump relation:

$$\Gamma''' = \frac{-q_{iv}''' - q_{il}'''}{H_{fg}} \quad (2-140)$$

where:

$$q_{iv}''' = h_{iv} A_i \frac{T_{sat} - T_v}{V_c} \quad (2-141)$$

and

$$q_{il}''' = h_{il} A_i \frac{T_{sat} - T_l}{V_c} \quad (2-142)$$

are the interfacial heat transfer rates for the vapor and liquid respectively. A_i is the interfacial area, and h_{iv} and h_{il} are the interfacial heat transfer coefficients; these are discussed in Section 5.

Similarly, the wall heat transfer rate terms assume the following form:

$$q_{wv}''' = h_{wv} A_w \frac{T_w - T_v}{V_c} \quad (2-143)$$

and

$$q_{wl}''' = h_{wl} A_w \frac{T_w - T_l}{V_c} \quad (2-144)$$

The wall heat transfer coefficients are discussed in Section 6.

The wall friction term in the momentum equation assumes the form

$$L_{fric} = \frac{f_{wm}}{2D_h} \rho_m U_m |U_m| \quad (2-145)$$

where D_h is a hydraulic diameter and f_{wm} is the two-phase friction factor for the mixture.

2-5 ONE-DIMENSIONAL COMPONENT COMPUTATIONAL CELL STRUCTURE (MODEL AS CODED)

2-5-1 Introduction

A one-dimensional component is divided into a number of one-dimensional computational cells as shown in Figure 2-8. The five partial differential equations are solved using a staggered difference scheme in which the mixture velocity is obtained at the cell interfaces, and the void fraction, pressure and liquid, and vapor temperatures are obtained at the cell centers. We shall use subscript j to denote a cell centered quantity and subscripts $j-1/2$ and $j+1/2$ to denote the cell interfaces.

2-5-2 One-Dimensional Component Computational Mesh

The geometry of the mass and energy control volumes is characterized by five independent variables: axial length ΔX_j , volume V_j , cross-sectional areas at the cell faces $A_{j-1/2}$, $A_{j+1/2}$, and the hydraulic diameter D_h . All of these are specified by the user. Associated with each fluid cell is a one-dimensional heat slab. This has a surface area in contact with the fluid which is consistent with the volume and length of the energy control volume. The geometry of the heat slab is characterized by a radius and a thickness.

The momentum control volume is centered at the cell interface $j+1/2$ and has faces at the cell centers on either side i.e., at j and $j+1$. The geometry of the momentum control volume is characterized by the length,

$$\overline{\Delta X}_{j+1/2} = \frac{1}{2} (\Delta X_j + \Delta X_{j+1}) \quad (2-146)$$

volume,

$$\overline{V}_{j+1/2} = \frac{1}{2} (V_j + V_{j+1}) \quad (2-147)$$

flow areas,

$$A_j = \frac{V_j}{\Delta X_j} \quad (2-148)$$

$$A_{j+1} = \frac{V_{j+1}}{\Delta X_{j+1}} \quad (2-149)$$

and the hydraulic diameter D_h . The geometry of the momentum control volume is principally determined by the geometry of the corresponding mass and energy control volumes.

2-5-3 One-Dimensional Component Finite Difference Formulation

The one-dimensional hydrodynamic equations have been formulated in two separate finite difference forms. The first form of the difference equations is semi-implicit and has a timestep size stability limit of the form⁽¹⁹⁾

$$\Delta t < \left| \frac{\Delta X}{U_m} \right| \quad (2-150)$$

where ΔX is the cell length and U_m is the mixture velocity (see Section 2-7-3 for other timestep controls). In blowdown applications, the use of the semi-implicit scheme at break locations generally leads to prohibitively small timestep sizes due to the high velocities and fine spatial discretization

adjacent to the break. To alleviate this problem, a fully-implicit form of the finite difference equations is available for use in pipes where critical conditions are expected to occur.

Both formulations calculate certain quantities explicitly. Since the relative velocity and the two-phase wall friction factor are relatively weak functions of the principal solution variables, these are calculated explicitly at the start of the timestep.⁽²⁰⁾ The wall heat transfer terms are treated semi-implicitly and are sensitive to changes in the wall temperature, which is calculated explicitly. To avoid incurring any associated numerical instabilities, the timestep is controlled to limit the rate of change of wall temperature.

2-5-3-1 Semi-Implicit Formulation

Each of the averaged conservation equations described above is solved by differencing them on a staggered grid. The continuity and energy finite difference equations are obtained by integrating the differential equations over the mass and energy control volume (i.e., from $j-1/2$ to $j+1/2$) and over the timestep Δt . Similarly, the finite differenced mixture momentum equation is obtained by integrating the differential form over the momentum control volume. A superscript n is used to denote a quantity at the previous time level. No subscript over a quantity denotes the $n+1$ or new time level value. State variables such as densities and energies are normally only available at cell centers. However, to determine the convective flux derivatives it is necessary to provide averaged values for some of the cell center quantities at the cell interfaces:

$$\bar{f}_{j+1/2} = \beta_{j+1/2} f_j + (1 - \beta_{j+1/2}) f_{j+1} \quad (2-151)$$

and

$$\bar{f}_{j+1/2}^r = \beta_{j+1/2}^r f_j + (1 - \beta_{j+1/2}^r) f_{j+1} \quad (2-152)$$

where:

$$\beta_{j+1/2} = \begin{cases} 1 & U_{mj+1/2}^n > 0 \\ 0 & U_{mj+1/2}^n < 0 \end{cases} \quad (2-153)$$

$$\beta_{j+1/2}^r = \begin{cases} 1 & U_{rj+1/2}^n > 0 \\ 0 & U_{rj+1/2}^n < 0 \end{cases} \quad (2-154)$$

When the velocity is zero, the decision on which cell is the donor cell for the quantity depends on the pressure gradient and whether the cell face is undergoing a velocity reversal. The practice of donor celling the state variables for the convective fluxes leads to greater numerical stability than, for example, central differencing. It is convenient to define two finite difference divergence operators. The first is used for differencing mixture or individual phase fluxes:

$$\nabla_j (fU_m) = \frac{1}{V_j} \left[\bar{f}_{j+1/2} U_{m,j+1/2} A_{j+1/2} - \bar{f}_{j-1/2} U_{m,j-1/2} A_{j-1/2} \right] \quad (2-155)$$

and the second is used to difference fluxes associated with relative motion:

$$\nabla_j (fU_r) = \frac{1}{V_j} \left[\bar{f}'_{j+1/2} U_{r,j+1/2} A_{j+1/2} - \bar{f}'_{j-1/2} U_{r,j-1/2} A_{j-1/2} \right] \quad (2-156)^{(21)}$$

With this notation the finite difference equations are:

Mixture Continuity Equation [

]^{a,c} (2-157)

Vapor Continuity Equation [

]^{a,c}

Mixture Energy Equation [

] ^{a,c}

Vapor Energy Equation [

] ^{a,c}

Mixture Momentum Equation [

] ^{a,c}

In the mixture momentum equation, the convective derivative is donor celled as follows:

$$\left(\frac{\partial U_m}{\partial X} \right)_j = \beta_{j+1/2} \frac{U_{m_{j+1/2}}^n - U_{m_{j-1/2}}^n}{\Delta X_j} + (1 - \beta_{j+1/2}) \frac{U_{m_{j+3/2}}^n - U_{m_{j+1/2}}^n}{\Delta X_{j+1}} \quad (2-162)$$

Time levels were not assigned to the heat transfer and phase change terms because they involve a mixture of old and new time quantities. For the interfacial heat transfer, only the potential $(T_{sat} - T_v)$ is calculated at the new time level. For the phase change rate, the quantities $(T_{sat} - T_i)$ and $(H_g - H_f)$ are all evaluated at the new time level. The remaining interfacial functional dependence is treated explicitly. In the case of the wall heat transfer, only fluid temperatures T_v and T_i are evaluated at the new time.

The flux terms in Equations 2-158 to 2-161 are treated semi-implicitly; the old time level density or energy density is used with the new time level mixture velocity. The flux terms associated with the relative motion are treated entirely explicitly.

The mixture momentum equation deserves some comment. Both mixture and relative flux terms are treated explicitly. The pressure gradient is treated implicitly.⁽²²⁾ Equation 2-161 is actually solved using the old time pressures. However, following the solution of the mass and energy equations, the mixture velocities are updated to reflect the new time level in the pressure, thus leading to an implicit pressure dependence. The gravitational head term has been formulated in such a way as to accurately reflect the static pressure difference between the cell centers.

2-5-3-2 Fully Implicit Formulation

The fully implicit finite difference equations also use a donor cell averaging from the flux terms, and thus are very similar to the semi-implicit equations. With the notation of the preceding section, the equations are:

Mixture Continuity Equation [

]^{ac} (2-163)

Vapor Continuity Equation [$]^{a,c}$ **Mixture Energy Equation [** $]^{a,c}$ **Vapor Energy Equation [** $]^{a,c}$

Mixture Momentum Equation [

 J^{ac}

The major differences between these equations and those for the partially implicit scheme are as follows. The only variables that are not treated fully implicitly are the relative velocity, wall heat transfer, and wall friction coefficient. In addition, the convective derivative in the mixture momentum equation is calculated using central differencing. The use of central differencing for this term leads to a more precise representation of the pressure drops in components of non-uniform cross-section, but it is unstable with the semi-implicit scheme; therefore, it is not used in the semi-implicit scheme.

2-6 NUMERICAL SOLUTION METHOD

2-6-1 Introduction

The conservation equations and computational mesh used by WCOBRA/TRAC for the vessel and one-dimensional components were described in Sections 2-1 through 2-5. This section describes the numerical methods used to generate a solution to those sets of equations.

2-6-2 Vessel Component Numerical Solution

The equations shown in Sections 2-3 and 2-5 form a set of algebraic equations that must be solved simultaneously to obtain a solution for the flow fields involved. These equations must be simultaneously satisfied not only for each cell, but for the entire computational mesh. The numerical scheme chosen to solve these equations must be as efficient as possible to obtain a solution in a reasonable amount of computer time. While the equations can be solved directly using Gaussian elimination, the computer time required for problems with many mesh cells would be prohibitive. Therefore, it is desirable to reduce as much as possible the number and complexity of the equations being solved and use the most efficient scheme possible to obtain a final solution. Note that the equations in Sections 2-2 and 2-3 have already been greatly simplified over the conservation equations they are intended to represent since they are written in a semi-implicit form. It is assumed that these semi-implicit equations converge to the correct solution if a timestep size smaller than that required by the Courant criterion is used. The methods used to solve these equations will now be described.

2-6-2-1 Solution of the Momentum Equations

The momentum equations are solved first, using currently known values for all of the variables, to obtain an estimate of the new time flow. All explicit terms and variables in the momentum equation are computed in this step and are assumed to remain constant during the remainder of the timestep. The semi-implicit momentum equations have the following form:

Liquid

$$F_l = A_1 + B_1 \Delta P + C_1 F_l + D_1 F_v \quad (2-168)$$

Vapor

$$F_v = A_2 + B_2 \Delta P + C_2 F_l + D_2 F_v + E_2 F_e \quad (2-169)$$

Entrained Liquid

$$F_e = A_3 + B_3 \Delta P + D_3 F_v + E_3 F_e \quad (2-170)$$

A_1 , A_2 , and A_3 are constants that represent the explicit terms in the momentum equations such as the momentum efflux terms and the gravitational force. B_1 , B_2 , and B_3 are the explicit portion of the pressure gradient force term. C_1 and C_2 are the explicit factors that multiply the liquid flowrate in the wall and the interfacial drag terms. D_1 , D_2 , D_3 , E_2 , and E_3 are the corresponding terms that multiply the vapor and entrained liquid flowrates. F_l is the liquid mass flowrate, F_v is the vapor mass flowrate, and F_e is the entrained liquid mass flowrate. These equations may be written in matrix form as

$$\begin{bmatrix} C_1 - 1 & D_1 & 0 \\ C_2 & D_2 - 1 & E_2 \\ 0 & D_3 & E_3 - 1 \end{bmatrix} \begin{bmatrix} F_l \\ F_v \\ F_e \end{bmatrix} = \begin{bmatrix} -A_1 - B_1 \Delta P \\ -A_2 - B_2 \Delta P \\ -A_3 - B_3 \Delta P \end{bmatrix} \quad (2-171)$$

This expression is solved by Gaussian elimination to obtain a solution for the phasic mass flowrates as a function of the pressure gradient across the momentum cell, ΔP :

$$\begin{aligned} F_l &= G_1 + H_1 \Delta P \\ F_v &= G_2 + H_2 \Delta P \\ F_e &= G_3 + H_3 \Delta P \end{aligned} \quad (2-172)$$

The mass flowrates given by Equation 2-172 are computed based on the mass of each phase contained within the momentum control volume. Velocities may be computed from these flowrates using Equation 2-68. Once the tentative velocities have been obtained from the momentum equations, the continuity and energy equations can be solved.

2-6-2-2 Linearization of the Mass and Energy Equations

If the right hand side of each of the mass and energy equations is moved to the left hand side, and if the current values of all variables satisfy the equations, the sum of the terms on the left side should be identically equal to zero. The energy and mass equations will not generally be satisfied when the new velocities computed from the momentum equations are used to compute the convective terms in these equations. There will be some residual error in each equation as a result of the new velocities and changes in the magnitude of some of the explicit terms in the mass and energy equations, such as the vapor generation rate. The vapor mass equation, for example, has a residual error given by

$$E_{cv} = \frac{[(\alpha_v \rho_v)_J - (\alpha_v \rho_v)_J^n] A_{c_J}}{\Delta t} + \sum_{KA=1}^{NB} \frac{[(\alpha_v \rho_v)^{\tilde{v}} \tilde{U}_{vj} A_{mj}]_{KA}}{\Delta X_J} \quad (2-173)$$

$$- \sum_{KB=1}^{NB} \frac{[(\alpha_v \rho_v)^{\tilde{v}} \tilde{U}_{vj-1} A_{mj-1}]_{KB}}{\Delta X_J} - \sum_{KL=1}^{NKK} L_{KL} [(\alpha_v \rho_v)^{\tilde{v}} \tilde{W}_{vL}]_J - \frac{\Gamma_J}{\Delta X_J} - \frac{S_{cvJ}}{\Delta X_J}$$

All terms are computed using currently known values for each of the variables. The symbol \sim over the velocities indicates that they are the tentative values computed from the momentum equations, Equation 2-172. The mass equations for the liquid phases and the two energy equations also have residual errors: E_{α} , E_{ce} , E_{cv} , and E_{et} . The equations are simultaneously satisfied when E_{cv} , E_{α} , E_{ce} , E_{cv} , and E_{et} for all cells in the mesh simultaneously approach zero. The variation of each of the independent variables required to bring the residual errors to zero can be obtained using the block Newton-Raphson method. This is done by linearizing the equations with respect to the independent variables P , α_v , $\alpha_v H_v$, $(1-\alpha_v)H_t$, and α_e to obtain the following equation for each cell:

$$\begin{bmatrix}
 \frac{\partial E_{ct}}{\partial \alpha_v} & \frac{\partial E_{ct}}{\partial \alpha_v H_v} & \frac{\partial E_{ct}}{\partial (1-\alpha_v) H_t} & \frac{\partial E_{ct}}{\partial \alpha_e} & \frac{\partial E_{ct}}{\partial P_j} & \frac{\partial E_{ct}}{\partial P_{i=1}} & \dots & \frac{\partial E_{ct}}{\partial P_{i=NCN}} \\
 \frac{\partial E_{cv}}{\partial \alpha_v} & \frac{\partial E_{cv}}{\partial \alpha_v H_v} & \frac{\partial E_{cv}}{\partial (1-\alpha_v) H_t} & \frac{\partial E_{cv}}{\partial \alpha_e} & \frac{\partial E_{cv}}{\partial P_j} & \frac{\partial E_{cv}}{\partial P_{i=1}} & \dots & \frac{\partial E_{cv}}{\partial P_{i=NCN}} \\
 \frac{\partial E_{et}}{\partial \alpha_v} & \frac{\partial E_{et}}{\partial \alpha_v H_v} & \frac{\partial E_{et}}{\partial (1-\alpha_v) H_t} & \frac{\partial E_{et}}{\partial \alpha_e} & \frac{\partial E_{et}}{\partial P_j} & \frac{\partial E_{et}}{\partial P_{i=1}} & \dots & \frac{\partial E_{et}}{\partial P_{i=NCN}} \\
 \frac{\partial E_{ce}}{\partial \alpha_v} & \frac{\partial E_{ce}}{\partial \alpha_v H_v} & \frac{\partial E_{ce}}{\partial (1-\alpha_v) H_t} & \frac{\partial E_{ce}}{\partial \alpha_e} & \frac{\partial E_{ce}}{\partial P_j} & \frac{\partial E_{ce}}{\partial P_{i=1}} & \dots & \frac{\partial E_{ce}}{\partial P_{i=NCN}} \\
 \frac{\partial E_{cv}}{\partial \alpha_v} & \frac{\partial E_{cv}}{\partial \alpha_v H_v} & \frac{\partial E_{cv}}{\partial (1-\alpha_v) H_t} & \frac{\partial E_{cv}}{\partial \alpha_e} & \frac{\partial E_{cv}}{\partial P_j} & \frac{\partial E_{cv}}{\partial P_{i=1}} & \dots & \frac{\partial E_{cv}}{\partial P_{i=NCN}}
 \end{bmatrix}
 \begin{Bmatrix}
 d\alpha_v \\
 d(\alpha_v H_v) \\
 d[(1-\alpha_v) H_t] \\
 d\alpha_e \\
 dP_j \\
 dP_{i=1} \\
 \vdots \\
 dP_{i=NCN}
 \end{Bmatrix}
 = - \begin{Bmatrix} E_{ct} \\ E_{cv} \\ E_{et} \\ E_{ce} \\ E_{cv} \end{Bmatrix}
 \quad (2-174)$$

This equation has the form:

$$[R(X)] \{d(X)\} = -E \quad (2-175)$$

for each cell. Matrix $[R(X)]$ is the Jacobian Matrix of the system of equations evaluated for the set of independent variables given by the vector X , dX is the solution vector containing the linear variation of the independent variables, and $-E$ is a vector containing the negative of the residual errors required to bring the error for each equation to zero. The matrix $R(X)$ is composed of analytical derivatives of each of the terms in the equations with respect to the independent variables. The velocities are linearly dependent on the pressures, so derivatives of velocities with respect to pressure may be obtained directly from the momentum equations, Equation 2-172. The linear variation of velocity with respect to pressure is given by:

$$\begin{aligned}
dv_t &= H_1 (dP_J - dP_{J+1}) \\
dv_v &= H_2 (dP_J - dP_{J+1}) \\
dv_e &= H_3 (dP_J - dP_{J+1})
\end{aligned}
\tag{2-176}$$

The derivatives of the other dependent variables, such as ρ_t , ρ_v , H_t , and H_v , are obtained from the thermal equations of state and from fundamental identities involving partial derivatives. For example, the derivative of ρ_v with respect to the independent variable $\alpha_v H_v$ is given by:

$$\frac{\partial \rho_v}{\partial (\alpha_v H_v)} = \frac{\partial \rho_v}{\partial H_v} \frac{\partial H_v}{\partial (\alpha_v H_v)}
\tag{2-177}$$

The derivative $\partial \rho_v / \partial H_v$ is obtained directly from the thermal equation of state, while the derivative $\partial H_v / \partial \alpha_v H_v$ is obtained from the identity:

$$H_v = \frac{\alpha_v H_v}{\alpha_v}
\tag{2-178}$$

The term in the numerator is the independent variable with respect to which the derivative is being taken, and the denominator is the independent variable α_v which is assumed to be held constant while taking the derivative. From Equation 2-178 we then obtain:

$$\frac{\partial H_v}{\partial (\alpha_v H_v)} = \frac{1}{\alpha_v}
\tag{2-179}$$

Derivatives of the independent variables are obtained directly from Equation 2-172 and the comparable equations for the other four residual errors. For example, the derivative of the temporal term of Equation 2-173 with respect to α_v , is given by:

$$\frac{\partial (\alpha_v \rho_v)}{\partial \alpha_v} = \left(\rho_v \frac{\partial \alpha_v}{\partial \alpha_v} + \alpha_v \frac{\partial \rho_v}{\partial \alpha_v} \right) = \rho_v
\tag{2-180}$$

Once all of the derivatives for the five equations have been calculated, Equation 2-174 is reduced using Gaussian forward elimination to obtain solutions for the independent variables of the form:

$$dP_J = a_5 + \sum_{i=1}^{NCON} g_{5i} dP_i \quad (2-181)$$

and back substitution

$$d\alpha_e = a_4 + f_4 dP_J + \sum_{i=1}^{NCON} g_{4i} dP_i \quad (2-182)$$

$$d[(1-\alpha_v) H_t] = a_3 + e_3 d\alpha_e + f_3 dP_J + \sum_{i=1}^{NCON} g_{3i} dP_i \quad (2-183)$$

$$d(\alpha_v H_v) = a_2 + d_2 d[(1-\alpha_v) H_t] + e_2 d\alpha_e + f_2 dP_J + \sum_{i=1}^{NCON} g_{2i} dP_i \quad (2-184)$$

$$\begin{aligned} d\alpha_v = & a_1 + c_1 d(\alpha_v H_v) + d_1 d[(1-\alpha_v) H_t] \\ & + e_1 d\alpha_e + f_1 dP_J + \sum_{i=1}^{NCON} g_{1i} dP_i \end{aligned} \quad (2-185)$$

The computer time required to solve Equation 2-174 is greatly reduced if the nonlinear coefficients a_k through g_k are assumed to remain constant during a timestep and a solution is obtained only for the linearized system of equations (Equations 2-181 through 2-185). Timestep controls are then imposed to assure that the variation of the nonlinear terms between timesteps remains within acceptable limits so that a stable solution is obtained. A great savings in computer time is realized when this is done since the matrix equation, Equation 2-174, is reduced only once per timestep.⁽³⁰⁾

2-6-2-3 Solution of the System Pressure Matrix⁽³¹⁾

The linear variation of the pressure in cell J as a function of surrounding cell pressures is given by Equation 2-181. A similar equation may be derived for each cell in the mesh. This set of equations for the pressure variation in each mesh cell must be simultaneously satisfied. The solution to this equation set may be obtained by direct inversion for problems containing only a few mesh cells, or by using a Gauss-Siedel iterative technique for problems containing a large number of mesh cells.

The efficiency of the Gauss-Siedel iteration is increased in two ways. First, a direct inversion is carried out over groups of mesh cells specified by the user. The pressure variation for cells within the group are solved simultaneously while the pressure variations in surrounding mesh cells are assumed to have their last iterate value. A Gauss-Siedel iteration is then carried out over the groups of cells where the pressure variations of bounding cells for each group are updated with their last iterate value. As far as the iterative solution is concerned, solving groups of cells by direct inversion has the effect of reducing a large multidimensional problem down to a simpler one-dimensional problem that has the same number of cells as the large problem has groups of cells. Convergence difficulties that are typical of problems with large aspect ratios (long, narrow cells) are also eliminated by placing cells with large aspect ratios between them within the same solution group. The iteration is assumed to have converged when the change in linear pressure variation between timesteps is below a specified limit.

The second method for increasing the efficiency of the iteration involves obtaining the initial estimate for the pressure variation in each cell. This is done through a process called rebalancing. Rebalancing is simply the process of reducing the multidimensional mesh to a one-dimensional mesh for the vessel, and then obtaining a solution for the pressure variation at each level of the one-dimensional problem by direct inversion using the methods described above. The one-dimensional solution for the linear pressure variation at each level is then used as an initial guess for the linear pressure variation in each mesh cell on that level in the multidimensional problem. This process greatly enhances the rate of convergence in many problems since the one-dimensional solution generally gives a good estimate for the magnitude of the linear pressure variation in the multidimensional problem. Rebalancing is optional and must be specified by the user. If this option is not used, then the initial guess for the linear pressure variation in each cell is zero.

2-6-2-4 Cells Connected to One-Dimensional Components

The equation for the linear pressure variation in vessel mesh cells that connect to one-dimensional components is slightly more complicated than Equation 2-181 since the cell pressure is dependent on the pressures within the one-dimensional component. If the one-dimensional component forms part or all of a loop connection to one or more additional cells within the vessel, then the pressure variations within the one-dimensional components are functions of the pressure variation within each vessel mesh cell to which the loop connects. The equations for the one-dimensional components in each loop are reduced to the form: [

]^{a,c} (2-186)

where: [

]^{a,c} (2-187)

[

 J^{ac}

Combining Equations 2-186 and 2-187 produces: [

 J^{ac} (2-188)

for the linear variation in pressure for the vessel computational cell J . [

 J^{ac}

2-6-3 One-Dimensional Component Numerical Solution

One dimensional conservation equations are expressed by semi-implicit finite difference Equations 2-157 through 2-160 in a cell, and Equation 2-161 at a cell boundary. The noding of a one dimensional component with N cells is illustrated in Figure 2-8. Component boundaries in the figure are the left boundary (L), attached to node number 1, the right boundary (R), next to the last node N , and a tee boundary at cell number T .

The above set of algebraic equations is solved in the one-dimensional components in a manner similar to the vessel component discussed in Section 2-6-2 for the three-dimensional conservation equations. This section is developed in parallel to that section. In Section 2-6-3-1, momentum equations are solved. Mass and energy equations are then solved in Section 2-6-3-2. However, there is no need to construct and solve a system pressure matrix for the simple 1D component geometry. The component boundary conditions will be discussed in Section 2-6-3-3.

2-6-3-1 Solution of Momentum Equations

To solve the set of five algebraic equations, independent variables are selected first: pressure P , void fraction α , liquid temperature T_l , vapor temperature T_v , and mixture velocity U_m , where the scalar quantities are defined at the cell center j and U_m at the cell boundary $j-1/2$. The set of equations are

solved by the use of Newton-Raphson iteration. In the case of the mixture momentum Equation 2-161, $F_{mm,j-1/2}$ is expanded into a first order series as follows:

$$F_{mm,j-1/2} \approx F_{mm,j-1/2}^n + \frac{\partial F_{mm,j-1/2}}{\partial U_{m,j-1/2}} dU_{m,j-1/2} + \frac{\partial F_{mm,j-1/2}}{\partial P_j} dP_j + \frac{\partial F_{mm,j-1/2}}{\partial P_{j-1}} dP_{j-1} \quad (2-189)$$

where $F_{mm,j-1/2}^n$ is the value of $F_{mm,j-1/2}$ at the end of the previous timestep and the current variables are:

$$[\quad \quad \quad]^{a,c} \quad (2-190)$$

and so on. Thus, the formal solution for $F_{mm,j-1/2} = 0$ is expressed by: [

$$]^{a,c} \quad (2-191)$$

for $j=1, N+1$. It will be noticed that:

$$[\quad \quad \quad]^{a,c} \quad (2-192)$$

$$[\quad \quad \quad]^{a,c} \quad (2-193)$$

It is seen from Equation 2-191 that the coefficients $e_{j-1/2}$ and $f_{j-1/2}$ are constants depending only on the quantities of the previous timestep.

2-6-3-2 Solution of Mass and Energy Equations

The first four independent variables are collectively denoted by a vector. [

$$]^{a,c} \quad (2-194)$$

and another vector is formed of Equations 2-157 through 2-160 for the mass and energy equations: [

] ^{a,c} (2-195)

whose elements depend on \underline{X} . For the Newton-Raphson solution, \underline{E} is expanded into a first order series:
[

] ^{a,c}

Similar to construction of Equation 2-174 for the 3D solution method, the formal solution of Equation 2-191 is applied to the above equation. [

] ^{a,c}

where the coefficients of $d\underline{X}$ are Jacobian matrices. For the solution of $F=0$, we have: [

] ^{a,c} (2-198)

where \underline{C}_j , \underline{A}_j , and \underline{B}_j are (4x4) coefficient matrices.

2-6-3-3 Component Boundary Conditions

For a component, the mass and energy equations become: [

$$]^{a,c}$$

where L , R , and T are boundary conditions at the left, right, and tee boundaries of the one dimensional component, respectively. For example, [

$$]^{a,c}$$

for a velocity boundary condition or by incorporating the momentum equation, [

$$]^{a,c}$$

a pressure boundary condition can be imposed. At the right boundary, [

$$]^{a,c}$$

Thus, the solution of Equation 2-199 becomes [

$$]^{a,c} \quad (2-203)$$

Given velocity boundary conditions at the left, right, and tee boundaries of a one-dimensional component, therefore, the independent variables X_j are obtained at each cell center. For example, [

] ^{a,c} (2-204)

Applying this expression to Equation 2-191, the mixture velocities at the internal cell boundaries for $j = 2, \dots, N$ can be calculated.

If pressure boundary conditions are provided, then dU_L , dU_R , and dU_T in Equation 2-199 can be replaced by pressure at the respective boundary cells through the use of Equation 2-191 at the boundaries. The independent variables dX_j for $j = 1, \dots, N$ can be obtained by an expression similar to Equations 2-203 and 2-204 with dU being replaced by dP . Finally, the velocities at the internal cell boundaries as well as the component boundaries can be obtained by Equation 2-190.

2-6-3-4 Fully Implicit One-Dimensional Components

In the above sections, the solution method has been described for semi-implicit finite difference equations of one-dimensional conservation equations. The fully implicit difference Equations 2-163 to 2-167 are solved by WCOBRA/TRAC in a manner quite similar to the above semi-implicit solution, as shown in Takeuchi and Young (1988). The basic difference in the solution method comes from the mixture momentum equation. The semi-implicit momentum Equation 2-161 depends on the current values of $U_{m,j-1/2}$, P_j , and P_{j-1} . Therefore, the momentum equation was solved first as Equation 2-190, followed by mass and energy equations with (4x4) coefficient matrices. Consequently, Equation 2-198 for a semi-implicit component has a (4x4) blocked tridiagonal coefficient matrix.

The implicit momentum Equation 2-167, on the other hand, depends on the current values of not only $U_{m,j-1/2}$, P_j , and P_{j-1} , but also $U_{m,j+1/2}$, $U_{m,j-3/2}$, and ρ_j . Thus, the momentum equation cannot be solved by itself. In this situation, independent variables are chosen to be:

[

] ^{a,c} (2-205)

All the Equations 2-163 to 2-167 are collected in: [

] ^{a,c} (2-206)

Notice that the mixture velocity at the left hand end $j-1/2$ is coupled with the scalar quantities in cell j in vector $d\mathbf{X}$, as is the momentum equation. Furthermore, the momentum equation is placed in the middle of \mathbf{E} . Solution of $\mathbf{E}=0$ is obtained by the use of the Newton-Raphson method, and so the derived equation has the same expression as Equation 2-198. [

]^{a,c} (2-207)

However, $\underline{\mathbf{A}}$, $\underline{\mathbf{B}}$, and $\underline{\mathbf{C}}$ in Equation 2-207 are (5x5) coefficient matrices with conservation equations in the row placed in the order stated above, and \mathbf{S} is the constant source term.

Each cell is related to quantities in the nearest neighboring cells only. By assembling Equation 2-207 for a component with N cells, therefore, we again have a blocked tridiagonal system: [

]^{a,c}

While this implicit matrix equation has the same formal expression as the semi-implicit equation Equation 2-199, the contents of the coefficient matrices, the source vector, and the solution vector are greatly different. However, the boundary conditions of L , R , and T are the same as the semi-implicit case. Even if implicit one-dimensional components are connected each other, they are connected semi-implicitly, restricting the timestep size by the Courant condition. Because the boundary conditions are semi-implicit, their relationship to the network equations is the same as the other semi-implicit components.

2-6-4 Network Matrix Equation

In the above Sections 2-6-2 and 2-6-3, the solution method for a single component was discussed. Usually, several components are joined for modelling of a complex system by connecting boundaries of the components. The connected boundary conditions between the components are determined by a network equation in WCOBRA/TRAC, which is the subject of this section.

The WCOBRA/TRAC network matrix equations were described in general form by Takeuchi and Young (1988). However, the network equation can be better explained by an illustration of a sample network in Figure 2-9. Component 1 is a PIPE component with junction 1 at the left boundary and junction 2 at the right boundary. Component 2 is a TEE component whose primary tube has junctions 2, 3, and 5 at the left, right, and tee boundaries, respectively. The side tube, denoted as 2', has junctions 5 and 6 at the left and the right boundaries. Component 3 is a PIPE with junctions 3 and 4. Component 4 is an ACCUM component connected to component 2 at junction 6. Components 1 and 3 are connected to the vessel component at its cells V_1 and V_4 . For this system, the mixture momentum Equation 2-191 becomes: [

$$]^{a,c} \quad (2-209a)$$

[

$$]^{a,c} \quad (2-209b)$$

[

$$]^{a,c} \quad (2-209c)$$

[

$$]^{a,c} \quad (2-209d)$$

[

$$]^{a,c} \quad (2-209e)$$

[

$$]^{a,c} \quad (2-209f)$$

for the mixture velocity U_j at junction j , and where P_{i1} and P_{iN} are pressures in the first and the last cell of the component i . On the other hand, one of the solutions of the mass and energy equation (Equation 2-204), at the first and the last cells of the one-dimensional components are [

$$]^{a,c} \quad (2-210a)$$

[

$$]^{a,c} \quad (2-210b)$$

[

$$]^{a,c} \quad (2-210c)$$

$\mathbb{J}^{a,c}$
$$[\quad]^{a,c} \quad (2-212)$$

$$[\quad]^{a,c} \quad (2-213)$$

These relationships are represented in Equation 2-186 in a general expression. The boundary velocities at the other junctions become: [

$$]^{a,c} \quad (2-214)$$

for $J=2, \dots, 6$. It should be noted that coefficients B_{j1} and B_{j4} are usually not zero, indicating that the pressure change in the vessel cell at the 1D/3D junction influences all the boundary velocities in one timestep. This is a result of the implicit nature of the pressure terms in the semi-implicit scheme.

If the vessel component in Figure 2-9 were replaced by a one-dimensional component, mass and energy equations yield: [

$$]^{a,c} \quad (2-215)$$

$$[\quad]^{a,c} \quad (2-216)$$

at the first and the last cells. Applying these relations to Equation 2-203, a closed form solution is obtained: [

$$]^{a,c}$$

After solving this equation for the boundary velocities, the mass and energy relations of Equation 2-203 yields X for pressure, void fraction, liquid temperature, and vapor temperature. Then, the momentum Equation 2-191 gives the mixture velocities at the internal cell boundaries of all the components.

With the vessel component connected to the system as in Figure 2-9, the formal solutions of Equations 2-212 and 2-213 for the 1D/3D junction velocities are applied to the system pressure matrix Equation 2-187 for the 3D component to get the closed form, Equation 2-188. Once the system pressure matrix equation is solved, all the other independent variables are obtained at all the vessel cells by Equations 2-182 to 2-185. Pressure changes in the 3D cells at the 1D/3D junctions have been, of course,

obtained at this time. Then, Equation 2-211 is solved for the boundary velocities at the component boundaries in the entire system. Thus, Equations 2-203 and 2-191 give the solution for the independent variables of 1D components. The above process, in which a collection of the full component equations such as Equation 2-199 is reduced to the system pressure equation, will often be called IBKS-forward elimination. The terminology IBKS will be used later in the code description. The system pressure matrix equation in the closed form is the basis of the solution procedure. Once it is solved, the process is reversed to find solutions for the other variables, which is referred to as IBKS-backward substitution. It should be noted that there are several levels of different sets of forward elimination and back substitution within one outer iteration. The IBKS-process is the highest level in the iteration.

2-6-5 WCOBRA/TRAC Solution Routines

Subroutine TRANS drives the entire transient calculation. Simulation control in accordance with the input specified time domains is monitored by calls to TIMCHK. Timestep sizes are controlled by calling TIMSTP and NEWDLT which are discussed in Section 2-7. At every timestep, prepass calculations, outer iterations, and postpass calculations are performed under the control of TRANS. Figure 2-10 shows a logical tree with comments illustrating the functional scope of TRANS. Major subroutines under TRANS for the transient calculations are summarized in Section 2-6-5-1. One cycle of the outer iteration calculations is detailed in Section 2-6-5-2, where the relationship of the code with the previous equations is established.

2-6-5-1 Transient Calculation Routines

Prior to performing the iterative solution for each timestep, prepass calculations are made by subroutine PREP. Figure 2-11 outlines this procedure. The prepass calculations use the system state at the completion of the previous timestep to evaluate quantities to be used during the outer iterations. Separate prepass calculations are performed for the one-dimensional component network and for the vessel component. Subroutine PREPER controls the prepass calculations for the one-dimensional component network, and PREP3D governs the vessel component prepass calculations.

In the one-dimensional component prepass calculation, relative velocities, which are assumed fixed during the iterations, are evaluated in SLIP. The computed relative velocities are used to calculate liquid and vapor velocities in subroutine PREPER, which are in turn used in FWALL to calculate the two-phase wall friction factor. Heat transfer coefficients are returned by HTPPIPE.

The vessel component prepass calculation is performed by PREP3D, which updates boundary conditions and calls HEAT to determine the wall heat flux using heat transfer coefficients from HCOOL. The rod conduction equations are solved by subroutine TEMP and the quench front location and nodding is controlled by subroutine QFRONT.

The hydrodynamic state of the system is determined by a sequence of Newton-Raphson iterations that solve the linearized equations for each external loop and the vessel. Throughout the sequence of

iterations that constitute a timestep (called an outer iteration), the properties and variables evaluated during the prepass and previous postpass remain fixed. These include wall and rod temperatures, heat transfer coefficients, wall friction factors, and phase relative velocities.

The outer iteration is controlled by subroutine OUTER. Subroutine OUTER, as shown in Figure 2-12, completes a single cycle outer (Newton-Raphson) iteration of the linearized hydraulic equations for the external loops and the vessel. Each call to subroutine OUTER completes a single outer (Newton-Raphson) iteration. Both the forward elimination and backward substitution that sweep through the external loops are performed by subroutine OUT1D and its associated routines. The calculations that these routines perform are controlled by the variable IBKS, which is set by subroutine OUTER. Subroutine OUT3D solves the hydrodynamic equations for the vessel component ($IBKS = 0$), or merely updates boundary data ($IBKS = 1$).

All one-dimensional components in a particular external loop are handled by a single call to subroutine OUT1D. OUT1D invokes the appropriate component outer iteration subroutine and returns the data. The outer iteration subroutines for one-dimensional components use subroutine INNER to perform common functions. INNER retrieves boundary information from the boundary arrays, tests other boundary information for consistency, calls subroutine DF1D to perform the appropriate hydrodynamic calculation, and resets the boundary data arrays by calling subroutine J1D. Subroutine DF1D invokes subroutine DF1DI or DF1DS to perform fully or semi-implicit calculations, respectively.

Subroutine OUT3D solves the momentum, continuity and energy equations for the vessel component. Subroutines XSCHM, INTFR, FILLRO, and GSSOLV are the primary routines used by OUT3D to do this. XSCHM linearizes the equations and INTRF computes the interfacial drag and wall friction factors. FILLRO and GSSOLV solve the linear system by direct inversion or Gauss-Seidel iteration. The boundary data arrays are updated by OUT3D.

Having evaluated the system hydrodynamic state by a sequence of outer iterations, WCOBRA/TRAC performs a postpass to unfold the hydrodynamic variables and update the boundary data array. This postpass is performed by subroutine POST. The same subroutine also implements the timestep backup procedure when the outer iteration process fails to converge. When failure occurs, the outer iteration counter (OITNO) is set equal to -100 and subroutine POST is invoked. Under these conditions, POST returns the component data arrays to their state at the beginning of the timestep.

When the iteration converges successfully, POST calls the appropriate component postpass subroutines for the one-dimensional components and invokes subroutine POST3D for the vessel component. POST3D unfolds the values of the independent variables from the system matrix, updates the fluid densities and mass flowrates, and solves the drop interfacial area concentration equation.

Subroutine POST, as shown in Figure 2-13, performs the postpass calculation by unfolding the hydrodynamic variables in subroutine FPROP and THERMO for one-dimensional components and in subroutines SAT, VOLLIQ, and VOLVAP for the vessel component. Boundary arrays are updated in

subroutines SAVBD and SETBD for one-dimensional components and in SPLITIT for the vessel component. In addition, failure of the iteration is identified at this point using the convergence criteria in Section 2-7-2. In response, POST returns the component data arrays to their state at the beginning of the timestep and the timestep is repeated with a smaller timestep size. When the iteration converges successfully, POST calls the one-dimensional component and then vessel component postprocess routines. Other than hydrodynamic variables and boundary values, 1D component post calculation solves the heat conduction equation in CYLHT (n.b.; conduction equation for a vessel component is solved in prepass, op.cit.) and finds the maximum changes of pressure and structural temperatures per timestep in EVALDF. These maximum changes will be used in timestep size control as discussed in Section 2-7. In the vessel postpass calculation, the neutronic point kinetics equation is solved in LUCIFER, and subroutine BACOUT unfolds vessel component independent variables (n.b.; unfolding in one-dimensional components is performed by DF1DI and DF1DS with IBKS = 1 during the outer iterations).

2-6-5-2 Sequence of Outer Iteration Calculations

One cycle of the outer iteration consists of one-dimensional component calculations, vessel component calculations, and another pass of one-dimensional component calculations. This sequence of calculations is described below. Subroutine OUTER is the driver of one cycle of the outer iterations which calls OUT1DN for the 1D series of computations and OUT3D for the vessel computations. Subroutines OUT1D, INNER, J1D, DF1DS, and DF1DI are used to solve one-dimensional component conservation equations. Vessel equations are solved by the subroutines XSCHM, REDUCE, FILLRO, and GSSOLV.

First, IBKS=0 is set in OUTER to initialize the IBKS-forward elimination step in an outer iteration. Then, OUTER calls OUT1DN, which subsequently calls OUT1D loop by loop. OUT1D disassembles one loop into components and calls the routines DF1DS or DF1DI component by component in a preset order. Routines DF1DS and DF1DI solve the one-dimensional thermal-hydraulic equations for each component, subject to velocity boundary conditions.

[

] ^{ac}.

[

] ^{a.c.}

At the end of one component calculation, INNER calls J1D to update the boundary data with the just computed data and stores the data to BD(i), to be subjected to the next component in a preset calculation order.

The above process is repeated over the components of a loop. Then another loop is selected by OUT1DN and components are ordered by OUT1D to be processed until all the one-dimensional components are updated. At the completion, the network equation has been constructed. This equation is solved in OUT1DN by calling subroutines SOLVE and BACSUB for the boundary velocities at 1D/1D and 1D/3D junctions.

After the network equation is solved, control returns to OUTER where the one-dimensional component data are transferred to vessel calculations by parameters $AP(i,j)$ with 1D/3D junction number, coefficient f in Equations 2-192 or 2-193, the 1D/3D boundary velocity change, and PSNEW with the pressure change rate in the one-dimensional component cell adjacent to the 1D/3D junction. Including mass, energy, and momentum sources at the junctions, XSCHM computes coefficient matrices of the vessel momentum, mass, and energy equations.

[

] ^{a.c.}

[

] ^{a.c.} [] ^{a.c.} (2-218)

where superscript m is for the m -th outer iteration. Since all the boundary velocities are updated, the remaining independent variables in one-dimensional components are computed in DF1DI or DF1DS: [

]^{ac} (2-219)

which corresponds to Equation 2-203. With the computed pressure and fluid temperatures, subroutine THERMO is called to generate other hydraulic properties. Finally, OUT3D is called to renew the boundary data, at 1D/3D junctions.

This completes the one cycle of outer iteration. Convergence of iterations is discussed in the next section.

2-7 TIMESTEP SIZE AND CONVERGENCE CRITERIA

2-7-1 Introduction

WCOBRA/TRAC contains logic to control the timestep size and the rate at which it changes. Control of the timestep size is accomplished through user specified convergence criteria. This section describes these convergence criteria. Sections 19-1-2 and 25-5 of WCAP-12945-P-A (Bajorek et al., 1998) present the results of sensitivity studies on these criteria and identifies the values that are appropriate in determining the code uncertainty.

2-7-2 Coded Convergence Criteria

As described in the previous sections, the non-linear thermal-hydraulic conservation equations are discretized and linearized to semi-implicit difference equations which are solved iteratively. One outer iteration (Newton-Raphson) consists of IBKS-forward elimination and backward substitution, that is, a sequence of one-dimensional loop calculations, three-dimensional vessel calculation, and another pass of the one-dimensional loop calculations. The set of calculational steps is iteratively processed.

The computed results of the outer iterations are evaluated by the following convergence criterion:

$$\text{VARERM} < \text{EPSO}$$

where VARERM is the maximum pressure change rate of all components in an iteration, and EPSO is the user specified maximum pressure change in a single iteration.

If this condition is satisfied, the iteration is completed and the computation is allowed to proceed to the next timestep.

If the outer iteration does not converge within an input specified maximum number of iterations, OITMAX, the outer iteration, is considered to have failed. All fluid conditions are reset to the previous timestep value, the timestep size is reduced by half, and the calculation is repeated.

2-7-3 Timestep Size Control⁽²⁵⁾

WCOBRA/TRAC contains separate algorithms to increase and decrease the timestep size, DELT. A promotional algorithm allows DELT to increase when all of the convergence criteria have been satisfied. An inhibitive algorithm restricts DELT to sizes within those permitted by the convergence criteria to ensure computational stability.

The timestep size is regulated by convergence criteria selected by the user and several internal controls by the code. Internal controls on the timestep size are a result of limits placed on the iteration count, the Courant limit, and the vessel vapor fraction change. User selected convergence criteria include specifications of vessel and one-dimensional component pressure change limits, phasic enthalpy change limits (vessel), phasic temperature change limits (one-dimensional components), a fuel rod clad temperature change limit and a one-dimensional component heat structure temperature change limit. The effect of these limits on timestep size are as follows:

[

] ^{a.c.}

[

] ^{a.c.}

[

] ^{a.c.}

[

] ^{a.c.}

[

] ^{a.c.}

These limits restrict the timestep size when fluid conditions are rapidly changing and increase the timestep for a slower transient. At the beginning of a steady-state calculation, the timestep size is set to the minimum allowable timestep size, DTMIN. Often, at the start of a large break LOCA, the Courant limits and pressure change simulation become timestep controlling parameters. The timestep size typically increases with the promotional algorithm to the maximum allowable timestep size, DTMAX, or the size limited by the Courant condition.

2-7-4 Numerical Stability

To achieve numerical stability while maintaining reasonable computing time, discontinuities both in time and space must be eliminated. Several ramps are applied generally within WCOBRA/TRAC. One type of ramp eliminates discontinuities in calculated physical quantities as the void fraction varies from 0 to 1.0. Since different physical models for interfacial shear and heat transfer are used, for example, ramps are applied to assure a smooth transition in the calculated variable as the void fraction changes. Different ramps are used, as described in the following sections.

Generally, all phasic constitutive variables, such as shear and heat transfer coefficients, are ramped to zero as the phase is depleted in a cell. The ramps are applied over a small range of void fraction, usually less than one percent.

In addition to smoothing over void fraction, smoothing over time is also implemented. This is done by applying the following formula to constitutive variables:

$$y(t+\Delta t) = y_c^a y(t)^{1-a} \quad (2-220)$$

where $y(t+\Delta t)$ is the quantity which will be used in the new timestep, y_c is the quantity as calculated by models and correlations, $y(t)$ is the quantity as used in the previous timestep, and a is a number between 0 and 1.0.

[

]'.c.

2-8 REFERENCES

Bajorek, S. M., et al., 1998, "Code Qualification Document for Best Estimate LOCA Analysis," WCAP-12945-P-A, Volume 1, Revision 2, and Volumes 2 through 5, Revision 1, and WCAP-14747 (Non-Proprietary).

Ishii, M., 1977, "One-Dimensional Drift-Flux Model and Constitutive Equations for Relative Motion Between Phases in Various Two-Phase Flow Regimes," ANL-77-47.

Takeuchi, K. and Young, M. Y., 1988, "A Coupling Method of 1D/1D and 1D/3D Junctions for an Implicit WCOBRA/TRAC," ANS Trans., Vol. 57, pg. 353.

Thurgood, M. J., et al., 1983, "COBRA/TRAC - A Thermal-Hydraulics Code for Transient Analysis of Nuclear Reactor Vessels and Primary Coolant Systems," Vol. 1, PNL-4385, NUREG/CR-3046.

2-9 RAI LISTING

1. RAI1-1 (Note: The letter next to superscript 1 refers to the corresponding subsection of RAI1-1)
 RAI1-1a (refers to WCAP-12945, Rev. 1, page 2-30; now page 2-21)
 RAI1-1b (refers to WCAP-12945, Rev. 1, top of page 2-29; now page 2-19)
 RAI1-1c
 RAI1-1d (refers to WCAP-12945, Rev. 1, page 2-36; now page 2-26)
 RAI1-1e (refers to WCAP-12945, Rev. 1, page 2-39; now page 2-28)
 RAI1-1f
 RAI1-1qq
 RAI1-1rr
2. RAI1-4 (refers to WCAP-12945, Rev. 1, page 2-20; now page 2-13)
3. RAI1-5 (refers to WCAP-12945, Rev. 1, page 2-22; now page 2-15)
4. RAI1-6 (refers to WCAP-12945, Rev. 1, page 2-36; now page 2-26)
5. RAI1-7 (refers to WCAP-12945, Rev. 1, page 2-10; now page 2-7)
6. RAI1-8
7. RAI1-9 (refers to WCAP-12945, Rev. 1, page 2-36; now page 2-24)
8. RAI1-10
9. RAI1-11
10. RAI1-12

11. RAI1-13
12. RAI1-14
13. RAI1-15 (refers to WCAP-12945, Rev. 1, page 2-42; now page 2-31)
14. RAI1-16
15. RAI1-18 (refers to WCAP-12945, Rev. 1, page 2-57; now page 2-43)
16. RAI1-17
17. RAI1-19
18. RAIS-1 (refers to WCAP-12945, Rev. 1, page 2-57; now page 2-42)
19. RAIS-2 (refers to WCAP-12945, Rev. 1, page 2-63; now page 2-47)
20. RAIS-3 (refers to WCAP-12945, Rev. 1, page 2-63; now page 2-48)
21. RAIS-4 (refers to WCAP-12945, Rev. 1, page 2-64; now page 2-49)
22. RAIS-5 (refers to WCAP-12945, Rev. 1, page 2-67; now page 2-51)
23. RAIS-6 (refers to WCAP-12945, Rev. 1, page 2-11; now page 2-7)
24. RAIS-7 (refers to WCAP-12945, Rev. 1, page 2-16; now page 2-11)
25. RAIS-8 (refers to WCAP-12945, Rev. 1, page 2-99; now page 2-74)
26. RAIS-9 (refers to WCAP-12945, Rev. 1, page 2-28; now page 2-19)
27. RAIS-10 (refers to WCAP-12945, Rev. 1, page 2-32; now page 2-22)
28. RAIS-11 (refers to WCAP-12945, Rev. 1, page 2-57, 2-66; now page 2-50)
29. RAIS-13 (refers to WCAP-12945, Rev. 1, page 2-40, 2-41; now page 2-31)
30. RAIS-14 (refers to WCAP-12945, Rev. 1, page 2-74, 2-77; now page 2-58)
31. RAIS-15
32. RAIS-12 (refers to WCAP-12945, Rev. 1, page 2-40; now page 2-29)

Note: RAIS-# denote supplemental RAIs.

Table 2-2 Code Backup Limits	

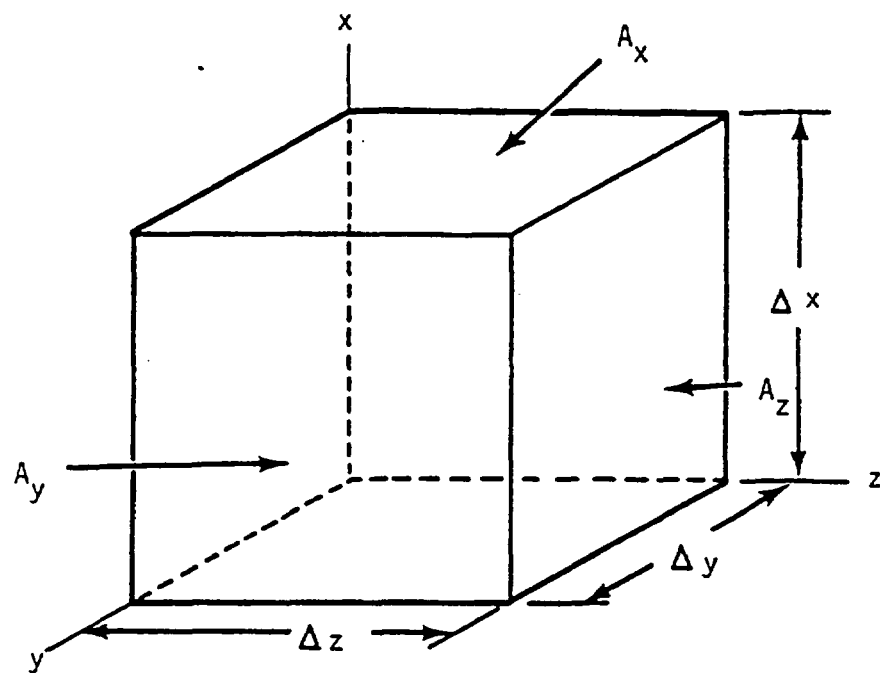


Figure 2-1. Control Volume for Cartesian Coordinates

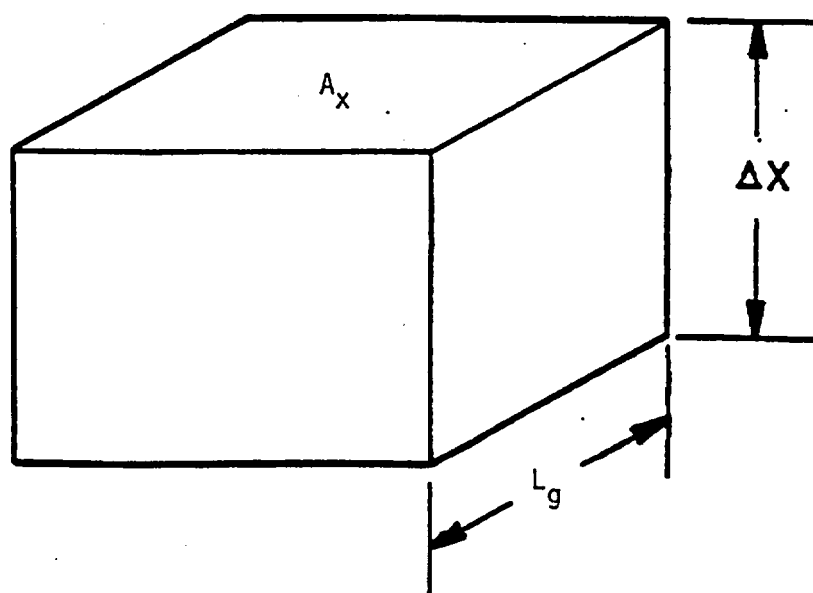


Figure 2-2. Basic Mesh Cell

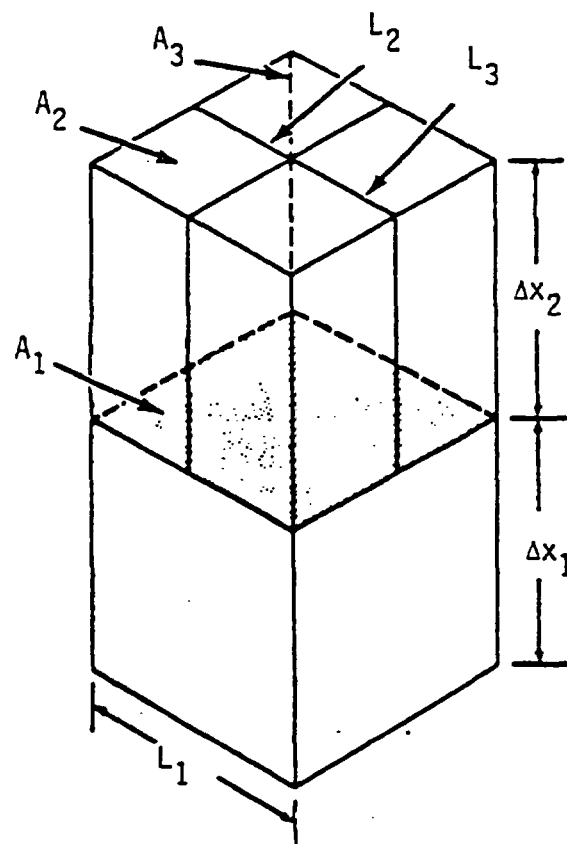


Figure 2-3. Variable Mesh Cell

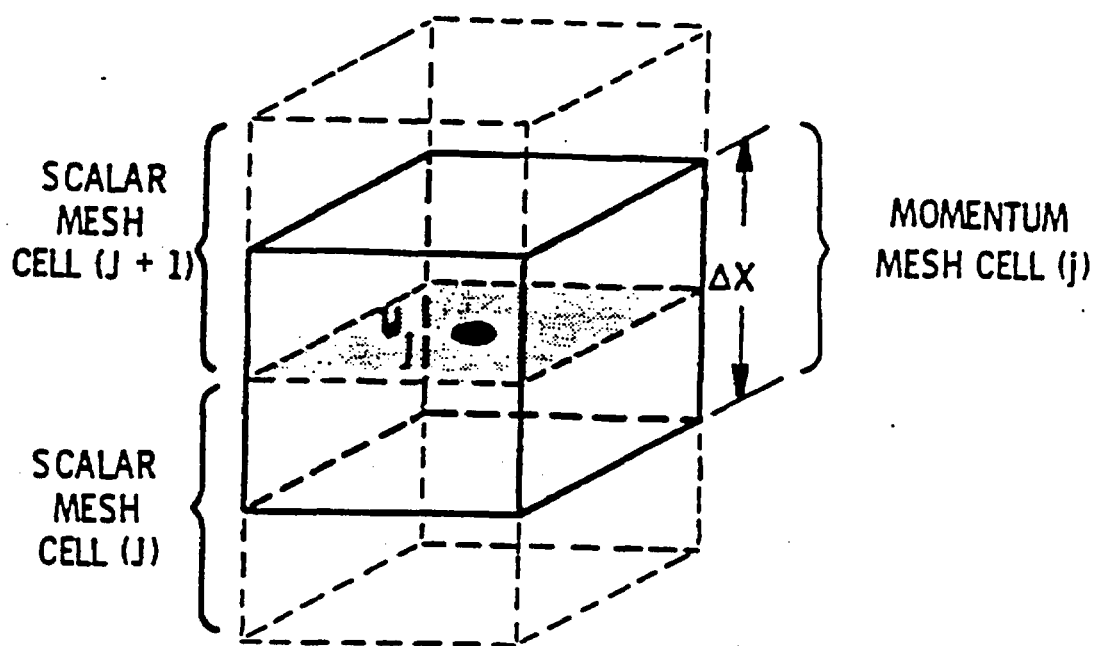


Figure 2-4. Mesh Cell for Vertical Velocities

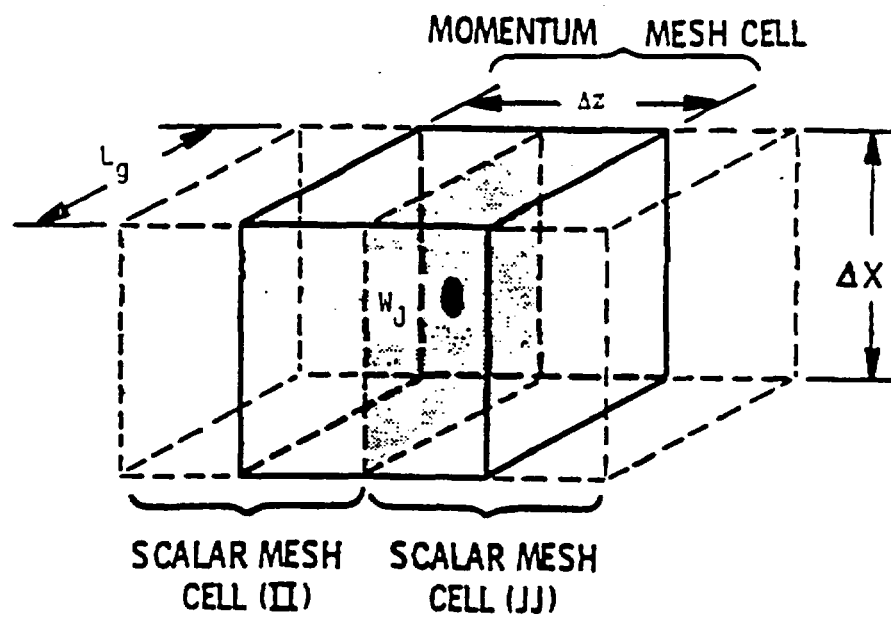


Figure 2-5. Mesh Cell for Transverse Velocities

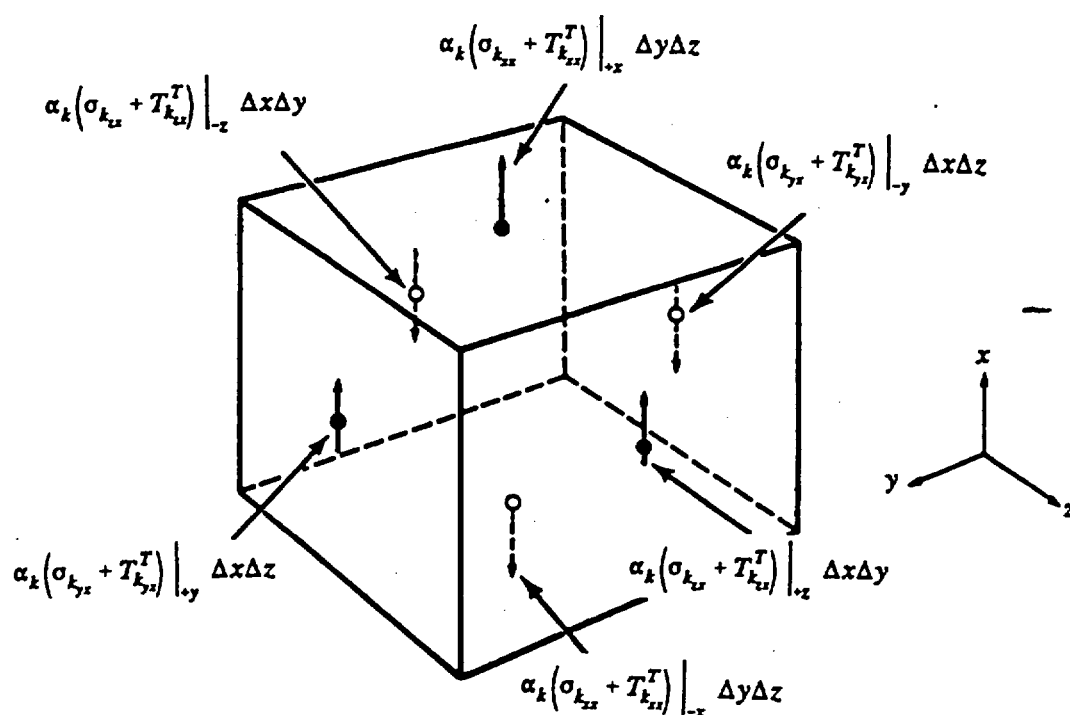


Figure 2-6. Vertical Stresses Acting on a Vertical Momentum Cell

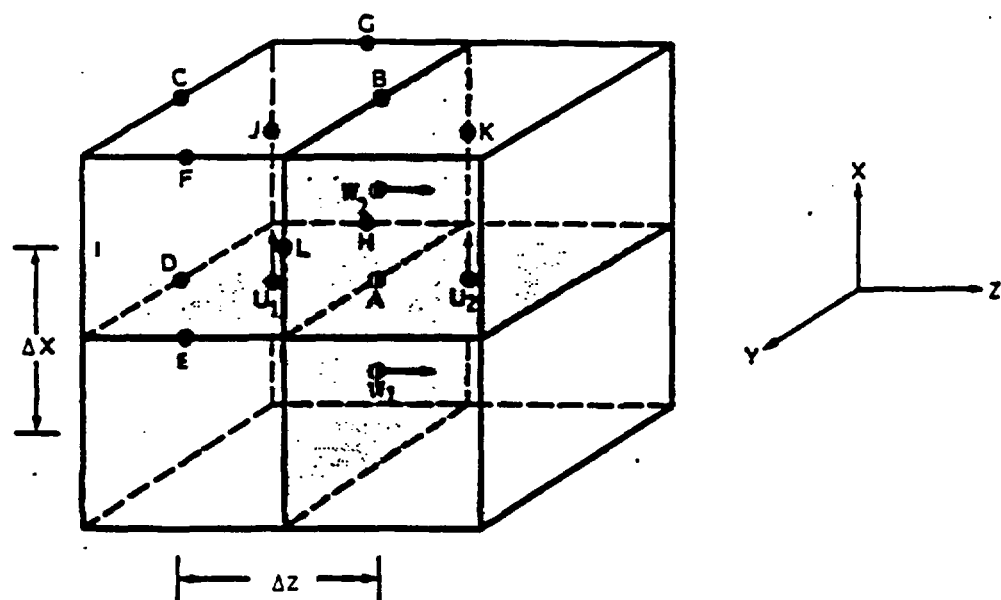


Figure 2-7. Velocity Gradient for Point A

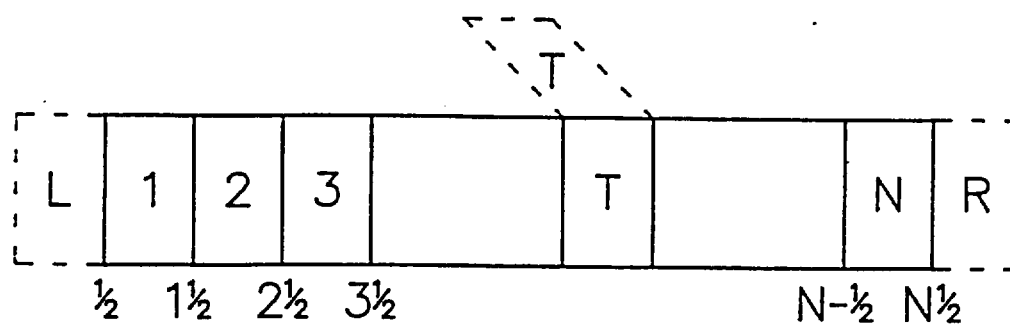


Figure 2-8. One-Dimensional Computational Cell Structure

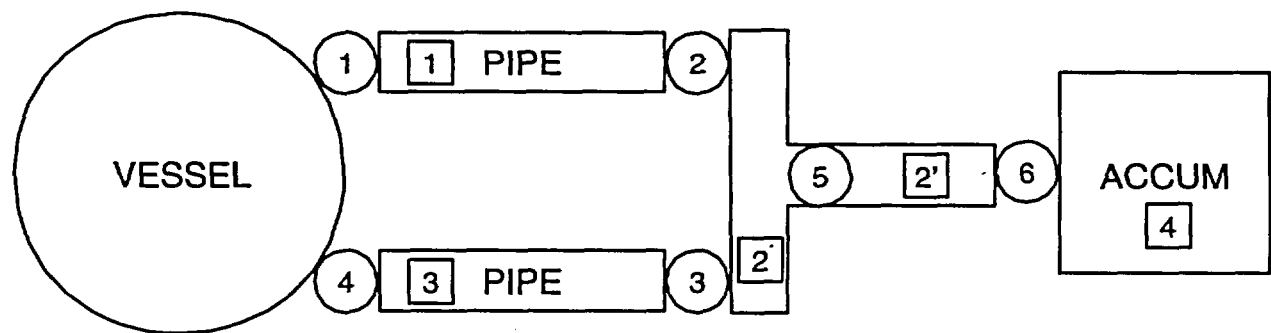


Figure 2-9. Sample Model of a Thermal-Hydraulic Network

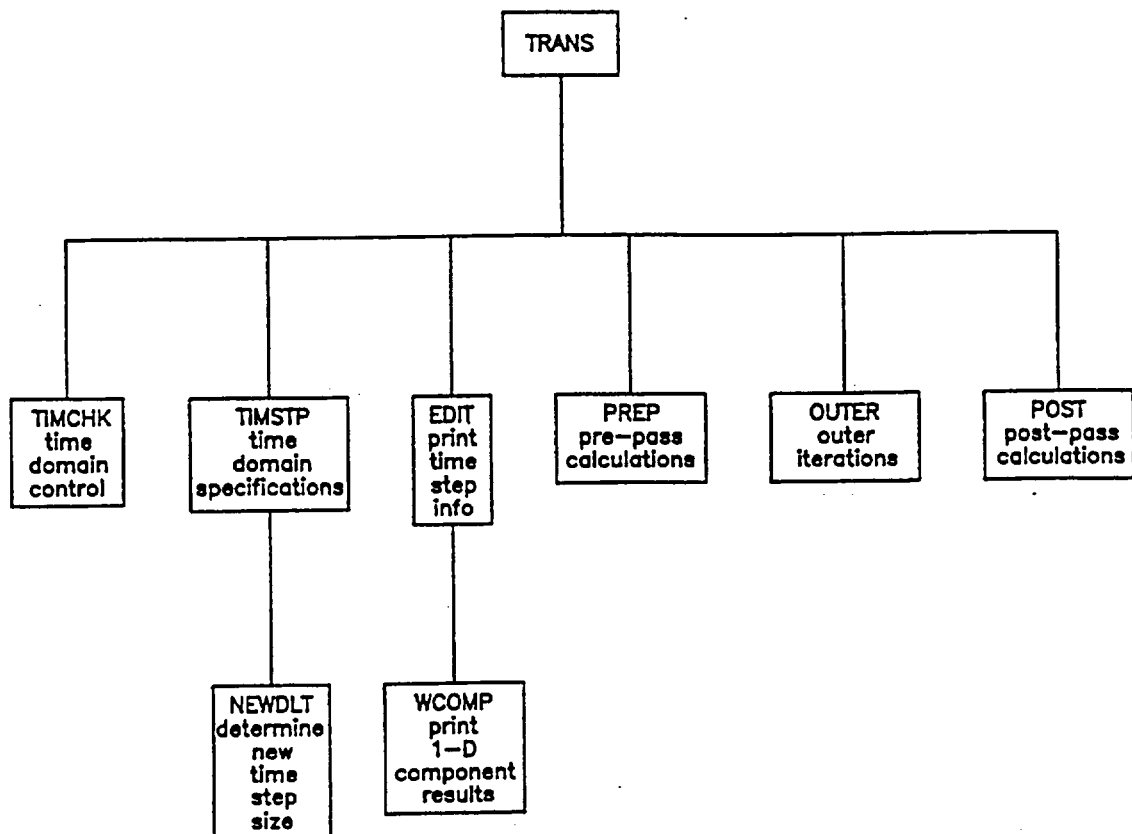


Figure 2-10. Numerical Solution Routines

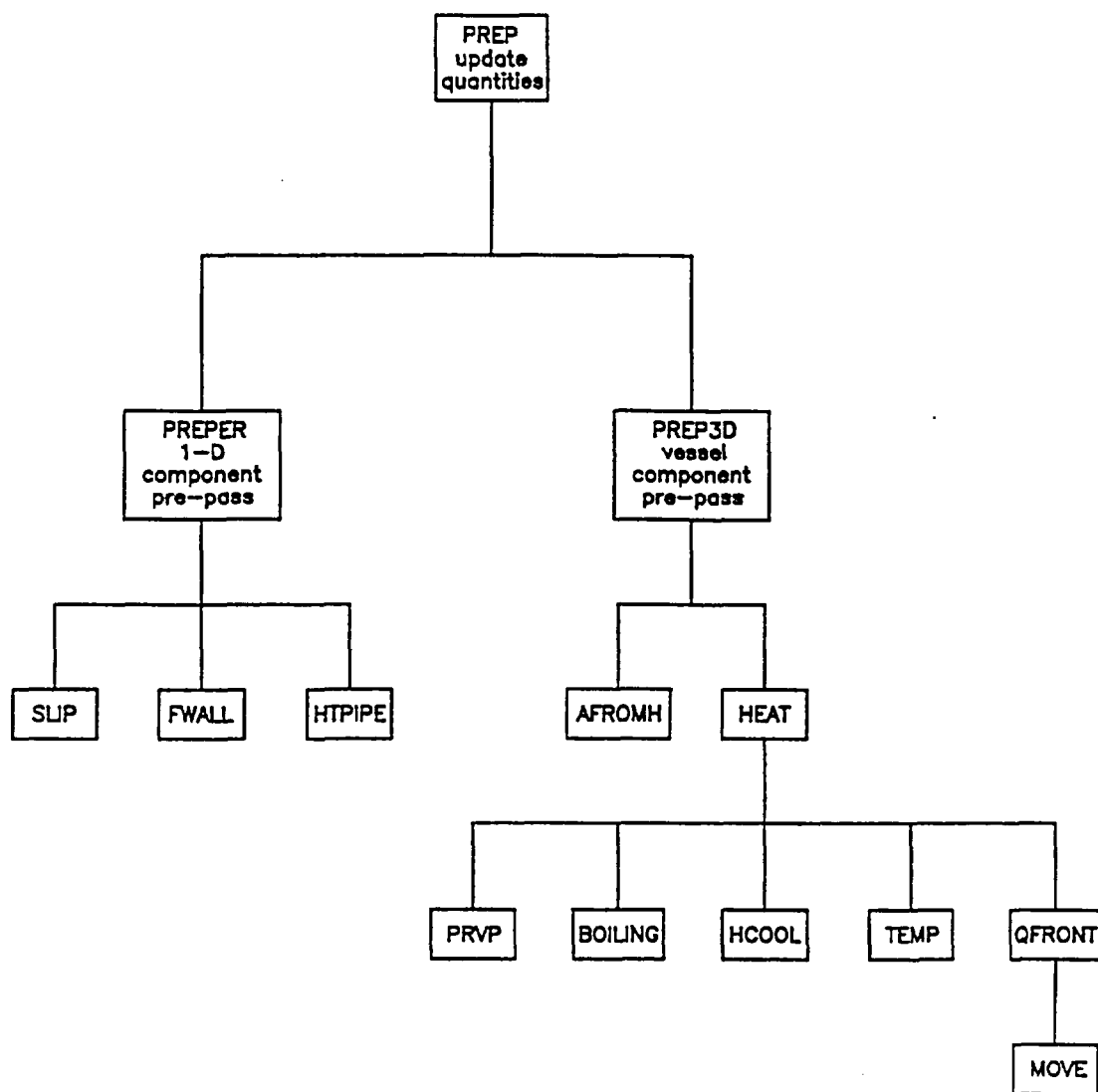


Figure 2-11. WCOBRA/TRAC Prepass Calculation Routines

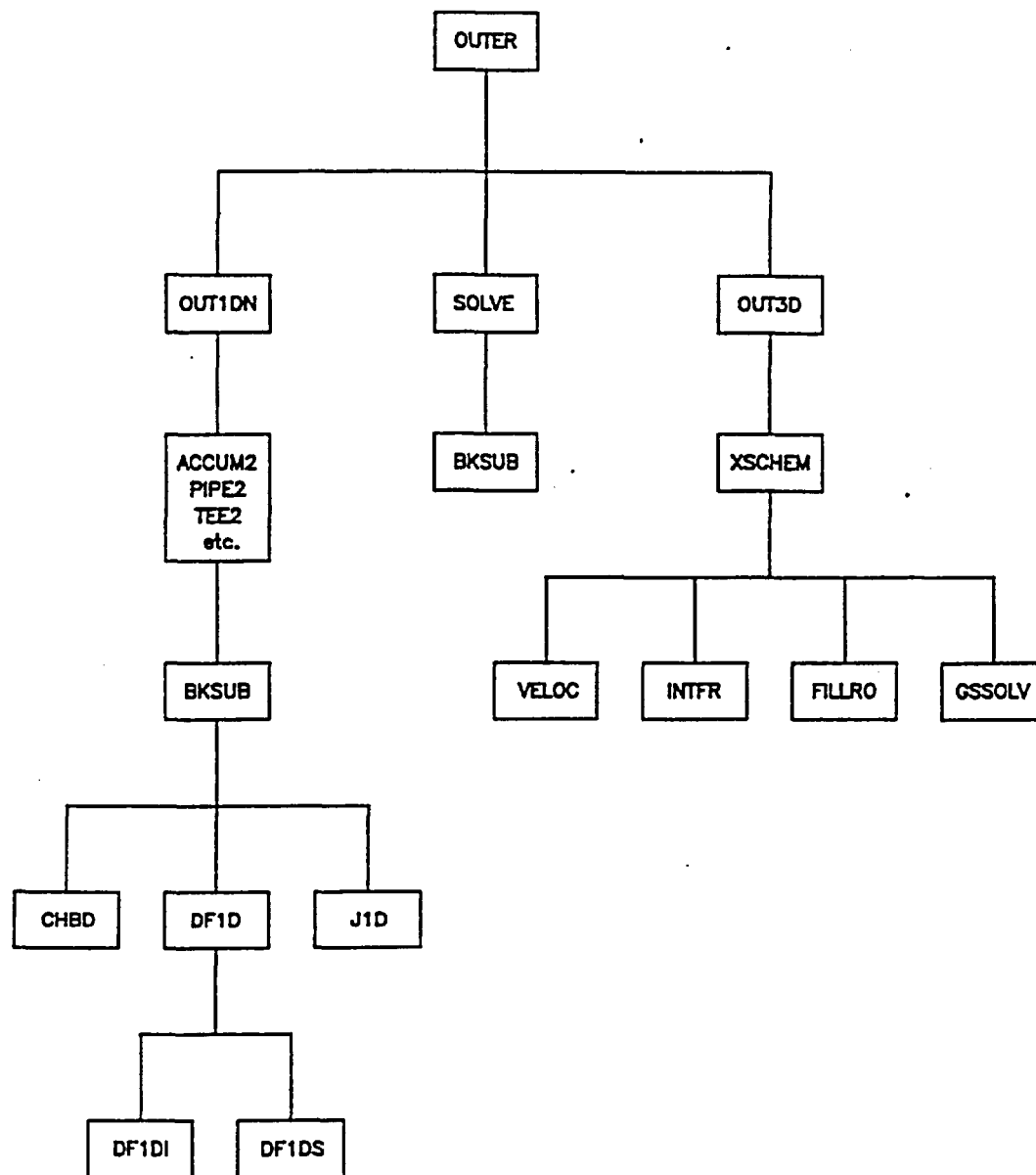


Figure 2-12. WCOBRA/TRAC Outer Iteration Routines

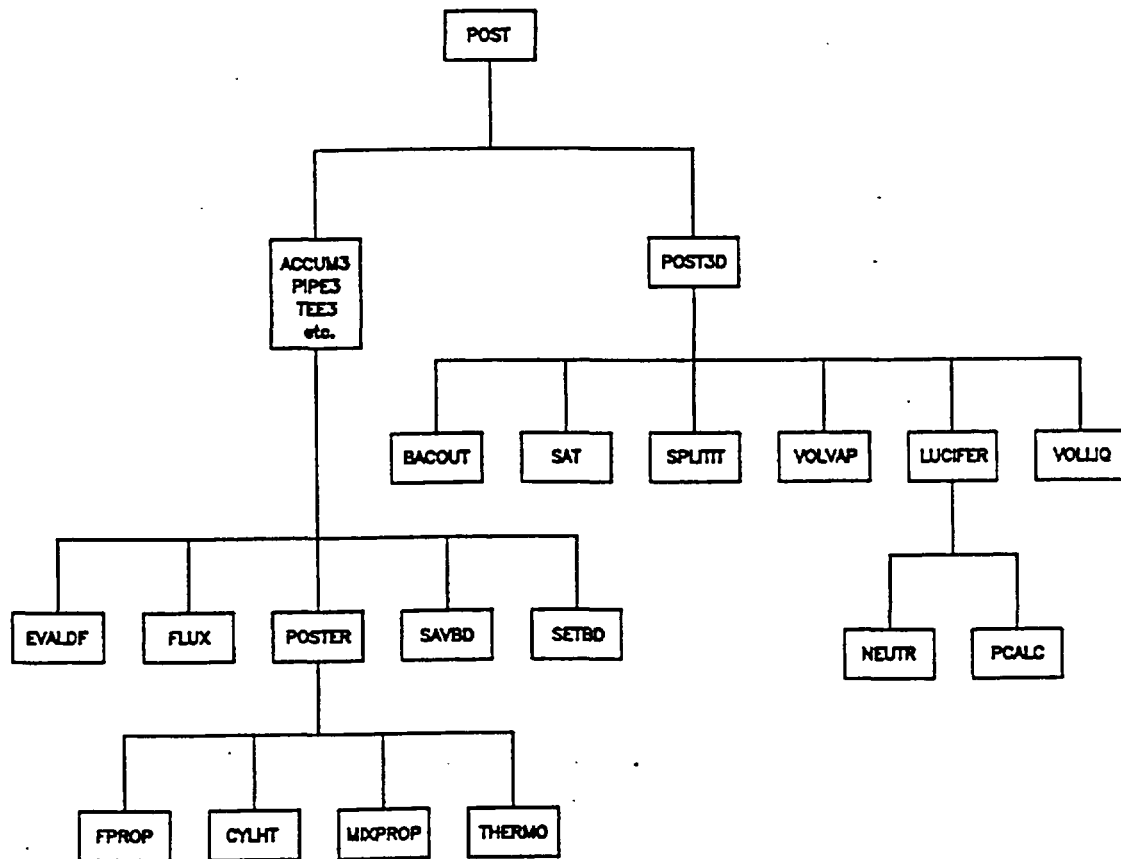


Figure 2-13. WCOBRA/TRAC Routines for Post Pass Calculations

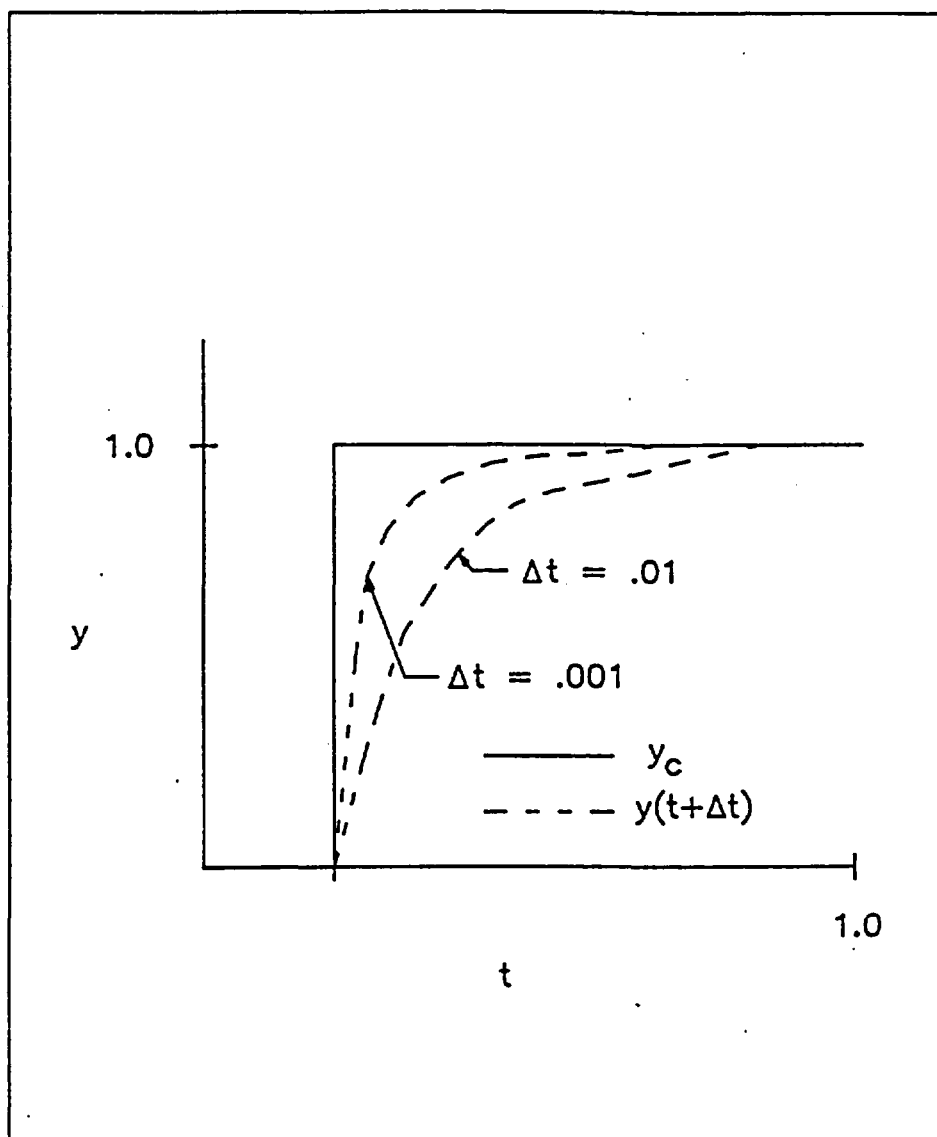


Figure 2-14. Effect of Numerical Damping on Transient Value of y

3 WCOBRA/TRAC FLOW REGIME MAPS AND INTERFACIAL AREA

3-1 INTRODUCTION

Two-phase flow patterns are described by the use of flow regime maps. Subsequent calculations for interfacial heat and mass transfer, interfacial drag, and wall drag depend on the flow regime indicated by the flow regime maps. The WCOBRA/TRAC code uses three flow regime maps to determine the type of two-phase flow in the reactor coolant system. Two flow regime maps are used in the vessel component. These are the "hot wall" flow regime map and the "normal wall" flow regime map. The normal wall flow regimes are also referred to as the "cold wall" flow regimes. The hot wall flow regime map is selected when a wall surface temperature exceeds the critical heat flux temperature, while the normal wall flow regime map is used when the wall is expected to be fully wetted. A third flow regime map, similar to the vessel component normal wall flow regime map, is used for the one-dimensional components. This section includes descriptions of the flow regimes and the calculation of interfacial areas in the vessel and one-dimensional components.

3-2 VESSEL COMPONENT NORMAL WALL FLOW REGIMES

3-2-1 Introduction

The vessel component normal wall flow regime selection logic is used when there are no heated structures within the computational cell with a surface temperature exceeding

$$T_w = \begin{cases} 705.3^\circ F \\ T_{CHF} \end{cases} \quad (3-1)$$

This temperature selection criteria assumes that below the critical heat flux temperature, the wall is fully wettable and the surface temperature at the critical heat flux is approximated by $T_{CHF} \approx (T_{sat} + 75)^\circ F$. The upper limit of 705.3°F corresponds to the critical temperature of water. It is assumed that for cells in which a metal surface temperature exceeds the criteria given by Equation 3-1, liquid can only partially wet the wall and the hot wall flow regime is used.

The normal wall flow regimes, shown in Figure 3-1, are the following: small bubble (SB), small to large bubble (SLB), churn-turbulent (CT), and film/drop (FD). Selection logic for the normal wall flow regimes is shown in Figure 3-2.

The following subsections describe each regime in the vessel component and specify the range of conditions for which each regime can occur. In addition, the interfacial area estimated for each regime is described. The interfacial area is used in the calculation of interfacial drag and interfacial heat transfer, which are described in Sections 4 and 5.

Before selecting a flow regime and performing calculations, a check is made to assure that the local flow regime is consistent with the global flow pattern. This is done by checking the void fraction difference between two axial mesh cells. The void fraction difference between cells is

$$\Delta\alpha_v = \alpha_v(i, j+1) - \alpha_v(i, j) \quad (3-2)^{(1)}$$

where i is a channel index and j is an axial node index.

If the void fraction difference $|\Delta\alpha_v| > [\]^{ac}$, a ramp is identified as [

$$]^{ac} \quad (3-3)^{(1)}$$

and the void fractions used in calculations of the interfacial quantities in determining flow regime transitions for mesh cell (i, j) are re-defined as [

$$]^{ac} \quad (3-6)^{(1)}$$

If the mesh cell $(i, j-1)$ is in the film/drop or a hot wall regime, α_v and α_t are re-set for subsequent calculations as [

$$]^{ac} \quad (3-7)^{(1)}$$

and [

$$]^{ac} \quad (3-8)^{(1)}$$

If α_v^{ac} , an inverted pool is assumed and the void fractions used to determine the flow regime and interfacial terms in cell (i, j) are [

$$\alpha_v^{ac} \quad (3-11)^{(1)}$$

When a large void gradient between two cells is not present, the void fractions at the momentum cell center are assumed to be [

α_v^{ac} . That is,

$$\alpha_v^{ac} \quad (3-12)$$

[

$$\alpha_v^{ac} \quad (3-14)$$

After these void fractions (α_v , α_t , α_c) are determined, the flow regime and interfacial terms are calculated. The following sections describe the flow regimes and the determination of interfacial area for each regime. The subsections for each normal wall flow regime follow in order of increasing void fraction. First the small bubble regime is described, followed by the small to large bubble regime, the churn-turbulent regime, and then the film/drop regime.

3-2-2 Small Bubble Regime

Model Basis The WCOBRA/TRAC small bubble flow regime is assumed to exist for void fractions up to α_v^{ac} . This regime models what is generally referred to as bubbly flow. In this flow regime, the vapor phase is assumed to consist of dispersed spherical bubbles in a continuous liquid phase. As the void fraction increases above α_v^{ac} , the small to large bubble flow regime is selected and the transition from bubbly flow to slug flow is modelled.

Transition from bubbly flow to slug flow occurs when the dispersed bubbles agglomerate. When the dispersed bubble density becomes sufficiently large, the bubbles become closely packed and the collision rate increases. Griffith and Wallis (1961) conducted experiments with air-water mixture in tubes with diameters up to 1.0 inches and observed that below a void fraction of 0.18 there was no indication of slug formation. Additional experiments by Griffith and Snyder (1964) indicated that the void fraction where the bubbly to slug transition occurs is in the range of 0.25 to 0.30.

Other investigators obtained similar conclusions on the bubbly-slug flow transition point. In a semi-theoretical approach, Radovicich and Moissis (1962) postulated that the maximum void fraction for bubbly flow is attained when the bubble collision frequency becomes very large, which they concluded to be at a void fraction of 0.30. Mishima and Ishii (1984)⁽²⁾ used and also recommended a value of 0.30 for the transition point between the bubbly and slug flow.

Model as Coded The selection of vessel flow regime takes place in subroutine INTFR. Calculations are performed to determine the interfacial drag and interfacial heat transfer coefficients, [

]^{a,c} (3-16)

The interfacial area used in the interfacial drag coefficient calculations is then estimated as [

]^{a,c}:

$$N_b = 2000./\text{maximum}(\alpha_v, 0.001) \quad (3-18)^{(4)}$$

[

]^{a,c}

[

]^{ac} (3-19)

where [

]^{ac} (3-20)

or [

]^{ac} (3-21)

The interfacial area for interfacial heat transfer coefficient calculations is [

]^{ac} (3-22)

Scaling Considerations The model for the small bubble regime is based on motion of an individual bubble in a flow stream. Therefore, no scale bias is introduced. The transition point from bubbly flow to slug flow, $\alpha_{SB} \approx [\quad]^{ac}$, is close to the theoretical transition, which is also scale independent. Therefore, although there is little information on flow pattern transitions for large diameter pipes, the transition point $\alpha_{SB} \approx [\quad]^{ac}$ appears to be generally applicable. In the application of WCOBRA/TRAC to pressurized water reactors, typical fuel assemblies have a hydraulic diameter of approximately 0.5 in., which is within the range of tube diameters that were used in determining the transition point between the bubbly and slug flow. The flow regime tests thus provide reasonable assurance that the transition boundary between bubbly and slug flow is appropriate for flow in a reactor core. Simulations of experimental tests of differing scale using WCOBRA/TRAC are reported in Volumes 2 and 3 of WCAP-12945-P-A (Bajorek et al., 1998). The agreement between predicted and test data indicates that flow regime transition criteria assumed in WCOBRA/TRAC are sufficiently accurate for PWR analysis.

The effect of scale on the small bubble transition boundary was also considered by Chow et al. (1989). In that study, the WCOBRA/TRAC normal wall flow regime map was assessed by comparing it to the vertical flow regime map by Taitel, Bornea, and Dukler (1980), shown in Figure 3-3. The Taitel-Bornea-Dukler map was found to have a small scale dependence on D_h for the bubbly flow boundaries. Figure 3-4 shows the WCOBRA/TRAC normal wall flow regime map as a function of volumetric flux. As described in the reference, these boundaries were obtained by assuming steady flow conditions,

deriving the relative velocity obtained from a force balance, and using the interfacial shear models described in Section 4. The flow regime boundary between small bubble and the small to large bubble regime is seen to agree well with the Dukler map.

Conclusions The void fraction used in WCOBRA/TRAC as the upper limit of the small bubble regime is consistent with the experimental observations of Griffith and co-workers. Slugs, referred to as large bubbles in WCOBRA/TRAC, are not permitted to form below $\alpha_{SB} = [\quad]^{ac}$. This value is in general agreement with the proposed mechanisms of slug formation (suggested by Radovich and Moissis-1962, and by Mishima and Ishii-1980). For void fractions above $\alpha_b = [\quad]^{ac}$, WCOBRA/TRAC assumes the small to large bubble regime, which provides a continuous transition from small to large bubbles (slugs). Thus, WCOBRA/TRAC at a void fraction of $\alpha_b = [\quad]^{ac}$ still assumes that part of the flow consists of discrete small bubbles. Therefore, the transition point assumed in WCOBRA/TRAC between the small bubble and small to large bubble regimes is in good agreement with the transition points reported in the published literature.

3-2-3 Small to Large Bubble Regime

Model Basis The small to large bubble transition regime in WCOBRA/TRAC models the transition from bubbly flow to slug flow. This flow regime is more commonly known as the slug flow or the bubbly/slug flow regime. In the WCOBRA/TRAC normal wall flow regime map, this small to large bubbly regime is assumed for void fractions $[\quad]^{ac}$. The lower limit for transition into this regime from the small bubble regime was discussed in the previous section. The upper limit is based on the postulate of Taitel, Bornea, and Dukler (1980), who considered spherical bubbles arranged in a cubic lattice. They reported that at a void fraction of $\alpha_v = 0.52$, stationary bubbles would begin to touch and implied that this void fraction must represent the theoretical upper limit of bubbly flow. WCOBRA/TRAC uses a value of $\alpha_b = [\quad]^{ac}$ to approximate this condition.

The small to large bubble regime models the growth of large vapor slugs and thus approximates the transition from bubbly to slug flow. The flow in this regime is assumed to consist of several large bubbles and many small spherical bubbles in the continuous liquid. In the small to large bubble regime, the vapor is partitioned into a small bubble field with a void fraction $\alpha_{SB} = [\quad]^{ac}$, and the remaining vapor is used to form one or more large bubbles. Figure 3-5 shows this process pictorially. As the vapor fraction increases, the size of the large bubble increases until it is equal to the hydraulic diameter of the computational cell or $[\quad]^{ac}$, whichever is less. The large bubble is held at this constant value as the vapor fraction continues to increase. Thus, there can be more than one large bubble in each computational cell, and the interfacial area is dependent on the cell size. Figure 3-5 shows a case where there is sufficient vapor to form 1 and 2/3 large bubbles in the computational cell.

Model as Coded Calculations for the small bubble regime as described in Section 3-2-2 are performed assuming all of the vapor is in the form of small bubbles and the interfacial area is stored as a temporary variable. Calculations assuming that all of the vapor is in the form of large bubbles are performed next.

The large bubble calculations and the interpolation of the small and large bubble values for the small to large bubble regime are described below.

The large bubble radius is selected to be [

$$]^{ac} (3-23)^{(7,3)}$$

where r_{SB} is the bubble radius assuming all of the vapor is in the form of small bubbles and r_{LB} is the bubble radius for the large bubbles. The expression for r_{LB}^* is coded in subroutine INTFR as [

$$]^{ac} (3-28)$$

Substituting Equation 3-27 into Equation 3-28 gives V_{LB} as [

$$J^{ac}.$$

For large bubbles, the interfacial area in a computational cell is equal to the surface area of a single bubble times the number of bubbles in the cell. Expressing the number of large bubbles in the computational cell as [

$$J^{ac} \quad (3-32)$$

and assuming all of the vapor is in the form of large bubbles, the large bubble interfacial area is [

$$J^{ac} \quad (3-33)$$

or [

$$J^{ac} \quad (3-34)$$

This expression is used in the calculation of the large bubble interfacial drag coefficient.

A_{iLB} is then modified to avoid a large dependence on the adjacent void fraction: [

$$J^{ac} \quad (3-35)^{(8)}$$

Finally, the interfacial area in the small to large bubble regime is calculated by ramping the small bubble and large bubble areas: [

$$J^{ac}.$$

Equation 3-37 can be shown to be the as-coded expression: [

$$J^{ac} \quad (3-38)$$

Scaling Considerations The small to large bubble regime, similar to the small bubble regime, is based on the behavior of a single bubble in a flow field. The use of mesh cell volume to determine the large bubble size, however, indicates that noding selection can influence calculations for this regime. Chow et al. (1989), however, found the small to large bubble flow regime boundaries in WCOBRA/TRAC to be relatively scale independent, as shown in Figure 3-4. That finding is consistent with the Taitel-Bornea-Dukler map, which shows no scale dependence for the slug flow regime, as shown in Figure 3-3. Therefore, the WCOBRA/TRAC small to large bubble regime does not contribute to a scale bias.

Conclusions The WCOBRA/TRAC model for the small to large bubble regime is consistent with experimental observations on the growth and agglomeration of large bubbles and the formation of slug flow. Simulations of separate and integral effects tests discussed in Volumes 2 and 3 of WCAP-12945-P-A apply this model when slug flow was considered possible in experimental tests. Therefore, the uncertainty introduced by the small to large bubble regime assumptions are included in the overall WCOBRA/TRAC bias and uncertainty.

3-2-4 Churn-Turbulent Flow Regime

Model Basis As the vapor content of the flow increases, the large bubbles will begin to coalesce. This marks the beginning of the transition into churn-turbulent flow. The churn-turbulent flow regime is assumed to occur above a void fraction of $\alpha_{LB} = []^{ac}$. This regime is assumed at void fractions above α_{LB} until a stable liquid film is achieved. The void fraction at which a stable liquid film will exist depends on the flow channel size and the vapor velocity. The critical void fraction α_{crit} is determined from a force balance between the disruptive force of the pressure gradient over the crest of waves on the film and the restraining force of surface tension. The expression for α_{crit} is derived in Section 4.

Model as Coded Calculations to determine the critical void fraction marking the upper limit of the churn-turbulent flow regime and the interfacial area are performed in subroutine INTFR. The critical void fraction α_{crit} is limited to a value no less than $[]^{ac}$, and is given by [

$$]^{ac} \quad (3-39)^{(10)}$$

If $0.5 < \alpha < \alpha_{crit}$, the churn-turbulent regime is assumed to exist. The droplet diameter is calculated in the film/drop regime as [

$$]^{ac} \quad (3-40)^{(11)}$$

where $A_{i,d}'''$ is the drop interfacial area density and is determined from solution of the interfacial area transport equation, described in Section 3-3-7.

The interfacial area for continuous liquid-vapor interfacial drag is calculated assuming a [

$$]^{ac} \quad (3-41)^{(12)}$$

and for droplets that occur, the interfacial area assumes [

$$J^{a,c} \quad (3-42)$$

For interfacial heat transfer, the interfacial area is [

$$J^{a,c} \quad (3-43)$$

where [

$$J^{a,c}.$$

Scaling Considerations The model of the churn-turbulent flow regime was assessed by Chow et al. (1989). The transition boundaries of the churn-turbulent flow regime were found to be relatively insensitive to scale, as shown in Figure 3-4.

Conclusions The churn-turbulent flow regime model has been assessed by the WCOBRA/TRAC simulations of the APWR two-phase pressure drop tests and with the UPTF, CCTF, and LOFT integral tests. The uncertainty in modelling churn-turbulent flow is accounted for in the WCOBRA/TRAC bias and uncertainty.

3-2-5 Film/Drop Flow Regime

Model Basis At a void fraction above $\alpha_v = \alpha_{crit}$, the flow is considered to consist entirely of film/drop flow. As long as the vapor velocity is sufficiently high to entrain drops, a drop field will be maintained. The transition between film and droplet flow is predicted based on the models used for entrainment and interfacial drag between the vapor and the drops.

Model as Coded The interfacial areas for continuous liquid film and drops in the film/drop regime are calculated in the same way as they are for churn-turbulent flow. As before, in the film/drop regime the drop diameter is calculated as [

$$]^{a,c} \quad (3-45)^{(29)}$$

where $A_{i,d}'''$ is the drop interfacial area density.

The interfacial area for continuous liquid-vapor interfacial drag is calculated as [

$$]^{a,c} \quad (3-46)^{(12)}$$

and the drop interfacial area is [

$$]^{a,c} \quad (3-47)$$

For the interfacial heat transfer, the interfacial area is adjusted to provide a smoother transition between two adjacent hydraulic cells and is calculated as [

$$]^{a,c} \quad (3-48)$$

where, [

$$]^{a,c} \quad (3-49)$$

Scaling Conclusions The model for the film/drop flow regime was assessed by Chow et al. (1989). The transition boundary between the film/drop regime and the churn-turbulent regime was found to be somewhat dependent on scale, as shown in Figure 3-4. For large hydraulic diameters, the boundary agrees with that given by Taitel, Bornea, and Dukler (1980) in Figure 3-3.

Conclusions The film/drop regime model has been assessed by WCOBRA/TRAC simulations of the APWR two-phase pressure drop tests and by simulation of the UPTF, CCTF, and LOFT integral tests. The uncertainty in modelling film/drop flow is accounted for in the WCOBRA/TRAC bias and uncertainty.

3-3 VESSEL COMPONENT HOT WALL FLOW REGIMES

3-3-1 Introduction

This section describes the hot wall flow regime map used in the WCOBRA/TRAC vessel component.

During the initial part of blowdown in a PWR, departure from nucleate boiling (DNB) occurs and the core undergoes a rapid heatup. After DNB, liquid-wall contact is prevented by the rapid evaporation of water, and the flow regimes are significantly different from the two-phase flow regimes that occur for an unheated surface. This flow regime is available only for channels with heated structures.

The "hot wall" flow regimes are assumed when a momentum cell contains a heated surface with a temperature exceeding the value of T_w given by Equation 3-1. These hot wall regimes describe the structure and hydrodynamics of the highly non-homogeneous, thermal non-equilibrium two-phase flow encountered during blowdown and reflood. The hot wall flow regimes include the subcooled inverted annular flow regime, the inverted liquid slug flow regime, the dispersed droplet flow regime, the falling film flow regime and the top deluge flow regime. Figure 3-6 presents an illustration of the hot wall flow regimes, and Figure 3-7 shows a schematic of the hot wall regime selection logic. The following sections describe each of these flow regimes, and determine the interfacial area used in interfacial drag and heat transfer calculations.

3-3-2 Inverted Annular Flow Regime

Model Basis An inverted annular flow regime is assumed during upflow when the continuous liquid phase is subcooled. In the inverted annular flow regime, the continuous liquid is assumed to be separated from the wall by a thin film of vapor. This assumed flow structure is in agreement with that observed in the experiments conducted by DeJarlais (1983). The interfacial areas calculated for the liquid annular column and any droplets present in the flow are consistent with this flow structure. For the continuous liquid, the interfacial area density is [

$$J^{ac} \quad (3-50)^{(12)}$$

and for droplets the interfacial area density $A_{i,d}'''$ is determined from the solution of the drop interfacial area transport equation.

Model as Coded For continuous liquid, the interfacial area for the subcooled inverted annular flow regime is coded as [

$$]^{a,c} (3-51)^{(12)}$$

and for the droplets by [

$$]^{a,c}.$$

Scaling Considerations The model for the inverted annular flow regime has been verified through its use in simulations of the FLECHT-SEASET, FLECHT Low Flooding Rate, FLECHT Top Skewed Power, FEBA, and NRU separate effects reflood tests. Each of these tests modelled full-scale PWR fuel bundles.

Conclusions The inverted annular flow regime has been verified through simulations of reflood separate effects tests and integral effects tests that are reported in Volumes 2 and 3 of WCAP-12945-P-A. The uncertainty in modelling this regime is accounted for in the overall WCOBRA/TRAC code bias and uncertainty.

3-3-3 Inverted Liquid Slug Flow Regime

Model Basis The inverted liquid slug flow regime, also referred to as the liquid chunk regime, models the flow pattern following breakup of the continuous liquid column in the inverted annular regime. In this regime, the annular liquid column disintegrates due to growth of unstable waves that form on the interface. The liquid slugs that form are large, nearly filling the channel flow area, and are themselves unstable. These slugs eventually break up into smaller discrete droplets.

The interfacial area for the liquid slugs is estimated assuming the continuous liquid slugs are spherical. The interfacial area of the slugs is

$$A_{i,s}''' = N_s''' \pi D_s^2 \quad (3-53)$$

where D_s is the liquid slug diameter and N_s''' is the number density of slugs:

$$N_s''' = \frac{\alpha_l}{\frac{\pi D_s^3}{6}} \quad (3-54)$$

The interfacial area density of the slugs then becomes

$$A_{i,s}''' = \frac{6 \alpha_t}{D_s} \quad (3-55)$$

Assuming the slugs have a diameter [$d_s^{(13)}$] yields for slug interfacial area [$A_{i,s}^{ac}$] (3-56)

The slug diameter is based on the assumption that an inverted annular column will break up initially into drops whose dimensions are approximately equal to the wavelength of the surface instability which forms on the liquid column. Data by DeJarlais (1983) indicates that for conditions typical of those in a PWR core channel during reflood, the characteristic surface wavelength is about 0.75 of the liquid column diameter. The liquid column diameter is assumed to be equal to the channel diameter, because the inverted liquid slug regime is expected to occur at low void fraction.

Model as Coded The interfacial area of the liquid slug in the inverted slug flow regime is coded as [$A_{i,s}^{ac}$] (3-57)

where A_x is the flow area in the momentum cell, and ΔX is the cell height.

The interfacial area for any droplets that may appear in the inverted liquid slug regime is [$A_{i,d}^{ac}$] (3-58)

Scaling Considerations The model for the inverted annular flow regime has been verified through its use in simulations of the FLECHT-SEASET, FLECHT Low Flooding Rate, FLECHT Top Skewed Power, FEBA, and NRU separate effects reflood tests. Each of these tests modelled full-scale PWR fuel bundles.

Conclusions The inverted annular flow regime has been verified through simulations of reflood separate effects tests and integral effects tests that are reported in Volumes 2 and 3 of WCAP-12945-P-A. The uncertainty in modelling this regime is accounted for in the overall WCOBRA/TRAC code bias and uncertainty.

3-3-4 Dispersed Droplet Flow Regime

Model Basis The dispersed droplet flow regime is characterized by small liquid drops surrounded by a continuous vapor phase. Entrainment of continuous liquid in the inverted slug regime allows for a smooth transition into the dispersed droplet flow regime. The dispersed droplet regime can exist at all void fractions if entrainment mechanisms create this field.

Model as Coded The interfacial area in this regime is determined directly from solution of the drop interfacial area transport equation, as described in Section 3-3-7.

The interfacial area for the dispersed droplets is given by [

$$]^{ac} \quad (3-59)$$

The droplet diameter used to calculate the drop Reynolds number for the interfacial drag and heat transfer is given by Equation 3-45.

Scaling Considerations The model for dispersed droplet flow is scale independent. The model has been verified through simulations of FLECHT-SEASET, FLECHT Low Flooding Rate, FLECHT Top Skewed Power, FEBA, and NRU separate effects reflood tests. Each of these tests modelled full-scale PWR fuel bundles.

Conclusions The dispersed droplet flow regime model has been verified through a large number of simulations of reflood, blowdown, and refill separate effects tests in addition to simulations of large scale integral test facilities. The uncertainty in modelling this regime is accounted for in the overall WCOBRA/TRAC code bias and uncertainty.

3-3-5 Falling Film Regime

Model Basis Although the normal direction for reflood is from the bottom of the core, a top quench front is assumed to exist if the momentum cell above the cell in a hot wall flow regime (inverted annular, inverted liquid slug, dispersed droplet) contains no surfaces with a temperature greater than T_{CHF} . If the void fraction is greater than []^{ac}, the falling film flow regime is assumed.

The interfacial area and diameter of droplets in the flow field are determined in the same way as described in the dispersed droplet flow regime. The interfacial area per unit volume for the film is [

$$]^{ac} \quad (3-60)$$

Model as Coded The interfacial area for the falling film is calculated as [

$$]^{ac} \quad (3-61)$$

and the interfacial area for the droplets is again given by [

$$]^{ac} \quad (3-62)$$

Scaling Considerations The models for the falling film regime are verified through their use in simulations of the G-1 loop and G-2 loop blowdown tests, the G-2 loop refill tests, and the CCTF upper plenum injection tests. Each of these tests were full-scale in height. The G-1 and G-2 test bundles contained 448 and 336 rods each respectively and the CCTF facility contained 32 rod bundles. Thus, the models for the falling film regime have been tested against data from tests that were full-scale in height and were varied in scale radially.

Conclusions The falling film flow regime model has been used in simulations of blowdown and refill separate effects tests, and in the CCTF integral tests. The uncertainty in modelling this regime is accounted for in the overall WCOBRA/TRAC code bias and uncertainty.

3-3-6 Top Deluge Flow Regime

Model Basis The top deluge flow regime is similar to the falling film regime except that top deluge is assumed when the void fraction is less than $[]^{ac}$. Like the falling film regime, a top quench front is assumed to exist if the momentum cell above the cell in a hot wall regime contains rods with temperatures less than T_{CHF} . In the deluge flow regime the flow is assumed to consist of large liquid slugs having diameters equal to the flow channel hydraulic diameter.

Model as Coded The interfacial area and drop size for droplets that occur in the top deluge regime are determined in the same way as described for the dispersed droplet flow regime. The interfacial area for the liquid slugs is [

$$]^{ac} \quad (3-63)^{(14)}$$

The interfacial area of the drops is [

] ^{a,c} (3-64)

Scaling Considerations The model of the top deluge flow regime is verified through its use in simulations of the G-1 loop and G-2 loop blowdown tests, the G-2 loop refill tests and the CCTF upper plenum injection tests. Each of these tests were full-scale in height. The G-1 and G-2 test bundles contained 448 rods and 336 rods each respectively, and the CCTF facility contained 32 rod bundles. Thus, the model of the falling film regime has been tested against data from tests that were full-scale in height and were varied in scale radially.

Conclusions The model for the top deluge flow regime has been verified through its use in blowdown and refill separate effects tests and in CCTF integral effects tests. The uncertainty in modelling this regime is accounted for in the overall WCOBRA/TRAC code bias and uncertainty.

3-3-7 Interfacial Area Transport Equation

Model Basis The interfacial area of the entrained droplet field is determined by solving an interfacial area transport equation:

$$\frac{dA_{i,d}'''}{dt} + \nabla \cdot (A_{i,d}''' \underline{U}_e) = \dot{A}_{i,E}''' + \dot{A}_{i,\Gamma}''' \quad (3-65)^{(16,31)}$$

$$\left[\begin{array}{c} \text{Rate of} \\ \text{Change of} \\ \text{Interfacial Area} \\ \text{Concentration} \end{array} \right] + \left[\begin{array}{c} \text{Rate of} \\ \text{Efflux of} \\ \text{Interfacial Area} \\ \text{Concentration} \end{array} \right] = \left[\begin{array}{c} \text{Rate of} \\ \text{Interfacial Area} \\ \text{Concentration} \\ \text{Generation by} \\ \text{Entrainment and} \\ \text{Deposition} \end{array} \right] + \left[\begin{array}{c} \text{Rate of} \\ \text{Interfacial Area} \\ \text{Concentration} \\ \text{Change Due to} \\ \text{Phase Change} \end{array} \right]$$

Model as Coded The interfacial area transport equation given by Equation 3-65 is solved in subroutine POST3D for $A_{i,d}'''$ with an explicit method. Equation 3-65 is written as [

] ^{a,c}

The change in drop interfacial area due to phase change within the cell is calculated from a mass balance:
[

$]^{ac}.$

Since [

$]^{ac}.$

Relating volume and surface area by [

$]^{ac} \quad (3-70)$

Equation 3-69 becomes [

$]^{ac}.$

The drop interfacial area concentration is then calculated. The net contribution to interfacial area from incoming and outflowing streams is evaluated and added to Equation 3-71 along with the entrainment component, as shown below: [

$$j^{a,c} \quad (3-72)^{(16,18,31)}$$

The interfacial area concentration given by Equation 3-72 is then compared to possible lower limits, and the final value of $A_{i,d}'''$ is selected as [

$$j^{a,c} \quad (3-73)^{(17)}$$

The drop interfacial area for entrained flow is given by [

$$j^{a,c} \quad (3-74)^{(18)}$$

Scaling Considerations The interfacial area transport equation is not dependent on scale. One of the lower limits imposed on $A_{i,d}'''$ depends on mesh size, but that limit is rarely applied. As a result, the calculation of $A_{i,d}'''$ is not considered to be scale dependent.

Conclusions The interfacial area transport equation is used in nearly all WCOBRA/TRAC simulations. The uncertainty of this model is therefore accounted for in the overall WCOBRA/TRAC code bias and uncertainty.

3-4 ONE-DIMENSIONAL COMPONENT FLOW REGIMES

3-4-1 Introduction

This section describes the flow regime map used in the one-dimensional components. This flow regime map was originally developed and used in the TRAC-PD2 code (Liles et al., 1981). The same map is used for both vertical and horizontal components. The map assumes the existence of four flow regimes: bubbly, slug, churn, and annular mist. The bubbly flow regime occurs for void fractions $\alpha \leq 0.3$, the slug regime for $0.3 < \alpha \leq 0.5$, the churn regime for $0.5 < \alpha < 0.75$, and the annular-mist regime for

$\alpha \geq 0.75$. In addition, the slug flow regime does not occur if the total mass flux is greater than $2700 \text{ kg/m}^2\text{-s}$. The basic WCOBRA/TRAC one-dimensional component flow regime map is shown in Figure 3-8. The crosshatched sections represent regions where values are interpolated between two flow regimes. For the churn flow regime, values of the interfacial heat transfer coefficients are interpolated between values at $\alpha = 0.5$ and $\alpha = 0.75$ rather than using separate correlations for churn flow. The transition from slug to bubbly flow for mass fluxes higher than $2000 \text{ kg/m}^2\text{-s}$ also used interpolation to smoothly change regimes over the range $2000 < G < 2700 \text{ kg/m}^2\text{-s}$. Single phase liquid is assumed if $\alpha < 1.0 \times 10^{-6}$ and single phase vapor when $\alpha > 0.999999$.

The flow regime map described below is applied to the calculation of interfacial area for heat transfer only. As described in Section 4-7, correlations are used to describe the relative velocity between the phases. These correlations assume similar basic flow regimes, but the transition boundaries occur at different void fractions.

3-4-2 Bubbly Flow Regime

Model Basis Bubbly flow occurs for the range $0 \leq \alpha \leq 0.30$. The transition point $\alpha = 0.30$ between bubbly and slug flow is that value postulated by Radovich and Moissis (1962) and by Mishima and Ishii (1980). Bubbly flow is also assumed when $0.30 < \alpha < 0.50$ and the mass flux is greater than $2700 \text{ kg/m}^2\text{-s}$. This limit is based on the work by Choe, Weinberg, and Weisman (1976).

The total interfacial area within a cell is determined assuming a constant bubble Weber number:

$$We_b = \frac{\rho_t U_r^2 D_b}{\sigma} = 7.5 \quad (3-75)$$

or

$$D_b = \frac{We_b \sigma}{\rho_t U_r^2} \quad (3-76)$$

where D_b is the bubble diameter. The value $We_b = 7.5$ was originally based on TRAC predictions of the Creare low subcooling downcomer tests (Crowley, Block, and Cary, 1977).

A uniform bubble distribution is assumed, and the total interfacial area in a cell is given by

$$A_{i,bubbly} = \frac{6\alpha}{D_b} V_c \quad (3-77)$$

where V_c is the cell volume.

Model as Coded The bubble diameter from Equation 3-76 is restricted to values between [$j^{ac(19)}$]

The interfacial area is calculated with Equations 3-75 and 3-76, and coded as [

$$j^{ac} \quad (3-78)$$

If the surface area is very small, this area can become small enough to allow significant nonequilibrium to occur. [

$$j^{ac} \quad (3-79)^{(20)}$$

[

$$j^{ac} \quad (3-80)^{(20)}$$

The interfacial area used in the bubbly flow regime is the larger of $A_{i,bubbly}^*$ and $A_{i,bubbly}^{**}$: [

$$j^{ac} \quad (3-81)$$

Scaling Considerations WCOBRA/TRAC simulations of the Westinghouse 1/3-scale steam/water mixing tests and the UPTF full-scale hot leg steam/water mixing test have been performed and results have been compared to experimental data. The WCOBRA/TRAC model of the test facility was composed of one-dimensional components. The results of these simulations did not indicate a dependency on scale.

Conclusions The models and correlations for the bubbly flow regime have been verified through WCOBRA/TRAC simulations of the Westinghouse 1/3-scale steam/water mixing tests, the full-scale UPTF steam/water mixing tests, and through their use in the loop components of the LOFT and CCTF integral tests. The uncertainty and reliability of these models is accounted for in the overall WCOBRA/TRAC code bias and uncertainty.

3-4-3 Slug Flow Regime

Model Basis When the vapor void fraction is $0.3 < \alpha \leq 0.5$ and the cell-average mass flux is less than $2000 \text{ kg/m}^2\text{-s}$, the flow enters the slug flow regime. At the upper void fraction limit, $\alpha = 0.5$, 40 percent of the vapor is assumed to exist in the form of trailing bubbles with the remainder contained in the slug.⁽²¹⁾ If the mass flux is greater than $2700 \text{ kg/m}^2\text{-s}$, all of the vapor is assumed to exist as a bubbly flow. In the slug regime, the interfacial area is determined by a linear combination of areas derived from small bubbles based on Weber number and large vapor slugs based on pipe diameter.

Model as Coded The slug flow regime is modelled by defining a parameter X_{slug} and using it to modify the interfacial area. X_{slug} is defined as [

$$]^{ac} \quad (3-82)$$

$$[$$

$$]^{ac}$$

Then, for void fractions greater than 0.3, α_b^* is defined as [

$$]^{ac}.$$

The interfacial area for the bubbles in slug flow is calculated as [

$$]^{ac} \quad (3-84)^{(23)}$$

As had been noted in the discussion on bubbly flow, for small relative velocities the interfacial area given by Equation 3-84 can become small enough to allow significant non-equilibrium to occur. To prevent this in the bubbly flow regime, the [

$$]^{ac} \quad (3-85)^{(22)}$$

For the slugs, the interfacial area is assumed to be: [

$$J^{a,c} \quad (3-85b)$$

Viewing the slug as a cylinder inside a pipe, and using Equation 3-60, it can be shown that [

$$J^{a,c} \quad (18)$$

The total interfacial area in the slug regime is the sum of the areas calculated by Equations 3-85 and 3-85b.

Scaling Considerations WCOBRA/TRAC simulations of the Westinghouse 1/3-scale steam/water mixing tests and the UPTF full-scale hot leg steam/water mixing test have been performed and results have been compared to experimental data. The WCOBRA/TRAC model of the test facility was composed of one-dimensional components, and the slug flow regime was predicted to have occurred. The results of these simulations do not indicate a dependence on scale. This implies that the models used for the slug flow regime are not strongly dependent on scale.

Conclusions The models and correlations for the slug flow regime have been verified through WCOBRA/TRAC simulations of the Westinghouse 1/3-steam/water mixing tests, the full-scale UPTF steam/water mixing tests, and through their use in the loop components of the LOFT and CCTF integral tests. The uncertainty and reliability of these models is accounted for in the overall WCOBRA/TRAC code bias and uncertainty.

3-4-4 Churn Flow Regime

Model Basis The churn flow regime is assumed in the range $0.5 < \alpha < 0.75$. The churn flow regime is modelled in WCOBRA/TRAC one-dimensional components as a simple transition between bubbly or slug and annular-mist flows. The interfacial area for the churn flow regime is estimated using interfacial areas calculated for the bubbly, slug, and annular-mist regimes and a weighing factor to insure the regimes merge smoothly.

Model as Coded Interfacial areas are first calculated for the bubbly/slug regimes $A_{i,bubbly}$ or $A_{i,slug}$, and for the annular-mist regime $A_{i,am}$. The interfacial area for the churn flow regime is then calculated using a [

$$]^{ac} \quad (3-86)$$

where [

$$]^{ac} \quad (3-87)$$

The interfacial area for the annular mist regime, $A_{i,am}$, is described in Section 3-4-5 and is given by Equation 3-98.

The ramping factor α^* is given by [

$$]^{ac}.$$

Scaling Considerations WCOBRA/TRAC simulations of the Westinghouse 1/3-scale steam/water mixing tests and the UPTF full-scale hot leg steam/water mixing test have been performed, and results have been compared to experimental data. The WCOBRA/TRAC model of the test facility was composed of one-dimensional components, and the churn flow regime was predicted to have occurred. The results of these simulations do not indicate a dependence on scale. This implies that the models used for the churn flow regime are not strongly dependent on scale.

Conclusions The models and correlations for the churn flow regime have been verified through WCOBRA/TRAC simulations of the Westinghouse and 1/3-scale steam/water mixing tests, the full-scale UPTF steam/water mixing tests, and through their use in the loop components of the LOFT and CCTF integral tests. The uncertainty and reliability of these models is accounted for in the overall WCOBRA/TRAC code bias and uncertainty.

3-4-5 Annular-Mist Flow Regime

Model Basis The annular-mist flow regime is assumed when $0.75 < \alpha < 0.999999$. Both liquid films and entrained droplets are modelled. A simple entrainment correlation, based on a critical droplet Weber number, is used to determine the fraction of liquid that is present in the flow as drops. The remainder is assumed to remain in the liquid film. The entrainment fraction F_e is determined from an empirical correlation given by

$$F_e = 1 - \exp \left[-0.23 \left(U_v - U_e^* \right) \right] \quad (3-89)^{(24)}$$

where the velocity for the onset of entrainment U_e^* is determined from a force balance between the gravity and drag forces on a droplet which gives the relation

$$U_e^* = 2.33 \left[(\rho_l - \rho_v) \frac{We_d \sigma}{\rho_v^2} \right]^{1/4} \quad (3-90)$$

The correlation given by Equation 3-90 was developed as part of the TRAC-PD2 code (Liles et al., 1981). Liles et al. (1988) reported that this expression was found to provide a better representation of entrainment in the intermediate range of vapor velocities than the Kataoka and Ishii correlation (1982).

The critical Weber number for droplets is assumed to be constant:

$$We_d = \frac{\rho_v U_r^2 D_d}{\sigma} = 4.0 \quad (3-91)$$

Liles et al. (1981) made tests on the sensitivity of TRAC-PD2 to We_d and found the results were not strongly influenced by variations of We_d between 2 and 12.

The film interfacial area is calculated as

$$A_{i, film} = (1 - F_e) \pi D_h \Delta X \quad (3-92)^{(25)}$$

and the droplet interfacial area by

$$A_{i,mist}^* = 6 F_e (1-\alpha) V_c \rho_v \frac{U_r^2}{We_d \sigma} \quad (3-93)$$

If the droplet area given by Equation 3-93 becomes too small, significant nonequilibrium can occur. To protect against this, a droplet interfacial area assuming a minimum drop number density []^{ac} is calculated as⁽²⁶⁾

$$A_{i,mist}^{**} = 4.83598 V_c [F_e (1-\alpha)]^{2/3} N_{d,min}^{1/3} \quad (3-94)^{(20)}$$

The maximum of $A_{i,mist}^*$ and $A_{i,mist}^{**}$ is then used as the droplet interfacial area.

Model as Coded The entrainment fraction F_e is calculated as [

$$]^{ac} \quad (3-95)^{(27)}$$

where the velocity for onset of entrainment is calculated from Equation 3-90.

The drop diameter is calculated with limits on the minimum and maximum size as [

$$]^{ac} \quad (3-96)^{(27)}$$

This diameter is used to calculate the drop Reynolds number Re_d that is used in determining the interfacial heat transfer coefficient.

The interfacial area for drops is then calculated as [

$$]^{ac} (3-97)^{(28)}$$

where F_c is calculated from Equation 3-95 and the void fraction α is limited to values between 0.75 and 0.999.

The interfacial area for the annular mist regime, $A_{i,am}$, that is used in determining interfacial area for churn-turbulent flow is simply the sum of the film and mist interfacial areas: [

$$]^{ac} (3-98)$$

where $A_{i,film}$ is given by Equation 3-92 and $A_{i,mist}$ by Equation 3-97.

Scaling Considerations WCOBRA/TRAC simulations of the UPTF full-scale hot leg steam/water mixing test have been performed and the results have been compared to experimental data. The WCOBRA/TRAC model of this UPTF test was composed of one-dimensional components and the annular-mist regime was predicted to have occurred. The results of these simulations demonstrate the ability of the code to calculate annular-mist flow at full-scale and obtain acceptable agreement with data.

Conclusions The models and correlations for the annular-mist flow regime have been verified through simulations of the UPTF steam/water mixing tests and their use in the LOFT and CCTF integral tests.

3-5 REFERENCES

Bajorek, S. M., et al., 1998, "Code Qualification Document for Best Estimate LOCA Analysis," WCAP-12945-P-A, Volume 1, Revision 2, and Volumes 2 through 5, Revision 1, and WCAP-14747 (Non-Proprietary).

Choe, W. G., Weinberg, L., and Weisman, J., 1976, "Observations and Correlation of Flow Pattern Transitions in Horizontal Concurrent Gas-Liquid Flow," Two-Phase Transport and Reactor Safety, Veziroglu, T. N. and Kakac, S., editors, Vol. IV, pp. 1357-1393.

Chow, S. K., et al., 1989, "Assessment of Scaling Uncertainties for PWR Plant Large-Break LOCA Analysis," EPRI NP-6602.

Crowley, C. J., Block, J. A., and Cary, C. N., 1977, "Downcomer Effects in a 1/15-Scale PWR Geometry: Experimental Data Report," Creare Inc, NUREG-0281.

DeJarlais, G., 1983, "An Experimental Study of Inverted Annular Flow Hydrodynamics Utilizing An Adiabatic Simulation," ANL-83-44, NUREG/CR-3339.

Griffith, P. and Snyder, G. A., 1964, "The Bubbly-Slug Transition in a High Velocity Two-Phase Flow," MIT Report 5003-29 (TID-20947).

Griffith, P. and Wallis, G. B., 1961, "Two-Phase Slug Flow," J. Heat Transfer, Vol. 83, pp. 307-320.

Kataoka, I. and Ishii, M., 1982, "Mechanism and Correlation of Droplet Entrainment and Deposition in Annular Two-Phase Flow," ANL-82-44, NUREG/CR-2885.

Liles, D. R. et al., 1988, "TRAC-PF1/MOD1 Correlations and Models," NUREG/CR-5069, Los Alamos Report, LA-11208-MS.

Liles, D. R., et al., 1981, "TRAC-PD2, An Advanced Best Estimate Computer Program for Pressurized Water Reactor Loss-of-Coolant Accident Analysis," NUREG/CR-2054.

Mishima, K. and Ishii, M., 1980, "Theoretical Prediction on Onset of Horizontal Slug Flow," J. Fluids Eng., Vol. 102, pp. 441-445.

Mishima, K. and Ishii, M., 1984, "Flow Regime Transition Criteria for Upward Two-Phase Flow in Vertical Tubes," Int. J. Heat Mass Transfer, Vol. 27, No. 5, pp. 723-737.

Radovicich, N. A. and Moissis, R., 1962, "The Transition from Two-Phase Bubble Flow to Slug Flow," MIT Report 7-7673-22.

Taitel, Y., Bornea, D., and Dukler, A. E., 1980, "Modelling Flow Pattern Transitions for Steady Upward Gas-Liquid Flow in Vertical Tubes," AIChE J., Vol. 26, No. 3, pp. 345-354.

3-6 RAI LISTING

1. RAI1-20
2. RAI1-21
3. RAI1-22 (refers to WCAP-12945, Rev. 1, page 3-6; now page 3-4)
4. RAI1-23
5. RAI1-24
6. RAI1-25 (refers to WCAP-12945, Rev. 1, page 3-7; now page 3-5)
7. RAI1-26
8. RAI1-27

- 9. RAI1-28
- 10. RAI1-29
- 11. RAI1-30
- 12. RAI1-31
- 13. RAI1-32 (refers to WCAP-12945, Rev. 1, page 3-21; now page 3-15)
- 14. RAI1-33
- 15. RAI1-34
- 16. RAI1-35
- 17. RAI1-36
- 18. RAI1-37
- 19. RAI1-38 (refers to WCAP-12945, Rev. 1, page 3-32; now page 3-22)
- 20. RAI1-39
- 21. RAI1-40 (refers to WCAP-12945, Rev. 1, page 3-33; now page 3-23)
- 22. RAI1-41
- 23. RAI1-42
- 24. RAI1-43
- 25. RAI1-44
- 26. RAI1-45 (refers to WCAP-12945, Rev. 1, page 3-38; now page 3-27)
- 27. RAI1-46
- 28. RAI1-47
- 29. RAI1-77
- 30. RAI1-1(h)
- 31. RAI1-1(i)

Figure 3-1. Normal Wall Flow Regimes

Figure 3-2. Normal Wall Flow Regime Selection Logic

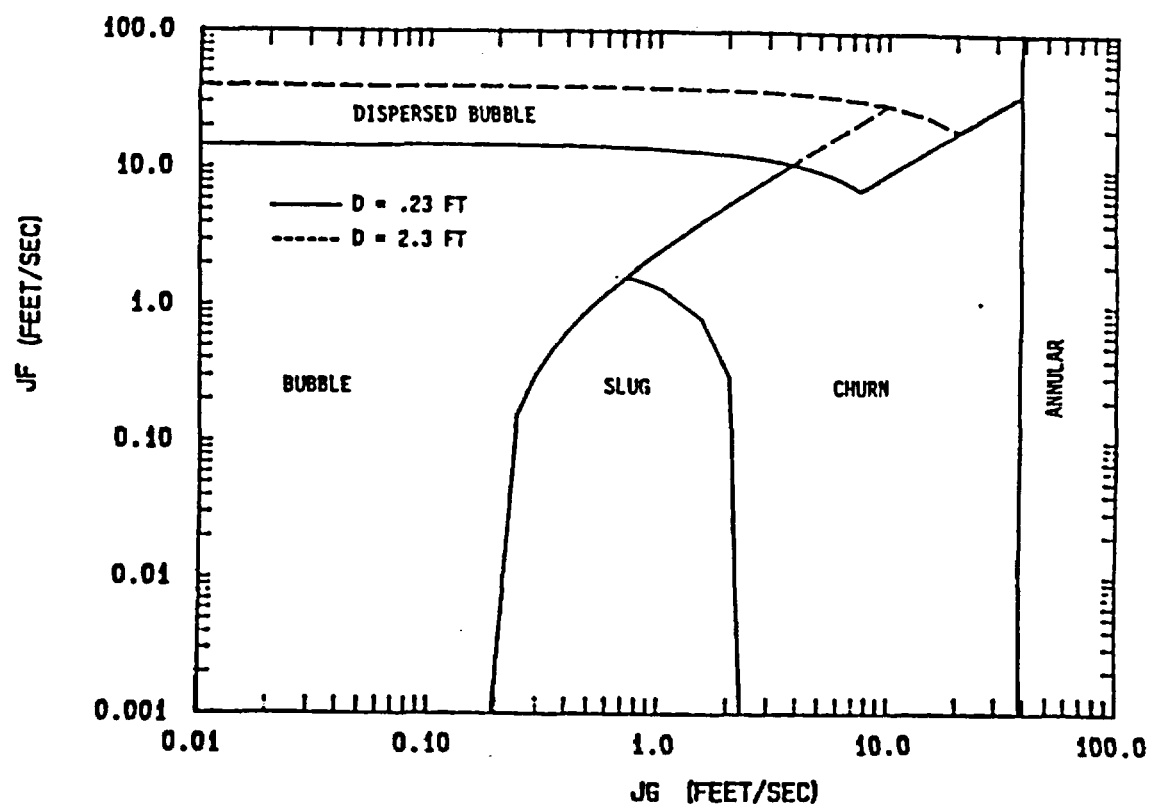


Figure 3-3. Effect of Scale on Vertical Upflow Flow Regime Transitions Predicted by Taitel, Bornea, and Dukler (1980)

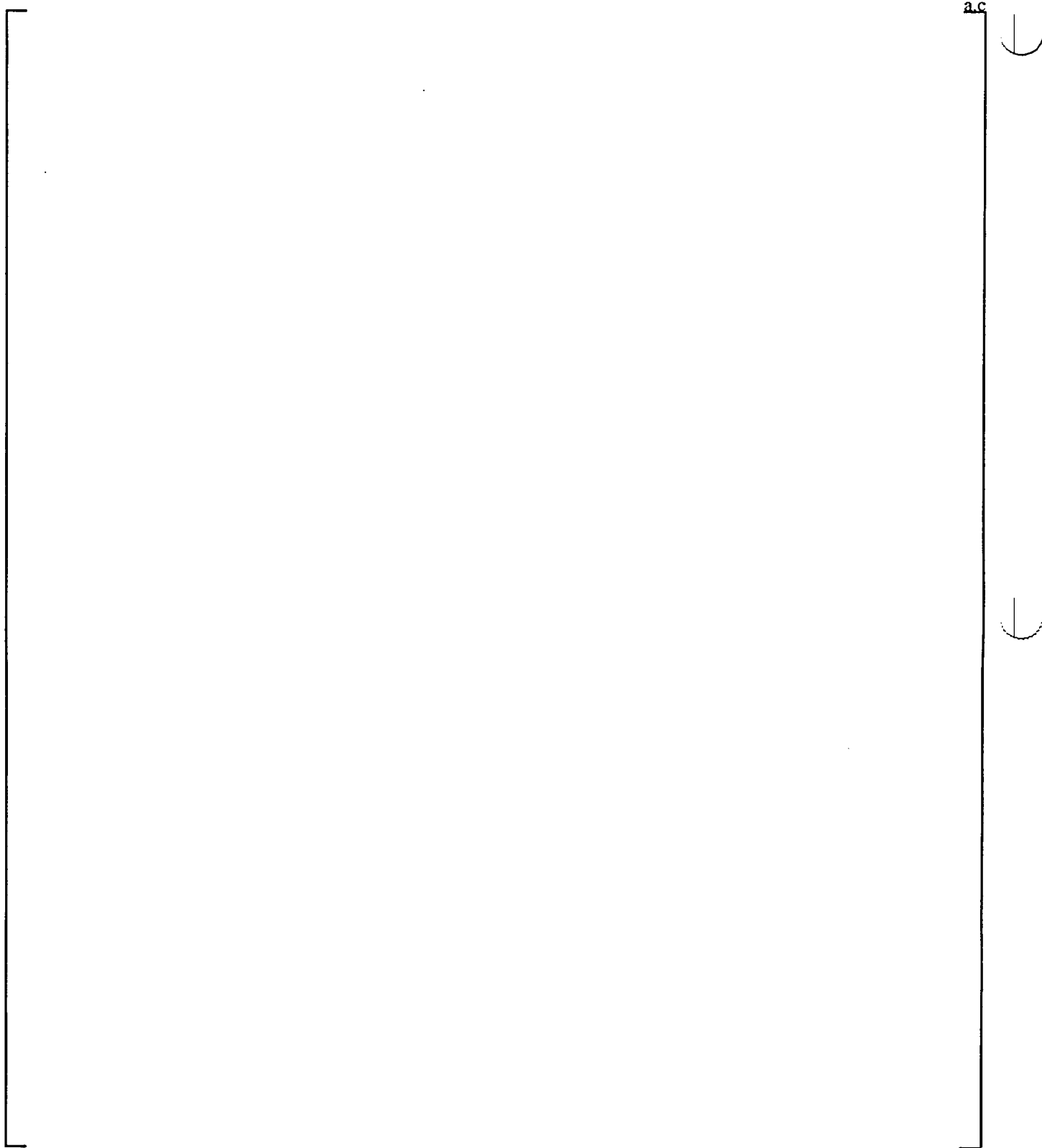


Figure 3-4. Effect of Scale on Vertical Upflow Flow Regime Transitions Predicted by WCOBRA/TRAC

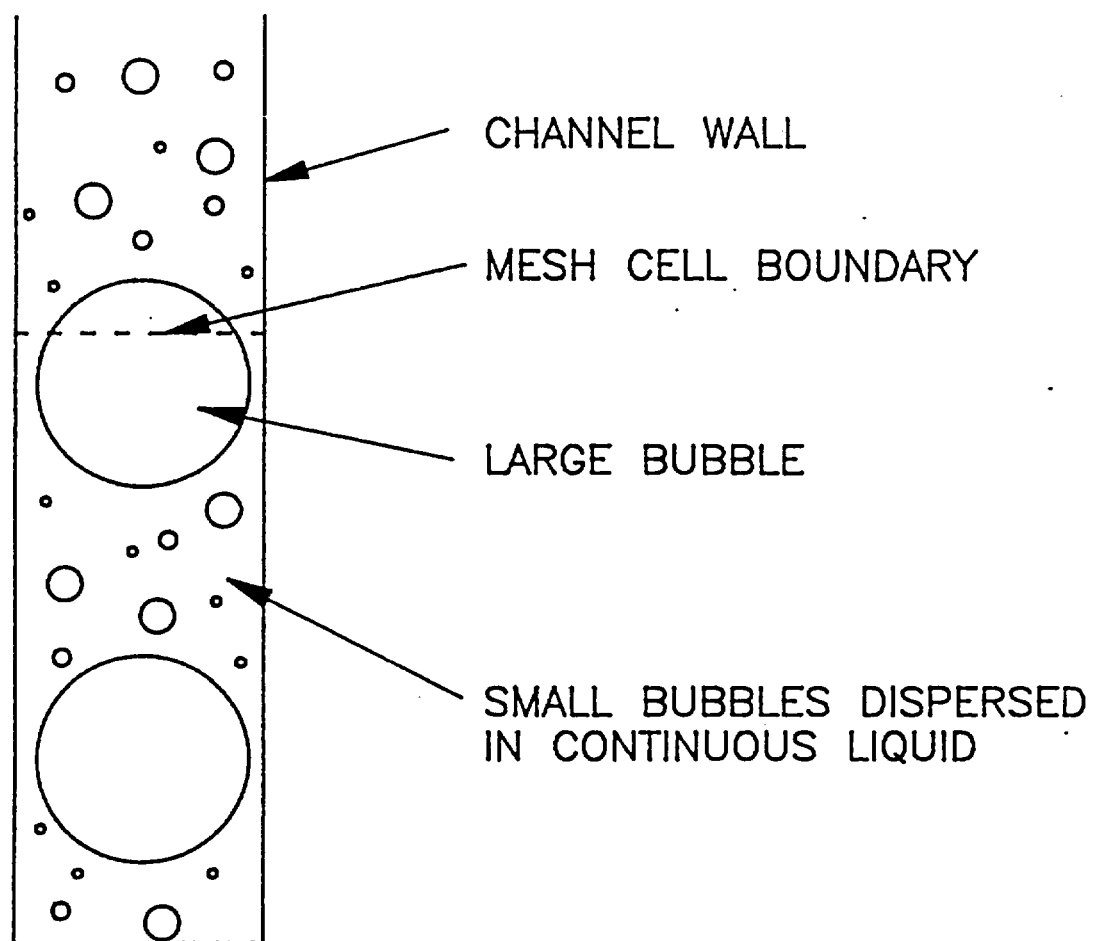


Figure 3-5. Small to Large Bubble Regime - Formation of Large Bubbles

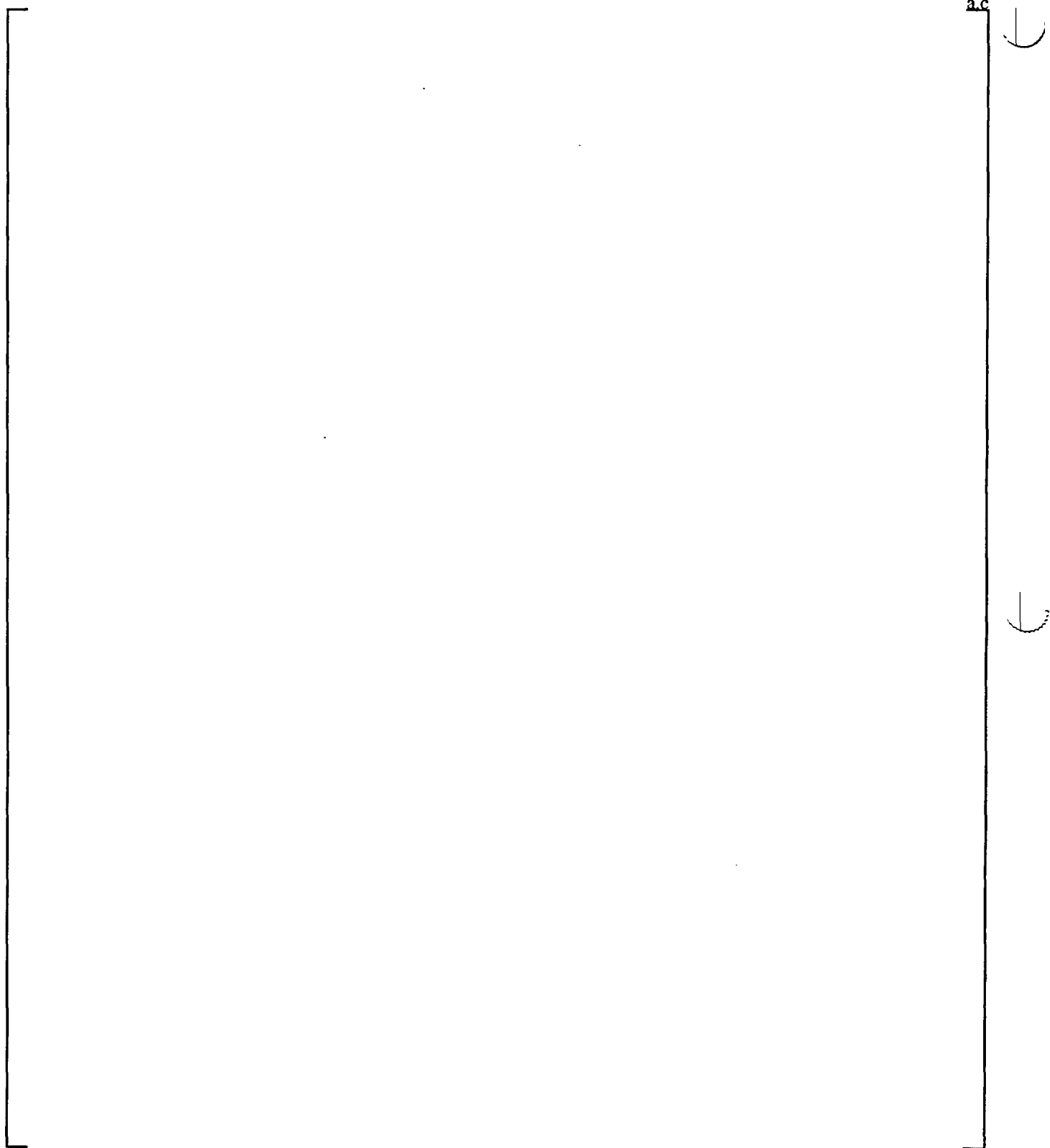


Figure 3-6. Vessel Component Hot Wall Flow Regimes

Figure 3-7. Hot Wall Flow Regime Selection Logic

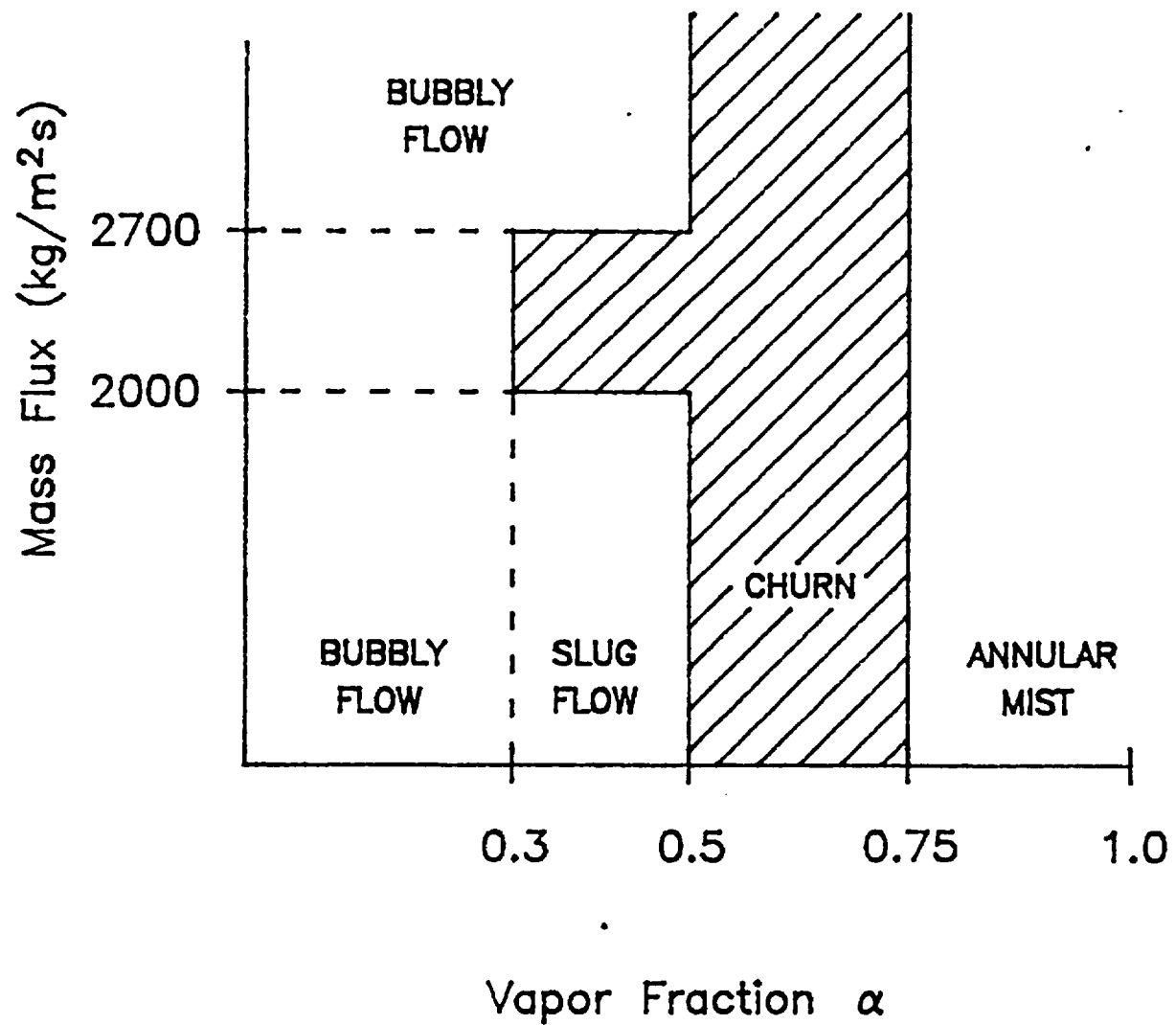


Figure 3-8. One-Dimensional Component Flow Regime Map

a.c

Figure 3-9. One-Dimensional Component Churn Flow Ramping Factor

4 WCOBRA/TRAC MOMENTUM TRANSFER MODELS

4-1 INTRODUCTION

The momentum equations used for the WCOBRA/TRAC vessel component and loop components have been described in Section 2. There are specific terms in these equations that model the wall-to-fluid drag for each phase and the vapor-to-liquid drag. The constitutive relationships which characterize the wall and interphase drag account for the wall frictional force on the fluid, as well as the interfacial forces which occur as a result of momentum exchange between the phases flowing together within a channel. The interfacial drag models and correlations used in WCOBRA/TRAC are flow regime dependent. These expressions for the interfacial drag force also assume that the force is proportional to the square of the relative velocity between the phases. In the WCOBRA/TRAC vessel model, there exist two liquid fields such that different expressions are used to calculate the interfacial drag term for the entrained droplet and the continuous liquid fields within a computational cell.

As mentioned above, the interfacial drag relationships are flow regime dependent. Thus, the interfacial area, liquid content, and resulting frictional relationships between the phases will change as the flow regime changes. As a result, the interfacial drag relationship will be dependent on the cell void fraction and the total local mass flux through the cell at any one time. The flow regimes used in WCOBRA/TRAC have been discussed in Section 3 of this report and the interfacial drag models and their basis for each flow regime are described in this section.

Since the WCOBRA/TRAC vessel component interfacial drag uses the formulation of two separate liquid fields, entrained and continuous film flow, this permits the use of more basic, microscopic models to describe the interfacial drag. In addition, the use of two liquid fields permits more accurate modelling of the reactor vessel geometric details such as spacer grids, top and bottom fuel nozzles (tie plates), downcomer, lower plenum, and the complex flow passages in the upper core plate and structures. More detailed modelling of these geometries allows the code to calculate, more accurately, a variety of hydraulic conditions such as countercurrent flow, flooding, entrainment and de-entrainment.

WCOBRA/TRAC vessel component also has the capability of modelling turbulent effects within the continuous phases. The turbulence model in the original COBRA/TRAC code uses a simplified version of the Ishii (1975) mixing length model. The effects of the turbulence models are to reduce gradients within the continuous liquid or vapor between adjacent subchannels thereby promoting heat transfer without mass transfer by mixing. The coarse noding used in WCOBRA/TRAC precludes the use of those models because the lateral length scale between adjacent channels greatly exceeds the subchannel hydraulic diameter which is used as the basis for the mixing length. If the code were used in a true subchannel basis, then the turbulence formulation given in the original COBRA/TRAC code would be applicable.

The WCOBRA/TRAC one-dimensional loop components use a five equation drift flux formulation to solve the system of two-phase flow equations as described in Section 2. The flow regime dependence of

the frictional drag is characterized by the relative velocity, which is flow regime dependent. This then determines the mixture velocity and the resulting two-phase multiplier and pressure drop.

The interfacial drag models, in conjunction with the flow regime modelling used in WCOBRA/TRAC, have been verified over a wide range of hydraulic conditions typical of a postulated large break LOCA transient. New experimental data have become available on full scale reactor hardware and components from the Upper Plenum Test Facility (UPTF) experiments. These experiments are modelled with WCOBRA/TRAC, as described in Sections 14 and 15 of WCAP-12945-P-A (Bajorek et al., 1998), to verify the total integrated interfacial drag - flow regime package. Other, smaller scale experiments have also been used to verify the WCOBRA/TRAC interfacial drag models.

4-2 VESSEL COMPONENT WALL SHEAR MODELS

Model Basis: The vessel momentum equations described in Section 2-3-3-2 define the wall drag coefficient in units which, when multiplied by the new time phasic velocity, will yield force per unit length on the phase. However, as described in Section 2-6-2, the phasic mass flow rates are the actual solution variables. The wall drag coefficients described here are defined in terms of the units in which they are derived in subroutine INTFR. The wall shear stress components for axial flow in the vessel are expressed as:

$$\tau'_{wx,l} = K_{wx,l} \rho_l \alpha_l \underline{U}_l A_x \quad (4-1a)$$

$$\tau'_{wx,v} = K_{wx,v} \rho_v \alpha_v \underline{U}_v A_x \quad (4-1b)$$

$$\tau'_{wx,e} = K_{wx,e} \rho_e \alpha_e \underline{U}_e A_x \quad (4-1c)$$

and for lateral flow by:

$$\tau'_{wz,l} = K_{wz,l} \rho_l \alpha_l \underline{W}_l A_z \quad (4-2a)$$

$$\tau'_{wz,v} = K_{wz,v} \rho_v \alpha_v \underline{W}_v A_z \quad (4-2b)$$

$$\tau'_{wz,e} = K_{wz,e} \rho_e \alpha_e \underline{W}_e A_z \quad (4-2c)$$

where:

$\tau'_{wA,k}$ = wall shear stress per unit length
 subscript $A = X$ for axial flow and $A = Z$ for lateral flow
 for phase k where $k = \ell, v, e$,

$K_{wA,k}$ = wall drag coefficient times fluid velocity
 ρ_k = phasic density
 α_k = phasic volumetric fraction
 v_k = phasic velocity.

The wall shear stress is assumed to be carried by the continuous liquid field when the wall is wet, except at very high vapor fractions. [

] ^{ac}:

[

] ^{ac}.

The friction factors for the liquid and vapor fields are:

$$f_{wt} = \text{maximum} \begin{cases} 64 / Re_\ell & (\text{laminar}) \\ 0.0055 + 0.55Re_\ell^{-1/3} & (\text{turbulent}) \end{cases} \quad (4-5a)^{(2)}$$

$$f_{wv} = \text{maximum} \begin{cases} 64 / Re_v & (\text{laminar}) \\ 0.0055 + 0.55Re_v^{-1/3} & (\text{turbulent}) \end{cases} \quad (4-5b)^{(2)}$$

The Reynolds number for each phase is based on the phasic mass velocity

$$Re_t = \frac{D_h |G_{x,t}|}{\mu_t} \quad (4-6a)$$

$$Re_v = \frac{D_h |G_{x,v}|}{\mu_v} \quad (4-6b)$$

The wall shear models for the lateral directions are similar to those for the axial or vertical direction. The same friction factor relationships given in Equations 4-5a and 4-5b are used, and the form loss coefficients for lateral flow are user input.

For all flow regimes, a shear term associated with an input form loss is also considered. [

] ^{ac} (4-7c)⁽⁵⁾

Similar expressions hold for the lateral flow equations.

In summary, the wall drag coefficient is defined as follows for the continuous liquid in the cold wall regime: [

] ^{ac} (4-9)

Combining and using Equations 4-7a, 4-8, and 4-9, [

$$]^{ac} \quad (4-10)$$

Similarly, in the hot wall regime, [

$$]^{ac} \quad (4-11)$$

Model as Coded: For bubbly, film, and single-phase liquid, the wall-vapor friction factor (f_{wv}) is set equal to zero. For single-phase vapor, and inverted annular and droplet (no film flow) flow regimes, the wall-liquid friction factor (f_{wl}) is set equal to zero.

The axial flow models are described first. The liquid and vapor Reynolds numbers are calculated using Equations 4-6a and 4-6b, and the friction factors by Equations 4-5a and 4-5b. The phasic frictional pressure drops are calculated as: [

$$]^{ac} \quad (4-12b)$$

where:

$\bar{\rho}_l$ = average liquid density between mesh cells

$\bar{\rho}_v$ = average vapor density between mesh cells

The axial wall drag coefficient for the liquid phase is calculated as: [

$$]^{ac} \quad (4-13)^{(3)}$$

and the axial wall drag coefficient for the vapor phase is calculated as: [

$$]^{ac} \quad (4-14)$$

The first term of Equation 4-14 is zero except at vapor fractions near one. For the entrained field, the wall drag coefficient has only the form loss term: [

$$]^{ac} \quad (4-15)$$

[

$$]^{ac} \quad (4-16)$$

and [

$$]^{ac} \quad (4-17)$$

where F_{SPV} and F_{SPL} are defined as: [

$$]^{ac} \quad (4-18)$$

and, [

$$]^{ac} \quad (4-19)$$

The functions F_{SPV} and F_{SPL} provide a smooth transition of the wall friction term from one field to another as a phase is depleted.

In the hot wall flow regime, the axial wall drag coefficient is calculated as: [

$$]^{ac} (4-20)^{(3)}$$

The continuous liquid phase coefficient is [

$$]^{ac} (4-21)^{(3)}$$

[

$]^{ac}$. The single-phase friction factor for transverse flow is calculated using the same correlations for friction factors given in Equations 4-5a and 4-5b for each phase. For transverse flow, the phasic Reynolds numbers are calculated as: [

$$]^{ac} (4-23b)$$

[

 $]^{ac}.$

The single-phase frictional pressure drop between two adjacent channels through the gap become: [

 $]^{ac}.$

For the cold wall flow regimes, lateral drag coefficients are calculated as: [

 $]^{ac}$

[

] ^{a,c}

and, [

] ^{a,c}

The values of F_{SPV} and F_{SPL} are given by Equations 4-18 and 4-19.

For the hot wall flow regime, [

] ^{a,c} (4-30)

The next section discusses use and calculation of form loss coefficients in more detail.

Scaling Considerations: The wall friction models, as defined in the above subsections, are scale independent. The friction factor relationships given in Equations 4-5a and 4-5b agree with existing friction factor relationships found in text books (Vennard, 1961). The laminar friction factor is obtained from a momentum balance in laminar flow and the turbulent relationship agrees with the smooth pipe data of Nikuradse (1933).⁽⁴⁾ The key assumption is the void fraction weighting of the form losses as shown in Equations 4-7a to 4-7c. The WCOBRA/TRAC wall friction model has been compared to the two phase flow data in complex geometries for different experiments.^(5,6) In these experiments, the static pressure as well as the local void fraction were measured for channels with multi-hole plates. As shown

in these sections, the WCOBRA/TRAC predicted pressure drop and void fractions are in excellent agreement with the test data, for both the frictional pressure losses as well as the form losses.

| In Volumes 2 and 3 of WCAP-12945-P-A, heated wall pressure drop comparisons are also shown for rod bundle experiments and again indicate good agreement with the test data.

Conclusions: The WCOBRA/TRAC vessel wall shear models use a system of consistent correlations for the friction and form loss components for axial and lateral flow. The WCOBRA/TRAC use of an entrained liquid field in addition to a continuous liquid field results in partitioning the form losses by each fraction of the flow for the total loss. This particular feature of the vessel wall shear models has been verified on full-scale, two-phase flow experiments on simulated reactor hardware. There have been other full-scale simulations with WCOBRA/TRAC such that there are no scaling effects with the vessel wall shear model. The uncertainties in this particular model are accounted for in the overall WCOBRA/TRAC code uncertainty.

4-3 VESSEL COMPONENT FORM LOSS

Model Basis: WCOBRA/TRAC vessel component models a form loss as defined in Section 4-2. The form loss coefficient is directly input into the code for both axial and lateral flows. The user has two options when modelling an unrecoverable pressure loss due to area changes: to model the true area change, or to use the nominal area and input a loss coefficient that has been adjusted for the area change. Both methods are used in WCOBRA/TRAC when modelling true area changes. However, the WCOBRA/TRAC numerics will calculate an unrecoverable pressure loss which is nearly the same as that which one would normally input. Therefore, care must be used when modelling true area changes such that unrecoverable losses are not accounted for twice in the calculation.

Model As Coded: WCOBRA/TRAC solves the momentum equations on a control volume extending from the midpoint of one continuity cell, to the midpoint of the next continuity cell as seen with the dashed lines in Figure 4-1. The momentum equations from Section 2-3 can be reduced to the one-dimensional, single-phase, steady, frictionless form, and applied to the one-dimensional mesh shown in Figure 4-1. For simplicity it will be assumed that the flow is upward, so that the donor cell is the cell below. Since the lateral momentum equations are differenced in a similar manner, the conclusions which will be drawn below apply to the lateral flow through the gaps as well.

The expression for the axial pressure difference across a momentum cell neglecting friction and density changes is: [

$$J^{ac} \quad (4-31)$$

This equation can be applied to a sudden expansion, a sudden contraction, or a combination of both where successive pressure differences across several cells are combined to get the total pressure difference. For example, for a sudden contraction, Equation 4-31 applied successively across two consecutive cells in Figure 4-1 (where $j = 1$) yields:

Sudden Contraction: [

] ^{a,c} (4-32)

Adding the pressure drops for each cell in Equation 4-32 results in [

] ^{a,c} (4-33)

From Figure 4-1, $A_2 = A_3 = A_T$ and $A_1 = A_p$, and $U_1 = U_0 = U_p$, while $U_2 = U_3 = U_T$.

Using the continuity equation,

$$A_T \rho U_T = A_p \rho U_p \quad (4-34)$$

or

$$U_p = \frac{A_T}{A_p} U_T = R U_T \quad (4-35)$$

such that Equation 4-33 becomes [

] ^{a,c} (4-36)

Rearranging, Equation 4-36 yields: [

$$]^{a,c} \quad (4-37)$$

Normalizing the pressure change to the dynamic head at the minimum area gives [

$$]^{a,c} \quad (4-38)$$

for a sudden contraction. Similarly, for a sudden expansion in which the expansion occurs across one cell: [

$$]^{a,c} \quad (4-39)$$

and for a combination contraction/expansion in which the contraction occurs across one cell, [

$$]^{a,c} \quad (4-40)$$

The expression for the expansion is the same as would be predicted by the Bernoulli equation. The other expressions are more complicated and result from the differencing technique used. In Tables 4-1 to 4-3, the pressure difference predicted by the above equations is compared to data from King and Brater (1963).

[

$$]^{a,c}.$$

[

]'.c.

Scaling Considerations: The loss coefficients that are normally used in codes like WCOBRA/TRAC are derived from full-scale and scaled experimental test data, and in many cases are standardized and available in handbooks of hydraulic resistance (Crane, 1969). For specific nuclear reactor geometries and area changes in the reactor vessel, loss coefficients and unrecoverable pressure drop information is obtained from scale model experiments. These experimental loss coefficients and pressure drops are used as a guide to adjust the form loss coefficients in regions of the vessel where the geometries are complex.

WCOBRA/TRAC method of applying the form loss coefficients is verified by comparing the WCOBRA/TRAC steady-state flow and pressure distributions to calculated PWR steady-state conditions. WCOBRA/TRAC has also been compared to single phase and two-phase pressure drop experiments on prototypical reactor internals hardware which contained restrictive multi-hole plates. The comparisons of WCOBRA/TRAC predictions with the pressure drop and void fraction data was excellent, as shown in Volumes 2 and 3 of WCAP-12945-P-A.

Conclusions: The form loss coefficients are user inputs to the calculation and are dependent on the geometry and the method of modelling the area changes in the model. Explicitly modelled area changes require a small adjustment of the form loss coefficient using the guidance provided above. For cases where no area change is modelled, explicitly standard experimentally determined loss coefficients are used.

4-4 VESSEL COMPONENT INTERFACIAL SHEAR MODELS

As described in Section 3, flow regime maps are used in the vessel component of WCOBRA/TRAC. The normal or cold wall flow regime map is used unless there is a structure in the computational cell that has a surface temperature in excess of [

]'.c.

If heated rods exist in the computational cell with temperatures in excess of the above criteria, the flow regime is based on the hot wall flow regime map. This means that care must be used when modelling situations with hot and cold wall structures, since if both are in the same cell, the code will assume that all walls are hot; i.e., no liquid film on the walls. Conversely if the wall temperature is below the criteria, the code will use the cold wall flow regime with a liquid film on the wall.

The vessel momentum equations described in Section 2 require the interfacial drag coefficient in units which, when multiplied by the new time velocity difference between the phases, will yield force per unit length for that phase. During the numerical solution, these coefficients are divided by the appropriate phasic densities, when the phasic mass flowrate is solved for. In subroutine INTFR, the interfacial drag coefficients are defined based on phasic velocity, as shown below. The average interfacial drag force per unit length between the vapor and continuous liquid is defined as

$$\tau'_{ix,v} = K_{ix,v} U_v \quad (4-41)$$

where:

- $\tau'_{ix,v}$ is the force per unit length on the liquid by the vapor,
- $K_{ix,v}$ is the flow regime dependent interfacial drag coefficient, and
- U_v is the relative velocity between the vapor and the continuous liquid.

A similar expression exists for the drag force between the vapor and entrained liquid. This expression is given as

$$\tau'_{ix,ve} = K_{ix,ve} U_{ve} \quad (4-42)$$

where:

- $\tau'_{ix,ve}$ is the force per unit length on the entrained liquid phase by the vapor,
- $K_{ix,ve}$ is the flow regime dependent interfacial drag coefficient, and
- U_{ve} is the relative velocity between the vapor and the entrained phase

When calculating the relative velocity between the phases, the value generally assumed is the [

$$]^{a,c} \quad (4-43)$$

where $W_{v,max}$ is the maximum lateral relative velocity and U_v is the axial relative velocity for the cell. However, in some cases, this value is modified as described in the Model as Coded sections. When the value has been modified, it is expressed as U_r .

4-4-1 Small Bubble Flow Regime Interfacial Drag

Model Basis: For the bubbly regime, the general form of the interfacial drag coefficient is

$$K_{iX,v} = C_{Db} \rho_l |\underline{U}_v| A_{p,b} / 2\Delta X \quad (4-44)^{(7)}$$

where $A_{p,b}$ is the total projected area of the bubbles in the volume. For spherical bubbles, this results in

$$A_{p,b} = N_b \pi r_b^2 \quad (4-45)$$

where N_b is the number of bubbles in the cell, and r_b is the bubble radius. This can be shown to be equivalent to [

$$J^{ac} \quad (4-46)$$

where $A_{i,b}$ is the bubble interfacial area, described in Section 3. Two alternate forms of the interfacial drag coefficient are obtained: [

$$J^{ac} \quad (4-47b)$$

Similarly, for lateral flow, [

$$J^{ac} \quad (4-48b)$$

Expressions for the bubble drag coefficient (C_{Db}) are discussed by Ishii (1977) and Ishii and Chawla (1979). The drag coefficients are Reynolds number dependent and closely related to the drag coefficients for single bubbles and drops in an infinite medium. The drag coefficient for a single bubble in an infinite

liquid medium is shown in Figure 4-2. The bubble is considered to behave as a solid sphere in the viscous regime. At a higher Reynolds number, the bubble is characterized by a distorted shape and irregular motion. In this distorted particle regime the drag coefficient decreases with the Reynolds number. As the Reynolds number further increases, the bubble becomes spherical-cap shaped and the drag coefficient becomes constant.

As discussed by Ishii (1979), in the viscous regime the drag coefficient of a single particle in a multiparticle system may be assumed to have the same functional form as that of a single particle in an infinite medium, provided that the Reynolds number is computed using the appropriate mixture viscosity. Therefore, in the viscous regime the drag coefficient on a bubble is given by

$$C_{Db} = \frac{24}{Re_b} (1.0 + 0.1 Re_b^{0.75}) \quad (4-49)$$

where:

$$Re_b = \frac{2r_b \rho_t |U_w|}{\mu_{m_b}} \quad (4-50)$$

and

$$\mu_{m_b} = \mu_t (1 - \alpha_v)^{-2.5 \frac{(\mu_v + 0.4\mu_t)}{(\mu_v + \mu_t)}} \quad (4-51)$$

(also given by Ishii). In the distorted particle regime, it is again assumed that the drag coefficient for a particle in a multiparticle system is the same as that of a single particle in an infinite medium with the Reynolds number based on a mixture viscosity. In addition, it is assumed that churn-turbulent flow always exists in the distorted particle regime. Under these conditions, a particle tends to move in the wake caused by other particles. Therefore, the velocity used in the drag coefficient and Reynolds number should be the drift velocity, $U_{vj} = (1 - \alpha_v) U_w$. The drag coefficient in the distorted particle regime is then

$$C_{Db} = \frac{\sqrt{2}}{3} N_\mu Re_b' (1 - \alpha_v)^2 \quad (4-52)^{(8,9)}$$

where:

$$N_\mu = \frac{\mu_t}{\left[\rho_t \sigma \sqrt{\frac{\sigma}{g(\rho_t - \rho_v)}} \right]^{1/2}} \quad (4-53)^{(8,9)}$$

$$Re'_b = \frac{2r_b \rho_t (1 - \alpha_v) |U_{vt}|}{\mu_m} \quad (4-54)^{(8,9)}$$

and

$$\mu_m = \frac{\mu_t}{(1 - \alpha_v)} \quad (4-55)^{(8,9)}$$

The $(1 - \alpha_v)^2$ in the expression for the drag coefficient results from using the drift velocity to compute the drag force.

Churn-turbulent flow is also assumed for the cap bubble regime where

$$C_{Db} = \frac{8}{3} (1 - \alpha_v)^2 \quad (4-56)$$

For the large-bubble flow regime, Equation 4-49 is assumed to apply down to the limit of Newton's regime where the drag coefficient for a single solid sphere becomes constant at a value of 0.45. Within Newton's regime the large bubbles are assumed to move with respect to the average volumetric flux and, therefore,

$$C_{Db} = 0.45 (1 - \alpha_v)^2 \quad (4-57)^{(10)}$$

The mixture viscosity is used in Re'_b (Equation 4-59) because a particle moving in a multiparticle system experiences a greater resistance than a single particle in an infinite medium. As it moves it must deform not only the fluid, but the neighboring particles as well. The effect is seen by the particle as an increased viscosity.

The terminal relative velocity between the bubble and liquid is also calculated from a bubble rise model given by Ishii (1977) as:

$$U_{rb} = 1.414 \left[\sigma g_c (\rho_l - \rho_v) / \rho_l^2 \right]^{25} / (1 - \alpha_v) \quad (4-58)^{(11)}$$

The bubble size is assumed to depend on a Weber number criterion:

$$r_b = 0.5 We_b \sigma g_c / (\rho_l U_{rb}^2) \quad (4-59)^{(12)}$$

where $We_b = 10$.

[

] ^{ac} (4-60)⁽¹³⁾

If large heat releases exist at a solid boundary within the cell, then vapor is assumed to concentrate as a film at the wall. The interfacial shear between the vapor film and the bulk liquid is then determined by assuming a transition inverted slug regime described in Section 4-4-6.

Model as Coded: The WCOBRA/TRAC coding logic uses the above correlations with consistency checks to establish limits on parameters such as relative velocities and bubble size before the interfacial drag is calculated. The relative velocity is compared using different methods and the minimum value is used in the bubble Weber number and drag coefficient. The reason for this is that in the small bubble regime the interfacial area is large and would lead to excessively large forces if a large relative velocity were used.

The relative velocity to be used in Equation 4-44 is initially set at the local vector sum value ($U_r = \underline{U}_{vt}$), given in Equation 4-43. It is then limited as follows.

The first limit is calculated by [

] ^{ac} (4-61)⁽¹⁴⁾

[

$$]^{a,c} \quad (4-62)$$

and the drift velocity is determined by [

$$]^{a,c} \quad (4-63)$$

The second limit is calculated by [

$$]^{a,c} \quad (4-64)^{(16)}$$

[

$$]^{a,c}.$$

The value of U , used in Equation 4-44 is then: [

$$]^{a,c} \quad (18)$$

Next, the bubble drag coefficient is calculated, using Equations 4-49, 4-52, 4-56, and 4-57. [

$$]^{a,c}.$$

[

$$]^{a,c} \quad (19)$$

The interfacial drag between the continuous liquid and the vapor in the small bubble regime is calculated as [

$$]^{a,c} \quad (4-66)$$

where the interfacial area $A_{i,SB}$ is given in Equation 3-17. If there is significant⁽²⁰⁾ vapor generation at the wall, the interfacial drag is ramped between the small bubble value calculated from Equation 4-66 and the inverted slug value as [

$$]^{a,c} \quad (4-67)^{(20)}$$

The hot wall drag coefficient, $K_{ix,vl,HW}$ is calculated from Equation 4-105.

The value of F_T is given as [

$$]^{a,c} \quad (4-68)^{(20)}$$

where U_{rb} is calculated from Equation 4-58 and [

$$]^{a,c} \quad (4-69)^{(20)}$$

where A_x is the cell momentum area in the axial direction and Γ_v (Equation 5-102) is the cell vapor generation rate and Q_{wt} and Q_b are the heat flow from wall to liquid and the subcooled boiling heat flow, respectively (Section 6-2). To illustrate the effect of the ramps and limits described above, Equation 4-67 was evaluated as a function of \underline{U}_{vt} for typical fluid conditions, and plotted in Figure 4-3a. It can be seen that, at high heat flux and high relative velocities, the interfacial drag factor approaches a value more typical of separated, rather than bubbly, flow.

For lateral flow through gaps, the procedure is similar, with the following differences: the relative velocity is limited to a maximum value of [$]^{a,c}$. The more complicated channel model is not used because, in general, gaps tend to have a large flow area, and the flow velocities are relatively small. [

$$]^{a,c} \quad (21)$$

The lateral flow interfacial drag uses the same expression for bubble drag coefficient except that the vector sum relative velocity is used in the Reynolds number as described earlier. The bubble drag coefficient for lateral flow uses the same logic as the axial or vertical flow. The interfacial area is calculated in the same fashion for the lateral flow as the axial flow, except the velocity is the lateral relative velocity for the gap flow. The lateral flow interfacial drag is given as [

$$J^{ac}.$$

Scaling Considerations: The formulation used in the small bubble regime is scale independent, since it is based on an individual bubble in the flow stream. Therefore, no scale dependence or bias would be introduced into the calculation by this model. Since the small bubble regime would be only a small region in the reactor core, before the flow regime would transition to other regimes, the noding selection used could influence the size of this regime and how it is weighted with other regimes. There is a small region of bubbly flow in the FLECHT-SEASET, FLECHT, and FEBA reflood heat transfer experiments. These effects are examined in Section 12 of WCAP-12945-P-A and should not influence the PWR calculation since the same noding approach is used in the code assessment as is used in the PWR calculations. In this case, any uncertainties in averaging due to node size is accounted for in the WCOBRA/TRAC code validation and uncertainty analysis.

Conclusions: The small bubble regime models are based on the work of Ishii and Chawla (1979), which represents the current state of knowledge in this area. The same coding logic is used to represent the axial bubble behavior as well as the gap or lateral bubble effects. These models have been compared to rod bundle pressure drop data on different rod arrays such that the uncertainty of these models is accounted for in the overall WCOBRA/TRAC code uncertainty.

4-4-2 Small-to-Large Bubble Flow Regime Interfacial Drag

Model Basis: The approach used for the large bubble regime is similar to that for the small bubble regime. The small bubbles are primarily in the viscous regime where $1.0 \leq Re_b \leq 1000$ whereas the larger bubbles may be in Newton's Regime where $Re_b \geq 1000$. In the Newton Regime the large bubbles are assumed to move with the average volumetric flux in the flow.

[

$$J^{ac}.$$

As discussed by Ishii (1977) the presence of other particles affects the resulting drag for a multi-particle system. This effect is corrected by using the appropriate mixture viscosity for multi-particle systems. As a single bubble moves in a multi-particle system, it deforms not only the neighboring fluid, but the other particles as well. The individual particle or bubble is, in turn, distorted by its neighbors as it moves through the fluid. This effect is seen as an increased fluid viscosity. The bubble Reynolds number is defined as Equation 4-50 with the mixture viscosity correction given as Equation 4-51.

[

] ^{ac}. In the Newton regime, the large bubbles are assumed to move relative to the average volumetric flux such that

$$C_{Db} = C_{Db} (1 - \alpha_v)^2 \quad (4-71)$$

where the $(1 - \alpha_v)^2$ term results from using the drift velocity to calculate the drag force, and C_{Db} is the maximum drag from Equation 4-49 or a value of [] ^{ac}.

The same basis is used for the transverse drag relationships in this regime. [

] ^{ac}.

Model as Coded: The interfacial drag between the continuous liquid and vapor in the small-to-large bubble regime is calculated as [

$$] \quad (4-72)$$

where $A_{i, LB}$ is given by Equation 3-34. The calculation for the large bubble regime follows the same general procedure as the small bubble model, where $|\underline{U}_v|$ is modified by the limits described by Equation 4-65.

For conditions in which there is a large vapor generation rate at the wall, the [

$$] \quad (4-73)$$

$$[\dots]^{ac}.$$

The interfacial drag coefficient between the continuous liquid and vapor for the small to large bubble regime is then calculated by [

$$]^{ac} \quad (4-74)$$

$$[\dots]^{ac} \quad (4-75)$$

which can be shown to be the as-coded expression: [

$$]^{ac} \quad (4-76)^{(22)}$$

The term α_{SB} represents the upper bound of the small bubble regime, assumed to be 0.20.

The bubble drag relationship for the lateral flow through the gaps for the small-to-large bubble and large bubble regime are the same as the axial flow coding logic. As mentioned earlier, the lateral relative velocity along with the gap bubble radius is used to calculate the bubble Reynolds number for the bubble drag coefficient. The small-to-large bubble range is the same for the lateral flow as the axial flows given in Equation 4-72.

The effect of the models, ramps, and limits on the axial interfacial drag factor for this flow regime is shown in Figure 4-3b, and indicates similar trends as the small bubble regime.

Scaling Considerations: As described in Section 4-4-1, the noding selection could influence this flow regime and how it is weighted with other regimes. The verification of this model with noding similar to PWR noding is given in Section 12 of WCAP-12945-P-A. It indicates that the model, in conjunction with other models for bubble size and void fraction, represents the measured void fraction from the FLECHT-SEASET experiments below the quench front. Since these experiments preserve full-scale core geometry, potential scaling bias is eliminated.

Conclusions: The bubble drag coefficient and interfacial drag relationships are consistent between lateral flow and axial flow in the WCOBRA/TRAC model. The drag relationships are based on the extensive work by Ishii and Chawla (1979). There are a number of rod bundle experiments with different rod array sizes which will experience the small bubble and small-to-large bubble regime following rod quench. These experiments have been examined to compare the measured and predicted pressure distributions and indicate good agreement with the WCOBRA/TRAC models. The uncertainty in these models is accounted for in the overall WCOBRA/TRAC uncertainty.

4-4-3 Churn-Turbulent Flow Regime Interfacial Drag

Model Basis: The churn-turbulent regime is assumed to be a combination of the large bubble regime and the film/drop regime. The model basis for the film/drop regime is described in Section 4-4-4.

Model as Coded: The interfacial drag is calculated from the selected drag coefficient and the relative velocity as previously described in Section 4-4-2: [

$$]^{ac} \quad (4-77)$$

where the interfacial area $A_{i, LB}$ is given by Equation 3-34. The same ramp as in Section 4-4-2 is applied to consider the vapor generation rate at the wall-by-wall heat transfer.

The interfacial drag relationships for the film/drop component are described in Section 4-4-4.

For the churn-turbulent regime, a [

$$]^{ac} \quad (4-78)$$

where: [

$$]^{ac} \quad (4-79)^{(22)}$$

where $\alpha_{LB} = [\quad]^{ac}$, and α_{crit} is given as [

$$]^{ac} \quad (4-80)$$

The same logic is used in the lateral direction to combine large bubble and film/drop components.

Scaling Considerations: This model for interfacial drag has some scale dependence. Ishii (1977) attempted to compensate for the interaction effects of one bubble or groups of bubbles on each other through adjustments of the effective viscosity. A comparison of the void fraction predicted by WCOBRA/TRAC and the FLECHT-SEASET pressure drop data (from corrected ΔP cells) below the quench front shows good agreement, as shown in Section 12 of WCAP-12945-P-A.

Conclusions: Although the model has some scale dependence, the coding logic will limit the bubble sizes based on the true physical dimensions for the problems. In addition, the churn-turbulent interfacial drag models have been verified using prototypical rod bundle data with different rod array sizes such that the uncertainty of these models is accounted for in the total WCOBRA/TRAC code uncertainty.

4-4-4 Film/Drop Flow Regime

Model Basis: This section describes the interfacial drag models between the vapor and continuous liquid for the wetted wall film flow regime. The interfacial drag between the vapor and entrained liquid for this regime is the same as that for the hot wall dispersed droplet flow regime, and is discussed in Section 4-4-7. As shown in Section 3, when the vapor content in the flow exceeds a critical void fraction, and the wall is below the wetted wall temperature criteria, the film is assumed to become stable and liquid can no longer bridge the channel.

In the film regime, the general form of the interfacial drag coefficient is, for axial flow, [

$$]^{ac} \quad (4-81)$$

where $A_{i,film}$ is the interfacial area in the volume. For a thin liquid film, the interfacial area is [

$$]^{ac} \quad (4-82)$$

For lateral flow, the expression for interfacial area is [

$$]^{a,c} \quad (4-83)$$

where the gap is viewed as a series of N_g vertical slots of height ΔX .

With the above equations, alternate versions of Equation 4-81 are defined: [

$$]^{a,c} \quad (4-85)$$

The friction factor ($f_{i,FD}$) for film flow is dependent on whether the film is stable or unstable. It has been observed experimentally that the onset of film instability causes a sudden increase in system pressure drop. This is a result of increased roughness of the liquid film caused by large, unstable waves. The film friction factor for stable film flow in tubes has been studied by Wallis (1969), and Henstock and Hanratty (1976) have correlated a large amount of cocurrent and countercurrent film flow data for unstable films.

Henstock and Hanratty's correlation is of the form,

$$f_{i,HH} = f_s \left\{ 1 + 1400F \left[1 - \exp \left(-\frac{1}{G} \frac{(1 + 1400F)^{3/2}}{13.2F} \right) \right] \right\} \quad (4-86)$$

where:

$$G = \frac{\rho_t g D_h}{\rho_v U_v^2 f_s} \quad (4-87)$$

and

$$F = \frac{m^+}{Re_v^{0.9}} \frac{\mu_t}{\mu_v} \sqrt{\frac{\rho_v}{\rho_t}} \quad (4-88)$$

with

$$m^+ = [(0.707 Re_t^{0.5})^{2.5} + (0.0379 Re_t^{0.9})^{2.5}]^{0.40} \quad (4-89)$$

and [

$$]^{ac} \quad (4-90)$$

[$]^{ac}$. The single-phase friction factor is different from that given in the Henstock and Hanratty (1976) paper which was:

$$f_s = 0.046 Re_v^{-20} \quad (4-91)$$

[

$$]^{ac}.$$

For stable films, the annular flow interfacial correlation developed by Wallis (1969) is used:

$$f_{i,w} = 0.005(1 + 75(1 - \alpha_v)) \quad (4-92)^{(6)}$$

[

$$]^{ac}.$$

As discussed in Section 3, the transition to churn-turbulent (large bubble) regime begins at a void fraction of [$]^{ac}$ percent and continues until a stable film is achieved. The void fraction at which a stable liquid film will exist depends on the flow channel size and the vapor velocity. The critical void fraction is determined from a force balance between the disruptive force of the pressure gradient over the crest of waves on the film and the restraining force of surface tension. The resulting expression for the critical vapor fraction is [

$$]^{ac} \quad (4-93)^{(23)}$$

The critical void fraction is limited to a minimum value of $[\]^{ac}$, the value at which waves can be expected to bridge across the flow channel and cause a transition to churn-turbulent flow.

The interfacial drag logic for the lateral flow is simplified relative to the vertical flow since the film flow between the gaps is assumed to be stable and the Wallis interfacial friction factor given in Equation 4-92 is used. $[\]^{ac}$.

Model as Coded: $[\]^{ac}$.

$[\]^{ac}$. The interfacial drag is calculated as, $[\]^{ac}$.

$[\]^{ac}$ (4-94)

where the interfacial area is given by Equation 3-46.

For lateral flow through the gaps, the interfacial friction factor is calculated using $[\]^{ac}$.

$[\]^{ac}$ (4-95)

where the factor of 2 in Equation 4-85 has been taken into account, and giving a lateral drag coefficient of $[\]^{ac}$.

$[\]^{ac}$ (4-96)

Scaling Considerations: The Wallis friction factor for film, Equation 4-92 has been examined for horizontal and vertical flow from pipe sizes ranging from 1-inch to 3-inch diameter as shown in Figure 4-4. The Hanstock and Hanratty film friction model has also been compared to vertical film flow data on diameter of 0.503 inches to 2.5 inches over a range of different fluid velocities and pressures. The comparison of their correlation to data is shown in Figure 4-5. This comparison shows that the correlation provides a good fit to the data over a range of scales. WCOBRA/TRAC has been compared

to annular pressure drop data on full-scale reactor internals. The agreement between the measured pressure drop, pressure distribution, and void fraction with the WCOBRA/TRAC prediction is excellent, indicating the models used in this flow regime do not have a scale bias.

Conclusions: The film wall drag models have been compared for both horizontal and vertical flows over a wide range of geometries and hydraulic diameters. WCOBRA/TRAC has been used with these models to calculate the two-phase pressure drops in an annular film flow regime. The uncertainty of this model is included in the total code uncertainty for WCOBRA/TRAC.

4-4-5 Inverted Annular Flow Regime

Model Basis: An inverted annular flow regime is assumed if the continuous liquid phase is subcooled and the surrounding surface is hot and dry. This regime consists of a liquid core surrounded by a vapor film.

For inverted annular flow, the interfacial friction factor is [

$$]^{ac} \quad (4-97)^{(24)}$$

Model as Coded: WCOBRA/TRAC calculates the continuous liquid enthalpy and compares it to the saturated liquid enthalpy in the cell. If the liquid is subcooled and the wall is in the hot wall regime, the flow regime is inverted annular. If the liquid enthalpy is saturated or superheated, the code assumes the inverted liquid slug regime.

The interfacial friction factor is set to $f_{i,JVA} = [\quad]^{ac}$, taking into account the factor of 2 in Equation 4-81 as defined earlier in this section. The interfacial drag for the axial momentum equation then is set to

$$K_{iX,vl,JVA} = f_{iX,JVA} \rho_v |U_{vl}| A_{i,filn} / \Delta X \quad (4-98)$$

where the interfacial area is given by Equation 3-51.

The interfacial drag and friction models are simplified for the lateral flow in the inverted annular and inverted annular slug regimes. [

direction of [$]^{ac}$. A drag coefficient in the lateral

$$]^{ac} \quad (4-99)^{(24)}$$

is used, and the radius of the chunk of liquid is [

$$]^{ac} (4-100)^{(24)}$$

The interfacial drag coefficient becomes [

$$]^{ac} (4-101)$$

where $|\underline{W}_v|$ is the lateral relative velocity between the continuous liquid and the vapor.

Scaling Considerations: Inverted annular flow can most commonly occur during a rapid reflood process when subcooled liquid is forced into the core either at the beginning of reflood, or when the nitrogen pressurizes the downcomer. When this situation occurs, the subcooled continuous liquid is forced into the bundle at a much higher velocity than the quench front velocity on the rods, and a thin vapor film exists on the rods' surface, separating it from the liquid core. Inverted annular flow was observed in the FLECHT and FLECHT-SEASET rod bundle experiments. These experiments are full-length tests using prototypical rod dimensions and spacings such that the geometric effects for this flow regime are preserved, and there are no scaling effects. The experimental conditions were varied over wide ranges to insure that the PWR plant conditions were covered. WCOBRA/TRAC has been compared to these reflood experiments as shown in Section 12 of WCAP-12945-P-A. The comparisons of heat transfer, quench front movement, and pressure drop are good indicators that WCOBRA/TRAC predicts interfacial drag in the inverted annular flow regime with reasonable accuracy.

Conclusions: The inverted annular interfacial drag model used in WCOBRA/TRAC is derived from the annular film flow model used for high void fraction wetted wall flows. The inverted annular interfacial drag model has been verified on full-scale prototypical rod bundle experiments for different rod arrays. The uncertainty of this model is included in the overall WCOBRA/TRAC uncertainty.

4-4-6 Inverted Liquid Slug Regime

Model Basis: As the liquid flow in the inverted annular flow regime is heated by wall heat transfer, the liquid core is accelerated by the increased vapor content of the flow. When the liquid reaches the saturation temperature, it no longer can condense the vapor and the liquid begins breaking into ligaments or chunks--into a dispersed droplet flow as it progresses up along the heated channel. The interfacial

friction is calculated assuming an unstable liquid film surface exists on the large liquid ligaments or drops as: [

$$]^{a,c} \quad (4-102)^{(25)}$$

This equation is []^{a,c} times⁽²⁵⁾ the Wallis (1969) equation for stable liquid films discussed earlier, given as Equation 4-92.

The interfacial area is calculated assuming that the liquid slugs are spherical, and have a diameter []^{a,c} of the channel diameter, as described in Section 3-3-3.

Model as Coded: The axial flow interfacial drag coefficient is calculated as:

$$K_{iX,v,IVS} = f_{i,IVS} \rho_v |U_v| A_{i,IVS} \quad (4-103)$$

where the friction factor is calculated from Equation 4-102 and the interfacial area for the liquid slug regime is

$$A_{i,IVS} = \frac{4A_X}{D_h} \alpha_i \quad (4-104)$$

where α_i is the minimum of the liquid void fraction in the mesh cell $\alpha_i(i,j)$ and the average liquid void is given by Equation 3-13.

Note that the ΔX term is absent from both equations, so the resulting expression is equivalent to that in Equation 4-81.

This is further modified by [

$$]^{a,c} \quad (4-105)^{(20,26)}$$

The lower limit is necessary to allow for [

$$]^{a,c}.$$

The lateral flow interfacial drag for the inverted slug regime is calculated in the same fashion as the inverted annular regime, as described in the previous section.

Scaling Considerations: As mentioned in Section 4-2-6, the inverted annular flow regime, continues to develop due to the heat transfer from the walls. The inverted slug regime is a transition from the inverted annular flow regime, where the liquid column breaks up into ligaments or large liquid slugs and then to dispersed droplets.

The interfacial drag in the inverted liquid slug regime will be somewhat sensitive to the number of heated surfaces/volume since the vapor layers along the heated rods will be growing. The liquid will not be continuous, but will still be trapped between the heated surfaces. Again, the reflood experiments used to verify the WCOBRA/TRAC code have full-height and full-scale subchannel dimensions prototypical of PWR fuel bundles such that no scaling effects should exist for these models. Different rod array geometries were also examined for bottom flooding, top flooding, and blowdown situations where this regime could exist.

Conclusions: The inverted slug regime is a transition hot wall regime where the liquid is breaking up into a dispersed droplet flow regime. The WCOBRA/TRAC models have been verified on full-length rod bundles over a wide range of PWR conditions. Since the rod bundles have prototypical dimensions, there are no scaling concerns. The uncertainty in this particular model is accounted for in the overall WCOBRA/TRAC code uncertainty.

4-4-7 Dispersed Droplet Flow Regime

Model Basis: As discussed in Section 2, WCOBRA/TRAC has a separate entrained liquid field. The droplet drag model is based on the work by Ishii (1977) using the analogy of a single drop in an infinite vapor medium to a single bubble in an infinite liquid field. The droplet drag models discussed in this section are used for both the hot wall and cold wall flow regimes. The interfacial friction coefficient used is

$$K_{iX,ve,DD} = 0.375 \frac{C_{Dd}}{r_d} \alpha_e \rho_v |U_{ve}| \quad (4-106)$$

where:

C_{Dd} is the droplet drag coefficient,

r_d is the droplet radius,

α_e is the entrained liquid fraction in the flow, and

$|\underline{U}_{ve}|$ is the vector sum relative velocity between the vapor and the entrained droplet, and is given as

$$U_{ve} = \sqrt{\max(W_{ve})^2 + U_{ve}^2} \quad (4-107)$$

It is assumed that the drops are in the Newton Regime where the droplet Reynolds number is large. The droplet drag coefficient that is used in this is assumed to be: [

] ^{a,c} (4-108)

Bird, Stewart, and Lightfoot (1960) recommend a value of 0.44 for the droplet drag in the Newton Regime while Ishii and Chawla (1979) recommend a value of 0.45.

The droplet sizes used in WCOBRA/TRAC are discussed in Section 5 and have as their basis drop sizes measured in the FLECHT-SEASET program (Lee, N. et al., 1982). The drop size is calculated as [

] ^{a,c} (4-109)⁽²⁶⁾

Model As Coded: The current droplet diameter is first established via Equation 4-109.

The droplet interfacial drag is then calculated as

$$K_{ix,ve,DD} = \frac{0.125 C_{Dd} A_{i,drop} \rho_v |\underline{U}_{ve}|}{\Delta X} \quad (4-110)^{(27)}$$

where:

$$A_{i,drop} = A_{i,d}''' A_x \Delta X \quad (4-111)$$

The droplet drag relationships for a cold wall are identical, except that there is no check on the drop size relative to the hydraulic diameters. If the drops were as large as the hydraulic diameter, they would intersect the liquid films on the wall and the channel would be filled with liquid. This would result in a different flow regime.

The lateral flow droplet calculation uses the average droplet radius calculated in each of the adjacent cells from Equation 4-109. The droplet drag coefficient for lateral flow is a constant value, $C_{Dd} = []^{a.c(27)}$, and the lateral droplet drag coefficient is calculated as

$$K_{iZ,ve,DD} = 0.375 C_{Dd} \rho_v | \underline{W}_{ve} | \alpha_e L_g \Delta X / r_d \quad (4-112)^{(27)}$$

Scaling Considerations: The hot wall interfacial droplet drag effects have been verified by comparing WCOBRA/TRAC to full height heated rod bundle experiments which have the same physical dimensions as PWR fuel assemblies. The calculated droplet sizes for different FLECHT-SEASET experiments are compared to high speed movie data in Section 13-4 of WCAP-12945-P-A, as well as the measured droplet velocities.

Since both the droplet velocities and the calculated drop sizes agree reasonably well with the measured data, the droplet drag relationships described above, which would determine the resulting drop velocities, provide a reasonably good model for the dispersed droplet flow. Again, since the rod bundle experiments have been performed on full-scale bundle simulations, the droplet interfacial drag models are applicable to the PWR.

Conclusions: There is consistency in how the droplet flow is modelled both axially and laterally. The same relationships for droplet drag are used for each drag coefficient formulation. The drop field models have been verified against full-scale prototypical data such that no scaling effects exist. The model uncertainties are included in the overall WCOBRA/TRAC code uncertainty.

4-4-8 Falling Film Flow Regime

Model Basis: As fuel rods quench from the top, a liquid film is formed on the rods behind the quench and sputtering front. Liquid is de-entrained from the upward flowing dispersed droplet flow to provide liquid source for the film on the rods. The interfacial drag relationships on the film behind the top quench front are the same as those for annular film flow except that the interfacial friction uses the Wallis (1969) friction factor given in Equation 4-92. [

$]^{a.c}$. Therefore, the interfacial friction coefficient for falling films is

$$f_{iX,FF} = 0.005 (1 + 75 \alpha_i) \quad (4-113)$$

In the falling film regime, the gap or transverse flow film interfacial drag is calculated in the same fashion as the annular film flow drag discussed earlier in Section 4-4-4. The lateral flow of drops which are sputtered from the top down quench front would be handled in the same fashion as the droplet flow discussed in Section 4-4-7.

Model as Coded: The interfacial drag coefficient is given as

$$K_{iX,tv,FF} = f_{iX,FF} \rho_v |U_v| A_{i,fil} / \Delta X \quad (4-114)$$

where $f_{iX,FF}$ is from Equation 4-113 and $A_{i,fil}$ is calculated from Equation 3-61.

The interfacial drag is always calculated if a cold wall is present in the cell. If the cell void fraction is greater than $[]^{ac}$, then the flow regime is a falling film regime with upward flowing entrained droplets. If the void fraction is below $[]^{ac}$ and the liquid flow is from the top, then the interfacial drag is ramped between the top deluge regime and the falling film regime. The top deluge interfacial drag coefficients will be discussed in Section 4-4-9.

Scaling Considerations: WCOBRA/TRAC simulations of the G-1 and G-2 loop experiments, in addition to the simulation of CCTF Run 76 predicted a falling film regime near the top of the heater rods after they had quenched. The G-1 and G-2 loop tests used full-size, full-height test bundles, and the CCTF facility modelled a full-height core. Since these tests are full- and/or large-scale, there should be no scaling concerns.

Conclusions: The falling film models have been used in the simulation of top-down quench experiments with prototypical geometry over a wide range of conditions. The uncertainty of these models is accounted for in the overall uncertainty of the WCOBRA/TRAC code.

4-4-9 Top Deluge Flow Regime

Model Basis: When the walls are hot and a large amount of liquid flows downward into a computational cell, the flow regime is called the top deluge. This flow regime is similar to the liquid slug regime for upflow as discussed in Section 4-4-6. The top deluge regime is assumed present at void fractions less than $[]^{ac}$. Physically, the top deluge regime could occur with large liquid injection rates in a PWR upper plenum due to upper plenum injection or upper head injection. The top deluge regime would also occur during blowdown when the core flow reverses and large amounts of liquid either drain out of the upper head or plenum and are forced into a hot core. PWR with combined injection, hot leg, and cold leg accumulators, where the hot leg accumulators inject large liquid flows in the upper plenum, could also experience the top deluge flow regime.

Model As Coded: The droplet drag coefficient is calculated as the maximum of

$$C_{Dd} = \frac{24}{Re_v} \left[1.0 + 0.1 Re_v^{.75} \right] \quad (4-115)^{(28)}$$

where Re_v is the vapor Reynolds number in the cell based on local vapor properties; and [

$$]^{a,c} \quad (4-116)^{(28)}$$

The interfacial drag coefficient for top deluge regime is calculated as

$$K_{iX,M,TD} = 0.125 C_{Dd} \rho_v |U_v| A_{i,fil} / \Delta X \quad (4-117)^{(28)}$$

where the interfacial area is given by Equation 3-63.

The low vapor fraction for this regime implies that the liquid is filling most of the channel. Note that the velocity used in Equation 4-117 is the relative velocity between the continuous liquid and the vapor, rather than the entrained liquid to vapor, since the liquid slugs are modelled by the continuous liquid field. Again, the model represents large liquid slugs or chunks which would nearly fill the channel and would capture any small droplets in the channel.

[

]^{a,c}.

Scaling Considerations: The top deluge model is similar to the liquid slug model for upflow. The basic correlations that are used are scale dependent because they depend on the channel hydraulic diameter.

Blowdown experiments have been performed on the Westinghouse G-1 and G-2 test facilities that simulate reverse flow blowdowns with and without upper head injection. The experiments with upper head injection will result in lower void fractions in the upper portion of the test bundle such that WCOBRA/TRAC will be in the top deluge regime for a portion of the transient. Since these experiments have been performed on prototypical rod bundles with different rod array sizes at full-scale there are no scaling effects that need to be considered. The agreement of the test data with the WCOBRA/TRAC predictions for heat transfer is reasonable and indirectly shows that the proper interfacial area is calculated for this flow regime.

Conclusions: The top deluge flow regime models have been verified on full-length rod bundles with prototypical fuel rod array sizes over a range of conditions which cover PWR conditions. The uncertainties in the models is accounted for in the overall WCOBRA/TRAC code uncertainties.

4-5 VESSEL COMPONENT INTERCELL DRAG

Model Basis: WCOBRA/TRAC calculates an additional interfacial drag force for interfacial shear that occurs at mesh cell boundaries. These interfaces are detected by changes in void fraction between adjacent cells, and can occur on either horizontal or vertical cell boundaries.

The intercell drag model is used to help calculate counter current flow limitation (CCFL) situations where there is liquid flowing downward against vapor upflow. The intercell drag models are applied between channels where liquid can pool, such as on the top of the upper core plate in the reactor upper plenum, and channels representing vapor jets through holes in the upper core plate, for example. The intercell drag models will calculate a drag force on the pooled liquid in the adjacent cell as well as the reaction force on the vapor jet. The details of the model are given below.

For two cells, i and j , connected to each other by a vertical or lateral connection, an intercell interface is assumed when []^{a,c}, so that cell i is on the vapor side of the interface and cell j is on the liquid side. The drag force is a function of the difference between the vapor velocity in cell i and the liquid velocity in cell j , and is given by

$$F_{I,X} = f_i \frac{1}{2} \rho_v (U_{v,i} - U_{l,j}) (U_{v,i} - U_{l,j}) A_{I,X} \quad (4-118)$$

for the vertical direction and

$$F_{I,Z} = f_i \frac{1}{2} \rho_v (W_{v,i} - W_{l,j}) (W_{v,i} - W_{l,j}) A_{I,Z} \quad (4-119)$$

for the lateral direction, where [

$$]^{a,c} \quad (4-120)^{(29)}$$

In these equations $A_{I,X}$ and $A_{I,Z}$ are the appropriate intercell areas. The intercell interfacial force is added to the liquid momentum equation in cell j (on the liquid side of the interface) and subtracted from the vapor momentum equation in cell i (on the vapor side).

Model as Coded: The code logic checks [

] ^{ac}. If such

cells are identified, the code will calculate an intercell drag force. [

$$]^{ac} \quad (4-121)$$

where $\Delta\alpha_i$ is the difference in liquid fraction between adjacent cells. This difference is an estimate of the contact area between vapor and liquid at the cell interface. Since the absolute value is used, the area is always a positive number. The intercell drag force becomes [

$$]^{ac} \quad (4-122)$$

where ΔU_{ij} is the difference between the vapor velocity in cell j and the liquid velocity in cell i , and is used as the relative velocity for the interfacial drag as given in Equation 4-118. This additional drag component will be added or subtracted depending on the cell void fraction. For the liquid rich cell, the interfacial force is added to the liquid momentum equation in that cell. For the adjacent vapor rich cell, this interfacial drag force is subtracted from the vapor momentum equation in the cell.

The code also checks for void differences on horizontal interfaces. In this case, the lateral velocity components are used for the liquid and vapor velocities. The interfacial area for the horizontal calculation is [

$$]^{ac} \quad (4-123)$$

where ΔZ is the lateral distance between the centerlines of the two adjacent cells. [

$$]^{ac}.$$

Scaling Considerations: The intercell drag model has no direct scale dependence, but it can be noding dependent since the geometric areas, cell sizes, gaps, and interfacial areas are all directly used in the drag calculations. The use of a constant interfacial friction factor such as $f_i = []^{ac}$ simulates a rough surface for all Reynolds numbers of interest, and has an equivalent roughness of $\epsilon/D_H = []^{ac}$. This roughness would simulate surface waves which are roughly $[]^{ac}$ of the pipe or channel hydraulic diameter. The use of this friction factor is an assumption which is verified by comparisons to experimental data. The experiments which can be used to confirm the intercell drag model are experiments such as the UPTF, CCTF, and SCTF which measure liquid levels in the upper plenum above a simulated core plate. The results of these experiments are discussed in Volume 3 of WCAP-12945-P-A. To address the scalability question, the experiments were modelled in the same manner as the PWR such that the geometry effects, which enter the intercell frictional drag calculation, are preserved between the PWR and the experiments. Also, the UPTF used full-scale reactor hardware components such that this intercell frictional drag model was verified at full-scale.

Conclusions: The intercell drag model relationships can depend on the method of modelling critical areas where counterflow can occur. The same modelling and noding technique was used on the large scale systems tests, such as LOFT, UPTF, CCTF, SCTF, and others, is the same as the PWR. The uncertainty of this model is accounted for in the overall uncertainty of the WCOBRA/TRAC code.

4-6 VESSEL COMPONENT ENTRAINMENT AND DE-ENTRAINMENT MODELS

4-6-1 Introduction

The drag between the vapor and continuous liquid results in either liquid entrainment, where the liquid moves from the continuous liquid field to the entrained liquid field due to the interfacial shear forces of the vapor acting on the liquid, or liquid de-entrainment caused by the entrained liquid interacting with the continuous liquid in the form of liquid film on structures. For liquid de-entrainment, the liquid moves from the entrained phase to the continuous liquid phase. The models for the different entrainment and de-entrainment mechanisms will be discussed below.

4-6-2 Entrainment in Film Flow

Model Basis: Entrainment of liquid drops from the continuous liquid phase can occur under a variety of conditions. The physical models used to determine the average net mass rate of entrainment and the entrained drop size will be different for each condition. Entrainment mechanisms that may have a significant influence on reactor thermal-hydraulics include entrainment from liquid films, reflood entrainment, entrainment resulting from vapor bubbling through liquid pools, and entrainment resulting from vapor flow across rod structures such as the upper plenum internals of a PWR.

The net mass entrainment rate is defined as

$$S = S''' V \quad (4-124)$$

where V is the cell volume.

The net mass entrainment rate (S) has units of mass per unit time and is the net result of the opposing mechanisms of entrainment (S_E) and de-entrainment (S_{DE}). Models for the entrainment rate, de-entrainment rate, and drop formation size are discussed below.

In addition to the entrainment rate, the rate of change of interfacial area of the entrained liquid field must be determined for use in the interfacial area transport equation (Section 3). The rate of change of total droplet area due to entrainment and de-entrainment is

$$\dot{A}_{i,E} = \frac{3 S_E}{\rho_l r_{d,E}} - \frac{3 S_{DE}}{\rho_l r_{d,DE}} \quad (4-125)$$

where $r_{d,E}$ is the radius of the entrained droplet, and $r_{d,DE}$ is the radius of the de-entrained droplet. $r_{d,DE}$ is assumed to be the cell average droplet diameter, while $r_{d,E}$ depends on the entrainment mechanism.

The contribution to droplet area resulting from droplet breakup mechanisms is also calculated. This term is calculated as [

$$]^{ac} \quad (4-126)^{(30)}$$

where S_{BR} is the mass flow of drops being broken, $r_{d,0}$ is the original drop size, and $r_{d,1}$ is the new drop size. This equation is derived in subsequent sections.

[

$$]^{ac}.$$

The void fraction at which a stable liquid film will exist depends on the flow channel size and the vapor velocity. The critical void fraction is determined from a force balance between the disruptive force of the pressure gradient over the crest of waves on the film and the restraining force of surface tension, as described in Section 3. The resulting expression for the critical vapor fraction is,

$$\alpha_{crit} = 1.0 - 2.0\sigma/(\rho_v |\underline{U}_v|^2 D_h) \quad (4-127)$$

The critical void fraction is limited to a minimum value of []^{ac}, the value at which waves can be expected to bridge across the flow channel and cause a transition to churn flow. The interfacial geometry of the churn-turbulent flow is treated as a linear interpolation between bubble flow and film flow. The flow is considered to consist entirely of bubbly flow as described above at a void fraction of []^{ac}, and entirely of film flow at the critical void fraction. Entrainment of liquid from the continuous liquid field

into the droplet field is allowed in this flow regime. The entrainment rate is interpolated between 0.0 at a void fraction of $[\]^{ac}$ to the full value given by the entrainment correlations at the critical void fraction. This provides a smooth transition into film or film mist flow. It should be noted that as long as the vapor velocity is sufficiently high to carry liquid drops away, the film mist flow regime will be maintained. This is consistent with Dukler's et al. (1979) explanation for the transition to film flow. This transition is predicted by the code based on the models used for the entrainment rate and interfacial drag between the vapor and drops.

Liquid entrainment is generated from the random perturbations in the flow which cause the development of a wavy interface on the film. These waves will grow as a result of the hydrodynamic and surface tension forces acting on the wave. Eventually the amplitude of the wave becomes so large that the pressure differential over the wave exceeds the restraining force of surface tension, and the wave breaks toward the gas core. The resulting drops are then carried along with the vapor. The shape and size of the wave depends on whether the film flow is cocurrent or countercurrent. Lower-amplitude roll waves with drops being sheared off of the wave crest are typical of cocurrent flow (Ishii and Grolmes, 1975). Abrupt, large-amplitude waves are typical of countercurrent flow (Lovell, 1977). This may be partially attributed to the fact that higher vapor velocities are required to cause vertical cocurrent upflow. As a result, the film thickness and wave amplitudes are generally smaller than those found in countercurrent vertical flow, which occurs at lower vapor velocities. Also, in countercurrent flow the shear forces act in opposition to gravity, causing larger wave amplitudes.

In countercurrent flow, the entrainment rate (S_E) is taken to be [

$$]^{ac} \quad (4-128)$$

The critical liquid fraction is defined as

$$\alpha_{t,crit} = (1 - \alpha_{crit}) \quad (4-129)$$

where α_{crit} is given by Equation 4-127.

It is assumed that all liquid in excess of that required for a stable film is removed from the film and enters into the entrained liquid phase, where it is treated as drops. In reality, some of this liquid may be in the form of waves which travel upward while the bulk of the film flows down. The gross flow split between the amount of liquid flowing down and that flowing up in the form of drops and waves is obtained by the above assumption.

For cocurrent film flow, Whalley et al. (1973) have correlated entrainment data with the parameter

$$S_k = k_s \tau_i / \sigma \quad (4-130)$$

where k_s , the equivalent sand roughness, is used as the length scale for the entrainment force due to surface tension, and τ_i is the interfacial shear stress. Wurtz (1978) later modified the above correlation by multiplying it by the dimensionless velocity $|\underline{U}_v| \mu_t / \sigma$ to compare with a larger variety of data. This velocity was also used by Paleev and Filippovich (1966) to correlate air-water entrainment data. This resulting correlating parameter became:

$$S_u = \frac{k_s \tau_i |\underline{U}_v| \mu_t}{\sigma^2} \quad (4-131)$$

and was then used to obtain a relationship for the entrainment rate. This relationship is

$$S_E = 0.41 S_u P_w \Delta X \quad (4-132)$$

where ΔX is the vertical dimension of the mesh cell and P_w is the wetted perimeter. This empirical correlation is used to determine the entrainment rate for cocurrent film flow. The equivalent sand roughness is given as

$$k_s = [0.57] \delta + [6625.0 \text{ ft}^{-1}] \delta^2 - [3.56 \times 10^6 \text{ ft}^{-2}] \delta^3 + [1.5736 \times 10^9 \text{ ft}^{-3}] \delta^4 \quad (4-133)^{(31)}$$

where δ is the film thickness and:

$$\tau_i = \frac{f_i}{2} \rho_v |\underline{U}_v|^2 \quad (4-134)$$

Correlations for the interfacial friction factor (f_i) have been given with the interfacial drag models discussed in Section 4-4-5.

The size of drops formed by entrainment from films has been characterized by Tatterson et al. (1977). Their results are used for both cocurrent and countercurrent flow. The drop formation radius is given by

$$r_{d,E} = 0.0056 \left(\frac{D_h \sigma}{\frac{f_s}{2} \rho_v |\underline{U}_v|^2} \right)^{1/2} \quad (4-135)^{(67)}$$

where f_s is defined in Equation 4-91.

Model as Coded: [

]ac.

A modified relative velocity is calculated as: [

$$]^{a,c} \quad (4-136)^{(32)}$$

where α_l is the average liquid fraction between adjacent axial cells J and $J+1$.

The entrainment rate is calculated by assuming that all liquid in excess of that calculated from Equation 4-129 is entrained. The entrainment rate is the difference between the film flowrate calculated using the cell liquid fraction, and the critical liquid fraction:⁽³²⁾ [

$$]^{a,c}$$

where $\alpha_{l,crit}$ is calculated from Equation 4-127 using U_{RI} :

$$\alpha_{l,crit} = 4 C_1 \sigma / (\rho_v U_{RI}^2 D_h) \quad (4-138)^{(33)}$$

where [$]^{a,c}$

The liquid film velocity $U_{l,j}$ is the cell J film velocity. [

$]^{a,c}$. The cell flowrate is calculated from the cell edge flowrate by [

$$]^{a,c} \quad (4-139)$$

where J denotes the cell center, and j denotes the cell edge. As described in Section 2, during solution of the momentum equation, the mass flowrate at the cell edge (i.e., within the momentum cell) is solved. The average phase fraction between cells is used to denote the cell edge phase fractions. When calculating entrainment processes, cell centered flow quantities are employed.

[

$$]^{a,c}.$$

Scaling Considerations: The basis for these film entrainment models is small-scale experiments which isolate each phenomenon. The entrainment rate formulation given by Equation 4-132 is mesh cell length dependent.⁽³⁴⁾ However, this dependence reflects the length of the surfaces with films which are generating the entrained liquid. Other parameters in the entrainment model given in Equation 4-132 are local flow, interfacial friction, and the channel geometry. These models have been verified against different scaled experiments, as shown in Volume 3 of WCAP-12945-P-A, which have structures similar to a PWR such that film entrainment from these structures should be prototypical.

Sources of verification of the film entrainment model are the Upper Plenum Test Facility (UPTF) ECC bypass tests, as well as the UPTF Upper Plenum Injection Test. In both of these experiments, the walls were cold and had liquid films from which entrainment could be generated. Also, both experiments had cocurrent flows as well as countercurrent flows. The UPTF experiments were full-scale, so there were no scaling distortion effects. These experiments and the calculated results are reported in Section 14-4 of WCAP-12945-P-A and Section 4-3 of WCAP-14449-P-A (Dederer et al., 1999).

Conclusions: The film entrainment models are based on local fluid conditions and have been verified with both scaled and full-scale experiments over a wide range of conditions. Section 18 of WCAP-12945-P-A concluded that ECC bypass and entrainment from the upper plenum to the hot legs are overpredicted, both resulting in conservative biases. Section 4-3 WCAP-14449-P-A also demonstrated that entrainment from the upper plenum to the hot legs is overpredicted for UPI plants.

4-6-3 Entrainment During Bottom Reflood

Model Basis: This model is available for channels with heated structures only. When the cladding temperature is above the surface rewetting temperature, a film boiling heat transfer mechanism will be established. This may correspond to either a dispersed flow regime or an inverted-annular, two-phase flow regime, depending upon the liquid content of the flow, the liquid subcooling, and the vapor velocity. As the cladding temperature is reduced because of the cooling provided by film boiling, the cladding will enter a transition boiling, and finally a nucleate boiling regime. High flowrates of superheated vapor result from the steam generated as the rods are quenched. Vapor velocities are usually high enough to entrain significant fractions of the liquid in the form of drops. This droplet entrainment is beneficial since it enhances heat transfer downstream of the quench front by desuperheating the steam and contributing to the total steam flowrate as the drops evaporate.

Several mechanisms for the formation of droplets during reflood can be postulated. The droplets may be formed by the breakup of the inverted annular liquid core because of surface instabilities if the liquid is subcooled. If the liquid is saturated, droplets may be formed by bubbles breaking through the surface of the liquid.

In COBRA/TRAC and WCOBRA/TRAC MOD7, the entrainment rate was given (Thurgood et al., 1983) by

$$S_E = (\alpha_v U_v / U_{crit})^2 \dot{m}_v \quad (4-140)^{(35)}$$

where \dot{m}_v is the vertical vapor mass flowrate and U_{crit} is the vertical vapor velocity required to lift a droplet, with radius defined by the critical Weber criterion against gravity. The critical velocity is obtained from a balance between the drag force and gravity force acting on the drop,

$$U_{crit} = \left(\frac{4We_d}{3C_{Dd}} \right)^{1/4} \left(\frac{\sigma g \Delta \rho}{\rho_v^2} \right)^{1/4} \quad (4-141)^{(36)}$$

A Weber number of []^{ac} (typical of reflood in the FLECHT tests) and a droplet drag coefficient of []^{ac} are used.⁽³⁶⁾ The use of the vapor flowrate, \dot{m}_v , in Equation 4-139 reflects the effect of vapor generation at the quench front on droplet formation.

In Kataoka (1983), models for entrainment from pools were developed, and several correlations were presented. Entrainment is defined as:

$$E = \frac{\rho_l j_{te}}{\rho_v j_v} \quad (4-141a)$$

where the entrainment E was expressed as the ratio of the mass flux of the entrained droplets to the mass flux of the gas. Kataoka and Ishii noted that E depends on the gas flux and the height above the top of the liquid pool. For a given height above the pool, the entrainment was reported as proportional to the gas flux as:

$$E \propto j_v \quad \text{for low gas flux}$$

$$E \propto j_v^{3-4} \quad \text{for intermediate gas flux}$$

$$E \propto j_v^{7-20} \quad \text{for high gas flux}$$

Equation 4-140 can be recast and written in terms of Kataoka and Ishii's definition for entrainment as, [

$$]^{ac} \quad (4-141b)$$

This shows that the entrainment model in WCOBRA/TRAC for bottom reflood is proportional to j_v^2 , and is consistent with the work by Kataoka and Ishii for low gas flux. For reflood, with high vapor generation, the high and intermediate gas flux regimes are likely. What this implies, is that the WCOBRA/TRAC MOD7 model has a weaker dependence on j_v than should be expected.

In addition, Kataoka and Ishii provide information that suggests that the upper limit of "4.0" in the as-coded original expression may be too restrictive at low pressure. Kataoka and Ishii give⁽³⁸⁾

$$E = 0.00484 \frac{\Delta p}{\rho_g} \quad (4-141c)$$

as appropriate for an upper limit on entrainment. This becomes greater than 4.0 below about 30 psia and increases rapidly with lower pressures. Thus, even if there is sufficient vapor flow at low pressure, the "4.0" upper limit could impose too low a limit on the entrainment.

The work by Kataoka and Ishii suggests two modifications to the existing WCOBRA/TRAC model that would increase entrainment. First, the exponent of the αU_v term should be increased from 2 to something higher. Second, the upper limit of 4.0 could be increased, which would allow more entrainment at low pressure. The final expression for bottom reflood entrainment used in WCOBRA/TRAC MOD7A is: [

]^{a,c}.

The droplet formation diameter for bottom reflood entrainment is taken as [

]^{a,c} (4-142)

where: [

]^{a,c} (4-143a)⁽³⁷⁾

and [

]^{a,c} (4-143b)⁽³⁷⁾

where $W_e = 7.5$

The droplet size Equations 4-143a and 4-143b are estimates of the reflood droplet size based on FLECHT data. Equation 4-143a is based on an equation originally developed for the BART code (Young et al., 1984); and then adapted to an earlier version of the vessel model called COBRA-TF, which was then used to assess FLECHT tests (Hochreiter et al., 1986). In the BART code, the initial droplet size is defined by (after combining Equations 2-115 and 2-71 in Young):

[]^{ac} (4-143c)

This equation was simplified by using a hydraulic diameter which was an average of the "large" and "small" Westinghouse fuel rod designs. The following table shows rod pitch, rod diameter, and hydraulic diameter for 15x15 and 17x17 fuel (the same geometry was used in FLECHT COSINE and FLECHT SEASET), and the average of the two.

Array Type	Rod Pitch (in)	Rod Diam (in)	D_h (ft)
15x15	0.563	0.422	0.0334
17x17	0.496	0.374	0.0386
		AVERAGE D_h :	0.036

If the averaged value of D_h is used in Equation 4-143c, and is combined with the constant, the value []^{ac} is obtained, which compares with the value coded of []^{ac}. This equation is also used in Hochreiter et al. (1986), Equation 2-50, the only difference being that the g term is also combined with the constant: []^{ac}, which compares with the reported value of []^{ac}.

The simplification of using an average hydraulic diameter, while unnecessary, reflects the fact that the scatter in droplet diameters is such that the effect of hydraulic diameter cannot be discerned over the narrow range of interest.

Equation 4-143b uses the Weber number criterion to establish the maximum droplet size which can be entrained.

The liquid which is being shattered into drops is assumed to be suspended above a pool through which vapor is flowing at a flux $j_v (= \alpha U_v)$. The relative velocity between the vapor and the liquid above the pool is therefore the vapor velocity above the pool, which is approximated by j_v .

The droplet size data is tabulated in Lee et al., (1982). The droplet size data ranges from 0.002 to 0.006 feet. When the data was plotted against droplet velocity, no clear trend was observed. The various equations, and the minimum allowed value from Equation 4-142 are compared to this data range in Figure 4-6a for 40 psia. Equation 4-143a estimates the midpoint of the data range, and includes a pressure effect through the vapor density. Equation 4-143b assures that if vapor volumetric flux is high, the predicted droplet size approaches the minimum of the range. A second comparison at 20 psia is shown in Figure 4-6b.

Near the quench front, the measured droplet size was somewhat larger, with a minimum value of 0.0033 ft⁽⁶⁶⁾. This value is used as a lower bound in Equation 4-142 for bottom reflood.

Model as Coded: Entrainment due to bottom flooding is assumed if the flow regime in the cell is a hot wall regime, and if the vapor velocity in the cell is upward.

Equation 4-141d is evaluated as follows: [

$$]^{ac} \quad (4-144)^{(38)}$$

where \bar{m} is the average vapor flow in the cell.

[

$$]^{ac}.$$

The ratio of local to cell averaged vapor fraction and vapor density is a consequence of the fact that the vapor mass flowrate, solved for in the momentum equation, is defined at the cell edge, and is based on average fluid properties between adjacent cells (Section 2-3-3-2). The vapor mass flowrate within the cell is calculated from the relation [

$$]^{ac} \quad (4-145)$$

where j and J denote the cell edge and cell center, respectively. The value of U_T is given by Equation 4-69.

A further check on the entrainment is made by calculating a minimum velocity needed to lift a droplet upward against gravity. In this case, the minimum vapor velocity is given as [

$$]^{ac} \quad (4-146)$$

where the drop diameter is given in Equation 4-142 and is the minimum of these choices. The droplet drag coefficient is C_{D0} in Equation 4-146. If the vapor velocity is less than C_{D0} times $U_{v,min}$, then the entrainment rate calculated in Equation 4-144 is modified by

$$C_{D0}^{(38)} \quad (4-147)$$

When U_v is greater than C_{D0} times $U_{v,min}$, the velocity ratio given in Equation 4-147 is 1.0, and the full entrainment calculated from Equation 4-144 is used. If U_v is less than $U_{v,min}$ then no entrainment is calculated. As U_v increases, more entrainment is calculated, as given in Equation 4-147. Finally, the entrained flow entering the cell is subtracted from the entrainment, which is calculated from Equation 4-147.

Equation 4-147 gives the incremental amount of entrained liquid which should be added to the entrained liquid field in the cell. Once the flow is entrained, the droplet drag relationships discussed in Section 4-4-7 will convect the entrained droplets axially as well as in the transverse directions.

Scaling Considerations: The basic model formulation for entrainment has no scale dependent parameters, and the droplet Weber numbers given in Equations 4-140 to 4-144 come from high speed movies of FLECHT reflood experiments which were performed using prototypical geometries, flow, pressures, and powers. The FLECHT and FLECHT-SEASET reflood experiments were especially designed to obtain the necessary data for developing and verifying reflood codes. The drop sizes chosen for the initial reflood drop size are based on this data. Another source of validation for the reflood entrainment model is void fraction distribution or overall mass inventory calculated for the FLECHT-SEASET reflood experiments. These tests are consistent flooding rate experiments so that a cold test bundle would fill at a prescribed flooding rate. However, a hot bundle will fill much more slowly because of the vapor generation and resulting liquid entrainment caused by quenching and cooling the hot rods. As shown in Section 12 of WCAP-12945-P-A, WCOBRA/TRAC predicts the FLECHT-SEASET void fraction data quite well and also predicts the bundle mass storage as a function of time. Predicting the correct bundle mass storage as a function of time is an indication that the entrainment rate is also being predicted correctly since the entrainment rate is the difference between the inlet mass flow and the bundle storage rate. Since the FLECHT-SEASET tests have full-scale rod bundle dimensions, there are no scaling issues with the WCOBRA/TRAC entrainment model.

Conclusions: The entrainment models for bottom reflood have been verified by comparison to full-length rod bundle experiments with prototypical dimensions such as the FLECHT, FLECHT-SEASET, FEBA, and the NRU nuclear rod bundle reflooding experiments. These experiments cover the full range of expected conditions for PWR reflood. The uncertainty and reliability of the entrainment models is accounted for in the overall WCOBRA/TRAC code uncertainty.

4-6-4 Entrainment During Top Down Reflood

Model Basis: There are two mechanisms for entrainment in top down reflood, upper plenum injection, or top spray situations. The first mechanism is the breakup of pooled liquid films on reactor internals hardware as the liquid falls through holes, slots, or slits in the hardware, into the core. The second mechanism is entrainment from falling films at the top quench front where the film flow exceeds the quench rate of the rod and the excess liquid is sputtered off the hot surface. The model for entrainment from the top down quench front will be discussed first.

When the top ends of a fuel or heater rod quench, a quench front moves down the rods by axial conduction. A liquid film follows the quench front down the rods toward the sputtering or quench front. It is assumed that the entrainment rate from a falling film top quench front is equal to the liquid film flowrate reaching the quench front, (\dot{m}_t) , minus the vapor generation rate at the quench front,

$$S_E = \dot{m}_t - \Gamma_q''' V \quad (4-148)$$

Droplets are assumed to be generated at the sputtering front (quench front) with a drop size which is selected as [

] ^{a.c} (4-149)⁽³⁹⁾

The falling liquid film behavior is handled using the models previously discussed in Section 4-4-2 for both vertical and lateral flow. The droplet behavior is handled using the dispersed droplet models for vertical and lateral flow discussed in Section 4-4-7.

The model for the breakup of pooled liquid films is discussed next.

The drop size model for the sputtering quench front is based on top spray heat transfer experiments, typical of a BWR. When Westinghouse began analysis of the Westinghouse G-2 refill experiments (Hochreiter et al., 1976), which were low pressure rod bundle film boiling experiments with significant liquid injection into the upper plenum, it was found that the entrained droplet size, using a sputtering front model, would yield drops which were too small, resulting in excess over cooling compared to the G-2 test data.

When examining the tests and the code predictions, it was felt that the main reason for the higher predicted heat transfer was the drop size the code was choosing. The flows in these experiments were sufficiently small that the injected water would de-entrain, pool and fall, or be forced through the upper fuel nozzle simulation which was a plate with several small diameter holes. This plate was designed to be hydraulically similar to a PWR top fuel nozzle plate.

It was felt that the dominant drop size which would fall through the rod bundle would be determined from drops which were formed at the fuel nozzle simulation plate or top spacer grid as the liquid fell or was forced through the holes in the plate. Therefore, a drop size model was developed to calculate the size of droplets which would be formed as the liquid flowed through hardware at the top of the fuel assembly into the heated portion of the core. Wallis (1969) presented a model for a single drop falling through an area restriction, or orifice. For liquid velocity less than the critical velocity derived from Equation 9.8 of Wallis (1969),

$$V_{L,LIM} = \frac{2.5}{D_h} \left(\frac{\sigma^3}{\rho_l^2 g (\rho_l - \rho_v)} \right)^{\frac{1}{4}} \quad (4-150a)$$

Equation 12.1 of Wallis (1969) is used to estimate the drop diameter.

$$\frac{D_d}{2} = \left(\frac{\sigma(D_H/2)}{g(\rho_l - \rho_v)} \right)^{\frac{1}{3}} \quad (4-150b)$$

For liquid velocity greater than this limit, the liquid will form an unstable liquid jet which breaks up to form drops with a radius equal to

$$r_{OR} = 1.9 R_o \quad (4-150c)^{(40)}$$

from Wallis, Equation 12-3, where

r_{OR} is the drop radius formed from the liquid jet as the water flows through the orifice, and

R_o is the radius of the orifice plate or hole size.

For plates which have multihole geometries such as the G-2 top fuel nozzle simulation, a PWR top fuel nozzle core plate, or a top spacer grid, this formulation was generalized to

$$D_{OR} = 1.9 D_h \quad (4-151)$$

where:

D_{OR} is the droplet diameter formed at the orifice or area reduction, and

D_h is the hydraulic diameter which characterizes the plates or hardware where the liquid pools and flows through.

Again, the above formulation is valid for situations in which the vapor-to-liquid velocities are small, such that there is small interfacial shear on the liquid as it flows through the area reduction or orifice.

If the liquid flow is being accelerated through the plate holes by steam, there is a possibility that the liquid will be shattered into smaller drops by the large relative liquid and vapor velocities. The dimensionless group which describes the largest stable droplet size to be formed under these conditions is the Weber number given as

$$We_{crit} = \frac{\rho_v (U_v - U_l)^2 D_{OR}}{\sigma} \quad (4-152)$$

Experiments have shown that $We_{crit} \approx 12$ for this situation (Wallis, 1969).

In a situation where there is top down flooding with a top quench front, two different drop sizes will be calculated: the large drops which are generated from the hardware at the top of the rod bundle with drop sizes calculated with Equation 4-151, and drop sizes generated at the quench front which are calculated using Equation 4-149. The drops from the hardware will flow down into the channel between the heated rods, while the smaller drops will sputter off the heated surface into the channel flow area. It is assumed that these drops can be treated as a single droplet field of average diameter as determined by the interfacial area transport equation. The large drop sizes, which are generated from the hardware, will dominate so that the resulting drop size is closer to the large hardware generated drops, not the very small sputtering front drops. The model then represents the sweeping up of the smaller drops, or the coalescence of the smaller drops by the large droplets in the channel. The effect of this model for top down flooding is to reduce the interfacial area between the liquid and vapor such that reduced interfacial heat transfer occurs, the steam superheats to higher temperatures, and the overall heat transfer from the heated surface decreases.

The above models are used for downflow at void fractions above $\alpha_v \geq [\quad]^{ac}$.

Model as Coded: For the entrainment from the sputtering front the code calculates the maximum liquid available for entrainment as given in Equation 4-148 as [

$]^{ac} \quad (4-153)$

where $\alpha_{t,j+1}$ is the upstream cell liquid fraction, $\dot{m}_{x,t,j}$ is the liquid downflow, and $\alpha_{t,j}$ is the averaged liquid fraction between the current cell and the donor cell.

This is further modified by comparing the void fraction for the liquid film to the critical liquid void fraction for a stable liquid as [

$$]^{ac} \quad (4-154)$$

The coding logic chosen for the top down flooding droplet size model chooses a maximum droplet size as specified in Equation 4-149. [

$$]^{ac}.$$

For the breakup of pooled liquid films, the code examines changes in the momentum area along the channel to determine if the drop size should be recalculated with the drop orifice equation given in Equation 4-151. For momentum area changes greater than [$]^{ac}$, the drop size is recalculated using the hydraulic diameter in the reduced area channel. Fuel rod grid locations are also checked to see if the grid area reduction is significant relative to the channel area, and the drop size can be calculated at the gridded locations using the grid hydraulic diameter.

For the orifice droplet equation, drops are assumed to be formed by the reactor hardware where an area reduction of greater than [$]^{ac}$ occurs. [

$$]^{ac}.$$

That is: [

$$]^{ac} \quad (4-155)$$

If a grid exists in the cell, the incoming drop size is compared to that calculated with Equation 4-151⁽⁴¹⁾ using the grid hydraulic diameter, and the minimum drop size is used.

That is: [

$$]^{ac} \quad (4-156)$$

The rate of change of the interfacial area due to the droplet diameter change is given as

$$\dot{A}_{i,OR} = \frac{dA_i'''}{dt} A_X \Delta X \quad (4-157)$$

where A_i''' is the interfacial area/volume. Equation 4-157 can be approximated as

[

] ^{a.c.}

The interfacial area upstream of the restrictive plate is [

] ^{a.c.} (4-159)

where:

N_d is the number of drops/volume, and

D_{UP} is the drop size upstream of the plate.

The plate will reform the drops with a new drop diameter given from Equations 4-155 or 4-156, depending on whether the plate or grid is more limiting. The interfacial area downstream of the plate or grid is: [

] ^{a.c.} (4-160)

where D_{OR} is the new drop size, and $N_{d,new}$ is the new number of droplets. The volume of drops are preserved such that the new number of drops becomes: [

] ^{a.c.} (4-161)

The interfacial area change across the plate or grid then becomes: [

] ^{a.c.} (4-162)

or [

]^{a,c} (4-163)

However, the entrained void fraction upstream of the plate or grid is: [

]^{a,c} (4-164)

Substituting Equation 4-164 into Equation 4-163, the interfacial area change becomes: [

]^{a,c} (4-165)

The rate of change of interfacial area from Equation 4-158 then becomes: [

]^{a,c} (4-166)

which is programmed as [

]^{a,c} (4-167)

| for downflow. [

]^{a,c} (4-168)

[

]^{a,c}.

A further test is used on the calculated drop size (D_{OR}) for large drops. [

]^{a,c}

becomes:[

] ^{a,c} (4-169)

The model described above causes entrained droplets flowing through the orifice plate to change size. Continuous liquid flowing through the orifice is also assumed to be completely entrained into the droplet field. This is done by calculating an orifice entrainment rate as [

] ^{a,c} (4-170)

where $\alpha_{l,j}$ is the upstream cell liquid fraction. The droplet size associated with this entrainment is D_{OR} , calculated from Equation 4-155 or 4-156.

Using Equation 4-125, the contribution to the entrainment interfacial area density change is

$$\dot{A}_{i,E} = \frac{6 (S_E + S_{E,OR})}{\rho_l D_{OR}} \quad (4-171)$$

This equation assumes that, in a cell containing an orifice plate, entrainment from all sources leads to drops of size D_{OR} .

The interfacial area shifts to a larger or smaller value depending on the drop size generated by the models described above. If drops generated in the cell are one half the original size or smaller, this is reflected in the interfacial area source term as an increase in the interfacial area. This increase in area will usually improve the interfacial heat transfer in a dispersed flow situation by de-superheating the steam temperature such that the wall is exposed to a lower sink temperature.

The above model and approach are for downflow. The code logic is applied in the dispersed flow film boiling regime, [^{a,c}. The interfacial area generation term is added to other sources of interfacial area generation as a source term for the total interfacial area transport equation, which is solved for the next time step.

Scaling Considerations: The falling film entrainment model is a basis model which does not have any scale dependent parameters. This model is used for all reflood and blowdown situations and has been verified on full-length heated rod bundles with prototypical dimensions and rod arrays, such that there should be no scaling effects.

The droplet entrainment model for top down flooding uses a generalization of the Wallis orifice droplet formulation which models the complex flow passages with a hydraulic diameter. This model has been validated against the G-1 and G-2 blowdown data as described in Section 11 of WCAP-12945-P-A. It has also been applied in analyses of the CCTF tests with upper plenum injection (UPI), and the UPTF - UPI injection test as described in WCAP-14449-P-A (Dederer et al., 1999). This model generalizes the

Wallis equation and uses the hydraulic diameter of the structure as the dimension to set the droplet diameter for the entrained flow coming into the core from the upper plenum. Using the hydraulic diameter will permit the modelling of all the wetted surfaces and flow passages found in the complex upper core plate, top fuel nozzle, and spacer grids. Normally either the top nozzle or the top most spacer grid is limiting and results in the smallest droplet diameter being formed. This particular model will set the initial drop size entering the bundle. The drops can be further broken up by the grids as they are accelerated down through the bundle.

Conclusions: The generalization of the Wallis orifice equation for drop formation has been verified on several different hardware geometries which are similar to real PWR hardware. The G-1 and G-2 blowdown experiments use prototypical Westinghouse mixing vane and non-mixing vane grids, and a fuel assembly tie plate similar to an actual fuel assembly. The UPTF-UI test series uses actual PWR hardware for top fuel assembly nozzles and spacer grids. The CCTF tests use hardware which is also similar to actual PWR fuel assembly components. Therefore, the models have been verified on prototypical components at full scale. Any uncertainty in these models is reflected in and accounted for in the overall WCOBRA/TRAC code uncertainty calculations.

4-6-5 Spacer Grid Droplet Breakup Model

Model Basis: Spacer grids are structural members in the reactor core which support the fuel rods at a prescribed rod-to-rod pitch. All fuel assemblies have grids at the same elevations across the core. Because the grids are at the same elevations, no flow bypass or flow redistribution occurs. Since the grid reduces the fuel assembly flow area, the flow is contracted and accelerated, and then expands downstream of each gridded layer in the core. As the flow is accelerated within the grid and then expands downstream, it reestablishes the thermal boundary layers on the fuel rod, which increases local heat transfer within and downstream of the grid.

Several single-phase experiments clearly showed that the continuous phase heat transfer downstream of a spacer grid can be modelled on entrance effect phenomena where the abrupt contraction and expansion result in establishment of a new thermal boundary layer on the heated surface downstream of the grid. This entrance effect heat transfer decays exponentially downstream of the grid, and the local Nusselt number decreases exponentially downstream of the grid. The enhancement of the convective heat transfer is described in Section 6-2-10.

When the flow is a two-phase dispersed droplet flow, characteristic of a calculated PWR blowdown or reflood, the grids can promote additional heat transfer effects. Since the grids are unpowered, they can quench before the fuel rods. If the grids quench, they can create additional liquid surface area, which can help desuperheat the vapor temperature in the nonequilibrium two-phase droplet flow. A wetted grid will have a higher interfacial heat transfer coefficient compared to the droplets, since the relative velocity for the vapor flow relative to the liquid film is larger. The models accounting for the wetted grid effect are described in Section 5-2-10.

In addition to grid rewetting, the grids can also cause shattering of the entrained droplets into smaller, more easily evaporated droplet fragments. The evaporation of the smaller shattered droplets provides an additional steam source, which decreases the stream superheated temperature and also increases the convective heat transfer coefficient. This section describes how the droplet breakup at grids is accounted for in WCOBRA/TRAC.

Wachters and Westerling (1966) studied drops impinging on a plate and classified the droplet fragmentation in terms of the perpendicular Weber number

$$We_d = \frac{\rho_t D_0 U_p^2}{\sigma} \quad (4-172)$$

where U_p is the drop velocity perpendicular to the plate and D_0 is the incoming drop size. Extensive experiments were also performed by Takeuchi et al. (1982) on droplets normally impacting on a hot plate. Liquid deforms as a circular sheet, then disintegrates into fine droplets. The splashed droplet diameter was also reported as a function of the droplet's perpendicular Weber number.

Since the grid thickness is usually less than the droplet diameter during a typical reflood transient, the impact phenomena for a droplet on a grid should be different from that found by Wachters (1966) and Takeuchi (1982). From movies of reflood tests conducted by Japan Atomic Energy Research Institute (Okubo and Sugimoto, 1984), the entrained droplets were clearly observed to break into finer sizes after impaction on the grid structure. However, no further study was performed on droplet breakup phenomena. Experiments which concentrated on the study of the droplet impingement on the spacer grid can be found from the tests conducted by the Central Electricity Generating Board (CEGB) of the United Kingdom, (Adams and Clare (1983, 1984), by S. L. Lee et al. (1982, 1984a,b) at the University of New York at Stony Brook, and by Yao, Hochreiter, and Cai (1988) from Westinghouse/ Carnegie-Mellon University.

When an entrained droplet impacts on the grid strap, the droplet is split into two liquid sheets flowing along each side of the grid strap, as shown in Figure 4-7(a). Detailed photographic studies from the above references indicated the mass and the trajectory angle of the split liquid sheet varied with the impact conditions, such as the incoming drop velocity, grid strap-to-droplet thickness ratio, and the degree of asymmetry between the droplet and grid center. For a high velocity droplet impacting on a wide grid, the resulting trajectory angle is large, which results in significant generation of microdrops. A low velocity droplet impacting on a thin grid will be sliced into two liquid sheets which reform into two large drops with very few micro drops being generated. For high velocity droplets the splashed liquid sheet expands and a cylindrical rim forms at the free edge of the liquid sheet. The cylindrical rim was observed to be a source of small droplets. A thinner liquid sheet will generate finer droplets. Based on these observations, the size of broken droplets should be a function of two major dimensionless parameters, namely the droplet Weber number (We_d) as defined in Equation 4-172 and the ratio of grid thickness to incoming droplet diameter (w/D_0).

The droplet off-set parameter, Δ defined in Figure 4-7(b), was also reported by Yao, Hochreiter, and Cai (1988) as a parameter affecting the size of the generated small droplets. However, the off-set parameter can be absorbed in the parameter (w/D_0) and the break-up efficiency in the droplet break-up correlation to be described below.

Following the first impact, the shattered droplets will either flow away with the steam and provide some grid cooling by film boiling if the grid is nonwetable, or help in quenching of the grid and formation of a liquid film on the grid surface if the grid is wettable. If a liquid film is formed, new drops may be generated through entrainment mechanisms either from the liquid film on the grid or from the liquid sheet flowing away from the trailing edge of the grid. Adams and Clare (1984) also observed that the drop size entrained from liquid sheets flowing away from the trailing edge of a wetted grid is similar to the drop size before the impact, which is consistent with the WCOBRA/TRAC film entrainment model for quenched grids. It is concluded that the small droplet formation occurs primarily at the first impact rather than from subsequent droplet entrainment off the grid.

The leading edge of a wetted grid may be covered by a thick film, if the local vapor velocity is low, or a thin film if the local vapor velocity is high enough to push the liquid film upward (Figure 4-7c). The droplet breakup mechanism is expected to be different in these two situations. Droplet breakup into sizes significantly smaller than the incoming droplet size was observed to occur at droplet Weber numbers of 80 or higher (Yao, Hochreiter, and Cai, 1988, Figure 11).⁽⁴³⁾ This Weber number corresponds to a droplet velocity of approximately 15 ft/s, the minimum vapor velocity for droplet breakup is therefore expected to be 25 ft/s or greater, which, in addition to evaporation of the liquid to superheated steam, would lead to a thin film on the grid. This likely situation is further supported by measurements in Lee et al. (1982) which indicated that the shattered droplets were of similar size whether the grid was wet or dry. In the case of a wet grid with a thin film or a dry grid, the droplet breakup mechanism was found to result primarily from the impact of the droplet on the grid leading edge. In experiments by Yao, Hochreiter, and Cai (1988), the leading edge condition for the wet grid cases was similar to the thin film case (Figure 4-7c), since the test was designed to let the droplets fall onto the grid. The film would then drain from the grid strap away from the leading edge.

The broken small droplets measured by Lee et al. (1982, 1984a,b), either with dry grid or wet grid were found to be of similar size, supporting the conclusion that a thin film covers the grid. Yao, Hochreiter, and Cai also observed that the small droplet sizes under a cold grid impact were only slightly larger than that when the grid was hot. In the test by Yao, Hochreiter, and Cai, since the droplet was falling downward, the leading edge condition for both cold grid and hot grid for high vapor velocity were very close to that shown in Figure 4-7c.⁽⁴⁴⁾ The leading edge impact is the most important break-up mechanism, the drop size distributions for either cold or hot (i.e., wet or dry) grids should be similar since the condition of the leading edges are similar.

As the entrained droplets impact a grid spacer, some may pass through without contact while some will impact on the grid structure. The droplets which impact on the grid will be broken into many or few

microdrops depending on how the drop hit the grid. The size of the shattered droplets is represented by the following formula [

$$]^{ac} \quad (45)$$

D_{small} is the Sauter mean diameter of the shattered drop, D_0 is the diameter of incoming drop, and w is the grid strap width.

The correlation given by Equation 4-173 is a refinement to earlier models which reflects the effects of different grid thickness to droplet diameter ratios at high Weber numbers. [

$$]^{ac}.$$

Model as Coded: WCOBRA/TRAC has the coding and input logic to locate the grid structure within the core channels for any PWR fuel design. Once the grid is located, the drop size approaching the grid is calculated from the entrained flow and the droplet number density in the upstream cell

$$D_d = \frac{6 \alpha_e}{A_{i,d}^{///}} \quad (4-174)$$

If the calculated drop size from Equation 4-174 is less than []^{ac} feet in diameter, the drops are not allowed to be further broken up by the grids and the grid droplet logic is bypassed. A droplet Weber

number is calculated for the incoming droplets in the cell using Equation 4-172. If the droplet Weber number is less than $[]^{ac}$, it is assumed that the drops do not have sufficient inertia to be broken-up by the grids and the grid logic is bypassed. For droplet Weber numbers greater than $[]^{ac}$, the droplet breakup model given in Equation 4-173 is used to calculate the shattered drop-to-incoming-drop ratio after the drops pass through the grid. This ratio is then used to calculate the small droplet diameter after passing through the grid, by multiplying the calculated droplet ratio by the incoming droplet diameter.

The rate of change of the interfacial area due to the droplet breakup is given as

$$\dot{A}_{i,GR} = \frac{dA_{i,d}'''}{dt} A_X \Delta X \quad (4-175)$$

where $A_{i,d}'''$ is the interfacial area/volume.

Equation 4-175 can be approximated as [

$$]^{ac} \quad (4-176)$$

where $\Delta A_i''' = A_{i,new}''' - A_i'''$ is the change in the interfacial area.

The interfacial area upstream of the grid is

$$A_{i,d}''' = \pi D_d^2 N_d \quad (4-177)$$

where:

N_d is the number of drops/volume, and

D_d is the drop size upstream of the grid and is determined from the interfacial area transport equation, described in Section 3.

The grid will shatter a fraction of the drops which impact the grid. The drop volume is preserved such that if a fraction (F_s) of the drops are shattered, the number of new small drops are given as [

$$]^{ac} \quad (4-178)$$

such that the new interfacial area downstream of the grid is [

$$]^{ac} \quad (4-179)$$

The change in the interfacial area ΔA_i^{ac} is calculated by using Equation 4-179 and subtracting Equation 4-177 as [

$$]^{ac} \quad (4-180)$$

but [

$$]^{ac} \quad (4-181)$$

such that by substituting Equation 4-181 into Equation 4-180, and then putting the result into Equation 4-176, the rate of change of the interfacial area becomes [

$$]^{ac} \quad (4-182)^{(46)}$$

Equation 4-182 is programmed as [

$$]^{ac} \quad (4-183)$$

The value of F_s is [

$]^{ac}$. This area is input and depends on the grid design and the fuel type.

Unlike the orifice breakup model, only the entrained droplet field is considered for breakup through grids. This is because the grid droplet breakup mechanism occurs only in dispersed droplet flow in the hot wall regime.

Scaling Considerations: The grid droplet breakup model is a basic model which accounts for the physical geometry of the fuel assembly spacer grids and is not scale dependent. However, the droplet breakup model is empirical and does depend upon the specified geometry of the spacer grid in the fuel assembly. The grid droplet breakup model development was based on droplet size data which is characteristic of PWR reflood situations as well as prototypical spacer grid structures. The total model

was verified by comparing the resulting film boiling heat transfer in rod bundles for different types of spacer grids. In particular, the FEBA experiments were modelled with and without a mid-plane spacer grid, the FLECHT and FLECHT-SEASET experiments were modelled using simple egg-crate spacer grids, and the G-1 and G-2 blowdown and reflood experiments were modelled using 15x15 and 17x17 Westinghouse production mixing vane grids. Inclusion of the spacer grid droplet breaking model improved the WCOBRA/TRAC predictions of these experiments. Since these experiments were all full-length with prototypical rod array geometries and grids, there are no scaling effects which need to be considered.

Conclusions: A droplet breakup model for spacer grids has been developed to represent the actual effects of the grids on the entrained two-phase flow at high void fractions, $\alpha_v \geq []^{ac}$. The model has been verified against a range of full-length rod bundle experiments with prototypical geometries and different grid designs in blowdown and reflood situations. The uncertainty in this model is addressed in the overall WCOBRA/TRAC code uncertainty calculations.

4-6-6 De-entrainment in Film Flow

Model Basis: Liquid film flow can exist on any structural surface which is in the wetted wall regime, such as the reactor upper plenum structures, vessel wall, core barrel wall, the ends of the fuel rods which are quenched, and other structures.

The deposition of entrained drops on this liquid film occurs as a result of random turbulent motions that impart transverse velocity to the drops, bringing them into contact with the solid surfaces or liquid films within the flow channel. The rate at which this occurs has been correlated by Cousins et al. (1965) using a drop concentration gradient diffusion model in which the concentration at the wall is assumed to be zero. Cousins' model is used to determine the de-entrainment rate for film flow as

$$S_{DE} = k_g \Delta C P_w \Delta X \quad (4-184)$$

where:

k_g is the mass transfer coefficient,
 P_w is the wetted perimeter,
 ΔX is the cell height,

and where ΔC is the concentration gradient for the channel as given by

$$\Delta C = \frac{\alpha_e P_t}{\alpha_e + \alpha_v} \quad (4-185)$$

The mass transfer coefficient, (k_g) , has been found to be a function of surface tension (Whalley, 1973). This function is represented by⁽⁶⁸⁾

$$k_{\sigma} = \text{maximum} \begin{cases} 3.0492 (10^{12}) \sigma^{5.3054} \\ 12.491 \sigma^{0.8968} \end{cases} \quad (4-186)$$

and is compared with the Whalley data in Figure 4-9.

The de-entraining flow is assumed to carry with it droplets of average size as calculated from the cell interfacial area transport equation (Section 3-3-7).

Model as Coded: [

] ^{a,c}.

The mass flow of de-entrained droplets goes into the liquid film flow field. The de-entrainment rate also is reflected as a loss of interfacial area in the interfacial area transport equation discussed in Section 3-3-7, using Equation 4-125.

Scaling Considerations: The de-entrainment model, as developed from small scale data, does have the surface geometric effects directly included in the formulation through the wetted perimeter and the cell length. The use of the cell length can make the model nodding sensitive. Thus, the model must be examined at several scales, and the nodding should be consistent with the PWR nodding.

The droplet de-entrainment is most critical for ECC bypass calculations and reflood calculations since de-entrainment can represent liquid mass that is retained in the reactor vessel. WCOBRA/TRAC has been compared to the different scaled ECC bypass experiments at 1/15, 1/5, and full-scale UPTF data. As shown in Section 18 of WCAP-12945-P-A, WCOBRA/TRAC has a tendency to over-predict bypass as facility size is increased to full scale. For reflood situations, WCOBRA/TRAC has been compared to CCTF, SCTF, and UPTF data for de-entrainment effects in the reactor upper plenum. The UPTF-UPI and non-UPI experiments are full-scale simulations for upper plenum de-entrainment behavior. As seen in Section 18 of WCAP-12945-P-A, and Section 4-3 of WCAP-14449-P-A, WCOBRA/TRAC under-predicts de-entrainment for the full-scale facilities during a simulated reflood transient. Therefore, since the WCOBRA/TRAC models have been verified up to full-scale and since the same nodding is used for WCOBRA/TRAC PWR simulations, there are conservative biases due to scaling effects of this model.

Conclusions: The WCOBRA/TRAC simulations have been performed, at different scales, for the film de-entrainment model for ECC bypass and upper plenum de-entrainment. These simulations have shown conservative biases at full scale for this model.

4-6-7 Crossflow De-entrainment

Model Basis: Entrained liquid carried into the reactor upper plenum during reflood can de-entrain on the reactor structures as the two-phase mixture flows across these structures and out of the hot legs of the reactor. This cross flow de-entrainment will result in creating liquid films on the structures which can flow downward to create a liquid pool at the horizontal upper core plate.

The model used in the code employs de-entrainment fractions obtained in the upper plenum de-entrainment experiments of Dallman and Kirchner (1980) where:

$$S_{DE} = \eta_{NR} \alpha_e \rho_t |U_e| L_g \Delta X \quad (4-187)$$

The de-entrainment fraction (η_{NR}) is user input and depends on the reactor design. Following the recommendations of Dallman and Kirchner (1980) the de-entrainment fraction for an array of tubes is given by

$$\eta_{NR} = 1 - (1 - \eta_R)^N \quad (4-188)$$

with

$$\eta_R = \eta_l (1 + 4.5\beta^2) \quad (4-189)$$

from Chen (1955) where

- η_R = the de-entrainment fraction for a single row of tubes,
- N = the number of rows of tubes,
- β = the diameter-to-pitch ratio of the array, and
- η_l = the de-entrainment fraction for a single tube (0.19 for cylindrical tubes and 0.27 for square tubes.)

In the reactor situation, the square cross section tubes represent control rod guide tube structures while the circular tubes represent support column structures.

The experiments performed by Dallman and Kirchner were for air/water flows and a single structure (either a cylinder or square tube). There were different size cylindrical structures examined, ranging up to ~4.0 inches in diameter, with variations in air and droplet velocities. These authors obtained the single structure de-entrainment data for cylinders or square tubes, which is the basis for Equation 4-189. They examined the effects of the droplet Weber number defined as

$$We_d = \frac{\rho_t U_d^2 D_d}{\sigma} \quad (4-190)$$

which characterizes the drop splashing and splattering effects at high values of We_d and []^{a,c}. The range of drop Weber numbers investigated ranged from 2500 to 7000 which compares to drop velocities from 10 m/sec to 18 m/sec. These drop velocities are more characteristic of the region close to the hot leg nozzle where the flow is accelerating toward the nozzle from the upper plenum. The data indicated that the single structure de-entrainment was independent of the drop Weber number over the range of the data, and a consistent value could be used for the de-entrainment fraction. The values given by the authors are best fit to the data.

The extrapolation of these de-entrainment measurements of isolated structures in air-droplet cross flow to multiple structures in close proximity, e.g., a row of cylinders, has been investigated by Chen (1955) and Davies (1952). The work of Chen is the most directly applicable to the PWR situation.

Chen used cylinders with very small diameters—a few millimeters. Therefore, application of Equation 4-188 to the present work must be verified at larger geometries. Chen assumed that for an array the flow is completely mixed between rows, and the changes in drop size and velocity spectra do not change the local de-entrainment efficiencies markedly from those of the first row. With these assumptions, Chen developed an equation for multi-row de-entrainment efficiency (η_{NR}) as

$$\eta_{NR} = A[1 - C(1 - \eta_{R1}) \dots (1 - \eta_{RN})], \quad (4-191)$$

where C is a complicated geometric parameter dependent upon array pitch diameter ratios, staggered versus in-line arrays, etc., A has a value of unity for a staggered array with no line of sight through the array, and η_{RN} is the capture efficiency of the n^{th} row. Equation 4-189 is used to calculate η_R for the de-entrainment from the first row and Equation 4-191 or Equation 4-188 is used to calculate the de-entrainment from multi rows of tubes using $C = 1$ and $A = 1$ in Equation 4-191. Thus a prediction can be made of the multiple tube array de-entrainment efficiency using only isolated tube measurements.

Model as Coded: The de-entrainment fractions given in Equations 4-189 and 4-191 are geometry dependent since N , β , and η_{la} which represent the crossflow de-entrainment geometry in that particular cell, are input.

The source term for de-entrainment is then calculated as [

$$]^{a,c} \quad (4-192)$$

where η_{NR} is given in Equation 4-188 or 4-191 and [

$$]^{a,c} \quad (4-193)$$

where $\dot{m}_{z,e}$ is the mass flow of the entrained phase in the cross-flow or lateral directions. [

$$]^{a,c}.$$

Scaling Considerations: The experiments by Dallman and Kirchner (1980) were performed on scaled structures, but used typical droplet velocities and drop sizes. The key parameter is the blockage effects of these structures on the cross-flow, both the size and number of rows of structures. Other experiments such as CCTF and SCTF have scaled reactor internal structures which can de-entrain the droplets from a two-phase mixture crossflowing toward the hot legs. In these experiments, there are competing effects of liquid de-entrainment as well as liquid entrainment from the falling films and pools that exist in the simulated upper plenum. Therefore, the data, in the form of pressure drop readings, give the net de-entrainment for the experiment as a function of time. Full-scale upper plenum de-entrainment data is also available from the UPTF test facility in West Germany. In these experiments, the radial dimensions from the core to the hot legs are preserved, as well as the drop sizes, drop velocities, and the steam velocity. The structures in UPTF are actually larger than those in a Westinghouse PWR. The comparisons of WCOBRA/TRAC to the pressure drop data from CCTF, UPTF, and SCTF is shown in Volume 3 of WCAP-12945-P-A. These simulations used the same noding as the PWR to address scale effects. The agreement is acceptable considering the data uncertainties. Since these tests cover the ranges of sizes and number of rows of structures typical of a PWR, this model has been verified at different scales up to full-scale.

Conclusions: The cross-flow de-entrainment model was developed in the basis of scaled tests with fluid conditions, drop sizes, velocities, and vapor velocities, that are typical of PWR conditions. This model, in conjunction with other entrainment and de-entrainment models, has been compared to both scaled and full-scale data which covers the expected thermal-hydraulic conditions and geometries for a PWR. Section 18 of WCAP-12945-P-A concludes that the net effect of the entrainment and de-entrainment models results in an over-prediction of hot leg entrainment and steam binding for plants with cold leg ECCS injection. Section 4-3 of WCAP-14449-P-A demonstrates that this conclusion is also valid for UPI plants.

4-6-8 De-entrainment at Area Changes

Model Basis: Droplets will de-entrain at area changes on the wetted wall flow regimes by contacting the walls or surfaces of the reduced area channel for axial and lateral flow. The drops are assumed to de-entrain anytime the area changes, regardless if the actual area is normal or inclined toward the flow. These drops will then form liquid films on those surfaces which will drain.

De-entrainment can be expected to occur as droplets, formed during reflood, flow through the upper tie plate. Droplets that strike the solid portions of the tie plate de-entrain and provide the initial liquid for the top quench front. This type of de-entrainment is accounted for using [

]^{ac}. The reduced area acts to sweep the drops out of the entrained flow field since it is assumed the drops flow normal to the flow area and impact the area reduction.

De-entrainment is not calculated for cells in the hot wall flow regime. De-entrainment on spacer grids is separately accounted for in the spacer grid model. Most area de-entrainment will occur outside the core region since the core region has a constant flow area, and is usually in the hot wall regime.

The area change de-entrainment model is also generalized to treat droplets which are flowing vertically upward toward a horizontal surface or downward toward a pool that exists on a horizontal surface. In both cases, all the entrained flow flowing normal to these surfaces is de-entrained into the liquid field.

Model as Coded: The de-entrainment for an area change is calculated as [

$$]^{a,c} \quad (4-195)$$

where $A_{x,j}$ is the momentum (cell edge) area, and $A_{x,j}$ is the cell nominal area.

This equation de-entrains some of the entrained liquid flow entering at the bottom of a cell if the top of the cell has a reduced flow area; it de-entrains some of the entrained liquid flow entering at the top of the cell if the bottom of the cell has a reduced flow area. As described previously, the cell centered entrained flowrate ($\dot{m}_{x,e,j}$) is obtained from the cell edge flowrate ($\dot{m}_{x,e,j}$) by taking the appropriate ratios of fluid properties (see for example, Equation 4-145).

Scaling Considerations: This model has no scale dependence as such and simply models the geometric changes seen in the flow channels. This particular model has been tested at different scales from the CCTF and SCTF experiments for reflood, as well as the full-scale UPTF experiments for upper plenum de-entrainment, and the LOFT experiments. The CCTF and SCTF have scaled prototypical hardware in the upper plenum and CCFL region above the fuel such that the area ratios were typical of a PWR. Similarly, the UPTF used full-scale hardware in the CCFL region, core plate, downcomer, and upper plenum, so not only was the area ratio preserved but the areas were prototypical. In LOFT, the fuel assembly hardware at the top of the assemblies was prototypical. The upper plenum structures were also prototypical, particularly the guide tubes. There is no direct verification of this particular model, since no instrumentation was available to measure liquid film flow at the area change locations. However, the model is logical since the drops would have sufficient inertia such that they would impact a flow structure rather than flow around such structures.⁽⁴⁸⁾

Conclusions: The area change de-entrainment model is a logical application of WCOBRA/TRAC which uniquely models the entrained droplet field. There are experiments which have the same types of area reductions that occur in a PWR at the same locations in the simulated reactor vessel. Experiments such

as LOFT, CCTF, SCTF, and UPTF all have area reductions and prototypical hardware designs such that any uncertainty in this particular model is reflected in the overall WCOBRA/TRAC uncertainty.

4-6-9 De-entrainment at Solid Surfaces and Liquid Pools

Model Basis: Entrained liquid flow is assumed to de-entrain under the following additional conditions:

- a) Flow of entrained droplets into a cell with a solid surface at the opposite cell face, and
- b) Flow of entrained droplets into a cell which is in a bubbly flow regime.

Model as Coded: For the cases above the de-entrainment rate is calculated as [

]^{ac}.

Scaling Considerations: This model has no scale dependence as such since complete de-entrainment on either horizontal surfaces or low void fraction pools is assumed. The model assumptions are logical since the entrained drops should have sufficient inertia to impact a solid wall in a cell of one exist, rather than flowing around the obstruction. Drops flowing into a cell with a low void fraction, typical bubbly flow regime, would be expected to de-entrain since they would mix with the continuous liquid in the cell.

Conclusions: Models for de-entrainment at solid surfaces and on liquid pools have been included in the WCOBRA/TRAC model. The models are logically based and are consistent with the WCOBRA/TRAC formulation for the entrained liquid field. Experiments such as UPTF, CCTF, and SCTF have horizontal surfaces for de-entrainment, and some experiments also have liquid pools formed on horizontal surfaces. WCOBRA/TRAC has been compared to these experiments such that any uncertainty in these assumptions are reflected in the overall WCOBRA/TRAC code uncertainty.

4-7 ONE-DIMENSIONAL COMPONENT MOMENTUM TRANSFER MODELS

4-7-1 Introduction

The equation formulation for the one-dimensional component portion of the WCOBRA/TRAC code uses a five equation drift flux formulation as described in Section 2. The momentum losses due to friction and form losses use the mixture velocity U_m as the reference velocity head. The mixture velocity is calculated by solving the mixture momentum equation. Constitutive equations for the relative velocity are then used to obtain the liquid and vapor velocities.

The total pressure gradient calculated in the mixture momentum equation is expressed as the sum of the frictional dissipation, acceleration head, and potential head terms. Under single-phase flow conditions, pressure drops associated with frictional losses are correlated as functions of fluid velocity, fluid density, fluid viscosity, channel hydraulic diameter, and surface roughness of the channel wall. When a two-phase mixture is flowing in a channel, a correction to the single-phase frictional loss is necessary to account for added dissipation between phases and interactions with the channel walls. This correction factor is the two-phase flow multiplier and is a feature in four of the five friction-factor options available for the one-dimensional components.

The one-dimensional friction factor is defined as

$$f = \frac{\left(\frac{\Delta P}{\Delta x} \right)_f D_h}{2\rho_m U_m |U_m|} \quad (4-197)$$

where $(\Delta P/\Delta x)_f$ is the pressure gradient associated with frictional losses.

The user has several different friction factor relationships for two-phase flow. The options available to calculate f are:

NFF	=	0	=	constant value (user input),
NFF	=	1	=	homogeneous model,
NFF	=	2	=	Armand correlation,
NFF	=	3	=	CISE correlation,
NFF	=	4	=	modified annular flow model, and
NFF	=	5	=	Chisholm correlation,

where NFF is a user-supplied index. Using a negative value of the index results in an automatic calculation of an appropriate form-loss coefficient in addition to the selected two-phase flow friction factor if there are abrupt area changes.

The annular flow model (NFF = 4), is used for the one-dimensional components in WCOBRA/TRAC, and is described below.

4-7-2 Annular Flow Friction Factor Model

Model Basis: The basis for the annular model choice is that for the majority of the calculated transient the reactor coolant will be in an annular flow with liquid films on the inside walls and a highly voided ($\alpha > 0.9$) mixture flowing through the system as it depressurizes and refloods. After a few seconds, for the large break, the reactor coolant system is at void fractions in excess of 80 percent, while later in time, during reflood, the void fraction exceeds 90 percent everywhere on the loops.

The annular flow friction-factor method from Hirt and Romero (1975)⁽⁵⁰⁾ is adopted with a modification at high vapor fractions. The single-phase friction factor (f_{sp}) from Govier and Aziz (1972)⁽⁵⁰⁾ is

$$f_{sp} = a + bRe^{-c}, \quad (4-198)$$

where:

$$a = 0.026 \left(\frac{k}{D_h} \right)^{0.225} + 0.133 \left(\frac{k}{D_h} \right) \quad (4-199)$$

and

$$b = 22.0 \left(\frac{k}{D_h} \right)^{0.44} \quad (4-200)$$

with

$$c = 1.62 \left(\frac{k}{D_h} \right)^{0.134} \quad (4-201)$$

where k/D_h is the relative pipe wall roughness. A value of $k = 5.0 \times 10^{-6}m$, which is intermediate between drawn tubing and commercial piping, is used for the absolute pipe roughness. The annular flow friction factor is then

$$f = f_{sp} \varphi^2 \quad (4-202)^{(52)}$$

where the two-phase multiplier is defined as

$$\varphi^2 = \frac{\rho_l U_l^2}{\rho_m U_m^2} \quad (4-203)^{(51)}$$

where U_l is the liquid field velocity and U_m is the mixture velocity.

Model as Coded: The annular flow friction model will calculate the friction factor for the two-phase mixture using Equations 4-198 to 4-201 if the volume weighted cell void fraction is less than or equal to 0.9. The resulting two-phase flow friction factor becomes

$$CFZ_A = 2f_{sp} \bar{\rho}_l U_l^2 / (\bar{\rho}_m U_m^2) \quad (4-204)^{(52)}$$

where $\bar{\rho}_l$, $\bar{\rho}_m$ are the "cell volume weighted" liquid and mixture densities (see below). The single-phase friction factor (f_{sp}) is calculated from Equations 4-198 to 4-201 where the Reynolds number is defined as

$$Re = \bar{\rho}_t U_t D_h / \bar{\mu}_t \quad (4-205)$$

where again $\bar{\rho}_t$ and $\bar{\mu}_t$ are the "cell volume weighted" liquid density and viscosity, while D_h is the hydraulic diameter for the cell of interest. In one-dimensional components, the momentum equation is solved at the cell face between two cells. Values of density, viscosity, and void fraction are thus needed at the cell face. To avoid discontinuities in performing the calculations discussed above, the density, viscosity, and void fraction are "volume averaged" using upstream and downstream cell values. The void fraction for example, is estimated at the cell face as:

$$\bar{\alpha} = \frac{(\alpha_u V_u + \alpha_d V_d)}{V_u + V_d} \quad (4-205a)$$

where V represents the cell volume, and the subscripts "u" and "d" denote the upstream and downstream cells, respectively.

If the "cell volume weighted"⁽⁵³⁾ void fraction is greater than 0.9 but less than 0.9995, then the two-phase multiplier is linearly ramped between the annular flow two-phase friction multiplier and the homogeneous two-phase friction multiplier. The homogeneous two-phase flow multiplier is calculated using a mixture viscosity defined as

$$\frac{1}{\mu_m} = \frac{x}{\mu_v} + \frac{(1-x)}{\mu_t} \quad (4-206)$$

from McAdams (1942). The single-phase friction factor for the homogeneous two-phase flow multiplier is given as:

$$f_{sp} = \begin{cases} 0.046 Re^{-0.2} & (Re \geq 5000) \\ 0.032 - 5.25 \times 10^{-6} (Re - 500) & (500 < Re < 5000) \\ 0.032 & (Re < 500) \end{cases} \quad (4-207)^{(54)}$$

If the Reynolds number is expressed in terms of the mixture density, velocity, and viscosity and Equation 4-206 is used for a mixture viscosity, the homogeneous two-phase flow Reynolds number is:

$$Re = \bar{\rho}_m \bar{U}_m D_h / \bar{\mu}_m \quad (4-208)^{(54)}$$

Using this definition of the two-phase Reynolds Number, the two-phase homogeneous multiplier becomes

$$\Phi_{HM}^2 = [1 + x (\mu_t / \mu_v - 1)]^{-2} \quad (4-209)^{(54)}$$

using the mixture viscosity relationship given in Equation 4-206. The homogeneous quality is calculated from the volume weighted cell void fraction as

$$x_h = \frac{1}{1 + \left(\frac{1 - \bar{\alpha}}{\bar{\alpha}} \right) \frac{\bar{\rho}_l}{\bar{\rho}_v}} \quad (4-210)$$

where $\bar{\rho}_l$, $\bar{\rho}_v$ are the "cell volume weighted" densities. The code will calculate the quality from Equation 4-210, the two-phase multiplier from Equation 4-209, the single-phase friction factor, then the two-phase friction as:

$$CFZ_H = 2.0 f_{sp} \Phi_{HM}^2 \quad (4-211)$$

A linear void fraction ramp is used between $\bar{\alpha} = 0.9$ to $\bar{\alpha} = 0.9995$ to weight the two-phase friction factor between the annular model and the homogeneous two-phase model as:

$$CFZ = (1 - WF) CFZ_A + (WF) CFZ_H \quad (4-212)$$

where:

$$WF = \begin{matrix} \text{maximum} \\ \left\{ \begin{matrix} 1.0 \\ \frac{\bar{\alpha} - 0.90}{0.0995} \\ 0.0 \end{matrix} \right\} \end{matrix} \quad (4-213)$$

Scaling Considerations: The annular flow friction factor model was developed from small diameter tube data as discussed by Hirt and Romero (1975). However, the WCOBRA/TRAC verification efforts have tested this particular model at several different scales and geometries with the LOFT, CCTF, and full-scale UPTF test data as discussed in Volume 3 of WCAP-12945-P-A. Comparison of measured versus predicted pressure drops in the loop components for other different experiments have compared quite well for these experiments which use similar noding as the PWR model. Thus there is no scale bias in the annular flow friction factor model that requires modification of the model.

Comparisons of the TRAC PD2 two-phase multiplier to the data from Collier et al. (1972) is shown in Figures 4-10 to 4-13. As these figures indicate, the agreement is very good considering the wide range of flows, pressures, and void fractions.

Conclusions: The one-dimensional two-phase friction model is based on two-phase tube data. The model is particularly valid for the annular flow regime which is expected to occur in the PWR loops for most, if not all, the large LOCA transients. The model has been validated with experiments at several

scales and no scaling effects were observed. The uncertainty of this model is accounted for in the overall WCOBRA/TRAC uncertainty.

4-7-3 Relative Velocity Models

Model Basis: The mixture velocity is calculated by solving the mixture momentum equation. The complimentary relation to determine both liquid and vapor phase velocities is given by a correlation for the relative velocity as discussed above. To formulate relevant quantities, Ishii's formulation (1977) is followed by taking cross-sectional averages in a pipe:

$$\langle F \rangle = \frac{1}{A} \int F dA \quad (4-214)$$

and the averages weighted by liquid and vapor fractions as

$$\langle \langle F_k \rangle \rangle \equiv \frac{1}{A \langle \alpha_k \rangle} \int \alpha_k F_k dA \quad (4-215)^{(55)}$$

for $k = v$ and $k = l$. Noting that $\alpha = \alpha_v$ and $1 - \alpha = \alpha_l$, Ishii showed that the mixture velocity determined by the mixture momentum equation has the following relationship to the local phase quantities:

$$U_m = \frac{\langle \rho_m U_m \rangle}{\langle \rho_m \rangle} = \frac{\rho_v \langle \alpha \rangle \langle \langle U_v \rangle \rangle + \rho_l (1 - \langle \alpha \rangle) \langle \langle U_l \rangle \rangle}{\rho_v \langle \alpha \rangle + \rho_l (1 - \langle \alpha \rangle)} \quad (4-216)$$

The vapor and liquid velocities are related to each other through the mean drift velocity (\bar{U}_{vj}), which is related to the relative velocity (U_R) by

$$\bar{U}_{vj} = \langle \langle U_v \rangle \rangle - \langle j \rangle \quad (4-217)$$

and

$$\bar{U}_{vj} = (1 - \langle \alpha \rangle) U_R \quad (4-218)$$

where:

$$U_R = \langle \langle U_v \rangle \rangle - \langle \langle U_l \rangle \rangle \quad (4-219)$$

Typically, experiments measure the weighted mean drift velocity, related to \bar{U}_{vj} by

$$\langle \langle U_{vj} \rangle \rangle = \bar{U}_{vj} - (C_o - 1) \langle j \rangle \quad (4-220)$$

where C_o is the distribution parameter defined by $C_o = \langle \alpha j \rangle / (\langle \alpha \rangle \langle j \rangle)$.

To apply the experimentally determined drift velocity to calculate U_R , $\langle \langle U_{vj} \rangle \rangle$ and $\langle \langle U_t \rangle \rangle$ are eliminated from Equations 4-216, 4-218, and 4-220, to obtain:

$$U_R = \frac{U_m + \langle \langle U_{vj} \rangle \rangle / (C_o - 1)}{\frac{\langle \alpha \rangle \rho_v}{\langle \rho_m \rangle} + \frac{1 - C_o \langle \alpha \rangle}{C_o - 1}} \quad (4-221)^{(56)}$$

At this point, the averaging brackets will be dropped.

The distribution parameter C_o , as defined in the previous paragraphs, is a measure of the degree of global slip present in the two-phase mixture. At low void fractions, the phases are usually well mixed and the degree of local slip is small. However, redistribution of the vapor phase into the region of high mixture velocity can lead to a significant departure from homogeneous flow.

At high void fractions, the flow regime is usually well separated as in annular flow. The local slip is high in this case, and effects of void redistribution are less pronounced.

At these high void fractions, C_o should be viewed not as a distribution parameter but as the component of the local slip which depends on the mixture velocity.

Vertical Drift Flux Correlations

Drift velocities for various flow regimes are:

$$U_{vj, \text{ bubbly}} = 1.41 \left[\frac{\sigma \Delta \rho g}{\rho_t^2} \right]^{1/4}, \quad (4-222)^{(57)}$$

for the churn-turbulent flow regime, from Ishii (1977),

$$U_{vj, \text{ slug}} = 0.345 \left[\frac{D_h \Delta \rho g}{\rho_t} \right]^{1/2}, \quad (4-223)$$

for the slug flow regime, from Zuber and Findlay (1965), and

$$U_{vj, \text{ am}} = (C_o - 1) \left[\frac{D_h (1 - \alpha) \Delta \rho g}{0.015 \rho_t} \right]^{1/2} \quad (4-224)^{(57)}$$

for the annular-mist flow regime, from Ishii (1977).

The distribution parameter C_o is defined as [

$$]^{ac} \quad (4-225)$$

for churn-turbulent and slug flow, from Zuber and Findlay and as [

$$]^{ac} \quad (4-226)$$

for annular flow, from Ishii (1977). The constant C_1 is set to 4 in the reference, but is modified in WCOBRA/TRAC as discussed below.

Horizontal Drift Flux Correlations

In horizontal flow, the liquid and vapor phases also tend to move relative to one another under the influence of the pressure gradient. Usually, this movement has been quantified in terms of the slip ratio (U_v/U_l).

It is assumed that Ishii's annular flow model for vertical flow applies to horizontal flow if $U_{vj} = 0$. The horizontal flow model for annular flow becomes

$$U_r = \frac{U_m}{\frac{\alpha \rho_v}{\rho_m} + \frac{1 - C_o \alpha}{C_o - 1}} \quad (4-227)$$

It can be shown that the slip ratio is

$$\frac{U_v}{U_l} = \frac{C_o(1 - \alpha)}{1 - \alpha C_o} = S \quad (4-228)^{(58)}$$

where:

$$C_o = 1 + \frac{1 - \alpha}{\alpha + C_1 \sqrt{\frac{\rho_v}{\rho_l}}} \quad (4-229)^{(58)}$$

Using the above expression for C_o , it can also be shown that

$$\frac{U_v}{U_t} = \frac{1 + C_1 \sqrt{\frac{\rho_v}{\rho_t}}}{C_1 \sqrt{\frac{\rho_v}{\rho_t}}} \quad (4-230)^{(58)}$$

This expression for the slip ratio is compared to data from Thom (1964) in Table 4-4. It can be seen that Equation 4-230 with $C_1 = []^{ac}$ shows good agreement with data. In a similar manner, it is assumed that for horizontal churn-turbulent or slug flow, the relative velocity can be obtained by setting $U_{vj} = 0$ and using $C_o = 1.1$ in Equation 4-221.⁽⁵⁹⁾

Model as Coded: The relative velocity is calculated in subroutine SLIP. All fluid and mixture properties are donor cell values. The three drift velocities defined by Equations 4-222 to 4-224 are calculated, as are the distribution parameters defined by Equations 4-225 and 4-226. To provide for a smooth transition between horizontal and vertical orientation, the constant g is replaced by $g \cos \theta$, where θ is the angle of inclination of the pipe from the vertical.

The code logic then checks for horizontal or vertical flow and if $\cos \theta$ is less than 1×10^{-5} , the flow is assumed to be horizontal and U_{vj} is set to 0. For vertical flow the drift velocities are calculated from Equation 4-222 to Equation 4-224 and the minimum⁽⁶⁰⁾ value of U_{vj} is used. The distribution parameter C_o is calculated from Equation 4-229, compared to a C_o value of $[]^{ac}$.⁽⁶⁰⁾ If the void fraction is less than 0.999, the slip ratio is calculated from Equation 4-228 using the value of C_o , as specified in Table 4-4. If α is greater than 0.999, the slip ratio is calculated from Equation 4-230. The relative velocity is then calculated from Equation 4-221 using Equation 4-228 such that $[$

$$U_R = \frac{U_m + U_{vj}/(C_o - 1)}{\frac{\alpha \rho_v}{\rho_m} + \frac{1.0}{S - 1.0}} \quad]^{ac} \quad (4-231)$$

The use of minimum U_{vj} and C_o is in effect a choice of flow regimes. It can be shown that the transition from slug or churn-turbulent flow to annular flow occurs at a void fraction ranging from 0.8 to 0.9,⁽⁶¹⁾ depending on the pipe diameter. This is a reasonable transition point, and closely approximates the flow regime map used for the interfacial heat transfer in the vessel component.

Scaling Considerations: The relative velocity models are developed from tube experiments for both air/water and steam/water situations. These models, however, have been successfully applied to larger scale pipes with the WCOBRA/TRAC validation as shown in Volume 3 of WCAP-12945-P-A for both blowdown and reflood situations. Several experiments such as LOFT, CCTF, and SCTF include two-phase data in pipes. In addition, Westinghouse small-scale and full-scale UPTF steam/water mixing tests were also used for validation. The agreement between the test pressure drop data and the code predictions is good.

Therefore, while the relative velocity models and the two-phase friction multiplier were developed on small-scale tests, these models have been verified on larger scales, up to full-scale, and are considered acceptable for PWR applications.

Conclusions: The WCOBRA/TRAC one-dimensional components, while using a more simplified treatment of two-phase flow, can predict the flow regime dependent phase slip for horizontal and angled pipes. The models used for the drift velocity have been derived from smaller scale requirements, but have been verified against larger scale tests, up to full-scale. No scale dependent bias was detectable from these comparisons. Therefore, the model uncertainty for the one-dimensional components is accounted for in the overall WCOBRA/TRAC code uncertainty.

4-7-4 One-Dimensional Component Form Loss

Model Basis: Pressure changes due to irrecoverable form losses are modelled by specifying an appropriate input loss coefficient which is user specified and depends upon the geometry being modelled. As in the case of the vessel component, however, care must be taken to properly specify these losses, taking into account the numerics used such that there is no double accounting of the losses in the calculation.

Model as Coded: Because of the numerical scheme used for WCOBRA/TRAC one-dimensional components, the pressure difference calculated for area changes is different than would normally be expected. The following discussion applies to all one-dimensional components except for pipes which use the implicit pipe scheme. As discussed in the vessel component section, the momentum differencing scheme can affect the unrecoverable losses that should be added to the input.

For incompressible, single-phase, frictionless, steady flow, the momentum equation used is the same as the Bernoulli equation and is as follows:

$$\frac{1}{\rho} \frac{\partial P}{\partial X} + \frac{U \partial U}{\partial X} = 0 \quad (4-232)$$

For semi-implicit pipes, this equation is differenced as:

$$-\rho U_j (U_j - U_{j-1}) = P_j - P_{j-1} \quad (4-233)$$

where the nomenclature shown in Figure 4-14 is used.

When this equation is applied over several cells in which area changes are modelled, a pressure loss is predicted. This loss will be compared to standard methods, which use the Bernoulli equation.

Sudden Expansion

Application of the Bernoulli equation to the geometry of the sudden expansion in Figure 4-14 yields

$$P_1 + \frac{\rho U_1^2}{2} = P_3 + \frac{\rho U_3^2}{2} \quad (4-234)$$

The continuity equation gives:

$$U_3 = U_1 A_1 / A_3 \quad (4-235)$$

Combining Equations 4-235 and 4-234 results in the recoverable pressure drop of

$$\Delta P = (A_1 / A_3)^2 - 1 \quad (4-236)$$

where the nondimensional recoverable pressure drop is defined as:

$$\Delta P = 2(P_1 - P_3) / \rho U_1^2 \quad (4-237)$$

Nonrecoverable losses for sudden expansions can be accounted for in Equation 4-236 by adding a loss coefficient calculated from:

$$K = (1 - A_1 / A_3)^2 = 2 \Delta P_{irr} / \rho U_1^2 \quad (4-238)$$

Adding Equation 4-237 and Equation 4-238 gives the total pressure difference as:

$$\Delta P_T = (A_1 / A_3)^2 - 1 + (1 - A_1 / A_3)^2 \quad (4-239)$$

or

$$\Delta P_T = 2(A_1 / A_3) (A_1 / A_3 - 1) \quad (4-240)$$

yielding

$$\Delta P_T = 2R (R - 1) \quad (4-241)$$

where $R = A_1 / A_3$.

The total pressure difference calculated using Equation 4-241 is compared to experimentally derived values in Table 4-5. There is disagreement between predicted and measured pressure losses at large values of R , possibly because friction has not been explicitly modelled in this simplified analysis. The negative pressure change indicates, as expected, that there is a pressure recovery in the expansion section.

We will now calculate the pressure loss which would be predicted by WCOBRA/TRAC in this simplified situation, using Equation 4-233.

Equation 4-233 can be used to predict the pressure difference for the sudden expansion at various points along the duct as (Figure 4-14):

$$[\dots]^{a,c} \quad (4-242)^{(62)}$$

Eliminating P_2 , and since $U_2 = U_1$, [

$$]^{a,c} \quad (4-243)^{(62)}$$

Because of the staggered mesh, the pressure change is spread over two cells. The total pressure change, normalized to the dynamic pressure in the smaller area, is: [

$$]^{a,c} \quad (4-244)^{(62)}$$

or [

$$]^{a,c} \quad (4-245)$$

where:

$$\Delta P_{1D} = \frac{2(P_1 - P_3)}{\rho U_1^2} \quad (4-246a)$$

$$R = A_1/A_3 \quad (4-246b)$$

Comparing Equation 4-245 with Equation 4-241 it is seen that [

$$]^{a,c}.$$

The Sudden Contraction

Using the same approach as before, application of the Bernoulli equation to the sudden contraction shown in Figure 4-15 leads to

$$\Delta P = 1 - R^2 \quad (4-247)$$

where $R = A_3/A_1$ and

$$\Delta P = 2(P_1 - P_3)/\rho U_3^2 \quad (4-248)$$

Note that, consistent with standard practice, the pressure difference is normalized to the dynamic pressure in the smaller of the two flow areas.

As before, a loss coefficient is used to account for irrecoverable pressure losses in the Bernoulli equation. The loss coefficient data for sudden contractions can be obtained from Weisbach (1855) and Kays and London (1955):

$$K = 0.5 - 0.7R + 0.2R^2 \quad (4-249)$$

from fitting the data of Massy (1968). Table 4-6 compares the experimental data from Weisbach to the fitted expression given in Equation 4-249. The agreement is good except for small R values.

Equations 4-249 and 4-247 can be combined to predict the total pressure change for an abrupt contraction. This prediction is compared in Table 4-7 to the data of King and Brater (1963).

If the one-dimensional component difference equation (Equation 4-233), is applied to the sudden contraction shown in Figure 4-13, then [

$$]^{ac} \quad (4-250)$$

Table 4-8 shows the comparison of the normalized pressure drops predicted by Equation 4-250 to the measured total pressure drop data from King and Brater. [

$$]^{ac}.$$

Contraction and Expansion

In the absence of viscous effects, the pressure would be completely recovered downstream of an equal area contraction and expansion as shown in Figure 4-15, by applying the Bernoulli equation. The one-dimensional component equations, however, will not predict complete pressure recovery for this configuration. The semi-implicit equations for this configuration become

$$\left. \begin{aligned} P_1 - P_0 &= -\rho U_1 (U_1 - U_0) \\ P_2 - P_1 &= -\rho U_2 (U_2 - U_1) \\ P_3 - P_2 &= -\rho U_3 (U_3 - U_2) \end{aligned} \right\} \quad (4-251)$$

Using the same approach as before, the total pressure difference normalized to the velocity in the minimum area, is [

$$J^{ac} \quad (4-252)$$

However, it turns out that [

$$J^{ac}.$$

Smooth Area Reductions

The sudden contraction and expansion represent upper limits to the expected pressure change through flow restrictions. A smooth nozzle will have very small losses.

Nozzles will be modelled simply in one-dimensional components, with a small number of cells. However, this will lead to pressure drops similar to those calculated for sudden contractions and expansions. If more cells were used to model the area reductions, it can easily be shown that the pressure drop will approach zero as the number of cells becomes large. However, this is not a practical solution because computing costs will become prohibitive. A recommended approach, if modelling the area change is necessary, is to incorporate a loss coefficient into the one-dimensional component model which cancels the predicted $\Delta P(\text{TRAC})$.

In the implicit pipe numerical scheme, the momentum flux terms are centrally differenced:

$$P_J - P_{J-1} = \rho U_J (U_{J+1} - U_{J-1})/2 \quad (4-253)$$

It can be shown that in the absence of friction or form losses, this scheme predicts pressure changes identical to the Bernoulli equation, and for combined contractions and expansions the pressure is fully recovered. However, the junction between the implicit pipe and the vessel or another one-dimensional pipe is solved semi-implicitly, and the prior conclusions apply.

Scaling Considerations There are no scale dependent parameters in the TRAC form loss methodology. The geometry should be accurately represented by the code, and the unrecoverable loss should be accounted for when using input form loss coefficients. The one-dimensional model has been verified at different scales on loop configurations similar to a PWR by simulating the LOFT, CCTF, SCTF, and UPTF experiments. No scale dependent bias has been observed in the calculated results.

Conclusions The following approach is taken for modelling flow restrictions in one-dimensional components.

a) [

] ^{a,c}.

b) [

] ^{a,c}.

c) [

] ^{a,c}.

One-Dimensional/Vessel Junctions: The pressure change calculated at a vessel/one-dimensional component junction requires special consideration. Figure 4-17 illustrates the momentum cell used at the junction. When the mixture is flowing from the vessel to the pipe, the mixture velocity at point zero is assumed to be equal to the mixture velocity at point one. Consequently, Equation 4-233 will predict in the absence of friction or other losses:

$$P_0 - P_1 = 0 \quad (4-254)$$

When a gap is specified, or when the connection is at the top or bottom of the cell, the momentum at point zero is assumed to be the value at the opposite face of the cell, as shown in Figure 4-17.

One important vessel/pipe junction is the broken cold leg nozzle. It can be visualized as shown in Figure 4-18. Fluid in the annular downcomer converges on the nozzle, where it must then make a turn into the nozzle. We apply the Bernoulli equation from point zero to point two in Figure 4-17:

$$P_0 = P_2 + \frac{1}{2} \rho U_2^2 \quad (4-255)$$

This is the recoverable loss for the nozzle.

For a typical PWR geometry, the irrecoverable loss through the nozzle has been calculated to be $K = [\quad]^{a,c}$ from the UPTF data (Section 16-5 of WCAP-12945-P-A). The equation for irrecoverable loss is

$$P_0 - P_2 = K \frac{\rho U_2^2}{2} \quad (4-256)$$

Combining the recoverable losses Equation 4-255 and irrecoverable loss, Equation 4-256, the total pressure change for a typical PWR geometry is: [

] ^{a.c.}

4-8 CRITICAL FLOW MODEL

In the event of a hypothetical Large Break Loss of Coolant Accident (LBLOCA) in a PWR, the rate of depressurization of the primary loop is dominated by the rate of fluid discharge at the break. During the blowdown phase of the LOCA, the discharge will be choked (critical flow).

There are two options available in WCOBRA/TRAC. The first option is to choose the TRAC/PD2 approach which does not have a critical flow model as such, but relies on the ability of the one-dimensional conservation equations and the constitutive relations to provide 'natural choking.' The second option is to choose the critical flow packages from TRAC-PF1/MOD1. The following sections give descriptions to both options.

4-8-1 Natural Choking Approach (TRAC-PD2)

Model Basis: The original critical flow calculation in WCOBRA/TRAC is based on TRAC/PD2 (Liles et al., 1981) approach. The calculation relies on the ability of the one-dimensional conservation equations (two continuity, two energy, and one momentum) and the constitutive relations for interfacial heat transfer, relative velocity, wall friction, and wall heat transfer to provide 'natural choking.' So that critical flow can be predicted, the region in which the critical plane is expected must be nodalized using a component with cells of very small length. Fully-implicit numerics option must be used to avoid the penalty of small timesteps imposed by Courant-Freidrichs-Lewy (CFL) conditions.

Model as Coded: For one-dimensional components that use the semi-implicit numerics, a limiting velocity condition is imposed. The magnitude of the mixture velocity is constrained to be less than the velocity of a compressibility wave in a homogeneous mixture given by:

$$a = \left[\frac{\alpha \rho_m}{\rho_v} \left(\frac{\partial \rho_v}{\partial P} \right)_s + \frac{(1 - \alpha) \rho_m}{\rho_t} \left(\frac{\partial \rho_t}{\partial P} \right)_s \right]^{-1} \quad (4-258)^{(63)}$$

as described by Wallis (1969), where a is the sonic velocity.

The natural choking model predicts the detailed pressure gradient in the pipe up to the choking plane. To calculate this pressure gradient, detailed nodalization is required in the vicinity of the critical discharge

plane. A typical (guillotine) break requires approximately 20 small fluid cells for each of the break locations, broken loop and vessel side break, as well as an equal number of heat transfer nodes.

The use of small cells in the break pipes can lead to numerical difficulties (and a significant increase in computing time) during portions of the transient when low velocities are encountered adjacent to the breaks. This can be avoided, but places an additional burden on the user to modify the component data on a restart.

Scaling Considerations: The TRAC-PD2 natural choking model was compared to a range of critical flow experiments in the original TRAC-PD2 code validation efforts. The results of that validation effort were analyzed to determine the model bias and uncertainty (Dederer et al., 1988) and it was found that the TRAC natural choking model had an average bias of 1.2 and an uncertainty of 0.2, where the bias is the average of the measured test flowrate divided by the code calculated flowrate, for several different tests, test configurations, and test diameters. A bias of 1.2 means that on the average, the TRAC-PD2 model over predicts the measured critical flow by 20 percent. The tests that were examined are given in the reference by Dederer et al. and included the Marviken tests, Brookhaven nozzle tests, and the French Moby Dick tests.

Conclusions: The comparisons of the TRAC-PD2 and TRAC-PF1 critical flow models indicate the TRAC-PF1 model has a smaller bias and is more accurate for PWR calculations. Therefore, the TRAC-PF1 model was programmed into the current version of the WCOBRA/TRAC code.

4-8-2 Critical Flow Model (TRAC-PF1)

Model Basis: The TRAC-PF1/MOD1 two-phase, two-component, choked-flow model was developed from first principles using the characteristic analysis approach. The TRAC-PF1/MOD1 subcooled choked-flow model is a modified form of the Burnell model.

In general, choking calculations can be done simply by using a sufficiently fine mesh for components with smooth area changes. However, the TRAC-PF1/MOD1 quasi-steady choked-flow model saves computational time because it allows a much coarser mesh. For components with abrupt area changes, a one-dimensional fine mesh can cause erroneous natural-choking results. For all such cases, a separate choking model is almost a necessity. Thus, a choking model not only improves computational efficiency but also accounts for effects such as sharp area changes and frictional pressure losses.

The critical flow model contains three basic models which are used depending on the void fraction as follows:

$\alpha < 0.01$	subcooled model
$0.01 < \alpha < 0.10$	interpolation region
$0.10 < \alpha < 0.999$	two-phase model
$0.999 < \alpha$	single-phase vapor model

The interpolation region is necessary to avoid the discontinuity between the critical flowrates calculated by the subcooled and two-phase models. In this region the liquid and vapor velocities are linearly interpolated with void fraction. A similar interpolation region at $\alpha = 0.999$ is unnecessary because the critical flowrates calculated by the two-phase model naturally approach those of single-phase vapor.

The precise nature of the void fraction used to determine which model is used is dependent on the length-to-diameter ratio as determined from the geometry of the adjacent donor cell

$$L/D = \frac{\Delta X}{2} \left(\frac{\pi}{\Delta V/\Delta X} \right)^{\frac{1}{2}} \quad (4-259)$$

where ΔV and ΔX are the adjacent cell volume and length.

The models used for determining the void fraction for both $L/D < 1.5$ and $L/D \geq 1.5$ assume that the two-phases are in equilibrium at the choking plane (which is taken to be at the cell edge). For both types of model stagnation conditions are also calculated at the cell center, but in different ways.

For $L/D < 1.5$ the stagnation conditions are calculated directly from the cell center conditions as supplied to the critical flow model from the calling routine. Thus, stagnation conditions are calculated as follows:

$$H_{o_c} = x_c \left(H_{v_c} + \frac{1}{2} U_{v_c}^2 \right) + (1-x_c) \left(H_{t_c} + \frac{1}{2} U_{t_c}^2 \right) \quad (4-260)$$

or

$$H_{o_c} = H_{m_c} + x_c \frac{1}{2} U_{v_c}^2 + (1-x_c) \frac{1}{2} U_{t_c}^2 \quad (4-261)$$

and

$$S_{o_c} = X_c S_{v_c} + (1 - X_c) S_{t_c} \quad (4-262)$$

where the subscript "c" is the cell center.

For $L/D \geq 1.5$ the thermodynamic condition at the cell center is converted to an equivalent equilibrium condition assuming constant enthalpy, i.e.,

$$\alpha_{eq} = \frac{x_{eq} \rho_{t_c}^{sat}}{\rho_{v_c}^{sat} + x_{eq} (\rho_{t_c}^{sat} - \rho_{v_c}^{sat})} \quad (4-263)$$

where:

$$x_{eq} = \frac{H_{m_c} - H_{t_c}^{sat}}{H_{v_c}^{sat} - H_{t_c}^{sat}} \quad (4-264)$$

and saturated conditions correspond to the cell center pressure P_c . The stagnation enthalpy and entropy are determined as in Equations 4-260 and 4-262, except that x_{eq} is used and the thermodynamic quantities are taken at saturation.

For $L/D < 1.5$, α_c is used to determine which model is used (subcooled or two-phase), while for $L/D \geq 1.5$, α_{eq} is used.

Subcooled Model: The subcooled critical velocity (a_{sc}), is taken as the maximum of a homogeneous equilibrium value a_{HE} and a velocity determined from application of Bernoulli's equation:

$$a_{sc} = \text{maximum} \{a_{HE}, a_{Be}\} \quad (4-265)$$

where:

$$a_{HE} = F_e / \rho_{m_e} \quad (4-266)$$

and

$$a_{Be} = \left(U_{t_c}^2 + \frac{(P_c - P_{nuc})}{\rho_{t_e}} \right)^{\frac{1}{2}} \quad (4-267)$$

where P_{nuc} is the nucleation pressure.

The mass flux (F_e) is the maximum mass flux at the cell edge consistent with assuming an isentropic expansion from the cell center stagnation conditions to an equilibrium state at the cell edge. The degree of freedom with which the mass flux is maximized is the pressure at the cell edge.

Thus

$$F_e = \rho_{m_e}^{sat} \left(2 (H_{o_c} - H_{m_e}^{sat}) \right)^{1/2} \quad (4-268)$$

is maximized where $H_{m_e}^{sat}$ and $\rho_{m_e}^{sat}$ are defined in terms of the edge quality (x_e) and the saturation values of the individual phase quantities, i.e.,

$$H_{m_e}^{sat} = x_e H_{v_e}^{sat} + (1 - x_e) H_{l_e}^{sat} \quad (4-269)$$

and

$$\frac{1}{\rho_{m_e}^{sat}} = \frac{x_e}{\rho_{v_e}^{sat}} + \frac{1-x_e}{\rho_{l_e}^{sat}} \quad (4-270)$$

and the edge quality is determined isentropically:

$$x_e = \frac{s_{o_e} - s_{l_e}^{sat}}{s_{v_e}^{sat} - s_{l_e}^{sat}} \quad (4-271)$$

The value of critical velocity so obtained is equal to the homogeneous equilibrium value for cell center conditions which are at equilibrium, but can significantly deviate from the homogeneous equilibrium value when nonequilibrium effects are evident.

For the alternative critical velocity (a_{Be}), the driving force is the pressure gradient between the cell center and the nucleation pressure at the cell edge. Because of nucleation delay effects, the nucleation pressure (P_{nuc}) can be considerably lower than the local saturation pressure (P_{sat}). The delay in nucleation is modelled using a correlation developed by Alamgir and Lienhard (1981), and Jones (1980).

$$P_{nuc} = P_{sat} - \max \left\{ 0.0, 0.258 \sigma^{1.5} \left(\frac{T_{l_e}}{T_{crit}} \right)^{13.76} \frac{(1 + 13.25 \Sigma^{0.8})^{\frac{1}{2}}}{(k_B T_{crit})^{\frac{1}{2}} (1 - \rho_v/\rho_l)} - \frac{27}{2} (0.072)^2 \rho_{l_e} \left(\frac{A_e}{A_c} \right)^2 U_{l_e}^2 \right\} \quad (4-272)$$

The rate of depressurization Σ is determined from the pressure gradient between the cell center and the cell edge:

$$\Sigma = \frac{|U_{l_e}| (P_c - P_e)}{1.01325 \times 10^{11} \Delta X/2} \quad (4-273)$$

The first term in Equation 4-272 represents the static depressurization effect and is based on classical nucleation theory (Alamgir and Lienhard, 1981). The second term accounts for turbulent fluctuations in the flowing liquid (Jones, 1980).

Two-phase Model: In the absence of a noncondensable field, the equations describing the two-phase critical flow model are as shown below.

(a) Overall Mass Conservation

$$\frac{\partial \rho_m}{\partial t} + \frac{\partial}{\partial Z} (\rho_m U_m) = 0 \quad (4-274)$$

(b) Momentum Conservation for the Liquid Field

$$\begin{aligned} (1-\alpha)\rho_l \frac{\partial U_l}{\partial t} + (1-\alpha)\rho_l U_l \frac{\partial U_l}{\partial Z} + (1-\alpha) \frac{\partial P}{\partial Z} \\ + C_{vM} \alpha(1-\alpha)\rho_m \left[\frac{\partial U_l}{\partial t} + U_v \frac{\partial U_l}{\partial Z} - \frac{\partial U_v}{\partial t} - U_l \frac{\partial U_v}{\partial Z} \right] = 0 \end{aligned} \quad (4-275)$$

(c) Momentum Conservation for the Vapor Field

$$\begin{aligned} \alpha\rho_v \frac{\partial U_v}{\partial t} + \alpha\rho_v U_v \frac{\partial U_v}{\partial Z} + \alpha \frac{\partial P}{\partial Z} \\ + C_{vM} \alpha(1-\alpha)\rho_m \left[\frac{\partial U_v}{\partial t} + U_l \frac{\partial U_v}{\partial Z} - \frac{\partial U_l}{\partial t} - U_v \frac{\partial U_l}{\partial Z} \right] = 0 \end{aligned} \quad (4-276)$$

(d) Overall Energy Conservation

$$\frac{\partial}{\partial t} (\rho_m s_m) + \frac{\partial}{\partial Z} [\alpha\rho_v U_v s_v + (1-\alpha)\rho_l U_l s_l] = 0 \quad (4-277)$$

Note that all nondifferential source terms have been omitted, since these do not enter into the characteristic analysis (which is the method by which Equations 4-274 to 4-277 are solved).

The latter terms in the momentum equations represent the virtual mass force. This force is responsible for accelerating one phase with respect to the other, and is thought to be important in modelling critical flow phenomena (Drew et al., 1979). The particular form chosen for the virtual mass force is symmetric, frame invariant, and the coefficient $C_{vM}\alpha(1-\alpha)$ is chosen to permit a smooth transition as either phase becomes depleted. The value of C_{vM} used is 10.0.⁽⁶⁴⁾ Note that thermal equilibrium is assumed, and that the entropy gains associated with interphase mass transfer and relative acceleration have been neglected in the energy equation.

Choosing P , α , U_v and U_t as the independent variables which are to be solved for, it is convenient to cast Equations 4-274 and 4-277 into a form that involves only derivatives in these variables. (The momentum equations are already in this form.) Then, Equations 4-274 to 4-277 may be written as:

$$\underline{A} \cdot \frac{\partial \underline{U}}{\partial t} + \underline{B} \cdot \frac{\partial \underline{U}}{\partial Z} = 0 \quad (4-278)$$

where:

$$\underline{U} = (P, \alpha, U_v, U_t)^T \quad (4-279)$$

and

$$\underline{A} = \begin{vmatrix} \frac{\partial \rho_m}{\partial P} & \rho_v - \rho_t & 0 & 0 \\ 0 & 0 & \alpha \rho_v + C_{vM} \alpha (1 - \alpha) \rho_m & -C_{vM} \alpha (1 - \alpha) \rho_m \\ 0 & 0 & -C_{vM} \alpha (1 - \alpha) \rho_m & (1 - \alpha) \rho_t + C_{vM} \alpha (1 - \alpha) \rho_m \\ \frac{\partial(\rho_m s_m)}{\partial P} & \rho_v s_v - \rho_t s_t & 0 & 0 \end{vmatrix} \quad (4-280)$$

$$\underline{B} = \begin{vmatrix} \frac{\partial(\rho_m U_m)}{\partial P} & \rho_v U_v - \rho_t U_t & \alpha \rho_v & (1 - \alpha) \rho_t \\ \alpha & 0 & \alpha \rho_v U_v + C_{vM} \alpha (1 - \alpha) \rho_m U_t & C_{vM} \alpha (1 - \alpha) \rho_m U_v \\ 1 - \alpha & 0 & -C_{vM} \alpha (1 - \alpha) \rho_m U_t & (1 - \alpha) \rho_t U_t + C_{vM} \alpha (1 - \alpha) \rho_m U_v \\ \alpha U_v \frac{\partial(\rho_v s_v)}{\partial P} & \rho_v U_v s_v - \rho_t U_t s_t & \alpha \rho_v s_v & (1 - \alpha) \rho_t s_t + (1 - \alpha) U_t \frac{\partial(\rho_t s_t)}{\partial P} \end{vmatrix} \quad (4-281)$$

The system of Equations 4-279 is solved using the method of characteristics. The characteristic polynomial is

$$\det (\underline{A}\lambda - \underline{B}) = 0 \quad (4-282)$$

Choking occurs when the signal, which propagates with the largest velocity relative to the fluid, is just stationary, i.e.,

$$\operatorname{Re}(\lambda_i) = 0 \text{ for some } i, \text{ and}$$

$$\operatorname{Re}(\lambda_j) > 0 \text{ for } j \neq i.$$

Since it is fourth order, Equation 4-278 can in principle be solved analytically; however, the critical model uses a numerical method which permits extensions to higher orders (required for the noncondensable and nonequilibrium effects). The method of solution to Equation 4-278 is as follows. The thermodynamic state at the cell edge is estimated by iterating for the cell edge pressure that maximizes the mass-flux (in exactly the same way as for the subcooled model). A value for the cell edge void fraction is subsequently backed-out from the densities:

$$\alpha_e = \frac{\rho_{m_e}^{sat} - \rho_{l_e}^{sat}}{\rho_{v_e}^{sat} - \rho_{l_e}^{sat}} \quad (4-283)$$

where:

$\rho_{m_e}^{sat}$, $\rho_{v_e}^{sat}$, $\rho_{l_e}^{sat}$ are the mixture, vapor, and liquid densities at saturation conditions on the cell edge.

If α_e is found to be outside the void fraction range for the two-phase model, control is passed, as appropriate, to the subcooled or single-phase vapor models. Having established the cell edge thermodynamic properties, the vapor velocity is iterated in an effort to find a solution $\lambda_i = 0$ to Equation 4-282. During this iterative process the liquid velocity is calculated from the vapor velocity using a constant value for the slip, and all other variables are kept fixed. With these velocities determined, the coefficients of matrix A are computed and the full characteristic polynomial is solved for all roots. The roots are then checked to ensure that the correct solution has been found, i.e., the phase velocities correspond to the minimum root. Interpolation with the subcooled model is then performed if required.

First the phasic velocities which result in $\operatorname{Det}(B)=0$ (matrix B is shown in Equation 4-281) while keeping the slip constant, are found through iteration. Using these velocities, the eigenvalues for $A^{-1}B$ (matrix A is shown in Equation 4-280) are calculated. Standard matrix solver packages (LIN-PACK and EISPACK) are used to calculate both the determinant (through LU factorization) and the eigenvalues (through EISPACK's standard set for general matrices). The largest value of the real part of the eigenvalues is checked for the choking condition ($\operatorname{Real}(\text{root}) < 1\%$ of adiabatic sonic velocity) for confirmation. If this condition is satisfied, the mixture velocity is calculated from the phasic velocities⁽⁶⁵⁾.

Single-phase Vapor Model: The single-phase vapor choking velocity is calculated by isentropically expanding the vapor to maximize the mass flux. This is performed using basically the same technique as for the subcooled model.

Model as Coded: The TRAC-PF1/MOD1 (Liles et al., 1988) choked flow-package of subroutines as implemented in WCOBRA/TRAC is reasonably self-contained and consists of the following:

- (i) Subroutine CHOK, which provides the entry point into the package and governs the entire calculational sequence. This routine, together with SOUND, contains all the physics of the model,
- (ii) Subroutine SOUND, which calculates the cell edge thermodynamic state from the cell center conditions while maximizing the mass flux, and
- (iii) A self-contained set of numerical routines that perform matrix operations. These are only required by the two-phase model.

The package also requires access to a number of external routines and common blocks which are generic in nature. Routines CHOK and SOUND use:

- (i) SATPRS, which determines the saturation pressure corresponding to a given temperature; this routine was added to the package,
- (ii) THERMO, which calculates various thermodynamic quantities given temperature and pressure,
- (iii) ERROR, which handles error conditions, and
- (iv) RHOLIQ, which calculates the density of liquid.

The interface between the entry routine CHOK and the WCOBRA/TRAC one-dimensional component hydrodynamic routines DF1DS and DF1DI was accomplished via an independent routine called PF1CHK. The main task of this routine is to determine whether the choked-flow package is called. For critical conditions to be calculated, the following conditions must be satisfied:

- (i) The face area is greater than 10^{-10} m^2 ,
- (ii) The model is switched on (which is the default),
- (iii) The cell face is not part of a component that has just been solved,
- (iv) The cell face is not adjacent to a FILL component,
- (v) The vapor velocity is greater than 15 m/s,

- (vi) If ICFLOW=1 (the default) the component must be adjacent to a BREAK component,
- (vii) If ICFLOW=2, the cell face must be flagged by the user with the ICFLG input data,
- (viii) A_e/A_c must be less than 1.01,
- (ix) The cell face does not have a momentum source associated with it (as might be the case for TEEs and PUMPS), and
- (x) The flow must be co-current.

Following the call to CHOK, the indicator ICHOK is examined to determine whether choking occurred. If it did, an indicator is set for that cell face, and the new time level mixture velocity is updated using the critical conditions. This mixture velocity is used to limit the flow in the pressure solution step as described below.

After obtaining the critical mixture velocity, the global junction velocity matrix is formed with the critical mixture velocity at the break. Note that the critical mixture velocity is introduced in the forward pass rather than after the back substitution pass, which results in a more stable solution⁽⁶⁵⁾.

Implementation with the WCOBRA/TRAC Semi-Implicit Numerics

For the one-dimensional components, WCOBRA/TRAC solves the mixture continuity, vapor continuity, mixture momentum, mixture energy and vapor energy conservation equations. The relative velocity between the phases is specified explicitly in the form of correlations. A prerequisite (but not necessarily sufficient condition) for these equations to be solved using a semi-implicit numerical method is that the magnitude of the timestep is constrained by the CFL condition. The scheme used in WCOBRA/TRAC is similar (but not identical) to that described by Liles and Reed (1978). [

]^{a,c}.

Because the momentum equation is evaluated independently of the other equations, the implementation of the choked-flow model is straightforward. Following the determination of the mixture velocity from the momentum equation, the interface routine PF1CHK is called and the mixture velocity is limited to the critical value.

Implementation with the WCOBRA/TRAC Fully-Implicit Numerics

For the one-dimensional components, WCOBRA/TRAC solves the mixture continuity, vapor continuity, mixture momentum, mixture energy, and vapor energy conservation equations. The relative velocity between the phases is specified explicitly in the form of correlations. The conservation equations and constitutive relations (except those which determine the interphase relative velocity) are all treated implicitly, but certain parts of the source terms are treated semi-implicitly. Although this requires

significantly greater computation than the semi-implicit numerics, the method is more robust and has the advantage that the timestep size is permitted to violate the Courant condition. It is therefore particularly suited to the calculation of critical flows.

The numerical strategy for solving the conservation equations is based upon an application of a linear Newton-Raphson iteration procedure. The fully-implicit numerical solution is performed in routine DF1DI. This routine is called independently for each one-dimensional component (excluding the boundary condition components FILL and BREAK), and solves the two-phase equations for all the cells in the component simultaneously. (The fully-implicit method does not currently extend across component boundaries.) The simultaneous solution is performed as follows: given the five conservation equations in finite-difference form, it is desired to solve for the following basic variables, pressure, void fraction, liquid temperature, vapor temperature, and mixture velocity. However, the equations also contain references to other quantities such as densities and internal energies. To avoid this problem, the finite-difference equations are linearized; and it is convenient to do so, not with the basic variables described above, but with a set of variations. Thus each equation is reduced to a linear combination of the variations: δP , $\delta \alpha$, $(1 - \alpha)\delta T_l$, $\alpha\delta T_v$, δU_m . The process of linearizing the set of equations is equivalent to a Newton-Raphson iteration with 5N independent variables.

Scaling Considerations: The incorporation of the TRAC-PF1 critical flow model in the WCOBRA/TRAC reduces the bias in the WCOBRA/TRAC critical flow calculations, resulting in more accurate critical flow predictions. In Volume 3 of WCAP-12945-P-A, the TRAC-PF1 critical flow model has been compared to the Marviken (1982) critical flow data as well as the LOFT data. No scale effect has been observed in these comparisons for the TRAC-PF1 critical flow model. In the PWR calculations, the break size is ranged over the uncertainty of the critical flow model such that the break flow model uncertainty is directly addressed in the PWR calculations.

Conclusions: The critical flow model needed in the WCOBRA/TRAC code has been changed from the natural choking model in TRAC PD2 to the TRAC-PF1 model. Using the TRAC-PF1 model reduces the code bias and results in a more accurate calculation. The uncertainty in the critical flow model is accounted for in the PWR calculations which range the break flow over the model uncertainties.

4-8-3 Post Critical Flow Model

At high pressures, the flowrate from the broken pipes in a PWR simulation is calculated using a critical flow model as described in the previous section. It was found as a result of numerous plant simulations that the transition from critical flow to post critical flow was not handled well by the code in some cases. Typically, post critical flow (i.e., unchoked flow) occurs if the reservoir pressure is less than twice the receiver pressure. At the point where the flow no longer became choked in the WCOBRA/TRAC PWR calculation, the mixture velocity was still high (over 100 ft/s). Large pressure gradients were created partly because of the natural choking inherent in the TRAC-PD2 momentum equations, and partly due to condensation. In addition, condensation transients caused pressure and density oscillations in the vessel cell connected to the pipe. Both these factors caused large oscillations in break flowrates. As a result, break flowrates from two nearly identical calculations would sometimes diverge near the end of

blowdown, resulting in varying amounts of ECCS retained in the vessel, and significant swings in PCT. A post critical flow model was developed to help reduce this sensitivity.

The critical flow model works by specifying the mixture velocity at the boundary between the broken PIPE and the BREAK. [

] ^{a,c}. The flow usually becomes post critical when the vessel pressure falls below about 100 psia. At this point, mixture velocities are still quite high (> 100 ft/s). These high velocities, along with condensation transients in the vessel late in blowdown, led to large oscillations in break flow. To prevent the large oscillations, and the potentially unrealistic sensitivity on PCTs, the following model was developed.

[

] ^{a,c} (4-284)

[

] ^{a,c} (4-286)

[

] ^{a,c} (4-287)

[

]^{ac}.

The critical flow model is applied in the hydrodynamic subroutines DF1DI and DF1DS. In both routines, the post critical mixture velocity can be calculated after the pass through the critical flow model. If the pressure in the vessel cell falls below []^{ac} the containment pressure, then the post critical flow model is activated. [

]^{ac}

[

]^{ac} (4-289)

between limits of 0 and 1.

4-9 REFERENCES

Adams, J. E. and Clare, A. J., 1983, "A Preliminary Study of Droplet Breakup at PWR Spacer Grids," Central Electric Generating Board, PWR/HTWS/P Pg. 130.

Adams, J. E. and Clare, A. E., 1984, "Droplet Breakup and Entrainment at PWR Spacer Grids," International Workshop on Fundamental Aspects of Post-Dryout Heat Transfer, Salt Lake City.

Alamgir, M. and Lienhard, J. H., 1981, "Correlation of Pressure Undershoot During Hot Water Depressurization," Transactions of the ASME, Journal of Heat Transfer, Vol. 103, pp. 52-55.

Archer, W. H., 1913, Trans. ASCE. Vol. 76, Pg. 999.

Bajorek, S. M., et al., 1998, "Code Qualification Document for Best Estimate LOCA Analysis," WCAP-12945-P-A, Volume 1, Revision 2, and Volumes 2 through 5, Revision 1, and WCAP-14747 (Non-Proprietary).

Bird, R. B., Stewart, W. E., and Lightfoot, E. N., 1960, Transport Phenomena, John Wiley and Sons.

Chen, C. Y., 1955, "Filtration of Aerosols by Fibrous Model," Chem. Rev., Vol. 55, pg. 595.

Collier, J. G. et al., 1972, "Two-Phase Pressure Drop and Void Fractions in Tubes," AERE-R-6454, HTFS Design Report 15 (HTFS-DR-15).

Cousins, L. B., et al., 1965, "Liquid Mass Transfer in Annular Two-Phase Flow," Paper C4 presented at the Symposium on Two-Phase Flow Volume 2, Exeter, England, pp. 401-430.

Crane, C. O., 1969, "Flow of Fluids Through Valves, Fittings, and Pipe," Technical Paper No. 410 published by Crane Co.

Dallman, J. C. and Kirchner, W. L., 1980, Los Alamos Scientific Laboratory, "De-entrainment Phenomena on Vertical Tubes in Droplet Cross Flow," USNRC Report, NUREG/CR-1421.

Davies, C. N., 1952, "The Separation of Airborne Dust and Particles," Proc. Inst. Mech. Engrs. (London), Vol B1, pg. 185.

Dederer, S. I., et al., 1988, "Westinghouse Large Break LOCA Best Estimate Methodology, Volume 2, Application to Two-Loop PWR's Equipped with Upper Plenum Injection," WCAP-10924 P-A.

Dederer, S. I., et al., 1999, "Application of Best Estimate Large Break LOCA Methodology to Westinghouse PWRs with Upper Plenum Injection," WCAP-14449-P-A, Revision 1, and WCAP-14450-NP-A, Revision 1 (Non-Proprietary).

Drew, D., et al., 1979, "The Analysis of Virtual Mass Effects in Two-Phase Flow," International Journal Multi-phase Flow, Vol. 5, pp. 233-242.

Dukler, A. E., and Smith, L., 1979, "Two-Phase Interactions in Countercurrent Flow Studies of the Flooding Mechanism," NUREG/CR-0617.

Govier, G. W., and Aziz, K., 1972, The Flow of Complex Mixtures in Pipes, Von Nostrand Reinhold, New York.

Henstock, W. H. and Hanratty, T. J., 1976, "The Interfacial Drag and the Height of the Wall Layer in Annular Flows," AIChE Journal, Vol. 22, No. 6, pp. 990-1000.

Hirt, C. W., and Romero, N. C., 1975, "Application of a Drift-Flux Model to Flashing in Straight Pipes," LA-6005-MS (Los Alamos National Laboratory).

Hochreiter, L. E., et al., 1986, "Analysis of FLECHT-SEASET 163-rod Blocked Bundle Data Using COBRA-TF," NUREG/CR-4166.

Idel'Chik, I. E., 1960, "Handbook of Hydraulic Resistance," AEC-tv-6630.

Ishii, M., 1975, Thermo-Field Dynamic Theory of Two-Phase Flow, Eyrolles.

Ishii, M., 1977, "One-Dimensional Drift Flux Model and Constitutive Equations for Relative Motion Between Phases in Various Two-Phase Flow Regimes," Argonne National Laboratory, ANL-77-47.

- Ishii, M. and Chawla, T. C., 1979, "Local Drag Laws in Dispersed Two-Phase Flow," NUREG-CR-1230, ANL-79-105.
- Ishii, M. and Grolmes, M. A., 1975, "Inception Criteria for Droplet Entrainment in Two-Phase Concurrent Film Flow," AIChE Journal, Vol. 21, No. 2, pg. 308.
- Jones, O. C., 1980, "Flashing Inception in Flowing Liquids," ASME Journal of Heat Transfer, Vol. 102 pp. 439-444.
- Kataoka, I., and Ishii, M., 1983, "Mechanistic Modeling and Correlations for Pool Entrainment Phenomenon," NUREG/CR-3304.
- Kays, W. M. and London, A. L., 1955, Compact Heat Exchangers, McGraw-Hill Publishers.
- King, H. W. and Brater, E. F., 1963, Handbook of Hydraulics, McGraw Hill Book Company, Inc., New York, pp. 6-21.
- Lee, N., et al., 1982, "PWR FLECHT-SEASET Unblocked Bundle Forced and Gravity Reflood Task: Data Evaluation and Analysis Report," NUREG/CR-2256.
- Lee, S. L., et al., 1982, "Re-entrainment of Droplets from Grid Spacers in Mist Flow Portion of a LOCA Reflood of a PWR, NRC/ANS Topical Meeting on Basic Thermal Hydraulic Mechanisms in LWR Analysis," NUREG/CR-0043.
- Lee, S. L., 1984a, "Measurement of Grid Spacer's Enhanced Droplet Cooling Under Reflood Condition in a PWR by LDA," Department of Mechanical Engineering, SUNY at Stony Brook.
- Lee, S. L., et al., 1984b, "A Study of Droplet Hydrodynamics Across a Grid Spacer," NUREG/CR-4034.
- Liles, D. R., et al., 1981, "TRAC-PD2, An Advanced Best-Estimate Computer Program for Pressurized Water Reactor Loss-of-Coolant Accident Analysis," NUREG/CR-2054.
- Liles, D. R., et al., 1988, "TRAC-PF1/MOD1 Correlations and Models," NUREG/CR-5069.
- Liles, D. R. and Reed, W. H., 1978, "A Semi-Implicit Model for Two-Phase Fluid Dynamics," Journal of Computational Physics, Vol. 26, pp. 390-407.
- Lovell, T. W., 1977, "The Effect of Scale on Two-Phase Countercurrent Flow Flooding in Vertical Tubes," Masters Thesis, Thayer School of Engineering, Dartmouth College.
- "The Marviken Full-Scale Critical Flow Tests-Summary Report," 1982, EPRI-NP-2370 Volume 1, Report MXC 301.
- Massey, B. S., 1968, Mechanics of Fluids, Van Nostrand Co., New York.

McAdams, W. H., 1942, "Vaporization Inside Horizontal Tubes-II-Benzene-Oil Mixtures," Trans. ASME, Vol. 64, Pg. 193.

Nikuradse, J., 1933, "Strömungsgesetze in Rauhen Rohren," VDI-Forschungshelf, 361, 1933 or NACA-TM-1292.

Okubo, T. and Sugimoto, J., 1984, "Overview of JAERI's 17x17 Type Small Scale Reflood Experiments," JAERI.

Paleev, I. I. and Filippovich, B. A., 1966, "Phenomena of Liquid Transfer in Two-Phase Dispersed Annular Flow," International Journal Heat Mass Transfer, 9, pp. 1089-1093.

Takeuchi, K., et al., 1982, "Experimental Studies on the Behavior of a Small Droplet Impinging Upon a Hot Surface," Proceedings of the Second International Conference on Liquid Atomization and Spray Systems, pp. 397-404.

Tatterson, D. F., et al., 1977, "Drop Sizes in Annular Gas-Liquid Flows," AIChE Journal, Vol. 23, No. 1, pp. 68-76.

Thom, J. R. S., 1964, "Prediction of Pressure Drop During Forced Circulation Boiling of Water," International Journal Heat Mass Transfer, Vol. 7, pg. 709.

Thurgood, M. J., et al., 1983, "COBRA/TRAC - A Thermal-Hydraulics Code for Transient Analysis of Nuclear Reactor Vessels and Primary Coolant Systems," Vol. 1, PNL-4385, NUREG/CR-3046.

Vennard, J. K., 1961, Elementary Fluid Mechanics, Fourth Edition, John Wiley Sons's Publishers.

Wachters, L. H. J. and Westerling, N. A. J., 1966, "The Heat Transfer From a Hot Wall to Impinging Water Drops in a Spheroidal State," Chem. Eng. Sci., Vol. 21, pp. 1047-1056.

Wallis, G. B., 1969, One-Dimensional Two-Phase Flow, McGraw-Hill.

Weisbach, 1855, Die Experimental Hydraulic, Friburg, Germany, J. S. Englehart, pg. 133.

Whalley, P. B., et al., 1973, "Experimental Wave and Entrainment Measurements in Vertical Annular Two-Phase Flow," AERE-R7521, Atomic Energy Research Establishment, Harwell, England.

Wurtz, J., 1978, "An Experimental and Theoretical Investigation of Annular Steam-Water Flow in Tubes and Annuli at 30 to 90 Bar," Report No. 372, RISO National Laboratory, Denmark.

Yao, S. C., Hochreiter, L. E., and Cai, K. Y., 1988, "Dynamics of Droplets Impacting on Thin Heated Strips," Journal of Heat Transfer, Vol. 110, pg. 214.

Young, M. Y., et al., 1984, "BART-A1: A Computer Code for the Best Estimate Analysis of Reflood Transients," WCAP-9561-P-A.

Zuber, N. and Findlay, J. A., 1965, "Average Volumetric Concentration in Two-Phase Flow Systems," Journal of Heat Transfer, ASME, pg. 453.

4-10 RAI LISTING

1. RAI1-48 (refers to WCAP-12945, Rev. 1, page 4-4, now page 4-3)
2. RAI1-49 (refers to WCAP-12945, Rev. 1, pages 4-4, 4-5, now page 4-3)
3. RAI1-51 (refers to WCAP-12945, Rev. 1, page 4-7, 4-9, 4-11, 4-12, now pages 4-5, 4-7, 4-8, and 4-9)
4. RAI1-52 (refers to WCAP-12945, Rev. 1, page 4-13, now page 4-9)
5. RAI1-50 (refers to WCAP-12945, Rev. 1, page 4-13, now pages 4-4 and 4-9)
6. RAI1-68 (refers to WCAP-12945, Rev. 1, page 4-13, and 4-40 now pages 4-9 and 4-27)
7. RAI1-53 (refers to WCAP-12945, Rev. 1, page 4-22, now page 4-15)
8. RAI1-54 (refers to WCAP-12945, Rev. 1, page 4-25, now pages 4-16 and 4-17)
9. RAI1-55 (refers to WCAP-12945, Rev. 1, page 4-25, now pages 4-16 and 4-17)
10. RAI1-56 (refers to WCAP-12945, Rev. 1, page 4-26, now page 4-17)
11. RAI1-57 (refers to WCAP-12945, Rev. 1, page 4-26, now page 4-18)
12. RAI1-58 (refers to WCAP-12945, Rev. 1, page 4-26, now page 4-18)
13. RAI1-59 (refers to WCAP-12945, Rev. 1, page 4-27, now page 4-18)
14. RAI1-60 (refers to WCAP-12945, Rev. 1, page 4-27, now page 4-18)
15. RAI1-61 (refers to WCAP-12945, Rev. 1, page 4-28, now page 4-19)
16. RAI1-62 (refers to WCAP-12945, Rev. 1, page 4-28, now page 4-19)
17. RAI1-63a (refers to WCAP-12945, Rev. 1, page 4-28, now page 4-19)
18. RAI1-63b (refers to WCAP-12945, Rev. 1, page 4-29, now page 4-19)
19. RAI1-64 (refers to WCAP-12945, Rev. 1, page 4-29, now page 4-19)
20. RAI1-65 (refers to WCAP-12945, Rev. 1, page 4-29, now pages 4-20 and 4-31)
21. RAI1-66 (refers to WCAP-12945, Rev. 1, page 4-30, now page 4-20)
22. RAI1-67 (refers to WCAP-12945, Rev. 1, page 4-33, now pages 4-23 and 4-24)
23. RAI1-69 (refers to WCAP-12945, Rev. 1, page 4-40, now page 4-27)
24. RAI1-70 (refers to WCAP-12945, Rev. 1, page 4-43, now pages 4-29 and 4-30)
25. RAI1-71 (refers to WCAP-12945, Rev. 1, page 4-45, now page 4-31)
26. RAI1-72 (refers to WCAP-12945, Rev. 1, page 4-46 and 4-48, now pages 4-31 and 4-33)
27. RAI1-73 (refers to WCAP-12945, Rev. 1, page 4-49, now pages 4-33 and 4-34)
28. RAI1-74 (refers to WCAP-12945, Rev. 1, page 4-52, now page 4-36)
29. RAI1-75 (refers to WCAP-12945, Rev. 1, page 4-54, now page 4-37)
30. RAI1-81 (refers to WCAP-12945, Rev. 1, page 4-58, now page 4-40)
31. RAI1-76 (refers to WCAP-12945, Rev. 1, page 4-62, now page 4-42)
32. RAI1-78 (refers to WCAP-12945, Rev. 1, page 4-63, now page 4-43)
33. RAI1-79 (refers to WCAP-12945, Rev. 1, page 4-63, now page 4-43)
34. RAI1-80 (refers to WCAP-12945, Rev. 1, page 4-64, now page 4-44)
35. RAI1-82 (refers to WCAP-12945, Rev. 1, page 4-65, now page 4-44)
36. RAI1-83 (refers to WCAP-12945, Rev. 1, page 4-66, now page 4-45)

37. RAI1-84 (refers to WCAP-12945, Rev. 1, pages 4-66, now page 4-46; RAI response included in following text)
38. RAI1-85 (refers to WCAP-12945, Rev. 1, pages 4-66 to 4-68, now pages 4-46, 4-48, and 4-49)
39. RAI1-86 (refers to WCAP-12945, Rev. 1, page 4-70, now page 4-50)
40. RAI1-87 (refers to WCAP-12945, Rev. 1, page 4-71, now page 4-51)
41. RAI1-88 (refers to WCAP-12945, Rev. 1, page 4-74, now page 4-53)
42. RAI1-89 (refers to WCAP-12945, Rev. 1, page 4-75, now page 4-54)
43. RAI1-90 (refers to WCAP-12945, Rev. 1, page 4-83, now page 4-59)
44. RAI1-91 (refers to WCAP-12945, Rev. 1, page 4-83, now page 4-59)
45. RAI1-92 (refers to WCAP-12945, Rev. 1, page 4-83, now page 4-60)
46. RAI1-93 (refers to WCAP-12945, Rev. 1, page 4-87, now page 4-62)
47. RAI1-94 (refers to WCAP-12945, Rev. 1, page 4-95, now page 4-67)
48. RAI1-95 (refers to WCAP-12945, Rev. 1, page 4-97, now page 4-68)
49. RAI1-96 (refers to WCAP-12945, Rev. 1, page 4-98, now page 4-69)
50. RAI1-97a,b (refers to WCAP-12945, Rev. 1, page 4-100, now page 4-71)
51. RAI1-97c (refers to WCAP-12945, Rev. 1, page 4-102, now page 4-71)
52. RAI1-98 (refers to WCAP-12945, Rev. 1, page 4-102, now page 4-71)
53. RAI1-99 (refers to WCAP-12945, Rev. 1, page 4-102, now page 4-72)
54. RAI1-100 (refers to WCAP-12945, Rev. 1, page 4-103, now page 4-72)
55. RAI1-101 (refers to WCAP-12945, Rev. 1, page 4-105, now page 4-74)
56. RAI1-102 (refers to WCAP-12945, Rev. 1, page 4-107, now page 4-75)
57. RAI1-103 (refers to WCAP-12945, Rev. 1, pages 4-107 and 4-108, now page 4-75)
58. RAI1-104 (refers to WCAP-12945, Rev. 1, page 4-109, now pages 4-76 and 4-77)
59. RAI1-105 (refers to WCAP-12945, Rev. 1, page 4-110, now page 4-77)
60. RAI1-106 (refers to WCAP-12945, Rev. 1, page 4-110, now page 4-77)
61. RAI1-107 (refers to WCAP-12945, Rev. 1, page 4-111, now page 4-77)
62. RAI1-108 (refers to WCAP-12945, Rev. 1, page 4-117, now page 4-80)
63. RAI1-109 (refers to WCAP-12945, Rev. 1, page 4-125, now page 4-84)
64. RAI1-110 (refers to WCAP-12945, Rev. 1, page 4-134, now page 4-89)
65. RAIF-9 (refers to WCAP-12945, Rev. 1, page 4-136, now pages 4-91 and 4-93)
66. Additional discussion on droplet size is in the MOD7A Report, located after RAI2-69
67. RAI1-77 (refers to WCAP-12945, Rev. 1, page 4-62, now page 4-42)
68. RAIF-3

Table 4-1 Sudden Contraction

[
			J ^{ac}

Table 4-2 Sudden Expansion

[

J^{ac}.

Table 4-3 Combination			
[
] ^{a,c}

Note: ΔP (exp) calculated by adding losses due to contraction and expansion.

Table 4-4 Comparison of Thom's Slip Ratios and Ishii C_o and Modified C_o			
[
] ^{a,c}

Table 4-5 Comparisons of TRAC Predicted Expansion Pressure Loss to Test Data			
[
] ^{a,c}

Note: The values of $\Delta P(\text{exp})$ are obtained from Archer (1913).

Table 4-6 Comparisons of Abrupt Contraction Loss Coefficients		
[
] ^{a,c}

Table 4-7 Comparison of Predicted Contraction Pressure Loss to Test Data		
[
		$J^{a,c}$

Table 4-8 Comparison of Normalized Contraction Pressure Loss with Test Data			
[
			$J^{a,c}$

Table 4-9 Comparison of TRAC Predicted Loss With Test Data for Combined Contraction and Expansion				
[
				$J^{a,c}$

where $R = A2/A3$

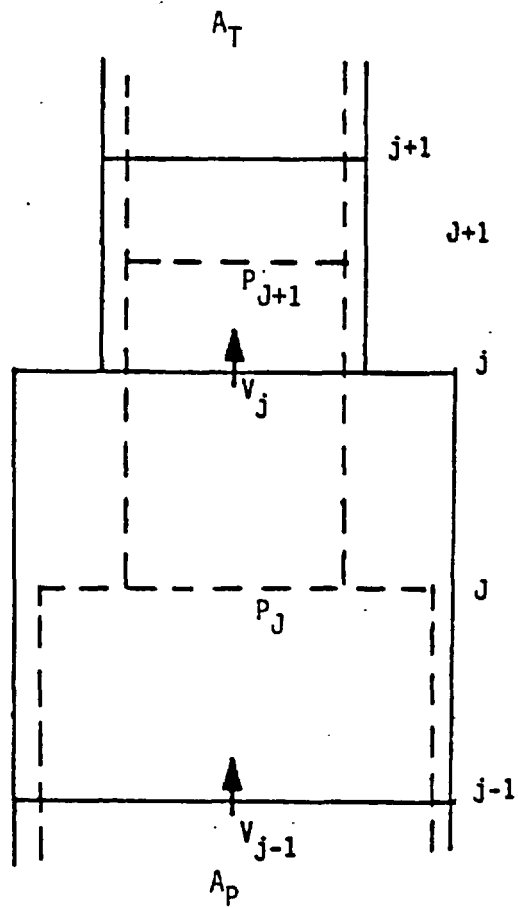


Figure 4-1. One-Dimensional Vessel Channel with Area Change

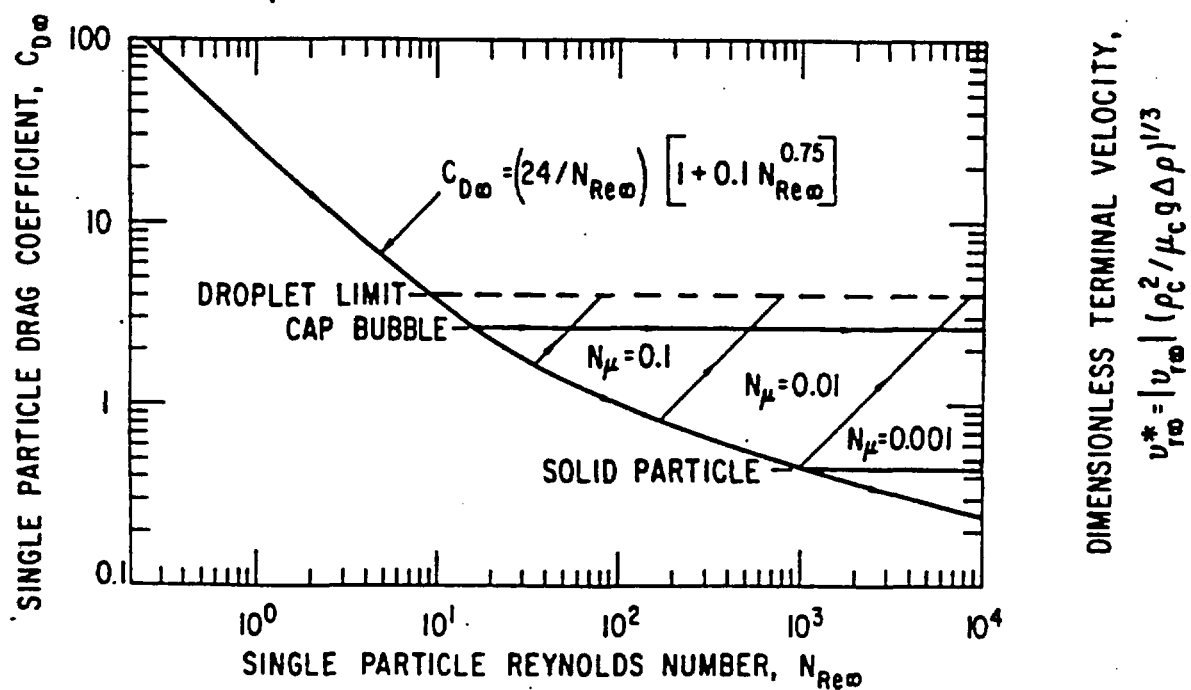


Figure 4-2. Bubble Drag Coefficients (Ishii and Chawla, 1979)

a,c

Figure 4-3. Effect of Ramps On Interfacial Friction Factor. (a) Small Bubble Regime, (b) Large Bubble Regime

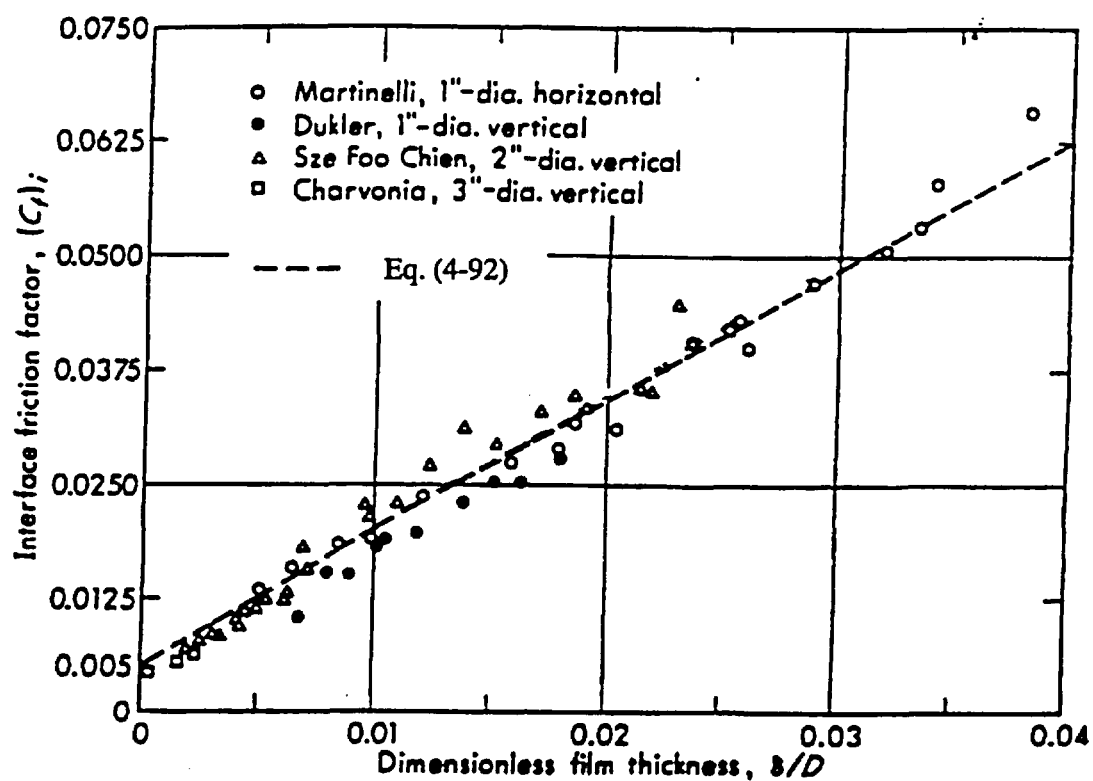
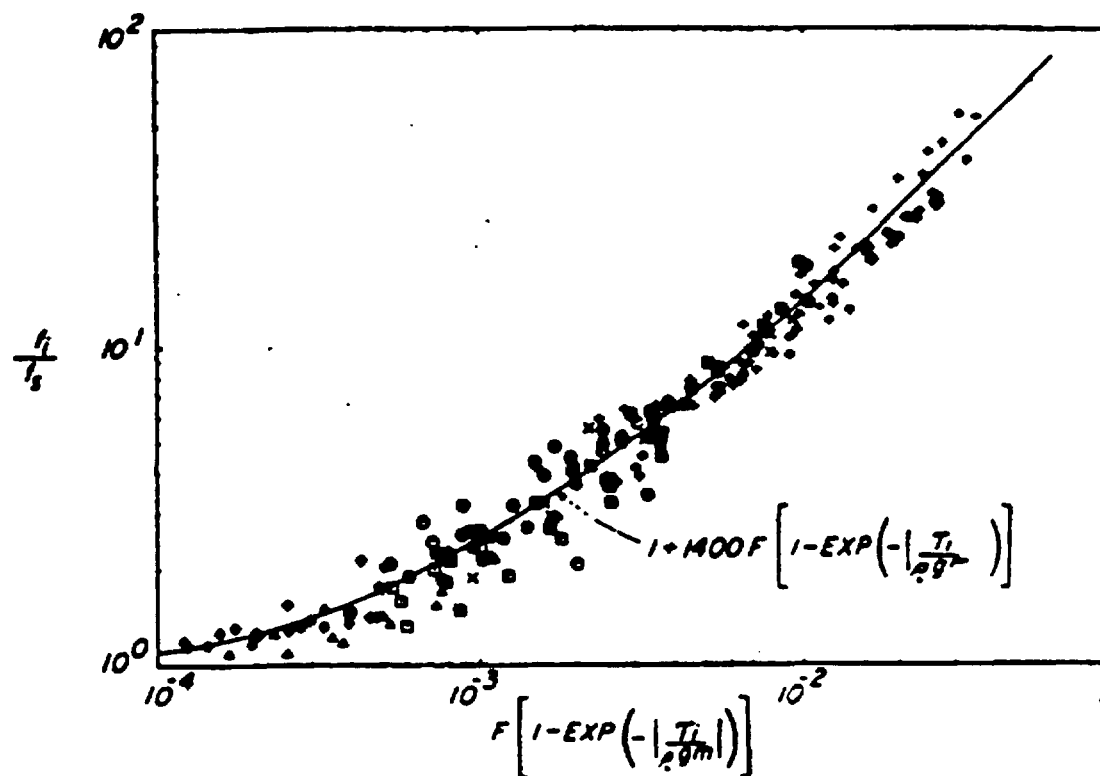


Figure 4-4. Interfacial Friction Factor for Smooth Films (Wallis, 1969)



Final form of friction factor correlation, vertical flows

Figure 4-5. Hanstock and Hanratty (1976) Film Flow Interfacial Shear

**Figure 4-6a. Comparison of Droplet Data Range and Droplet Size Limits^(37,39)
in WCOBRA/TRAC at 40 psia**

a,c

**Figure 4-6b. Comparison of Droplet Data Range and Droplet Size Limits^(37,39)
in WCOBRA/TRAC at 20 psia**

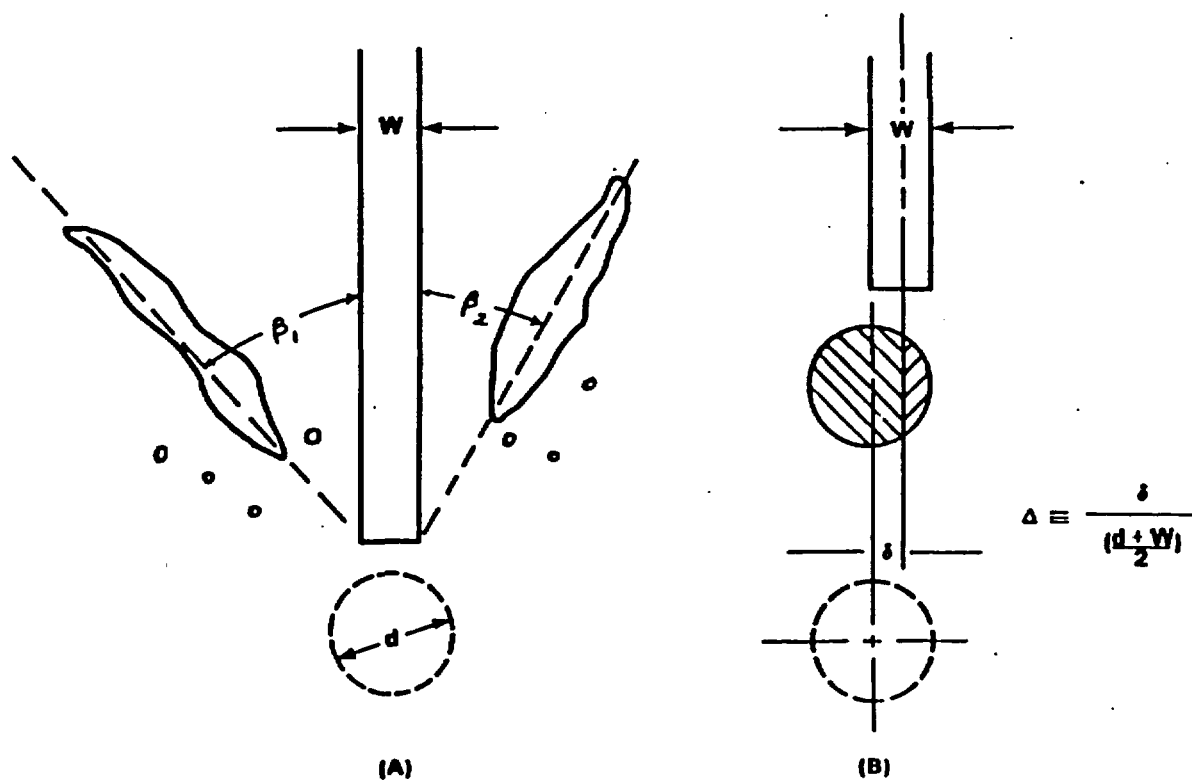


Figure 4-7. Impingement of a Droplet on a Grid Spacer

(a) Shattering Process

(b) Definition of Droplet Offset Parameter

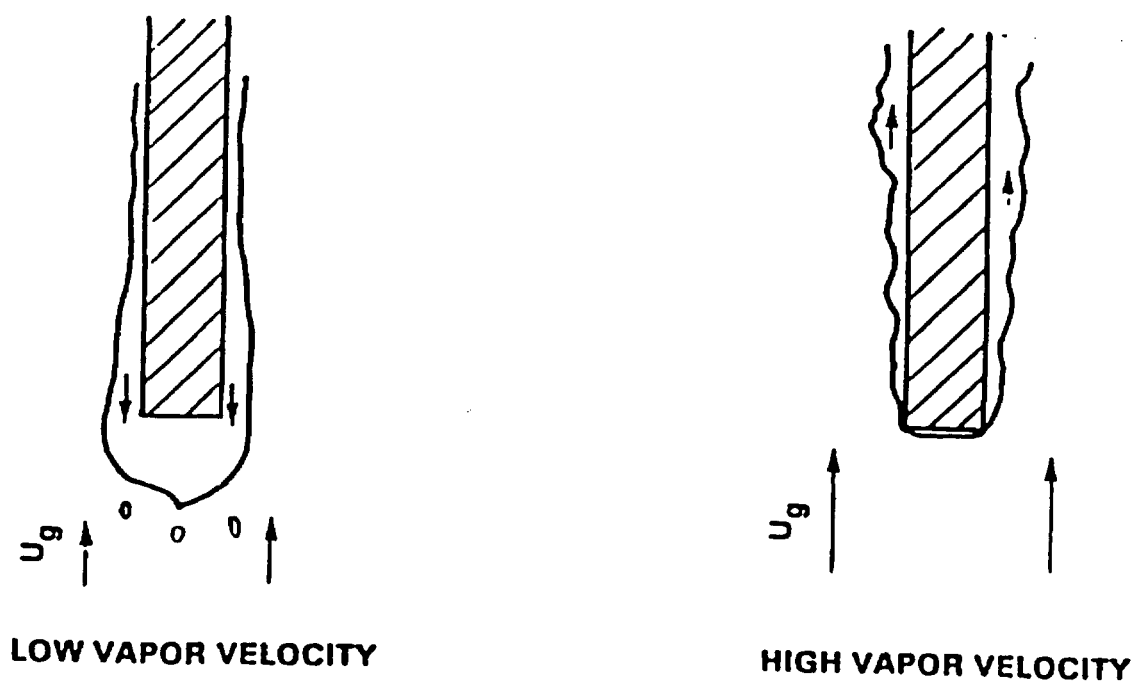


Figure 4-7c. Leading Edge of a Wetted Grid; Effect of Vapor Velocity⁽⁴⁵⁾

Figure 4-8. The Relationship of Droplet Diameter Ratio Versus Droplet Weber Number

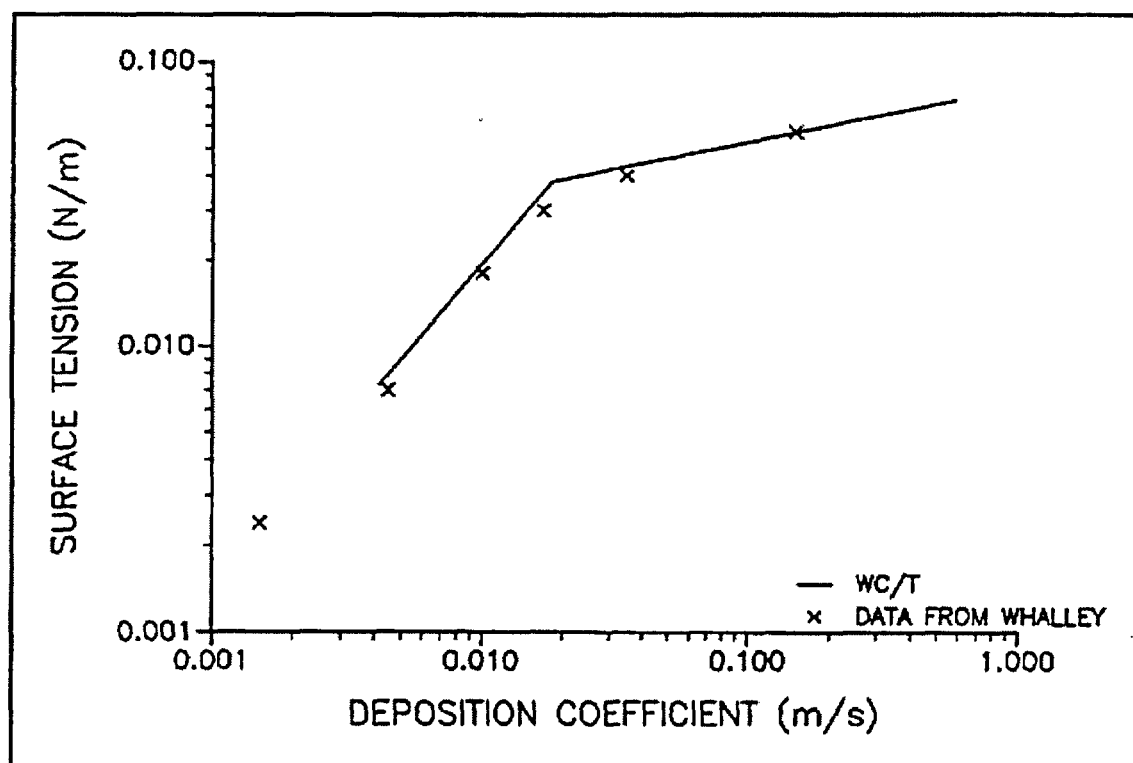


Figure 4-9. Comparison of CQD Equation 4-186 with Data from Whalley (1973)

Figure 4-10. Comparison of TRAC-PD2 Two-Phase Multiplier to Collier et al. (1972) Data, Case 1

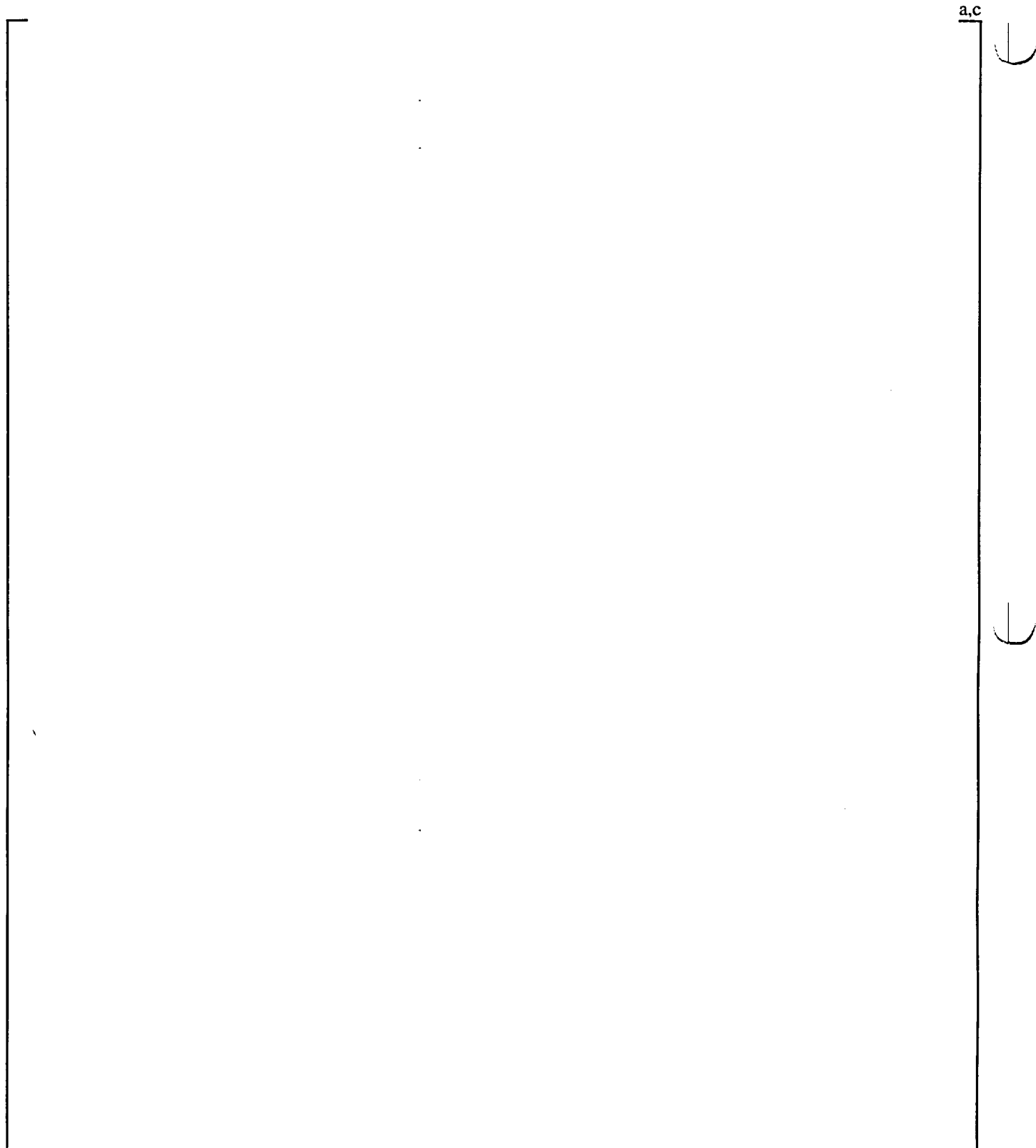


Figure 4-11. Comparison of TRAC-PD2 Two-Phase Multiplier to Collier et al. (1972) Data, Case 2

Figure 4-12. Comparison of TRAC-PD2 Two-Phase Multiplier to Collier et al. (1972) Data, Case 3

a,c

Figure 4-13. Comparison of TRAC-PD2 Two-Phase Multiplier to Collier et al. (1972) Data, Case 4

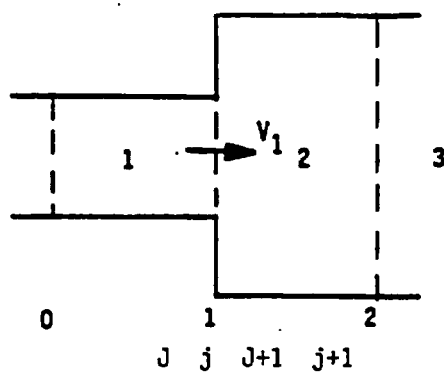


Figure 4-14. Sudden Expansion in 1-D Component

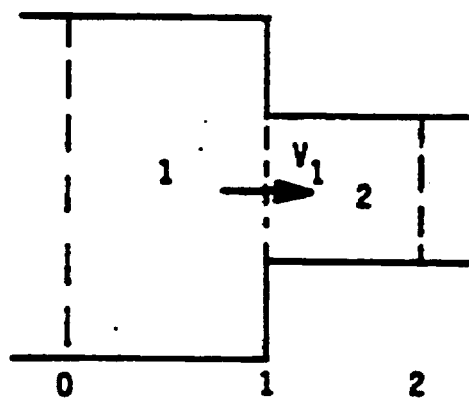


Figure 4-15. Sudden Contraction in 1-D Component

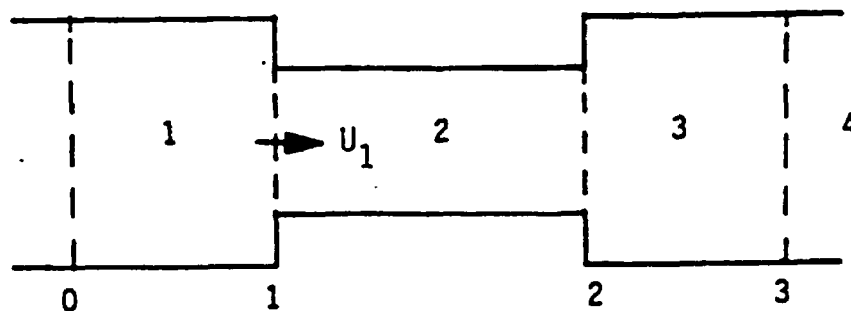


Figure 4-16. Contraction and Expansion in 1-D Component

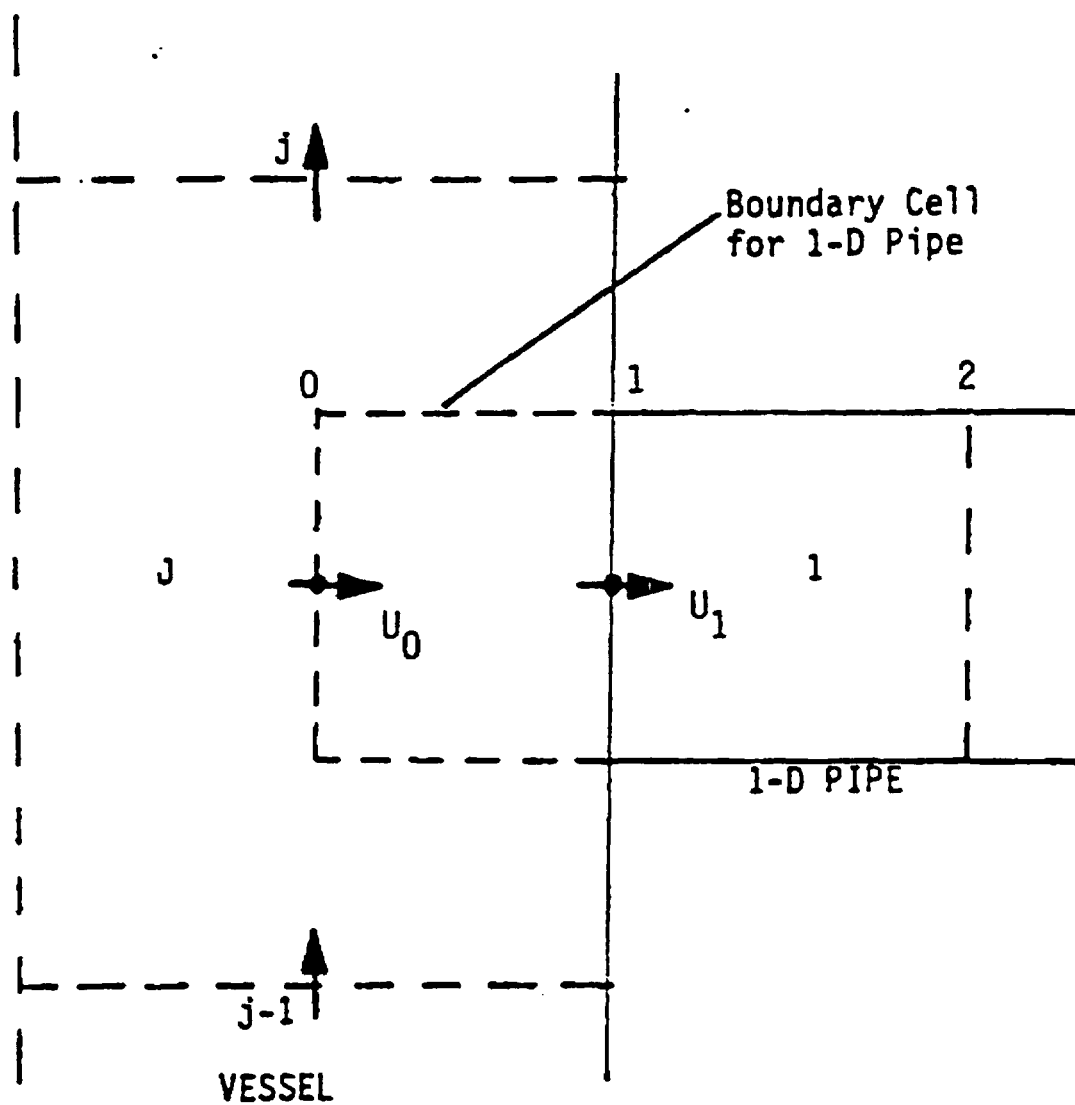
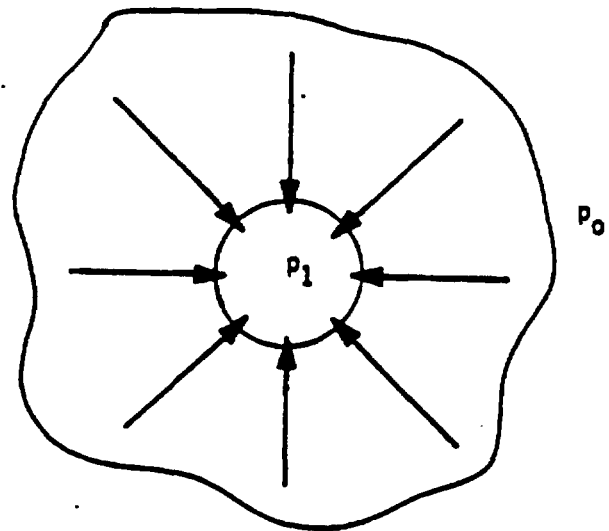
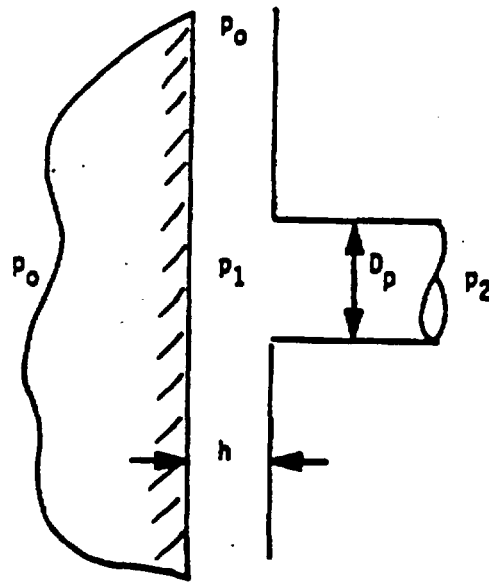


Figure 4-17. 1-D / Vessel Junction



(a)



(b)

Figure 4-18. Broken Cold Leg Nozzle Junction to Vessel

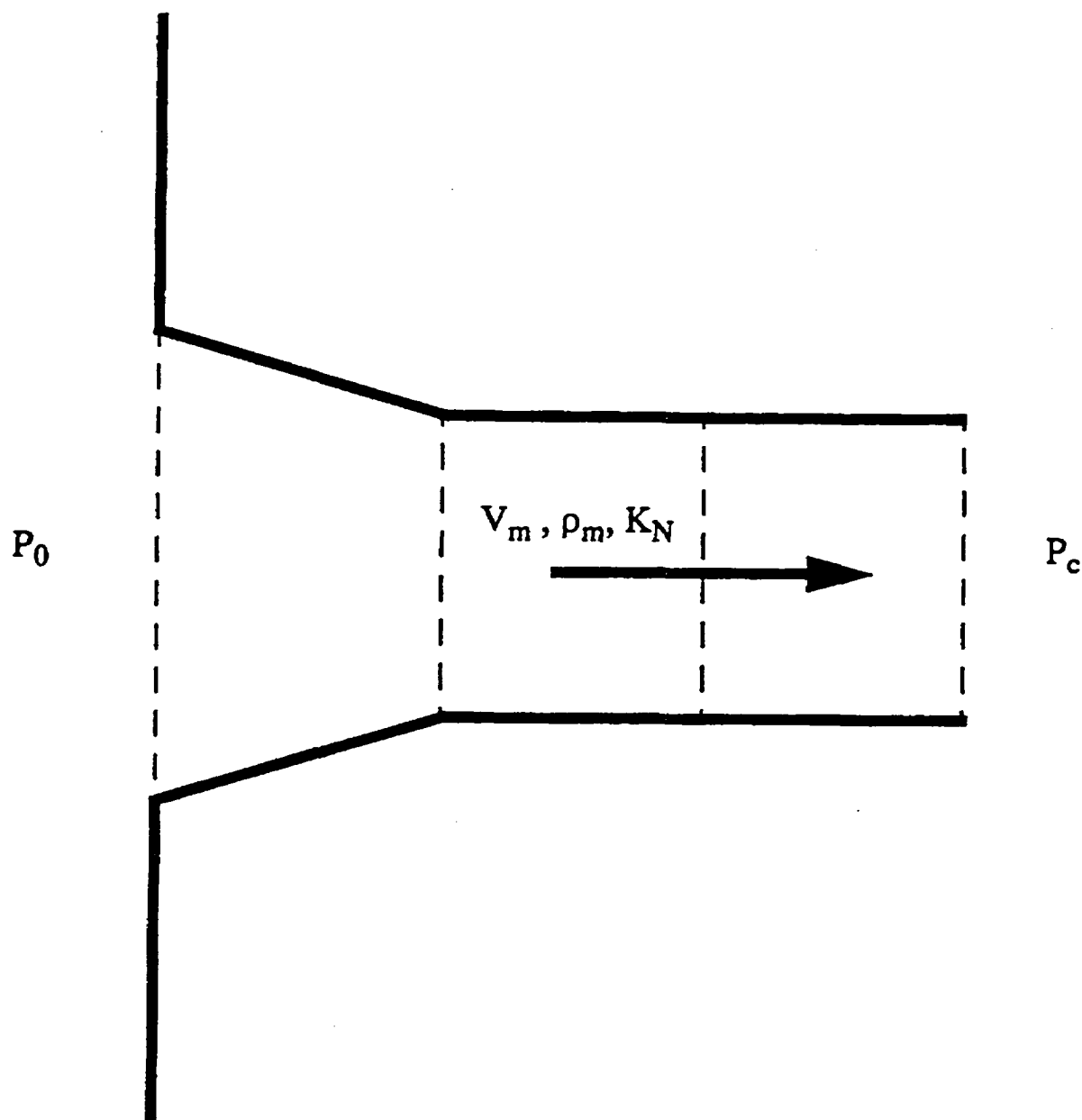


Figure 4-19. Pipe for Revised Critical Flow Model

5 WCOBRA/TRAC INTERFACIAL HEAT AND MASS TRANSFER MODELS

5-1 INTRODUCTION

The heat and mass transfer between the liquid and vapor phases depends on the interfacial heat transfer coefficient h_i and the interfacial area A_i . WCOBRA/TRAC combines these quantities into interfacial heat transfer factors ($h_i A_i$) for the vessel component and into liquid side (ALV) and vapor side (CHTI) interfacial heat transfer factors in the one-dimensional components. Section 3 discussed calculation of the interfacial area. This section describes the models, correlations, and assumptions used in the WCOBRA/TRAC vessel and one-dimensional components to determine the interfacial heat transfer coefficients and calculation of the interfacial heat transfer factors. The interfacial heat transfer coefficients depend on the flow regime and on whether the fluid is subcooled or superheated.

In a large break LOCA, and in the integral and separate effects tests that approximate parts of a LOCA, not all of the interfacial heat transfer terms are of equal importance. In the vessel, evaporation of saturated liquid droplets and films into superheated vapor is clearly the most dominant interfacial heat transfer process. Condensation to subcooled liquid also occurs as ECC liquid enters the vessel or the loops. Superheated liquid and subcooled vapor are inherently unstable and are rarely encountered. Thus, the interfacial heat transfer coefficients from the interface to superheated vapor and from the interface to subcooled liquid are the most important terms to consider.

The following sections describe, by flow regime, the correlations used for h_i , and calculation of the interfacial heat transfer factors in the WCOBRA/TRAC vessel and one-dimensional components.

5-2 VESSEL COMPONENT INTERFACIAL HEAT AND MASS TRANSFER MODELS

5-2-1 Small Bubble Regime

Model Basis In the small bubble flow regime, the vapor side heat transfer coefficient for superheated vapor is assumed to be a constant:

$$h_{i, SHV} = 2.78 \frac{Btu}{ft^2-s-^{\circ}F} \quad (5-1)^{(1)}$$

For subcooled vapor, a large constant value is assumed for the interfacial heat transfer coefficient:

$$h_{i, SCV} = 2780.0 \frac{Btu}{ft^2-s-^{\circ}F} \quad (5-2)^{(1)}$$

The interfacial area for subcooled vapor is [

$$J^{a,c} \quad (5-3)^{(2)}$$

where $A_x \Delta X$ is the cell volume.

The expression given by Equation 5-3 is essentially a [

$J^{a,c}$. The constant coefficient was originally arrived at by making assumptions on bubble or drop size, although it should be taken mainly as an empirical constant.

In the small bubble regime, the liquid side interfacial heat transfer coefficient to subcooled liquid is calculated using a correlation by [

$$J^{a,c} \quad (5-4)^{(3)}$$

where,

$$Re_b = \frac{\rho_t U_{br} D_b}{\mu_t} \quad (5-5)$$

Use of this equation in the small bubble regime assumes [

$$J^{a,c} \quad (4)$$

For superheated liquid, a large value is assumed in order to drive the liquid towards saturation:

$$h_{i,SHL} = 278.0 \frac{Btu}{ft^2-s-^{\circ}F} \quad (5-6)^{(1)}$$

Model As Coded Calculations of the interfacial heat transfer coefficients and the quantities $(h_i A_i)$ for each regime are performed in subroutine INTFR. Only the $(h_i A_i)$ terms are returned for use by the rest of the code, so their calculations will be described in this section.

For evaporation to superheated vapor in the small bubble regime, $(h_i A_i)$ is coded as

$$(h_i A_i)_{SB,SHV} = h_{i,SHV} A_{i,SB} \quad (5-7)$$

where $h_{i,SHV}$ is given by Equation 5-1 and the interfacial area is given by Equation 3-22.

For superheated liquid evaporation ($h_i A_i$) is

$$(h_i A_i)_{SB,SHL} = 278.0 A_{i,SB} \quad (5-8)$$

The condensation terms in the small bubble regime are calculated as discussed in the following paragraphs.

For subcooled vapor,

$$(h_i A_i)_{SB,SCV} = h_{i,SCV} A_{i,SCV} \quad (5-9)$$

For subcooled liquid, the interfacial area is subjected to an additional ramp if there is a large void fraction gradient. If the difference in void fraction between two adjacent hydraulic cells is greater than $[]^{a.c.}$, indicating that a transition to large bubble or churn-turbulent flow occurs nearby, the interfacial area is modified in the following manner:

$$A_{i,SCL} = F_{\Delta\alpha} A_X + (1 - F_{\Delta\alpha}) A_{i,SB} \quad (5-10)^{(5)}$$

where A_X is the cell axial flow area and $A_{i,SB}$ is the small bubble interfacial area from Equation 3-22.

[

$]^{a.c.}$

The interfacial heat transfer coefficient to subcooled liquid is calculated using Equation 5-4 and

[

$$]^{a.c.} (5-11)^{(6)}$$

where,

[

$]^{a.c.}$

[

$$j^{a,c}$$

it follows that [

$$j^{a,c} \quad (5-12)^{(1,6)}$$

The interfacial heat transfer factor for subcooled liquid in the small bubble regime is then calculated as [

$$j^{a,c} \quad (5-13)$$

where the interfacial area $A_{i,SCL}$ is given by Equation 5-10.

Scaling Considerations The models and correlations for the $(h_i A_i)$ terms for the small bubble regime were used in WCOBRA/TRAC simulations of LOFT, CCTF, SCTF, UPTF integral tests and the FLECHT series and FEBA reflood experiments. These test facilities covered a wide range of scale including PWR full scale geometries. These tests, and the WCOBRA/TRAC simulations of them, are described in Volumes 2 and 3 of WCAP-12945-P-A (Bajorek et al., 1998). These WCOBRA/TRAC simulations did not indicate a bias due to scale. The small bubble regime was predicted to occur during portions of these simulations, implying that either the correlations are scale independent, or at least do not contribute towards making the overall results a strong function of scale.

Conclusions The key process for the small bubble regime is the flow of saturated steam bubbles in subcooled water. Other combinations are unlikely to occur during a LOCA. For this combination, the interfacial heat transfer is modelled with an appropriate expression. The small bubble flow regime was predicted to occur in many of the WCOBRA/TRAC simulations of experimental tests. The accuracy and reliability of the models and correlations representing the small bubble regime $(h_i A_i)$ is thus included in the overall code bias and uncertainty.

5-2-2 Small to Large Bubble Regime

Model Basis In the small to large bubble regime, large vapor bubbles (slugs) are gradually calculated to form above a void fraction of $[]^{ac}$, while a dispersion of small bubbles is assumed to exist in the continuous liquid phase. The interfacial area for large bubbles was described in Section 3-2-3.

The interfacial heat transfer coefficient to large bubbles for superheated vapor uses the correlation suggested by Lee and Ryley (1968):

$$h_{i,LR} = \frac{k_v}{D_h} (2.0 + 0.74 Re_b^{1/2} Pr_v^{1/3}) \quad (5-14)^{(7)}$$

The Lee-Ryley correlation was originally developed for the evaporation of droplets in superheated steam.

The value of $h_{i,LR}$ given by Equation 5-14 assumes all of the vapor is in the form of large bubbles in calculating the bubble Reynolds number Re_b and that the bubbles nearly fill the hydraulic cell, making $D_b \approx D_h$. The use of this correlation in this regime is an extrapolation. However, bubbles of superheated steam are unlikely to occur extensively in a LOCA transient, since the large interfacial area will quickly drive the steam to saturation.

For superheated liquid, a constant value is assumed,

$$h_{i,SHL} = 278.0 \frac{Btu}{ft^2-s-^{\circ}F} \quad (5-15)$$

[

]^{ac}.

For subcooled vapor, a constant value is assumed for the interfacial heat transfer coefficient:

$$h_{i,SCV} = 2780.0 \frac{Btu}{ft^2-s-^{\circ}F} \quad (5-16)$$

Model as Coded The calculations of the interfacial heat transfer coefficients and the quantity $(h_i A_i)$ are performed in subroutine INTFR. In the small to large bubble regime, values of $(h_i A_i)$ for large bubbles are ramped with $(h_i A_i)$ for small bubbles to obtain a $(h_i A_i)$ for the small to large bubble regime. The small bubble values were discussed in Section 5-2-1.

The quantities $(h_i A_i)$ for large bubbles are calculated as follows.

For superheated vapor,

$$(h_i A_i)_{LB,SHV} = h_{i,LR} A_{i,SLB} \quad (5-17)^{(42)}$$

where $A_{i,SLB}$ is given by Equation 3-36, and $h_{i,LR}$ is from Equation 5-14.

For superheated liquid,

$$(h_i A_i)_{LB,SHL} = h_{i,SHL} A_{i,SLB} \quad (5-18)$$

For subcooled liquid, the interfacial area is modified if there is a large void fraction gradient ($\Delta\alpha > [0.2]^{ac}$) between two adjacent hydraulic cells, indicating a more separated flow regime. When the void gradient is large, the interfacial area for subcooled liquid is calculated as [

$$]^{ac} \quad (5-19)$$

where A_x is the cell flow area, $A_{i,SLB}$ is given by Equation 3-36 and [

$$]^{ac}.$$

The subcooled liquid term $(h_i A_i)$ is then calculated as [

$$]^{ac} \quad (5-20)^{(8)}$$

where $h_{i,RCL}$ is given by Equation 5-4, $h_{it,max}$ by Equation 5-12 and $A_{i,SCL}$ by Equation 5-19.

After these calculations are performed for large bubbles, the final values of $(h_i A_i)$ for the small to large bubble regime are obtained. The ramp between the small bubble and large bubble values is the same as that described in Section 3-2-3, so only the final expressions are listed here. These are:

For superheated vapor, [

$$]^{ac} \quad (5-21)$$

For superheated liquid, [

$$]^{ac} \quad (5-22)$$

For subcooled liquid, [

$$]^{a,c} \quad (5-23)$$

and for subcooled vapor, [

$$]^{a,c} \quad (5-24)$$

Scaling Considerations The interfacial heat transfer correlations in the small to large bubble regime are verified through their use in the simulation of the LOFT, CCTF, SCTF, and FLECHT-SEASET tests reported in Volumes 2 and 3 of WCAP-12945-P-A. Bubbly and slug flow were expected to have occurred in the lower plenums and lower parts of the rod bundles in these tests. WCOBRA/TRAC simulations of these experimental results showed periods in which the small to large bubble flow regime was predicted to occur, thus applying the correlations discussed in this section.

Conclusions As with the small bubble regime, the key process is the flow of saturated vapor bubbles in subcooled water. An appropriate expression is used for this process. The interfacial heat transfer correlations for the small to large bubble regime are based on fairly simple models for the vapor side heat transfer and were originally verified for a limited range of conditions. The simulations of experimental tests with a wide range of scale and conditions using WCOBRA/TRAC show that these correlations may be applied to PWR type geometries and conditions. It is unlikely that a bubbly flow regime with superheated vapor will exist, so these simplifications are justified. The reliability of these correlations is reflected in the overall WCOBRA/TRAC code bias and uncertainty for LOCA analysis.

5-2-3 Churn-Turbulent Regime

Model Basis In the churn-turbulent flow regime, flow is transitioned from large bubble at $\alpha_{LB} = [0.5]^{a,c}$ to film at $\alpha = \alpha_{crit}$ as described in Section 3. Droplets can appear in the flow from entrainment and from adjoining channels.

For superheated vapor, the interfacial heat transfer coefficient from the liquid film is based on

$$h_{i,v} = \frac{f_{i,l} \rho_v C_{pv} |U_v|}{2 Pr_v^{2/3}} \quad (5-25)^{(9)}$$

For superheated vapor from droplets, the interfacial heat transfer coefficient is given by the Lee-Ryley (1968) correlation:

$$h_{i,LR} = \frac{k_v}{D_d} \left[2.0 + 0.74 Re_d^{1/2} Pr_v^{1/3} \right] \quad (5-26)$$

For superheated liquid films, there are three possible expressions for the interfacial heat transfer coefficient. The first of these expressions is derived from the Colburn analogy⁽¹¹⁾ (Colburn, 1933) using friction factors by Hughmark (1973): [

$$j^{ac} \quad (5-27)^{(10)}$$

where: [

$$j^{ac} \quad (5-28b)^{(10)}$$

The second expression is from conduction through a liquid film:

$$h_i^* = \frac{2k_l}{\delta_l} \quad (5-29)^{(12)}$$

where δ_l is the liquid film thickness, and the third assumes the constant value

$$h_i^{**} = 278.0 \quad (5-30)$$

The interfacial heat transfer coefficient from the interface to the liquid for liquid drops is from Andersen (1973):

$$h_{i,drop} = C \frac{\pi^2}{3} \frac{k_l}{r_d} \quad (5-31)^{(1)}$$

where the value of C is taken as []^{ac} ⁽¹³⁾

The interfacial heat transfer coefficient from the interface to subcooled liquid films is also based on the Hughmark (1973) expression:

$$h_{i,SCLM} = h_{i,HM} \quad (5-32)$$

where $h_{i,HM}$ is given by Equation 5-27. This value is limited by the upper limit heat transfer coefficient described in Section 5-2-1, as shown in the next section.

For subcooled liquid drops, the expression from Andersen (1973) is again applied:

$$h_{i,SCL,ve} = h_{i,drop} \quad (5-33)^{(14)}$$

where $h_{i,drop}$ is from Equation 5-31.

The interfacial heat transfer coefficient from the interface to subcooled vapor is assumed to be a large constant for both liquid films and droplets to drive the vapor towards saturation. The value given by Equation 5-16 is again applied.

Model as Coded Calculations of the interfacial heat transfer coefficients for the churn-turbulent regime are performed in subroutine INTFR. The evaporation and condensation ($h_i A_i$) terms are calculated for large bubbles, as described in Section 5-2-2, and for annular films and drops as described below. The interfacial heat transfer coefficient is then calculated for the churn-turbulent regime using a linear interpolation of the large bubble values at $\alpha_{LB} = []^{ac}$ and the film/drop values at α_{crit} , where α_{crit} is calculated using Equation 3-39.

The term ($h_i A_i$) from the interface to vapor for liquid films and drops in superheated vapor is calculated as [

$$]^{ac} \quad (5-34)$$

where $h_{i,vl}$ is calculated by Equation 5-25, $h_{i,LR}$ is given by Equation 5-26 and the interfacial areas are given by Equations 3-42 and 3-43.

For superheated liquid, ($h_i A_i$) is calculated as [

$$]^{ac} \quad (5-35)$$

where $h_{i,HM}$, h_i^* and h_i^{**} were given by Equations 5-27, 5-29, and 5-30, $A_{i,film}$ is given by 3-43, and $A_{i,drop}$ is given by Equation 3-42.

The interfacial area used with the Hughmark (1973) correlation, $A_{i,film}^*$, is a modification of the film interfacial area to take into account a large void fraction gradient, and is calculated as [

$$]^{ac} \quad (5-36)$$

where $F_{\Delta\alpha}$ is shown in Figure 5-2, A_x is the cell flow area, and $A_{i,film}$ was given by Equation 3-43.

For subcooled liquid, the interfacial heat transfer coefficient from the interface to the liquid is calculated as [

$$]^{ac} \quad (5-37)$$

subject to the upper limit on the liquid side interfacial heat transfer coefficient described in Section 5-2-1. In Equation 5-37 $h_{i, HM}$, $h_{i, drop}$ and $h_{i, max}$ are given by Equations 5-27, 5-31 and 5-12 respectively. The interfacial areas $A_{i, film}^*$ and $A_{i, drop}$ are calculated with Equations 5-36 and 3-42.

The quantity $(h_i A_i)$ for subcooled vapor is calculated as

$$(h_i A_i)_{FD, SCV} = h_{i, SCV} A_{i, SCV} \quad (5-38)$$

where $h_{i, SCV}$ is an assumed large constant value given by Equation 5-16 and $A_{i, SCV}$ is given by Equation 5-3.

[

$$]^{ac} \quad (5-39)$$

where [

$$]^{ac}.$$

The $(h_i A_i)$ terms for interfacial heat transfer in the churn-turbulent regime are then calculated as

$$(h_i A_i)_{CT, SHV} = F_{CT} (h_i A_i)_{FD, SHV} + (1 - F_{CT}) (h_i A_i)_{LB, SHV} \quad (5-40)$$

$$(h_i A_i)_{CT, SHL} = F_{CT} (h_i A_i)_{FD, SHL} + (1 - F_{CT}) (h_i A_i)_{LB, SHL} \quad (5-41)$$

$$(h_i A_i)_{CT, SCL} = F_{CT} (h_i A_i)_{FD, SCL} + (1 - F_{CT}) (h_i A_i)_{LB, SCL} \quad (5-42)$$

$$(h_i A_i)_{CT, SCV} = 2780.0 A_{i, SCV} \quad (5-43)$$

Scaling Considerations The interfacial heat transfer correlations in the churn-turbulent regime are verified through their use in the simulation of the LOFT, CCTF, SCTF, and UPTF tests reported in Volume 3 of WCAP-12945-P-A. Churn-turbulent and annular flows were expected to have occurred in the downcomer, upper, and lower plenums and lower parts of the rod bundles in these tests. WCOBRA/TRAC simulations of these experimental results showed periods in which the churn-turbulent regime was predicted to occur, thus applying the correlations discussed in this section.

Conclusions The interfacial heat transfer correlations for the churn-turbulent regime were originally verified for a limited range of conditions. The simulations of experimental tests with a wide range of scale and conditions using WCOBRA/TRAC show that these correlations may be applied to PWR type geometries and conditions. The reliability of these correlations is reflected in the overall WCOBRA/TRAC code bias and uncertainty for LOCA analysis.

5-2-4 Film/Drop Regime

Model Basis The film/drop regime is assumed to exist when the vapor fraction is greater than the critical vapor fraction for transition to annular flow (α_{crit}). The value of α_{crit} was described in Section 3-2-4, and is given by Equation 3-39.

The correlations for interfacial heat transfer coefficient in the film/drop flow regime are the same as those in the churn-turbulent regime. The difference between the film/drop regime ($h_i A_i$) and the churn-turbulent regime ($h_i A_i$) enters through the interfacial areas A_i of the two regimes. In the churn-turbulent regime, the interfacial area is dominated by the large bubble area. In the film/drop regime, the entrainment rate is high, and the ($h_i A_i$) term due to droplets thus has the greater importance.

Model as Coded For superheated vapor, the interfacial heat transfer factor is calculated as [

$$]^{ac}.$$

For superheated liquid, ($h_i A_i$) is calculated as [

$$]^{ac} \quad (5-45)$$

[
 $]^{ac}.$

The interfacial area used with the Hughmark (1973) correlation $A_{i, film}^*$ is a modification of the film interfacial area and is calculated as [

$]^{ac}.$

For subcooled liquid, the interfacial heat transfer coefficient from the interface to the liquid is calculated as [

$]^{ac} \quad (5-47)$

The quantity $(h_i A_i)$ for subcooled vapor is calculated as

$$(h_i A_i)_{FD, SCV} = h_{i, SCV} A_{i, SCV} \quad (5-48)$$

where $h_{i, SCV}$ is an assumed large constant value given by Equation 5-16 and $A_{i, SCV}$ is given by Equation 5-3.

Scaling Considerations The interfacial heat transfer correlations in the film/drop regime are verified through their use in WCOBRA/TRAC simulations of LOFT, CCTF, SCTF, and UPTF tests reported in Volume 3 of WCAP-12945-P-A of this report. These tests encompassed the range of radial and vertical scales up to that of a full-scale PWR. This regime in WCOBRA/TRAC was also considered by Chow et al. (1989), and no bias relative to scale was found.

Conclusions The interfacial heat transfer correlations for the film/drop regime were originally verified for a limited range of conditions. The simulation of experimental tests using WCOBRA/TRAC demonstrate that these correlations may be applied to PWR type geometries and conditions. The reliability of these correlations is accounted for in the overall WCOBRA/TRAC code bias and uncertainty.

5-2-5 Inverted Annular Regime

Model Basis The inverted annular flow regime is selected when the liquid is subcooled, and the cell contains a heated structure with a surface temperature exceeding $T_{sat} + [\quad]^{ac}$. The continuous liquid in this regime is assumed to be in an annular column separated from the wall by a thin film of vapor.

The interfacial heat transfer coefficient from both continuous liquid and droplets to superheated vapor is based on a correlation by Forslund and Rohsenow (1968). This expression is

$$Nu_d = 2 + 0.55 Re_d^{1/2} Pr_v^{1/3} \quad (5-49)^{(15)}$$

where the Prandtl number is evaluated at the vapor film temperature.

The Forslund-Rohsenow correlation is modified as suggested by Yuen and Chen (1978) to account for the reduction in the drop heat transfer due to evaporation. Yuen and Chen recommend for interfacial heat transfer from drops the expression

$$Nu_d (1+B) = 2 + 0.6 Re_d^{1/2} Pr_v^{1/3} \quad (5-50)^{(1,16)}$$

where the mass transfer number B is defined as

$$B = \frac{H_v - H_f}{H_{fg}} \quad (5-51)$$

For the subcooled continuous liquid and droplets, the interfacial heat transfer coefficient is assumed to be given by

$$h_{i,ve}^* = C \frac{\pi^2}{3} \frac{k_t}{R_d} \quad (5-52)^{(1)}$$

for droplets, and for continuous liquid by [

$$]^{ac} \quad (5-53)^{(1)}$$

with C , assumed to be $C = [\quad]^{ac}$.

For subcooled vapor, a large interfacial heat transfer coefficient is assumed:

$$h_{i,SCV} = 2780 \frac{Btu}{ft^2-s-^{\circ}F} \quad (5-54)$$

Model as Coded Interfacial areas for the inverted annular column and for droplets that may appear were described in Section 3-3-2. Values of $(h_i A_i)$ are calculated in subroutine INTFR and returned to subroutine XSCHEM for use in the solution of the conservation equations.

The $(h_i A_i)$ for superheated vapor is calculated as

$$(h_i A_i)_{IVA,SHV} = h_{i,FR,vl} A_{i,film} + h_{i,FR,ve} A_{i,drop} \quad (5-55)$$

where $h_{i,FR,vl}$ and $h_{i,FR,ve}$ are modified versions of the Forslund-Rohsenow correlation, coded in subroutine INTFR as [

$$]^{ac} \quad (5-56)^{(15,16)}$$

and [

$$]^{ac}.$$

The interfacial areas $A_{i,film}$ and $A_{i,drop}$ are given by Equations 3-51 and 3-52, respectively.

For subcooled liquid, the $(h_i A_i)$ term is calculated by [

$$]^{ac} \quad (5-58)$$

where $h_{i,vl}^*$ is determined from Equation 5-53, $h_{i,ve}^*$ from Equation 5-52, and $h_{it,max}$ from Equation 5-12.

The $(h_i A_i)$ term for subcooled vapor is calculated as

$$(h_i A_i)_{IVA,SCV} = h_{i,SCV} A_{i,SCV} \quad (5-59)$$

where $h_{i,SCV}$ and $A_{i,SCV}$ are calculated by Equations 5-54 and 5-3, respectively.

Although not used in the inverted annular regime, a value of $(h_i A_i)$ for superheated liquid is also calculated. This term is calculated as

$$(h_i A_i)_{IVA,SHL} = 278.0 A_{i,film} + 27.8 A_{i,drop} \quad (5-60)^{(17)}$$

Scaling Considerations The interfacial heat transfer correlations for the inverted annular flow regime are verified through their use in simulations of the FLECHT-SEASET, FLECHT Low Flooding Rate, FLECHT Top Skewed Power, FEBA, and NRU separate effects reflood tests. Each of these were full scale PWR geometries.

Conclusions The key process in the inverted annular regime is condensation to the subcooled liquid $(h_i A_i)_{IVA,SHV}$. Appropriate correlations were selected to represent these terms. The models and correlations for this regime were applied in a large number of separate and integral effects tests. Therefore, the uncertainty in these expressions is accounted for in the overall WCOBRA/TRAC code bias and uncertainty.

5-2-6 Inverted Liquid Slug Regime

Model Basis The inverted liquid slug regime is selected when the liquid is saturated or superheated and the cell contains a heated structure with a surface temperature exceeding $T_{sat} + [\quad]^{\circ}C$. The continuous liquid in this regime is assumed to be in the form of large liquid slugs. Droplets occur through entrainment.

The interfacial heat transfer coefficient from the liquid and droplets interface to superheated vapor in this regime is also estimated using the modified Forslund-Rohsenow (1968) correlation. This correlation was originally developed to determine the interfacial heat transfer coefficient from droplets to superheated vapor and is described in Section 5-2-5.

For superheated liquid, the heat transfer coefficient from the interface to the liquid is assumed to be a constant value of

$$h_{i,vl} = 278.0 \frac{Btu}{ft^2-s-^{\circ}F} \quad (5-61)$$

for continuous liquid and

$$h_{i,ve} = 27.8 \frac{Btu}{ft^2-s-^{\circ}F} \quad (5-62)$$

for drops.

For subcooled vapor, a large interfacial heat transfer coefficient is assumed,

$$h_{i,scv} = 2780 \frac{Btu}{ft^2-s-^{\circ}F} \quad (5-63)$$

Model as Coded Interfacial areas for the inverted liquid slugs and for droplets were described in Section 3-3-3. Values of $(h_i A_i)$ are calculated in subroutine INTFR and returned to subroutine XSCHEM for use in solution of the conservation equations.

The $(h_i A_i)$ for superheated vapor is calculated as

$$(h_i A_i)_{IVS,SHV} = h_{i,FR,vl} A_{i,filn} + h_{i,FR,ve} A_{i,drop} \quad (5-64)$$

where $h_{i,FR,vl}$ and $h_{i,FR,ve}$ are modified versions of the Forslund-Rohsenow (1968) correlation, coded in INTFR as [

$$]^{ac} \quad (5-65)^{(16)}$$

and [

$]^{ac}$.

The interfacial areas $A_{i,filn}$ and $A_{i,drop}$ are given by Equations 3-57 and 3-58, respectively.

For the superheated liquid, the value of $(h_i A_i)$ is calculated from

$$(h_i A_i)_{IVS,SHL} = h_{i,vl} A_{i,filn} + h_{i,ve} A_{i,drop} \quad (5-67)$$

where $h_{i,vl}$ and $h_{i,ve}$ are the constant values given by Equations 5-61 and 5-62.

The $(h_i A_i)$ term for subcooled vapor is calculated as

$$(h_i A_i)_{IVS,SCV} = h_{i,SCV} A_{i,SCV} \quad (5-68)$$

where $h_{i,SCV}$ and $A_{i,SCV}$ are calculated by Equations 5-63 and 5-3, respectively.

Although not used explicitly in the inverted liquid slug regime, a value of $(h_i A_i)$ for subcooled liquid is also calculated. This term is calculated as

$$(h_i A_i)_{IVS,SCL} = \text{minimum} \begin{cases} h_{i,vl}^* A_{i,flm} + h_{i,ve}^* A_{i,drop} \\ h_{il,max} (A_{i,flm} + A_{i,drop}) \end{cases} \quad (5-69)^{(17)}$$

where $h_{i,vl}^*$ is given by Equation 5-53, $h_{i,ve}^*$ by Equation 5-52, and $h_{il,max}$ by Equation 5-12.

Scaling Considerations The interfacial heat transfer correlations for the inverted liquid slug flow regime are verified through their use in simulations of the FLECHT-SEASET, FLECHT Low Flooding Rate, FLECHT Top Skewed Power, FEBA, and NRU separate effects reflood tests. Each of these were full-scale assembly dimensions. Simulations were also performed for the LOFT, CCTF, and SCTF integral effects tests. CCTF and SCTF were full-scale in height and LOFT about one-half scale in height. Thus, the correlations for this regime have been assessed by tests using mainly full scale PWR geometries.

Conclusions The key process in the inverted liquid slug flow regime is evaporation to superheated vapor $(h_i A_i)_{IVS,SHV}$. An appropriate correlation is used to represent this term. The models and correlations for this regime were applied in a large number of separate and integral effects tests. Therefore, the uncertainty in these expressions is accounted for in the overall WCOBRA/TRAC code bias and uncertainty.

5-2-7 Dispersed Droplet Flow Regime

Model Basis The dispersed droplet flow regime occurs when the continuous liquid field becomes completely entrained. Interfacial heat transfer is then due to droplets only.

The interfacial heat transfer coefficient to superheated vapor is given by the [

$$]^{a,c} \quad (5-70)$$

where the mass transfer number B from Yuen and Chen (1978) is

$$B = \frac{H_v - H_f}{H_{fg}} \quad (5-71)$$

For the interfacial heat transfer coefficient to superheated liquid, a constant value is assumed:

$$h_{i,ve} = 27.8 \frac{BTU}{ft^2-s-^{\circ}F} \quad (5-72)$$

The interfacial heat transfer coefficient to subcooled liquid droplets is calculated using the equation by Andersen (1973):

$$h_{i,ve}^* = C \frac{\pi^2}{3} \frac{k_f}{R_d} \quad (5-73)^{(1)}$$

with $C = [\quad]^{a,c}$.

For subcooled vapor a large interfacial heat transfer coefficient is assumed

$$h_{i,SCV} = 2780 \frac{Btu}{ft^2-s-^{\circ}F} \quad (5-74)$$

Model as Coded The quantity $(h_i A_i)$ for the dispersed droplet regime is calculated as follows.

For superheated vapor,

$$(h_i A_i)_{DD,SHV} = h_{i,FR,ve} A_{i,drop} \quad (5-75)$$

For superheated liquid,

$$(h_i A_i)_{DD,SHL} = h_{i,ve} A_{i,drop} \quad (5-76)$$

For subcooled liquid,

$$(h_i A_i)_{DD,SCL} = \text{minimum} \begin{cases} h_{i,ve}^* A_{i,drop} \\ h_{it,max} A_{i,drop} \end{cases} \quad (5-77)$$

and for subcooled vapor,

$$(h_i A_i)_{DD,SCV} = h_{i,SCV} A_{i,SCV} \quad (5-78)$$

where $A_{i,drop}$ is given by Equation 3-74 and $A_{i,SCV}$ by Equation 5-3.

Scaling Considerations The interfacial heat transfer correlations for the dispersed droplet flow regime are verified through their use in simulations of the FLECHT-SEASET, FLECHT Low Flooding Rate, FLECHT Top Skewed Power, FEBA, and NRU separate effects reflood tests, the G-1 and G-2 blowdown tests, and the G-2 refill tests. Each of these were full-scale assembly dimensions. Simulations were also performed for the LOFT, CCTF, and SCTF integral effects tests. CCTF and SCTF were full-scale in height and LOFT about one-half scale. Thus, the correlations for this regime have been assessed by tests using mainly full-scale PWR geometries.

Conclusions The key process in the dispersed droplet flow regime are condensation to the subcooled drops $(h_i A_i)_{DD,SCL}$ and evaporation to superheated vapor $(h_i A_i)_{DD,SHV}$. Appropriate correlations were selected to represent these terms. The models and correlations for this regime were applied in a large number of separate and integral effects tests. Therefore, the uncertainty in these expressions is accounted for in the overall WCOBRA/TRAC code bias and uncertainty.

5-2-8 Falling Film Regime

Model Basis The falling film regime is selected in a cell when the [J^{ac} . Both continuous liquid films and droplets occur.

The correlations used for the interfacial heat transfer coefficients in the falling regime have all been described in previous sections. The modified Forslund-Rohsenow correlation is used for superheated vapor, the Andersen correlation is used for subcooled liquid, and constant values are used for h_i for subcooled vapor and superheated liquid.

Model as Coded In the falling film regime, the $(h_i A_i)$ terms are calculated as follows.
For superheated vapor,

$$(h_i A_i)_{FF,SHV} = h_{i,FR,v} A_{i,film} + h_{i,FR,ve} A_{i,drop} \quad (5-79)$$

For subcooled liquid, [

$$J^{ac} \quad (5-80)$$

For superheated liquid,

$$(h_i A_i)_{FF,SHL} = h_{i,vl} A_{i,film} + h_{i,ve} A_{i,drop} \quad (5-81)$$

and for subcooled vapor,

$$(h_i A_i)_{FF,SCV} = h_{i,SCV} A_{i,SCV} \quad (5-82)$$

where,

$h_{i,FR,vl}$ is given by Equation 5-56,

$h_{i,FR,ve}$ is given by Equation 5-57,

$h_{i,vl}^*$ is given by Equation 5-53,

$h_{i,ve}^*$ is given by Equation 5-52,

$h_{i,vl}$ is given by Equation 5-61,

$h_{i,ve}$ is given by Equation 5-62,

$h_{i,SCV}$ is given by Equation 5-63,

$h_{il,max}$ is given by Equation 5-12,

$A_{i,film}$ is given by Equation 3-61,

$A_{i,drop}$ is given by Equation 3-62,

$A_{i,SCV}$ is given by Equation 5-3.

Scaling Considerations The interfacial heat transfer correlations in the falling film regime are verified through their use in simulations of the G-1 loop and G-2 loop blowdown tests, the G-2 loop refill tests, and the CCTF upper plenum injection tests. Each of these tests were full scale in height. The G-1 and G-2 test bundles contained 448 and 336 rods each, respectively, and the CCTF facility contained 32 rod bundles. Thus, the interfacial heat transfer models for the falling film regime have been tested against data from tests that were full scale in height and varied in scale radially.

Conclusions The key processes in the falling film regime are condensation to the subcooled liquid $(h_i A_i)_{FF,SCL}$ and evaporation to superheated vapor $(h_i A_i)_{FF,SHV}$. Appropriate correlations were selected to represent these terms. The models and correlations for this regime were applied in a large number of separate and integral effects tests. Therefore, the uncertainty in these expressions is accounted for in the overall WCOBRA/TRAC code bias and uncertainty.

5-2-9 Top Deluge Flow Regime

Model Basis The top deluge regime is selected in a cell when the []^{ac}. Both continuous liquid and droplets can occur; however, since entrainment is low, most of the liquid remains in the continuous liquid field. Thus, for interfacial heat transfer, the $(h_i A_i)$ for continuous liquid is of greater importance.

The models and correlations for the top deluge regime are the same as those described previously.

Model as Coded The interfacial heat transfer terms for the top deluge flow regime are coded identically to those for the falling film regime. Thus, for superheated vapor,

$$(h_i A_i)_{TD,SHV} = h_{i,FR,v}^* A_{i,film} + h_{i,FR,ve}^* A_{i,drop} \quad (5-83)$$

For subcooled liquid, [

$$]^{ac} \quad (5-84)$$

For superheated liquid,

$$(h_i A_i)_{TD,SHL} = h_{i,v} A_{i,film} + h_{i,ve} A_{i,drop} \quad (5-85)$$

and for subcooled vapor,

$$(h_i A_i)_{TD,SCV} = h_{i,SCV} A_{i,SCV} \quad (5-86)$$

where,

$h_{i,FR,v}$ is given by Equation 5-56,

$h_{i,FR,ve}$ is given by Equation 5-57,

$h_{i,v}^*$ is given by Equation 5-53,

$h_{i,ve}^*$ is given by Equation 5-52,

$h_{i,v}$ is given by Equation 5-61,

$h_{i,ve}$ is given by Equation 5-62,

$h_{i,SCV}$ is given by Equation 5-63,

$h_{it,max}$ is given by Equation 5-12,

$A_{i, film}$ is given by Equation 3-63,

$A_{i, drop}$ is given by Equation 3-64,

$A_{i, SCV}$ is given by Equation 5-3.

Scaling Considerations The interfacial heat transfer correlations in the top deluge flow regime are verified through their use in simulations of the G-1 loop and G-2 loop blowdown tests, the G-2 loop refill tests, and the CCTF upper plenum injection tests. Each of these tests were full scale in height. The G-1 and G-2 test bundles contained 448 and 336 rods each, respectively, and the CCTF facility contained 32 rod bundles. Thus, the interfacial heat transfer models for the falling film regime have been tested against data from tests that were full scale in height and varied in lateral scale.

Conclusions The key processes for interfacial heat transfer in the top deluge regime are condensation to subcooled liquid $(h_i A_i)_{TD, SCL}$ and evaporation to super heated vapor $(h_i A_i)_{TD, SHV}$. Appropriate correlations were selected to represent these terms. These models and correlations have been applied in the simulations of separate and integral effects tests. Therefore, the uncertainty in these expressions is accounted for in the overall WCOBRA/TRAC code bias and uncertainty.

5-2-10 Effect of Grid Spacers on Interfacial Heat Transfer

Model Basis Spacer grids have an important effect on interfacial heat transfer. Since the grids are unpowered and have a large surface area to volume ratio, they can quench before the fuel rods. If the grid quenches, a liquid film can cover the grid, which creates an additional liquid surface area. This thin liquid film readily evaporates and acts to desuperheat the vapor in a non-equilibrium two-phase droplet flow. Because the grid blocks a portion of the fuel assembly flow area, the velocity of the vapor passing through the grid is higher than velocities nearby in the fuel bundle. As a result the vapor-film relative velocity at the grid is larger, so that a wetted grid has a higher interfacial heat transfer coefficient compared to nearby droplets.

The additional interfacial heat transfer due to a wetted grid is accounted for in WCOBRA/TRAC by an additional $(h_i A_i)$ term which augments the $(h_i A_i)$ term calculated for the droplet flow. Since the grid height is small compared to the height of the momentum cell in which it is placed and the fuel rods are not yet quenched, a continuous liquid film is not formed in the momentum cell by de-entrainment from the droplet field. Thus, mass conservation calculations are unaffected by the assumption that a thin film is assumed to form on the grid. Rather, mass that would form the liquid film is left in the droplet field and the evaporation of this mass is taken into account through an $(h_i A_i)$ term calculated for the wetted grid, $(h_i A_i)_{grid}$. A simple radiation heat transfer model is used to determine if the grid can be wetted. This grid rewet model is described in Section 6-2-10.

[

]^{a,c}.

Since the grid itself is located at $X = 0$, this expression for interfacial heat transfer from the film becomes [

$$]^{a,c} \quad (5-89)^{(19)}$$

In Equation 5-89, the exponent on the [

$$]^{a,c}.$$

The liquid film interfacial area $A_{i,grid}$ is assumed to be equal to the grid metal surface area.

Model as Coded For a grid to rewet, its temperature must be below the rewet temperature, and there must be sufficient liquid in the flow to form a film. Calculations are first performed in subroutine HEAT to determine the grid temperature T_{grid} . A flag to indicate if the grid can rewet, I_{wet} , is passed from HEAT to subroutine INTFR, where the interfacial heat transfer calculations are performed. The value of I_{wet} is [

$$]^{a,c} \quad (5-90)^{(20)}$$

where T_{grid} is the grid temperature. Section 6-2-10 describes the calculation of the grid temperature.

The value of $(h_i A_i)$ is then calculated as [

$$]^{a,c} \quad (5-91)$$

where $h_{i,grid}$ is determined by Equation 5-88 and $A_{i,grid}$ is the grid surface area. The term F_{SPV} is given by [

$$]^{a.c.} \quad (21)$$

Finally, the interfacial heat transfer factor for superheated vapor is augmented by $(h_i A_i)_{grid}$:

$$(h_i A_i)_{fr,SHV} = (h_i A_i)_{fr,SHV}^* + (h_i A_i)_{grid} \quad (5-93)^{(22)}$$

where the flow regime "fr" in this case may be any of the hot wall flow regimes where the void fraction can be greater than []^{a.c.} (23). The term $(h_i A_i)_{fr,SHV}^*$ is the interfacial heat transfer factor calculated for each regime as described in previous sections.

Scaling Considerations The grid model, including the grid interfacial heat transfer augmentation, has been used in WCOBRA/TRAC simulations of FLECHT/SEASET, FLECHT Low Flooding Rate, FLECHT Top-Skewed Power, FEBA, CCTF, and SCTF reflood tests, and the ORNL THTF, G-1 loop, and G-2 loop blowdown tests. The test bundles in these experiments were full scale in height and used prototypic PWR spacer grids, including both mixing vane and non-mixing vane grid types. The grid models were developed based on data for full scale grids.

Conclusions The grid interfacial heat transfer augmentation model has been tested with a large number of simulations using WCOBRA/TRAC, as shown above. The uncertainty and reliability of this model is thus accounted for in the WCOBRA/TRAC overall code bias and uncertainty.

5-2-11 Effect of Noncondensables⁽²⁴⁾

Model Basis The rate of steam condensation is suppressed in the presence of a noncondensable gas such as nitrogen or hydrogen. Numerous experimental studies have demonstrated this effect, including those by Dehbi, Golay, and Kazimi (1991) and Slegers and Seban (1970).

Prediction methods for the extent of condensation suppression for a given concentration of noncondensable gas in the bulk fluid, however, are lacking. The current state-of-the-art in modelling

condensation has not identified a fully reliable means of estimating condensation interfacial heat transfer coefficients for steam in the presence of a noncondensable gas.

Noncondensable gases can arise in a PWR from several sources during a loss-of-coolant accident. As the RCS de-pressurizes, dissolved gas will come out of solution throughout the primary side. During accumulator injection, some of the nitrogen cover gas can be swept into the cold legs and additional nitrogen can flow into the system after most of the accumulator water inventory has been depleted. Air from the containment can be ingested into the RCS at the break during the refill phase of a LOCA. Hydrogen, resulting from cladding oxidation, can also be present in the RCS.

WCOBRA/TRAC provides the user with two methods to model the effects of a noncondensable gas during a LOCA. Each method suppresses condensation in the vessel component through the application of a $[\quad]^{ac}$ to the liquid side ($h_i A_i$) for subcooled liquid and to the vapor side ($h_i A_i$) for subcooled vapor. This section describes each of the noncondensable gas condensation suppression methods in WCOBRA/TRAC.

Method 1: [

$]^{ac}$.

[

$]^{ac}$.

Method 2: [

$]^{ac}$.

Model as Coded The accumulator nitrogen ramp function used in Methods 1 and 2 is: [

$]^{a,c}.$

The containment ramp function for Method 1 is calculated as [

$]^{a,c}.$

For Method 2, the condensation suppression ramp is calculated as: [

$]^{a,c}$ (5-95b)

The ramp suppresses condensation when [$]^{a,c}.$

The noncondensable gas suppression ramps are applied during the calculation of interfacial mass transfer. This is described in Section 5-2-12.

Scaling Considerations The containment and accumulator ramps associated with modelling the effect of a noncondensable gas are used only in a PWR analysis (with the exception of a brief part of the LOFT simulations). Their use do not affect the simulations of the experimental tests that determined the code bias and uncertainty. The possible bias to scale of these models is of no concern.

Conclusions A discussion of the effect of noncondensable gases on the PWR transient and PCT is presented in Section 25-8 of WCAP-12945-P-A. Although the models are simple, simulation results indicate that they provide an adequate approximation of the condensation suppression process. The simplicity of the models are taken into account when estimating the overall PCT.

5-2-12 Vessel Component Interfacial Mass Transfer

Model Basis The vessel component model for interfacial mass transfer is obtained from the energy jump condition by neglecting the mechanical terms and averaging. Wheeler et al. (1986), showed that this yields

$$\Gamma''' = \frac{-q_{il}''' - q_{iv}'''}{\Delta H_{lv}} \quad (5-96)$$

where

$$\Delta H_{lv} = H_g - H_l \text{ for vaporization} \quad (5-96a)$$

$$\Delta H_{lv} = H_v - H_f \text{ for condensation}$$

The interfacial heat transfer for phase k , q_{ik}''' is given by

$$q_{ik}''' = (h_i A_i''') (T_{sat} - T_k) \quad (5-97)$$

where h_i is the interfacial heat transfer coefficient and A_i''' is the average interfacial area per unit volume.

In the vessel component, the vapor generation rate is divided into five components, two for each phase, depending on whether the phase is superheated or subcooled, and one representing boiling at the wall. The total vapor generation rate is given by the combination of these five components.

The interfacial transfer terms associated with each phase when the phases are in disequilibrium were described in the previous sections. One way for nonequilibrium conditions to be created is for the liquid or vapor phase to receive heating or cooling from an external surface. The models used to calculate the heat transfer between the external surface ("wall") and the phases are described in the next section. In nearly all situations, some portion of the total wall heat flux from the wall is considered to flow from the wall directly to the phase. Subsequent heating or cooling of that phase then results from interfacial heat and mass transfer as described in this section.

For most heat transfer regimes, some portion of the total heat flux from the wall is allocated to a term Q_b or $h_{wb} (T_w - T_{sat})$ called the "boiling heat flux." This term then appears as an additive term in the net evaporation rate. The reason for doing this is to more accurately model situations such as subcooled

nucleate boiling. In this heat transfer regime, the bulk fluid is still subcooled, but the liquid layer near the wall has reached saturation. Additional heating of this liquid layer creates bubbles, which then enter the bulk liquid and condense. Use of the boiling term allows vapor to be created via the net evaporation term, even though the liquid is subcooled. Because WCOBRA/TRAC uses only one liquid energy equation, if the wall heat flux were to be allocated only to the liquid, vapor generation would not occur until the bulk fluid became saturated and slightly superheated.

A similar situation exists for film boiling situations in which the bulk liquid is subcooled. The vapor generation occurs at the interface between the liquid and the thin vapor film surrounding the wall as heat is conducted across the vapor film. Although the vapor film is superheated, most of the heat passes directly to the liquid layer. As more vapor is created, the film thickens and the hot wall begins to superheat the vapor, which then loses its superheat by interfacial heat transfer.

Transition boiling is a situation in which part of the wall is transferring directly to the vapor, and part of the wall is transferring directly to the liquid, usually at a high heat flux rate. Under these conditions, it is more numerically stable to pass the wall heat directly to the boiling term, rather than allow the liquid to superheat and then evaporate.

The way in which the total heat flux from the heat transfer models is split up among Q_{wt} , Q_{wv} , and Q_b is described for each heat transfer regime in Section 6.

The net vapor generation rate is given as the sum of four interfacial components, given below, and the boiling term.

Superheated Vapor (SHV),

$$\Gamma_{SHV}^{///} = \frac{(h_i A_i^{///})_{fr,SHV} (H_v - H_g)}{C_{pv} (H_g - H_l)} \quad (5-98)$$

Superheated Liquid (SHL),

$$\Gamma_{SHL}^{///} = \frac{(h_i A_i^{///})_{fr,SHL} (H_l - H_f)}{C_{pl} (H_g - H_l)} \quad (5-99)$$

Subcooled Liquid (SCL),

$$\Gamma_{SCL}^{///} = \frac{(h_i A_i^{///})_{fr,SCL} (H_l - H_f)}{C_{pl} (H_v - H_f)} \quad (5-100)$$

Subcooled Vapor (SCV),

$$\Gamma_{SCV}''' = \frac{(h_i A_i)'''_{fr,SCV} (H_v - H_g)}{C_{pv} (H_v - H_g)} \quad (5-101)$$

where " fr " denotes the flow regime dependence.

The total vapor generation rate is given by

$$\Gamma''' = (\Gamma_{SHV}''' + \Gamma_{SHL}''') + (\Gamma_{SCL}''' + \Gamma_{SCV}''') + Q_b''' / (H_g - H_l) \quad (5-102)$$

which is seen to be the sum of the evaporative and condensive contributions, plus the boiling term.

The fraction η of the total vapor generation coming from the entrained liquid is given by [

$$J^{ac} \quad (5-103)^{(25)}$$

for evaporation, and for condensation by [

$$J^{ac} \quad (5-104)^{(25)}$$

Model as Coded Calculations are first performed as described in Sections 5-2-1 through 5-2-9 to determine $(h_i A_i)$ for each flow regime and fluid condition (SHV, SHL, SCV, SCL). If there is a grid, the $(h_i A_i)$ value for superheated vapor is augmented by $(h_i A_i)_{grid}$ as described in Section 5-2-10. The calculation of the interfacial mass transfer is performed next in subroutine XSCHM.

It is convenient to discuss the interfacial heat transfer factors $(h_i A_i)$ for this calculation in terms of the array variable representing $(h_i A_i)$ at mesh cell (I,J).

Thus, for any flow regime "*fr*" let

$$HASHV(I,J) = (h_i A_i)_{fr,SHV} \quad (5-105)$$

$$HASHL(I,J) = (h_i A_i)_{fr,SHL} \quad (5-106)$$

$$HASCV(I,J) = (h_i A_i)_{fr,SCV} \quad (5-107)$$

$$HASCL(I,J) = (h_i A_i)_{fr,SCL} \quad (5-108)$$

A temporary interfacial area is defined as [

$$J^{ac} \quad (5-109)^{(26)}$$

where A_x is the flow area in cell (I,J) and ΔX is the cell height.

Finally, the interfacial heat transfer factors for the cell (I,J) are calculated as [

$$J^{ac} \quad (5-113)^{(27)}$$

The individual components of the interfacial mass transfer are calculated as [

$$J^{ac} \quad (5-114)$$

[

]^{ac} (5-117)

where Q_b^* is defined by Equation 6-180.

The condensation suppression ramps F_{ACC} and F_{CONT} are calculated as described in Section 5-2-11.

The numerical ramps F_{CGL} , F_{CGV} , and F_{DUM3} are applied to avoid sharp discontinuities in Γ''' as the flow approaches single-phase. They are given by [

]^{ac} (5-120)^{(29)}

Finally, the interfacial mass transfer is calculated as the sum of the evaporative and condensive terms:

$$\Gamma''' = (\Gamma'''_{SHV} + \Gamma'''_{SHL}) + (\Gamma'''_{SCL} + \Gamma'''_{SCV}) \quad (5-121)$$

Scaling Considerations The vessel model for interfacial mass transfer is not dependent on scale.

Conclusions The model for interfacial mass transfer is based on conservation principles and is approximated only where the flow approaches single-phase. Nearly all of the simulations reported in Volumes 2 and 3 of WCAP-12945-P-A include two-phase flow and some degree of thermal nonequilibrium. As such, the interfacial mass transfer model in WCOBRA/TRAC has been verified against experimental data. The inaccuracy introduced by the numerical ramps is thus accounted for in the overall code bias and uncertainty.

5-3 ONE-DIMENSIONAL COMPONENT INTERFACIAL HEAT AND MASS TRANSFER MODELS

5-3-1 Bubbly Flow Regime

Model Basis As discussed in Section 3-4-2, the bubbly flow regime is assumed in one-dimensional components when the void fraction is less than []^{ac} for mass fluxes greater than 2700 kg/m²-s. The interfacial heat transfer coefficient for the bubbly flow regime is estimated as follows.

For subcooled liquid, the interfacial heat transfer coefficient is calculated assuming a constant Stanton number: [

$$]^{ac} \quad (5-122)$$

A constant Stanton number approach has been suggested by several investigators for predicting the condensation rates on highly turbulent subcooled liquid jets. A comprehensive review of these studies was presented by Theofanous (1979). The Theofanous model also contains a correction factor term based on the jet shape. For highly turbulent liquid jets, the Stanton number is given by

$$St = 0.02 \left(\frac{L}{D} \right)^{-1/2} \quad (5-123)$$

where (L/D) is the jet length to diameter ratio. A comparison of Equation 5-123 with experimental results is shown in Figure 5-3. [

] ^{ac}. In WCOBRA/TRAC then, the Stanton number becomes, [

$$]^{ac} \quad (5-124)$$

For superheated liquid, the interfacial heat transfer coefficient used is the maximum calculated by the Lee-Ryley correlation (1968) and the bubble growth model of Plesset and Zwick (1954).

The subcooled model does not have a flow regime dependent interfacial area. Instead it uses the wall surface area in the cell. This is likely to underestimate the interfacial area at low void fractions.⁽³⁰⁾

The Lee-Ryley correlation in its original form is given by Equation 5-14. In the one-dimensional components, the Lee-Ryley correlation is modified and given by

$$h_{il,SHL} = \frac{k_l}{D_b} \left[2.0 + 0.74 Re_b^{1/2} \right] \quad (5-125)^{(31)}$$

where:

$$Re_b = \frac{\rho_l U_r D_b}{\mu_l} \quad (5-126)$$

These expressions differ from the original Lee-Ryley (1968) correlation in that the vapor properties are replaced by liquid properties, and the liquid Prandtl number is assumed to be unity. In effect, the bubbles are assumed to behave as spheres.

The second correlation used is based on the bubble growth model of Plesset and Zwick (1954). It is assumed that heat transfer from the liquid is conduction limited and that all of the heat goes into vapor generation. The Plesset and Zwick model for WCOBRA/TRAC one-dimensional components is coded as

$$h_{il,SHL}^* = \left(\frac{k_l}{D_b} \right) \frac{12}{\pi} (T_l - T_{sat}) \frac{\rho_l C_{pf}}{\rho_v (H_v - H_l)} \quad (5-127)^{(32,33)}$$

A multiplier is used with this expression to drive the fluid towards saturation.⁽³³⁾

For superheated vapor, the vapor side interfacial heat transfer coefficient assumes a constant Nusselt number of []^{a,c}, and the interfacial heat transfer coefficient becomes: [

$$]^{a,c} \quad (5-128)^{(34)}$$

For subcooled vapor, the interfacial heat transfer coefficient also assumes a constant Nusselt number of []^{a,c} and, [

$$]^{a,c} \quad (5-129)^{(33,34)}$$

A multiplier is used to drive the subcooled vapor towards saturation.⁽³³⁾

Model as Coded Calculations of the interfacial heat transfer coefficients and the interfacial areas are performed in subroutine DF1DI for fully implicit components and in subroutine DF1DS for semi-implicit components. The liquid side heat transfer factor ALV_{bubbly} and the vapor side heat transfer factor $CHTI_{bubbly}$ are calculated as follows:

For subcooled liquid, the liquid side interfacial heat transfer factor is calculated as [

$$]^{a,c} \quad (5-130)^{(35)}$$

where A_w is the wall surface area, and $h_{it,max}$ is the diffusion limited interfacial heat transfer coefficient given by Equation 5-12.

For superheated liquid, the interfacial heat transfer factor is calculated as [

$$]^{a,c} \quad (5-131)^{(35)}$$

where $h_{it,SHL}$ and $h_{it,SHL}^*$ are given by Equations 5-125 and 5-127, respectively, and the interfacial area $A_{i,bubbly}$ is given by Equation 3-81.

The multiplier F_{SHL} is a function of the liquid superheating and is used to drive the liquid phase towards saturation. This term is calculated as: [

$$]^{a,c} \quad (5-132)$$

For superheated vapor, $CHTI$ is calculated as

$$CHTI_{bubbly,SHV} = h_{i,SHV} A_{i,bubbly} \quad (5-133)$$

where $h_{i,SHV}$ is a constant given by Equation 5-128.

For subcooled vapor, $CHTI$ is calculated as [

$$]^{ac} \quad (5-134)^{(35)}$$

The multiplier F_{scv} is a function of the vapor subcooling and is used to drive the vapor phase towards saturation. This term is calculated as: [

$$]^{ac} \quad (5-135)$$

Scaling Considerations WCOBRA/TRAC simulations of the Westinghouse 1/3-scale steam/water mixing tests and the UPTF full-scale hot leg steam/water mixing test have been performed and results have been compared to experimental data. The WCOBRA/TRAC model of these facilities was composed of one-dimensional components. The results of these simulations did not indicate a dependency on scale.

Conclusions The models and correlations for the bubbly flow regime have been verified through WCOBRA/TRAC simulations of the Westinghouse 1/3-scale steam/water mixing tests, the full-scale UPTF steam/water mixing test, and in the loop components of the LOFT and CCTF integral tests. The uncertainty and reliability of these models is accounted for in the overall WCOBRA/TRAC code bias and uncertainty.

5-3-2 Slug Flow Regime

Model Basis When the cell void fraction is between []^{ac}, and the average mass flux is less than $2000 \text{ kg/m}^2\text{-s}$, the slug flow regime is assumed. When the mass flux is between 2000 and $2700 \text{ kg/m}^2\text{-s}$, the flow is assumed to be in transition between slug and bubbly flow. In both the slug and slug and bubbly transition, bubbles and slugs are assumed to coexist. After calculating the interfacial heat transfer areas and the vapor-side and liquid side interfacial heat transfer coefficients, the heat transfer factors for slug and bubbly/slug transition flows are calculated as

$$ALV = h_{i,bubbly} A_{i,bubbly} + h_{i,slug} A_{i,slug} \quad (5-136)$$

and

$$CHTI = h_{iv,bubbly} A_{i,bubbly} + h_{iv,slug} A_{i,slug} \quad (5-137)$$

For both subcooled and superheated liquids, the interfacial heat transfer coefficient for the slug portion of the flow field is calculated assuming a constant Stanton number of [

$$]^{a,c} \quad (5-138)^{(36)}$$

For superheated and subcooled vapor bubbles, a constant Nusselt number is assumed [

$$]^{a,c} \quad (5-139)$$

and for superheated and subcooled vapor slugs, [

$$]^{a,c} \quad (5-140)$$

which is the same as that used for bubbly flow.

Model as Coded For the slug and slug/bubbly transition flow, calculations are first performed to determine the interfacial area and heat transfer coefficients for bubbly flow. Values of ALV and $CHTI$ for the slug flow regime are then calculated as follows.

For subcooled liquid, ALV is calculated in the same way as it was for bubbly flow: [

$$]^{a,c} \quad (5-141)^{(36,37)}$$

where A_w is the wall surface area and $h_{it,max}$ is given by Equation 5-12.

For superheated liquid, ALV is calculated as [

$$]^{a,c} \quad (5-142)^{(36,37,38)}$$

where $ALV_{bubbly,SHL}$ is given by Equation 5-131, $h_{it,slug}$ by Equation 5-138, $A_{i,slug}$ by Equation 3-85b, and F_{SHL} by Equation 5-132.

For superheated vapor, $CHTI$ is calculated as

$$CHTI_{slug,SHV} = h_{iv,bubbly} A_{i,bubbly} + h_{iv,slug} A_{i,slug} \quad (5-143)$$

where the interfacial areas $A_{i,bubbly}$ and $A_{i,slug}$ are given by Equations 3-85 and 3-85b, respectively, and the heat transfer coefficients are given by Equations 5-139 and 5-140.

For subcooled vapor, $CHTI$ is calculated as [

$$]^{a,c} \quad (5-144)$$

where $h_{iv,slug}$ is given by Equation 5-140 and the interfacial areas by Equations 3-85 and 3-85b. The multiplier F_{SCV} is given by Equation 5-135.

Scaling Considerations WCOBRA/TRAC simulations of the Westinghouse 1/3-scale steam/water mixing tests and the UPTF full-scale hot leg steam/water mixing test have been performed and results have been compared to experimental data. The WCOBRA/TRAC model of these facilities was composed of one-dimensional components, and the slug flow regime was predicted to have occurred. The results of these simulations did not indicate a dependency on scale. This implies that the models used for the slug flow regime are not strongly dependent on scale.

Conclusions The models and correlations for the slug flow regime have been verified through WCOBRA/TRAC simulations of the Westinghouse 1/3-scale steam/water mixing tests, the full-scale UPTF steam/water mixing test, and in the loop components of the LOFT and CCTF integral tests. The uncertainty and reliability of these models is accounted for in the overall WCOBRA/TRAC code bias and uncertainty.

5-3-3 Churn Flow Regime

Model Basis The churn flow regime is assumed when [$]^{a,c}$. This regime is modelled as a simple transition between the bubbly or slug and annular-mist flow regimes. Interfacial areas and heat transfer coefficients are calculated for the slug and annular-mist flow regimes, and then values for the churn regime are calculated using the weighting factor α^* , given by Equation 3-88 described in Section 3-4-4.

Model as Coded The values of ALV and $CHTI$ for the churn flow regime are coded as follows: [

$$]^{a,c} \quad (5-145)^{(37)}$$

where A_w is the wall surface area, and $h_{it,max}$ is given by Equation 5-12.

For superheated liquid, [

$$]^{a,c} \quad (5-146)$$

where, α^* is given by Equation 3-88, and

$$ALV_{am} = ALV_{film} + ALV_{mist} \quad (5-147)$$

$$ALV_{bs} = ALV_{bubbly,SHL} + h_{it,slug} A_{i,slug} \quad (5-148)$$

The terms $ALV_{bubbly,SHL}$, $h_{it,slug}$, and $A_{i,slug}$ are given by Equations 5-131, 5-138, and 3-85b. Terms for the annular-mist regime are described in the next section.

For superheated vapor, [

$$]^{a,c} \quad (5-149)$$

where,

$$CHTI_{bs} = h_{iv,bubbly} A_{i,bubbly} + h_{iv,slug} A_{i,slug} \quad (5-150)$$

and,

$$CHTI_{am} = CHTI_{film} + CHTI_{mist} \quad (5-151)$$

The terms $CHTI_{film}$ and $CHTI_{mist}$ are described in the next section.

For subcooled vapor, [

$$]^{a,c} \quad (5-152)$$

Scaling Considerations WCOBRA/TRAC simulations of the Westinghouse 1/3-scale steam/water mixing tests and the UPTF full-scale hot leg steam/water mixing test have been performed and results have been compared to experimental data. The WCOBRA/TRAC model of these facilities was

composed of one-dimensional components, and the churn flow regime was predicted to have occurred. The results of these simulations did not indicate a dependency on scale. This implies that the models used for the churn flow regime are not strongly dependent on scale.

Conclusions The models and correlations for the churn flow regime have been verified through WCOBRA/TRAC simulations of the Westinghouse 1/3-scale steam/water mixing tests, the full-scale UPTF steam/water mixing test, and in the loop components of the LOFT and CCTF integral tests. The uncertainty and reliability of these models is accounted for in the overall WCOBRA/TRAC code bias and uncertainty.

5-3-4 Annular-Mist Flow Regime

Model Basis The annular mist flow regime is assumed when []^{a,c}. Both a liquid film and droplets may exist at the same time. Entrainment determines the amount of liquid in each field. Interfacial heat transfer terms *ALV* and *CHTI* are calculated separately for each field.

The interfacial heat transfer coefficient for subcooled liquid (both film and drops) is given by: [

$$]^{a,c} \quad (5-153)$$

For superheated liquid droplets, the interfacial heat transfer coefficient is

$$h_{il,mist} = \frac{Ck_l}{D_l} \quad (5-154)$$

where the constant *C* has been set to the value []^{a,c}, which implies that the thermal boundary layer in the drops is approximately one-thousandth of the drop diameter.⁽³⁸⁾

For superheated liquid films, [

$$]^{a,c} \quad (5-155)^{(38)}$$

The interfacial heat transfer coefficient from films to superheated vapor is calculated from [

$$]^{a,c} \quad (5-156)$$

From mist to superheated vapor, the Lee-Ryley (1968) correlation is used:

$$h_{iv,mist} = \frac{k_v}{D_d} \left[2 + 0.74 Re_v^{1/2} Pr_v^{1/3} \right] \quad (5-157)$$

Model as Coded For the annular-mist flow regime, calculations for *ALV* and *CHTI* are performed as follows.

For subcooled liquid, *ALV* is calculated as [

$$]^{ac} \quad (5-158)^{(37,39)}$$

where A_w is the wall surface area, and $h_{it,max}$ is given by Equation 5-12.

For superheated liquid, *ALV* is calculated as [

$$]^{ac} \quad (5-159)^{(39)}$$

where,

$$ALV_{am,film} = h_{it,film} A_{it,film} F_{SHL} \quad (5-160)$$

[

$$]^{ac} \quad (5-161)^{(39)}$$

In these expressions, $h_{it,mist}$ and $h_{it,film}$ are given by Equations 5-154 and 5-155, while the interfacial areas are given by Equations 3-92 and 3-97 respectively, and F_{SHL} is given by Equation 5-132.

For superheated vapor,

$$CHTI_{am,SHV} = h_{iv,mist} A_{iv,mist} + h_{iv,film} A_{iv,film} \quad (5-162)$$

where $h_{iv,mist}$ is given by Equation 5-157 and $h_{iv,film}$ by Equation 5-156. $A_{i,film}$ and $A_{i,mist}$ are given by Equations 3-92 and 3-97.

For subcooled vapor, the interfacial heat transfer coefficients $h_{iv,film}$ and $h_{iv,mist}$ are augmented by a factor to provide large values with high vapor subcooling. The interfacial heat transfer factor for subcooled vapor is calculated as [

$$]^{ac} \quad (5-163)^{(39)}$$

where $h_{iv,film}$ and $h_{iv,mist}$ are given by Equations 5-156 and 5-157, and F_{SCV} is given by Equation 5-135.

Scaling Considerations WCOBRA/TRAC simulations of the Westinghouse 1/3-scale steam/water mixing tests and the UPTF full-scale hot leg steam/water mixing test have been performed and results have been compared to experimental data. The WCOBRA/TRAC model of these facilities was composed of one-dimensional components, and the annular-mist flow regime was predicted to have occurred. The results of these simulations did not indicate a dependency on scale.

This implies that the models used for the annular-mist regime are not strongly dependent on scale.

Conclusions The models and correlations for the annular-mist flow regime have been verified through WCOBRA/TRAC simulations of the Westinghouse 1/3-scale steam/water mixing tests, the full-scale UPTF steam/water mixing test, and in the loop components of the LOFT and CCTF integral tests. The uncertainty and reliability of these models is accounted for in the overall WCOBRA/TRAC code bias and uncertainty.

5-3-5 Effect of Noncondensables

Model Basis The rate of steam condensation is suppressed in the presence of a noncondensable gas such as nitrogen or hydrogen. WCOBRA/TRAC accounts for this effect in the one-dimensional components by simple multipliers applied to condensation interfacial heat transfer coefficients. WCOBRA/TRAC provides the user with two methods to model the effects of noncondensable gas during a LOCA. These methods were described in Section 5-2-11. Additional assessment of the effect of noncondensables is provided in Section 25-8 of WCAP-12945-P-A.

Model as Coded The numerical ramp functions used in the one-dimensional components values for F_{ACC} and F_{CONT} are the same as those given by Equations 5-94 and 5-95a for Method 1. For Method 2, the value of F_{CONT} is calculated as [

]^{a,c}.

The interfacial heat transfer coefficients are then adjusted if $T_l < T_{sat}$ as

$$ALV_{NC} = F_{CONT} F_{ACC} ALV_{fr} \quad (5-165)$$

$$CHTI_{NC} = F_{CONT} F_{ACC} CHTI_{fr} \quad (5-166)$$

where ALV_{fr} and $CHTI_{fr}$ are the liquid side and vapor side interfacial heat transfer factors without noncondensables as described in Sections 5-3-1 through 5-3-4.

Scaling Considerations The containment and accumulator ramps associated with modelling the effect of a noncondensable gas are used only in a PWR analysis (with the exception of a brief part of the LOFT simulations). Their use does not affect the simulations of the experimental tests that determined the code bias and uncertainty. The possible bias to scale of these models is of no concern.

Conclusions A discussion on the use of the accumulator model and application of the condensation suppression ramps to account for the effect of noncondensable gases on the PWR transient and PCT is presented in Sections 16-2 and 25-8 of WCAP-12945-P-A. Although the models are simple, simulation results indicate that they provide an adequate approximation of the condensation suppression process. The simplicity of the models are taken into account when estimating the overall PCT.

5-3-6 One-Dimensional Component Interfacial Mass Transfer

Model Basis The interfacial mass transfer rate is calculated in WCOBRA/TRAC one-dimensional components after the interfacial heat transfer factors have been determined. The interfacial heat transfer rate is obtained by combining the volume averaged liquid side and vapor side heat transfer rates given as:

$$q_{il}''' = ALV \left(\frac{T_{sat} - T_l}{V_C} \right) \quad (5-167)$$

and

$$q_{iv}''' = CHTI \left(\frac{T_{sat} - T_v}{V_C} \right) \quad (5-168)$$

The interfacial mass transfer rate is determined using a simple thermal energy jump condition where the interfacial heat transfer factors for each flow regime are determined as described in Sections 5-3-1 through 5-3-5.

The interfacial heat transfer is given by

$$q_{it} = ALV (T_{sat} - T_l) \quad (5-169)$$

$$q_{iv} = CHTI (T_{sat} - T_v) \quad (5-170)$$

and the interfacial mass transfer is

$$\Gamma'' = \frac{-q_{it} - q_{iv}}{H_{fg}} \quad (5-171)$$

where a positive quantity represents vapor generation.

Model As Coded The value of *ALV* and *CHTI* used depends on the fluid superheating and subcooling. That is,

$$ALV = \begin{cases} ALV_{fr,SHL} & \text{if } T_l > T_{sat} \\ ALV_{fr,SCL} & \text{if } T_l < T_{sat} \end{cases} \quad (5-172)$$

and

$$CHTI = \begin{cases} CHTI_{fr,SHV} & \text{if } T_v > T_{sat} \\ CHTI_{fr,SCV} & \text{if } T_v < T_{sat} \end{cases} \quad (5-173)$$

where the interfacial heat transfer factors for each flow regime "*fr*" are determined as described in Sections 5-3-1 through 5-3-5. Then, the interfacial heat transfer is calculated as (in the coding, the sign convention is reversed):

$$q_{it} = F_0 \frac{\alpha(1-\alpha)}{\alpha_0(1-\alpha_0)} ALV(T_l - T_{sat}) \quad (5-174)$$

$$q_{iv} = \frac{\alpha(1-\alpha)}{\alpha_0(1-\alpha_0)} CHTI(T_v - T_{sat}) \quad (5-175)$$

and finally,

$$\Gamma''' = \frac{q_{it} + q_{iv}}{H_{fg}} \quad (5-176)$$

The terms F_0 and α_0 are defined as [

$$]^{ac} \quad (5-177)$$

and [

$$]^{ac} \quad (5-178)$$

to provide implicit ramping as the fluid approaches single-phase conditions.

Scaling Considerations The model for interfacial mass transfer in WCOBRA/TRAC one-dimensional components is scale independent.

Conclusions The model for interfacial mass transfer has been used in WCOBRA/TRAC simulations of LOFT, CCTF, SCTF, and UPTF. Any uncertainty in this model is thus accounted for in the overall WCOBRA/TRAC code bias and uncertainty.

5-4 REFERENCES

Andersen, J. G. M., 1973, "REMI/HEAT COOL, a Model for Evaluation of Core Heat Up and Emergency Core Spray Cooling System Performance for Light Water Cooled Nuclear Power Reactors," Report 296, RISO National Lab Denmark.

Asaka, H., Murao, Y., and Kukita, Y., 1989, "Assessment of TRAC-PF1 Condensation Heat Transfer Model for Analysis of ECC Water Injection Transients," J. Nuclear Sci. Tech., 26 (11), pp. 1045-1057.

| Bajorek, S. M., et al., 1998, "Code Qualification Document for Best Estimate LOCA Analysis,"
| WCAP-12945-P-A, Volume 1, Revision 2, and Volumes 2 through 5, Revision 1, and WCAP-14747
| (Non-Proprietary).

Chow, S. K., et al., 1989, "Assessment of Scaling Uncertainties for PWR Plant Large-Break LOCA Analysis," EPRI NP-6602.

Colburn, A. P., 1933, "A Method of Correlating Forced Convection Heat Transfer Data and a Comparison With Fluid Friction," Trans Am Inst Chem Eng, Vol. 29, pp. 174-210.

Collier, J. G., 1981, Convective Boiling and Condensation, McGraw Hill, New York, pp. 118-121.

Dehbi, A. A., Golay, M. W., and Kazimi, M. S., 1991, "The Effects of Noncondensable Gases on Steam Condensation Under Turbulent Natural Convection Conditions," Rpt. No. MIT-ANP-TR-004, Dept. of Nucl. Engr., MIT.

Dimenna, R. A., et al., 1988, "RELAP5/MOD2 Models and Correlations," NUREG/CR-5194 EGG-2531.

Dittus, F. W., and Boelter, L. M. K., 1930, "Heat Transfer in Automobile Radiators of the Tubular Type," University of California Engineering Publications.

Forslund, R. P., and Rohsenow, W. M., 1968, "Dispersed Flow Film Boiling," J. Heat Transfer, Vol. 87, pp. 399-407.

Hughmark, G. A., 1973, "Film Thickness Entrainment and Pressure Drop in Upward Annular and Dispersed Flow," AIChE J., Vol. 19, pp. 1062-1065.

Lee, K., and Ryley, D. J., 1968, "The Evaporation of Water Droplets in Superheated Steam," Trans A.S.M.E. J Heat Transfer, Vol. 90, pp. 445-451.

Liles, D. R., et al., 1988, "TRAC-PF1/MOD1 Correlations and Models," NUREG/CR-5069, Los Alamos Report, LA-11208-MS.

Plesset, M. S. and Zwick, S. A., 1954, "The Growth of Vapor Bubbles in Superheated Liquids," J App Phys, Vol. 25, pp. 493-500.

Rowe, P. N., Claxton, K. T., and Lewis, J. B., 1965, "Heat and Mass Transfer from a Single Sphere in an Extensive Flowing Fluid," Trans. Instn. Chem. Engrs., 43, T14-T31.

Slegers, L. and Seban, R. A., 1970, "Laminar Film Condensation of Steam Containing Small Concentrations of Air," Int. J. Heat Mass Trans., Vol. 13, pp. 1941-1947.

Theofanous, T. G., 1979, "Modelling of Basic Condensation Processes," Presented at WRSR Workshop on Condensation, Silver Springs MD.

Thurgood, M. J., et al., 1983, "COBRA/TRAC-A Thermal-Hydraulics Code for Transient Analysis of Nuclear Reactor Vessels and Primary Coolant Systems, Development Assessment and Data Comparisons," Vol. 4, NUREG/CR-3046, PNL-4385.

Wallis, G. B., 1968, "Use of the Reynolds Flux Concept for Analyzing One-Dimensional Two-phase Flow, Part I, Derivation and Verification of Basic Analytical Techniques," Int. J. Heat Mass Transfer, Vol. II, pp. 445-458.

Wheeler, C. L., et al., 1986, "COBRA-NC: A Thermal-Hydraulic Code for Transient Analysis of Nuclear Reactor Components," Vol. 1, NUREG/CR-3262, PNL-4710.

Yao, S. C., Hochreiter, L. E., and Leech, J. J., 1982, "Heat Transfer Augmentation in Rod Bundles Near Grid Spacers," J. Heat Transfer, Vol. 104, pp. 76-81.

Young, M. Y., et al., 1984, "BART-A1: A Computer Code for Best Estimate Analysis of Reflood Transients," WCAP-9561-P/A.

Yuen, M. C., and Chen, L. W., 1978, "Heat-Transfer Measurements of Evaporating Liquid Droplets," Int J Heat and Mass Transfer, Vol. 21, pp. 537-542.

5-5 RAI LISTING

1. RAI1-111
2. RAI1-112
3. RAI1-113
4. RAI1-114
5. RAI1-115 (refers to WCAP-12945, Rev. 1, pages 5-9, 5-14, and 5-18; now pages 5-6, 5-9, and 5-12)
6. RAI1-116
7. RAI1-117
8. RAI1-118
9. RAI1-119
10. RAI1-120
11. RAI1-121
12. RAI1-122
13. RAI1-123 (refers to WCAP-12945, Rev. 1, page 5-13; now page 5-8)
14. RAI1-124
15. RAI1-125
16. RAI1-126
17. RAI1-127
18. RAI1-128
19. RAI1-129
20. RAI1-130
21. RAI1-131 (refers to WCAP-12945, Rev. 1, page 5-37; now page 5-24)
22. RAI1-132

- | 23. RAI1-133 (refers to WCAP-12945, Rev. 1, page 5-37; now page 5-24)
- 24. RAI1-134
- 25. RAI1-135
- 26. RAI1-136
- 27. RAI1-137
- 28. RAI1-138
- 29. RAI1-139
- | 30. RAI1-140 (refers to WCAP-12945, Rev. 1, page 5-49; now page 5-33)
- 31. RAI1-141
- 32. RAI1-142
- | 33. RAI1-143 (refers to WCAP-12945, Rev. 1, pages 5-50 and 5-51; now pages 5-33 and 5-34)
- 34. RAI1-144
- 35. RAI1-145
- | 36. RAI1-146 (refers to WCAP-12945, Rev. 1, page 5-54; now page 5-36)
- 37. RAI1-147
- 38. RAI1-148
- 39. RAI1-149
- 40. RAI1-150
- 41. MOD7A Report, located after RAI2-69
- 42. RAI1-28

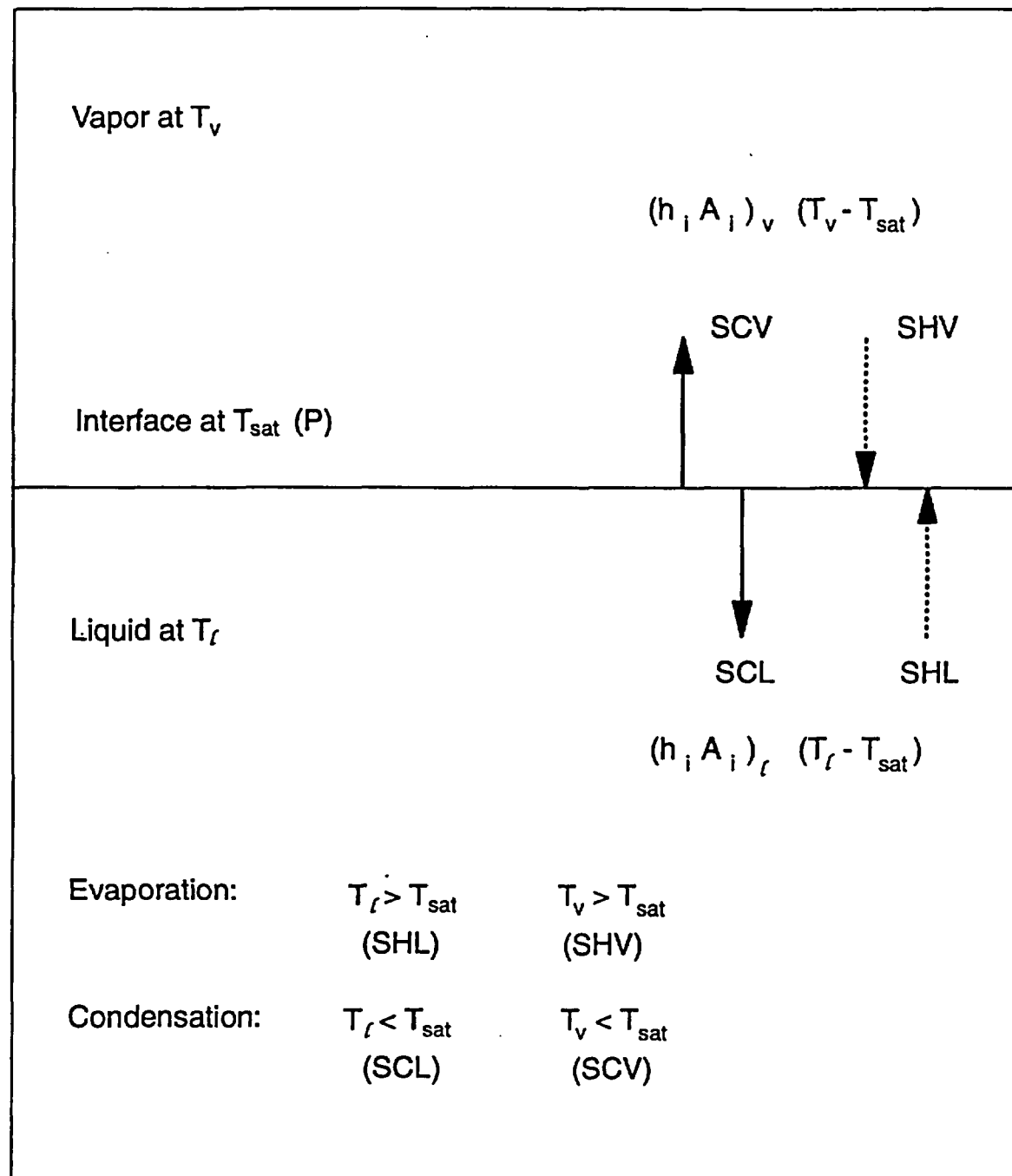


Figure 5-1. Description of Interfacial Heat Transfer⁽⁴⁰⁾

Figure 5-2. Large Void Fraction Gradient Ramp for Subcooled Liquid Interfacial Area

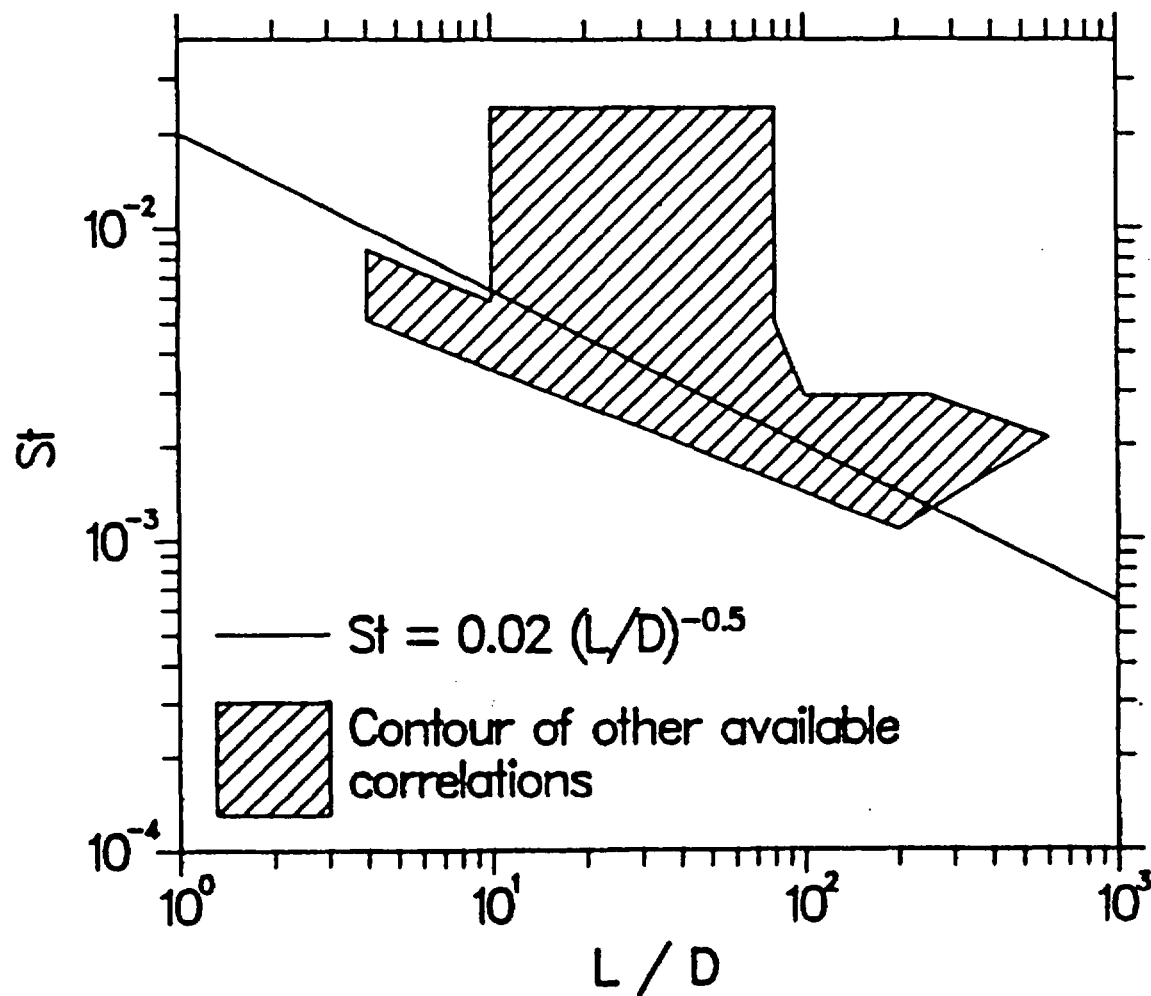


Figure 5-3. Comparison of the Theofanous (1979) Interfacial Heat Transfer Correlation to Others (Liles et al., 1988)

6 WCOBRA/TRAC WALL HEAT TRANSFER MODELS

6-1 INTRODUCTION

This section describes the wall to fluid heat transfer models in WCOBRA/TRAC. These models and correlations determine the temperature response of the fuel, cladding, and structural components of a PWR during normal operations and transients. Separate heat transfer packages are used for the vessel (COBRA/TF) and one-dimensional (TRAC-PD2) components. In general, the two packages are similar for pre-CHF heat transfer. For post-CHF heat transfer, the vessel component contains models that are more refined. This is due to the intended application of each package. The vessel component heat transfer package is used in the core and reactor vessel, where post-CHF heat transfer and dispersed droplet film boiling in particular are expected to be important. Other RCS structures such as the loop piping, pumps, and steam generators utilize the one-dimensional component heat transfer package. Post-CHF heat transfer is much less common in these components and does not require the same amount of detail as the vessel.

For both the vessel and one-dimensional components, the heat transfer calculations are performed at the beginning of each time step before the hydrodynamic solution. The heat transfer coefficients based on the previous time step fluid conditions are used to advance the conduction solution in the affected material structures. Heat release rates are explicitly coupled to the hydrodynamic solution as source terms in the fluid energy equation. The coupling of the heat transfer rate to the fluid energy equation is described in Section 6-2-11 for the vessel component and in Section 6-3-11 for one-dimensional components.

6-2 VESSEL COMPONENT WALL HEAT TRANSFER MODELS

The vessel heat transfer package consists of a library of heat transfer correlations and the selection logic to determine which correlation is appropriate for a given set of hydrodynamic conditions. The heat transfer correlations and selection logic produce a continuous boiling curve, as shown in Figure 6-1. The heat transfer regime selection logic is shown in Figure 6-2. The following list gives the heat transfer regimes used in the WCOBRA/TRAC vessel component heat transfer package.

- | | |
|--------|--------------------------------------|
| Mode 1 | Single-phase liquid convection (SPL) |
| Mode 2 | Single-phase vapor convection (SPV) |
| Mode 3 | (currently not assigned) |
| Mode 4 | Subcooled nucleate boiling (SCNB) |
| Mode 5 | Saturated nucleate boiling (NUCL) |

Mode 6	Transition boiling (TRAN)
Mode 7	Inverted annular film boiling (IAFB)
Mode 8	Inverted annular dispersed flow (IADF)
Mode 9	Dispersed droplet film boiling (DFFB)

Figure 6-3 shows a heat transfer regime map, indicating where each of the modes apply.

For each regime, three heat transfer coefficients are determined. These are: h_{wv} , the heat transfer coefficient from the wall to vapor, h_{wl} the heat transfer coefficient from the wall to liquid for sensible heat, and h_{wb} the heat transfer coefficient from the wall to liquid for latent heat. The use of h_{wl} and h_{wb} to partition the heat transfer to the fluid phases is discussed in Section 6-2-11. The following sections describe, by heat transfer regime, the correlations used by the vessel component to determine h_{wv} , h_{wl} , and h_{wb} .

6-2-1 Convection to Single-Phase Vapor

Model Basis Heat transfer to single-phase vapor (SPV) is assumed when $\alpha_v > [\quad]^{ac}$. The WCOBRA/TRAC vessel component uses a set of four correlations to determine the heat transfer coefficients for convection to single-phase vapor. The maximum value of these four correlations is chosen as the heat transfer coefficient to be used to calculate the heat flux to provide a continuous and smooth transition between heat transfer regimes. These correlations are the McAdams (1954) correlation for turbulent natural convection, a constant Nusselt number value for laminar forced convection, the Dittus-Boelter (1930) equation, and an expression proposed by Wong and Hochreiter (1981) for turbulent forced convection. This section presents each correlation and describes its basis.

The McAdams correlation for turbulent free convection over vertical plates and cylinders is given by

$$h_{wv, nc} = 0.13 \left(\frac{k_v}{L} \right) (Gr_v Pr_v)^{0.33} \quad (6-1)$$

where the Grashof number (Gr_v) is defined by

$$Gr_v = \frac{g\beta|T_w - T_v|L^3\rho_v^2}{\mu_v^2} \quad (6-2)$$

with the Prandtl number (Pr_v) defined by

$$Pr_v = \frac{\mu_v C_{pv}}{k_v} \quad (6-3)$$

The form of the McAdams correlation results from the analysis of the boundary layer on a vertical surface, at uniform temperature and in an infinite fluid at rest. It is assumed that the flow in the boundary layer is buoyancy induced, and is primarily parallel to the surface. Although the coefficients for this correlation were originally developed by fitting the equation to data from vertical flat plates in air, the McAdams correlation has also been found to provide good estimates of the heat transfer coefficients for vertical planes and short horizontal surfaces in water, oils, alcohols, and air. This correlation is valid in the range $10^9 < GrPr < 10^{13}$.

For laminar flow, the heat transfer coefficient for vapor is determined assuming a constant Nusselt number of 10. Thus, for laminar vapor flow the heat transfer coefficient is given by

$$h_{wv,lam} = 10 \left(\frac{k_v}{D_h} \right) \quad (6-4)^{(71)}$$

where k_v is the film thermal conductivity for vapor.

This expression for the laminar flow heat transfer coefficient is in the same form as that for fully developed laminar flow in a circular pipe with a constant wall heat flux. The Nusselt number for internal tube flow with constant wall heat flux is 4.364. For laminar external flows, it has been shown that the calculated Nusselt number is higher. Kim (1979) showed that the Nusselt number for an infinite rod bundle with a square rod to pitch ratio of 1.33 is 7.86.

For forced turbulent flow, convective vapor heat transfer coefficients are determined by the Dittus-Boelter (1930) equation and a correlation proposed by Wong and Hochreiter (1981) that was based on experimental rod bundle data. The Dittus-Boelter equation was originally developed for turbulent flow within smooth tubes in automobile radiators. It has since proven acceptable for many other applications involving turbulent flows. It is given by

$$h_{wv,DB} = 0.023 \left(\frac{k_v}{D_h} \right) \left(\frac{G_v D_h}{\mu_v} \right)^{0.8} (Pr_v)^n \quad (6-5)$$

where $n = 0.4$ for heating and $n = 0.3$ for cooling. All vapor properties are evaluated at the mean film temperature.

The expression proposed by Wong and Hochreiter (1981) is

$$h_{wv,WH} = 0.0797 \left(\frac{k_v}{D_h} \right) \left(\frac{G_v D_h}{\mu_v} \right)^{0.6774} (Pr_v)^{0.333} \quad (6-6)$$

This correlation is a linear regression fit to experimental data obtained from steam cooling heat transfer tests run in a 17x17 rod bundle. This correlation predicts heat transfer coefficients that are larger than those predicted by the Dittus-Boelter equation for Reynolds numbers less than 25,000.

Model as Coded The set of four correlations are coded as presented above, with all fluid properties evaluated at the mean film temperature. These correlations are applied to both vertical and horizontal surfaces in the vessel and use the hydraulic diameter of the flow channel, D_h , as the characteristic length.

For heated structures, the heat transfer coefficient to single-phase vapor is calculated as

$$h_{wv,FC} = \text{maximum} \begin{cases} h_{wv,DB} \\ h_{wv,WH} \\ h_{wv,lam} \\ h_{wv,nc} \text{ (if } Re_v < [2000]^{a,c} \end{cases} \quad (6-7)^{(2)}$$

When the Reynolds number is less than []^{a,c}, the McAdams correlation for turbulent natural convection is also considered.

Continuity between free and forced convection and between laminar and turbulent flow is assured by selecting the maximum value of the heat transfer coefficients. Figure 6-4 compares the expressions in Equation 6-7 for $Pr = 1$. The Dittus-Boelter equation is coded with the [

] ^{a,c}.

If grids are present in the flow, the convective heat transfer to single-phase vapor is enhanced. This is accounted for by multiplying the convective heat transfer coefficient by a factor F_{grid} that models the grid effect. Then,

$$h_{wv,SPV} = F_{grid} h_{wv,FC} \quad (6-8)$$

The effect of the grid on convective heat transfer and calculation of F_{grid} is described in Section 6-2-8. For unheated structures, $F_{grid} = 0$ and $h_{wv,FC}$ is selected as the maximum of $h_{wv,DB}$, $h_{wv,lam}$, and $h_{wv,nc}$. Since the Wong-Hochreiter correlation was developed for rod bundles, it is not used for unheated structures.

The single-phase vapor regime is assumed when $\alpha_v > [\quad]^{ac}$. Only heat transfer to vapor is calculated, and for this regime,

$$h_{wt,SPV} = 0 \quad (6-9)$$

and

$$h_{wb,SPV} = 0 \quad (6-10)^{(49)}$$

Scaling Considerations Each of the four correlations used to calculate the single-phase heat transfer coefficient to vapor scale by using an appropriate characteristic length. In WCOBRA/TRAC, the channel hydraulic diameter is used for the characteristic length. The McAdams correlation is not affected by choice of the characteristic length since that term cancels out of the expression for the heat transfer coefficient. The hydraulic diameter affects the calculation of the natural convection heat transfer coefficient only through its use in the Reynolds number in the selection logic to determine the appropriate heat transfer mode. Therefore, the scale dependence of the McAdams (1954) correlation is not large.

The correlation by Wong and Hochreiter (1981) was developed directly from experimental data from a full scale rod bundle. Therefore, the only scale dependent concern is over the application of this correlation to rod bundle arrays different from the 17x17 rod bundle used to generate the experimental data on which this correlation is based. Therefore, the set of equations used by WCOBRA/TRAC to calculate single-phase vapor heat transfer coefficients is not strongly dependent on scale.

Conclusions The expressions used to determine the wall to vapor heat transfer coefficient for single-phase vapor are well known. The set of correlations used for this heat transfer coefficient has been assessed in the separate and integral effects tests simulated by WCOBRA/TRAC and detailed in Volumes 2 and 3 of WCAP-12945-P-A (Bajorek et al., 1998). FLECHT-SEASET, FLECHT Low Flooding Rate, FLECHT Top Skewed Power, FEBA, and NRU reflood separate effects tests, in addition to the CCTF, SCTF, and LOFT integral effects tests, show significant fractions of the rod bundles in this heat transfer regime. Thus, the uncertainty in these models and correlations are accounted for in the overall WCOBRA/TRAC code bias and uncertainty.

6-2-2 Convection to Single-Phase Liquid⁽²⁾

Model Basis The WCOBRA/TRAC vessel heat transfer routines employ two correlations to calculate the heat transfer coefficients to single-phase liquid. For laminar flow, the heat transfer coefficient is limited to the value recommended by Kim (1979):

$$h_{wt,lam} = 7.86 \left(\frac{k_t}{D_h} \right) \quad (6-11)^{(1)}$$

where k_f is the fluid thermal conductivity for the liquid.

For turbulent flow, the Dittus-Boelter correlation is used to calculate the single-phase heat transfer coefficient to liquid:

$$h_{wt,DB} = 0.023 \left(\frac{k_f}{D_h} \right) \left(\frac{G_t D_h}{\mu_t} \right)^{0.8} (Pr_t)^n \quad (6-12)$$

where $n = 0.4$ for heating and $n = 0.3$ for cooling. All liquid properties are evaluated at saturation based on the bulk liquid pressure and enthalpy.

Model as Coded The Dittus-Boelter correlation is coded as listed with $n = 0.4$ for all usage. Heat transfer coefficients are calculated using the Dittus-Boelter correlation and the expression for laminar external tube flow, and the maximum value is selected as the heat transfer coefficient for forced convection to single-phase liquid. Natural convection heat transfer is not considered. The correlation is also applied in the transition region between laminar and fully turbulent flow.

The wall to liquid single-phase heat transfer coefficient is calculated as

$$h_{wt,SPL} = \text{maximum} \begin{cases} h_{wt,lam} \\ h_{wt,DB} \end{cases} \quad (6-13)^{(3)}$$

A heat transfer coefficient to vapor for the single-phase liquid regime is also calculated, as described in Section 6-2-1, and

$$h_{wv,SPL}^* = h_{wv,SPV} \quad (6-14)$$

To obtain $h_{wt,SPL}$ and $h_{wv,SPL}$ and account for liquid deficient heat transfer, a ramp is defined:

[

$$]^{ac} \quad (6-15)^{(4)}$$

where $\alpha_{SPV} = [\quad]^{ac}$,

and the single-phase liquid regime heat transfer coefficient to vapor is calculated as

$$h_{wv,SPL} = (1 - F_{liq}) h_{wv,SPL}^* \quad (6-16)$$

The effect of $(1 - F_{liq})$ is to set the vapor phase heat transfer coefficient to 0.0, except at very high void fraction.

Since for the single-phase liquid regime $T_l < T_{sat}$, boiling does not occur and

$$h_{wb,SPL} = 0. \quad (6-17)^{(49)}$$

Scaling Considerations In the two correlations for heat transfer to single-phase liquid, scaling is accounted for by selection of an appropriate hydraulic diameter. In Equation 6-12, the heat transfer coefficient is seen to be a weak function of D_h and thus is not a strong function of scale.

Conclusions The correlations used to determine the heat transfer coefficient from the wall to single-phase liquid have been assessed by their use in a large number of WCOBRA/TRAC simulations. These simulations include the FLECHT-SEASET, FLECHT Low Flooding Rate, FLECHT Top Skewed Power, FEBA, and NRU separate effects reflood tests where heat transfer to single-phase liquid was predicted at the bottom most parts of the test bundles, well below the quench front. This regime also occurred in the CCTF, SCTF, and LOFT integral tests. In the LOFT simulations, this regime is important in obtaining an acceptable steady-state simulation of the facility. Thus, the uncertainty in modelling this heat transfer regime is included in the overall WCOBRA/TRAC code bias and uncertainty.

6-2-3 Saturated and Subcooled Nucleate Boiling

Model Basis When the wall temperature is greater than saturation but less than the temperature at the critical heat flux and liquid is present, the Chen (1963) correlation is used. This correlation assumes that both nucleation and convective mechanisms occur and that the contributions made by the two mechanisms are additive. The Chen correlation automatically makes the transition to single-phase forced convection at low wall superheat, and to pool boiling at low flowrate. The convective component is represented by a Dittus-Boelter type of expression where the thermal conductivity, Reynolds number, and the Prandtl number are replaced by effective values associated with the two-phase flow. To account for increased convection caused by the formation of vapor bubbles, a multiplier is applied to the convective part of the correlation.

A Forster-Zuber (1955) type of pool boiling equation is used for the nucleate boiling component of the correlation. The pool boiling expression relates a bubble Nusselt number to a bubble Reynolds number and a liquid Prandtl number. It can be shown that the product of growth rate and bubble radius is constant for a given superheat. In pool boiling and convective boiling, the superheat is not constant

across the boundary layer. This effect can be neglected in pool boiling since the boundary layer is generally large in comparison to the vapor bubble. In convective boiling, however, the boundary layer is thinner and the temperature gradients steeper. The difference between the wall superheat and the mean superheat to which the bubble is exposed must be considered. A suppression factor, S_{CHEN} , is used to modify the nucleate boiling part of the correlation and account for this effect.

The equations for the Chen correlation are as follows:

$$h_{CHEN} = h_{FC} + h_{NB} \quad (6-18)$$

where:

$$h_{FC} = 0.023 F_{CHEN} \left(\frac{k_f}{D_h} \right) Re_t^{0.8} Pr^{0.4} \quad (6-19)$$

with

$$Re_t = \frac{G_t D_h}{\mu_f} \quad (6-20)^{(11)}$$

and

$$h_{NB} = 0.00122 S_{CHEN} \left(\frac{k_f^{0.79} C_{pf}^{0.45} \rho_f^{0.49} g_c^{0.25}}{\sigma^{0.5} \mu_f^{0.29} H_{fg}^{0.24} \rho_g^{0.24}} \right) (T_w - T_{ff})^{0.24} (P_w - P)^{0.75} \quad (6-21)$$

where F_{CHEN} is the Reynolds number factor shown in Figure 6-5 as a function of the inverse Martinelli factor, χ_{TT}^{-1} . The boiling suppression factor S_{CHEN} is shown in Figure 6-6, and P_w is the saturation pressure corresponding to T_w .

The inverse Martinelli factor is given by

$$\chi_{TT}^{-1} = \left(\frac{x}{1-x} \right)^{0.9} \left(\frac{\rho_f}{\rho_g} \right)^{0.5} \left(\frac{\mu_g}{\mu_f} \right)^{0.1} \quad (6-22)$$

and the Reynolds number factor is determined as

$$F_{CHEN} = \begin{cases} 1.0 & ; \chi_{TT}^{-1} < 0.1 \\ 2.34 (\chi_{TT}^{-1} + 0.213)^{0.736} & ; \chi_{TT}^{-1} > 0.1 \end{cases} \quad (6-23)$$

The boiling suppression factor recommended by Thurgood (1983) is given by

$$S_{CHEN} = \begin{cases} [1 + 0.12 Re_{2\phi}^{1.14}]^{-1} & ; Re_{2\phi} < 32.5 \\ [1 + 0.42 Re_{2\phi}^{0.78}]^{-1} & ; 32.5 < Re_{2\phi} < 50.9 \\ 0.1 & ; Re_{2\phi} > 50.9 \end{cases} \quad (6-24)^{(73)}$$

where:

$$Re_{2\phi} = (10^{-4}) Re_t F_{CHEN}^{1.25} \quad (6-25)$$

Note that the limit in Equation 6-24 has been modified from 70 to 50.9 (Thurgood et al., 1983) to make the transition more continuous.

Subcooled Nucleate Boiling

The Chen (1963) correlation, though developed for saturated boiling, may be extended into the subcooled region. As discussed above, the Chen correlation superimposes a forced convective and nucleate boiling component. For subcooled boiling,

$$q_{SCNB}'' = q_{FC}'' + q_{NB}'' \quad (6-26)$$

The nucleate boiling heat flux is evaluated as

$$q_{NB}'' = h_{NB} (T_w - T_{sat}) \quad (6-27)$$

where h_{NB} is defined by Equation 6-21 above, and the suppression factor, S_{CHEN} , is calculated from Equation 6-24. The forced convection heat flux is computed from Equation 6-19 using subcooled liquid properties and setting the flow factor, F_{CHEN} , to unity so that

$$q_{FC}'' = 0.023 \left(\frac{k_t}{D_h} \right) Re_t^{0.8} Pr_t^{0.4} (T_w - T_t) \quad (6-28)^{(5)}$$

where T_t is the local bulk fluid temperature and

$$Re_t = \frac{G_t D_h}{\mu_t} \quad (6-29)$$

Moles and Shaw (1972) compared the Chen correlation to boiling data for several fluids and reported satisfactory agreement for low to moderate subcoolings.

During subcooled boiling, vapor generation occurs and a significant void fraction ($\alpha_v \sim 0.6$) may exist despite the presence of subcooled water. In this regime, four processes are of interest:

1. forced convection to liquid,
2. vapor generation at the wall,
3. condensation near the wall, and
4. bulk condensation (subcooled liquid core).

Condensation occurring because of the presence of vapor in the subcooled liquid core is calculated implicitly during the solution of the energy equations and does not affect the determination of phasic heat inputs. Forced convection to liquid is treated using Equation 6-28 for the heat input to the liquid energy equation. The nucleate boiling component of the Chen correlation Equation 6-21 defines the amount of heat available to cause vapor generation at the wall.

The near-wall condensation is estimated using the Hancox-Nicoll (1971) correlation for heat flux at the point where all the bubbles generated collapse in the near-wall region:

$$q_{HN}'' = 0.4 \left(\frac{C_{pf} \mu_f}{D_h} \right) \left(\frac{G_t D_h}{\mu_f} \right)^{0.662} (T_{sat} - T_t) \quad (6-30)^{(7)}$$

where T_{sat} is the local saturation temperature.

The heat flux dissipated in near-wall condensation for a flowing system is calculated as

$$q_{cond}'' = q_{HN}'' - q_{SPL}'' \quad (6-31)$$

Subtracting the near wall condensation from the amount of energy available for vapor generation yields

$$q_{\Gamma} = (q_{NB}'' - q_{cond}'') A_w \quad (6-32)$$

However, a fraction of q_{Γ} is expended to heat up the subcooled liquid "pumped" into the saturated thermal boundary layer. This fraction is given by the Rouhani and Axelsson (1970) model:

$$\epsilon_p = \frac{(\rho_f/\rho_g)(H_f - H_t)}{H_{fg} + (\rho_f/\rho_g)(H_f - H_t)} \quad (6-33)^{(8,9)}$$

and

$$\epsilon_{\Gamma} = (1 - \epsilon_p) = \frac{H_{fg}}{H_{fg} + (\rho_f/\rho_g)(H_f - H_t)} \quad (6-34)^{(8,9)}$$

where:

ϵ_p = fraction of heat to boundary layer

ϵ_{Γ} = fraction of heat causing vapor generation

Finally, the amount of energy available for vapor generation is

$$q_{\Gamma} = (q_{NB}'' - q_{cond}'') \epsilon_{\Gamma} A_w \quad (6-35)$$

and, adding all the heat inputs to the liquid

$$q_t = [q_{SPL}'' + (1 - \epsilon_{\Gamma})q_{NB}'' + \epsilon_{\Gamma}q_{cond}''] A_w \quad (6-36)$$

The heat source term for vapor generation, q_{Γ} , enters the liquid energy equation as an explicit vapor generation rate and will partially condense because of the implicit bulk condensation.

Model as Coded Nucleate boiling heat transfer coefficients are calculated when the wall temperature is

$$T_{sat} \leq T_{wall} < T_{CHF}$$

Calculations are first performed in subroutine BOILING to determine X_{TT}^{-1} , $Re_{2\phi}$, F_{CHEN} and S_{CHEN} . To obtain χ_{TT}^{-1} , the quality is calculated as [

$$]^{a,c} \quad (6-37)$$

The inverse Martinelli factor is then calculated as [

$$]^{a,c} \quad (6-38)^{(54)}$$

For saturated liquid ($T_t \geq T_{sat}$), the convective enhancement factor F_{CHEN} is calculated: [

$$]^{a,c} \quad (6-39)^{(6,54)}$$

and the value of $Re_{2\phi}$ is

$$Re_{2\phi} = (10^{-4}) F_{CHEN}^{1.25} Re_t \quad (6-40)$$

For subcooled liquid, χ_{TT}^{-1} is not calculated and $Re_{2\phi}$ is calculated as

$$Re_{2\phi} = (10^{-4}) Re_t \quad (6-41)$$

which is equivalent to assuming $F_{CHEN} = 1.0$ in Equation 6-40.

The boiling suppression factor is then calculated for both saturated and subcooled liquid as [

$$]^{a,c} \quad (6-42)^{(6,54)}$$

The $(P_w - P)$ term in the Chen correlation is approximated as [

$$]^{a,c} \quad (6-43)^{(10)}$$

where: [

$$]^{a,c} \quad (6-44)$$

For saturated nucleate boiling, the heat transfer coefficient to liquid for latent heat is calculated as

$$h_{wt,NB} = F_{CHEN} h_{wt,SPL} + h_{NB} \quad \text{where:} \quad (6-45)^{(11)}$$

$$h_{NB} = 0.00122 S_{CHEN} \left[\frac{k_f^{0.79} C_{pf}^{0.45} \rho_f^{0.49} g_c^{0.25}}{\sigma^{0.5} \mu_f^{0.29} (H_{fg} \rho_g)^{0.24}} \right] (T_w - T_f)^{0.24} (P_w - P)^{0.75} F_B \quad (6-46)$$

and $h_{wt,SPL}$ is given by Equation 6-13.

The function F_B insures a smooth decrease in the boiling term as dryout occurs: [

$$]^{a,c} \quad (6-47)$$

The derivative of the Chen boiling heat transfer coefficient is used to calculate the wall to fluid heat transfer for nodes in the nucleate boiling regime as described in Section 6-2-11. This derivative is calculated as [

$$]^{ac} (6-48)^{(12)}$$

Since the liquid must be saturated to be in this regime and the interfacial heat transfer rates are high, all of the heat transfer results in evaporation. The heat transfer coefficient for latent heat ($h_{wb,NB}$) is set to 0.0 to avoid double accounting.

$$h_{wb,NB} = 0.0 \quad (6-49)^{(13,49)}$$

The heat transfer coefficient to vapor is calculated as it was for single-phase liquid. That is,

$$h_{wv,NB} = (1 - F_{liq}) h_{wv,SPV} \quad (6-50)$$

where F_{liq} is given by Equation 6-15. Equation 6-8 is used to calculate $h_{wv,SPV}$.

For subcooled nucleate boiling, a ramp is imposed on the correlation to avoid sharp discontinuities in the vapor generation rate at small liquid subcoolings. A subcooled boiling modifier is defined as [

$$]^{ac} (6-51)$$

This multiplier is used to determine the split between latent and sensible heating for subcooled liquid. A numerical ramp is applied between [$]^{ac}$ subcooling to gradually decrease F_{SCB}^* .

This function is defined as [

$$]^{a,c} \quad (6-52)$$

The subcooled boiling modifier is then calculated as [

$$]^{a,c} \quad (6-53)$$

for $(T_{sat} - T_f) > [\quad]^{a,c}$. For liquid subcoolings less than $[\quad]^{a,c}$, $F_{SCB} = 1.0$.

Subcooled nucleate boiling heat transfer coefficients are then estimated after calculating [

$$]^{a,c} \quad (6-54)$$

where the Hancox-Nicoll (1971) correlation is used to obtain q_{HN}'' , calculated by Equation 6-30 without modification.

The fraction of heat in subcooled boiling that goes into vapor generation F_{GAM} is then calculated as [

$$]^{a,c} \quad (6-55)^{(14)}$$

Finally, the subcooled nucleate boiling heat transfer coefficients are calculated as

$$h_{wt,SCNB} = h_{wt,SPL} + (1 - F_{GAM})h_{NB} \quad (6-56)^{(15)}$$

and

$$h_{wb,SCNB} = F_{GAM} h_{NB} \quad (6-57)^{(49)}$$

The heat transfer coefficient to vapor is zero except at very high void fractions and is given by:

$$h_{wv,SCNB} = (1 - F_{liq}) h_{wv,SPV} \quad (6-58)$$

with F_{liq} given by Equation 6-15 and $h_{wv,SPV}$ by Equation 6-8.

Scaling Considerations In the correlations used for subcooled and saturated nucleate boiling, the forced convection component scales with characteristic length, which is the flow channel hydraulic diameter. These correlations were assessed by examining a large number of WCOBRA/TRAC simulations of separate effects reflood tests below the quench front. These experiments used full scale fuel dimensions. These tests included FLECHT-SEASET, FLECHT Low Flooding Rate, FLECHT Top Skewed Power, FEBA, and NRU tests. These correlations were also used in simulations of the integral effects tests CCTF, SCTF, and LOFT. Thus, the model and correlations for subcooled and saturated nucleate boiling have been assessed over a range of scale typical of fuel assemblies in a PWR.

Conclusions The models and correlations used in WCOBRA/TRAC for subcooled and saturated nucleate boiling are expressions appropriate for these processes. These models were assessed by simulations of a large number of separate and integral tests. The uncertainty in these models is therefore accounted for in the overall WCOBRA/TRAC code bias and uncertainty.

6-2-4 Critical Heat Flux and Wall Temperature at CHF

Model Basis The intersection of the nucleate boiling and transition boiling heat transfer regimes occurs at the critical heat flux (CHF). To provide for an upper limit to the nucleate boiling regime and a continuous transition to other regimes, the CHF point (q_{CHF}'' , T_{CHF}) must be specified.

Three CHF regimes are considered: pool boiling, forced convective boiling departure from nucleate boiling (DNB), and annular film dryout.

Pool Boiling DNB Pool boiling DNB is selected when the mass flux is low ($G < 30^{(16)}$ g/cm²-sec) and the flow regime is not annular film flow. The pool boiling critical heat flux is given by modification of the Zuber et al. (1961) equation, as recommended by Bjornard and Griffith (1977):

$$q_{CHF}'' = 0.9 (1 - \alpha_v) \frac{\pi}{24} H_{fg} \rho_g^{0.5} [g_c g \sigma (\rho_f - \rho_g)]^{0.25} \quad (6-59)$$

Forced-Convection DNB Forced-convection DNB is considered when the mass flux is greater than 30 g/cm²-sec and the flow regime is not annular film flow. The critical heat flux is given by the Biasi et al. (1967) correlation which consists of two equations, one for low-quality CHF and one for high-quality CHF, and is given below:

$$q_{B1}'' = (5969500) G^{-1/6} [F(P) G^{-1/6} - x] D_h^{-n} \quad (6-60)^{(17,18)}$$

for low quality, and

$$q_{B2}'' = (11980000) H(P) (1-x) D_h^{-n} G^{-0.6} \quad (6-61)^{(17,18)}$$

for high quality, where:

q''	=	critical heat flux (Btu/hr-ft ²)
G	=	mass flux (g/cm ² -sec)
P	=	pressure (bars)
D_h	=	hydraulic diameter (cm)
x	=	quality
n	=	0.6 if $D_h < 1.0$ cm, $n = 0.4$ if $D_h > 1.0$ cm

and

$$F(P) = 0.7249 + 0.099 P \exp(-0.032 P) \quad (6-62)$$

$$H(P) = -1.159 + 0.149 P \exp(-0.019 P) + 8.99 P (10 + P^2)^{-1} \quad (6-63)$$

The critical heat flux is taken to be the maximum of that given by Equations 6-60 and 6-61:

$$q_{CHF}'' = \text{maximum} \begin{cases} q_{B1}'' \\ q_{B2}'' \end{cases} \quad (6-64)$$

Annular Film Dryout If annular flow exists, the departure from nucleate boiling is caused by film dryout. In this regime, the heat flux is not limited by a correlation, but rather forced convection vaporization exists until the film dries out. Film dryout is a complex function of the film flowrate, the applied heat flux, and the entrainment/de-entrainment rate, and is determined by the solution of the hydrodynamic equations. This approach was pioneered by Whalley, Hutchinson, and Hewitt (1973) and Whalley (1976) and has been applied successfully to the analysis of the single tube tests conducted by Bennett et al. (1967).

To be consistent with the remainder of the heat transfer package, the critical heat flux point for annular film dryout must be defined. A value of []^{ac} wall superheat has been selected and the critical heat flux is set to that given by the Zuber equation (Equation 6-59). The onset of film boiling is not affected

by this definition since film boiling is controlled by film dryout. The critical heat flux is ramped between the annular film dryout regime and the pool boiling and forced-convection DNB regimes.

Critical Heat Flux Temperature To define the boiling curve, it is necessary to know the surface temperature at which CHF occurs. An iterative procedure is used to find the wall temperature at which the heat flux from the Chen (1963) nucleate boiling correlation is equal to the critical heat flux. Thus,

$$q''_{CHEN}(T_{CHF}) = q''_{CHF} \quad (6-65)$$

Model as Coded Calculations to estimate the critical heat flux for vessel component structures are performed in subroutine BOILING. The search is currently limited to $T_F + 5 < T_{CHF} < T_F + 75$. The Biasi et al. (1967) correlation is evaluated first, and the Biasi critical heat flux is calculated as [

$$]^{a,c} \quad (6-66)^{(19)}$$

where q''_{B1} and q''_{B2} are calculated with Equations 6-60 and 6-61.

The Zuber et al. (1961) critical heat flux is then calculated as [

$$]^{a,c} \quad (6-68)$$

If the flow is approaching annular dryout, q_{CHF}^{**} is []^{a,c}, and

$$q_{CHF}^{**} = q_{CHF}^{**} F_D \quad (6-69)$$

where: [

$$]^{a,c} \quad (6-70)$$

The critical heat flux at the wall surface is then calculated by including a term to approximate the heat flux to vapor: [

$$]^{a,c} \quad (6-71)^{(20)}$$

where: [

$$]^{a,c} \quad (6-72)$$

and [

$$]^{a,c} \quad (6-73)^{(20)}$$

The term in Equation 6-71 representing the heat flux to vapor assumes that $\Delta T_{CHF} = []^{a,c}$.

Numerical damping is finally applied to avoid rapid changes with time. The critical heat flux then is [

$$]^{a,c} \quad (6-74)$$

where \tilde{q}_{CHF}'' is calculated by Equation 6-71 and q_{CHF}'' is the critical heat flux calculated for the previous time step.

Scaling Considerations The correlations used for critical heat flux scale with hydraulic diameter. These correlations were assessed against full scale fuel assemblies in nearly all of the WCOBRA/TRAC simulations of heated tests reported in Volumes 2 and 3 of WCAP-12945-P-A.

Conclusions The key process for critical heat flux in a fuel assembly during a LOCA is forced convection DNB at low quality and high flowrate. This process is represented in WCOBRA/TRAC by a correlation developed for these conditions.⁽²¹⁾

The models and correlations for critical heat flux have been assessed by their use in nearly all of the WCOBRA/TRAC simulations reported in Volumes 2 and 3 of WCAP-12945-P-A. Therefore, the uncertainty of these models is accounted for in the overall WCOBRA/TRAC code bias and uncertainty.

6-2-5 Transition Boiling

Model Basis The transition boiling heat transfer regime exists between the critical heat flux (T_{CHF} , q_{CHF}'') and the minimum film boiling point (T_{MIN} , q_{MIN}''). In this regime, liquid makes only intermittent contact with the wall. The vessel component in WCOBRA/TRAC uses three separate models to estimate the transition boiling heat transfer coefficient. These values are compared, and the maximum is used to calculate the transition boiling heat flux.

Model 1

The first model used to estimate transition boiling heat transfer coefficients is based on a mechanistic approach to the heat transfer. This model is similar to those suggested by Iloeje et al. (1974) and Ganic and Rohsenow (1977). Transition boiling heat transfer is assumed to be composed of both wet wall and dry wall heat transfer components. In this model, transition boiling heat flux is expressed as

$$q_{TBI}'' = q_{wv}'' + q_{rvv}'' + q_{rwe}'' + q_{dcht}'' \quad (6-75)$$

where:

- q_{wv}'' = heat transfer by convection to vapor
- q_{rvv}'' = radiation heat transfer to vapor
- q_{rwe}'' = radiation heat transfer to liquid droplets
- q_{dcht}'' = direct contact heat transfer to liquid

The heat transfer coefficient used to calculate the convective flux to vapor q''_{wv} is determined using the expressions described in Section 6-2-1. The radiative heat transfer terms q''_{rwv} and q''_{rwe} are calculated using the model by Sun, Gonzalez, and Tien (1976) and are discussed in Section 6-2-9.

The direct contact heat transfer term q''_{dcht} is composed of terms representing direct contact heat transfer to the continuous and entrained liquid fields as

$$q''_{dcht} = q''_{dcht,l} + q''_{dcht,e} \quad (6-76)$$

The direct contact heat transfer to the entrained field is calculated using a model developed by Forslund and Rohsenow (1968): [

$$]^{a,c} \quad (6-77)^{(22,23)}$$

[

$$]^{a,c} \quad (6-78)$$

The direct contact heat transfer to the continuous liquid field is modelled by assuming the liquid maintains wall contact only intermittently with an effectiveness, ϵ_{wet} . The continuous liquid direct contact heat transfer is given by

$$q''_{dcht,l} = h_{w\ell,SPL} \epsilon_{wet} (T_w - T_l) \quad (6-79)$$

The contact effectiveness is defined similar to Ganic and Rohsenow (1977) as [

$$]^{a,c} \quad (6-80)^{(24)}$$

In their original work, Ganic and Rohsenow assumed $m = 2$. However, this assumption gives unrealistic values at high pressure. Based on comparisons to Westinghouse G-1 and G-2 blowdown heat transfer experiments data and to ORNL high pressure blowdown data, the coefficient m is redefined to be [

$$]^{ac} \quad (6-81)$$

Figure 6-7 shows the effectiveness function compared to values obtained for droplets by Wachters and Westerling (1966), Corman (1966), Gaugler (1966), and Pedersen (1967) at atmospheric pressure. Figure 6-8 shows the variation of ϵ_{wet} as coded at higher pressure.

Model 2

The second model for transition boiling also expresses the heat flux as the sum of wet wall and dry wall contributions. The wet wall contribution to the heat flux is assumed to be a function of the critical and minimum film boiling heat fluxes:

$$q''_{TB2} = q''_{wv} + q''_{rvv} + q''_{wet} \quad (6-82)$$

but where

$$q''_{wet} = F_{wet} q''_{CHF} \quad (6-83)^{(27)}$$

where q''_{CHF} is the critical heat flux calculated from Equation 6-74. Bjornard and Griffith (1977) reported that the fraction of wetted wall F_{wet} given as

$$F_{wet} = \left(\frac{T_w - T_{MIN}}{T_{CHF} - T_{MIN}} \right)^2 \quad (6-84)$$

provides good agreement with data as described by Groenveld and Fung (1976) and with McCreery et al. (1977).

Model 3

A third transition boiling model is applied in the region near a top down quench front. For a top down quench, the void fraction can be very large (0.95 - 0.99) and yet still produce a significant quench rate. The transition boiling heat flux for this model is based on Zuber's estimate of the critical heat flux as

$$q_{TB3}'' = q_{wv}'' + q_{rvv}'' + q_{rwe}'' + q_{TQ}'' \quad (6-85)$$

but where [

$$]^{a,c} \quad (6-86)^{(25)}$$

where L_{QF} is the distance in feet from the top quench front and F_{wet} is given by Equation 6-84. The Zuber critical heat flux is given by [

$$]^{a,c} \quad (6-87)$$

Model as Coded The transition boiling heat transfer coefficients are calculated in subroutine *HCOOL* when the wall temperature is between T_{CHF} and T_{MIN} . These coefficients are calculated as follows.

The model for q_{TB1}'' uses a liquid contact effectiveness ϵ_{wet} that was defined by Equations 6-80 and 6-81. Limits are placed on the calculated value of ϵ_{wet} to insure that only reasonable values are employed in subsequent calculations. The maximum value allowed for ϵ_{wet} is $[]^{a,c}$. A value less than 1.0 is used based on the assumption that during stable nucleate boiling some fraction of the wall at any given moment is effectively covered by vapor. A minimum value of $= []^{a,c}$ is used as a lower limit for ϵ_{wet} . That is, [

$$]^{a,c} \quad (6-88)^{(26)}$$

where the exponent m is given by Equation 6-81.

The wet wall components of heat transfer for Model 1 and Model 2 are then calculated, and the maximum is selected:

$$q_{TB,wet}'' = \text{maximum} \left\{ \begin{array}{l} q_{dcht,t}'' + q_{dcht,e}'' \\ F_z F_{wet} q_{CHF}'' \end{array} \right. \quad (6-89)^{(27)}$$

where $q_{dcht,t}''$ is calculated by Equation 6-79, $q_{dcht,e}''$ by Equation 6-77, F_{wet} by Equation 6-84 and q_{CHF}'' by Equation 6-74 without modification.

The ramp F_z is included in Model 2 to insure a smooth transition to dispersed flow film boiling. It is calculated by [

$$]^{ac} \quad (6-90)$$

and is shown in Figure 6-9.

Model 3 is considered only if the wall location is within []^{ac} feet of a top quench front. For this model, the wetted wall fraction to account for dryout as [

$$]^{ac} \quad (6-91)$$

where: [

$$]^{ac} \quad (6-92)$$

Then, if L_{QF} is < []^{ac} feet, the wetted wall transition boiling heat flux is selected as [

$$]^{ac} \quad (6-93)$$

where $q_{TB,wet}^{''*}$ is from Equation 6-89 and Equation 6-87 is used to calculate the Zuber pool boiling DNB heat flux.

The transition boiling regime heat transfer coefficients are then calculated as [

$$]^{ac} \quad (6-94)^{(28,30,31)}$$

The first term in Equation 6-94 represents radiation from the wall to the liquid phase. It depends on the void fraction and is calculated using Equation 6-157 if $\alpha > []^{ac}$, with Equation 6-116 if []^{ac}, and with Equation 6-158 if $\alpha < []^{ac}$.⁽³²⁾

The heat transfer coefficient for latent heat is calculated as, [

] ^{ac} (6-95)^(28,29,30,49)

$$h_{wv,TB} = h_{wv,FC} + h_{rvv} \quad (6-96)^{(31)}$$

In these expressions, $h_{wt,SPL}$ is given by Equation 6-13 and $h_{wv,FC}$ by Equation 6-7. The term F_{SCB} accounts for the liquid subcooling (Section 6-2-3), and is calculated by Equation 6-53. The radiation heat transfer coefficients h_{rwt} and h_{rvv} are described in Section 6-2-9.

Scaling Considerations The set of correlations used for transition boiling heat transfer scale with hydraulic diameter. These correlations were assessed against data from full scale fuel assemblies in nearly all of the heated tests (reflood, blowdown, and integral) that are reported in Volumes 2 and 3 of WCAP-12945-P-A.

Conclusions Transition boiling remains one of the least understood heat transfer regimes. Liquid-wall contact does occur; however, the duration is difficult to quantify. The models for transition boiling account for the direct contact heat transfer process in addition to heat transfer to the vapor phase. The models have been assessed through WCOBRA/TRAC simulations of a large number of reflood, blowdown, refill, and integral tests. These simulations indicate a small region of transition boiling near the quench front. The uncertainty and reliability of these correlations is therefore included in the overall code bias and uncertainty.

6-2-6 Minimum Film Boiling Wall Temperature

Model Basis The transition boiling regime is bounded by the CHF point and the minimum stable film boiling point. It is assumed that the minimum film boiling temperature is the wall temperature that results in an instantaneous contact temperature equal to the homogeneous nucleation temperature, T_{hn} . Using a contact temperature correction to include the effects of surface thermal properties, the minimum film boiling temperature is

$$T_{MIN,hn} = T_{hn} + (T_{hn} - T_t) \left[\frac{(k\rho C_p)_k}{(k\rho C_p)_w} \right]^{1/2} \quad (6-97)^{(33)}$$

where the homogeneous nucleation temperature is given as a function of pressure by a simple curve fit:

$$T_{hn} = 705.44 - (4.722E-2) \Delta P_{crit} + (2.3907E-5) \Delta P_{crit}^2 - (5.8193E-9) \Delta P_{crit}^3 \quad (6-98)$$

where $\Delta P_{crit} = (3203.6 - P)$ psi.

The minimum film boiling temperature is specified as the larger of either Equation 6-97 or that given by Henry's modification (Henry, 1974) of the Berenson correlation:

$$T_{MIN, Henry} = T_B + 0.42 (T_B - T_l) \left\{ \left[\frac{(k\rho C_p)_h}{(k\rho C_p)_w} \right]^{1/2} \left[\frac{H_{fg}}{C_{pw} (T_B - T_{sat})} \right] \right\}^{0.6} \quad (6-99)^{(34)}$$

where:

$$T_B = T_{sat} + 0.127 \frac{\rho_v H_{fg}}{k_v} \left[\frac{g (\rho_f - \rho_g)}{(\rho_f + \rho_g)} \right]^{2/3} \left[\frac{g_c \sigma}{g (\rho_f - \rho_g)} \right]^{1/2} \left[\frac{\mu_v}{g (\rho_f - \rho_g)} \right]^{1/3} \quad (6-100)$$

Model as Coded The minimum film boiling temperature for all unheated structures (except for spacer grids; see Equation 6-167) is assumed to be $T_{MIN} = []^{ac}{}^{(35)}$. For heated structures, T_{MIN} is calculated as [

$$]^{ac} \quad (6-101)$$

Scaling The correlations used for predicting the minimum film boiling temperature depend on the thermal properties of the wall and of the coolant. This correlation does not depend on the system geometry, and is therefore scale independent.

Conclusions The minimum film boiling temperature has been found to occur over a range of values that depends on the fluid conditions and the surface properties. This is calculated in WCOBRA/TRAC by appropriate correlations, and the value of T_{MIN} is limited to a range of values observed in experiments. The correlations for T_{MIN} and the limitations on permissible values have been assessed by their use in

simulations of heated test facilities reported in Volumes 2 and 3 of WCAP-12945-P-A. These tests include the reflood, blowdown and refill separate effects tests, and the integral tests for CCTF, SCTF, and LOFT. Therefore, the uncertainty of these models is accounted for in the overall WCOBRA/TRAC code bias and uncertainty.

6-2-7 Inverted Annular Film Boiling

Model Basis The WCOBRA/TRAC vessel heat transfer package assumes that the flow has an inverted annular pattern if the wall temperature is greater than the minimum stable film boiling temperature, $T_w > T_{MIN}$, and the void fraction is less than $[]^{ac}$. Below a void fraction of $[]^{ac}$, the inverted annular film boiling heat transfer coefficient uses a modified form of the Bromley correlation (1950). The revised form of the Bromley correlation used in WCOBRA/TRAC is documented Pomerantz (1964). For void fractions in the range $[]^{ac}$, the heat transfer coefficients are interpolated between those of this version of the Bromley equation and heat transfer coefficients for dispersed droplet flow. The modified version of the Bromley equation, given by Pomerantz is

$$h_{Brom} = 0.62 \left(\frac{D_h}{\lambda} \right)^{0.172} \left[\frac{k_g^3 \rho_g (\rho_f - \rho_g) H_{fg} g}{D_h \mu_g (T_w - T_{sat})} \right]^{1/4} \quad (6-102)^{(36)}$$

where, the critical wavelength (λ) is

$$\lambda = 2\pi \sqrt{\frac{g_c \sigma}{g (\rho_f - \rho_g)}} \quad (6-103)$$

Wall to liquid core radiation heat flux is calculated as

$$q_{rwl}'' = \frac{\sigma_{SB}}{\frac{1}{\epsilon_w} + \frac{1}{1 - \epsilon_l}} (T_w^4 - T_{sat}^4) \quad (6-104)$$

where:

- σ_{SB} = Stefan-Boltzmann constant
- ϵ_w = wall emissivity
- ϵ_l = liquid emissivity

This model assumes that radiation takes place across an annular vapor gap to the liquid.

Then, for $\alpha_v [\quad]^{a,c}$, the heat flux in inverted annular flow is

$$q_{IAFB}'' = q_{Brom}'' + q_{w\ell}'' \quad (6-105)$$

If $[\quad]^{a,c}$, the inverted annular heat flux is interpolated between q_{IAFB}'' and the heat flux in dispersed flow film boiling, q_{DFFB}'' , which is described in Section 6-2-8.

Model as Coded Calculation of the inverted annular regime heat transfer coefficients are performed in subroutine *HCOOL*. Heat transfer coefficients are defined for the vapor phase and for sensible and latent heating of the liquid.

To estimate these heat transfer coefficients, the Bromley film boiling heat flux is estimated as

$$q_{Brom}'' = h_{Brom} (T_w - T_{sat}) \quad (6-106)$$

Since the Bromley correlation is derived from experiment, h_{Brom} includes the effect of heat transfer to vapor. Therefore, the heat flux to the liquid is estimated as

$$q_{w\ell}'' = q_{Brom}'' - (h_{wv,FC} + h_{rvv}) (T_w - T_v) \quad (6-107)^{(38)}$$

where $h_{wv,FC}$ is given by Equation 6-7, h_{rvv} by Equation 6-156, and $q_{dcht,e}''$ by Equation 6-128. The value of $q_{w\ell}''$ from Equation 6-107 is compared to the dispersed flow heat flux (described in the next section). If the dispersed flow heat flux is higher, then that heat transfer regime is assumed.

Vapor superheat and void fraction are taken into account by defining [

$$]^{a,c} \quad (6-108)^{(37)}$$

and calculating the liquid and vapor phase contributions from the Bromley correlation as

$$q_{w\ell,Brom}'' = (1 - F_{IAFB}) q_{w\ell}'' \quad (6-109)^{(38)}$$

and

$$q_{wv,Brom}'' = F_{IAFB} q_{wt}'' \quad (6-110)^{(38)}$$

with q_{wt}'' given by Equation 6-107.

For $\alpha_v < [\]^{ac}$, the regime is denoted as the Inverted Annular Film Boiling (IAFB) regime and the heat transfer given by

$$h_{wv,IAFB} = h_{wv,FC} + h_{rwv} + \frac{q_{wv,Brom}''}{(T_w - T_v)} \quad (6-111)^{(38)}$$

$$h_{wt,IAFB} = h_{rwt} \quad (6-112)$$

and

$$h_{wb,IAFB} = \frac{q_{wt,Brom}''}{(T_w - T_{sat})} \quad (6-113)^{(49)}$$

where:

- $h_{wv,FC}$ is given by Equation 6-7,
- h_{rwv} is given by Equation 6-156,
- h_{rwt} is given by Equation 6-158,
- $q_{wt,Brom}''$ is given by Equation 6-109 and,
- $q_{wv,Brom}''$ is given by Equation 6-110.

If $[\]^{ac}$, the heat transfer coefficients are calculated using a linear void fraction ramp between the Bromley heat flux and the dispersed droplet regime heat flux. In this void fraction range, the heat transfer regime is designated the Inverted Annular Dispersed Flow (IADF) regime.

The ramp is defined as $[$

$$]^{ac} \quad (6-114)$$

and the heat transfer coefficients for the Inverted Annular Dispersed Flow regime are calculated as

$$h_{wv,IADF} = (h_{wv,FC} + h_{rvv}) + F_{IADF} \frac{q_{wv,Brom}''}{(T_w - T_v)} \quad (6-115)^{(38)}$$

$$h_{wt,IADF} = F_{IADF} h_{rwt} + (1 - F_{IADF}) h_{rwe} \quad (6-116)$$

$$h_{wb,IADF} = F_{IADF} \frac{q_{wt,Brom}''}{(T_w - T_{sat})} + (1 - F_{IADF}) \frac{q_{dcht,e}''}{(T_w - T_{sat})} \quad (6-117)$$

where:

- $h_{wv,FC}$ is given by Equation 6-7,
- h_{rvv} is given by Equation 6-156,
- h_{rwt} is given by Equation 6-158,
- $q_{wt,Brom}''$ is given by Equation 6-109,
- $q_{wv,Brom}''$ is given by Equation 6-110, and
- $q_{dcht,e}''$ is given by Equation 6-128.

Figure 6-10 illustrates the effect of the various ramps in the film boiling regimes. As the wall temperature increases, a higher proportion of the overall heat transfer goes to the vapor phase while direct contact heat transfer and radiation to the liquid phases diminishes. As void fraction increases the heat transfer to the liquid phases decreases to zero.

Scaling Considerations The modified Bromley correlation (Equation 6-97) uses the hydraulic diameter (D_h) as the length scale. Bjornard and Griffith (1977) note that while there is some disagreement in the literature as to whether the hydraulic diameter, the rod diameter, or the critical wavelength should be used, all three yield virtually the same results. Thus, the Bromley correlation is seen to be relatively scale independent.

Conclusions The inverted annular heat transfer regime is characterized by the separation of the liquid field from the heated surface by a thin layer of vapor. Only a very limited amount of liquid-wall contact is assumed to be possible. The main components of the heat transfer are convection to vapor and thermal radiation to the inverted liquid annular column. As the inverted annular column breaks up, there is a transition to dispersed droplet film boiling.

These processes are represented in WCOBRA/TRAC by appropriate correlations. Each of the main mechanisms of heat transfer are modelled. A smooth transition to dispersed droplet film boiling is provided.

The models and correlations for the inverted annular heat transfer regime have been assessed through their use in reflood separate effects tests and in the CCTF, SCTF, and LOFT integral tests. In particular, inverted annular heat transfer is important in reflood separate effects tests with high reflood rates. The reliability and uncertainty in modelling inverted annular heat transfer is thus included in the WCOBRA/TRAC code bias and uncertainty.

6-2-8 Dispersed Flow Film Boiling

Model Basis Dispersed flow film boiling is assumed when the void fraction is greater than []^{a,c}. It is calculated as a "two-step" method where the dominant heat transfer mode is forced convection to superheated steam. The steam superheat is then determined by the interfacial heat transfer rate to the entrained droplets as part of the hydrodynamic solution. The dispersed flow film boiling heat flux is composed of four components.

The total heat flux is given by

$$q_{DFFB}'' = q_{cwv}'' + q_{rvv}'' + q_{rwe}'' + q_{dcht,e}'' \quad (6-118)$$

where:

$$\begin{aligned} q_{cwv}'' &= \text{convective heat flux to vapor} \\ q_{rvv}'' &= \text{radiative heat flux to vapor} \\ q_{rwe}'' &= \text{radiative heat flux to droplets} \\ q_{dcht,e}'' &= \text{drop-wall direct contact heat transfer} \end{aligned}$$

A discussion of each of these components of the dispersed flow heat flux follows.

Forced Convection to Vapor

The convective heat flux to vapor flowing through a rod bundle in a dispersed droplet flow is increased by the interfacial shear with the droplets and by an increase in the turbulence due to the support grids. In WCOBRA/TRAC, the convective flux to vapor in dispersed flow film boiling is expressed as

$$q_{cwv}'' = F_{2\phi} F_{grid} h_{wv,FC} (T_w - T_v) \quad (6-119)$$

where:

$$\begin{aligned} h_{wv,FC} &= \text{heat transfer coefficient to single phase vapor} \\ F_{2\phi} &= \text{two-phase enhancement factor} \\ F_{grid} &= \text{grid heat transfer enhancement factor} \end{aligned}$$

The heat transfer coefficient to single-phase vapor ($h_{wv,FC}$) is determined from Equation 6-7 (Section 6-2-1). Descriptions of the two-phase enhancement factor $F_{2\phi}$ and the grid heat transfer enhancement factor F_{grid} follow.

Two-Phase Enhancement Factor

Some dispersed flow experiments, such as those described by Spencer and Young (1980), Lee et al. (1981) and Drucker and Dhir (1984), have shown that interfacial shear between dispersed particles and a continuous phase increases the turbulence level and enhances the convective heat transfer. The two-phase enhancement factor for dispersed flow ($F_{2\phi}$) is approximated by an extension of the analogy between wall shear stress and heat transfer, described by Kays (1966) as follows:

The wall shear stress can be written as

$$\tau_w = \frac{1}{2} \rho_v f_w \frac{U_v^2}{D_h} \quad (6-120)^{(39)}$$

and the interfacial shear stress due to the droplets by

$$\tau_d = \frac{3}{4} \alpha_e \rho_v C_{Dd} \frac{(U_v - U_d)^2}{D_d} \quad (6-121)^{(39)}$$

and the total shear stress level for the two-phase dispersed flow field as

$$\tau_{2\phi} = \tau_w + \tau_d \quad (6-122)^{(39)}$$

where:

$$\begin{aligned} f_w &= \text{wall friction factor [} && \text{]}^{ac} \text{ (see note below)} \\ C_{Dd} &= \text{droplet drag coefficient} \\ D_d &= \text{drop diameter} \\ \alpha_e &= \text{volume fraction of entrained drops} \end{aligned}$$

From the momentum - heat transfer analogy, the turbulent convective heat transfer coefficient is proportional to the square root of the shear stress, given by Kays (1966) as

$$h_{wv,SPV} = \sqrt{\tau_w} \quad (6-123)^{(39)}$$

The two-phase enhancement factor can be defined as the ratio of convective heat transfer in a two-phase dispersed droplet field to that for a single phase vapor as

$$F_{2\phi} = \frac{h_{wnu,2\phi}}{h_{wnu,SPV}} = \sqrt{\frac{\tau_{2\phi}}{\tau_w}} \quad (6-124)^{(39)}$$

or, using Equation 6-122,

$$F_{2\phi} = \left(1 + \frac{\tau_d}{\tau_w} \right)^{1/2} \quad (6-125)^{(39)}$$

where from Equations 6-115 and 6-116 the shear stress ratio is

$$\frac{\tau_d}{\tau_w} = 1.5 \alpha_e \left(\frac{D_h}{D_d} \right) \left(\frac{C_{Dd}}{f_w} \right) \left(\frac{U_v - U_d}{U_v} \right)^2 \quad (6-126)^{(39)}$$

Instantaneous local values of the variables α_e , D_d , C_{Dd} , f_w , U_v , and U_d are used to evaluate Equation 6-126. A comparison of the two-phase enhancement inferred from FLECHT reflood tests is shown in Figure 6-11. The figure also shows a correlation for turbulence enhancement developed from separate air/water tests and from rod bundle tests at UCLA for EPRI by Drucker and Dhir (1984).

Grid Heat Transfer Enhancement Factor

Spacer grids are structural members in the reactor core which support the fuel rods at a prescribed rod-to-rod pitch. All fuel assemblies have grids at the same elevations across the core. Since the grid reduces

the fuel assembly flow area, the flow contracts and then expands downstream of each grid. As the flow is accelerated within the grid and then expands downstream, it disrupts and reestablishes the fluid and thermal boundary layers on the fuel rod increasing local heat transfer within and downstream of the grid. Several single-phase experiments clearly showed that the continuous phase heat transfer downstream of a spacer grid can be modelled as an entrance effect phenomenon in which the abrupt contraction and expansion result in the establishment of a new boundary layer downstream of the grid.

This entrance effect heat transfer decays exponentially downstream of the grid, as shown in Figure 6-12. Chiou, Hochreiter, and Young (1986) summarized the single phase and two-phase experiments that demonstrated the grid convective enhancement effect, and provided a complete description of the effect of grids on the flow.

The flow acceleration and consequent deceleration as the coolant flows past grid spacer cause a local increase in heat transfer rates downstream because of the creation of free turbulence and the separation and reestablishment of the boundary layer.

The correlation for single-phase enhancement downstream of a spacer grid used in WCOBRA/TRAC was [

]^{a,c}.

Radiation Heat Transfer in Dispersed Flow

The Sun, Gonzalez, and Tien (1976) model is used to account for radiation heat transfer to vapor and droplets in the dispersed flow film boiling regime. The dispersed flow is assumed to be optically thin, and the wall, vapor, and droplets are treated as individual nodes in a radiation heat transfer network. The thermal radiation heat transfer coefficients to vapor h_{rwv} , and to droplets h_{rwd} , are described in Section 6-2-9.

Droplet Impingement Heat Flux

The direct contact heat transfer for the dispersed droplet field is calculated using the model by Forslund and Rohsenow (1968): [

$$J^{a,c} \quad (6-128)^{(22)}$$

The term H_{fg}^* is given by [

$$J^{a,c} \quad (6-129)$$

Model as Coded The heat transfer coefficients for the dispersed flow film boiling regime are calculated in subroutine *HCOOL*. The heat transfer coefficients are calculated as follows:

$$h_{wv,DFFB} = F_{grid} F_{2\phi} h_{wv,FC} + h_{rwv} \quad (6-130)$$

$$h_{wt,DFFB} = h_{rwe} \quad (6-131)$$

$$h_{wb,DFFB} = \frac{q_{dcht,e}''}{(T_w - T_{sat})} \quad (6-132)^{(49)}$$

where:

$h_{wv,FC}$ is given by Equation 6-7,

h_{rwv} is given by Equation 6-156,

h_{rwe} is given by Equation 6-157,

$q_{dcht,e}''$ is given by Equation 6-128, and

F_{grid} is given by Equation 6-127.

The two-phase enhancement factor ($F_{2\phi}$) is calculated by Equation 6-125 and is limited to values within the range $1.0 \leq F_{2\phi} < []^{a,c}$.

Scaling Considerations The convective heat transfer correlations used in the dispersed flow film boiling regime scale with hydraulic diameter. The radiation heat transfer coefficients assume that the mean beam length is equal to the hydraulic diameter, so that h_{rwv} and h_{rwe} also scale with D_h . The direct contact heat transfer is scale independent.

The model for dispersed flow film boiling heat transfer was assessed by simulations of reflood, blowdown and refill separate effects tests. These tests utilized full-scale fuel assemblies and therefore validate the use of this model for analysis of PWR fuel bundles.

Conclusions The key process in dispersed flow film boiling is convective heat transfer to vapor. In the WCOBRA/TRAC model, this process is represented by appropriate convective heat transfer correlations and modified by factors to account for the effect of droplets and grids.

A large number of simulations of tests involving dispersed flow film boiling heat transfer have been performed using WCOBRA/TRAC. These tests include the FLECHT-SEASET, FLECHT Low Flooding Rate, FLECHT Top Skewed Power, FEBA, and NRU reflood separate effects tests, the G-1 and G-2 loop blowdown tests, G-2 refill tests, and the CCTF, SCTF, and LOFT integral tests. Thus, the uncertainty and reliability of the film boiling model is accounted for in the overall WCOBRA/TRAC code bias and uncertainty.

6-2-9 Thermal Radiation Heat Transfer

Model Basis Radiation heat transfer is calculated from the wall to vapor and droplets, and also from the wall to a continuous liquid field for an inverted annular flow. This section describes the calculation of the radiation heat transfer coefficients from wall to vapor (h_{rwv}), wall to droplets (h_{rwe}), and wall to liquid (h_{rwf}).

Radiation to vapor and droplets uses the model developed by Sun, Gonzalez, and Tien (1976). They showed that for a dispersed droplet flow, the wall, vapor, and droplets can be treated as single nodes in a radiation network analysis if the flow is assumed to be optically thin. The gray body factors are

$$F_{we} = \frac{1}{R_2 \left(1 + \frac{R_3}{R_1} + \frac{R_3}{R_2} \right)} \quad (6-133)$$

and

$$F_{wv} = \frac{1}{R_1 \left(1 + \frac{R_3}{R_1} + \frac{R_3}{R_2} \right)} \quad (6-134)$$

where:

$$R_1 = \frac{1 - \epsilon_v}{\epsilon_v (1 - \epsilon_v \epsilon_t)} \quad (6-135)$$

$$R_2 = \frac{1 - \epsilon_t}{\epsilon_t (1 - \epsilon_v \epsilon_t)} \quad (6-136)$$

$$R_3 = \frac{1}{1 - \epsilon_v \epsilon_t} + \frac{1 - \epsilon_w}{\epsilon_w} \quad (6-137)$$

with

$$\epsilon_v = 1 - \exp(-a_v L_b) \quad (6-138)$$

$$\epsilon_t = 1 - \exp(-a_t L_b) \quad (6-139)$$

The parameter L_b is the mean beam length and is assumed to be equal to []^{ac}. The terms a_v and a_t are the vapor and liquid absorption coefficients.

The liquid absorption coefficient is defined as

$$a_t = \psi_a \frac{\pi D_d^2 N_d}{4} \quad (6-140)$$

where D_d is a droplet diameter and N_d is a droplet number density. The parameter ψ_a is the absorption efficiency and has a value of []^{a,c} for drops in the range []^{a,c}.⁽⁴⁰⁾

The droplet number density can be expressed as

$$N_d = \frac{6 (1-\alpha_v)}{\pi D_d^3} \quad (6-141)$$

such that Equation 6-140 becomes

$$a_t = 1.11 \frac{(1-\alpha_v)}{D_d} \text{ (ft)}^{-1} \quad (6-142)^{(41)}$$

The vapor absorption coefficient is given by

$$a_v = \left(\frac{P}{14.7} \right) \left[5.6 \left(\frac{1000}{T_v + 460} \right)^2 - 0.3 \left(\frac{1000}{T_v + 460} \right)^4 \right] \text{ (ft)}^{-1} \quad (6-143)^{(42)}$$

which is from Abu-Romia and Tien (1967).

The fluid emissivities are then given by

$$\epsilon_v = 1 - \exp(-.85 a_v L_b) \quad (6-144)^{(42)}$$

and

$$\epsilon_t = 1 - \exp(-.85 a_t L_b) \quad (6-145)^{(42)}$$

where the beam length (L_b) is assumed to be equal to []^{a,c}. Additional information on Equations 6-143 to 6-145 can be found in Yao et al. (1979).

Radiation heat transfer from the wall to liquid in an inverted annular column is based on radiation between two concentric cylinders. The radiative heat flux from the wall to the liquid can be expressed as

$$q_{rad}'' = \frac{\sigma_{SB} (T_w^4 - T_{sat}^4)}{\frac{A_w}{A_t} \left(\frac{1}{\epsilon_t} \right) + \left(\frac{1}{\epsilon_w} - 1 \right)} \quad (6-146)^{(42)}$$

where A_w is the wall surface area, A_t is the inverted annular column surface area, ϵ_w and ϵ_t are the wall and liquid emissivities, and σ_{SB} is the Stefan-Boltzmann constant.

Model as Coded The radiation heat transfer coefficients are calculated in subroutines BOILING and HCOOL.

The liquid absorption coefficient is calculated as [

]^{a,c}.

The liquid emissivity is calculated as [

]^{a,c} (6-148)⁽⁴²⁾

where the mean beam length is assumed to be the []^{a,c}.

The vapor absorption coefficient is calculated as

$$a_v = \left(\frac{P}{14.7} \right) \left[5.6 \left(\frac{1000}{T_v + 460} \right)^2 - 0.3 \left(\frac{1000}{T_v + 460} \right)^4 \right] \quad (6-149)$$

and the vapor emissivity by [

] ^{a,c} (6-150)⁽⁴²⁾

The gray body factors are then calculated:

$$F'_{wv} = \frac{\sigma_{SB}}{R_1 \left(1 + \frac{R_3}{R_1} + \frac{R_3}{R_2} \right)} \quad (6-151)$$

[

] ^{a,c} (6-152)⁽⁴³⁾

where R_1 , R_2 , and R_3 are calculated by Equations 6-135 to 6-137, and the Stefan-Boltzmann constant is $\sigma_{SB} = 1.713 \times 10^{-9} \frac{\text{Btu}}{\text{hr-ft}^2-\text{°R}^4}$.

The term F'_{wt} is the gray body factor for inverted annular flow and is defined next.

The radiation heat transfer from the wall to an inverted annular column is calculated using Equation 6-146 with the assumptions that $\epsilon_w = []^{a,c(44)}$ and $\epsilon_t = []^{a,c(44)}$ [

] ^{a,c} (6-153)

An additional assumption is made that $\alpha_v \approx [\quad]^{ac(44)}$ (the $[\quad]^{ac}$) so that Equation 6-146 is reduced to

$$q''_{rwt} = F'_{wt} (T_w^4 - T_{sat}^4) \quad (6-154)$$

where: $[\quad]^{ac}$

$$]^{ac} (6-155)^{(42)}$$

The radiation heat transfer coefficients are then calculated as

$$h_{rwv} = F'_{wv} \frac{(T_w^4 - T_v^4)}{(T_w - T_v)} \quad (6-156)$$

$$h_{rwe} = F'_{we} \frac{(T_w^4 - T_{sat}^4)}{(T_w - T_l)} \quad (6-157)$$

$$h_{rwt} = F'_{wt} \frac{(T_w^4 - T_{sat}^4)}{(T_w - T_l)} \quad (6-158)$$

where F'_{wv} and F'_{we} are given by Equations 6-151 and 6-152 and $F'_{wt} = [\quad]^{ac}$. In Equations 6-157 and 6-158, it is assumed that the surface temperature of the liquid drops and liquid column is at saturation. For Equations 6-156 through 6-158, temperatures are converted to degrees Rankine.

Scaling Considerations The radiation heat transfer coefficients from wall to vapor and wall to drops assume the mean beam length is equal to $[\quad]^{ac}$.

$]^{ac}$. Scaling is

therefore not a concern.

Conclusions Radiation heat transfer tends to be a dominant mode of heat transfer only when the rod temperatures become very high ($> 2000^{\circ}\text{F}$). Simulations of the FLECHT-SEASET separate effects reflood tests were performed using WCOBRA/TRAC. Several tests were simulated, Test 31805 in particular, in which very high rod temperatures were measured. Therefore, the radiation heat transfer model uncertainty is thus accounted for in the overall WCOBRA/TRAC code bias and uncertainty.

6-2-10 Grid Rewet Model

Model Basis Spacer grids have important effects on heat transfer in a rod bundle. Since the grids are unpowered, they can quench before the fuel rods. When the grids quench, they create additional liquid surface area which de-superheats vapor in a non-equilibrium, two-phase, dispersed droplet flow. The film on a wetted grid also has a higher interfacial heat transfer coefficient as compared to the droplets, since the relative velocity at the grid is higher. Rewetting of the grids is important and must be accounted for in a best estimate analysis.

[

]^{ac} (6-159)

The grid temperature from Equation 6-159 is [

]^{ac}.

The radiation heat transfer from the rods to the grid is given by [

]^{ac}.

The grid is permitted to rewet if sufficient liquid is available, and if T_{grid} drops below the minimum film boiling temperature T_{MIN} .

Model as Coded The emissivities of the rod and the grid are assumed to be $\epsilon_w = \epsilon_{grid} = [\quad]^{a,c}$, and the value of D_{grid} is taken to be [

$$]^{a,c} \quad (6-162)^{(45)}$$

where P_{rod} is the fuel rod pitch.

The radiative heat flux to the grid is then calculated explicitly using the grid temperature from the previous time step T_{grid}^n as [

$$]^{a,c} \quad (6-163)$$

and the new time grid temperature is calculated as [

$$]^{a,c} \quad (6-164)$$

where: [

$$]^{a,c}.$$

The grid temperature is then numerically damped to prevent rapid changes as [

$$]^{a,c} \quad (6-166)$$

The minimum film boiling temperature for the grid is estimated as [

$$]^{ac} \quad (6-167)^{(46)}$$

where T_{MIN} is calculated by Equation 6-101. In effect, Equation 6-167 insures that the [

$]^{ac}$.

A flag to indicate possible grid rewet is then set:

$$I_{wet} = \begin{cases} 1 & \text{if } T_{grid} < T_{MIN,g} \\ 0 & \text{if } T_{grid} \geq T_{MIN,g} \end{cases} \quad (6-168)$$

This flag is then used as described in Section 5-2-10 in the calculation of interfacial heat transfer due to evaporation of the liquid film on the grid.

Scaling Considerations The grid rewet model is independent of scale, and depends on the structural design of the spacer grids and rod bundle arrays.

Conclusions The primary processes in the initial quenching of a grid are convection to steam and radiation from the rods. Because the grid strap mass is small, it is assumed to quickly rewet once a quench front is established. The simple WCOBRA/TRAC grid rewet model accounts for the convection and radiation processes by using appropriate expressions.

The grid rewet model has been assessed by its use in simulations of reflood separate and integral effects tests and in blowdown test simulations. Full size prototype PWR grids, as well as supplier grids, were modelled in these tests. The uncertainty and reliability of the grid rewet model is therefore included in the overall WCOBRA/TRAC code bias and uncertainty.

6-2-11 Wall to Fluid Heat Transfer

Model Basis The heat transfer coefficients h_{wv} , h_{wet} , and h_{wb} are used to determine the heat transfer to the vapor field, the combined liquid fields (continuous liquid and entrained liquid), and the fraction of the heat transfer from subcooled boiling that results in vapor generation. Sections 6-2-1 through 6-2-9 described the models and correlations used to determine the heat transfer coefficients for the vessel component. This section discusses the use of these coefficients in the determination of the wall to fluid heat transfer.

The heat transfer rates, used as boundary conditions in the fluid energy equations at each heat transfer node location, are given by

$$Q_{wv} = h_{vap} A_w (T_w - T_v) \quad (6-169)$$

$$Q_{wl} = h_{liq} A_w (T_w - T_l) \quad (6-170)$$

where A_w represents the heat transfer node surface area. The calculation of h_{vap} and h_{liq} from the values of h_{wv} , h_{wl} , and h_{wb} follow.

Model as Coded Calculations to determine h_{wv} , h_{wl} , and h_{wb} are performed in subroutine for the appropriate heat transfer regime. These coefficients are returned to subroutine HEAT, where h_{vap} and h_{liq} are calculated and used to determine Q_{wv} and Q_{wl} .

First, two ramps are defined which smooth changes in the heat transfer coefficients as one phase or another is depleted.

These are [

] ^{ac} (6-172)

The wall to vapor heat transfer coefficient is calculated using numerical damping with the new and old time step values as [

] ^{ac} (6-173)

and similarly, a wall to liquid heat transfer coefficient by [

$$]^{ac} \quad (6-174)$$

where the superscript n denotes the old time step value. The ratio of heat transfer for latent heat to the overall heat transfer to liquid is calculated as [

$$]^{ac} \quad (6-175)$$

For solution of the conduction equation, described in Section 7, the derivative of the wall to liquid heat transfer coefficient with respect to temperature is needed for heat transfer nodes in the nucleate boiling regime. This is calculated as [

$$]^{ac} \quad (6-176)^{(47)}$$

where $\frac{dh_{CHEN}}{dT_w}$ is given by Equation 6-48 for the nucleate boiling regime, but is 0.0 for all other regimes.

The wall to liquid heat transfer coefficient is then calculated as [

$$]^{ac} \quad (6-177)$$

where T_w^n is the wall temperature for the heat transfer node from the previous timestep. From the definition and use of $\frac{dh_{CHEN}}{dT_w}$ in Equation 6-176, $h_{liq} = h_{liq}^*$ from Equation 6-174 except for nucleate boiling.

The phasic heat transfer rates are then calculated as [

$$]^{ac} \quad (6-178)^{(48)}$$

and [

$$]^{a,c} (6-179)^{(48)}$$

The rate of heat transfer that causes subcooled boiling vapor generation Q_b , is calculated as [

$$]^{a,c} (6-181)$$

Scaling Considerations The above discussion is the coupling of the thermal-hydraulic calculation to the fuel rod and structural calculations such that scaling concerns are not applicable.

Conclusions The calculation of the phasic heat transfer rates use the conventional definition of heat flux. Ramps are imposed to insure smooth behavior as a phase is depleted, and numerical damping is used to prevent numerical oscillations that could result from the explicit/implicit coupling of the fluid and structures. All of the WCOBRA/TRAC simulations of heated tests provide verification of the model for phasic heat transfer.

6-3 One-Dimensional Component Wall Heat Transfer

This section describes the models and correlations used in WCOBRA/TRAC to determine the heat transfer coefficients in the one-dimensional components. The heat transfer coding logic in WCOBRA/TRAC for the one-dimensional components is from the TRAC-PD2 package as released by Los Alamos (Liles et al., 1981). The expressions and coding for this package are in the metric system of units. While the heat transfer logic in TRAC-PD2 can generate a full boiling curve with all the heat transfer regimes being modelled, the loops quickly void during the transient and are filled with vapor; so heat transfer rates are low, and single phase vapor convection is dominant. The exception is the steam generator, which is initially a heat sink during the early portion of blowdown, then becomes a heat source. For this situation, the dispersed flow film boiling model is important.

The selection and calculation of heat transfer coefficients is controlled by subroutine HTCOR, which defines eight different heat transfer regimes. These regimes and the code assigned identification number (IDREG) for each region are shown in Table 6-1.

The following sections discuss the correlations used in the regimes denoted in Table 6-1, in addition to calculations performed for the critical heat flux and the minimum stable film boiling temperature.

Figure 6-13 presents the coding logic that determines the heat transfer regime for WCOBRA/TRAC one-dimensional components.

6-3-1 Single-Phase Liquid Natural Convection

Model Basis Conventional heat transfer correlations are used for single-phase flow situations. The code has logic to determine natural convection, forced laminar convection or turbulent flow forced convection. Natural convection heat transfer is assumed when the quantity (Gr_t / Re_t^2) is greater than $[]^{a,c}$ or if $Re_t = 0.0$, where:

$$Re_t = \frac{\rho_t U_t D_h}{\mu_t} \quad (6-182)$$

and

$$Gr_t = \frac{g_c \beta |T_w - T_t| \rho_t^2 D_h^3}{\mu_t^2} \quad (6-183)$$

Heat transfer coefficients for laminar natural convection are calculated by the McAdams (1954) correlation:

$$h_{wt,inc} = 0.59 (Gr_t Pr_t)^{1/4} \frac{k_t}{D_h}, \quad (Gr_t Pr_t) \leq 10^9 \quad (6-184)$$

or by

$$h_{wt,inc} = 0.10 (Gr_t Pr_t)^{1/3} \frac{k_t}{D_h} \quad (6-185)$$

as suggested by Holman (1976) for turbulent flow.

Model as Coded The natural convection heat transfer coefficients $h_{wt,inc}$ and $h_{wt,nc}$ are calculated in subroutine HTCOR. The heat transfer coefficient to vapor $h_{wv,nc}$ is set to zero. All thermal properties except ρ_t and β are evaluated at the liquid temperature. The properties ρ_t and β are approximated as [

$]^{a,c}$ (6-186)

and [

$$]^{ac} \quad (6-187)$$

where T_{film} is the average of the wall and fluid temperatures.

The heat transfer coefficient selected by Subroutine HTCOR for this regime is the maximum value predicted by Equations 6-184 and 6-185. That is,

$$h_{wt,nc} = \text{maximum} \begin{cases} h_{wt,Inc} \\ h_{wt,mc} \end{cases} \quad (6-188)^{(50)}$$

By using the maximum, the laminar correlation is actually applied up to a value of $Gr_t \cdot Pr_t [\quad]^{ac}$.

Scaling Considerations The correlations used in the one-dimensional components for natural convection heat transfer use the hydraulic diameter as the characteristic length, rather than a vertical height which would be more appropriate. However, in turbulent natural convection, the heat transfer coefficient is not dependent on a characteristic dimension and in laminar natural convection, the heat transfer coefficient is only weakly dependent on the characteristic length.⁽⁵¹⁾

The most important region where natural convection heat transfer may occur during a LOCA transient is the steam generator secondary side. The heat transfer in this situation is from the secondary side fluid to the primary tube side dispersed flow two-phase mixture. Once the transient begins, the reactor power quickly drops to less than 5 percent of full power, and the secondary side heat transfer area is considerably over-sized relative to the full core power. The small uncertainty in the secondary side heat transfer coefficient will have almost no effect on the heat transfer to the primary fluid.

The WCOBRA/TRAC code has been compared to the CCTF experiments which have an unpressurized secondary side steam generator. The calculations indicate super-heating of the incoming primary two-phase mixture, which is consistent with the experimental data, as well as stratification of the secondary side through heat released by natural convection. Since the CCTF steam generators are full height and have similar tube diameter and pitches as a PWR steam generator, there should be no scale effects of the natural convection models.

Conclusions The natural convection heat transfer correlations used by the one-dimensional component heat transfer package are generally accepted correlations from the literature. These correlations have been tested in full height simulations in the CCTF experiments where they would have the greatest effect. Since these tests are full length and use prototypical PWR dimensions, there are no scale effects.

6-3-2 Single-Phase Liquid Forced Convection

Model Basis Heat transfer coefficients for both laminar and turbulent flows are calculated. For laminar flow, a theoretical analysis (Rohsenow and Choi, 1961) is used:

$$h_{wt,lfc} = 4.0 \frac{k_t}{D_h} \quad (6-189)$$

This equation represents a compromise between the analytically developed equations for uniform wall heat flux and uniform wall temperature for fully developed laminar flow in round tubes assuming a parabolic velocity profile. For the fully developed turbulent-flow regime, the Dittus-Boelter (1930) equation is used and is given by

$$h_{wt,lfc} = 0.023 \frac{k_t}{D_h} Re_t^{0.8} Pr_t^{0.4} \quad (6-190)$$

where the liquid Reynolds number is

$$Re_t = \frac{\rho_t U_t D_h}{\mu_t} \quad (6-191)$$

and the liquid Prandtl number is

$$Pr_t = \left(\frac{\mu_t c_p}{k} \right)_t \quad (6-192)$$

Model as Coded Both correlations given by Equations 6-189 and 6-190 are evaluated in subroutine CHEN and the maximum is selected as the single-phase liquid forced heat transfer coefficient.

The fluid properties in both correlations are evaluated at the liquid temperature and pressure. The velocity used to calculate the Reynolds number is the absolute value of the liquid velocity.

Scaling Considerations The laminar and turbulent flow correlation represent the geometry of the systems by the use of the hydraulic diameter, which is scale independent. These correlations have been applied on experiments with different scales to model the heat transfer in the one-dimensional components, such as CCTF, SCTF, and the LOFT loops. The most important loop component, from a heat transfer perspective, is the steam generator, since it can be a heat source or sink during the transient.

The CCTF generator used full height steam generator tubes with diameters which are typical of PWR steam generators, so that these correlations have been tested at full scale on the most important loop component.

Conclusions The one-dimensional, components use forced, convection heat transfer coefficients that are accepted correlations from the literature. These correlations have been assessed on large-to-full-scale components.

6-3-3 Nucleate Boiling

Model Basis The Chen correlation (1963) is used in the nucleate boiling heat transfer regime. The correlation assumes that both boiling and forced convective mechanisms occur and that the contributions made by the two mechanisms are additive. The convective component is assumed to be represented by a modified Dittus-Boelter (1930) equation where the thermal conductivity, Reynolds number, and Prandtl number are effective values associated with the two-phase flow. The liquid properties are used for the Reynolds number since a liquid film is assumed to exist on the wall. The values of the Prandtl number for liquid and vapor are normally of the same order of magnitude and it is reasonable to expect the two-phase Prandtl number to have a similar value. A parameter, $F_{CHEN} \geq 1.0$, which is a function of the Martinelli parameter (γ) is used to modify the convective part of the correlation, h_{forc} (called the macroterm), to account for increased agitation caused by the formation of vapor bubbles. The factor F_{CHEN} is the ratio of an effective two-phase Reynolds number to the single-phase liquid Reynolds number.

The basis for the nucleate boiling component of the correlation is the analysis of Forster and Zuber (1955) for pool boiling. Their analysis relates a bubble Nusselt number to a bubble Reynolds number and a liquid Prandtl number. It can be shown that the product of growth rate and bubble radius is constant for a given superheat. In pool boiling and convective boiling, the superheat is not constant across the boundary layer. In pool boiling, this effect can be neglected. In forced convective boiling, the boundary layer is thinner and temperature gradients are steeper. The difference between the wall superheat and the mean superheat to which the bubble is exposed must be considered. A suppression factor, S_{CHEN} , modifies the nucleate boiling part of the correlation, h_{nucb} (called the microterm), to account for this effect, and is a function of the two-phase Reynolds number.

The Chen model provides the transition from a liquid forced convection flow into fully developed nucleate boiling. As the quality in the flow increases, the two-phase convection increases and merges with the nucleate boiling portion of the correlation.

The equations for the Chen correlation are as follows:

$$h_{CHEN} = h_{forc} + h_{nucb} \quad (6-193)$$

where:

$$h_{forc} = 0.023 \frac{k_t}{D_h} \left(\frac{|U_t| \rho_t (1-\alpha) D_h}{\mu_t} \right)^{0.8} \left(\frac{\mu C_p}{k} \right)_t^{0.4} F_{CHEN} \quad (6-194)^{(52)}$$

and

$$h_{nucb} = 0.00122 \frac{k_t^{0.79} C_{pl}^{0.45} \rho_f^{0.49}}{\sigma^{0.5} \mu_f^{0.29} H_{fg}^{0.24} \rho_g^{0.24}} (T_w - T_{sat})^{0.24} (P_w - P)^{0.75} S_{CHEN} \quad (6-195)$$

with F_{CHEN} defined as

$$F_{CHEN} = 1.0, \quad \text{for } \chi_{TT}^{-1} \leq 0.10 \quad (6-196)$$

and

$$F_{CHEN} = 2.35 \left(\chi_{TT}^{-1} + 0.213 \right)^{0.736}, \quad \text{for } \chi_{TT}^{-1} > 0.10 \quad (6-197)$$

where:

$$\chi_{TT}^{-1} = (\text{Martinelli factor})^{-1} = \left(\frac{x}{1-x} \right)^{0.9} \left(\frac{\rho_f}{\rho_g} \right)^{0.5} \left(\frac{\mu_g}{\mu_f} \right)^{0.1} \quad (6-198)$$

and the suppression factor (S_{CHEN}) is defined as

$$S_{CHEN} = \left(1 + 0.12 Re_{2\Phi}^{1.14} \right)^{-1}, \quad Re_{2\Phi} < 32.5 \quad (6-199)$$

or

$$S_{CHEN} = \left(1 + 0.42 Re_{2\Phi}^{0.78} \right)^{-1}, \quad 32.5 \leq Re_{2\Phi} \leq 70.0 \quad (6-200)$$

and with the two-phase Reynolds number defined as

$$Re_{2\Phi} = 10^{-4} \frac{|U_t| \rho_t (1-\alpha) D_h}{\mu_t} F_{CHEN}^{1.25} \quad (6-201)$$

The Chen correlation provides the transition from forced convection liquid flow to nucleate boiling by enhancing the convective heat transfer with a two-phase Reynolds number and suppressing the boiling heat transfer as the convective portion of the heat transfer increases. As the void fraction or flow quality increases, the nucleation in the wall film becomes suppressed and the boiling contribution is decreased. Lahey and Moody (1977) have shown how the Chen correlation merges with the fully developed nucleate boiling correlation by Jens-Lottes (1951) and the high void fraction dryout correlation by Dengler and Addoms (1956). As Lahey and Moody indicate, the Chen correlation merges with the nucleate boiling correlation at low quality where the two-phase Reynolds number is low and also merges with the high quality dryout correlation as the quality increases and the convection is enhanced at the expense of the nucleate boiling term in the correlation.

Model as Coded The liquid heat transfer coefficient is calculated in subroutine CHEN and the vapor heat transfer coefficient is calculated in subroutine HVFILM. [

]^{a,c}. The liquid heat transfer coefficient is then given by [

]^{a,c}.

The Chen correlation was originally used in TRAC-PD2 for boiling in rod bundle arrays. The Chen correlation described here is used for loop components where the structure wall temperature exceeds T_{sat} and an evaporating liquid film exists on the walls. The components are mostly larger pipes whose geometry can be characterized by the hydraulic diameter. The void fraction in these structures is usually

very high, $\alpha > 0.96$, for most of the transient so that only a portion of the Chen correlation is used for the total heat transfer, while the forced convection to vapor is the primary mode of heat transfer.

Another location where the Chen correlation can be used is in the steam generator tubes as the reactor system depressurizes. This occurs very early in blowdown. Since the steam generators are vertical tubes, there should be no scaling effect. The WCOBRA/TRAC one-dimensional structure heat transfer models have been verified in different scaled tests such as LOFT and CCTF, when the walls were super-heated relative to the fluid. No scaling bias was observed in these simulations.

Conclusions Most of the data from which the correlations were developed were for boiling inside vertical tubes. The Chen correlation, although semi-empirical, does have a physical basis. It works well for a variety of fluids (including water), covers both the low- and high-quality regions, and transforms into the Forster-Zuber correlation for pool boiling at low flows.

6-3-4 Critical Heat Flux

Model Basis The critical heat flux is predicted by WCOBRA/TRAC for one-dimensional components using the Biasi correlation (1967) with modifications at low mass velocities and high void fractions.

The Biasi correlation consists of the following two equations, and the maximum CHF value calculated by these equations is used:

$$q''_{CHF} = \frac{1883}{D_h^m G^{1/6}} \left[\frac{F(P)}{G^{1/6}} - x \right] \quad (6-203)$$

and

$$q''_{CHF} = \frac{3780}{D_h^m G^{0.6}} H(P) (1-x) \quad (6-204)$$

where:

$$\begin{aligned} q''_{CHF} &= \text{critical heat flux, (W/cm}^2\text{)} \\ m &= 0.4 \text{ for } D_h \geq 1\text{cm, } 0.6 \text{ for } D_h < 1\text{cm,} \\ F(P) &= 0.7249 + 0.099P \exp(-0.032P), \\ H(P) &= -1.159 + \frac{8.99P}{10 + P^2} + 0.149P \exp(-0.019P), \\ D_h &= \text{diameter (cm),} \end{aligned}$$

G	=	mass flux ($g \cdot cm^{-2} \cdot s^{-1}$),
P	=	pressure (bar), and
x	=	equilibrium quality.

Typically Equation 6-203 is for low quality and Equation 6-204 is for high quality. For a given mass flux and tube diameter, the switch-over quality between the two equations is shown as a function of pressure in Figure 6-14 taken from Liles et al. (1988). As seen in this figure, the switch-over quality is not constant and varies between 0.3 and 0.68 within the pressure range of the Biasi correlation. It exhibits a peak between 2 and 3 MPa.

The Biasi correlation was originally correlated over a data base containing 4551 CHF data points. The ranges of the CHF parameters within this data base are as follows:

$$0.3\text{ cm} < D_h < 3.75\text{ cm}$$

$$20\text{ cm} < L < 600\text{ cm}$$

$$0.27\text{ MPa} < P < 14.0\text{ MPa}$$

$$10\text{ g} \cdot \text{cm}^{-2} \cdot \text{s}^{-1} < G < 600\text{ g} \cdot \text{cm}^{-2} \cdot \text{s}^{-1}$$

$$x_{inlet} < 0$$

$$\frac{1}{1 + \rho_t/\rho_v} < x < 1$$

Model as Coded The Biasi correlation is written in cgs units. Thus, Equations 6-203 and 6-204 yield the CHF in W/cm^2 . To obtain the CHF directly in W/cm^2 , Equations 6-203 and 6-204 are multiplied by 10^4 in the code. All the other constants remain unchanged.⁽⁵⁵⁾

In WCOBRA/TRAC, the critical heat flux calculations for one-dimensional components are done in subroutines CHF and CHF1, and are used in HTCOR. The critical heat flux temperature is needed in HTCOR to differentiate between the nucleate boiling and transition boiling regimes. The critical heat flux temperature is also needed for computing the heat transfer coefficient in the transition boiling regime.

In the subroutine CHF, the value of the critical heat flux calculated in subroutine CHF1 is used with the Chen nucleate boiling heat transfer correlation to obtain the corresponding critical heat flux temperature. This requires an iterative solution which is done by the Newton-Raphson procedures. The iteration is started by using []^{ac} as the initial guess. The latest calculated value of T_{CHF} is used in

subsequent iterations. The magnitude of the critical heat flux temperature is bound at the lower and upper ends as follows: [

] ^{ac} (6-205)

Scaling Considerations The Biasi correlation has been developed based on CHF test data for tubes from 0.12 inches in diameter to 1.47 inches in diameter and tube lengths up to 20 feet, which cover prototypical steam generator tube diameters.

The range of fluid conditions for which this correlation was developed covers expected PWR steam generator conditions during reflood. The correlation is being used in the geometry configuration and ranges for which it was originally developed. Therefore, no scaling bias is expected when applying this correlation for the steam generator component. The correlation has been tested in the WCOBRA/TRAC analysis of the LOFT and CCTF experiments, both of which have heated steam generators.

Conclusions The application of the Biasi correlation for the WCOBRA/TRAC one-dimensional components, the steam generator, is within the range of conditions for which the correlation was developed.

6-3-5 Transition Boiling

Model Basis The transition boiling regime spans the boiling curve between the critical heat flux and the minimum film boiling point. It is assumed that transition boiling heat transfer is composed of both nucleate boiling (wet-wall) and film boiling (dry-wall) heat transfer components. Each component is weighted by a factor F_{wet} , the fraction of wall area that is wet. The equations used in the transition boiling regime are from Bjornard and Griffith (1977):

$$q''_{tb} = F_{wet} q''_{CHF} + (1 - F_{wet}) q''_{MIN} \quad (6-206)$$

where:

$$F_{wet} = \left(\frac{T_w - T_{MIN}}{T_{CHF} - T_{MIN}} \right)^2 \quad (6-207)$$

such that the transition boiling heat transfer coefficient becomes

$$h_{tb} = q''_{tb} / (T_w - T_t) \quad (6-208)^{(56)}$$

In Equation 6-207, T_{MIN} is the wall temperature of the minimum stable film boiling point, while q''_{MIN} is the heat flux at that wall temperature. The transition boiling heat flux is simply a ramp between the critical heat flux (q''_{CHF}) heat flux at T_{CHF} to the film boiling heat flux, q''_{MIN} at T_{MIN} . The methods and correlations used to calculate q''_{MIN} and T_{MIN} will be discussed in following sections on film boiling.

Model as Coded⁽⁵⁷⁾ Calculations for the transition boiling regime are performed primarily in subroutine HTCOR. Subroutines CHEN, CHF, CHF1, DFHT, TMSFB, and HVFILM are called by HTCOR to perform various parameters such as the critical heat flux and minimum stable film boiling temperature. The transition boiling regime is assumed if,

$$T_w \leq T_{MIN}$$

$$T_w > T_{CHF}$$

$$x_{eq} < 1.0$$

where x_{eq} is the equilibrium quality defined as,

$$x_{eq} = \frac{(H_{mix} - H_f)}{H_{fg}}$$

where H is an enthalpy.

If the void fraction $\alpha > [\quad]^{ac}$, a single-phase heat transfer coefficient for the vapor phase, $h_{wv,spv}$, is calculated as described in Section 6-3-8.

A "total" transition boiling heat transfer coefficient is calculated as [

$$]^{ac} \quad (6-209)$$

where F_{wet} is defined by Equation 6-207. The critical heat flux is calculated as discussed in Section 6-3-4 and the heat flux at the minimum stable film boiling point is calculated as indicated in Section 6-3-6.

The liquid phase heat transfer coefficient is then calculated as [

$$]^{a,c} \quad (6-210a)$$

where the vapor phase heat transfer coefficient assumes film boiling and is calculated in subroutine HVFILM as, [

$$]^{a,c} \quad (6-210b)$$

[

$$]^{a,c} \quad (6-211a)$$

for the liquid phase heat transfer coefficient, and, [

$$]^{a,c} \quad (6-211b)$$

for the vapor phase heat transfer coefficient. Equation 6-211a linearly ramps the liquid phase coefficient to 0.0, and Equation 6-211b decreases the vapor phase coefficient to that of the single-phase vapor regime as the void fraction approaches 1.0.

Scaling Considerations The expressions used to calculate the transition boiling heat flux are based mainly on data from tubes and annuli. In WCOBRA/TRAC this transition boiling model is used primarily for steam generator tubes during reflood when a two-phase mixture enters the tubes. The steam generator tube wall temperature can be in the range where transition boiling is calculated to occur.

WCOBRA/TRAC has been verified against experiments, such as CCTF and LOFT, which have prototypical, full height, steam generator tubes with a hot pressurized secondary fluid as the heat source.

Conclusions A simple transition boiling model is used in the one-dimensional components to provide a smooth transition between the CHF point and the minimum film boiling point on the boiling curve. This model is most important in modelling the steam generator heat release during reflood and has been verified on prototypical steam generator data during reflood.

6-3-6 Minimum Film Boiling Temperature

Model Basis The minimum stable film boiling temperature T_{MIN} is the temperature at the intersection point between the transition boiling and the film boiling heat transfer regimes. It is also used in determining the transition boiling heat flux. In WCOBRA/TRAC one-dimensional components, the minimum film boiling temperature is calculated to be the maximum of the homogeneous nucleation temperature and the correlation by Iloeje et al. (1975). The homogeneous nucleation model for T_{MIN} is given as

$$T_{MIN,hn} = T_{crit} + (T_{crit} - T_l) R^{1/2} \quad (6-212)^{(57)}$$

where T_{crit} is the critical temperature of 705.2 °F and

$$R = \frac{(k\rho c_p)_l}{(k\rho c_p)_w} \quad (6-213)$$

is the ratio of the fluid properties at the fluid temperature and wall temperature, where the subscript l indicates liquid properties and the subscript w refers to wall properties.

T_{MIN} is also calculated using the Iloeje et al. (1975) correlation developed for liquid nitrogen. The Iloeje correlation is empirical and depends on the mass flux and equilibrium quality as follows:

$$T_{MIN,I} = T_{sat} + 0.29\Delta T_B (1.0 - 0.295x^{2.45}) [1.0 + (G \cdot 10^{-4})^{0.49}] \quad (6-214)^{(58)}$$

where:

$$\Delta T_B = 0.217 \frac{\rho_v H_{fg}}{k_v} \left[\frac{g(\rho_l - \rho_v)}{\rho_l + \rho_v} \right]^{2/3} \left[\frac{g_c \sigma}{g(\rho_l - \rho_v)} \right]^{0.5} \left[\frac{\mu_l}{g_o(\rho_l - \rho_v)} \right]^{1/3} \quad (6-215)^{(72)}$$

and x is the equilibrium quality.

[

] ^{a,c}

The liquid properties should be evaluated at the film temperature

$$T_{film} = 0.5(T_w + T_{sat}) \quad (6-216)$$

where T_{sat} is the saturation temperature.

There are limits placed on the Iloeje correlation as discussed below. The one-dimensional component heat transfer package logic chooses the maximum of the homogeneous nucleation value or the Iloeje value for T_{MIN} . That is

$$T_{MIN} = \text{maximum} \begin{cases} T_{MIN,hn} & \text{(Equation 6-212)} \\ T_{MIN,I} & \text{(Equation 6-214)} \end{cases} \quad (6-217a)$$

There are also limits placed on the Iloeje et al. (1975) correlation to keep it within its database. [

] ^{a,c}. The liquid properties are calculated at the film temperature as defined in Equation 6-216, and the vapor properties are evaluated at T_{sat} .

The heat flux at the minimum stable film boiling point, which is used in the transition boiling model is calculated as [

] ^{a,c} (6-217b)

where the radiation term is calculated as [

] ^{a,c} (6-217c)

and h_{diff} and $h_{wv,fb}$ are described in Section 6-3-7. ⁽⁵⁶⁾

Scaling Considerations The component where WCOBRA/TRAC may use the calculated value of T_{MIN} is in the steam generator during reflood. The homogeneous nucleation equation is a thermodynamic limit and as such does not have any scale dependency. The Iloeje et al. (1975) correlation is an empirical fit to water data and requires validation. The one-dimensional component heat transfer package has been

used in the analysis of the CCTF reflood test, which has full height steam generators. The tests use prototypical steam generator tube dimensions and lengths such that there should not be a scaling concern.

Conclusions Models have been developed to calculate the minimum wall temperature for film boiling. These models have been verified against prototypical data.

6-3-7 Film Boiling Heat Transfer

Model Basis The film-boiling heat-transfer regime incorporates several different correlations to describe fully-developed film boiling. The film boiling regime is assumed to occur when the wall temperature exceeds the minimum stable film boiling temperature ($T_w > T_{MIN}$). The wall-to-vapor and wall-to-liquid heat transfer are calculated separately. The wall-to-liquid heat transfer coefficient is assumed to be the sum of two components: radiation and dispersed flow film boiling. The film boiling liquid heat transfer coefficient is given by [

$$]^{a,c} \text{ (6-218)}$$

where the radiative component is [

$$]^{a,c} \text{ (6-219)}^{(59)}$$

and the dispersed flow film boiling portion is given as the modified Forslund-Rohsenow correlation (1968), where: [

$$]^{a,c} \text{ (6-220)}^{(62)}$$

In these correlations σ_{SB} is the Stefan-Boltzmann constant, ϵ_w is the wall emissivity (assumed to be [$]^{a,c}$),⁽⁵⁹⁾ and [

$$]^{a,c} \text{ (6-221)}$$

D_d is the droplet diameter based upon a critical Weber number (We_d) of [$]^{a,c}$.⁽⁵⁹⁾

$$D_d = \frac{We_d \sigma}{\rho_v (U_v - U_d)^2} \quad (6-222)$$

and σ is the surface tension. The value for the fraction of liquid entrained, (F_e) is found as [

$$]^{a,c} \quad (6-223)^{(60)}$$

for $|U_v| > U_{re}$, where: [

$$]^{a,c}.$$

The drop diameter in Equation 6-222 is restricted to the range [

$$]^{a,c} \text{ meters.}^{(61)}$$

The temperature ratio in Equation 6-220 [

$$]^{a,c}.$$

The wall-to-vapor film boiling heat transfer coefficient calculated in this heat transfer regime is the greater of the Dougall-Rohsenow (1963) correlation ($h_{wv,DR}$), the turbulent natural convection ($h_{wv,nc}$) correlations, and the Bromley correlation, $h_{wv,Brom}$.

The Dougall-Rohsenow (1963) correlation is given as follows:

$$h_{wv,DR} = 0.023 \frac{k_v}{D_h} \left[\frac{\rho_v \{ \alpha_v U_v + (1 - \alpha_v) U_t \} D_h}{\mu_v} \right]^{0.8} \cdot [Pr_v]^{0.4} \quad (6-225)$$

The Bromley (1950) correlation is given as

$$h_{wv,Brom} = 0.62 \left\{ \frac{\rho_v k_v^3 (\rho_t - \rho_v) g H_{fg}}{\mu_v (T_w - T_{sat}) \lambda} \right\}^{0.25} \quad (6-226)$$

where the critical wavelength is

$$\lambda = 2\pi \left[\frac{\sigma}{g(\rho_t - \rho_v)} \right]^{1/2} \quad (6-227)$$

The natural convection correlation to vapor is given from McAdams (1954) as

$$h_{wv,nc} = 0.13 k_v \left[\frac{\rho_v^2 g_c (T_w - T_v)}{\mu_v^2 T_v} \right]^{1/3} \cdot Pr_v^{1/3} \quad (6-228)$$

where, for the volumetric coefficient of expansion β , Equation 6-228 assumes:

$$\beta = \frac{1}{T_v} \quad (6-229)$$

Model as Coded Separate liquid and vapor heat transfer components are calculated for the film boiling heat transfer. For the heat transfer to liquid, the model calculates the radiation heat transfer and the Forslund and Rohsenow model for vapor void fractions $\leq [\]^{ac}$. Above $\geq [\]^{ac}$ the Forslund and Rohsenow model is not used. The entrainment fraction (F_e) in the Forslund and Rohsenow model is limited to values between $[\]^{ac}$ and 1.0.

For the heat transfer to vapor, in film boiling, the code chooses the largest of the h_{wv} correlations given in Equations 6-225, 6-226, and 6-228.

That is,

$$h_{wv,fb} = \text{maximum} \begin{cases} h_{wv,nc} \\ h_{wv,Brom} \\ h_{wv,DR} \end{cases} \quad (6-230)$$

For the Dougall-Rohsenow correlation, for void fractions above $[\]^{ac}$ is used to reach forced convection to vapor at $\alpha = 1.0$.

Scaling Considerations The correlations used for film boiling have been primarily developed on tube flow geometries. The most significant location where these correlations would be applied is the steam generator tubes during blowdown and reflood. The one-dimensional component film boiling model has been used to model the LOFT and CCTF tests, which have steam generator components that have prototypical PWR dimensions. No scale bias effects have been observed with these models.

Conclusions The film boiling models in WCOBRA/TRAC one-dimensional components model calculate the energy split between the liquid phase and vapor phase. These models have been verified on prototypical steam generator components in the LOFT and CCTF test simulations.

6-3-8 Convection to Single-Phase Vapor

Model Basis Heat transfer by convection to single-phase vapor is evaluated when the void fraction is greater than []^{a,c}.⁽⁶⁴⁾ In this heat transfer regime the vapor heat transfer coefficient is selected as the larger of the McAdams (1954) turbulent natural convection heat transfer coefficient $h_{wv,inc}$ or the forced convection heat transfer coefficient using the Dittus-Boelter (1930) equation $h_{wv,ffc}$. For turbulent natural convection, the McAdams (1954) correlation for turbulent natural convection from horizontal cylinders is used as

$$h_{wv,inc} = 0.13 (Gr_v \cdot Pr_v)^{1/3} \left(\frac{k_v}{D_h} \right) \quad (6-231)^{(63)}$$

where:

$$Gr_v = \frac{g_c \beta \rho_v^2 |T_w - T_v| D_h^3}{\mu_v^2} \quad (6-232)$$

[]^{a,c}

The Dittus-Boelter correlation is given as

$$h_{wv,ffc} = 0.023 Re_v^{0.8} Pr_v^{1/3} \left(\frac{k_v}{D_h} \right) \quad (6-233)$$

where:

$$Re_v = \frac{\rho_v |U_v| D_h}{\mu_v} \quad (6-234)$$

[]^{a,c}

Model as Coded The heat transfer coefficients for single-phase vapor are evaluated in subroutine HTCOR. The vapor heat transfer coefficient is found as follows:

$$h_{wv,spv} = \text{maximum} (h_{wv,inc}, h_{wv,ffc}) \quad (6-235)$$

This vapor heat transfer coefficient is used for h_{wv} in []^{a,c}, if ICHF = 0 is selected by the user. []^{a,c}.

Scaling Considerations The correlations used in heat transfer to single-phase vapor are well known and have been applied to a wide variety of fluids and geometries. The length scale does not appear in the expression for turbulent natural convection, and the Dittus-Boelter equation does not have a significant scale dependence.

Conclusions Existing, well known correlations are used for the single-phase vapor heat transfer. The application of these correlations is most important in the steam generator tubes, which is close to the original formulation for the correlations. These correlations have been tested on a wide range of scaled-to-full-scale system components as part of the WCOBRA/TRAC validation.

6-3-9 Heat Transfer to Two-Phase Mixtures⁽⁶⁵⁾

Model Basis For one-dimensional components, WCOBRA/TRAC includes a regime that is unique in that it is not part of the boiling curve discussed previously. The regime is used only when the input flag ICHF = 0 is specified, which instructs the component to ignore CHF calculations.

The liquid heat transfer coefficient uses the Rohsenow-Choi (1961) expression for laminar forced convection, $h_{wt,lfc}$, and the Dittus-Boelter (1930) correlation for turbulent forced convection, $h_{wt,tfc}$:

$$h_{wt,lfc} = \frac{4.0 k_t}{D_h} \quad (6-236)$$

and

$$h_{wt,tfc} = 0.023 \frac{k_t}{D_h} Re_m^{0.8} Pr_t^{0.4} \quad (6-237)$$

where:

$$Pr_t = \frac{C_{pt} \mu_t}{k_t} \quad (6-238)$$

$$Re_m = \frac{G_m D_h}{\mu_m} \quad (6-239)$$

and

$$\mu_m = \frac{1}{\frac{x}{\mu_v} + \frac{1-x}{\mu_l}} \quad (6-240)$$

The term μ_m is the two-phase viscosity proposed by McAdams, Woods, and Bryan (1942), x is the flow quality, and G_m is the product of mixture velocity (U_m), and mixture density (ρ_m). These equations are used for $\leq []^{ac}$ where the heat transfer to the vapor is assumed to be zero.

If the void fraction exceeds $\geq []^{ac}$, then heat transfer to the liquid is assumed to be zero. The vapor heat transfer coefficient is either the turbulent natural-convection heat transfer coefficient, $h_{wv,tn c}$, or the Dittus-Boelter correlation for turbulent forced convection to vapor, $h_{wv,tfc}$.

That is:

$$h_{wv,tn c} = 0.13 k_v \left[\frac{\rho_v^2 g |T_w - T_v|}{\mu_v^2 T_v} \right]^{0.333} Pr_v^{0.333} \quad (6-241)^{(65)}$$

and

$$h_{wv,tfc} = 0.023 \frac{k_v}{D_h} Re_v^{0.8} Pr_v^{1/3} \quad (6-242)$$

where:

$$Re_v = \frac{\rho_v U_v D_h}{\mu_v} \quad (6-243)$$

and

$$Pr_v = \frac{C_{pv} \mu_v}{k_v} \quad (6-244)$$

Model as Coded⁽⁶⁴⁾ The heat transfer coefficients for heat transfer in this regime are evaluated in subroutine HTCOR.

For void fractions above $\alpha = [\quad]^{a,c}$, with an equilibrium quality less than 1.0, the mixture is selected. Calculations to determine the single-phase vapor convective heat transfer coefficient are performed, and selected with Equation 6-246. Note that the vapor phase calculations in the mixture regime are the same as those in the single-phase vapor regime (IDREG = 6). That is, the vapor heat transfer coefficients calculated by either Equation 6-246 or 6-235 are identical. The coding for the vapor is redundant, since the code logic will pass through the single-phase vapor regime calculations if $\alpha > [\quad]^{a,c}$.

Turbulent and laminar liquid phase heat transfer coefficients are calculated with Equations 6-236 and 6-237. In the region where [

$]^{a,c}$. The liquid phase heat transfer coefficient in this range is calculated by selecting the maximum convective heat transfer coefficient:

$$\tilde{h}_{wl,2\phi} = \text{maximum} (h_{wl,lfc}, h_{wl,tfc}) \quad (6-245a)$$

and then linearly interpolating as: [

$$]^{a,c} \quad (6-245b)$$

The vapor phase heat transfer coefficients are also interpolated between the Equation 6-246 value at $\alpha = [\quad]^{a,c}$, and the value from Equation 6-235 at $\alpha = 1.000$. However, this operation is currently redundant since these equations produce the same value. For completeness, the vapor phase heat transfer coefficient is calculated as follows:

A temporary value for the mixture regime vapor phase heat transfer coefficient is determined from,

$$\tilde{h}_{wv,2\phi} = \text{maximum} (h_{wv,tmc}, h_{wv,tfc}) \quad (6-246a)$$

and then a linear interpolation with void fraction is performed to determine the final value when the void fraction is greater than [

$$]^{a,c} \quad (6-246b)$$

where $h_{wv,spv}$ is calculated by Equation 6-235.

[

]^{ac}.

Figure 6-15 clarifies the selection process. In this figure, it is assumed that ICHF = 0, so that post-CHF regimes are not considered. For equilibrium quality greater than or equal to 1.0, the single-phase vapor regime is chosen and the vapor heat transfer coefficient is calculated using Equation 6-235. The liquid phase heat transfer coefficient is set to 0.0 in this regime. [

]^{ac}. The liquid phase heat transfer coefficient is calculated using Equation 6-245 and the vapor phase heat transfer coefficient is set to 0.0.

Scaling Considerations The correlations used to determine the heat transfer coefficient in this regime scale weakly with hydraulic diameter.

Conclusions The WCOBRA/TRAC one-dimensional component heat transfer package provides extra flexibility for specifying two-phase heat transfer coefficients. This portion of the package is used only in one-dimensional components where CHF is not a consideration. Use of this model is not considered a major contributor to the code bias and uncertainty.

6-3-10 Condensation Heat Transfer

Model Basis WCOBRA/TRAC includes a separate heat transfer regime to account for condensation heat transfer in one-dimensional components. The equilibrium quality x , is compared to the value defined as $x_{CHEN} = []^{ac}$ to determine which set of condensation correlations to use for the wall condensation regime (IDREG=11). The limiting value, $x_{CHEN} = []^{ac}$, is based on the data used in development of the Chen correlation.⁽⁶⁶⁾ This can be observed in Table 7.2 of Collier and Thome (1994), which summarizes the data used in the development of the Chen model.

The vapor heat transfer coefficient for condensation is determined from the maximum of the McAdams (1954) correlation:

$$h_{wv,inc} = 0.13 \frac{k_v}{D_h} Gr_v^{1/3} Pr_v^{1/3} \quad (6-247)$$

and an approximation of the Dittus-Boelter (1930) equation as:

$$h_{wv,ffc} = 0.023 \frac{k_v}{D_h} \left[\frac{\rho_v U_v D_h}{\mu_v} \right]^{0.8} (Pr_v)^{1/3} \quad (6-248)$$

For the liquid phase, the condensation heat transfer coefficients are determined from the maximum of the Rohsenow and Choi (1961) value for laminar forced convection flow in a pipe:

$$h_{wt,ffc} = 4.0 \frac{k_t}{D_h} \quad (6-249)$$

and the Chen correlation with the suppression factor S_{CHEN} set to 0.0:

$$h_{wt,ffc} = 0.023 \frac{k_t}{D_h} \left[\frac{\rho_t U_t (1.0 - \alpha) D_h}{\mu_t} \right]^{0.8} (Pr_t)^{0.4} F_{CHEN} \quad (6-250)^{(52,67)}$$

where F_{CHEN} is defined in Equations 6-196 through 6-198. In evaluating F_{CHEN} for condensation, the minimum of x and $x_{CHEN} = []^{ac}$ is used for the quality.

Model as Coded⁽⁶⁶⁾ The condensation heat transfer regime (IDREG = 11) is assumed when the following conditions are each satisfied:

$$\begin{aligned} T_w &< T_{sat} \\ T_w &< T_t \\ \alpha &< []^{ac} \end{aligned}$$

If $x_{CHEN} < x < 1.0$, the condensation heat transfer coefficients are calculated as: [

$$]^{ac} \quad (6-252a)^{(66,68)}$$

where: [

$$]^{a,c} \quad (6-252b)$$

In Equation 6-252b, $h_{wt,lfc}$ is given by Equation 6-249, and $h_{wt,vfc}$ is given by 6-250.

If $x < x_{CHEN}$, the heat transfer coefficient for the liquid phase is calculated from the Chen correlation, with the suppression term $SCHEN = 0.0$ and the heat transfer coefficient for the vapor phase is set to 0.0. That is, [

$$]^{a,c} \quad (6-253)$$

and

$$h_{wv,cond} = 0.0 \quad (6-254)$$

where $h_{wt,lfc}$ is again given by Equation 6-249, and $h_{wt,vfc}$ by Equation 6-250.

[

$$]^{a,c}.$$

Scaling Considerations These correlations model condensation as a forced or natural convection process assuming that all the resistance to the condensation is at the vapor-liquid interface. These models have been used in condensation experiments for Westinghouse 1/3-scale and UPTF full-scale cold leg steam water mixing tests, and have been shown to be scale independent as seen in Section 15-3 of WCAP-12945-P-A.

Conclusions Condensation models are provided in the one-dimensional component heat transfer package. The condensation models in the one-dimensional heat transfer package were used in simulations of the Westinghouse 1/3-scale and UPTF full-scale steam-water mixing tests in which condensation was present. These models have also been used in simulations of the LOFT and CCTF integral tests.

6-3-11 Wall to Fluid Heat Transfer

Model Basis In the one-dimensional components, the total heat transfer from the wall is partitioned into the respective liquid and vapor phases. The total wall heat flux is given by

$$q_{total}'' = q_{wl}'' + q_{wv}'' \quad (6-255)$$

where:

$$q''_{wl} = h_{wl}(T_w - T_l) \quad (6-256)$$

and

$$q''_{wv} = h_{wv}(T_w - T_v) \quad (6-257)$$

The values of h_{wl} and h_{wv} are regime dependent and were described in the previous sections.

Model as Coded The calculation of the wall heat flux for one-dimensional components is controlled by subroutine HTCOR. The details of the individual models has been described above.

Scaling Conditions The details of each of the heat transfer correlations used for the wall-to-vapor and wall-to-liquid have been discussed in previous sections.

Conclusions The WCOBRA/TRAC one-dimensional heat transfer package uses correlations which have been tested by the simulation of different tests at different scales. The uncertainties of these correlations is accounted for in the overall WCOBRA/TRAC code uncertainties.

6-4 Heat Flux Splitting in WCOBRA/TRAC

In the preceding sections, three types of heat transfer coefficient were described: heat transfer to vapor (h_{wv}) (for example, Equation 6-4), heat transfer to liquid (h_{wl}) (for example, Equation 6-11), and heat transfer due to boiling, (h_{wb}) (for example, Equation 6-57). This section further describes how these components are derived from the overall heat transfer correlations.

WCOBRA/TRAC is similar to other two fluid models in that it requires the splitting of the heat flux from a heated surface to each phase being considered. In the calculation of a LOCA transient, the transition must be made from heat transfer entirely to the liquid (normal steady state conditions), to heat transfer partially to the liquid and partially to the vapor (transition boiling), to heat transfer entirely to the vapor (steam cooling), and back again (quenching and long term cooling). The problem encountered when doing this is also similar to other two fluid models; how to take heat flux correlations and models which describe the total heat flux from the wall to the fluid, and apportion this total heat flux properly among the phases being modelled in the code.

In WCOBRA/TRAC, the total heat flowrate is divided among three paths: the wall to liquid path (Q_{wl}), the wall to interface path (Q_{wi}), and the wall to vapor path (Q_{wv}) (note that Q_{wi} and h_{wi} are equivalent to Q_{wb} and h_{wb} in previous sections; the interface path description is felt to more accurately describe the process).

The heat flow to the bulk liquid (Q_{wl}) represents heat flow mechanisms in which energy is deposited, or mixed, into the bulk liquid phase, and where the driving force for such transfer is best described by the temperature difference between the wall and the bulk liquid. This energy transfer heats the liquid, raising its temperature. Examples of such mechanisms are:

Energy transferred by conduction or by turbulent eddies from the region near the wall surface.

Energy transferred by conduction or by turbulent eddies from the region near the vapor-liquid interface.

Energy deposited by radiation from the wall to the liquid.

The heat flow to the liquid interface (Q_{wi}) represents heat flow mechanisms in which energy is deposited locally in the liquid phase, near the interface between the liquid and either the wall or the vapor. Since the liquid near the interface is saturated when next to the vapor, and may also be saturated near the wall, the energy deposited will cause the liquid to evaporate or boil. The energy is therefore dissipated by local vapor generation before there is time to transfer the energy to the bulk fluid. The energy may ultimately be deposited into the bulk fluid as the generated vapor enters the main stream and condenses. Mechanisms in which energy is deposited this way are:

Energy transferred by nucleate boiling, where bubbles are created at the wall surface. These bubbles then detach and mix with the bulk liquid which may be subcooled.

Energy transferred by conduction across a thin vapor layer adjacent to the wall, to the vapor liquid interface, as in pool film boiling.

The wall to vapor heat flow (Q_{wv}) represents heat flow mechanisms in which energy is deposited in the bulk vapor phase. Examples of such mechanisms are:

Energy transferred by conduction or by turbulent eddies from the near-wall region.

Energy deposited by radiation from the wall to the vapor.

The wall to interface heat transfer is sometimes referred to as the "latent" heat transfer, while the other heat transfers are sometimes referred to as the "sensible" heat transfer.

The total heat flow from the wall is described by the following equation:

$$Q_w = Q_{wl} + Q_{wi} + Q_{wv}$$

$$Q_w = h_{wt} A_{wt} (T_w - T_l) + h_{wi} A_{wi} (T_w - T_i) + h_{wv} A_{wv} (T_w - T_v) \quad (6-258)$$

where h_{wl} , h_{wi} , and h_{wv} are the local heat transfer coefficients from the wall to the bulk liquid phase, the wall to the vapor liquid interface, and the wall to the bulk vapor phase. These will be described in more detail later. A_{wl} , A_{wi} , A_{wv} are the areas over which each process is assumed to take place. Described in terms of heat flux q (heat flow divided by total surface area), Equation 6-258 becomes:

$$q_w = q_{wl}\epsilon_{wl} + q_{wi}\epsilon_{wi} + q_{wv}\epsilon_{wv} \quad (6-259)$$

$$q_w = h_{wl}\epsilon_{wl}(T_w - T_l) + h_{wi}\epsilon_{wi}(T_w - T_i) + h_{wv}\epsilon_{wv}(T_w - T_v)$$

where the epsilons are the fractional areas for each path. The ϵ 's are somewhat analogous to the vapor fraction α , and the q 's are somewhat analogous to, for example, vapor volumetric flux j_v (total vapor flow divided by total flow area). Unlike the fluid phase situation, the heat transfer area fractions do not have to add up to 1.0. This is because different heat transfer mechanisms can easily be visualized as acting over the same surface area. Radiation to vapor, for example, acts over the entire surface area simultaneously with forced convection to vapor. However, in order to properly apply the model, the h 's and ϵ 's need to be defined consistent with the heat flux equation outlined above, and also consistent with a physical picture about the heat transfer mechanisms involved. How this is done for each heat transfer regime in WCOBRA/TRAC is described in the following section.

6-4-1 Single-Phase Liquid Forced Convection

In this regime, heat is transferred to the bulk liquid or vapor by conduction or by turbulent eddies. The Dittus-Boelter equation (Equation 6-12) is used for turbulent forced convection conditions, for example. The fractional areas along the various paths are: [

]^{a,c}

The overall heat flux is: [

]^{a,c} (6-260)

where: [

]^{a,c}

6-4-2 Saturated Nucleate Boiling

In this regime, the total heat flux is calculated using a model which accounts for nucleate boiling under forced convection conditions. The Chen correlation (Section 6-2-3) is an example of this type of model. This model assumes the heat transfer is made up of a forced convection component (q_{fc}), transferring sensible heat, and a nucleate boiling component (q_{nb}), transferring latent heat, as shown at the top of Figure 6-16. Consistent with assumptions made in other models of this type (for example Collier and Thome, 1994, page 260), the assumption is made that these contributions act over the entire surface and can be superimposed; that is: [

$$j^{a,c}$$

Equation 6-259 becomes: [

$$j^{a,c} \quad (6-261)$$

where: [

$$j^{a,c}$$

6-4-3 Subcooled Nucleate Boiling

In this regime, the total heat flux is calculated using Chen, but it is assumed that at high liquid subcoolings [

$$j^{a,c} \quad (6-262)$$

where: [

$$j^{a,c}$$

6-4-4 Transition Boiling

In this regime the surface is assumed to be dry and heat transfer to the vapor occurs by forced convection (q_{wl}), but the surface is contacted intermittently by liquid as illustrated in Figure 6-17. Since the wall temperature is relatively high, radiation to cooler vapor (q_{rv}) and liquid (q_{rl}) is assumed to take place. In this and in other models described below, radiation is always superimposed (i.e., acts over the entire surface). [

]^{a,c}. The resulting heat flux equation is: [

]^{a,c} (6-263)

where: [

]^{a,c}

6-4-5 Inverted Annular Film Boiling (IAFB)

In inverted annular film boiling, the wall is assumed to be dry, and covered by a vapor film surrounded by a more or less continuous liquid field (which may contain vapor), as shown at the bottom of Figure 6-18. [

]^{a,c}

[

 $j^{a,c}$ (6-264)

[

 $j^{a,c}$. The

resulting heat flux equation is: [

 $j^{a,c}$ (6-265)

where: [

 $j^{a,c}$

6-4-6 Inverted Annular Dispersed Flow Film Boiling (IADF) and Dispersed Droplet Film Boiling (DFFB)

The IADF regime is visualized as a dry wall surface surrounded by a discontinuous liquid field consisting of large drops whose surfaces approach the wall, and a population of small drops in the vapor field (top of Figure 6-18). [

 $j^{a,c}$

[

]^{a,c}. The

heat flux equation is: [

]^{a,c} (6-266)

where: [

]^{a,c}

In the instances where superposition is used, one of the heat flux components is assumed to dominate while the others represent perturbations, so the assumption introduces small errors. The potential also exists for compensating error if the functional dependence of a heat transfer component with flowrate or vapor fraction is incorrect, or if the phasic temperature, particularly of vapor, is not correctly calculated. The investigations in Appendix A of Volume 3 of WCAP-12945 are designed to find such compensating errors if they exist.

Note: In presentations of heat transfer coefficients calculated by WCOBRA/TRAC, the terms "HTCV" and "HTCL" are sometimes used. These are defined as follows:

$$HTCV = q_{wr} / (T_w - T_v)$$

$$HTCL = (q_{wi} + q_{wt}) / (T_w - T_l) \quad (6-268)$$

6-5 References

Abu-Romia, M. M., and Tien, C. L., 1967, "Appropriate Mean Absorption Coefficients for Infrared Radiation of Gases," J. Heat Transfer, 89, pp. 321-327.

Bajorek, S. M., et al., 1998, "Code Qualification Document for Best Estimate LOCA Analysis," WCAP-12945-P-A, Volume 1, Revision 2, and Volumes 2 through 5, Revision 1, and WCAP-14747 (Non-Proprietary).

Biasi, L., et al., 1967, "Studies on Burnout, Part 3," Energia Nucleare, Vol. 14, No. 9, pp. 530-536.

Bennett, A. W., et al., 1967, "Heat Transfer to Steam-Water Mixtures Flowing in Uniformly Heated Tubes in Which the Critical Heat Flux has been Exceeded," Report No. AERE-R5373, Atomic Energy Research Establishment, Harwell, England.

Bjornard, T. A. and Griffith, P., 1977, "PWR Blowdown Heat Transfer," Thermal and Hydraulic Aspects of Nuclear Reactor Safety, ASME, New York, Vol. 1, pp. 17-41.

Bromley, L. A. 1950, "Heat Transfer in Stable Film Boiling," Chemical Engineering Progress, Vol. 46, No. 5, pp. 221-226.

Chen, J. C., 1963, "A Correlation for Boiling Heat Transfer to Saturated Fluids in Convective Flow," ASME 63-HT-34.

Chiou, J. S., Hochreiter, L. E., and Young, M. Y., 1986, "Spacer Grid Heat Transfer Effects During Reflood," WCAP-10484. [].

Collier, J. G. and Thome, J. R., 1994, Convective Boiling and Condensation, 3rd Ed., Clarendon Press, Oxford.

Corman, J. C., 1966, "Water Cooling of a Thin, High Temperature Metal Strip," Ph.D. Thesis, Carnegie Institute of Technology.

Dengler, G. E. and Addoms, J. N., 1956, Chemical Engineering Progress Symposium, Ser. 52, No. 18, pp. 95-103.

Dittus, F. W. and Boelter, L. M. K., 1930, "Heat Transfer in Automobile Radiators of the Tubular Type," Publications in Engineering, 2, Univ. of California, Berkeley, pp. 443-461.

Drucker, M. and Dhir, V. K., 1984, "Studies of Single- and Two-Phase Heat Transfer in a Blocked Four-Rod Bundle," EPRI NP-3485.

Dougall, R. S. and Rohsenow, W. M., 1963, "Film Boiling on the Inside of Vertical Tubes with Upflow of the Fluid at Low Qualities," MIT Report 9079-26.

Forslund, R. P. and Rohsenow, W. M., 1968, "Dispersed Flow Film Boiling," J. Heat Trans., Vol. 90, No. 6, pp. 399-407.

Forster, H. K. and Zuber, N., 1955, "Bubble Dynamics and Boiling Heat Transfer," AICHE J., Vol. 1, pp. 532-535.

Gaugler, R. E. 1966, "An Experimental Study of Spray Cooling of High Temperature Surfaces," Ph.D. Thesis, Carnegie Institute of Technology.

Ganic, E. N. and Rohsenow, W. M., 1977, "Dispersed Flow Heat Transfer," Int. J. Heat and Mass Transfer, Vol. 20, pp. 855-866.

Groenveld, D. C. and Fung, K. K., 1976, "Forced Convective Transition Boiling - Review of Literature and Comparison of Predictive Methods," AECL-5543, Chalk River Nuclear Laboratories, Chalk River, Ontario.

Hancox, W. T. and Nicoll, W. B., 1971, "A General Technique for the Prediction of Void Distributions in Nonsteady Two-Phase Forced Convection," Int. J. Heat and Mass Transfer, Vol. 14.

Henry, R. E., 1974, "A Correlation for the Minimum Film Boiling Temperature," AIChE Symposium Series, Vol. 138, pp. 81-90.

Holman, J. P., 1976, Heat Transfer, 4th Edition, McGraw-Hill Co., New York.

Iloeje, O. C., et al., 1974, "A Study of Wall Rewet and Heat Transfer in Disposed Vertical Flow," MIT Report 72718-92.

Iloeje, O. C., et al., 1975, "An Investigation of the Collapse and Surface Rewet in Film Boiling in Vertical Flow," J. Heat Trans., Vol. 97, pp. 166-172.

Jens, W. H. and Lottes, P. A., 1951, "Analysis of Heat Transfer, Burnout, Pressure Drop and Density Data for High Pressure Water," USAEC Report ANL-4627.

Jones, O. C. and Bankoff, S. G., editors, 1977, "Thermal and Hydraulic Aspects of Nuclear Reactor Safety; Vol. 1: Light Water Reactors," ASME, New York.

Kays, W. M., 1966, Convective Heat and Mass Transfer, McGraw-Hill Book Company, New York.

Kim, J. H., 1979, "Heat Transfer in Longitudinal Laminar Flow Along Cylinders in a Square Array," Heat Transfer Over Rod or Tube Bundles, ASME, pp. 155-161.

Lahey, R. T. and Moody, F. J., 1977, The Thermal-Hydraulics of a Boiling Water Nuclear Reactor, American Nuclear Society.

Lee, N., et al., 1981, "PWR FLECHT SEASET Unblocked Bundle Forced and Gravity Reflood Task Data Evaluation and Analysis Report," NRC/EPRI/Westinghouse-10.

Lienhard, J. H. and Dhir, V. K., 1973, "Hydrodynamic Prediction of Peak Pool-Boiling Heat Fluxes from Finite Bodies," J. Heat Transfer, Vol. 95, No. 2, pp. 152-158.

Liles, D. R., et al., 1981, "TRAC-PD2: An Advanced Best-Estimate Computer Program for Pressurized Water Reactor Loss-of-Coolant Accident Analysis," Los Alamos National Laboratory Report, LA-8709-MS (NUREG/CR-2054).

Liles, D. R., et al., 1988, "TRAC-PF1/MOD1 Correlations and Models," NUREG-5069, LA-11208-MS.

McAdams, W. H., 1954, Heat Transmission, 3rd Edition, McGraw-Hill Co., New York.

McAdams, W. H., Woods, W. K., and Bryan, R. L., 1942, "Vaporization Inside Horizontal Tubes - II - Benzene-oil Mixtures," *Trans. ASME*, 64, 193.

McCreery, G. E., et al., 1977, "Thermal-Hydraulic Analysis of Semiscale MOD-1 Reflood Test Series (Gravity Feed Tests)," TREE - NUREG-1010.

Moles, F. D. and Shaw, J. F. G., 1972, "Boiling Heat Transfer to Subcooled Liquids Under Conditions of Forced Convection," Trans. Inst. Chem. Eng., Vol. 50.

Pedersen, C. O., 1967, "The Dynamics and Heat Transfer Characteristics of Water Droplets Impinging on a Heated Surface," Ph. D. Thesis, Carnegie Institute of Technology.

Pomerantz, M. L., 1964, "Film Boiling on a Horizontal Tube in Increased Gravity Fields," *J. Heat Transfer*, 86 (2), pp. 213-219.

Rohsenow, W. M. and Choi, H., 1961, Heat, Mass and Momentum Transfer, Prentice-Hall, Inc., New York.

Rouhani, S. Z. and Axelsson, E., 1970, "Calculation of Void Volume Fraction in Subcooled and Quality Boiling Regions," Int. J. Heat and Mass Transfer, Vol. 13.

Spencer, A. C. and Young, M. Y., 1980, "A Mechanistic Model for the Best-Estimate Analysis of Reflood Transients (the BART Code)," 19th National Heat Transfer Conference, Orlando, FL, HTD, Vol. 7.

Sun, K. H., Gonzalez-Santalo, J. M., and Tien, C. L., 1976, "Calculations of Combined Radiation and Convection Heat Transfer in Rod Bundles Under Emergency Cooling Conditions," ASME Journal of Heat Transfer.

Thurgood, M. J., et al., (1983), "COBRA/TRAC - A Thermal-Hydraulics Code for Transient Analysis of Nuclear Reactor Vessels and Primary Systems," Volume 1, NUREG/CR-3046.

Wachters, L. H. J. and Westerling, N. A. J., 1966, "The Heat Transfer From a Hot Wall to Impinging Water Drops in a Spheroidal State," Chem. Eng. Sci., Vol. 21, pp. 1047-1056.

Whalley, P. B., 1976, "The Calculation of Dryout in a Rod Bundle," Report No. AERE-R8319, Atomic Energy Research Establishment, Harwell, England.

Whalley, P. B., Hutchinson, P., and Hewitt, G. F., 1973, "The Calculation of Critical Heat Flux in Forced Convection Boiling," Report No. AERE-R7520, Atomic Energy Research Establishment, Harwell, England.

Wong, S. and Hochreiter, L. E., 1981, "Analysis of the FLECHT-SEASET Unblocked Bundle Steam Cooling and Boiloff Tests," NRC/EPRI/Westinghouse-8.

Yao, S. C., Hochreiter, L. E., and Dodge, C. E., 1979, "A Simple Method for Calculating Radiative Heat Transfer in Rod Bundles with Droplets and Vapor as Absorbing Media," J. Heat Transfer, 101, pp. 736-739.

Yao, S. C., Hochreiter, L. E., and Leech, J. J., 1982, "Heat Transfer Augmentation i Rod Bundles Near Grid Spacers," J. Heat Trans., Vol. 104, pp. 76-81.

Zuber, N., et al., 1961, "The Hydrodynamic Crisis in Pool Boiling of Saturated and Subcooled Liquids," International Developments in Heat Transfer, Int. Heat Transfer Conf., Boulder, Colorado, Part II, No. 27, pp. 23-236.

6-6 RAI Listing

1. RAI1-1, part (gg)
2. RAI1-152
3. RAI1-153
4. RAI1-154
5. RAI1-155
6. RAI1-156
7. RAI1-157
8. RAI1-158
9. RAI1-159
10. RAI1-160
11. RAI1-161
12. RAI1-162
13. RAI1-163
14. RAI1-164
15. RAI1-165
16. RAI1-166
17. RAI1-167
18. RAI1-168
19. RAI1-169

20. RAI1-170
- | 21. RAI1-171 (refers to WCAP-12945, Rev. 1 page 6-29; now page 6-20)
22. RAI1-172
23. RAI1-173
24. RAI1-174
25. RAI1-175
26. RAI1-176
27. RAI1-177
28. RAI1-178
29. RAI1-179
30. RAI1-180
31. RAI1-181
32. RAI1-182
33. RAI1-183
34. RAI1-184
35. RAI1-185
36. RAI1-186
37. RAI1-187
38. RAI1-188
- | 39. RAI1-189 (refers to WCAP-12945, Rev. 1, pages 6-47 and 6-48; now pages 6-33 and 6-34)
40. RAI1-190
41. RAI1-191
42. RAI1-192
43. RAI1-193
- | 44. RAI1-194 (refers to WCAP-12945, Rev. 1, page 6-58; now page 6-41)
- | 45. RAI1-195 (refers to WCAP-12945, Rev. 1, page 6-61; now pages 6-42 and 6-43)
- | 46. RAI1-196 (refers to WCAP-12945, Rev. 1, page 6-39; now page 6-26)
47. RAI1-197
48. RAI1-198
49. RAI1-199
50. RAI1-200
- | 51. RAI1-201 (refers to WCAP-12945, Rev. 1, page 6-71; now page 6-49)
52. RAI1-202
- | 53. RAI1-203 (refers to WCAP-12945, Rev. 1, page 6-77; now page 6-53)
- | 54. RAI1-204 (refers to WCAP-12945, Rev. 1, page 6-77; now page 6-53)
- | 55. RAI1-205 (refers to WCAP-12945, Rev. 1, page 6-80; now page 6-55)
- | 56. RAI1-206 (refers to WCAP-12945, Rev. 1, page 6-82; now page 6-56)
57. RAI1-207
- | 58. RAI1-208 (refers to WCAP-12945, Rev. 1, page 6-86; now page 6-59)
- | 59. RAI1-209 (refers to WCAP-12945, Rev. 1, page 6-88; now page 6-61)
- | 60. RAI1-210 (refers to WCAP-12945, Rev. 1, page 6-91; now page 6-62)
- | 61. RAI1-211 (refers to WCAP-12945, Rev. 1, page 6-89; now page 6-62)

- | 62. RAI1-212 (refers to WCAP-12945, Rev. 1, page 6-89; now page 6-61)
- | 63. RAI1-213 (refers to WCAP-12945, Rev. 1, page 6-93; now page 6-64)
- 64. RAI1-214 (this response added to main text)
- | 65. RAI1-215 (refers to WCAP-12945, Rev. 1, pages 6-95 and 6-97; now pages 6-66 and 6-68)
- | 66. RAI1-216 (refers to WCAP-12945, Rev. 1, page 6-97; now page 6-68. This response added to main text)
- 67. RAI1-217
- 68. RAI1-218
- 69. RAI1-219
- 70. not used
- 71. RAI1-151
- 72. RAI1-1, part (mm)
- 73. RAI1-1, part (hh)

Table 6-1
One-Dimensional Component Heat Transfer Regimes

IDREG	Heat Transfer Regime
1	Forced convection to single-phase liquid (<i>fc</i>)
2	Nucleate boiling (<i>nb</i>)
3	Transition boiling (<i>tb</i>)
4	Film boiling (<i>fb</i>)
6	Convection to single-phase vapor (<i>spv</i>)
7	Convection to two-phase mixtures (2ϕ)
11	Condensation (<i>cond</i>)
12	Natural convection to single-phase liquid (<i>nc</i>)

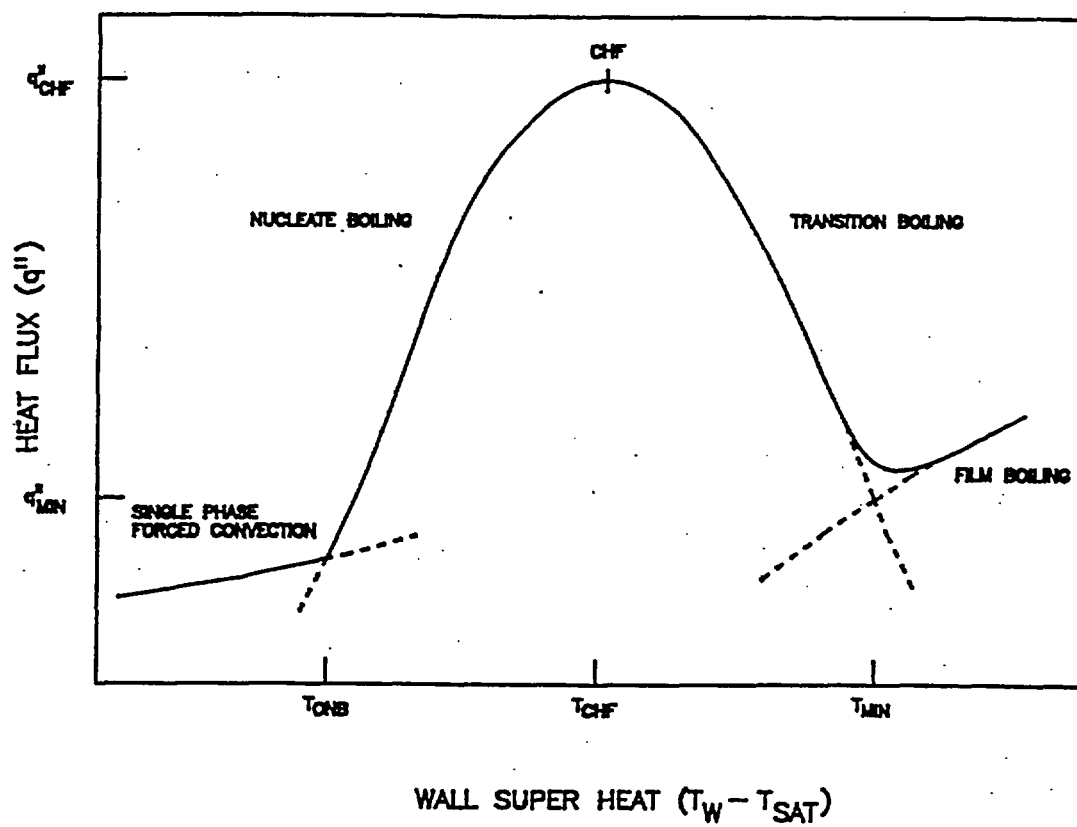


Figure 6-1. Boiling Curve

a.c

Figure 6-2. Heat Transfer Regime Selection Logic for Vessel Component

Figure 6-3. Heat Transfer Regime Map for Vessel Component⁽⁶⁹⁾

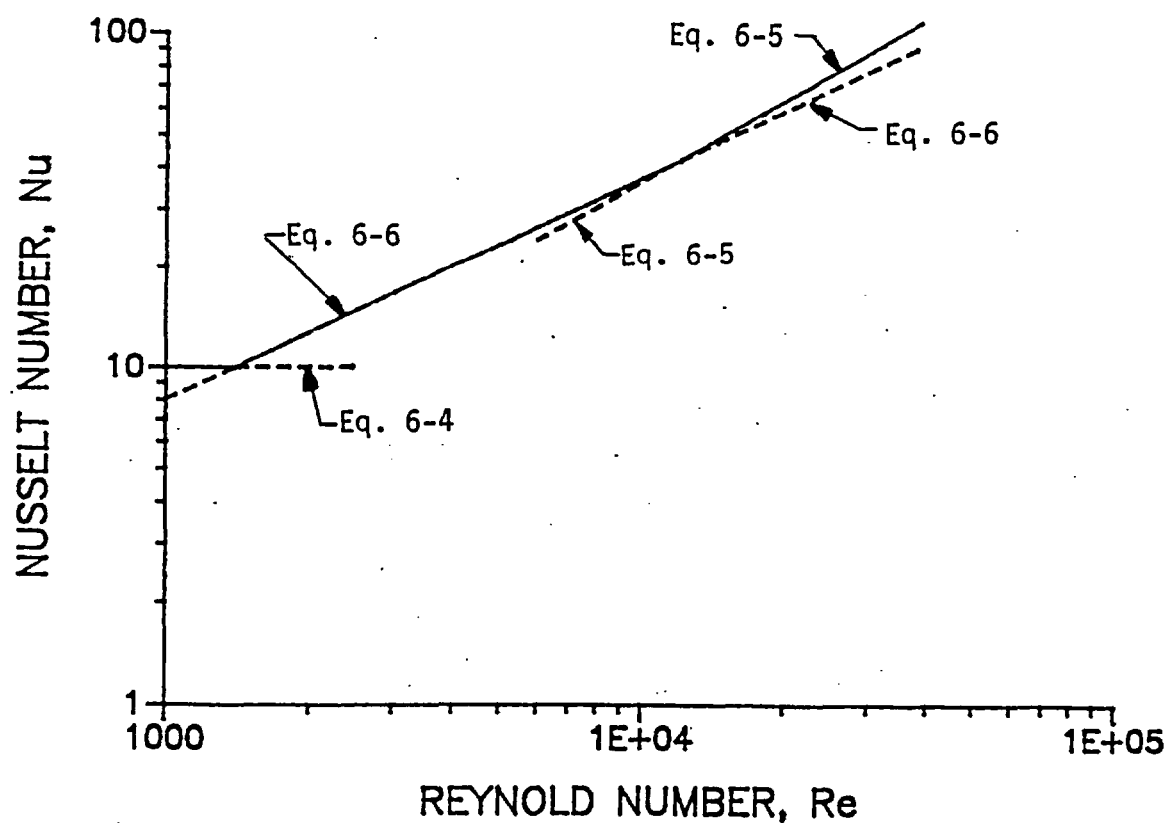


Figure 6-4. Heat Transfer Coefficient for Single-Phase Vapor

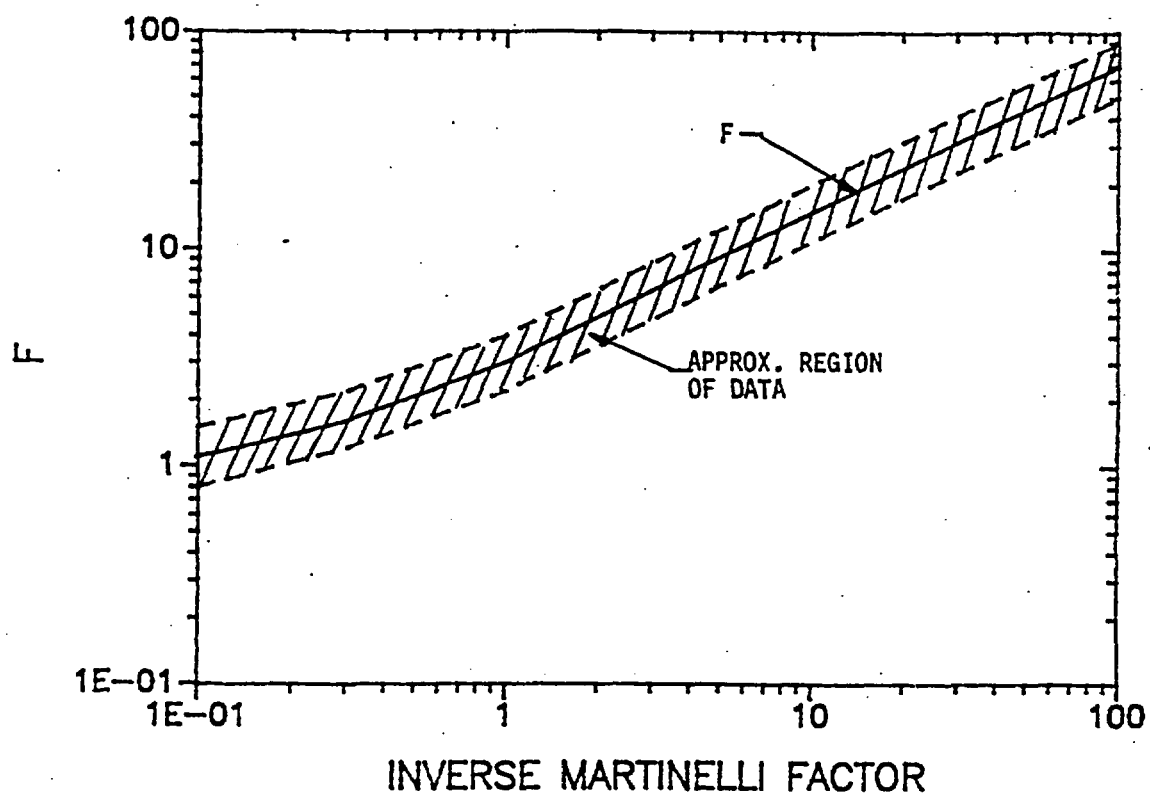


Figure 6-5. Chen Correlation Convective Multiplier F_{CHEN}

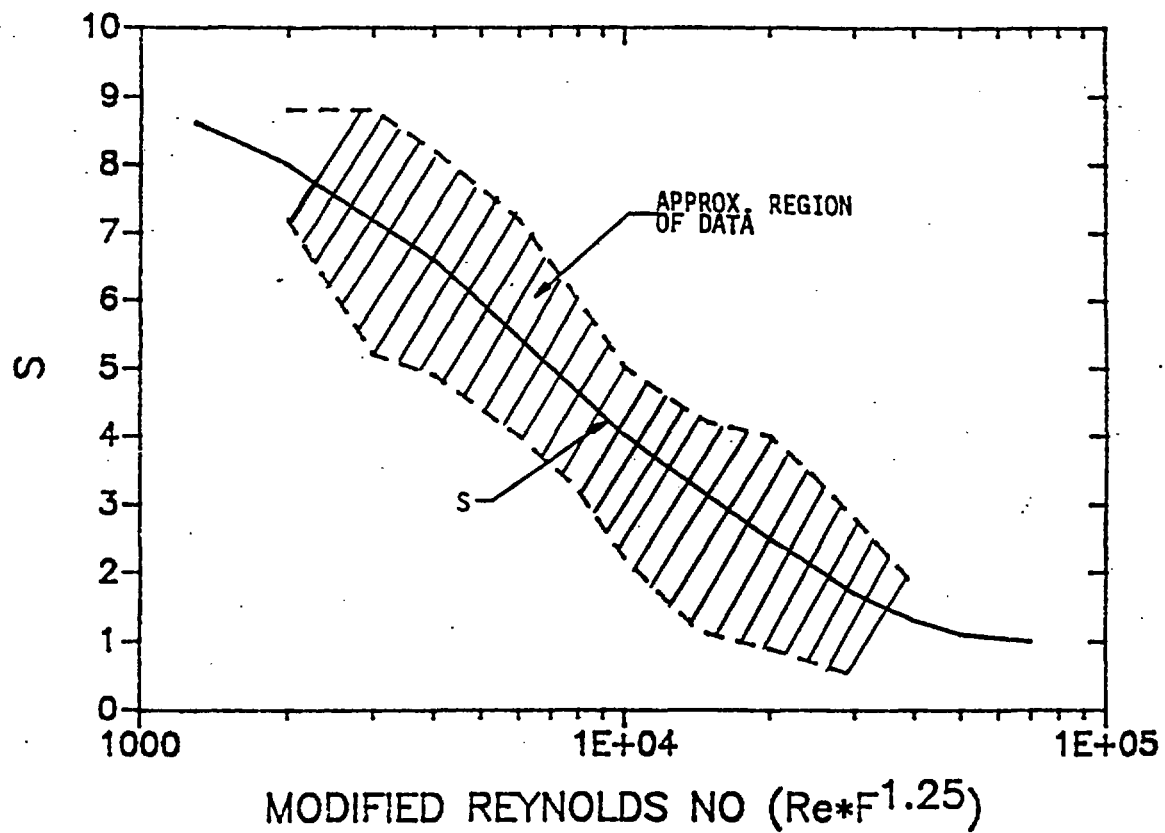


Figure 6-6. Chen Boiling Suppression Factor S_{CHEN}

a.c

Figure 6-7. Droplet Contact Effectiveness (as coded) at Atmospheric Pressure

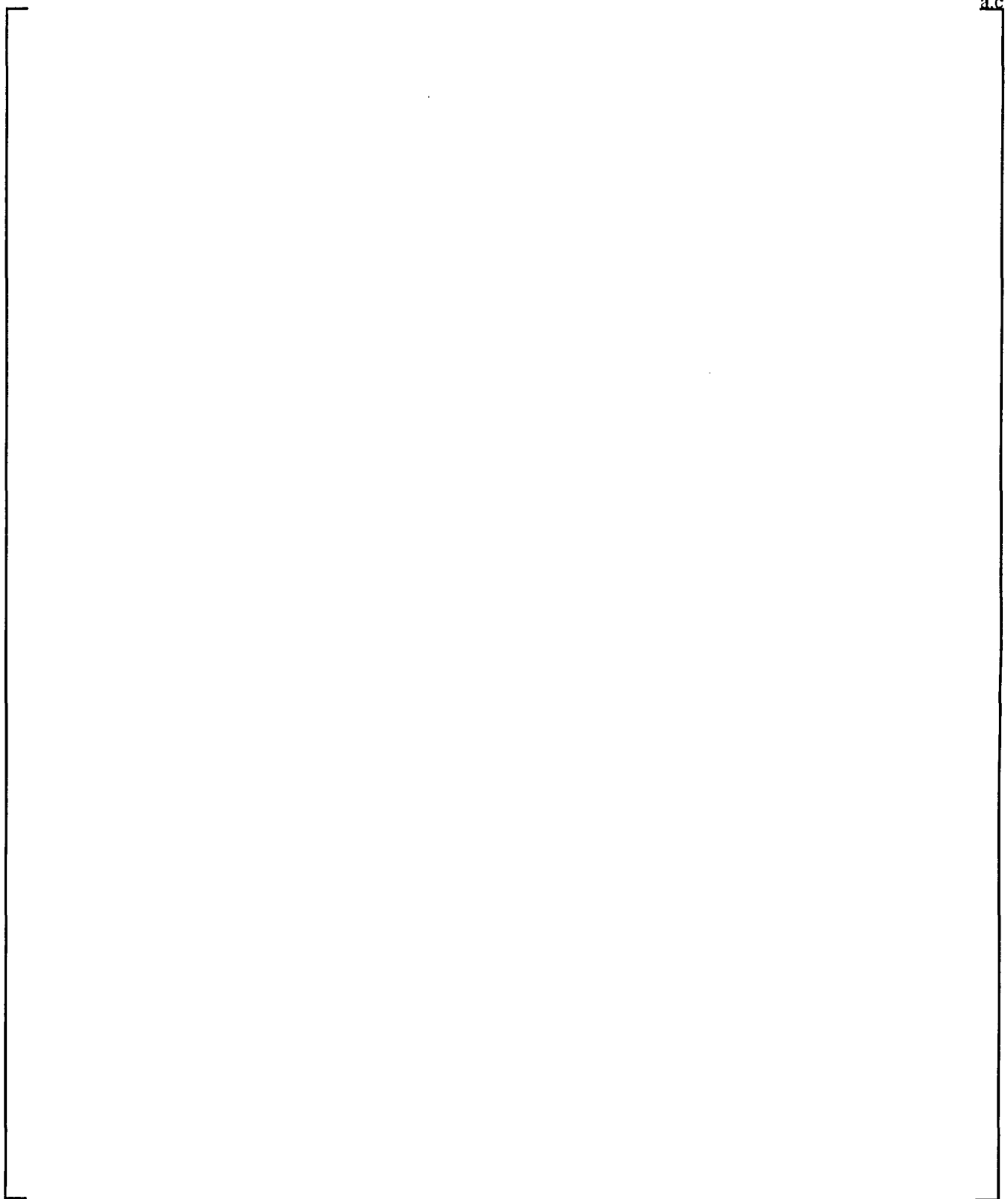


Figure 6-8. Droplet Contact Effectiveness (as coded) at High Pressure

a.c

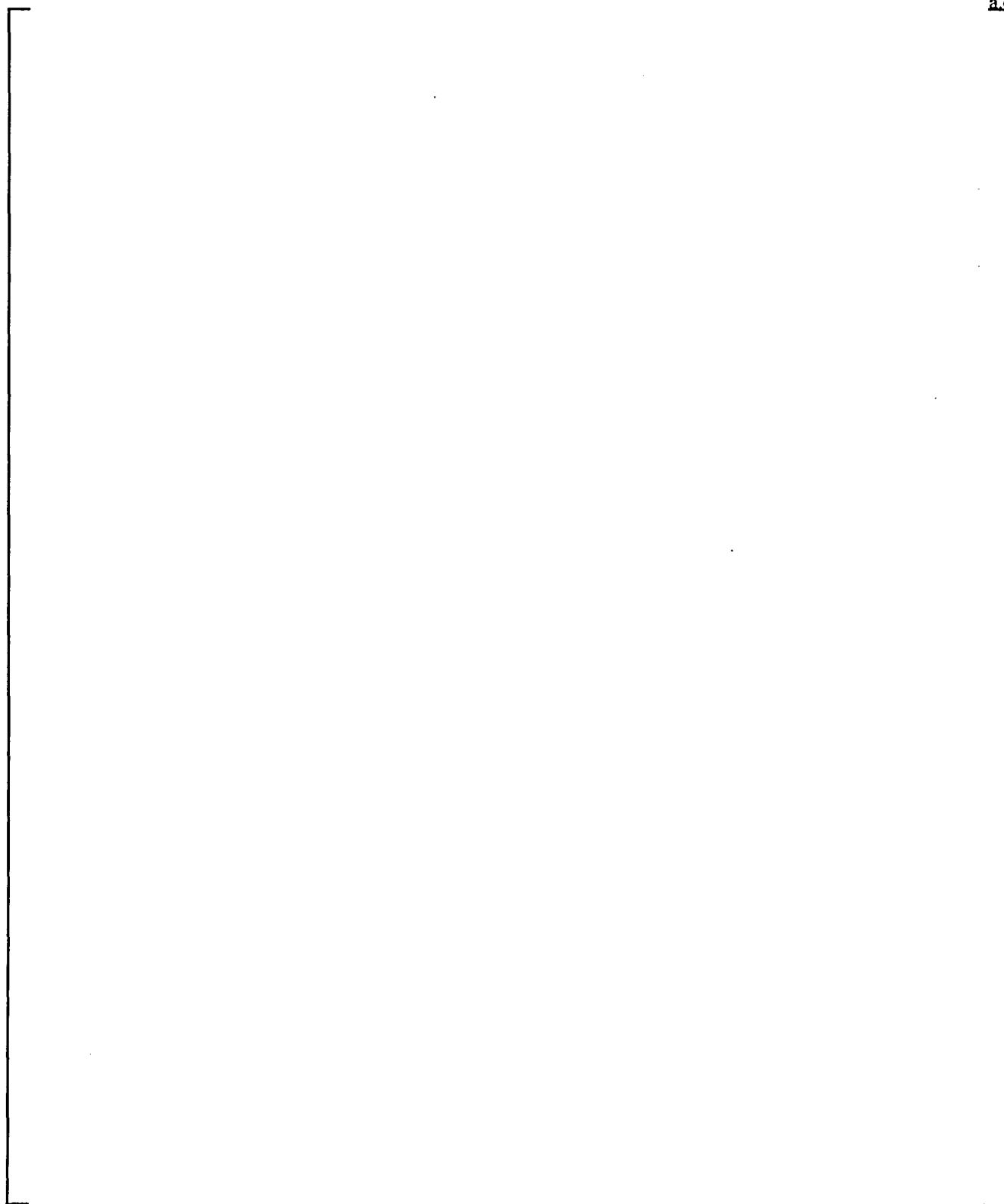


Figure 6-9. Transition Boiling (Model 2) Ramp F_z

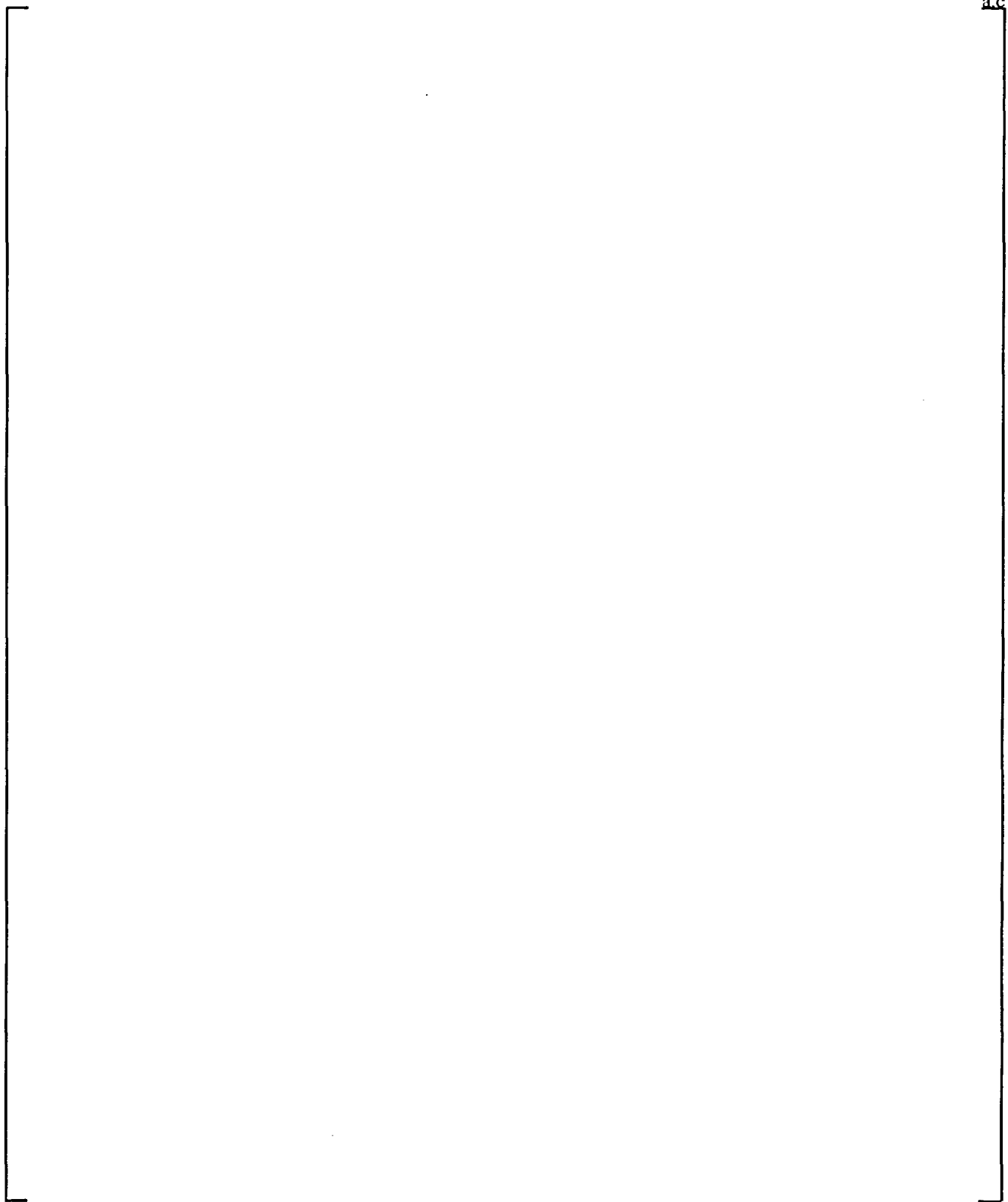


Figure 6-10. Film Boiling Model Components

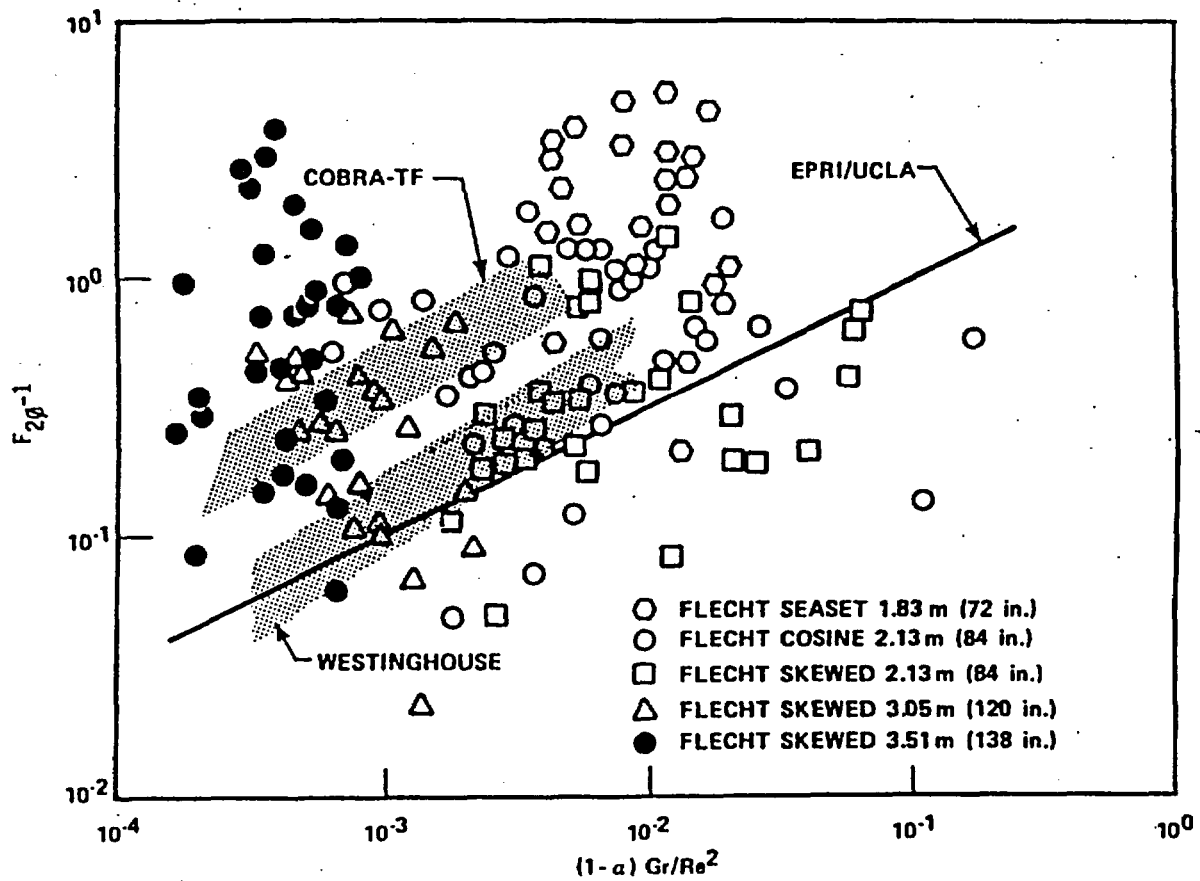
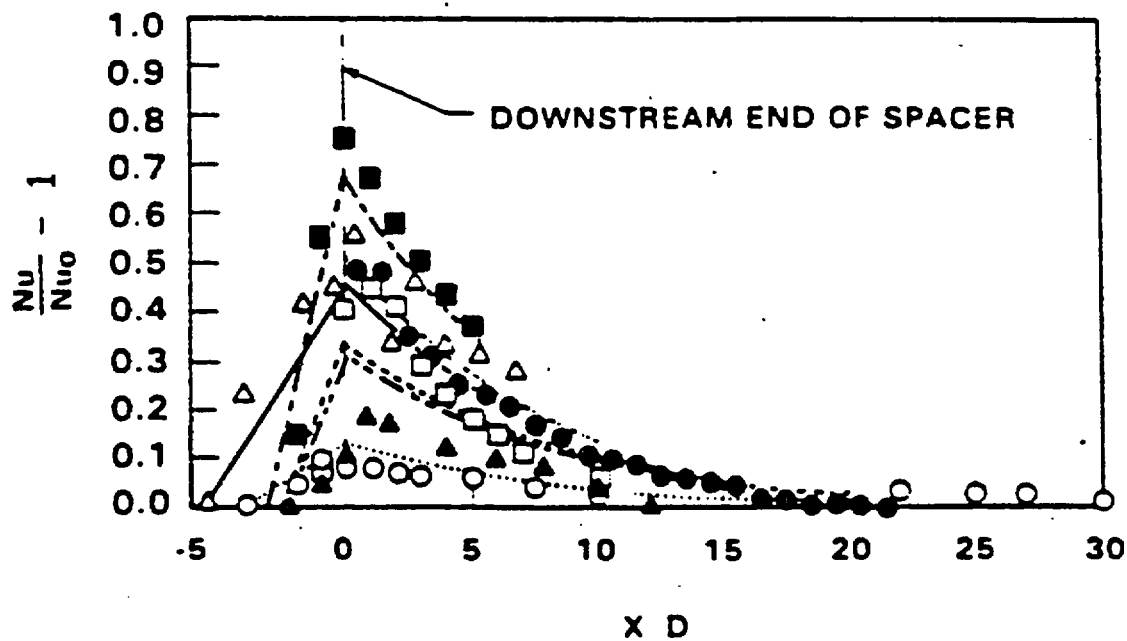


Figure 6-11. Enhancement of Convective Heat Transfer Due to Droplets



Type of grid
reported in reference

Calculated
 $\frac{Nu}{Nu_0} - 1$

Symbol	Author	Type of grid	$Re \times 10^{-4}$	ϵ	$= 5.55 \epsilon^2$
■	Rehme	B.3	12.7	0.348	0.672
△	Velcek	6 cm	15.5	0.289	0.463
●	Kidd	4.3	5	0.245	0.333
□	Krett	C	9.5	0.303	0.509
▲	Velcek	5 mm	12.5	0.237	0.311
○	Hudina	lb. smooth	1.5 - 5	0.156	0.135

Figure 6-12. Effect of Spacer Grids on Convective Heat Transfer

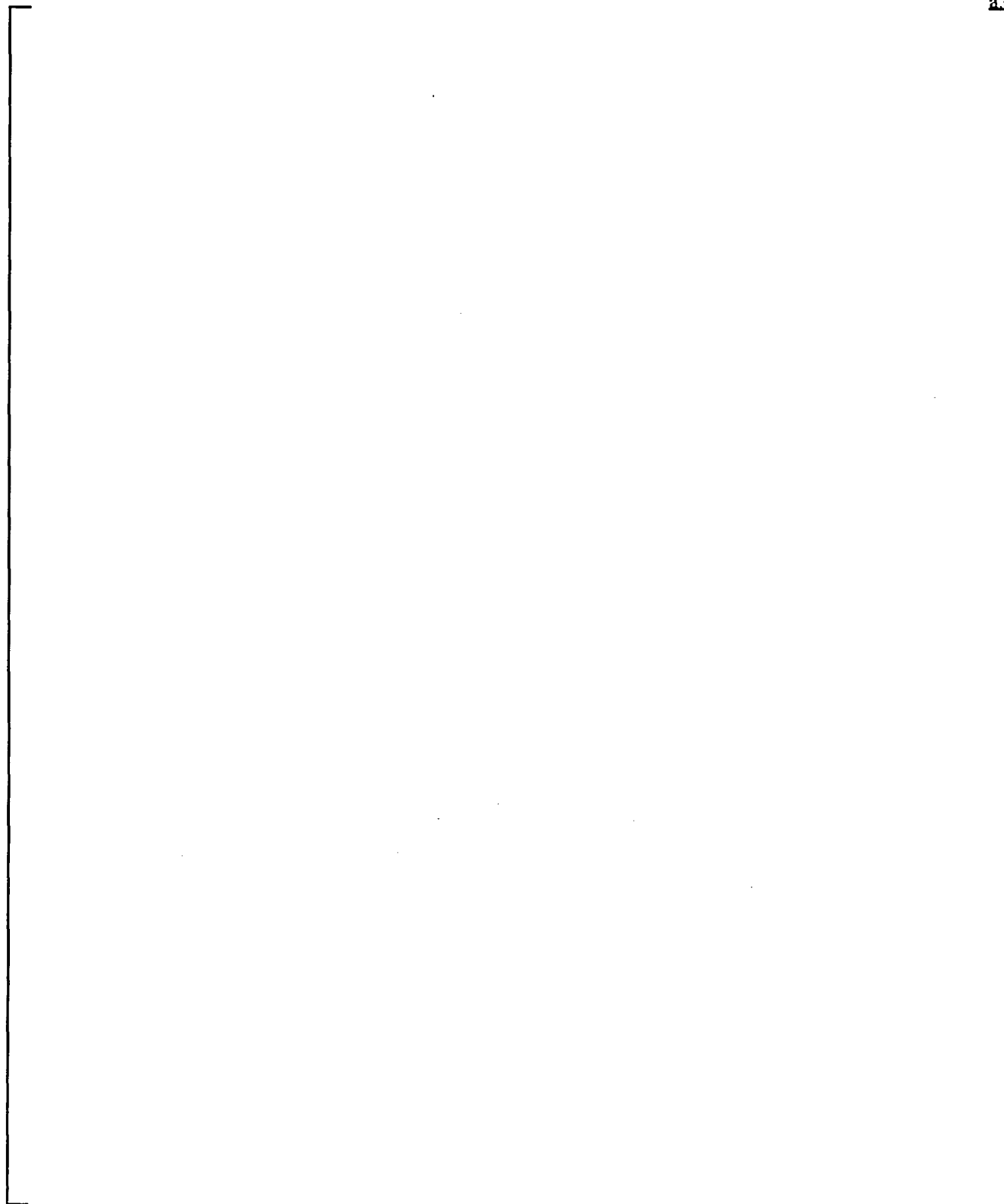


Figure 6-13. One-Dimensional Component Heat Transfer Regime Selection

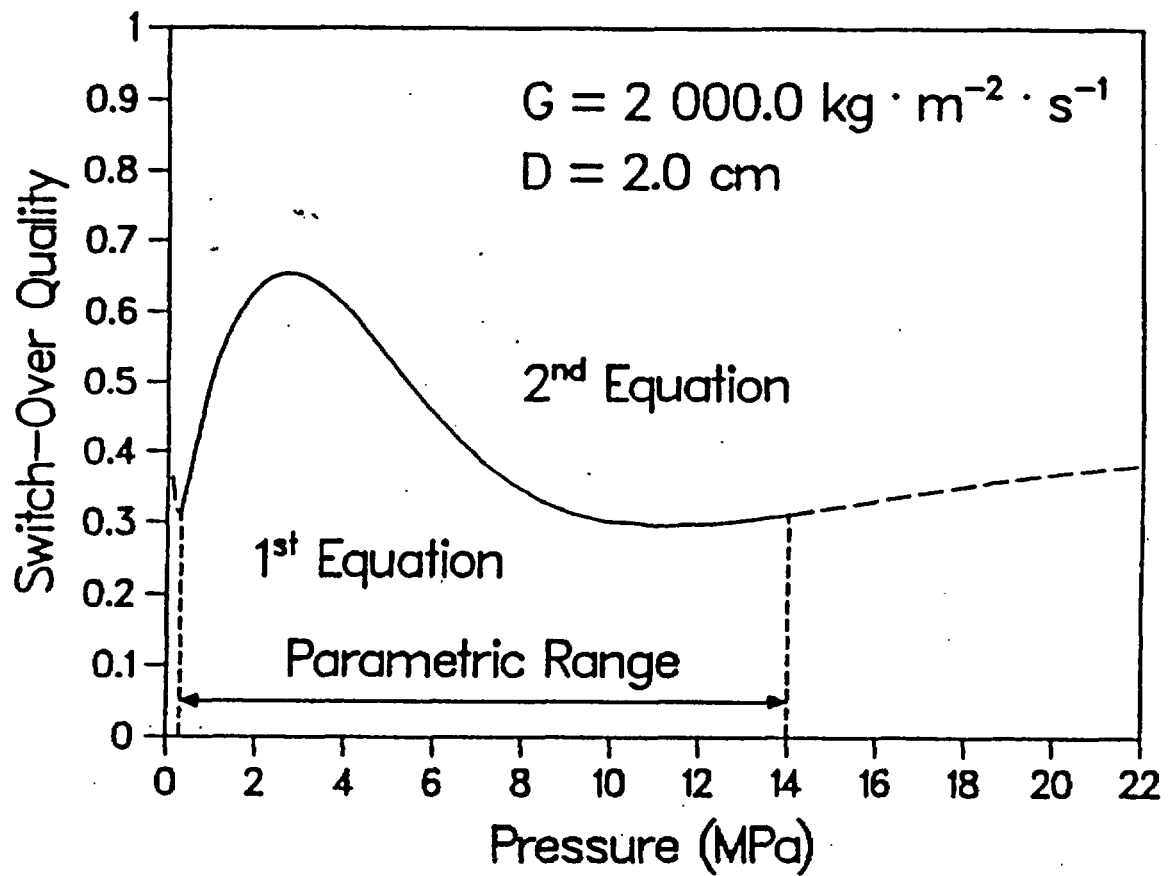


Figure 6-14. Biased CHF Correlation Switch Over Quality

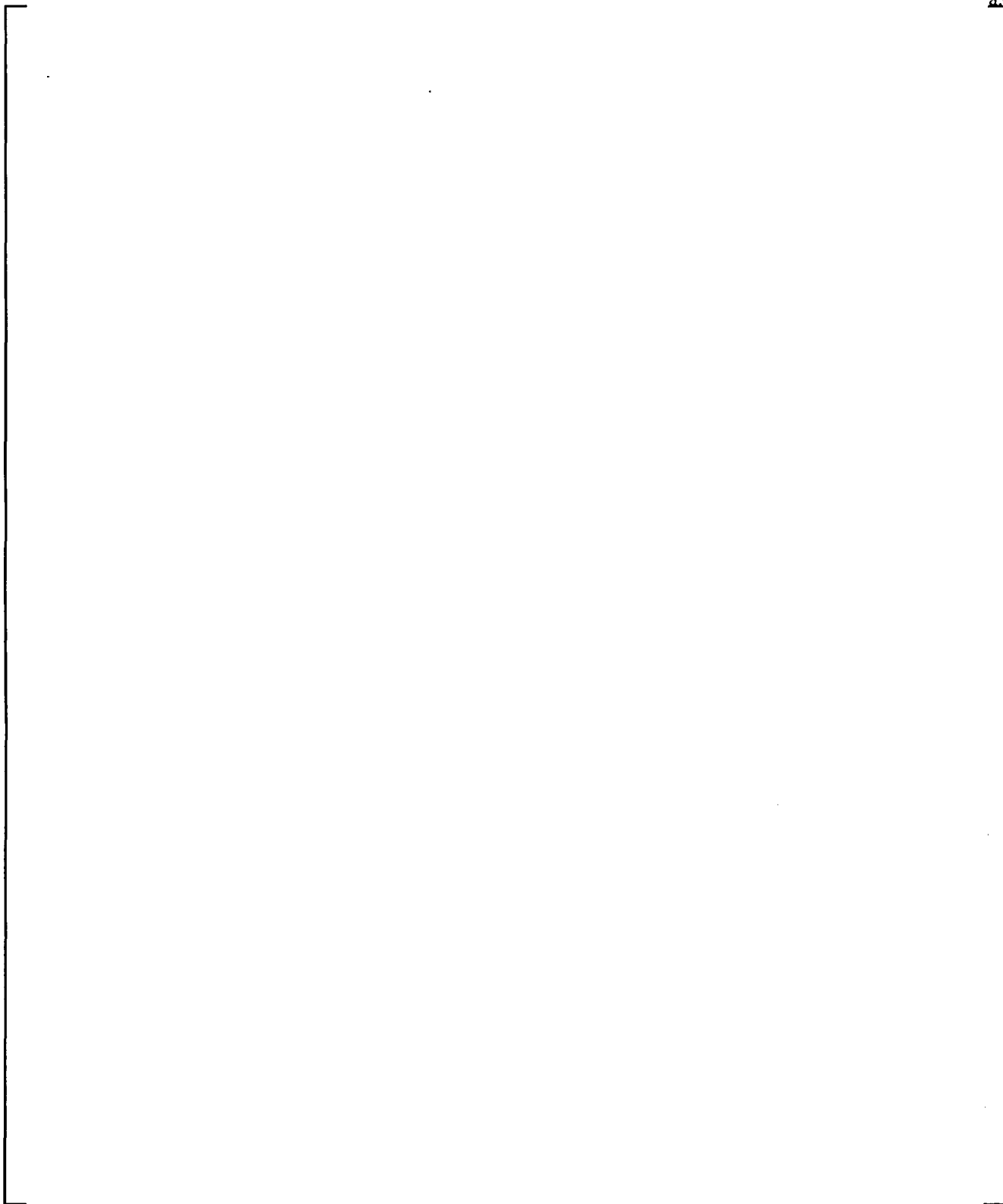


Figure 6-15. One-Dimensional Component Heat Transfer Regime Selection Process at High Void and Quality

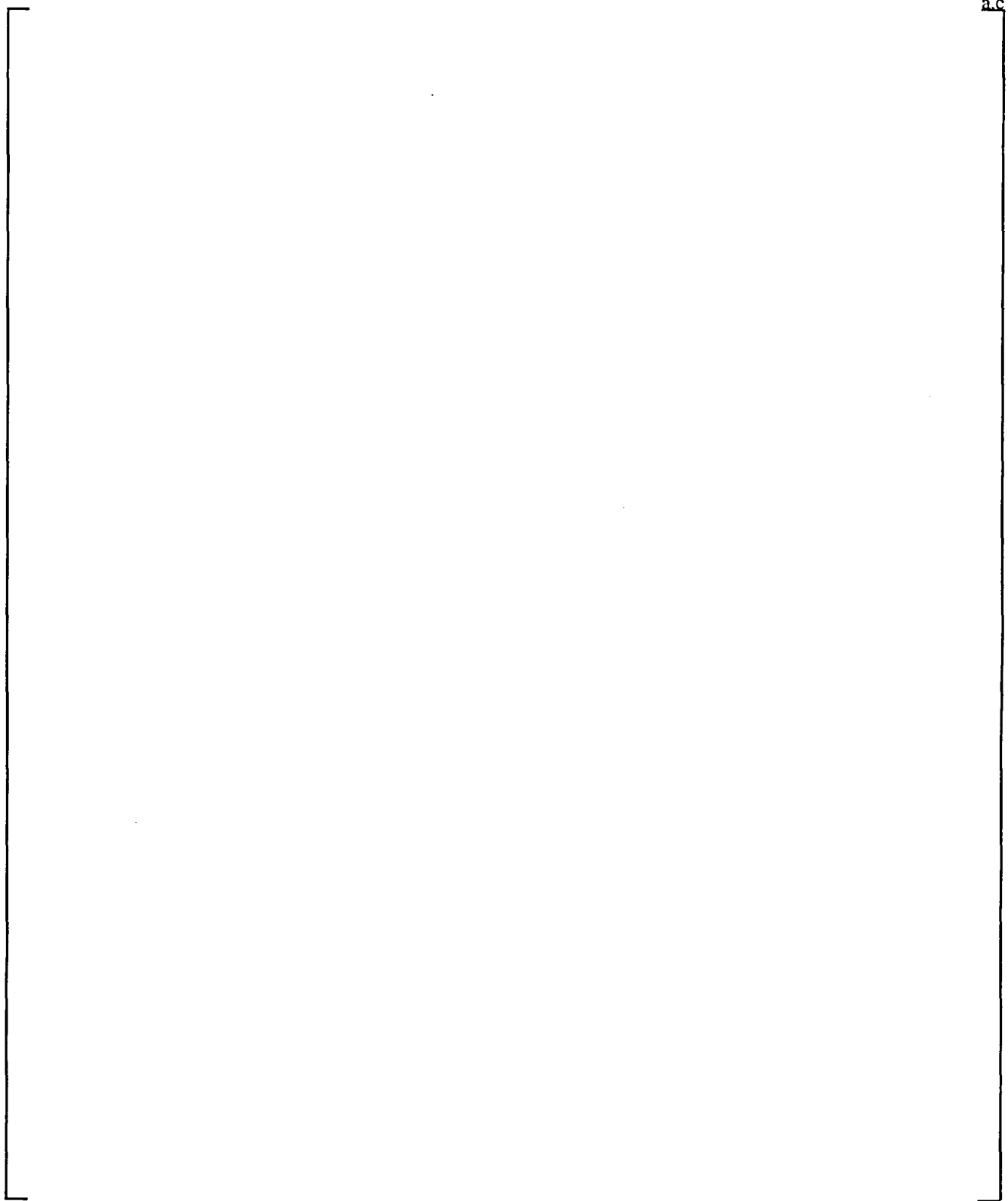


Figure 6-16. Heat Flux Paths for Nucleate Boiling

a.c

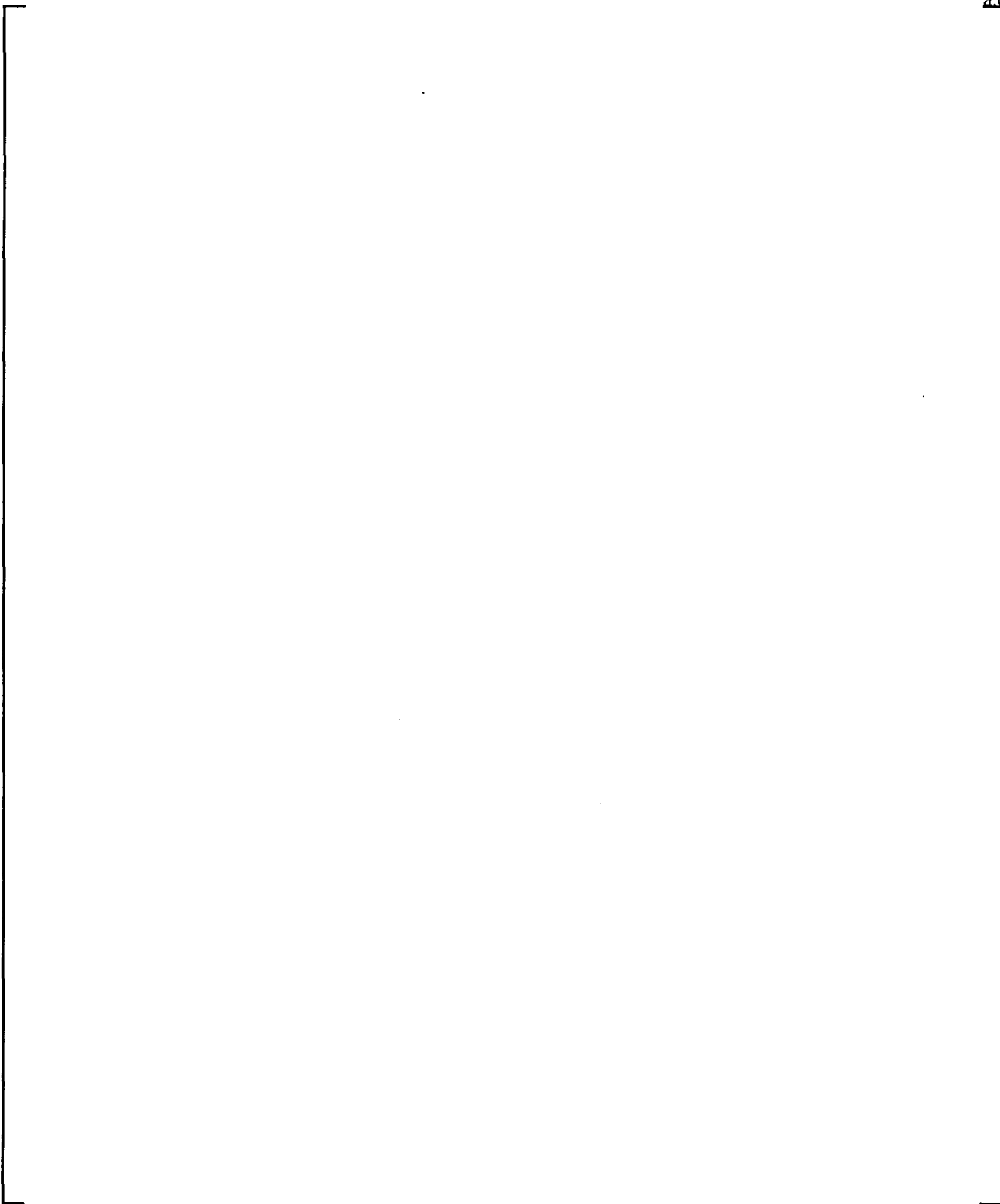


Figure 6-17. Heat Flux Paths for Transition Boiling and Dispersed Flow Film Boiling

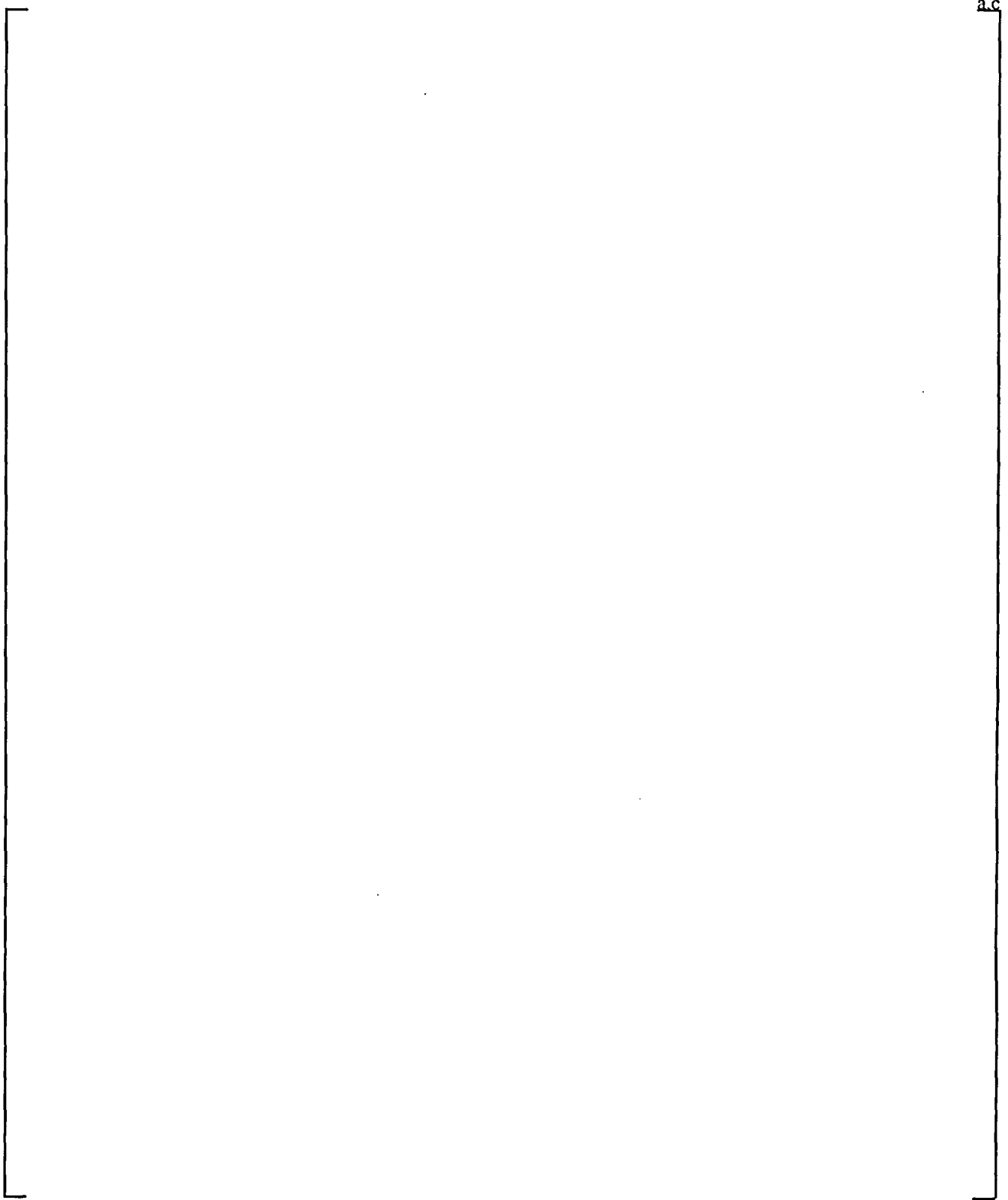


Figure 6-18. Heat Flux Paths for Film Boiling

7 WCOBRA/TRAC MODELS FOR HEATED AND UNHEATED STRUCTURES

7-1 INTRODUCTION

The WCOBRA/TRAC models for heated and unheated structures calculate the transient temperature response of the structures of interest, using the boundary conditions calculated by the heat transfer models and the fluid energy equations. This calculation consists of five major components:

- CONDUCTION MODEL specifies the conductor geometry and material properties, and solves the conduction equation.
- QUENCH FRONT MODEL a "fine mesh-rezoning" method that calculates quench front propagation due to axial conduction and radial heat transfer.
- GAP CONDUCTANCE MODEL a dynamic gap conductance model for a nuclear fuel rod.
- FUEL ROD DEFORMATION MODEL calculates the deformation of nuclear fuel rods, and the effects on core thermal-hydraulics.
- HEAT GENERATION MODEL determines the temporal and spatial variations in heat generation due to fission, gamma, and neutron energy deposition, fission product and actinide decay, and metal-water reaction in the cladding.

The conduction, quench front, gap conductance and fuel rod deformation models, and the metal-water reaction heat source are described in this section. The remaining heat sources are described in Section 8.

7-2 CONDUCTOR GEOMETRIES MODELLED IN THE VESSEL

WCOBRA/TRAC includes two general types of conductor models for the vessel component. The "rod" model is designed for heated structures such as nuclear fuel rods, heater rods, and tubes or walls which are expected to exceed the minimum film boiling temperature. This model allows the user to simulate most of the conductor geometries found in reactor vessels and heat transfer experiments. In addition, an "unheated conductor" model is provided for unpowered structures which are expected to remain below the minimum film boiling temperature.

Rods and unheated conductors are both used to model solid conducting structures in the vessel. There are two significant differences between them, however, one conceptual, the other numerical. Rods can model either active or passive elements, but unheated conductors are always passive. Unheated conductors cannot have internal heat sources. The quench front model with fine-mesh renoding can be applied to rods if needed, but unheated conductors are assumed never to require it.

A nuclear fuel rod model requiring minimal user input is built into the code as the "NUCL" rod option. Material properties can be specified by input or defaulted to uranium-dioxide and zircaloy.⁽¹⁾ The default properties are calculated using correlations from MATPRO-11 (Revision 1) (Hagman, Reymann, and Manson, 1980). The standard conductor geometry for a nuclear fuel rod is illustrated in Figure 7-1. Only cylindrical fuel rods with fluid thermal connections on the rod exterior are considered by this modelling option.

A dynamic gap conductance model based on the GAPCON (Beyer et al., 1975 and Lanning et al.) and FRAP (Dearian et al., 1977, Siefken et al., 1979, and Berna et al., 1978) computer codes is used for analyses of nuclear fuel rods. This model is discussed in Section 7-3-2. A fuel rod deformation model is also used for analyses of nuclear fuel rods. This model is discussed in Section 7-4.

Electric heater rods and other solid cylinders can be modelled with the "HROD" option. This option is available with the rod model and the unheated conductor model. These rods are modelled as concentric rings of different material regions, as shown in Figure 7-2. In each region the material type, number of radial nodes, width, and power factor are specified by input. Contact resistances are not calculated between material regions, but can be modelled by including a region one node wide with material properties that give it the appropriate thermal resistance.

Conductors, either tube or plate, with thermal connections to channels on either the inner or the outer surface are modelled with the "TUBE" and "WALL" options. The "WALL" option is available with the rod model and the unheated conductor model. The "TUBE" option is available with the unheated conductor model. The TUBE and WALL geometries, shown in Figure 7-3, are similar to the HROD geometry except for the interior coolant connections. Concentric and flat plate fuel elements, thermal walls and simple tubes can be modelled with these options.

Geometries simulated with the rod model may extend through any number of channel-splitting sections, but each heat transfer surface may only be connected to one channel in each section. Geometries simulated with the unheated conductor model may extend through one section only. Other limitations on the unheated conductor model are discussed in Section 7-6.

7-2-1 Conduction Equation

Model Basis The modelling requirements of the vessel component include the ability to simulate generalized conductor geometries (fuel rods, electric heater rods, tubes, and walls) and temperature-dependent material properties. To accomplish this, a finite-difference form of the conduction equation has been employed.

The difference equations are formulated using the "heat balance" approach (Trent and Welty, 1974) which easily accommodates the following features:

- unequal mesh spacing
- temperature-dependent material properties
- space-dependent material properties
- internal resistances (such as those due to gaps)
- radial heat generation profiles.

The finite-difference nodes of the conduction equation are modelled as control volumes connected by thermal resistances. They form a set of linearized equations solved by Gaussian elimination and back-substitution.

Model As Coded The radial conduction equation for a control volume can be derived from a simple heat balance. For node i of Figure 7-4 this is

$$(\rho C_p V)_i \frac{\partial T_i}{\partial t} = -Q_{i,i-1} - Q_{i,i+1} + Q_i''' V_i \quad (7-1)$$

where

- ρ = density (lbm/ft³)
- C_p = specific heat (Btu/lbm-°F)
- V_i = node volume (ft³)
- T_i = node temperature (°F)
- $Q_{i,i-1}$ = radial heat flow from node (i) to ($i-1$) (Btu/sec)
- $Q_{i,i+1}$ = radial heat flow from node (i) to ($i+1$) (Btu/sec)
- Q_i''' = volumetric heat generation rate (Btu/sec-ft³)

The locations of radial conduction nodes are automatically calculated for a conductor geometry type. Each material region is divided into a specified number of subregions of equal radial thickness, and a

conduction node is located at the center of mass of each subregion. This rule is followed for all nodes except the following:

- the node at the inside and outside surface of a "TUBE" or "WALL"
- outside surface of a heater rod
- fuel pellet exterior, cladding interior, and cladding exterior surface for a nuclear fuel rod.

For these surfaces, a subregion half as wide as the other subregions is defined, and the node is located on the surface. The noding within a nuclear fuel rod is illustrated in Figure 7-5. (The fuel centerline temperature is calculated by Hermite interpolation.)

The radial positions of the conduction nodes are fixed; relocation due to thermal expansion is not calculated. To prevent an apparent loss of mass from the conductor because of density change with temperature, the term (ρV) is evaluated at the cold state density and dimensions, and defines the mass M_i associated with node i . So Equation 7-1 becomes

$$(MC_p)_i \frac{\partial T_i}{\partial t} = -Q_{i,i-1} - Q_{i,i+1} + Q_i''' V_i \quad (7-2)$$

Heat transfer through a node is computed from the conductance (K) of the material and the temperature gradient across the node as

$$Q_{i,j} = -K_{i,j} (T_j - T_i) \quad (7-3)$$

and

$$K_{i,j} = K_{j,i} \text{ for } j = \begin{cases} i-1 \\ i+1 \end{cases}$$

The conductance is defined as the inverse of the thermal resistance (R) between nodes and is computed as

$$K_{i,i-1} = 1/(R_{i,i-1} + R_{i-1,i}) \quad (7-4)$$

Thermal resistances are calculated for each node as a function of geometry and thermal conductivity. (See Section 7-2-2 for a complete explanation of this procedure.)

Substituting Equation 7-3 into 7-2 gives

$$(MC_p)_i \frac{\partial T_i}{\partial t} = K_{i,i-1} (T_{i-1} - T_i) + K_{i,i+1} (T_{i+1} - T_i) + Q_i''' V_i \quad (7-5)$$

Forward differencing the temporal derivative in Equation 7-5 yields

$$\frac{(MC_p)_i}{\Delta t} (T_i - T_i^n) = K_{i,i-1} (T_{i-1} - T_i) + K_{i,i+1} (T_{i+1} - T_i) + Q_i''' V_i \quad (7-6)$$

where

$$\begin{aligned} \Delta t &= \text{time increment} \\ n &= \text{old time level (all other temperatures are at the new time level)} \end{aligned}$$

To solve this equation, an implicit formulation is applied in the radial direction and the equation solved by Gaussian elimination for all nodes at that axial level. Axial conduction, if used, is treated as an explicit source term. The finite-difference equation for node (*i*) is then:

$$\begin{aligned} \frac{(MC_p)_i}{\Delta t} (T_i - T_i^n) &= K_{i,i-1} (T_{i-1} - T_i) + K_{i,i+1} (T_{i+1} - T_i) \\ &+ K_{i,j-1} (T_{j-1}^n - T_i^n) + K_{i,j+1} (T_{j+1}^n - T_i^n) + Q_i''' V_i \end{aligned} \quad (7-7)$$

where the subscripts (*j+1*) and (*j-1*) represent the nodes at the same radial location and immediately above and below node *i*. If the stability criterion for the explicit axial conduction is exceeded, the timestep used in the conduction equation is divided into two or more smaller timesteps and the conduction equation is solved for each of these.

Variations of Equation 7-7 are defined for the boundary nodes. The boundary condition applied to the conduction equation can be adiabatic or a surface heat transfer coefficient. Adiabatic boundary conditions are assigned to the center nodes of solid cylindrical rods (nuclear and heater rods) and at any surface node not connected to the fluid. Heat transfer coefficient boundary conditions are applied at surfaces connected to the fluid.

The heat transfer is coupled to the fluid channel through the heat transfer coefficient boundary condition. For each surface heat transfer node, both a heat transfer coefficient and a fluid sink temperature are specified for each phase of the fluid. Thus, the rod heat flux is given by:

$$q'' = h_{wt} (T_w - T_t^n) + h_{wv} (T_w - T_v^n) \quad (7-8)$$

where h_{wt} is the total heat transfer coefficient to the liquid fields (Section 6). The fraction of the rod surface area in contact with a given phase is accounted for in the heat transfer modelling (e.g., $h_{wv} = 0$ for annular flow).⁽²⁾

The nucleate boiling heat flux depends very strongly on the wall surface temperature. Since the wall temperature is in turn affected strongly by the heat flux, the surface temperature solution may oscillate in

nucleate boiling unless the heat transfer and wall temperature solution are coupled implicitly. This is done non-iteratively by including the "linearized" derivative of the heat transfer coefficient with respect to temperature in the surface boundary condition. Therefore, the heat flux from the surface to phase (l) is given by:

$$q_l'' = h_{wl}^n (T_w - T_l^n) + \left(\frac{\partial h_{wl}^n}{\partial T_w} \right) (T_w - T_w^n) (T_w^n - T_l^n) \quad (7-9)$$

Rewriting Equation 7-7 for a surface node (w):

$$\begin{aligned} \frac{(MC_p)_w}{\Delta t} (T_w - T_w^n) &= K_{w,w-1} (T_{w-1} - T_w) + K_{w,j-1} (T_{j-1}^n - T_w^n) \\ &\quad + K_{w,j+1} (T_{j+1}^n - T_w^n) \\ &\quad - A_w \left[h_{wl}^n (T_w - T_l^n) + \left(\frac{\partial h_{wl}^n}{\partial T_w} \right) (T_w - T_w^n) (T_w^n - T_l^n) \right] \\ &\quad - A_w h_{wv}^n (T_w - T_v^n) + Q_w''' V_w \end{aligned} \quad (7-10a)$$

where A_w is the heated surface area. Equation 7-10 is solved simultaneously with a set of equations for the interior nodes to determine the new time temperatures.

Finally, the liquid phase heat transfer coefficient and the nucleate boiling heat flux are updated by,

$$h_{wl} = h_{wl}^n + \left(\frac{\partial h_{wl}^n}{\partial T_w} \right) (T_w - T_w^n) \quad (7-10b)$$

and

$$q_{wl}'' = h_{wl} (T_w - T_l^n) \quad (7-10c)$$

7-2-2 Calculation of Thermal Conductance

Model Basis The internode conductance, $(K_{i,i+1})$ between nodes i and $i+1$, as shown in Figure 7-6, is calculated from

$$K_{i,i+1} = 1/(R_{i,i+1} + R_{i+1,i}) \quad (7-11)$$

The thermal resistance $R_{i,i+1}$ is the resistance to heat flow from node i to the boundary between nodes i and $i+1$. The thermal resistance $R_{i+1,i}$ is the resistance to heat flow from node $i+1$ to the boundary between $i+1$ and i . Formulas for these resistances for both plate and cylindrical geometries are given below.

Model As Coded For a structure modelled as a flat plate, the steady, one-dimensional heat conduction equation with no internal generation is

$$\frac{d^2T}{dx^2} = 0 \quad (7-12)$$

with the boundary conditions (Figure 7-7)

$$\begin{aligned} x=0, & \quad T=T_1 \\ x=L, & \quad T=T_2 \end{aligned}$$

Integrating Equation 7-12 and applying the boundary conditions gives the following formula for temperature distribution in the plate:

$$T = (T_2 - T_1) \left(\frac{x}{L}\right) + T_1 \quad (7-13)$$

where L = thickness of the plate.

The rate of heat transfer, from the Fourier equation, is

$$q = -kA \frac{\partial T}{\partial x} = \frac{kA}{L} (T_1 - T_2) \quad (7-14)$$

where

k = thermal conductivity of the plate

A = surface area perpendicular to the direction of heat flow

If the heat transfer is thought of as energy being pushed down a temperature gradient against some thermal resistance, q can be expressed as

$$q = \frac{\Delta T}{R} \quad (7-15)$$

then

$$R = \frac{L}{kA} \quad (7-16)$$

Therefore, the resistance from node i to the boundary between i and $i+1$ for a flat plate is

$$R_{i,i+1} = \frac{\delta_{i,i+1}}{k_i A} \quad (7-17)$$

The total resistance from node i to node $i+1$ is $(R_{i,i+1} + R_{i+1,i})$. The conductance (K) between nodes i and $i+1$ is therefore

$$K_{i,i+1} = K_{i+1,i} = \frac{k_i k_{i+1} A}{k_{i+1} \delta_{i,i+1} + k_i \delta_{i+1,i}} \quad (7-18)$$

where

$\delta_{i,i+1}$ = distance from node i to boundary between nodes i and $i+1$ (Figure 7-6)

A = surface area perpendicular to the direction of heat flow

k_i, k_{i+1} = thermal conductivity of the material in node i and $i+1$, respectively.

For steady radial flow of heat through the wall of a hollow cylinder (Figure 7-8) the conduction is

$$\frac{1}{r} \frac{\partial}{\partial r} \left(r \frac{\partial T}{\partial r} \right) = 0 \quad (7-19)$$

with boundary conditions

$$r=r_1, T=T_1$$

$$r=r_2, T=T_2$$

Integration of Equation 7-19 yields

$$T = \frac{T_1 - T_2}{\ln \left(\frac{r_1}{r_2} \right)} \ln \left(\frac{r}{r_2} \right) + T_2 \quad (7-20)$$

The rate of heat flow is

$$q = -k(2\pi r \Delta X) \frac{\partial T}{\partial r} \quad (7-21)$$

$$= \frac{2\pi k \Delta X}{\ln \left(\frac{r_2}{r_1} \right)} (T_1 - T_2)$$

and the resistance is

$$R = \frac{\ln \left(\frac{r_2}{r_1} \right)}{2\pi k \Delta X} \quad (7-22)$$

where

ΔX = node length in axial direction.

Therefore, the resistance from node i to the boundary between i and $i+1$ for a cylinder is

$$R_{i,i+1} = \frac{\ln \left[\frac{(r_i + \delta_{i,i+1})}{r_i} \right]}{2\pi k (\Delta X)} \quad (7-23)$$

where

r_i = center of mass of node i

$\delta_{i,i+1}$ = radial distance from r_i to node boundary.

The total resistance between nodes i and $i+1$ is $(R_{i,i+1} + R_{i+1,i})$, so the conductance is

$$K_{i,i+1} = K_{i+1,i} = \frac{2\pi k_i k_{i+1} \Delta X}{k_{i+1} \ln (r_B/r_i) + k_i \ln (r_{i+1}/r_B)} \quad (7-24)$$

where $r_B = r_i + \delta_{i,i+1}$.

The formulation for the hollow cylinder applies also to solid cylinders, simply by assuming an adiabatic condition on the inside boundary.

7-3 FUEL ROD MODELLING

The fuel rod conductor has several special models to handle the unique situations that arise with heated conductors. These include a quench front renoding option and pellet-cladding gap conductance. These models are discussed in detail below.

7-3-1 Fuel Rod Quench Front Model

Model Basis Coupled thermal-hydraulic numerical simulations of rewetting encounter difficulties with large axial computational mesh spacing which cannot adequately resolve the axial profile of temperature and surface heat flux across the quench front. During quenching, the entire boiling curve -- from film boiling through transition boiling and critical heat flux to nucleate boiling -- can be encompassed by one hydrodynamic mesh cell. Constraining the entire cell to be in one boiling regime is nonphysical and results in stepwise cell-by-cell quenching, producing flow oscillations that can obscure the correct hydrodynamic solution. Consequently, an integration of the boiling curve shape through the hydrodynamic computational cell must be performed to determine the fluid heat input.

User-specified fixed heat transfer nodes and a fine mesh-rezoning technique (Kelly, 1979) are employed in the vessel component of WCOBRA/TRAC to surmount these difficulties. Fixed heat transfer nodes are used to model fuel rod conduction and cladding-fluid heat transfer with nodes that are smaller than the hydrodynamic cell size. These nodes are used throughout the transient. The fine mesh rezoning option allows the code to further resolve the quench front heat transfer. Fine mesh heat transfer cells with axial and radial conduction are superimposed upon the fixed heat transfer nodes, and a boiling heat transfer package is applied to each node.

By solving the two-dimensional conduction equation for a variable fine mesh at the quench front, propagation due either to quenching or dryout can be resolved and the surface heat flux integrated to provide the cell-averaged phasic heat inputs for the fluid energy equation. The resulting quench front velocity will be a function of:

- axial conduction
- boiling curve shape
- prequench heat transfer
- internal heat transfer within the rod.

Model as Coded Resolution of axial temperature and surface heat flux excursions is achieved by rezoning the heat conductor mesh in their vicinity. Figure 7-9 illustrates a typical axial noding scheme. When axial temperature differences between adjacent heat transfer nodes within a continuity cell exceed splitting criteria, an additional node is inserted halfway between the two original nodes. When the

splitting criteria are exceeded at a continuity cell boundary, one node is inserted below the boundary and another is inserted above the boundary. These scenarios are illustrated in Figure 7-10. The temperatures assigned to these nodes are computed so that energy is conserved. This splitting process continues (over a succession of timesteps) until the mesh is fine enough to resolve the surface temperature curve to the desired level of detail.

The correct temperature differences to be used as splitting criteria depend on the heat transfer regime. They are further modified by functions of the wall temperature (when the wall temperature is near the critical heat flux temperature) to ensure resolution of the surface heat flux profile in the vicinity of the quench front. The temperatures assigned to the inserted nodes are calculated from an energy balance:

$$C_{p_1} (T_1 - T_I) \frac{\Delta X}{2} + C_{p_2} (T_2 - T_I) \frac{\Delta X}{2} = 0$$

$$T_I = \frac{(C_p T)_1 + (C_p T)_2}{(C_{p_1} + C_{p_2})} \quad (7-25)$$

where the subscripts *I*, 1, and 2 represent the inserted and two original nodes, respectively.

Conversely, when a fine mesh has been established, but the disturbance has propagated downstream and the fine mesh is no longer necessary, adjacent nodes can be coalesced back down to one node. The decision to merge cells is based on minimum temperature differences between adjacent nodes. Eventually, all the fine mesh nodes in a region will coalesce, and only the original nodes will remain.

The fine mesh-rezoning model differs from other reflood models in that the fine mesh nodes are stationary and do not have a fixed mesh spacing. The fine mesh nodes are split to create a graduated mesh spacing that readjusts itself constantly to the changing axial temperature gradient. This approach permits node sizes small enough to resolve axial conduction and the boiling curve shape at the quench front, and yet minimizes the number of nodes required. It ensures conservation of stored energy when cells are added, and simplifies coupling with the hydrodynamic solution. Figures 7-11 and 7-12 (taken from a simulation of a FLECHT low flooding rate test) illustrate the resolution of the cladding temperature profile and the surface heat flux in the vicinity of the quench front.

7-3-2 Pellet-Cladding Gap Conductance Model

Model Basis The dynamic gap conductance model, originally developed for the VIPRE (Stewart et al., 1982) code, computes changes in the fuel rod structure and fill gas pressure that affect the gap conductance and fuel temperature during a transient. The method is based primarily on previous work on the GAPCON (Beyer et al., 1975, and Lanning et al., 1978) and FRAP (Dearien et al., 1977, Siefken et al., 1979, and Berna et al., 1978) series of fuel performance codes, but with the mechanics and fill gas pressure models greatly simplified. The material property correlations are taken exclusively from MATPRO-11 (Revision 1) (Hagman, Reymann, and Manson, 1980); refer to Section 10-4.

Model As Coded The pellet-cladding gap conductance has three components:

$$h_{gap} = h_{rad} + h_{gas} + h_{solid} \quad (7-26)$$

where

h_{rad} = gap conductance due to thermal radiation

h_{gas} = gap conductance due to conduction in the fill gas

h_{solid} = gap conductance due to physical contact between the fuel pellet and the cladding

Each of these terms has associated with it certain models and assumptions. These are discussed in detail below. In all models, the gap is assumed axisymmetric.

Radiant Heat Transfer

The gap conductance due to radiant heat transfer is the ratio of the gap radiant heat flux, q_r'' , to the temperature rise across the fuel/cladding gap

$$h_{rad} = \frac{q_r''}{T_1 - T_2} \quad (7-27)$$

The radiant heat flux leaving the fuel surface, q_r'' , is determined from the Stefan-Boltzmann equation using appropriate fuel cladding geometry factors, so that

$$q_r'' = \sigma_{SB} \left[\frac{1}{\epsilon_1} + \frac{A_1}{A_2} \left(\frac{1}{\epsilon_2} - 1 \right) \right]^{-1} [T_1^4 - T_2^4] \quad (7-28)$$

where

A_1 = fuel surface area (ft²)

A_2 = cladding surface area (ft²)

ϵ_1 = fuel surface emissivity

= min (0.8707, 1.311 - 2.447 x 10⁻⁴T(°R))

ϵ_2 = cladding surface emissivity

= 0.75

T_1 = fuel surface temperature (°R)

T_2 = cladding surface temperature (°R)

σ_{SB} = Stefan-Boltzmann constant (1.714x10⁻⁹ Btu/hr-ft²-°R⁴)

The emissivity of the fuel is taken from function FEMISS of MATPRO-11 (Revision 0) (Hagman and Reymann, 1979). The emissivity of the cladding inner surface is based on the data in subroutine ZOEMIS of MATPRO-11 (Revision 0).

Note that Revision 0 of function FEMISS has a lower bound of 0.4083, used for fuel temperatures in excess of 3230°F. Fuel surface temperatures never approach this value during any WCOBRA/TRAC calculation which satisfies the PCT acceptance criterion, so the absence of this lower limit is inconsequential.

Conduction Heat Transfer in the Fill Gas

Heat conduction through the fill gas is calculated using the model developed for GAPCON-2 based on a linear regression analysis of Ross-Stoudt data by Lanning and Hann (1975). For a normal open gap the conductance is

$$h_{gas} = \frac{k_{gas}}{\tau_g + 1.8 (g_1 + g_2)} \quad (7-29)$$

where

k_{gas} = fill gas mixture thermal conductivity (Btu/hr-ft-°F)

τ_g = gas gap width from deformation model (ft)

g_1 = fuel pellet temperature jump distances (ft)

g_2 = cladding temperature jump distances (ft)

The temperature jump distances compensate for the nonlinearity of the temperature gradient near the walls and the temperature discontinuities on the wall surface as illustrated in Figure 7-13. The nonlinear temperature gradient is due to the incomplete thermal mixing of the gas molecules near the surface. The surface temperature discontinuity results from the incomplete thermal accommodation of the gas molecules to the surface temperature.

The GAPCON-2 modification of the Lloyd model (Lloyd et al., 1973) is used to calculate the temperature jump distance. The Lloyd model compares well with available data and is used in both the FRAP and GAPCON-2 codes. The temperature jump distance term is evaluated with the relation^a

$$(g_1 + g_2) = 1.131(10^{-5}) \frac{k_{gas} (\bar{T}_g)^{1/2}}{P_{gas} \sum_{j=1}^6 \frac{a_j x_j}{(M_j)^{1/2}}} \quad (ft) \quad (7-30)$$

^a Note that the equation as written in the GAPCON-2 manual is in error.

where

$$\begin{aligned}
 k_{gas} &= \text{fill gas mixture thermal conductivity (Btu/hr-ft-}^\circ\text{F)} \text{ (Section 10-4)} \\
 \bar{T}_g &= \text{gas gap average temperature (}^\circ\text{K)} \\
 x_j &= \text{mole fraction of } j\text{th gas} \\
 M_j &= \text{molecular weight of } j\text{th gas} \\
 a_j &= \text{accommodation coefficient of } j\text{th gas} \\
 P_{gas} &= \text{fill gas pressure (psia)}
 \end{aligned}$$

Measurements for helium and xenon on UO_2 by Ullman, Acharya, and Olander (1974) show that accommodation coefficients are temperature-dependent and vary for different gases. These dependencies are incorporated by using the GAPCON-2 curve fits to the Ullman data.

$$a_{He} = 0.425 - 2.5(10^{-4})T$$

$$a_{Xe} = 0.749 - 2.3(10^{-4})T \quad (7-31)^{(3)}$$

where T is in Kelvin ($^\circ\text{K}$).

The accommodation coefficients for other gases are approximated using a linear interpolation between those of helium and xenon based on molecular weight. This was found to correlate the data of Thomas (1967) with reasonable accuracy.

The gas mixture conductivity (k_{gas}) is determined from the conductivities of the constituent gases using a simplified version of the model in the MATPRO-11 subroutine GTHCON. Since the code uses the temperature jump model described above, the free molecular convection (Knudsen) regime correction to the gas conductivity given in MATPRO is not required. The conductivities of helium, xenon, argon, krypton, hydrogen, and nitrogen gases are calculated using correlations from MATPRO-11 (Revision 1). The correlations compare favorably with the Chapman-Enskog theory used in GAPCON but are much easier to implement.

When fuel/cladding contact occurs, the heat conductance in the gas becomes

$$h_{gas} = \frac{k_{gas}}{\{1.8[C(R_1 + R_2) + g_1 + g_2] - 4.2(10^{-7})\}} \quad (7-32)$$

where

- k_{gas} = fill gas mixture thermal conductivity (determined as for open gap)
- g_1, g_2 = fuel pellet and cladding temperature jump distances (determined as for the open gap)
- C = $1.98 \exp [-8.8(10^{-5}) P_i]$, dimensionless constant where P_i is the contact pressure (in psi, determined by the fuel rod deformation model)

Fuel cladding contact is defined to occur when

$$\tau_g \leq 3.6 (R_1 + R_2) \quad (7-33)$$

where

- τ_g = gas gap width (from the fuel rod deformation model; discussed below)
- R_1 = mean surface roughness of fuel pellet
- R_2 = mean inside surface roughness

By this criterion, contact is assumed to occur because of waviness and mismatch of the fuel/cladding interface when the calculated gap width closes to within 3.6 times the combined surface roughnesses. This was determined by comparing measured gap widths with calculated gap widths from GAPCON (Hann, Beyer, and Parchen, 1973). A more complete discussion is available in the GAPCON-2 manual (Beyer et al., 1975).

Pellet-Cladding Contact Conductance

When the fuel and cladding are not in contact, h_{solid} must be zero. But when the deformation model determines that the gap between the fuel and cladding is small enough for contact to occur, the Mikic/Todreas model (Cooper, Mikic, and Yavonovich, 1969 and Todreas and Jacobs, 1973) is used to determine the contact conductance. Of the available models, it provides the best agreement with a wide range of contact conductance data (Lanning and Hahn, 1975 and Garnier and Begej, 1979).

In this model, h_{solid} is defined in terms of the physical properties of the materials and the geometry of the interface between them:

$$h_{solid} = \frac{5k_m}{(R_1^2 + R_2^2)^{1/2}} \left(\frac{P_{int}}{H_M} \right)^n \left(\frac{R_1}{\lambda_1} \right) \quad (7-34)$$

where

$$k_m = \frac{2k_1 k_2}{k_1 + k_2}$$

k_1 = fuel thermal conductivity (Btu/hr-ft-°F)

k_2 = cladding thermal conductivity (Btu/hr-ft-°F)

R_1 = mean fuel surface roughness (in.)

R_2 = mean cladding surface roughness (in.)

$\frac{P_{int}}{H_M}$ = the dimensionless ratio of the interface pressure to the Meyer hardness

$\frac{R_1}{\lambda_1}$ = the dimensionless ratio of the mean fuel surface roughness and wave length (distance between peaks)

The interfacial pressure (P_{int}) due to the differential fuel and cladding expansion, is calculated with the fuel rod deformation model and is nondimensionalized using the Meyer hardness calculated from MATPRO-11 (Revision 1) subroutine CMHARD (Hagman, Reymann, and Manson, 1980). The exponent, n , on the ratio of interfacial pressure to Meyer hardness is defined (Thomas, 1967) as

$$\begin{aligned} n &= 1.0 & (P_{int}/H_M) > 0.01 \\ n &= 0.5 & (P_{int}/H_M) < 0.0001 \end{aligned}$$

For the intermediate range, the ratio is held constant:

$$\left(\frac{P_{int}}{H_M}\right)^n = 0.01 \quad 0.0001 \leq (P_{int}/H_M) \leq 0.01$$

The ratio of fuel surface roughness to wave length is estimated as in GAPCON-2 by

$$\left(\frac{R_1}{\lambda_1}\right) = \exp[0.5285 \ln(R_1) - 5.738] \quad (7-35)$$

where R_1 = mean fuel surface roughness (microinches).

7-4 FUEL ROD DEFORMATION MODEL

Model Basis Fuel pellet and cladding dimensional changes will occur during a loss-of-coolant accident, as a result of the thermal and mechanical stresses present in a nuclear fuel rod. The fuel rod deformation model calculates these changes and their effects on the core transient thermal-hydraulics.

WCOBRA/TRAC calculates the effects of fuel rod deformation on the pellet-cladding gap conductance,

the cladding dimensions used in the conduction equation and the calculation of cladding oxidation, the cladding surface heat transfer area, and the continuity and momentum areas of the fluid cells associated with the fuel rods. The modelling of each of these effects is discussed in this section.

Model as Coded The fuel rod deformation mechanisms which are modelled in WCOBRA/TRAC are described in Section 7-4-1. The effects of fuel rod deformation on the core transient thermal-hydraulics are discussed in Section 7-4-2.

7-4-1 Deformation Mechanisms

Fuel Pellet Thermal Expansion

The axial and diametral thermal expansion of the fuel is calculated using the MATPRO-11 (Revision 1) (Hagrman, Reymann, and Manson, 1980) FTHEXP subroutine correlation for thermally induced strain in UO_2 . The correlation was simplified by omitting the corrections for molten fuel and mixed oxide (Pu). FTHEXP will return the same numerical value as the correlation in WCOBRA/TRAC, when FCOMP (weight percent PuO_2) is equal to zero, and when T (fuel temperature) is less than FTMELT (fuel melting temperature). This is apparent by inspection of the subroutine listing in MATPRO.

In this model, the radial cracks in the fuel are assumed to relieve the hoop and radial stresses, allowing unrestrained radial movement of the fuel in each concentric radial node. The total radial movement at the fuel pellet surface is the sum of the expansion in all the fuel nodes.

$$(\Delta r_{th})_{fuel} = \sum_{i=1}^{NFUEL} \epsilon_r(T_i) \Delta r_i \quad (7-36)^{(4)}$$

where

$$\begin{aligned} \epsilon_r(T_i)_j &= \text{thermal strain at axial node } j \text{ and radial node } i \\ &= 1 \times 10^{-5} T_i + 0.04 \exp(-5000/T_i) - 0.003 \\ T_i &= \text{node temperature (}^\circ\text{K)} \\ \Delta r_i &= \text{thickness of radial node } i \\ NFUEL &= \text{number of radial nodes in the fuel} \end{aligned}$$

The stress-free axial thermal expansion of the fuel pellet stack is calculated in an analogous manner. The fuel pellet stack length change due to the thermal expansion is

$$(\Delta \ell_{th})_{fuel} = \sum_{j=1}^{NDX} \epsilon_z(\bar{T}_j) \Delta X_j \quad (7-37)$$

where

$\varepsilon_z(\bar{T}_j)$ = thermal strain at axial node j based on volume-averaged radial node temperatures
 ΔX_j = height of axial node j
 NDX = number of axial nodes

Cladding Thermal Expansion

The axial and radial thermal expansion of the cladding are calculated using the CTHEXP subroutine correlations from Hagrman, Reymann, and Manson (1980). The radial thermal expansion is calculated as

$$(\Delta r_{th})_{clad} = \varepsilon_r(\bar{T}_j) \bar{r} \quad (7-38)$$

where

$\varepsilon_r(\bar{T}_j)$ = radial thermal strain at axial node j based on the average cladding temperature (Table 7-1)
 \bar{r} = cladding mean radius (cold)

The axial thermal expansion of the cladding is

$$(\Delta \ell_{th})_{clad} = \sum_{j=1}^{NDX} \varepsilon_z(\bar{T}_j) \Delta X_j \quad (7-39)$$

where

$\varepsilon_z(\bar{T}_j)$ = axial thermal strain at axial node j based on average cladding temperature at node j (Table 7-1)
 ΔX_j = height of axial node j

Cladding Elastic Deformation

When the pellet-cladding gap is open, elastic deformation of the cladding is driven by the difference between the fill gas and system pressures. If the gap closes, the cladding deformation is caused by the radial motion of the fuel. In both cases, the cladding is assumed sufficiently thin for the stress, strain, and temperature to be uniform throughout the cladding thickness.

In the open gap elastic deformation model, the cladding is considered as a thin cylindrical shell loaded by internal and external pressures. (Axisymmetric loading and deformation are assumed.) The radial and

axial elastic deformation is the result of hoop stress and axial stress caused by pressure difference. These stresses are given by the following equations:

$$\sigma_{\theta} = \frac{r_i P_i - r_o P_o}{\tau_c} \quad (7-40)$$

$$\sigma_z = \frac{\pi r_i^2 P_i - \pi r_o^2 P_o}{\pi(r_o^2 - r_i^2)} \quad (7-41)$$

where

- r_o = cladding outside radius
- r_i = cladding inside radius
- τ_c = cladding thickness
- P_i = internal fill gas pressure (P_G if the gap is open, Equation 7-46; P_{int} if the gap is closed, Equation 7-49)
- P_o = system pressure

The radial stress component is neglected, yielding the following relationships from Hook's Law:

$$\epsilon_{\theta} = \frac{\Delta r}{r} = \frac{1}{E}(\sigma_{\theta} - \nu \sigma_z) \quad (7-42)$$

$$\epsilon_z = \frac{\Delta \ell}{\ell} = \frac{1}{E}(\sigma_z - \nu \sigma_{\theta}) \quad (7-43)$$

where

- ϵ_{θ} = hoop strain
- ϵ_z = axial strain
- E = modulus of elasticity (Young's modulus)
- ν = Poisson ratio, $E/2G - 1$ where G = shear modulus

The modulus of elasticity and the shear modulus are shown in Table 7-2.

The relations for the cladding radial and axial elastic deformations, then, are

$$(\Delta r_{el})_{clad} = \epsilon_{\theta} \bar{r} \quad (7-44)$$

$$(\Delta \ell_{el})_{clad} = \sum_{j=1}^{NDX} \epsilon_z \Delta X_j \quad (7-45)$$

where

- ϵ_{θ} = hoop strain at axial node j
- \bar{r} = cladding mean radius
- ϵ_z = axial strain at axial node j
- ΔX_j = height of axial node j

The internal fill gas pressure used to determine the cladding elastic deformation when the gap is open is calculated from the relation

$$P_G = \frac{MR}{\frac{V_P}{T_P} + \sum_{j=1}^{NDX} \pi \Delta X_j \left[\frac{(r_{ci}^2 - r_{fo}^2)}{T_G} + \frac{r_v^2}{T_v} \right]_j} \quad (7-46)$$

where

- M = gram-moles of gas in fuel rod
- V_P = gas plenum volume, including effects of fuel and cladding axial expansion (ft³) (from Equations 7-37, 7-39, and 7-45)
- T_P = gas plenum temperature (°K) (defined as the temperature of the cladding at the top of the fuel rod + 10 °K)
- ΔX_j = computational cell length at axial level j (ft)
- r_{ci} = cladding inside radius including thermal and elastic expansion, and creep deformation (ft) (from Equations 7-38, 7-44, and 7-59)
- r_{fo} = fuel outside radius including thermal expansion (ft) (from Equation 7-36)
- R = gas constant (6.1313 ft-lbf/g-mole-°K)
- r_v = radius of central void (ft) (from input data)
- T_G = gas gap temperature (°K)
- T_v = central void temperature (°K)

This is a static lumped pressure model, similar to those in FRAP or GAPCON. The pressure is assumed uniform throughout the fuel rod, with constant fission gas inventory.

In the closed gap deformation model, the cladding is considered as thin-wall tubing with a specified displacement at the inside and pressure loading at the outside surface. The radial fuel displacement at which contact occurs can be calculated as

$$(\Delta r_{th})_{fuel} = (\Delta r_{th})_{clad} + (\Delta r_{cr})_{clad} + \tau_{g,cold} - \tau_g|_L \quad (7-47)$$

where

$$\begin{aligned} \tau_g|_L &= \text{fuel cladding gap width that defines the closed gap (i.e., } 3.6 (R_1 + R_2) \text{ as in Equation 7-33)} \\ \tau_{g,cold} &= \text{user-input cold fuel cladding gap width (including burnup-dependent effects)} \\ (\Delta r_{th})_{fuel} &= \text{fuel radial thermal expansion (Equation 7-36)} \\ (\Delta r_{th})_{clad} &= \text{cladding radial thermal expansion (Equation 7-38)} \\ (\Delta r_{cr})_{clad} &= \text{cladding creep deformation (Equation 7-59)} \end{aligned}$$

Fuel radial displacement due to contact is assumed negligible, so the radial elastic deformation of the cladding must be equal to the applied fuel displacement on the inside surface,

$$\begin{aligned} (\Delta r'_{th})_{fuel} &= (\Delta r_{th})_{fuel} - (\Delta r_{th})_{clad} - (\Delta r_{cr})_{clad} + \tau_g|_L - \tau_{g,cold} \\ (\Delta r_{el})_{clad} &= (\Delta r'_{th})_{fuel} \end{aligned} \quad (7-48)$$

The pellet-cladding interfacial pressure generated by the applied displacement can be computed using the equilibrium stress (Equations 7-40 and 7-41), Hook's Law (Equations 7-42 and 7-43), and the applied displacement $(\Delta r'_{th})_{fuel}$. The interfacial pressure is

$$P_{int} = \frac{(\Delta r'_{th})_{fuel} E \tau_c (r_o^2 - r_i^2)}{\bar{r} [r_i (r_o^2 - r_i^2) - r_i^2 \tau_c \nu]} + P_o \frac{r_o (r_o^2 - r_i^2) - r_o^2 \tau_c \nu}{r_i (r_o^2 - r_i^2) - r_i^2 \tau_c \nu} \quad (7-49)$$

where

$$\begin{aligned} (\Delta r'_{th})_{fuel} &= \text{applied fuel displacement in cladding (from Equation 7-48)} \\ E &= \text{modulus of elasticity} \\ \tau_c &= \text{cladding thickness} \\ r_o &= \text{cladding outside radius} \\ r_i &= \text{cladding inside radius} \\ \bar{r} &= \text{cladding mean radius} \\ \nu &= \text{Poisson's ratio for the cladding} \\ P_o &= \text{system pressure (on the outside surface of the cladding)} \end{aligned}$$

The elastic deformation when the gap is closed is evaluated using the relation in Equation 7-44, but the internal pressure P_i is defined as the interfacial pressure P_{int} from Equation 7-49 instead of the fill gas pressure P_G from Equation 7-46.

Cladding Creep Deformation

The high-temperature creep model is based on tests performed at the Berkeley Nuclear Laboratories in the United Kingdom. Three cladding material options are available. The first is used for analyses of Westinghouse manufactured Zircaloy-4 cladding, and is based on the work of Donaldson, Healey, and Horwood (1985). The second is used for analyses of Westinghouse manufactured ZIRLO™ cladding, and is based on the work of Donaldson and Barnes (1989), and Donaldson, Barnes, and Hall (1989). An additional option is available for analyses of the Sandvik manufactured Zircaloy-4 cladding used in the NRU experiments, and is based on the work of Donaldson, Horwood, and Healey (1982).

The Berkeley test data indicate that high-temperature creep of the cladding materials of interest is well described by a power law stress dependence and an Arrhenius temperature dependence.

$$d\epsilon/dt = A' \sigma^n \exp(-Q/RT) \quad (7-50)$$

where

$d\epsilon/dt$	=	creep rate (sec ⁻¹)
σ	=	hoop stress (MPa)
Q	=	activation energy, cal/gm-mole
R	=	gas constant, 1.987 cal/gm-mole/°K
T	=	temperature (°K)
t	=	time

and A' , n are material-specific functions of T and σ . This relationship for creep is commonly referred to as the Norton creep equation.

The time-dependent hoop stress is given by

$$\sigma(t) = (d(t)/2\tau(t)) P(t) \quad (7-51)$$

where

- $d(t)$ = mid-wall cladding diameter
- = $d_o (1 + \varepsilon(t))$, where d_o = initial mid-wall cladding diameter
- $\tau(t)$ = cladding thickness
- = $\tau_o / (1 + \varepsilon(t))$, where τ_o = initial cladding thickness
- $P(t)$ = cladding pressure differential
- $\varepsilon(t)$ = engineering strain

If the pressure is assumed to vary linearly over a small increment of time, such that,

$$P(t) = P_o + (dP/dt)\Delta t,$$

where

P_o = cladding pressure differential at the beginning of the timestep

the time-dependent stress is given by

$$\sigma(t) = \sigma_o (1 + \varepsilon(t))^2 (1 + ((dP/dt)/P_o)\Delta t), \quad (7-52)$$

where

σ_o = hoop stress at the beginning of the timestep.

If the temperature is assumed to vary linearly over a small increment of time, such that

$$T(t) = T_o + (dT/dt)\Delta t,$$

where

T_o = temperature ($^{\circ}\text{K}$) at the beginning of the timestep

then

$$\exp(-Q/RT(t)) = \exp(-Q/RT_o(1 + ((dT/dt)/T_o)\Delta t)) \quad (7-53)$$

A good approximation to this expression is

$$\exp(-Q/RT(t)) = \exp(-Q/RT_o)(1 + (dT/dt)(Q/RT_o^2)\Delta t) \quad (7-54)$$

provided that $|(dT/dt)(Q/RT_o^2)|\Delta t \leq 0.01$.

Substituting Equations 7-52 and 7-54 into 7-50 and allowing for the possibility of negative cladding pressure differentials yields

$$\begin{aligned} de/dt = & (|P_o|/P_o) A' \exp(-Q/RT_o) |\sigma_o|^n (1+\epsilon)^{2n} \\ & (1 + ((dP/dt)/P_o)\Delta t)^n (1 + (dT/dt)(Q/RT_o^2)\Delta t) \end{aligned} \quad (7-55)$$

The true strain is related to the engineering hoop strain by $e = \ln(1+\epsilon)$. Therefore, $de = d\epsilon/(1+\epsilon)$. If we define

$$\begin{aligned} C_1 &= (|P_o|/P_o) A' \exp(-Q/RT_o) |\sigma_o|^n \\ C_2 &= (dT/dt)(Q/RT_o^2) \\ C_3 &= (dP/dt)/P_o \end{aligned}$$

Equation 7-55 may be rewritten as

$$d\epsilon/(1+\epsilon)^{2n+1} = C_1((1+C_2\Delta t)(1+C_3\Delta t)^n)dt$$

or

$$(1+\epsilon)^{-(2n+1)}d\epsilon = C_1(1+C_3\Delta t)^n dt + C_1C_2\Delta t(1+C_3\Delta t)^n dt \quad (7-56)$$

Integration may be performed using standard integral tables (for example, Beyer, 1978) which yields

$$\begin{aligned} (-1/2n)((1+\epsilon)^{-2n} - 1) &= C_1/C_3^2((C_3-C_2)((1+C_3\Delta t)^{n+1} - 1)/(n+1) \\ &+ C_2((1+C_3\Delta t)^{n+2} - 1)/(n+2)) \end{aligned} \quad (7-57)$$

The engineering hoop strain in the timestep Δt is therefore

$$\epsilon = [(1 - 2n(\text{Right Hand Side of Equation 7-57}))^{-1/2n} - 1] \quad (7-58)$$

The creep model used in WCOBRA/TRAC calculates the incremental engineering hoop strain over a timestep Δt using Equation 7-58. The cladding creep deformation is then calculated as

$$(\Delta r_{cr})_{clad} = \varepsilon(t) \bar{r} \quad (7-59)$$

where

$\varepsilon(t)$ = engineering hoop strain at end of timestep
 \bar{r} = cladding mean radius.

The maximum timestep for the integration of the Norton creep equation is limited so that $|C_2| \Delta t \leq 0.01$, and the approximation to $\exp(-Q/RT(t))$ remains valid. Details of the model application for the three available cladding options are summarized below.

[]^{a,c}

Westinghouse Zircaloy-4 Cladding

Donaldson, Healey, and Horwood (1985) report Westinghouse manufactured Zircaloy-4 creep data obtained under constant pressure, constant temperature test conditions. Test specimens were heated to the specified temperature and the temperature was held constant for 10 minutes prior to pressurization. The creep test results indicate the existence of two types of creep behavior (Figure 7-14). Creep in the alpha and beta phases, and part of the mixed phase region, exhibits a high stress sensitivity typical of a dislocation climb mechanism. In the low stress/low temperature portion of the mixed phase region the stress sensitivity is significantly reduced. In this region, the creep mechanism is superplastic creep.

Donaldson, Healey, and Horwood (1985) report additional creep test data for [

] ^{a,c}

The creep rates shown in Figure 7-14 are programmed in WCOBRA/TRAC in the form

$$d\epsilon/dt = A\sigma^n \quad (7-60)$$

where the coefficients A and n are functions of temperature and the creep mechanism (Table 7-3). To determine the coefficients A', Q and n for integration of Equation 7-50, the following procedure is used:

a) [

$]^{a,c}$ (7-61)

where,

[

$]^{a,c}$

[

$]^{a,c}$

b) [

$]^{a,c}$

c) Calculate n from: [

$]^{a,c}$ (7-62)

d) [

$]^{a,c}$

e) Calculate Q from: [

$]^{a,c}$ (7-63)

f) Calculate A from: [

]^{ac} (7-64)

Westinghouse ZIRLO™ Cladding

Donaldson and Barnes (1989) and Donaldson, Barnes, and Hall (1989) report Westinghouse manufactured ZIRLO™ cladding creep data obtained under similar test procedures as were used for the Zircaloy-4 tests, with the following notable exception. [

]^{ac}

The ZIRLO™ cladding creep rates shown in Figure 7-15 are programmed in the form of Equation 7-60, with the coefficients A and n defined in Table 7-4. The procedure used to obtain the coefficients for the integration of the Norton creep equation is identical to that used for the Westinghouse Zircaloy-4 cladding option.

The ZIRLO™ cladding creep model used in WCOBRA/TRAC has previously been incorporated into the 1981 Evaluation Model with BASH and the NOTRUMP Evaluation Model (Davidson and Nuhfer, 1990). That reference describes a correction to the creep rate integration which is used in the alpha phase and the portion of the mixed phase region which exhibits dislocation creep, to more accurately predict the measured strain versus time. That correction is also used in WCOBRA/TRAC. Following integration of the Norton creep equation in the alpha phase and the mixed phase/dislocation creep regions, the strain accumulated during the timestep is reduced by an empirical expression which is a function of the strain accumulated in these regions, i.e.,

$$\epsilon_e = \frac{\epsilon}{(1+x)^m} \quad (7-65)$$

where

- ϵ_e = effective strain increment
- ϵ = strain increment calculated by Equation 7-58
- x = summation of ϵ_e in the strain hardening regimes
- m = []^{ac} for the alpha phase, []^{ac} for the mixed phase/dislocation creep region

Sandvik (NRU) Zircaloy-4 Cladding

Donaldson, Horwood, and Healey (1982) report creep data for Sandvik Zircaloy-4 cladding specimens in the alpha phase. Testing was confined to the high alpha phase temperature range, based on the expected range of interest for the NRU Materials Test program.

The alpha phase Sandvik Zircaloy-4 cladding creep rates shown in Figure 7-16 are programmed in the form of Equation 7-60, with the coefficients A and n defined in Table 7-5. [

] ^{ac} The procedure used to obtain the coefficients for the integration of the Norton creep equation is identical to that used for the Westinghouse Zircaloy-4 cladding option.

Cladding Rupture

Loss of coolant accidents result in depressurization of the reactor coolant system and heatup of the nuclear fuel rods, due to insufficient cooling. The resulting stresses on the cladding may be sufficiently high to cause rupture of the cladding. Correlations which predict the occurrence of cladding rupture and the resulting cladding strains have been incorporated into WCOBRA/TRAC for Zircaloy-4 cladding and for ZIRLO™ cladding. These correlations are described below.

Zircaloy-4 Cladding

Powers and Meyer (1980) have reviewed zircaloy cladding rupture data from a wide range of experimental facilities and have recommended the cladding rupture correlation developed by Chapman (1979). The correlation is given by:

$$T_R = 3960 - \frac{20.4\sigma_E}{1 + H} - \frac{8.51 \times 10^6 \sigma_E}{100 (1+H) + 2790 \sigma_E} \quad (7-66)$$

where

T_R = rupture temperature (°C)

σ_E = engineering hoop stress (kpsi)

H = min (1.0, heatup rate/28°C/sec)

This correlation has been incorporated into WCOBRA/TRAC, and is used to predict the occurrence of cladding rupture for nuclear fuel rods clad with Zircaloy-4.

The cladding heatup rate in WCOBRA/TRAC is treated in the same way as in the LOCTA-IV code (Bordelon et al., 1974). The approach can be explained by using Figure 7-17 which illustrates a number

of potential scenarios. The instantaneous heatup rate is used until the cladding temperature is within []^{a,c} of the cladding burst temperature. When this condition is reached (Point A) the cladding temperature and time are recorded to be used as a reference for the calculations. As long as the cladding temperature is [

$$]^{a,c} \quad (7-67)$$

where

[

]^{a,c}

[

]^{a,c}

A correlation for the Zircaloy-4 cladding strain following rupture has been developed using the single rod data compiled by Powers and Meyer (1980), additional single rod data reported by Erbacher et al. (1982), and proprietary single rod Zircaloy-4 data obtained by Westinghouse. Rod bundle data from the REBEKA and NRU test programs were also considered. The resulting correlation is shown with the database in Figure 7-18.⁽⁵⁾ The WCOBRA/TRAC correlation reflects the alpha phase and beta phase peaks, and []^{a,c}

[

]^{a,c}

ZIRLO™ Cladding

Westinghouse has conducted single rod burst tests of ZIRLO™ cladding over a wide range of cladding pressure differentials (100 to 2000 psi), and heatup rates (5 to 50°F/sec) (Davidson and Nuhfer, 1990). The test results have been correlated in the form of rupture temperature as a function of engineering hoop stress, consistent with the Chapman approach. However, the ZIRLO™ cladding rupture temperature correlation is not dependent on the heatup rate, as the data show no systematic heatup rate dependence.

The ZIRLO™ cladding rupture correlation was defined using the mean of the 10°F/sec heatup rate data. Figure 7-19 shows a comparison of the measured burst temperatures and those predicted by the correlation. The correlation predicts the data well over the entire range of heatup rates included in the test matrix.

A correlation for the ZIRLO™ cladding strain following rupture has been developed using the single rod burst test data reported in Davidson and Nuhfer (1990). The resulting correlation is shown with the database in Figure 7-20. The WCOBRA/TRAC correlation reflects the alpha phase and beta phase peaks, and []^{a,c}

[

] ^{a,c}

7-4-2 Effects of Fuel Rod Deformation on Core Thermal-Hydraulics

Transient Pellet-Cladding Gap

Prior to cladding rupture the pellet-cladding gap width is calculated as

$$\tau_g = \tau_{g,cold} - (\Delta r_{th})_{fuel} + (\Delta r_{th})_{clad} + (\Delta r_{el})_{clad} + (\Delta r_{cr})_{clad} \quad (7-68)$$

where

$$\begin{aligned} \tau_{g,cold} &= \text{input value for pellet-cladding gap width} \\ (\Delta r_{th})_{fuel} &= \text{pellet radial thermal expansion, from Equation 7-36} \\ (\Delta r_{th})_{clad} &= \text{cladding radial thermal expansion, from Equation 7-38} \\ (\Delta r_{el})_{clad} &= \text{cladding radial elastic deformation, from Equation 7-44} \\ (\Delta r_{cr})_{clad} &= \text{cladding radial creep deformation, from Equation 7-59} \end{aligned}$$

This gap width is used in Equation 7-33 to determine if the gap is open or closed. If the gap is open, the gap conductance is calculated as described in Section 7-3-2 with h_{solid} set to zero. If the gap is closed, the gap conductance is calculated as described in Section 7-3-2, with the interfacial pressure from Equation 7-49 used to evaluate h_{solid} .

After cladding rupture occurs the fuel rod deformation calculation is bypassed and the gap width at the time of rupture is used for the balance of the transient. The gap width at the burst evaluation in the hot rod is based on the hot rod burst strain, as described below.

After burst occurs in the hot rod, the outer radius of the heat transfer node containing the burst elevation is given by

$$(r_o)_{burst} = r_o (1 + \epsilon_{burst}) \quad (7-69)$$

where ϵ_{burst} is the hot rod burst strain, given by [

] ^{a,c}

The gap conductance for the heat transfer node containing the burst elevation is evaluated using the thermal conductivity of steam, after cladding rupture occurs.

Cladding Thermal Resistance

For analyses of nuclear fuel rods, the conduction model divides the fuel pellet into six radial nodes, and the cladding into two radial nodes. Node-to-node radial conduction is calculated using the conductance given by Equation 7-24. For undeformed cladding, the conductance is

$$K = \frac{2 \pi k_i k_o \Delta X}{k_o \ln \left(\frac{r_m}{r_i} \right) + k_i \ln \left(\frac{r_o}{r_m} \right)} \quad (7-70)$$

where

$$\begin{aligned}
 K &= \text{conductance between inner and outer cladding nodes} \left(\frac{\text{Btu}}{\text{hr } ^\circ\text{F}} \right) \\
 k_i, k_o &= \text{thermal conductivity of inner and outer cladding nodes} \left(\frac{\text{Btu}}{\text{hr } ^\circ\text{F}} \right) \\
 \Delta X &= \text{length of cladding (ft)} \\
 r_i &= \text{initial cladding inner radius (ft)} \\
 r_o &= \text{initial cladding outer radius (ft)} \\
 r_m &= 0.5 (r_i + r_o)
 \end{aligned}$$

The effects of cladding deformation on the cladding thermal resistance are accounted for by using the deformed dimensions r'_i , r'_o , and r'_m in Equation 7-70. Prior to burst, the deformed inner radius is approximated as

$$r'_i = r_i + (\Delta r_{th})_{clad} + (\Delta r_{el})_{clad} + (\Delta r_{cr})_{clad} \quad (7-71)$$

where the Δr terms are given by Equations 7-38, 7-44, and 7-59. The deformed outer radius is calculated by conserving the cladding mass.

After burst occurs, the inner and outer radii of the heat transfer node containing the burst elevation are calculated as described above, for the transient pellet-cladding gap width.

Deformation of the fuel pellet due to thermal expansion has a negligible effect on the pellet node-to-node conduction. Therefore, the conductance between the pellet nodes is based on the undeformed pellet dimensions.

Heat Transfer From Cladding to Fluid

The heat transferred from the cladding of a nuclear fuel rod to the fluid is dependent on the cladding surface heat transfer area (Equation 7-10). The cladding surface area of each heat transfer node is updated at each timestep, using the deformed cladding outer radius. The deformed cladding outer radius is calculated as described above.

Continuity and Momentum Cell Flow Areas

The flow areas of the continuity cells in the core region are updated at each timestep to reflect the cladding deformation of the rods within each cell. The flow areas of the momentum cells in the core region are updated at each timestep using the average outer rod diameter from the continuity cells above and below the center of the momentum cell.

If burst occurs for the hot assembly average rod, additional adjustments are made to the appropriate continuity and momentum cell flow areas to simulate flow blockage effects. Powers and Meyer (1980) have recommended a methodology for converting the cladding strain following rupture into an assembly flow area reduction factor. This conversion accounts for non-coplanar burst effects, flow area reduction versus strain, and the presence of thimble tubes and instrumentation tubes. This methodology has been applied to the cladding burst strain correlations shown in Figures 7-18 and 7-20. The resulting flow area reduction correlations are shown in Figures 7-22 and 7-23 for Zircaloy-4 and ZIRLO™ cladding materials, respectively.

The flow area reduction factor is applied to the nominal flow area of the continuity cell containing the hot assembly average rod burst elevation, to obtain the continuity area after burst. The continuity area reduction is ramped in over a period of 0.1 seconds, as shown in Figure 7-24. [

]^{a,c} (7-72)

where

[

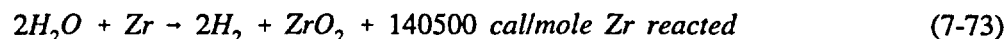
]^{a,c}

[

]^{a,c}

7-5 CLADDING REACTION MODEL

Model Basis The zirconium base metal used in modern nuclear fuel rod cladding materials undergoes the following exothermic reaction with water or steam:



This reaction may become significant under the high temperature conditions which may exist following a postulated LOCA.

At temperatures of about 1000°C or greater, the zirconium-water reaction follows a parabolic rate law:

$$W \, dW/dt = A \exp (-B/RT)$$

where

W = total oxygen consumed (gm/cm²)

A = constant ((gm/cm²)²/sec)

B = activation energy (cal/gm mole)

R = gas constant (1.987 cal/gm mole/°K)

T = temperature (°K)

WCOBRA/TRAC includes a cladding reaction model which calculates the oxide buildup throughout the transient and the resulting heat generation in the cladding. Options are available for Zircaloy-4 and ZIRLO™ cladding materials, as described below.

Model as Coded Cathcart and Pawel (1977) have examined the reaction of Zircaloy-4 in steam and have recommended a parabolic rate equation of

$$W \, dW/dt = 0.1811 \exp (-39940/RT) \quad (7-74)^{(6)}$$

The uncertainty of the data fit [

] ^{a,c}

The metal-water reaction calculation is performed in subroutine QOXIDE. The reaction rate of Equation 7-74 is converted to units of (ft Zr)²/sec assuming a density of 409 lb/ft³, resulting in

$$\tau \, d\tau/dt = 3.69E-5 \exp (-39940/RT) \quad (7-76)$$

where τ is the thickness of zirconium which has been reacted. Including the uncertainty on the reaction rate, given by Equation 7-75, rearranging and integrating over a timestep Δt yields

$$\int_{\tau_0}^{\tau} \tau \, d\tau = 3.69E-5 \int_0^{\Delta t} \exp (-39940/RT) (1 + \delta_{Zr-4}/100) \, dt \quad (7-77)$$

Timesteps in WCOBRA/TRAC are typically 0.01 seconds or less, due to hydraulic limitations. Therefore, the cladding temperature can be assumed constant over the timestep Δt , and Equation 7-77 may be integrated to yield

$$\frac{\tau^2 - \tau_o^2}{2} = 3.69E-5 \exp(-39940/RT) (1 + \delta_{Zr-4}/100) \Delta t \quad (7-78)$$

The thickness of cladding reacted at the end of the timestep is then given by

$$\tau = \left[\tau_o^2 + 7.38E-5 \exp(-39940/RT) (1 + \delta_{Zr-4}/100) \Delta t \right]^{1/2} \quad (7-79)$$

Burman (1990) has reported the high temperature oxidation kinetics behavior of the ZIRLO™ cladding material manufactured by Westinghouse. The parabolic rate equation recommended for the ZIRLO™ alloy was given as [

$$J^{ac} \quad (7-80)^{(9)}$$

with an uncertainty [

]

The fuel rod deformation model described in Section 7-4 calculates changes in the cladding dimensions throughout a LOCA transient. The deformed cladding dimensions are used in the cladding reaction model calculation, as described below.

Before cladding burst is predicted to occur, the metal-water reaction occurs on the cladding outer surface only. The heat generation rate is given by

$$q_o = Q_c \frac{\pi \left[(r'_{ox})^2 - (r'_{ox} - \Delta r_{ox})^2 \right] \Delta X}{\Delta t} \quad (7-83)$$

where

$$q_o = \text{heat generated by outer surface reaction} \left(\frac{\text{Btu}}{\text{sec}} \right)$$

$$Q_c = 1.123\text{E}6 \left(\frac{\text{Btu}}{\text{ft}^3} \right)$$

$$r'_{ox} = \text{outer surface oxide radius prior to new oxidation (ft)}$$

$$\Delta r_{ox} = \text{cladding thickness oxidized over the timestep (ft)}$$

$$\Delta X = \text{height of conduction node (ft)}$$

$$\Delta t = \text{timestep size (sec)}$$

Prior to burst, the fuel rod deformation model updates the cladding outer radius at each timestep. [

] ^{a,c} (7-85)

[

] ^{a,c}

Metal-water reaction on the cladding inner surface begins at the time the cladding bursts. Heat generation on the inner surface of the heat transfer node containing the hot rod burst elevation is calculated by [

$J^{a,c}$

The oxidation over the timestep is then calculated, and the heat generation is calculated using Equation 7-86.

7-6 UNHEATED CONDUCTOR MODELLING

Structural heat transfer surfaces in the vessel can be more efficiently modelled with the unheated conductor model. This option accesses the same conductor geometries (except for the nuclear fuel rod geometry) as the rod model, and uses the same heat transfer package. However, to economize computer time and storage, the unheated conductor model is limited in the following ways:

- No internal heat generation is included.
- Radial conduction only is used.
- No fine mesh-rezoning quench front model is included.
- Unheated conductors do not extend across section boundaries.

- The fluid solution cannot be forced into the "hot wall" flow regime.
- Vapor properties in the convective heat transfer correlations are evaluated at the bulk vapor temperature rather than the film temperature.
- The minimum film boiling temperature is set to a constant []^{a,c}.

These limitations only apply to the unheated conductor model and not to the rod model in general. Unheated conductors are used to model structural elements in the vessel for which expected peak temperatures are well below the minimum film boiling point.

7-7 CONDUCTOR MODELLING IN ONE-DIMENSIONAL COMPONENTS

Model Basis The temperature distribution within the walls of the one-dimensional components is determined by subroutine CYLHT. A solution is obtained from a finite-difference approximation to the one-dimensional conduction equation,

$$\rho C_p \frac{\partial T}{\partial t} = \frac{1}{r} \left[\frac{\partial}{\partial r} \left(rk \frac{\partial T}{\partial r} \right) \right] + q''' \quad (7-88)$$

Alternatively, a lumped parameter solution is employed if the user specifies one conduction node.

Model as Coded The finite-difference equations are derived by applying an integral method (Roache, 1972) to the elemental volumes shown in Figure 7-25. The general form for the volume i ($1 < i < N$) is

$$\begin{aligned} & \frac{r_{i-1/2} k_{i-1/2}}{\Delta r_{i-1}} T_{i-1} - \left\{ \frac{r_{i-1/2} k_{i-1/2}}{\Delta r_{i-1}} + \frac{r_{i+1/2} k_{i+1/2}}{\Delta r_i} \right. \\ & \left. + \frac{1}{2\Delta t} \left[\left(r_i \Delta r_{i-1} - \frac{\Delta r_{i-1}^2}{4} \right) (\rho C_p)_{i-1/2} + \left(r_i \Delta r_i + \frac{\Delta r_i^2}{4} \right) (\rho C_p)_{i+1/2} \right] \right\} T_i \\ & + \frac{r_{i+1/2} k_{i+1/2}}{\Delta r_i} T_{i+1} = -\frac{1}{2} \left\{ \left(r_i \Delta r_i - \frac{\Delta r_i^2}{4} \right) \left[\frac{(\rho C_p)_{i-1/2}}{\Delta t} T_i^n + q''' \right] \right. \\ & \left. + \left(r_i \Delta r_i + \frac{\Delta r_i^2}{4} \right) \left[\frac{(\rho C_p)_{i+1/2}}{\Delta t} T_i^n + q''' \right] \right\} \end{aligned} \quad (7-89)^{(11)}$$

The boundary conditions applied to the inner ($i=1$) and outer ($i=N$) surfaces are:

$$-k \frac{\partial T}{\partial r} \Big|_{i=1,N} = \pm [h_{wt}(T_t - T_i) + h_{wv}(T_v - T_i)] \quad (7-90)$$

Applying this boundary condition to the inner surface ($i=1$), for example,

$$\begin{aligned} - \left\{ \frac{r_{3/2} k_{3/2}}{\Delta r_1} + \frac{1}{2} \left[r_1 \Delta r_1 + \frac{\Delta r_1^2}{4} \right] \frac{(\rho C_p)_{3/2}}{\Delta t} \right\} T_1 + \frac{r_{3/2} k_{3/2}}{\Delta r_1} T_2 = \\ - \frac{1}{2} \left(r_1 \Delta r_1 + \frac{\Delta r_1^2}{4} \right) \left[\frac{(\rho C_p)_{3/2}}{\Delta t} T_1^n + q''' \right] \\ + r_1 [h_{wt}(T_1^n - T_t) + h_{wv}(T_1^n - T_v)] \end{aligned} \quad (7-91)$$

The resulting linear equations are solved in a sequential fashion for each of the cells in the component. For each cell a solution is achieved using Gaussian elimination.

If the user specifies one radial conduction node for the wall, the wall temperature is calculated using a lumped parameter solution:

$$\begin{aligned} T = \left\{ \frac{1}{2} \left(2\Delta r + \frac{\Delta r^2}{r_i} \right) \left(\frac{\rho C_p}{\Delta t} T^n + q''' \right) + h_{wt_i}(T_{t_i} - T^n) \right. \\ \left. + h_{wv_i}(T_{v_i} - T^n) - \left(1 + \frac{\Delta r}{r_i} \right) [h_{wt_o}(T^n - T_{t_o}) + h_{wv_o}(T^n - T_{v_o})] \right\} \\ \div \frac{1}{2} \left(2\Delta r + \frac{\Delta r^2}{r_i} \right) \left(\frac{\rho C_p}{\Delta t} \right) \end{aligned} \quad (7-92)$$

The subscripts i and o refer to the inner and outer radii, respectively.

7-8 SCALING CONSIDERATIONS

The vessel component rod and unheated conductor models, and the one-dimensional component conductor model, are used in analyses of nuclear reactors and simulations of experiments in which heat

transfer between structures and the fluid are important. The models are applied in a systematic manner in nuclear reactor analyses and simulations of experiments, as summarized below:

- For nuclear reactor analyses and simulations of experiments which use nuclear fuel rods (e.g., LOFT and NRU), the fuel rods are modelled using the NUCL rod option, and the dynamic gap conductance and fuel rod deformation models are employed. If high cladding temperatures are expected, the metal-water reaction model is also employed.
- For all simulations of experiments which include heat transfer, and in which quench front modelling is important (e.g., FLECHT, ORNL, CCTF, and FEBA), the same hydraulic node sizes are used as in the PWR analysis.
- The unheated conductor model and one-dimensional component conductor model are also applied in a consistent manner, for analyses of nuclear reactors and simulations of experiments.

[

] ^{a,c}

The simulations of the experiments cited above are used to assess the WCOBRA/TRAC models and the code uncertainty. Because of the consistent application of the models described in Section 7 in these simulations and in nuclear reactor analyses, and the use of full-length nuclear fuel rods and electrically heated rods in several of these experiments, there are no scaling uncertainties associated with the use of these models in analyses of nuclear reactors.

7-9 CONCLUSIONS

The WCOBRA/TRAC models for heated and unheated structures provide an appropriate means for calculating the transient temperature response of the structures found in nuclear reactors and the experiments of interest. These models are applied in a consistent manner in analyses of nuclear reactors and simulations of experiments. No scaling uncertainty is required for the use of these models in nuclear reactor analyses.

7-10 REFERENCES

Bajorek, S. M., et al., 1998, "Code Qualification Document for Best Estimate LOCA Analysis," WCAP-12945-P-A, Volume 1, Revision 2, and Volumes 2 through 5, Revision 1, and WCAP-14747 (Non-Proprietary).

Berna, G. A., et al., 1978, "FRAPCON-1: A Computer Code for the Steady-State Analysis of Oxide Fuel Rods," CDAP-TR-032-R1, Idaho National Engineering Laboratory, Idaho Falls, Idaho.

Beyer, C. E., et al., 1975, "GAPCON-THERMAL-2: A Computer Program for Calculating the Thermal Behavior of an Oxide Fuel Rod," BNWL-1898, Pacific Northwest Laboratory, Richland, Washington.

Beyer, W. H. (Ed.), 1978, CRC Standard Mathematical Tables, 25th Edition, CRC Press, Inc., West Palm Beach, Fla., pp. 326-327.

Bordelon, F. M., et al., 1974, "LOCTA-IV Program: Loss-of-Coolant Transient Analysis," WCAP-8301, Westinghouse Electric Corporation, Pittsburgh, PA. [PROPRIETARY].

Burman, D. L., 1990, "ZIRLO™ High Temperature Oxidation Tests," Appendix E to WCAP-12610, Westinghouse Electric Corporation, Pittsburgh, PA. [PROPRIETARY].

Cathcart, J. V. and Pawell, 1977, "Zirconium Metal-Water Oxidation Kinetics IV - Reaction Rate Studies," ORNL/NUREG-17, Oak Ridge National Laboratory, Oak Ridge, TN.

Chapman, R. H., 1979, "Multirod Burst Test Program Progress Report for April-June, 1979," NUREG/CR-1023, Oak Ridge National Laboratory, Oak Ridge, TN.

Cooper, M. G., Mikic, B. B., and Yavonovich, M. M., 1969, "Thermal Contact Conductance," Journal of Heat and Mass Transfer, Vol. 12.

Davidson, S. L. and Nuhfer, D. L. (Eds.), 1990, "VANTAGE+ Fuel Assembly Reference Core Report," WCAP-12610, Westinghouse Electric Corporation, Pittsburgh, PA. [PROPRIETARY].

Dearien, J. A., et al., 1977, "FRAP-S3: A Computer Code for the Steady-State Analysis of Oxide Fuel Rods -- Report I, Analytical Models and Input Manual," TFBP-TR-164, Idaho National Engineering Laboratory, Idaho Falls, Idaho.

Donaldson, A. T., Horwood, R. A., and Healey, T., 1982, "Biaxial Creep Deformation of Zircaloy-4 in the High Alpha Phase Temperature Range," TPRD/B/0100/N82, Central Electricity Generating Board - Berkeley Nuclear Laboratories, Berkeley, Gloucestershire, United Kingdom.

Donaldson, A. T., Healey, T., and Horwood, R. A., 1985, "Biaxial Creep Deformation of Zircaloy-4 PWR Fuel Cladding in the Alpha, (Alpha + Beta) and Beta Phase Temperature Ranges," Journal of the British Nuclear Energy Society, pp. 83-89.

Donaldson, A. T. and Barnes, J. P., 1989, "Creep Behavior of ZIRLO Clad at Temperatures in the Alpha Phase Range, 873-973K, and in the Beta Phase Range, 1273-1373K," RD/B/6245/R89, Central Electricity Generating Board - Berkeley Nuclear Laboratories, Berkeley, Gloucestershire, United Kingdom. [PROPRIETARY].

Donaldson, A. T., Barnes, J. P., and Hall, P. D., 1989, "Creep Behavior of ZIRLO Clad at Temperatures in the Duplex Phase Range, 1048-1183K," RD/B/6304/R89, Central Electricity Generating Board - Berkeley Nuclear Laboratories, Berkeley, Gloucestershire, United Kingdom. [PROPRIETARY].

Erbacher, F. J., et al., 1982, "Burst Criterion of Zircaloy Fuel Claddings in a Loss-of-Coolant Accident," Zirconium in the Nuclear Industry; Fifth Conference, ASTM STP 754, pp. 271-283.

Garnier, J. E. and Begej, S., 1979, "Ex-Reactor Determination of Thermal Gap and Contact Conductance Between Uranium Dioxide: Zircaloy Interfaces. Stage 1: Low Gas Pressure," NUREG/CR-0330, Pacific Northwest Laboratory, Richland, Washington.

Hagrman, D. L., and Reymann, G. A., 1979, "MATPRO-Version 11: A Handbook of Material Properties for Use in the Analysis of Light Water Reactor Fuel Rod Behavior," NUREG/CR-0497, Idaho National Engineering Laboratory, Idaho Falls, Idaho.

Hagrman, D. L., Reymann, G. A., and Manson, R. E., 1980, "MATPRO-Version 11: A Handbook of Materials Properties for Use in the Analysis of Light Water Reactor Fuel Rod Behavior," NUREG/CR-0497, Revision 1, Idaho National Engineering Laboratory, Idaho Falls, Idaho.

Hann, C. R., Beyer, C. E., and Parchen, L. J., 1973, "GAPCON-THERMAL-1: A Computer Program for Calculating the Gap Conductance in Oxide Fuel Pins," BNWL-1778, Pacific Northwest Laboratory, Richland, Washington.

Kelly, J. M., 1979, "Quench Front Modelling and Reflood Heat Transfer in COBRA-TF," Paper 79-WA/HT-63, ASME Winter Annual Meeting, New York, New York.

Lanning, D. D. and Hann, C. R., 1975, "Review of Methods Applicable to the Calculation of Gap Conductance in Zircaloy-Clad UO₂ Fuel Rods," BNWL-1894, Pacific Northwest Laboratory, Richland, Washington.

Lanning, D. D., et al., 1978, "GAPCON-THERMAL-3 Code Description," PNL-2434, Pacific Northwest Laboratory, Richland, Washington.

Lloyd, W. R., et al., 1973, "Heat Transfer in Multicomponent Monatomic Gases in the Low, Intermediate, and High Pressure Regime," paper presented at the Nuclear Thermionics Conference.

Powers, D. A., and Meyer, R. O., 1980, "Cladding Swelling and Rupture Models for LOCA Analysis," NUREG-0630, U.S. Nuclear Regulatory Commission, Washington, D.C.

Roache, P. J., 1972, Computational Fluid Dynamics, Hermosa Publishers, Albuquerque, NM.

Siefken, L. J., et al., 1979, "FRAP-T5: A Computer Code for Transient Analysis of Oxide Fuel Rods," NUREG/CR-0840, Idaho National Engineering Laboratory, Idaho Falls, Idaho.

Stewart, C. W., et al., 1982, "VIPRE-01 A Thermal-Hydraulics Analysis Code for Reactor Cores: Volume 1, Mathematical Modelling," NP-2511, Electric Power Research Institute, Palo Alto, California.

Thomas, L. B., 1967, Fundamentals of Gas-Surfacing Interactions, H. Saltsburg et al., Eds., Academic Press, New York, pp. 346-369.

Todreas, N. and Jacobs, G., 1973, "Thermal Contact Conductance of Reactor Fuel Elements," Nuclear Science and Engineering, Vol. 50, pg. 283.

Trent, D. S. and Welty, J. R., 1974, "A Summary of Numerical Methods for Solving Transient Heat Conduction Problems," Bulletin No. 49, Engineering Experimental Station, Oregon State University, Corvallis, Oregon.

Ullman, A., Acharya, R., and Olander, D. R., 1974, "Thermal Accommodation Coefficients of Inert Gases on Stainless Steel and UO₂," Journal of Nuclear Materials, Vol. 51, pp. 277-279.

7-11 RAI LISTING

1. RAI1-220
2. RAI1-221
3. RAI1-222
4. RAI1-223
5. RAI1-224
6. RAI1-225
7. RAI1-226
8. RAIF-attachment 8
9. RAI5-43
10. Letter, N. J. Liparulo (Westinghouse) to Document Control Desk (USNRC), "Presentation Material from WCAP-12945-P Review Status Meeting", NTD-NRC-95-4560, September 18, 1995.
11. RAID-attachment 6, item 9

Table 7-1 Cladding Thermal Expansion Correlations

$T < 1073^{\circ}\text{K}$		
$\epsilon_r = 6.721 \times 10^{-6} T - 0.00207$		
$\epsilon_z = 4.441 \times 10^{-6} T - 0.00124$		
$1073 \leq T \leq 1273^{\circ}\text{K}$		
Linear interpolation from the following table is used.		
T	ϵ_r	ϵ_z
1073	0.00514	0.00353
1083	0.00522	0.00353
1093	0.00525	0.00350
1103	0.00528	0.00346
1113	0.00528	0.00341
1123	0.00524	0.00333
1133	0.00522	0.00321
1143	0.00515	0.00307
1153	0.00508	0.00280
1163	0.00490	0.00250
1173	0.00470	0.00200
1183	0.00445	0.00150
1193	0.00410	0.00130
1203	0.00350	0.00116
1213	0.00313	0.00113
1223	0.00297	0.00110
1233	0.00292	0.00111
1243	0.00287	0.00113
1253	0.00286	0.00120
1263	0.00288	0.00130
1273	0.00290	0.00140
$T > 1273^{\circ}\text{K}$		
$\epsilon_r = 9.70 \times 10^{-6} T - 0.00945$		
$\epsilon_z = 9.70 \times 10^{-6} T - 0.0110$		

Table 7-2 Cladding Correlations for Modulus of Elasticity (E) and Shear Modulus (G)

$T < 1094^{\circ}\text{K}$
$E = 1.088 \times 10^{11} - 5.475 \times 10^7 T$
$G = 4.04 \times 10^{10} - 2.168 \times 10^7 T$
$1094 \leq T \leq 1239^{\circ}\text{K}$
$E = 4.893 \times 10^{10} - 4.817 \times 10^7 (T-1094)$
$G = 1.669 \times 10^{10} - 1.622 \times 10^7 (T-1094)$
$T > 1239^{\circ}\text{K}$
$E = 9.21 \times 10^{10} - 4.05 \times 10^7 T$
$G = 3.49 \times 10^{10} - 1.66 \times 10^7 T$

Table 7-4 Creep Correlation Coefficients for Westinghouse ZIRLO™ Cladding

[

]ac

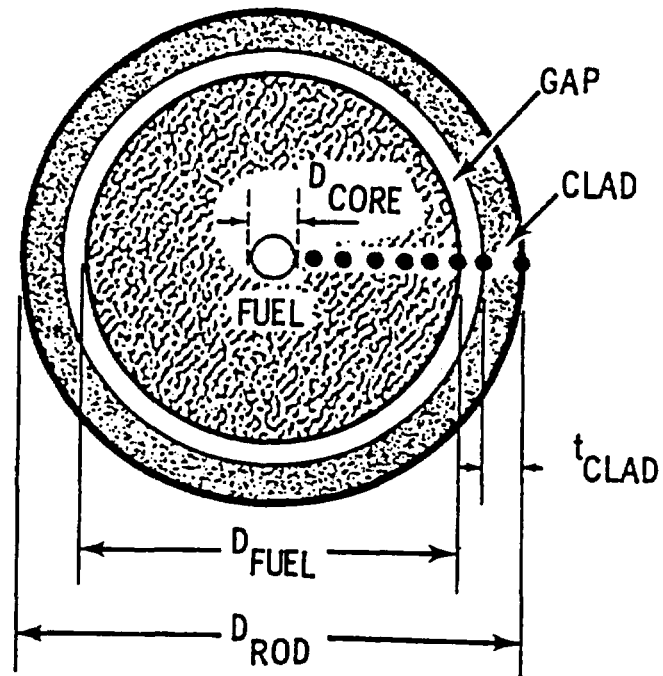


Figure 7-1. Nuclear Fuel Rod Geometry

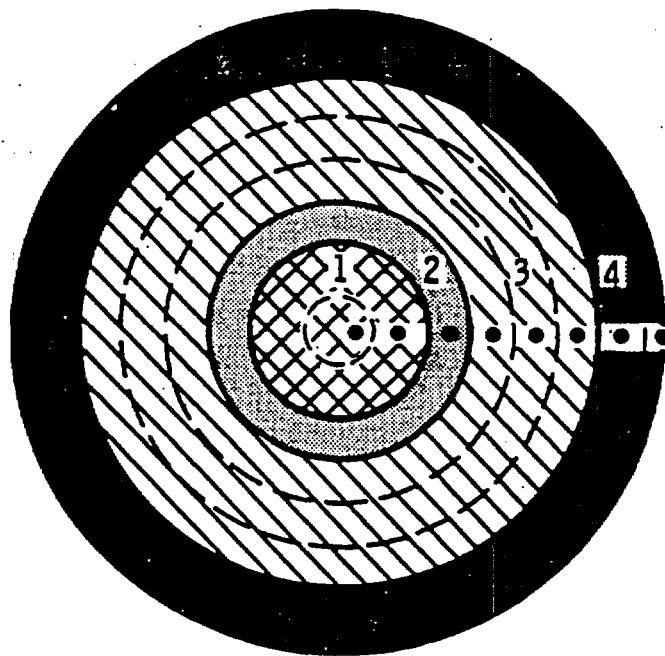


Figure 7-2. Heater Rod Geometry

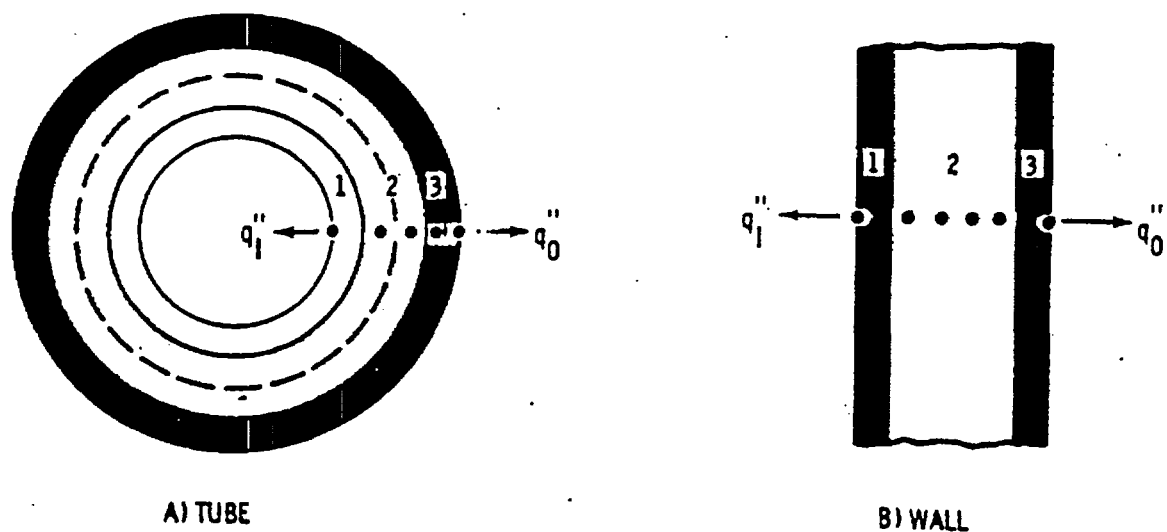


Figure 7-3. Tube and Wall Conductor Geometries

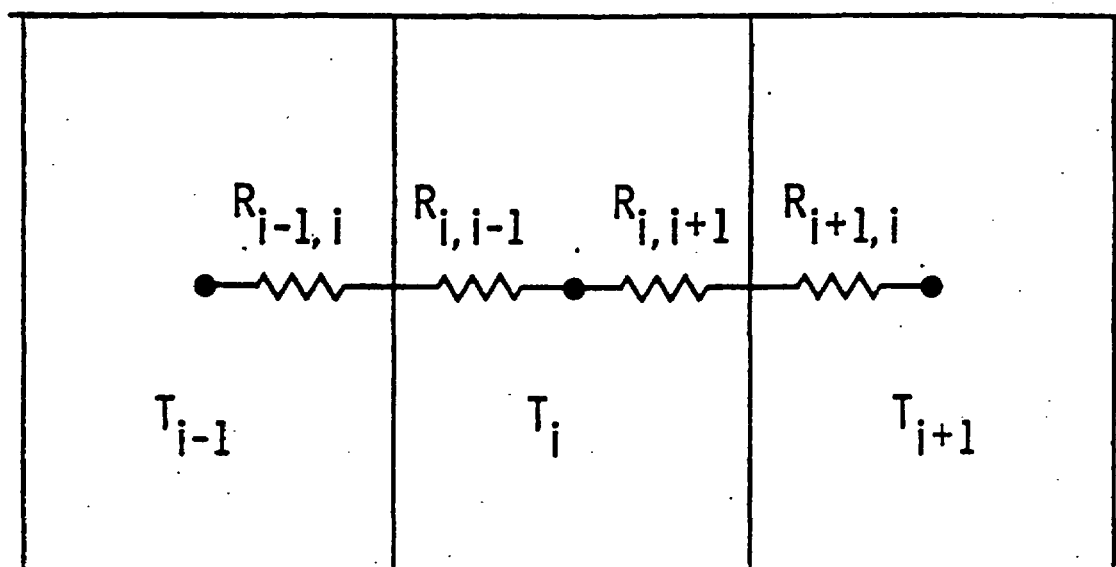


Figure 7-4. Control Volume for Heat Balance

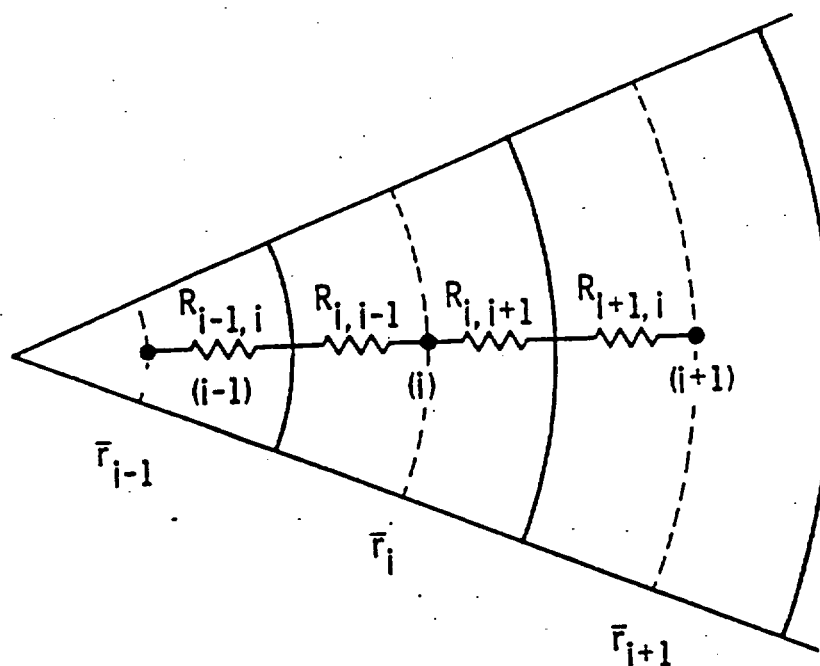


Figure 7-5. Noding for Fuel Rod Conduction Model

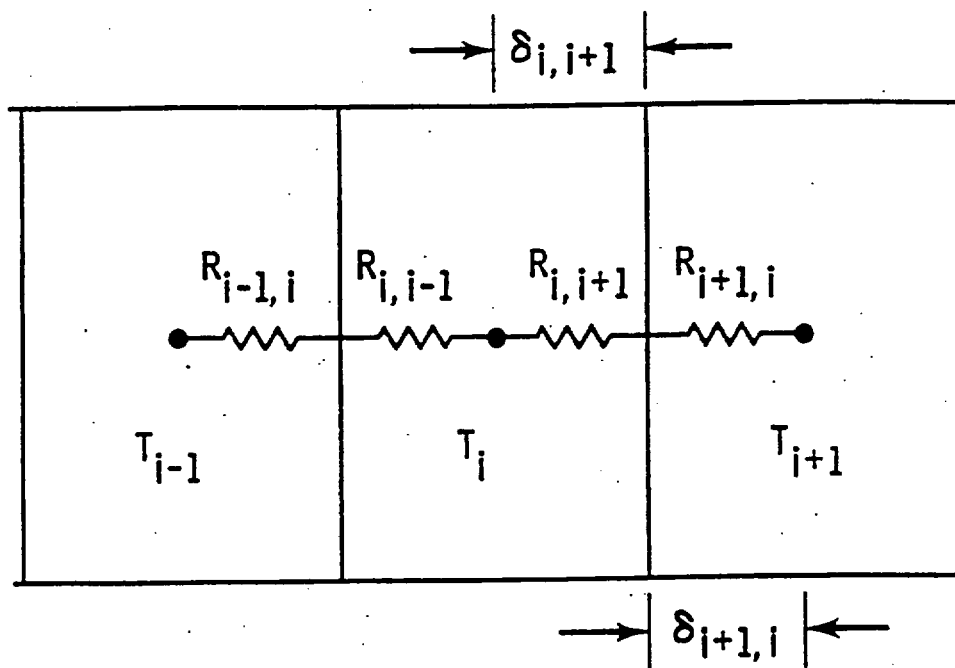


Figure 7-6. Conductance Between Nodes

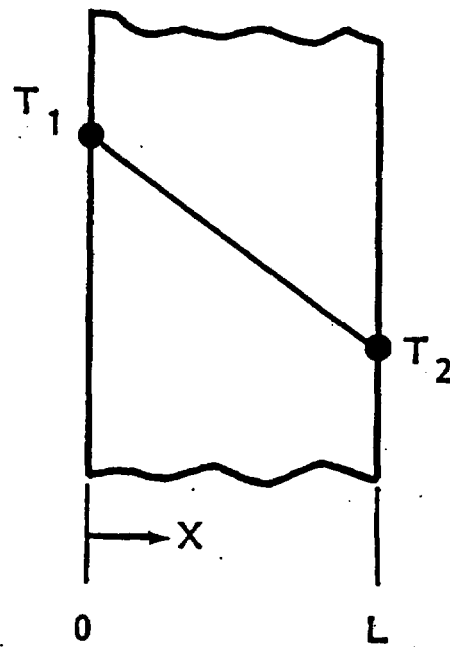


Figure 7-7. Steady-State Temperature Distribution in a Flat Plate with No Internal Heat Generation

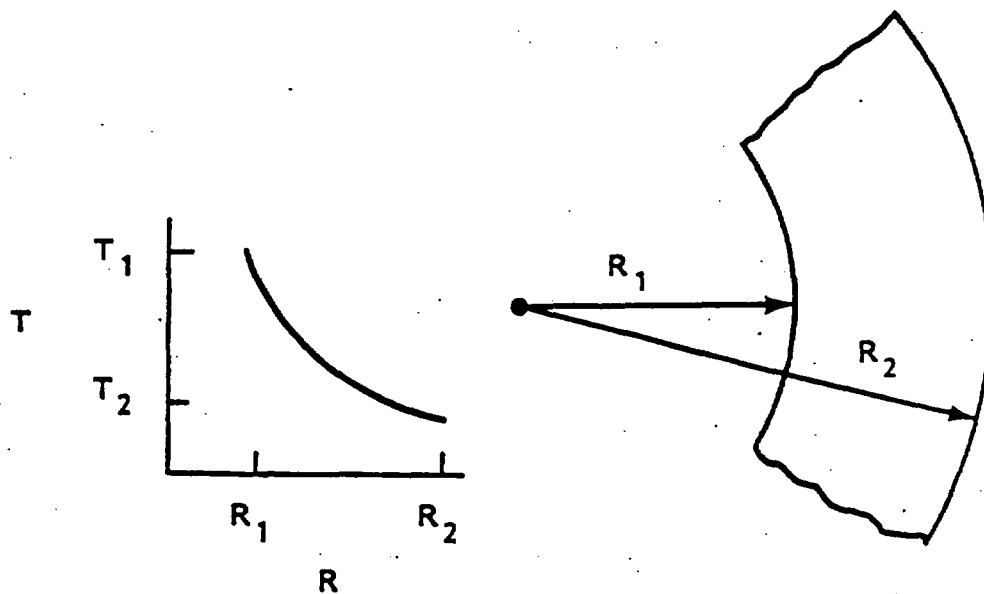


Figure 7-8. Steady-State Temperature Distribution in a Hollow Cylinder with No Internal Heat Generation

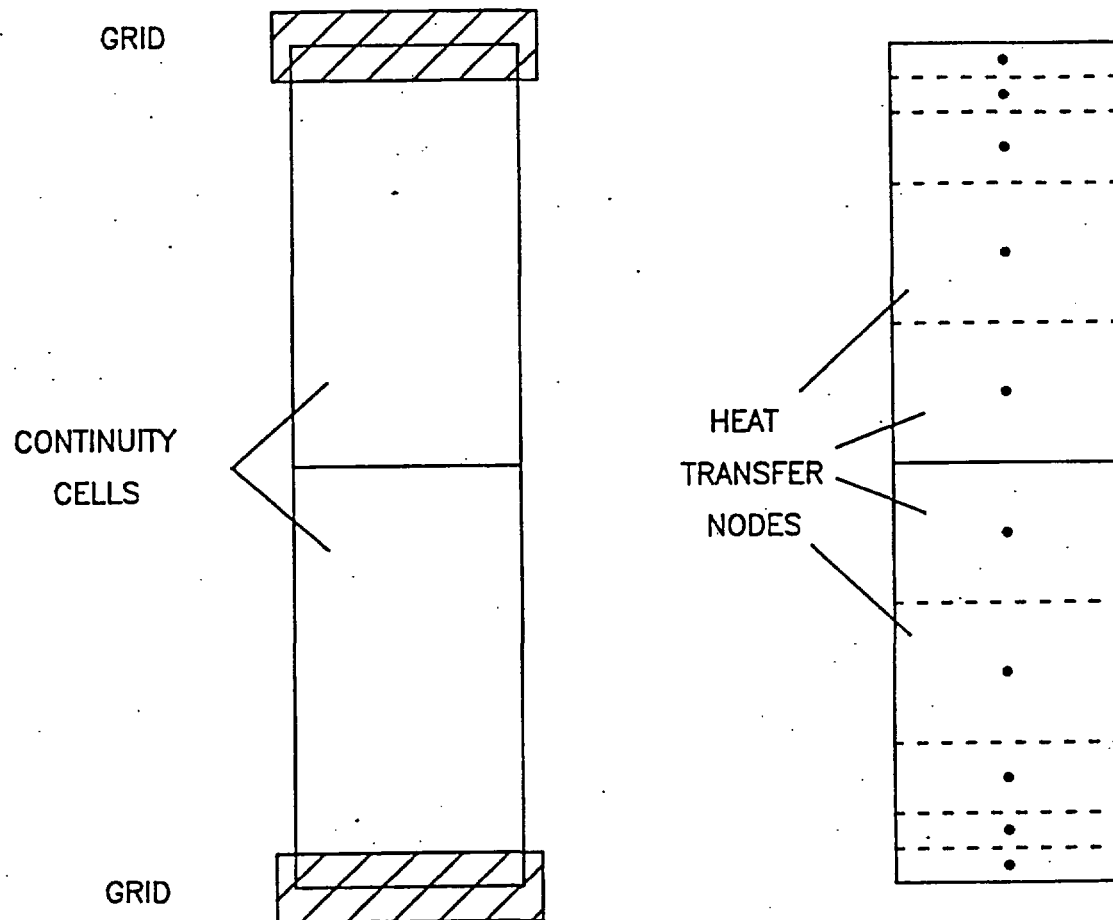
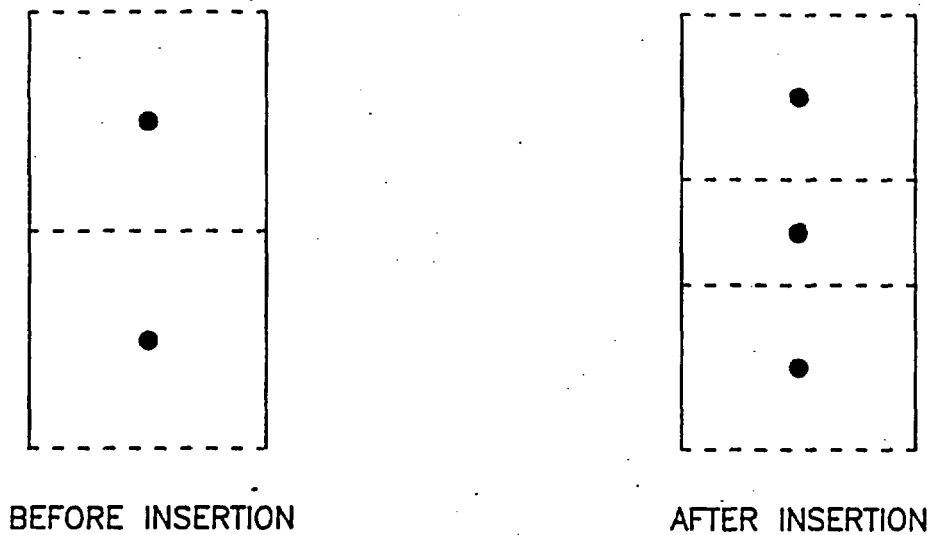
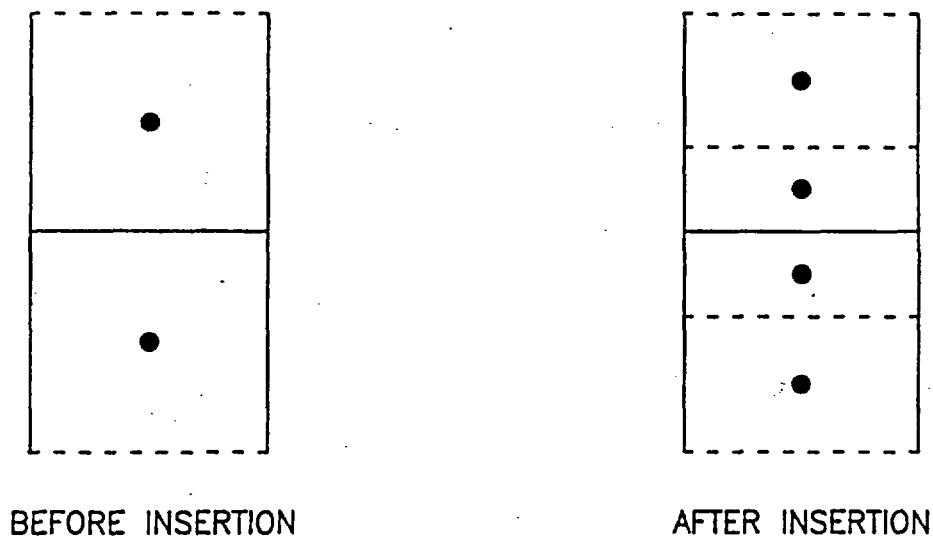


Figure 7-9. Typical Heat Transfer Noding Scheme



A.) WITHIN A CONTINUITY CELL



B.) AT CONTINUITY CELL BOUNDARY

Figure 7-10. Examples of Heat Transfer Node Insertion

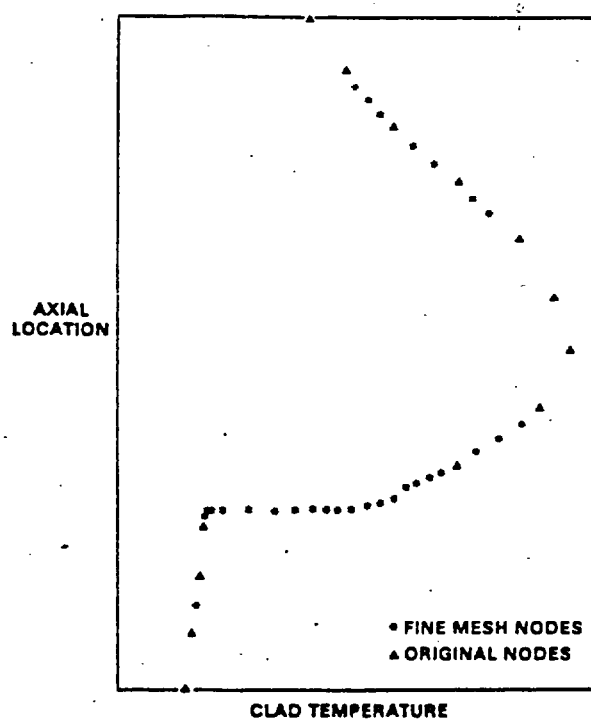


Figure 7-11. Cladding Temperature Profile with Fine Mesh Renoding

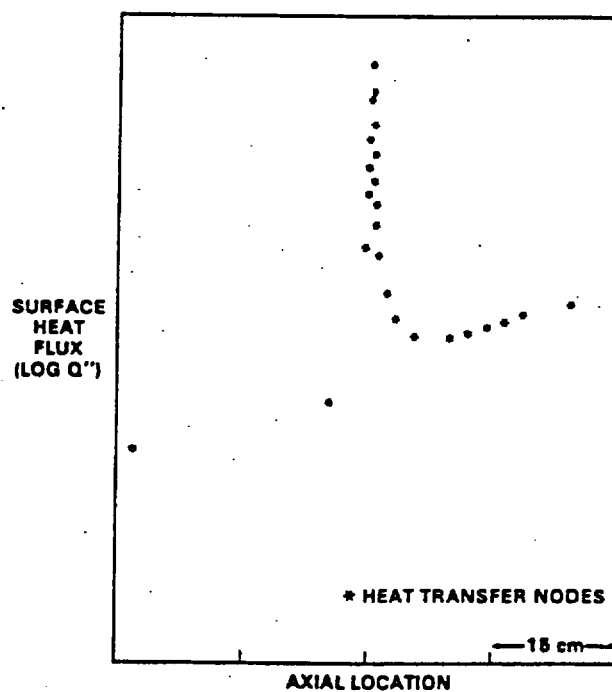


Figure 7-12. Surface Heat Flux Profile with Fine Mesh Renoding

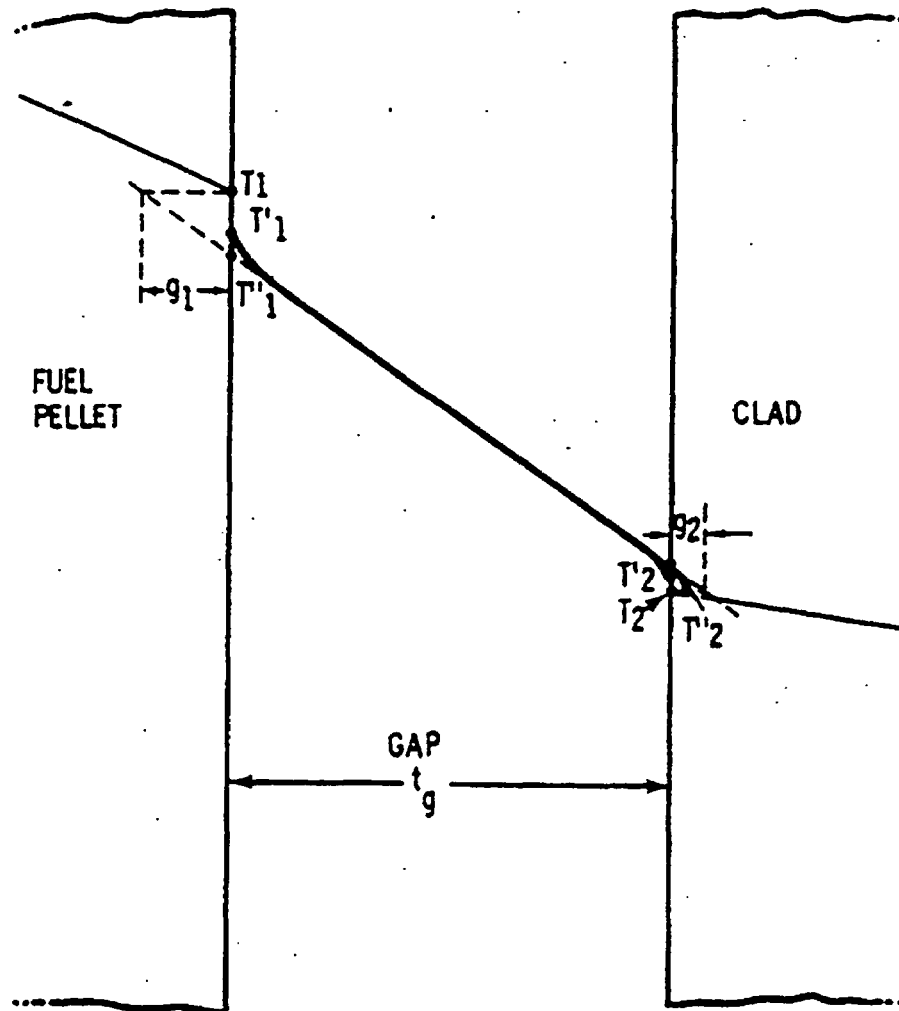


Figure 7-13. Temperature Jump Distances for an Ideal Gap

Figure 7-14. Instantaneous Creep Rates for Westinghouse Zircaloy-4 Cladding

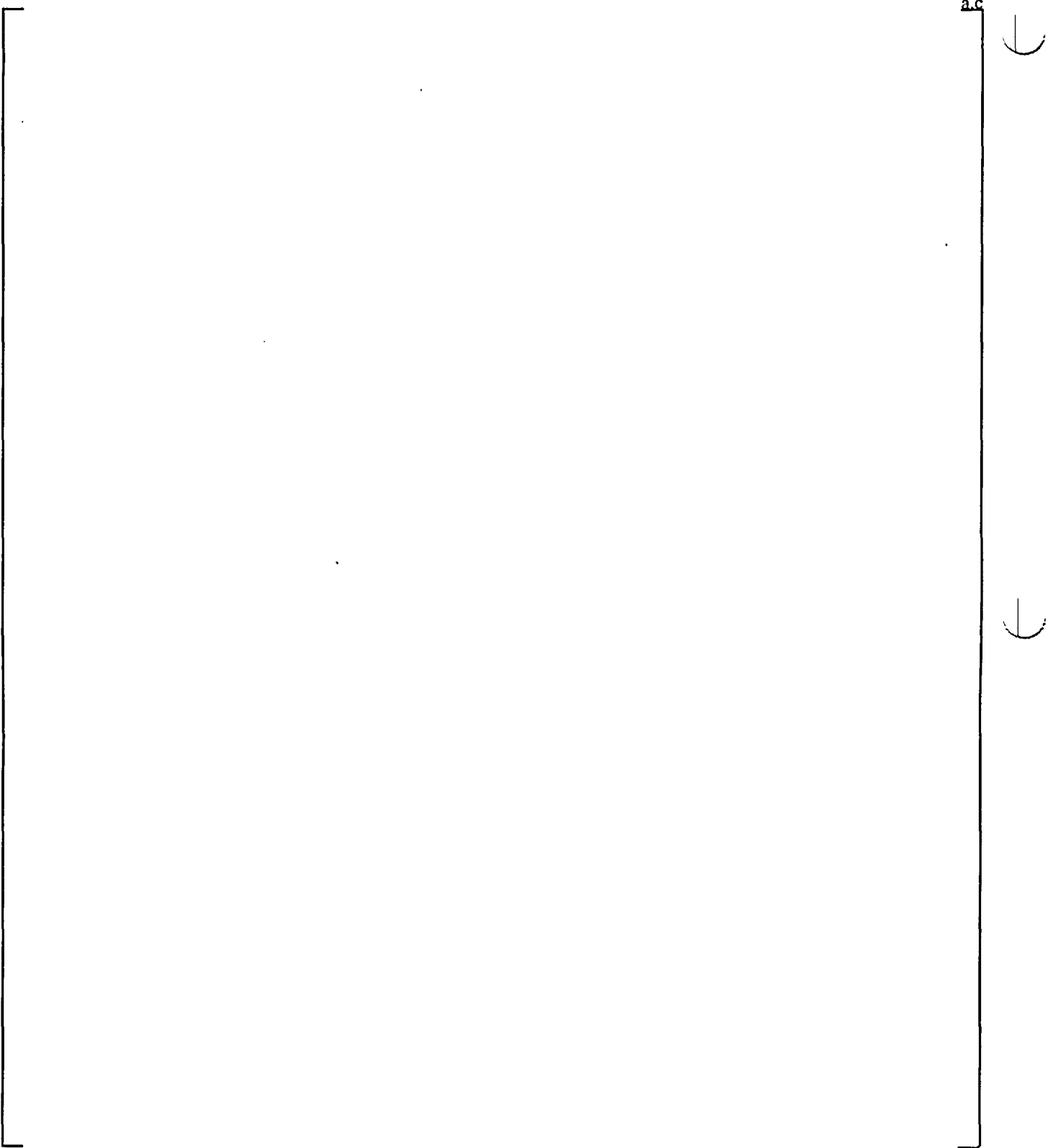


Figure 7-15. Instantaneous Creep Rates for Westinghouse ZIRLO™ Cladding

Figure 7-16. Instantaneous Creep Rates for Sandvik (NRU) Cladding

a.c.

Figure 7-17. Heatup Rate Scenarios

Figure 7-18. Circumferential Strain Following Rupture - Zircaloy-4 Cladding

a.c.

Figure 7-19. Burst Temperature Correlation - Westinghouse ZIRLO™ Cladding

a.c

Figure 7-20. Circumferential Strain Following Rupture - Westinghouse ZIRLO™ Cladding

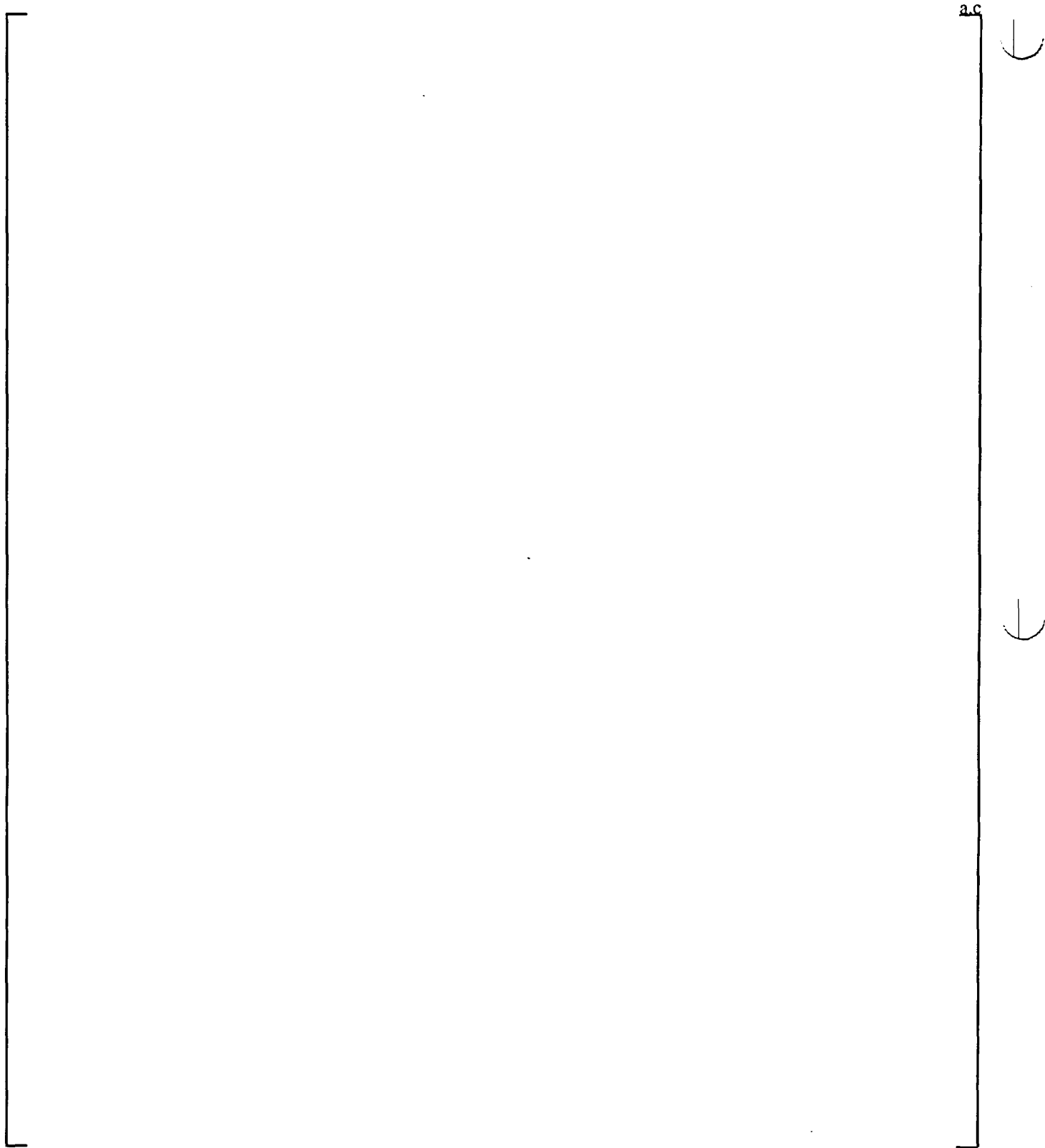


Figure 7-21. Rod Strain at Burst Elevation

Figure 7-22. Flow Area Reduction Due to Blockage - Zircaloy-4 Cladding

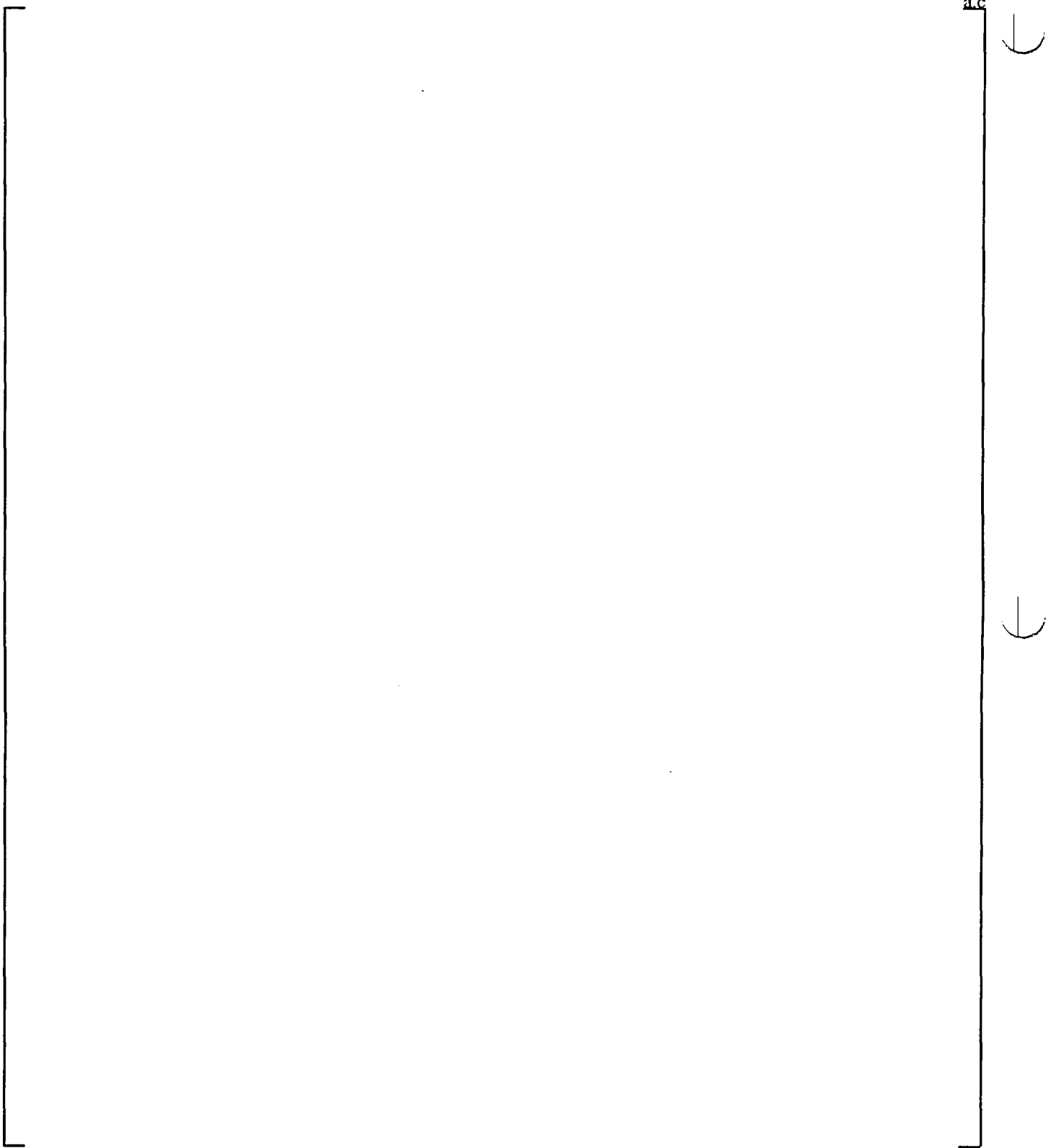


Figure 7-23. Flow Area Reduction Due to Blockage - ZIRLO™ Cladding

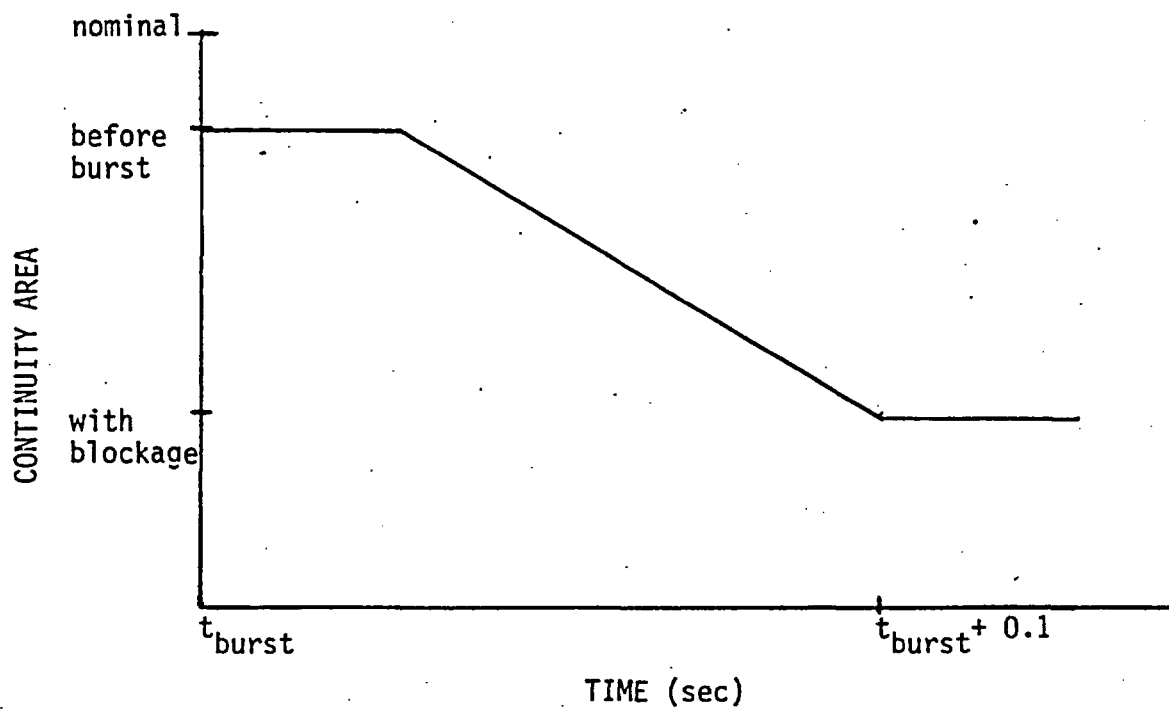


Figure 7-24. Application of Blockage Factor Following Hot Assembly Rod Burst

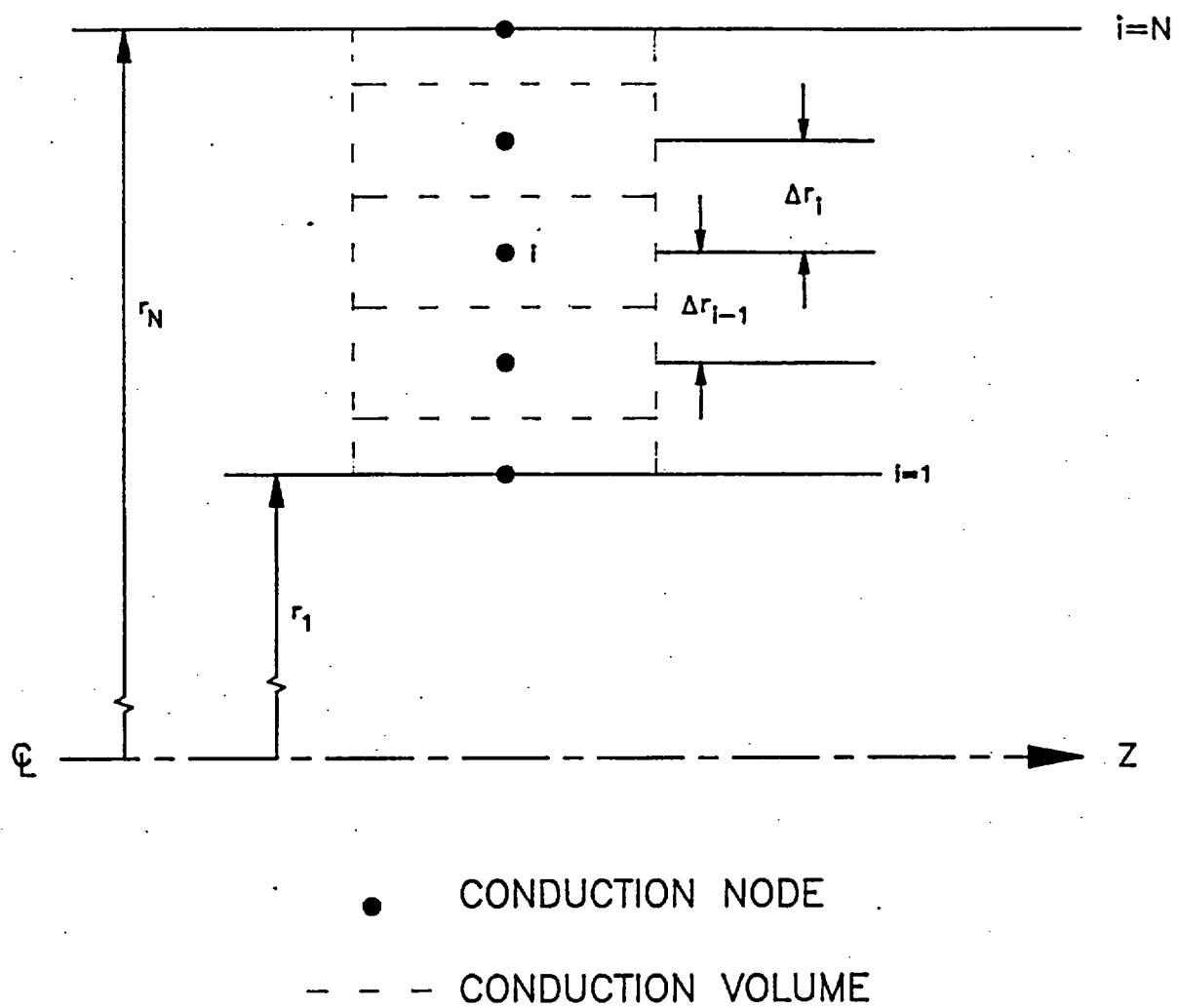


Figure 7-25. Geometry for One-Dimensional Component Conductor

8 WCOBRA/TRAC REACTOR KINETICS AND DECAY HEAT MODELS

8-1 INTRODUCTION

The heat sources during a postulated LOCA are important in determining the cladding heatup. It is important, therefore, to include all possible heat sources in an accurate way such that the PCT calculated from an analysis model is realistic without having an unnecessary penalty.

The primary heat sources during a LOCA are fission product decay heat, fission heat, actinide decay heat, stored energy, and cladding chemical reaction. The objective of this section is to summarize the models related to the first three heat sources, which have been programmed in the code WCOBRA/TRAC. The cladding chemical reaction was described in Section 7. The models described in this section are identical to the approved models which have been documented in Hochreiter et al. (1988).

The variables of each equation presented in this section are defined after each equation. The nomenclature of this section is independent of the nomenclature of the rest of this report.

8-2 DECAY HEAT SOURCE

Model Basis In general, the time-dependent decay activity for a given nuclide can be solved by the following relationship:

$$\begin{aligned} \frac{d}{dt} DH^i = & \alpha_i (\Sigma_F \phi) - \Gamma_i DH^i + \phi \sum_{j=1}^n DH^j \sigma_a^j A(i,j) \\ & + \sum_{j=1}^n \Gamma_j DH^j D(i,j) \end{aligned} \quad (8-1)$$

where:

- DH^i = the decay activity of the i-th decay heat pseudo-nuclide,
- α_i = the yield fraction of the i-th decay heat pseudo-nuclide directly from fission,
- Σ_F = the macroscopic fission cross section,
- $\Sigma_F \phi$ = the fission rate of the reactor of interest,
- Γ_i = the decay constant of the i-th decay heat pseudo-nuclide,
- ϕ = the neutron flux in the reactor of interest,

- σ_a^j = the microscopic absorption cross section of the j-th nuclide,
 $A(i,j)$ = the probability that absorption in the j-th isotope will produce the i-th isotope, and
 $D(i,j)$ = the probability that decay of the j-th nuclide will produce the i-th nuclide.

Equation 8-1 is numerically exact for the decay heat problem. However, the direct solution of Equation 8-1 involves 250 to 350 cross-coupled equations.

To simplify the preceding equation, three assumptions have been used to implement a generalized decay heat source consistent with ANSI/ANS 5.1-1971 Draft (1971) and ANSI/ANS 5.1-1979 (1978). The first two are:

- $A(i,j) = 0$
- $D(i,j) = 0$

That is, the contributions from the absorption in the j-th isotope and decay of the j-th isotope which will produce the i-th isotope are much less significant than the direct production, $(\alpha_i \sum_f \phi)$, and decay, $(\Gamma_i DH^i)$, except for very few nuclides in very high flux reactors. The third assumption is:

- Grouping of nuclides of similar time constants into a single pseudo-nuclide with the weighted average energy yield of all the nuclides involved.

The above assumption yields fewer equations to be solved with negligible loss in accuracy when the nuclide groups are chosen appropriately.

The final form of Equation 8-1 with the above assumptions is

$$\frac{d}{dt} DH^i = \alpha_i (\sum_f \phi) - \Gamma_i DH^i \quad (8-2)$$

Table 8-1 lists the standard data of α_i and Γ_i from the ANSI/ANS 5.1-1979 model for U-235, Pu-239 thermal fission, and U-238 fast fission.

The ANSI/ANS 5.1-1979 standard data are represented in an exponential form (MeV/fission):

$$DH(t,T) = \sum_{n=1}^3 w_n(BU,\epsilon) \left[\sum_{i=1}^{23} \frac{\alpha_i}{\Gamma_i} e^{-\Gamma_i t} (1 - e^{-\Gamma_i T}) \right] \quad (8-3)$$

where:

- t = time after shutdown (sec),
 T = irradiation time (sec), and,
 $w_n (BU, \epsilon)$ = fission fraction of the n-th fissile isotope as a function of burnup (BU) and initial enrichment (ϵ),

 $n=1$: U-235 Thermal Fission
 $n=2$: Pu-239 Thermal Fission
 $n=3$: U-238 Fast Fission.

Equation 8-3 is the general solution of Equation 8-2 for a constant fission rate for an irradiation time T followed by a zero fission rate for time t . WCOBRA/TRAC solves Equation 8-2 as the generalized differential equation representation of Equation 8-3 for U-235 and Pu-239⁽²⁾ thermal fission as well as U-238 fast fission. The energy yield constants are weighted by the appropriate fission rate fractions, $w_n (BU, \epsilon)$, as a function of initial enrichment and burnup within WCOBRA/TRAC.

The fission rate weighting was obtained from detailed physics evaluation of PWR fuel lattice designs. Figure 8-1 illustrates the U-235 thermal fission rate weighting obtained from these evaluations. Similarly, Figures 8-2 and 8-3 illustrate the Pu-239 thermal fission and U-238 fast fission weightings, respectively. The U-235 fission rate fraction presented in Figure 8-1 was evaluated as directed by ANSI/ANS 5.1-1979, as all fissions that are not U-238 or Pu-239.

The decay heat model within WCOBRA/TRAC has been benchmarked against the ANSI/ANS 5.1-1979 Standard. Table 8-2 presents the results of decay heat solved by Equation 8-2 in WCOBRA/TRAC and the standard form (Equation 8-3) for U-235 only. The difference between the two approaches is negligible. Similar comparisons exist for Pu-239 and U-238. WCOBRA/TRAC solves for the composite decay heat of the reactor of interest using the fission rate fractions derived from specific physics calculations for the fuel lattice design.

As for the ANSI/ANS 5.1-1971 model, the standard formulation is a piece-wise power fit over ranges of time from 0.1 seconds to 2×10^8 seconds (Table 8-3). The standard data have been refitted and incorporated in WCOBRA/TRAC in the same form as Equation 8-3, except only 11 groups instead of 69 groups of pseudo-nuclides were used.

Table 8-3 lists the fitted values of α_i and Γ_i of the ANSI/ANS 5.1-1971 model. It can be seen in Table 8-4 that the exponential form with the fitted coefficients generates results which deviate from the standard power form by about one percent.

8-3 FISSION HEAT

Model Basis The fission heat is treated using a point kinetics model. The derivation of the final form of the point kinetics model can be found in various nuclear reactor analysis textbooks, such as Henry (1975) and Glasstone and Sesonske (1967). The most familiar form of the point kinetics model is

$$\frac{dn}{dt} = \frac{\rho(t) - \bar{\beta}}{\ell^*} n(t) + \sum_{i=1}^6 \lambda_i C_i + S_e \quad (8-4)$$

and

$$\frac{dC_i}{dt} = \frac{\beta_i n(t)}{\ell^*} - \lambda_i C_i \quad (8-5)$$

where:

- n = neutron density,
- ρ = reactivity, $(k-1)/k$,
- β_i = the i -th group delayed neutron precursor yield fraction,
- $\bar{\beta} = \sum_{i=1}^6 \beta_i$,
- ℓ^* = effective neutron lifetime,
- λ_i = the i -th delayed neutron precursor time constant,
- C_i = the i -th delayed neutron precursor concentration, and,
- S_e = external source strength.

The assumptions in deriving Equations 8-4 and 8-5 are the time and space separability of the neutron density and six groups of delayed neutrons.

Once the neutron density $n(t)$ is solved from the point kinetics model, the fission power can be obtained by the equation

$$FH(t) = v n(t) \kappa \Sigma_f \quad (8-6)$$

where:

- v = neutron velocity,
- κ = prompt energy release per fission, and,
- Σ_f = macroscopic fission cross section.

The macroscopic fission cross section is a neutron energy dependent parameter. The moderator density affects the thermalization of neutrons. Therefore, the fission interaction frequency ($\nu\kappa\Sigma_f$) should be a function of moderator density. The moderator of a typical PWR is the primary loop coolant. During a LOCA, the coolant density will undergo a rapid change. Therefore, to assume $\nu\kappa\Sigma_f$ is a constant throughout the transient would be overly conservative (lower coolant density should result in harder neutron energy spectrum, hence lower thermal fission rate). A water-density-dependent form of fission interaction frequency ($\nu\kappa\Sigma_f$) has been incorporated in WCOBRA/TRAC, which is

$$\nu\kappa\Sigma_f(\rho_t) = A_0 + \sum_{n=1}^6 A_n \rho_t^n \quad (8-7)^{(1)}$$

where:

ρ_t = water density.

The seven coefficients ($A_0 - A_6$) are obtained by space/energy calculations for the fuel assembly of interest.

A series of detailed space/energy calculations have been performed for a typical fresh assembly to quantitatively evaluate fission rate per unit neutron density for water densities that occur during the LOCA transient. Table 8-5 lists the values of the 7 coefficients, and Figure 8-4 shows the calculated density dependence of $\kappa\Sigma_f$, which is normalized to the value at $\rho_t = 0.7 \text{ g/cm}^3$. [

]^a. Therefore, the modification of the fission frequency ($\nu\kappa\Sigma_f$) should be considered. This quantity, as with all other plant and reactor specific data, is modelled in WCOBRA/TRAC using input appropriate to the specific plant and reactor design being considered.

WCOBRA/TRAC explicitly models the burnup and initial enrichment dependence of kinetics data, i.e., groupwise delayed neutron fractions, groupwise delayed neutron time constants, prompt neutron lifetime, prompt energy release per fission, and total energy release per fission. Figure 8-5 presents the effective delayed neutron fraction as a function of burnup and initial enrichment. Figure 8-6 presents the prompt neutron lifetime as a function of initial enrichment and burnup. Figures 8-7 and 8-8 present the prompt and total energy release per fission as a function of initial enrichment and burnup, respectively. Figures 8-9 through 8-14 illustrate the groups 1 through 6 delayed neutron time constants as a function of initial enrichment and burnup. The data presented in Figures 8-5 through 8-14 were generated for typical Westinghouse fuel lattice designs.

8-4 ACTINIDE DECAY HEAT SOURCE⁽²⁾

Model Basis The time dependent actinide heat source due to the buildup and decay of U-239 and Np-239 is a relatively simple problem. The basic equations for U-239 and Np-239 are given below as Equations 8-8 and 8-9, respectively.

$$\frac{dU}{dt} = \bar{R}(BU, \epsilon)(v\Sigma_f n(t)) - \lambda_u U(t) \quad (8-8)$$

$$\frac{dNp}{dt} = \lambda_u U(t) - \lambda_n Np(t) \quad (8-9)$$

where:

- $U(t)$ = time-dependent U-239 concentration,
- $\bar{R}(BU, \epsilon)$ = U-238 capture to fission ratio, function of initial enrichment ϵ , and burnup (BU),
- $v\Sigma_f n(t)$ = time-dependent fission rate,
- λ_u = U-239 decay constant,
- $Np(t)$ = time-dependent Np-239 concentration, and,
- λ_n = Np-239 decay constant.

It is much more convenient to express the decay equations in terms of instantaneous decay power. Recall that decay power is simply the product of concentration, decay constant and energy release per decay as shown in Equations 8-10 and 8-11 for U-239 and Np-239, respectively:

$$P_u = q_u \lambda_u U(t) \quad (8-10)$$

$$P_n = q_n \lambda_n Np(t) \quad (8-11)$$

where:

- P_u = time dependent decay power due to U-239 decay,
- q_u = energy release per U-239 decay,
- P_n = time dependent decay power due to Np-239 decay and,
- q_n = energy release per Np-239 decay.

Equations 8-8 through 8-11 can now be combined into a form suitable for implementation as Equations 8-12 and 8-13 below:

$$\frac{dP_u}{dt} = \bar{R}\alpha_u(v\Sigma_F n(t)) - \lambda_u P_u \quad (8-12)$$

$$\frac{dP_n}{dt} = \frac{\lambda_u P_u(t)\alpha_n}{\alpha_u} - \lambda_n P_n \quad (8-13)$$

where:

$\alpha_u = q_u \lambda_u$, decay power yield per capture (MeV/sec/capture) for U-239, and
 $\alpha_n = q_n \lambda_n$, decay power yield per capture (MeV/sec/capture) for Np-239.

[]^{a.c.} With this assumption, the initial conditions for U-239 and Np-239 are described by Equations 8-14 and 8-15, respectively: [

] ^{a.c.} (8-15)

The values of constants required for explicit actinide representation were taken from ANSI/ANS 5.1-1979 and are presented in Table 8-6. The U-238 capture to fission ratio, \bar{R} , is a function of fuel lattice design, initial enrichment, and burnup. Figure 8-15 presents \bar{R} for a typical PWR fuel lattice design. ENDF-B/V data were used in PWR core depletion calculations to determine variations in \bar{R} with burnup and enrichment.

[] ^{a.c.} (8-16)⁽³⁾

where:

κ_f = total energy release per fission.

8-5 SPACE DEPENDENT HEAT SOURCE MODEL

Model Basis WCOBRA/TRAC models the space dependent composition and initial condition dimensions of the decay heat source. This model is based upon the space/time separability assumptions of the point reactor kinetics solutions as well as the input composition and initial condition description. WCOBRA/TRAC models decay heat using channel average compositions. Initial condition concentrations are input based on conservative irradiation history evaluations. Channel average compositions are realistic representations of decay heat in limiting elevations.

The basic space independent equations derived in Sections 8-1 and 8-2, are repeated below:

$$\frac{dn}{dt} = \frac{\rho(t) - \bar{\beta}}{\ell^*} n(t) + \sum_{i=1}^6 \lambda_i C_i(t) + S_e \quad (8-4)$$

$$\frac{dC_i}{dt} = \frac{n(t)\beta_i}{\ell^*} - \lambda_i C_i \quad (8-5)$$

$$\frac{d DH^j}{dt} = v \Sigma_f(t) n(t) \alpha_j - \Gamma_j DH^j \quad (8-2)$$

$$P(t) = FH(t) + \sum_j DH^j + AH(t) \quad (8-17)$$

$$FH(t) = \kappa v \Sigma_f(t) n(t) \quad (8-18)$$

where:

- $P(t)$ = time-dependent heat source,
- $n(t)$ = time-dependent neutron density,
- $\rho(t)$ = time-dependent reactivity defined as $(k-1)/k$,
- ℓ^* = prompt neutron lifetime,
- $\bar{\beta}$ = effective delay neutron fraction,
- λ_i = time constant for the i -th delayed neutron group
- S_e = external source strength,
- $v \Sigma_f(t)$ = time dependent interaction frequency for fission,
- β_i = effective delayed neutron fraction for the i -th group,

- DH^j = energy release rate of the j-th decay heat pseudo-nuclide,
 α_j = energy yield of the j-th decay heat pseudo nuclide,
 Γ_j = time constant of the j-th decay heat pseudo nuclide,
 κ = prompt energy release per fission,
 $FH(t)$ = time dependent fission heat, and
 $AH(t)$ = time dependent actinide heat.

Assuming space/time separability, Equation 8-17 can be expressed with a general time-independent space dependence for each basic heat source as Equation 8-19 below:

$$P_i(z, t) = F_i(z)FH(t) + \sum_j D_i^j(z)DH^j(t) + A_i(z)AH(t) \quad (8-19)$$

where:

- $P_i(z, t)$ = the heat-source as a function of elevation and time in the i-th xy channel,
 $F_i(z)$ = the elevation dependence of fission heat for the i-th xy channel,
 $D_i^j(z)$ = the elevation dependence of the j-th decay heat pseudo-nuclide for the i-th xy channel,
 and
 $A_i(z)$ = the elevation dependence of actinide heat for the i-th xy channel.

[

] ^{ac}

The decay heat source is most conveniently expressed in terms of the [

] ^{ac} (8-21)

where:

[

] ^{ac}.

Equation 8-21 is now solved for $D_i^j(z)$ as Equation 8-22 below: [

] ^{a,c} (8-22)

The space/time dependent heat source can now be expressed in terms of the fission distribution and the initial power by substituting Equation 8-22 into Equation 8-19 as Equation 8-23 below: [

] ^{a,c} (8-23)

Equation 8-23 can be further simplified by defining the [
] ^{a,c} as defined in Equation 8-24 below: [

] ^{a,c} (8-24)

Equation 8-24 is now solved for the initial condition for [
] ^{a,c} as Equation 8-25 below: [

] ^{a,c} (8-25)

Equation 8-25 is now substituted into Equation 8-23 to give the final form of the space/time dependent heat source as Equation 8-26 below: [

] ^{a,c} (8-26)

The remaining task is to provide initial conditions for Equations 8-4, 8-5, and 8-2 in terms of Equation 8-26. The first of these conditions is that the input power peaking $FT_i(z)$ be normalized to a reactor average value of unity. This relation is expressed for $FT_i(z)$ as Equation 8-27 below:

$$\frac{\sum_i \int_z FT_i(z) V_i(z) dz}{\sum_i \int_z V_i(z) dz} = 1.0, \quad (8-27)$$

where $V_i(z)$ is the volume of the i -th channel at elevation z . The second initial condition is that the initial reactor power, P_{TH} , be given by Equation 8-28 below:

$$P_{TH} = \sum_i \int_z V_i(z) P_i(z, 0) dz \quad (8-28)$$

The initial conditions of Equations 8-4, 8-5, and 8-2 can now be solved in terms of P_{TH} . First, it is necessary to derive the relations for $P_i(z, 0)$ as Equation 8-29 below (from Equations 8-26 and 8-20): [

$$]^{a,c} \quad (8-29)$$

Substituting Equation 8-25 into Equation 8-29 yields a statement of initial condition in terms of [$]^{a,c}$ as Equation 8-30: [

$$]^{a,c} \quad (8-30)$$

Finally, Equation 8-30 can be integrated over the entire reactor as specified in Equation 8-28, and [$]^{a,c}$ as shown in Equation 8-31 below: [

$$]^{a,c} \quad (8-31)$$

Now, solve for the initial neutron density $n(0)$ by substituting Equation 8-18 into Equation 8-31 to yield the initial conditions in terms of initial total power P_{TH} as Equation 8-32 below: [

$$]^{a,c} \quad (8-32)$$

Recall Equation 8-24 defines that [

$$]^{a,c} \quad (8-33)$$

where the two power distributions, $D_i(z)$ and $F_i(z)$, are normalized to a reactor average value of unity.

Equation 8-22 is now substituted into Equation 8-33 to yield an expression for $AVFR^j$ in terms of the fission peaking as Equation 8-34: [

] ^{ac} (8-34a)

and [

] ^{ac} (8-34b)

All that remains to be done is to solve for $F_i(z)$ in terms of $FT_i(z)$. Recall that Equation 8-27 requires that $FT_i(z)$ be normalized such that $P_i(z, 0)$ is given by Equation 8-35 below:

$$P_i(z, 0) = P_{AV}(0) FT_i(z), \quad (8-35)$$

where:

$$P_{AV}(0) = \frac{P_{TH}}{\sum_i \int_z V_i(z) dz} \quad (8-36)$$

Substituting Equation 8-30 into Equation 8-35 and rearranging gives Equation 8-37 below: [

] ^{ac} (8-37)

8-6 ENERGY DEPOSITION MODELLING

8-6-1 Introduction

WCOBRA/TRAC models the energy sources within the reactor fuel in three distinct categories. These categories are prompt fission, fission product decay, and actinide nuclide decay. The specific details of the energy source modelling can be found in (Hochreiter et al., 1988). The distribution of energy sources is, however, of no interest to the thermal and hydraulic modelling of deposition resulting from the various

distributed energy sources. The specific details of the methodology by which the spatial distribution of the energy sources is transformed into the spatial distribution of energy deposition are the subject of the following discussion.

The energy from fission events appears in varying forms with large differences in spatial transport characteristics. Table 8-7 illustrates a typical breakdown of the energy released due to a fission event and the relative spatial transport length of the component. The degree to which a radiation source will propagate through a medium is strongly related to whether the radiation is expressed as a charged particle (e.g., fission fragment or beta particle), an uncharged particle (e.g., neutron), or a photon, (e.g., gamma-ray). Charged particles emitted from within a nuclear fuel material are, from a practical viewpoint, unable to penetrate the confines of the fuel rod and, therefore, deposit essentially all of their energy within the fuel rod as heat. As illustrated in Table 8-7, the vast majority of the total energy released due to a fission event is expressed as the kinetic energy of the fission products. The fission fragments are emitted as highly charged particles essentially instantaneously after the fission event and are deposited almost exclusively within the fuel pin in which they are generated. The beta particle energy from both the decay of fission fragments and the transmutation of the actinide activation products are also charged particles which are, like the fission fragments, deposited almost exclusively within the fuel pin in which they are generated. The beta particle energy is released as a result of the radioactive decay process, which is not directly related to the fission rate; rather it is related to the concentration of the various radio-nuclides which compose the source. WCOBRA/TRAC explicitly models the spatial distribution and temporal relationships which describe all heat sources and deposits the energy from non-penetrating radiation sources []^{a,c}. The fraction of the total heat source which is deposited in this manner is independent of coolant conditions and ranges from []^{a,c} during steady state operation to []^{a,c}.

The balance of the energy released as a result of the fission event is expressed as uncharged particles, i.e., neutrons and gamma photon energy. These penetrating radiation sources, due to their lack of charged particles, easily escape the confines of the fuel rod and deposit their energy []^{a,c}. The deposition of the energy contained within these sources is quite important to the consequences of the LOCA transient since []^{a,c} of the decay power released during the LOCA transient is expressed as penetrating radiation. WCOBRA/TRAC models the spatial deposition of spatially varying penetrating radiation sources using a generalized energy deposition model, GEDM. The GEDM is []^{a,c} and relies on input to describe the energy deposition as a function of []^{a,c}. The formulation of the GEDM and the methodology for the generation of the model input follows. Illustrative examples are presented for a typical application. The application of the GEDM is restricted only to the []^{a,c}.

8-6-2 Generalized Energy Deposition Model

Generalized Energy Deposition Model (GEDM) Derivation

Model Basis The WCOBRA/TRAC GEDM utilizes the linear superposition of distribution sources to compute the spatial distribution of deposited energy due to a generalized distributed source. The energy deposition, modelled as either heat flux or volumetric, is based upon the results of detailed particle transport calculations which form the basis of the GEDM input. The WCOBRA/TRAC GEDM utilizes the relationship illustrated in Equation 8-38 below to account for the energy deposition as heat flux at the point of interest due to generalized penetrating and non-penetrating radiation source spatial distribution(s). [

] ^{a,c} (8-38)

where:

[

] ^{a,c}

The WCOBRA/TRAC GEDM utilizes the relationship in Equation 8-39 below to account for the energy deposition as volumetric coolant heating at the point of interest due to generalized penetrating and non-penetrating radiation source spatial distribution(s). [

] ^{a,c} (8-39)

where: [

] ^{a,c}

The GEDM transfer matrices Γ_{ij}^n and ϕ_{ij}^n represent []^{a,c},
 respectively. As stated above, the theoretical basis behind the GEDM transfer matrices is the
 []

[]^{a,c}. The GEDM transfer matrix elements are derived from []

[]^{a,c}. Equation 8-40 below describes
 the derivation of the GEDM []^{a,c} transfer matrix elements Γ_{ij}^n . []

[]^{a,c} (8-40)

where:

[]

[]^{a,c}

Equation 8-41 below describes the derivation of the GEDM []^{a,c} transfer matrix elements
 ϕ_{ij}^n . []

[]^{a,c} (8-41)

where:

[]

[]^{a,c}

The numeric values of $(1 - \beta_n)$ have been derived from the []
 []^{a,c}. Typical values for β_n are given in Table 8-8.

Generalized Energy Deposition Model (GEDM) Transfer Matrix Generation

The GEDM transfer matrix elements are the product of a [

] ^{a.c.}

[

chosen because it can [^{a.c.} The GEDM [^{a.c.} methodology was
matrices have been found to be independent of [^{a.c.} The GEDM transfer

] ^{a.c.}

[

^{a.c.} The following discussion will present a sample set of GEDM [^{a.c.}
^{a.c.} calculations that have been performed using the Westinghouse 15x15 fuel design. The methodology described below applies generically to all other fuel designs.

The current model for [

] ^{a.c.}

Gamma Transfer Matrix Generation Methodology

A series of [^{a.c.} calculations were performed for a typical 15x15 OFA fuel design at typical plant conditions. The purpose of these calculations was to quantify, in a generalized fashion, the relative distribution of gamma energy as [^{a.c.} throughout the reactor, parameterized as a function of [^{a.c.} DOT (Disney et al., 1970) was used as

the dimensional particle transport code for the examples presented in this report. The methodology presented within this report does not rely on the use of DOT, but rather on [

] ^{a,c}.

The dimensional problem was modelled as a [

] ^{a,c}.

The basic methodology employed in the generation of GEDM transfer matrix elements is the use of a [

] ^{a,c}.

Nuclear particle cross sections were taken from the familiar SAILOR (1985) and BUGLE-80 (1980) library, developed at the Oak Ridge National Laboratory as part of the Radiation Shielding Information Center (RSIC). [

] ^{a,c}.

Gamma kerma factors were taken from the BUGLE-80 library and used as [^{a,c}. The SAILOR/BUGLE-80 cross-section libraries are described in ORNL RSIC reports DLC-76 and DLC-75, respectively. The SAILOR basic multigroup cross sections were [

] ^{a,c}. The Kerma data used in the development of the [^{a,c} are presented in Table 8-11 and illustrated in Figure 8-20.

The final results of the [

] ^{a,c}.

The results of these calculations were then used to calculate the GEDM transfer matrix elements as shown in Equations 8-40 and 8-41 for [^{a,c} respectively. The results of this evaluation for the 15x15 fuel design are presented in Table 8-12.

The data presented in Table 8-12 quantifies the [

] ^{a,c}. A sample evaluation of the spatial energy deposition distributed using the data from Table 8-12 is presented in Figure 8-21 as the [

] ^{a,c},

respectively. Figure 8-22 illustrates the [

] ^{a,c}, respectively. These figures clearly illustrate the dependence of heat flux deposition on [^{a,c}.

Application of Generalized Energy Deposition Model (GEDM) within WCOBRA/TRAC

The data presented in Table 8-12 can be used directly in WCOBRA/TRAC provided that the [

]^{a,c}.

[

]^{a,c} can be found in Table 8-13 and demonstrates that the

[

]^{a,c}.

The relationship used to apply [

]^{a,c}. [

]^{a,c} (8-42c)

where:

- Γ_{ij} = problem specific transfer element,
- V_i = problem specific channel volume,
- Γ_{ij}^{ref} = reference transfer element, and
- V_{ij}^{ref} = reference channel volume.

The relationship used to apply [

] ^{ac}. [

] ^{ac} (8-43c)

where:

- ϕ_{ij} = problem specific transfer element,
- V_i = problem specific channel volume,
- ϕ_{ij}^{ref} = reference transfer element, and
- V_j^{ref} = reference channel volume.

As discussed above, WCOBRA/TRAC currently models [

] ^{ac}.

8-7 DECAY HEAT UNCERTAINTY EVALUATION

Decay heat uncertainty has been modelled in WCOBRA/TRAC through the use of pseudo-isotope energy yield, α_i , augmentation factors. The values of the augmentation factors are presented in Table 8-14. The values in Table 8-14 were generated using a least squares fit to the uncertainty data provided in ANSI/ANS 5.1-1979, and provide a conservative representation of the standard's quoted uncertainties. Figures 8-23 to 8-25 illustrate the fit deviation in both energy and decay heat versus cooling time. Figures 8-26 to 8-28 compare the predicted decay heat with uncertainties to the standard decay heat plus 2σ uncertainties.⁽⁴⁾

8-8 REACTOR POINT KINETICS VALIDATION

The WCOBRA/TRAC heat source model is a fully integrated model containing a total of [

] ^{a.c.}. The decay heat model validation was presented previously in Tables 8-2 and 8-4 against the ANSI/ANS 5.1 1979 and 1971 decay heat standards, respectively. WCOBRA/TRAC shows excellent agreement with the decay heat standard data.

The point kinetics model within WCOBRA/TRAC has been validated on a [^{a.c.} for two basic test problems. The first test problem is the time-dependent solution of a step reactivity input. Figures 8-29 through 8-31 illustrate the WCOBRA/TRAC point kinetics solution of reactor period for a step reactivity insertion of $+3.0 \times 10^{-3}$, $+1.5 \times 10^{-3}$, and $-3.0 \times 10^{-2} \Delta K$ in the absence of external feedback mechanisms, respectively. The WCOBRA/TRAC kinetics model stabilizes at a constant asymptotic reactor period after a short period of time. The asymptotic reactor period for a step reactivity insertion can be solved for analytically using the familiar Inhour Equation below:

$$\rho = \frac{\ell^*}{T} + \sum_{i=1}^6 \frac{\beta_i}{1 + \lambda_i T} \quad (8-44)$$

where T is the asymptotic reactor period.

Table 8-15 presents the calculated and theoretical asymptotic reactor period for these step insertions. WCOBRA/TRAC shows excellent agreement against this theoretical validation test.

[

] ^{a.c.}.

[

 $J^{a,c}$.

8-9 JUSTIFICATION OF SIMPLIFICATIONS AND ASSUMPTIONS

8-9-1 Actinide Decay Power

ANSI/ANS 5.1-1979 directs the user to evaluate the impact of other actinide isotopes. As stated previously, WCOBRA/TRAC explicitly models the decay power due to U-239 and Np-239 with the

[

 $J^{a,c}$.

Detailed calculations have been performed to evaluate the impact of the total actinide heat source. Table 8-16 presents the basic physical data for the [

 $J^{a,c}(S)$.

8-9-2 WCOBRA/TRAC Fission Energy Accounting

WCOBRA/TRAC explicitly accounts for the energy deposition due to fission by five basic mechanisms. Direct fission energy deposition due to fission fragments, prompt gamma reactions, and prompt beta reactions are a direct and immediate result of a fission event. These components, as well as the neutron slowing down deposition and structural material radiative capture mechanisms, are included explicitly in the prompt energy release per fission as illustrated in Figure 8-7. The basic physics data used to generate Figure 8-7 as a function of burnup and initial enrichment is based upon ENDF-B/V as utilized at Westinghouse for standard reactor design. Table 8-17 presents the prompt fission energy release,

radiative capture release, and average fission neutron energy utilized in the evaluation of the composite prompt energy release per fission. Thus, WCOBRA/TRAC complies with the standard's requirement to evaluate the energy release per fission including radiative capture in structural components.

8-9-3 Decay Heat Absorption Effects

ANSI/ANS 5.1-1979 directs the user that the basic decay heat data supplied within the standard is uncorrected for neutron capture effects. The standard supplies a means of correction for neutron capture as a function of irradiation time, shutdown time, and integrated fissions per initial fissile atom as shown in Equation 8-45 below:

$$G(t) = 1.0 + (3.24E-06 + 5.23E-10t)T^{0.4}\psi \quad (8-45)$$

where:

t = time after shutdown in seconds, ($t < 10,000$ sec)

T = irradiation time in seconds, ($T < 1.2614E+08$ sec)

ψ = fissions per initial fissile atom, ($\psi < 3.0$)

Integrated fissions per initial fissile atom have been evaluated for PWR fuel lattice designs, as illustrated in Figure 8-34, as a function [

$]^{ac}$. Thus, WCOBRA/TRAC conservatively accounts for neutron capture effects in the decay heat model as required by the standard.

8-10 GENERALIZED ENERGY DEPOSITION MODEL (GEDM) VALIDATION

The GEDM has been validated in two separate manners for application within WCOBRA/TRAC. The first validation calculation was performed to validate the [

$]^{ac}$

[

] ^{a,c}.

The final validation of the GEDM and input generation methodology was the comparison of the GEDM

[

] ^{a,c}. The results of this comparison are

given in Table 8-18. It is apparent from the [

] ^{a,c}.

8-11 INTERFACE BETWEEN NEUTRONICS AND THERMAL-HYDRAULICS MODELS

Figure 8-35 shows the calculation block diagram for WCOBRA/TRAC. The neutronics part of the calculation is performed by a subroutine within WCOBRA/TRAC called LUCIFER (Hochreiter et al., 1988). There are two options available for the neutronics calculations in terms of the reactivity feedback to LUCIFER. ⁽⁶⁾ The first option is the user supplied reactivity table. With this option, LUCIFER is essentially a stand alone code for calculating the power history associated with the reactivity table. The second option is the internal feedback option. The core average fuel temperature and coolant density calculated in WCOBRA/TRAC are fed back to LUCIFER for the reactivity calculation and the associated power history calculation. The calculated power history is then supplied to WCOBRA/TRAC as the heat source in the thermal-hydraulics calculations.

8-12 REACTOR KINETICS, DECAY HEAT, AND INTERFACE MODELS AS CODED

WCOBRA/TRAC solves the reactor kinetics, decay heat, and actinide decay heat models with a system of first-order ordinary differential equations of the form $y' = f(x,y)$ or $Ay' = f(x,y)$ with initial conditions, where A is a matrix of order N . The solution method is the backward differentiation formula (up to order 6), also called Gear's stiff method (1971). Because the basic formula is implicit, an algebraic system of equations must be solved at each step. The matrix in this system has the form $L = A + \eta J$, where η is a small number and J is the Jacobian.

The FORTRAN coding in WCOBRA/TRAC is consistent with the models described in this section.

8-13 REACTOR KINETICS, DECAY HEAT, AND INTERFACE MODELS SCALING CONSIDERATIONS

The models described in this section are scale independent.

8-14 CONCLUSIONS

The models and derivations described in this section have been reviewed and checked. It is concluded that the models are correct. The coding in WCOBRA/TRAC is found to be consistent with the models described in this section.

8-15 REFERENCES

ANSI/ANS 5.1-1971 Draft, 1971, "Proposed ANS Standard Decay Energy Release Rates Following Shutdown of Uranium Fueled Thermal Reactors," American Nuclear Society.

ANSI/ANS 5.1-1979, 1978, "Decay Heat in Light Water Reactors," American Nuclear Society.

BUGLE-80 Gamma Cross Sections, 1980, ORNL RSIC DLC-76.

Disney, R. K., et al., 1970, "Nuclear Rocket Shielding Methods, Modification, Updating, and Input Preparation," Volume 5, Two Dimensional Discrete Ordinates Transport Techniques, WANL-PR-(LL)-034, Westinghouse Astro Nuclear Laboratory.

DOT2W, "A Two-Dimensional Discrete Ordinates Computer Program," ORNL/RSIC CCC-89. Contributed by Westinghouse Advanced Reactors Division, Madison, PA, USA.

Gear, C. W., 1971, Numerical Initial-Value Problems in Ordinary Differential Equations, Prentice-Hall, Englewood Cliffs, New Jersey.

Glasstone, S. and Sesonske, A., 1967, Nuclear Reactor Engineering, Van Nostrand, New York.

Henry, A. F., 1975, Nuclear Reactor Analysis, The MIT Press, Cambridge, Mass. and London England.

Hochreiter, L. E., et al., 1988, "Westinghouse Large Break LOCA Best Estimate Methodology, Volume 1: Model Description and Validation, Addendum 2: Revised Appendix B: Heat Source Models," WCAP-10924-P-A, Revision 1.

SAILOR Gamma Cross Sections, 1985, ORNL RSIC DLC-75.

8-16 RAI LISTING

- | 1. RAI1-227 (refers to WCAP-12945, Rev. 1, page 8-12; now page 8-5)
- | 2. RAI1-228 (refers to WCAP-12945, Rev. 1, page 8-7; now page 8-3)
- 3. RAI1-229
- 4. RAI1-230
- | 5. RAI1-231 (refers to WCAP-12945, Rev. 1, page 8-45; now page 8-22)
- 6. RAI1-232
- 7. RAI1-1, item pp

Table 8-1 **ANSI/ANS 5.1-1979**
Decay Heat Standard Data for U-235 Thermal Fission

Group	α_i (MeV/f.sec)	Γ_i (sec ⁻¹)
1	6.5057E-01*	2.2138E+01
2	5.1264E-01	5.1587E-01
3	2.4384E-01	1.9594E-01
4	1.3850E-01	1.0314E-01
5	5.5440E-02	3.3656E-02
6	2.2225E-02	1.1681E-02
7	3.3088E-03	3.5870E-03
8	9.3015E-04	1.3930E-03
9	8.0943E-04	6.2630E-04
10	1.9567E-04	1.8906E-04
11	3.2535E-05	5.4988E-05
12	7.5595E-06	2.0958E-05
13	2.5232E-06	1.0010E-05
14	4.9948E-07	2.5438E-06
15	1.8531E-07	6.6361E-07
16	2.6608E-08	1.2290E-07
17	2.2398E-09	2.7213E-08
18	8.1641E-12	4.3714E-09
19	8.7797E-11	7.5780E-10
20	2.5131E-14	2.4786E-10
21	3.2176E-16	2.2384E-13
22	4.5038E-17	2.4600E-14
23	7.4791E-17	1.5699E-14

*read as 6.5057×10^{-1}

Table 8-1 **ANSI/ANS 5.1-1979**
(cont) **Decay Heat Standard Data for Pu-239 Thermal Fission**

Group	α_i (MeV/f.sec)	Γ_i (sec ⁻¹)
1	2.083E-01*	1.002E+01
2	3.853E-01	6.433E-01
3	2.213E-01	2.186E-01
4	9.460E-02	1.004E-01
5	3.531E-02	3.728E-02
6	2.292E-02	1.435E-02
7	3.946E-03	4.549E-03
8	1.317E-03	1.328E-03
9	7.052E-04	5.356E-04
10	1.432E-04	1.730E-04
11	1.765E-05	4.881E-05
12	7.347E-06	2.006E-05
13	1.747E-06	8.319E-06
14	5.481E-07	2.358E-06
15	1.671E-07	6.450E-07
16	2.112E-08	1.278E-07
17	2.996E-09	2.466E-08
18	5.703E-11	9.378E-09
19	5.703E-11 ⁽⁷⁾	7.450E-10
20	4.138E-14	2.426E-10
21	1.088E-15	2.210E-13
22	2.454E-17	2.640E-14
23	7.557E-17	1.380E-14

*read as 2.083×10^{-1}

Table 8-1 ANSI/ANS 5.1-1979 (cont) Decay Heat Standard Data for U-238 Fast Fission		
Group	α_i (MeV/f.sec)	Γ_i (sec ⁻¹)
1	1.2311E+0*	3.2881E+0
2	1.1486E+0	9.3805E-1
3	7.0701E-1	3.7073E-1
4	2.5209E-1	1.1118E-1
5	7.1870E-2	3.6143E-2
6	2.8291E-2	1.3272E-2
7	6.8382E-3	5.0133E-3
8	1.2322E-3	1.3655E-3
9	6.8409E-4	5.5158E-4
10	1.6975E-4	1.7873E-4
11	2.4182E-5	4.9032E-5
12	6.6356E-6	1.7058E-5
13	1.0075E-6	7.0465E-6
14	4.9894E-7	2.3190E-6
15	1.6352E-7	6.4480E-7
16	2.3355E-8	1.2649E-7
17	2.8094E-9	2.5548E-8
18	3.6236E-11	8.4782E-9
19	5.7030E-11	7.5130E-10
20	4.4963E-14	2.4188E-10
21	3.6654E-16	2.2739E-13
22	5.6293E-17	9.0536E-14
23	7.1602E-17	5.6098E-15

*read as 1.2311×10^0

Table 8-2 ANSI/ANS 5.1-1979
Decay Heat Model Comparison for Infinite Radiation of U-235

Time After Trip (sec.)	WCOBRA/TRAC (MeV/fission)	Standard (MeV/Fission)	$\Delta\%$
0	13.1825	13.183	- 0.003
1	12.3190	12.318	+ 0.008
10	9.5002	9.500	+ 0.007
20	8.4616	8.461	+ 0.003
40	7.4674	7.465	+ 0.036
100	6.2039	6.204	- 0.002
200	5.3744	5.374	+ 0.0002
400	4.6751	4.673	+ 0.04
1000	3.8013	3.801	0.0

ANSI/ANS 5.1-1979
Decay Heat Model Comparison for 10^6 Second Irradiation of U-235
From Zero Concentration

Time After Trip (sec.)	WCOBRA/TRAC (MeV/fission)	Standard (MeV/Fission)	$\Delta\%$
0	12.626	12.626	0.000
1	11.761	11.761	0.000
10	8.944	8.943	+ 0.015
20	7.907	7.905	+ 0.020
40	6.909	6.908	+ 0.012
100	5.648	5.647	+0.014
200	4.820	4.818	+ 0.034
400	4.118	4.117	+ 0.013
1000	3.245	3.245	0.000

Table 8-3 ANSI/ANS 5.1-1971
Decay Heat Standard Data for U-235 Thermal Fission

Standard Formulation

$$\frac{DH(t)}{DH_{\infty}} = At^B, \text{ where,}$$

t(sec)	A*	B
$0.1 \leq t < 10$	0.07236	-0.0639
$10 \leq t < 150$	0.09192	-0.181
$150 \leq t < 4 \times 10^6$	0.156	-0.283
$4 \times 10^6 \leq t \leq 2 \times 10^8$	0.3192	-0.335
EXPONENTIAL REPRESENTATION**		
	α_i	Γ_i
1	6.587E+00***	2.658E+00
2	1.490E-01	4.619E-01
3	2.730E-01	6.069E-02
4	2.173E-02	5.593E-03
5	1.961E-03	6.872E-04
6	1.025E-04	6.734E-05
7	4.923E-06	6.413E-06
8	2.679E-07	6.155E-07
9	1.452E-08	8.288E-08
10	1.893E-09	1.923E-08
11	1.633E-10	1.214E-09

* Includes 20% required Appendix K uncertainty

** Assumes 200 MeV/fission total recoverable energy

*** Read as 6.587×10^0

Table 8-4 ANSI/ANS 5.1-1971
Decay Heat Standard for U-235 Thermal Fission

Time After Trip	WCOBRA/TRAC (MeV/fission)	Standard (MeV/fission)	$\Delta\%$
0.1	16.549	16.766	-1.29
1	14.458	14.472	-0.094
10	12.095	12.118	-0.186
20	10.757	10.689	+0.632
40	9.409	9.429	-0.213
100	8.018	7.964	+0.675
200	6.869	6.899	-0.446
400	5.674	5.725	-0.888
1000	4.479	4.417	+1.39

Table 8-5 Typical Normalized Interaction Frequency Fit Data

[
] ^{a,c}

Table 8-6 Actinide Heat Source Data

Isotope	q(MeV)	α (MeV/Sec/Capture)	λ (Sec ⁻¹)
U-239	0.474	2.32834E-4	4.91E-4
Np-239	0.419	1.42879E-6	3.41E-6

Table 8-7 Typical Radiation Source Timing, Strength, and Range

WCOBRA/TRAC Energy Category	Radiation Type	Timing	Energy (MeV)	Range
Fission ^a	Fragments	Prompt	161.0	Very Short
Fission	Direct Gamma	Prompt	5.0	Long
Fission ^b	Capture Gamma	Prompt	~5.0	Long
Fission	Neutron	Prompt	5.0	Medium
Fission	Neutron	Delayed	0.04	Medium
Fission Fragment ^c Decay	Gamma	Delayed	6.5	Long
Fission Fragment Decay	Beta	Delayed	6.5	Short
Actinide Decay	Gamma	Delayed	0.4	Long
Actinide Decay	Beta	Delayed	0.4	Short

- a. Typical prompt fission energy source taken from "Nuclear Heat Transport," M. M. El-Wakil, American Nuclear Society, 1978.
- b. Typical BOL capture gamma energy source.
- c. Typical BOL decay heat source representative of ANSI/ANS 5.1-1979.

Table 8-8 Typical Values for Redistribution Fraction Values

[
] ^{a,c}

Table 8-9 Neutron Heating Transfer Model[illegible]

Table 8-10 Gamma Photon Energy Spectrum

[illegible]

Table 8-12 Typical 15x15 GEDM Gamma Transfer Matrix

[

] ^{a,c}

Table 8-13 [] ^{a,c}						
[]						

] ^{a,c}

Table 8-14 Decay Group Uncertainty Factors Per One Sigma (%)

Decay Group	U-235	Pu-239	U-238
1	20.00	30.00	12.00
2	18.00	25.00	14.00
3	3.90	7.00	19.50
4	3.10	4.60	19.80
5	2.60	4.20	20.20
6	2.25	3.90	11.20
7	1.95	3.80	6.80
8	1.85	4.00	5.70
9	1.75	4.00	5.50
10	1.70	4.20	5.30
11	1.65	4.50	5.10
12	1.65	4.50	5.00
13	1.80	4.90	4.70
14	2.00	5.00	3.80
15	2.00	5.00	3.40
16	2.00	5.00	3.60
17	2.00	5.00	3.90
18	2.00	5.00	4.70
19	2.00	5.00	5.00
20	2.00	5.00	5.00
21	2.00	5.00	5.00
22	2.00	5.00	5.00
23	2.00	5.00	5.00

Note: Above table quotes percent uncertainty by group for one-sigma uncertainty values from ANSI/ANS 5.1-1979. Two sigma values can be obtained by doubling the table values above.

Table 8-15 Point Reactor Kinetics Validation

<u>W</u> COBRA/TRAC		Inhour Solution ²	
$\Delta\rho$ (pcm)	T(sec) ¹	$\Delta\rho$ (pcm)	T(sec)
-30000	-80.707	-30027.1	-80.77
+300	+9.147	+300.002	+9.147
+150	+34.14	+150.001	+34.14

1. Observed asymptotic period
2. Data for each solution given below

Group	Beta	Lambda
1	3.5410E-04*	3.00
2	1.0104E-03	1.13
3	2.9479E-03	0.301
4	1.4271E-03	0.111
5	1.5313E-03	0.0305
6	2.2920E-04	0.0124

$\ell^* = 16.06 \mu\text{s}$, $\bar{\beta} = 0.0075$

*Read as 3.541×10^{-4}

Table 8-18 [] ^{a,c}								
[]								

] ^{a,c}

a.c

Figure 8-1. U-235 Fission Fraction



Figure 8-2. Pu-239 Fission Fraction

a.c

Figure 8-3. U-238 Fission Fraction

Figure 8-4. Calculated Normalized Macroscopic Cross Sections versus Core Average Water Density

a.c

Figure 8-5. $\bar{\beta}$ vs. Burnup at Various Enrichments

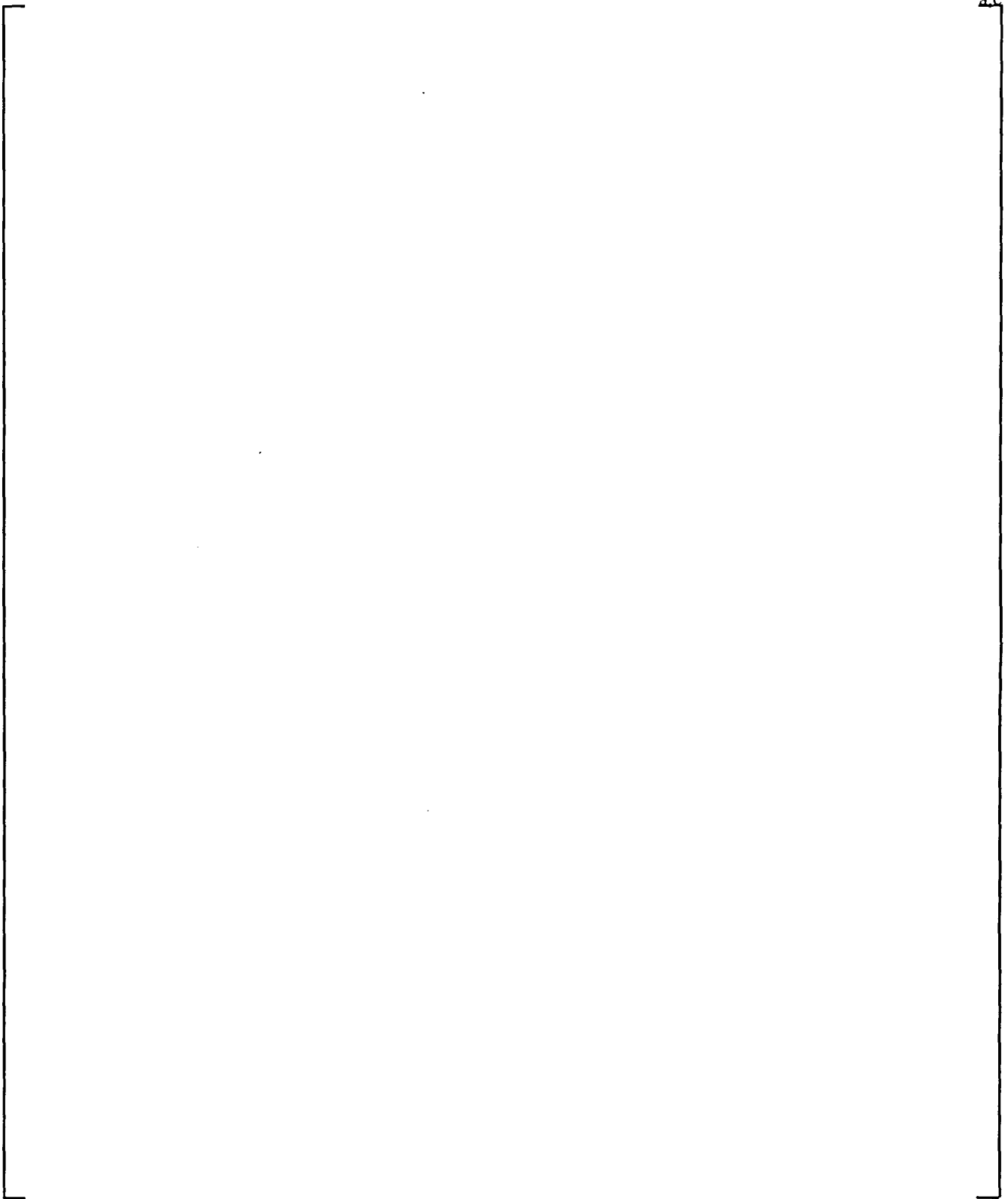


Figure 8-6. Prompt Neutron Lifetime

a.c

Figure 8-7. Prompt Energy Release

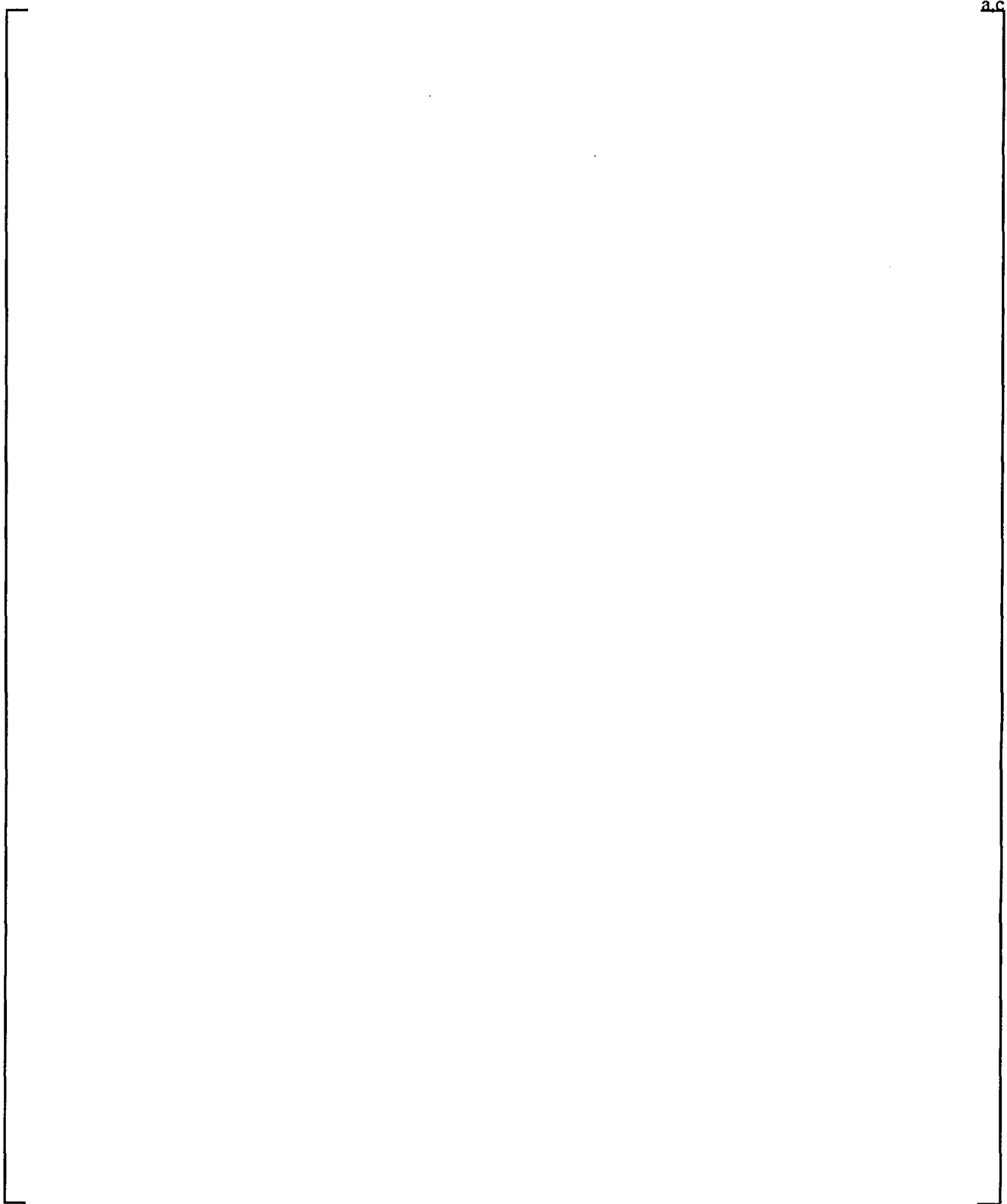


Figure 8-8. Total Energy Release

a.c

Figure 8-9. Delayed Group I Lambda

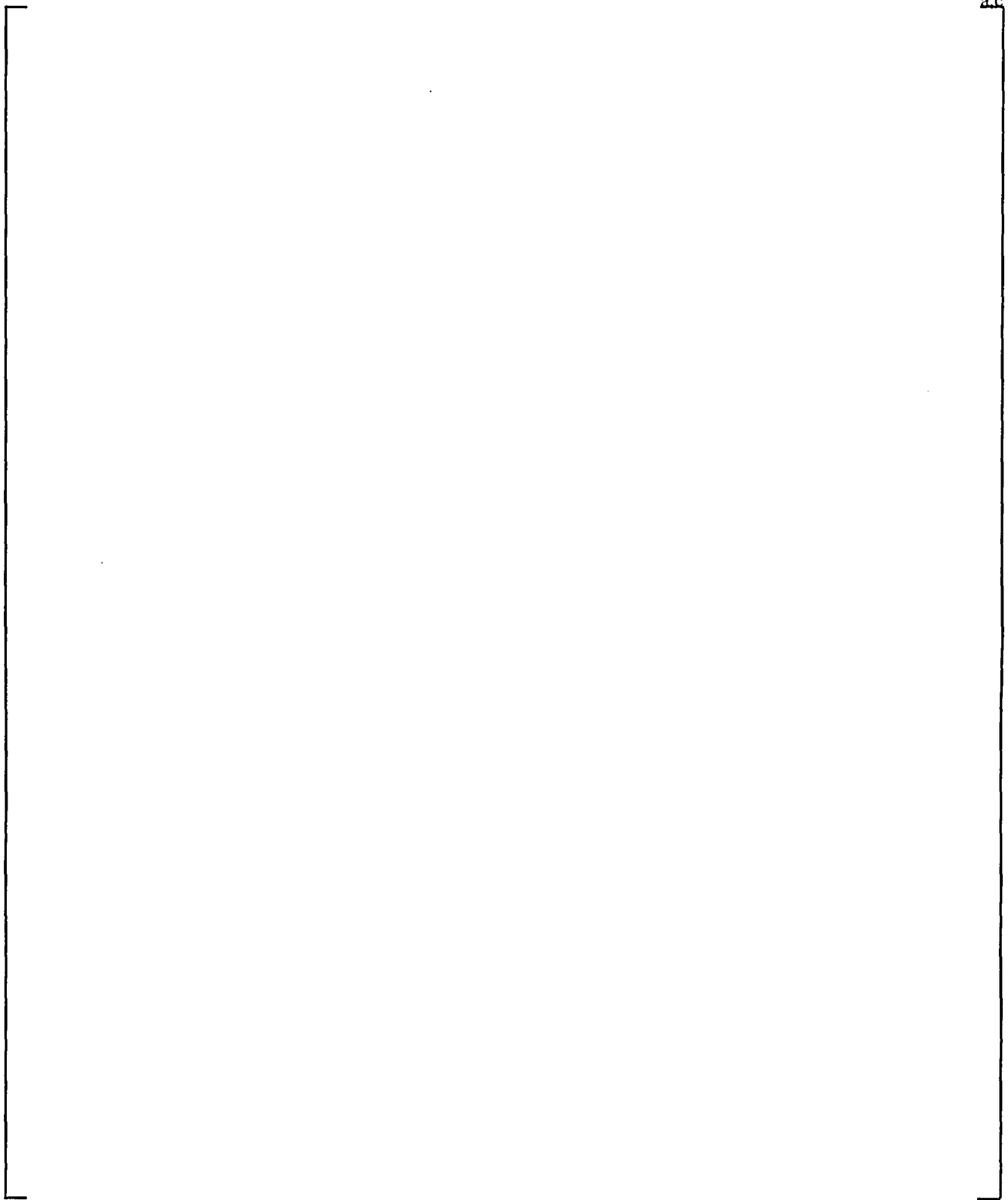


Figure 8-10. Delayed Group II Lambda

a.c

Figure 8-11. Delayed Group III Lambda

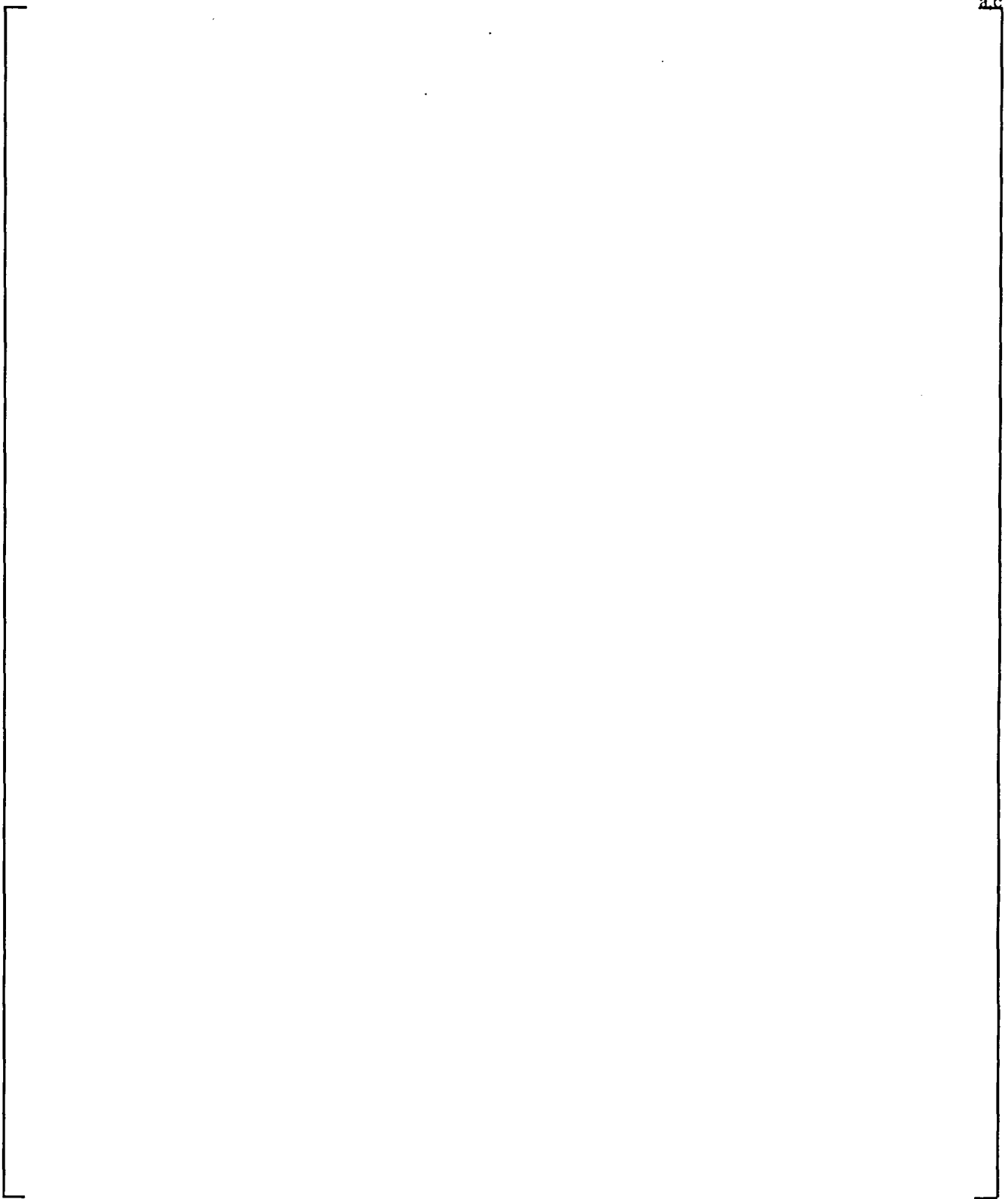


Figure 8-12. Delayed Group IV Lambda

a.c

Figure 8-13. Delayed Group V Lambda

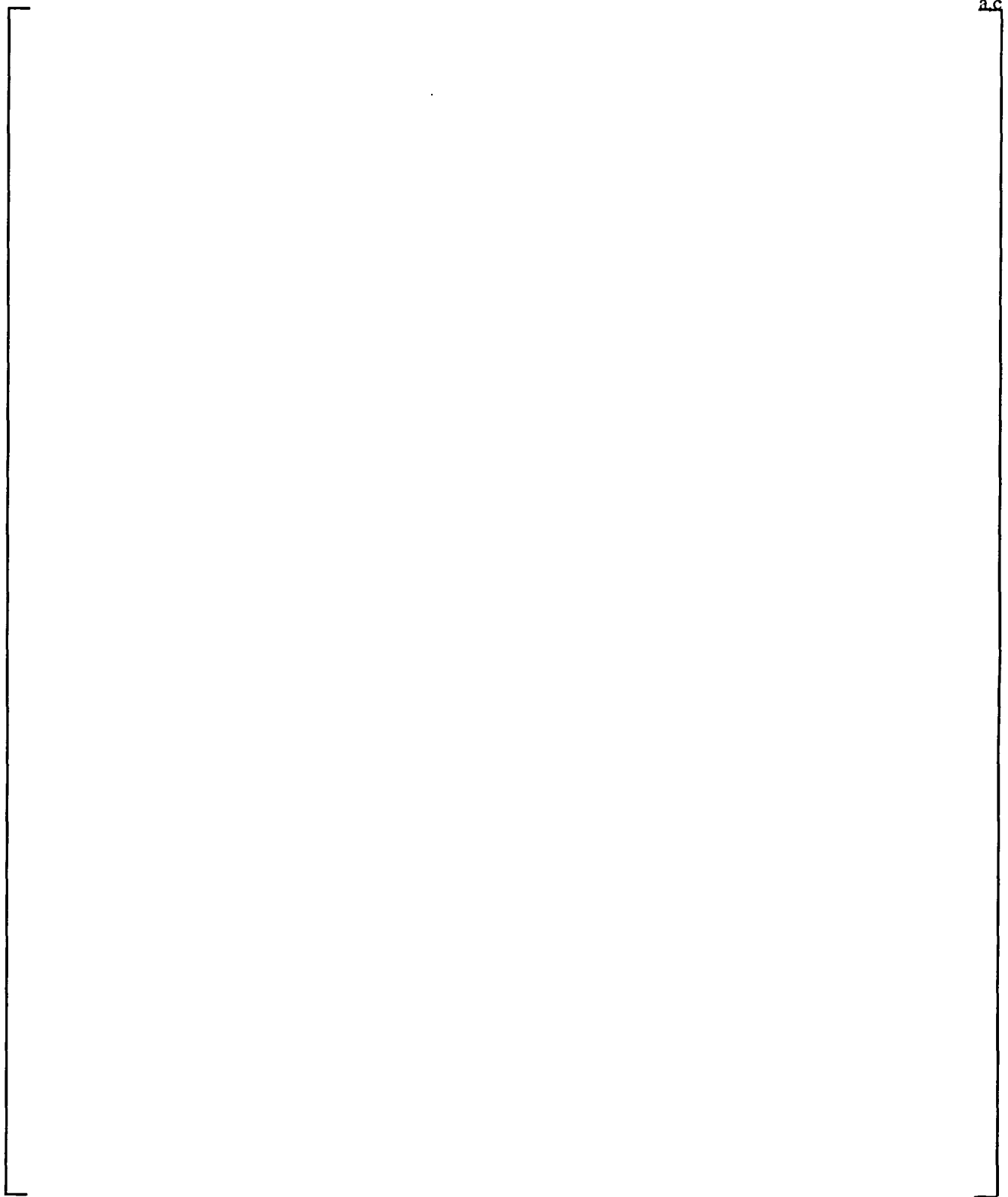


Figure 8-14. Delayed Group VI Lambda

a.c

Figure 8-15. U-238 Capture/Fission Ratio as a Function of Initial Enrichment and Burnup

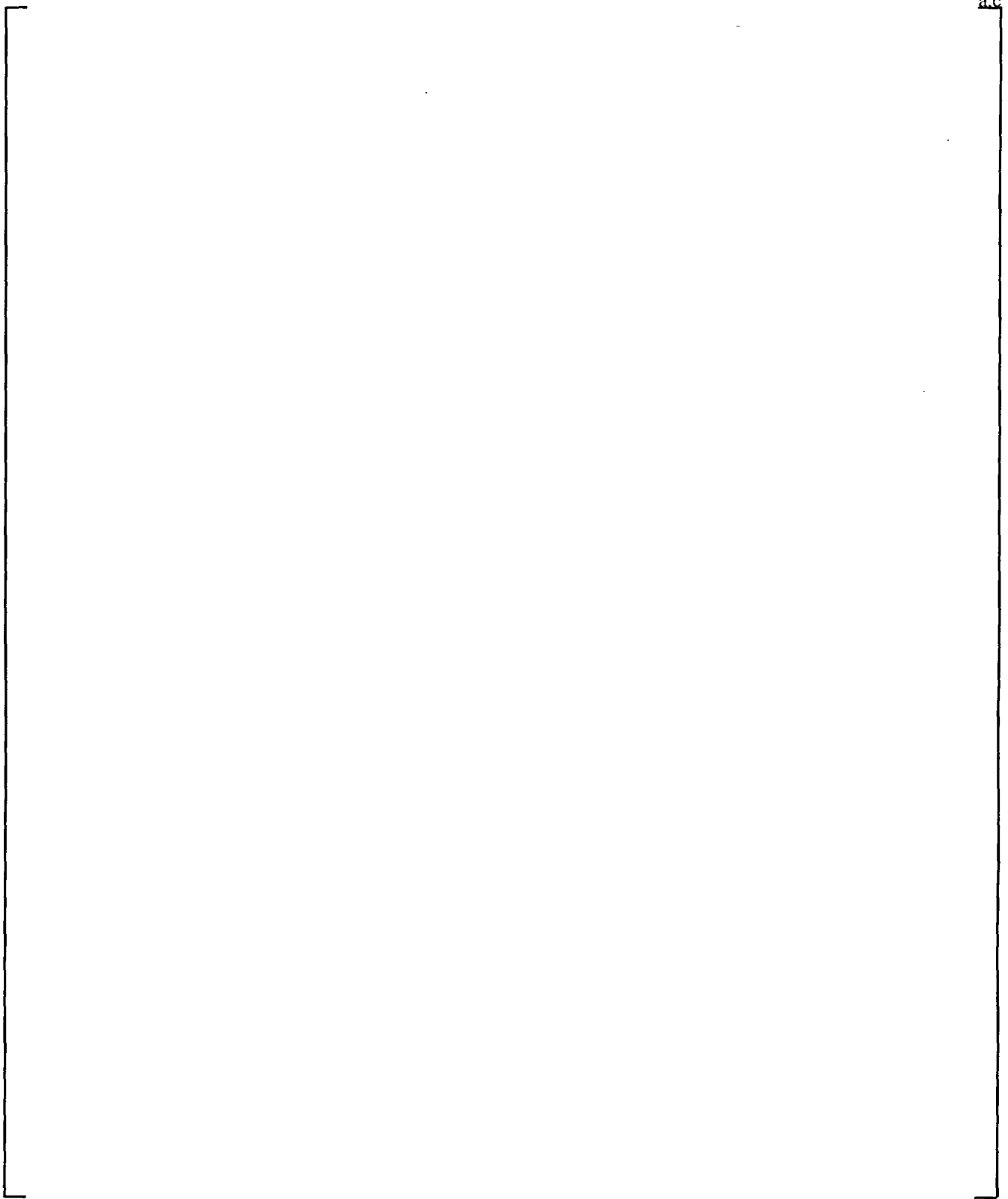


Figure 8-16. 15x15 Material Composition Assignment Layout

Figure 8-17. 15x15 Core Balance Fixed Source Distribution

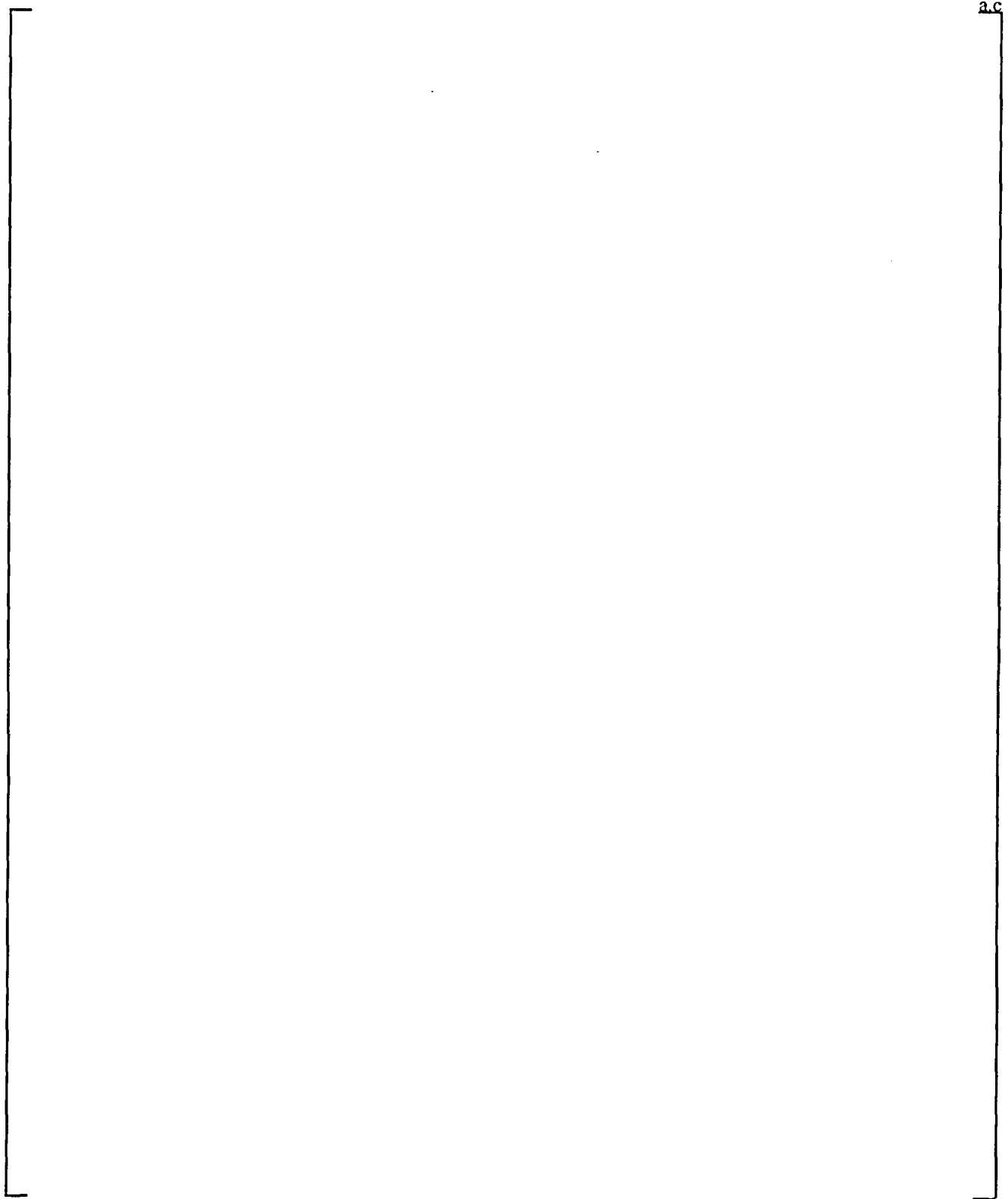


Figure 8-18. 15x15 Hot Assembly Fixed Source Distribution

a.c

Figure 8-19. 15x15 Hot Rod Fixed Source Distribution

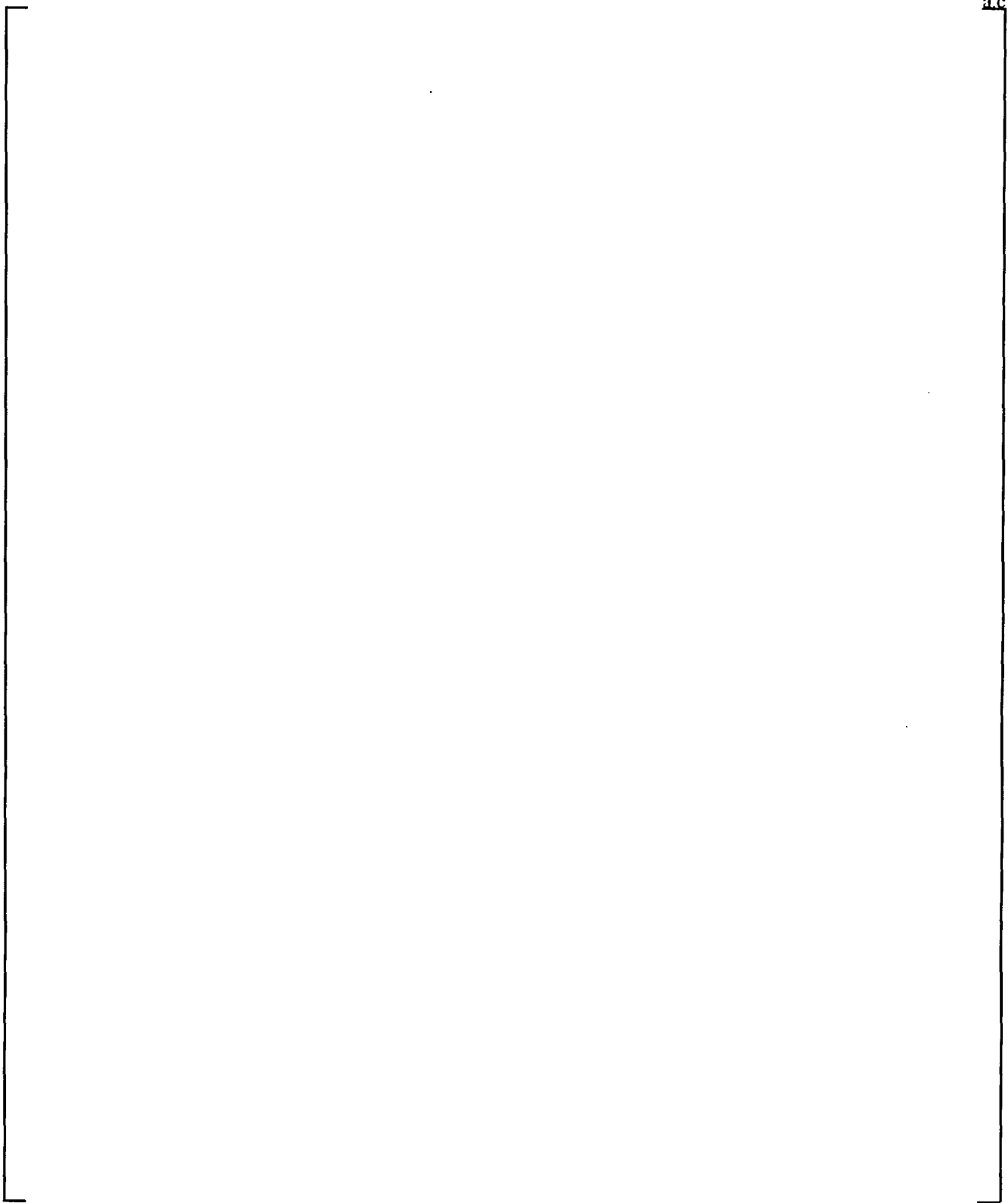


Figure 8-20. Gamma Kerma Cross Section Energy Dependence

a.c

Figure 8-21. Typical Heat Flux Deposition Fractions versus Coolant Density

Figure 8-22. Typical Heat Flux Deposition Fractions versus Coolant Density

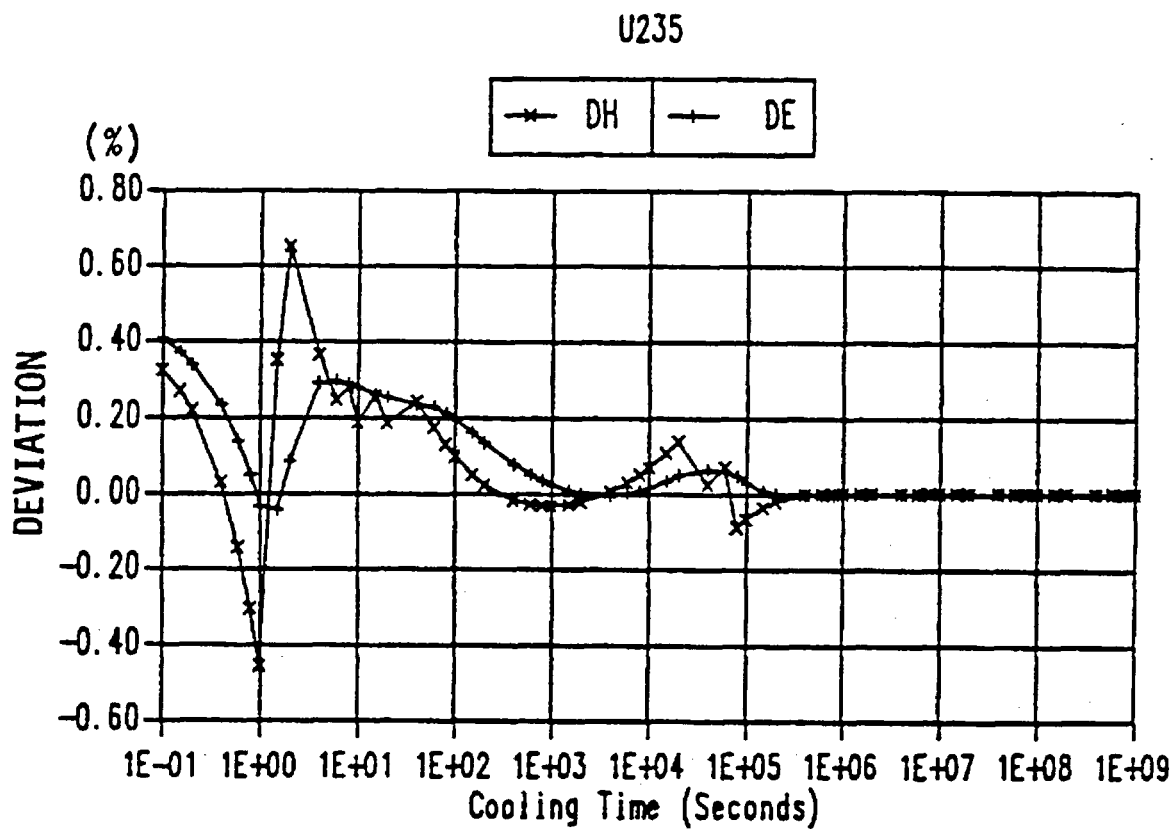


Figure 8-23. Percent Fit Deviations for U-235 ANSI/ANS 5.1 - 1979 Plus Two Sigma

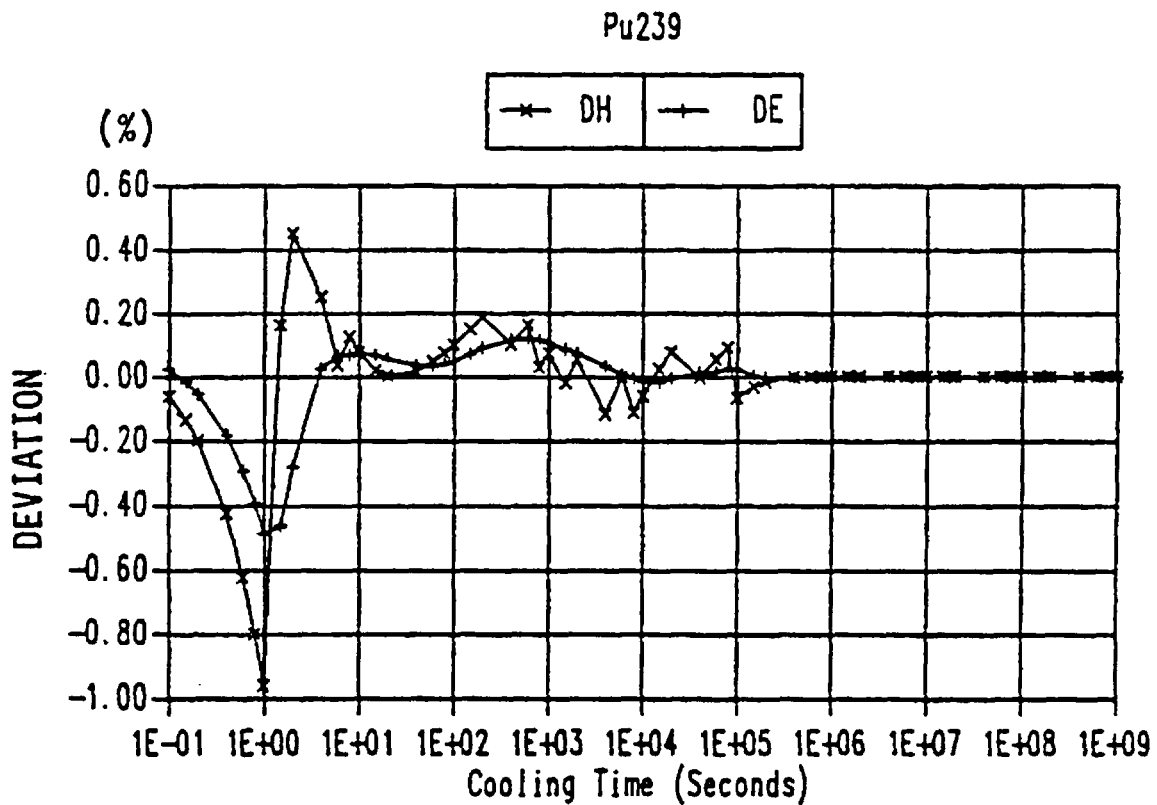


Figure 8-24. Percent Fit Deviations for Pu-239 ANSI/ANS 5.1 - 1979 Plus Two Sigma

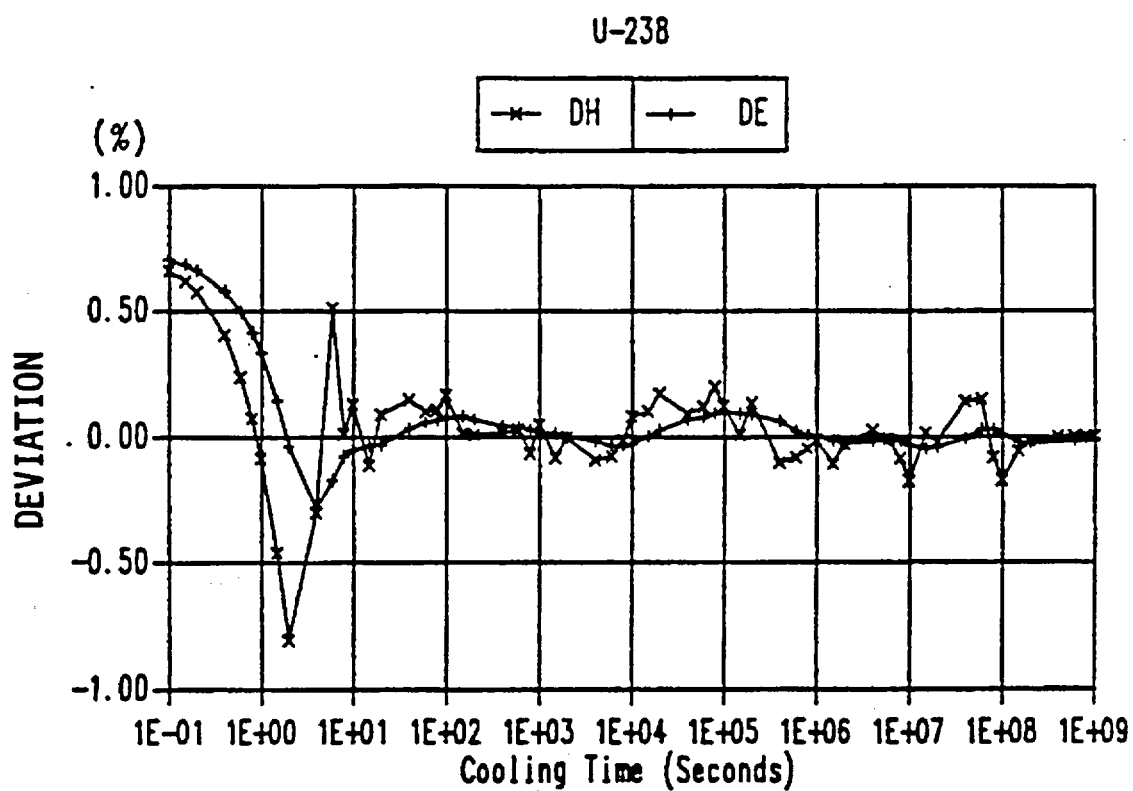


Figure 8-25. Percent Fit Deviations for U-238 ANSI/ANS 5.1 - 1979 Plus Two Sigma

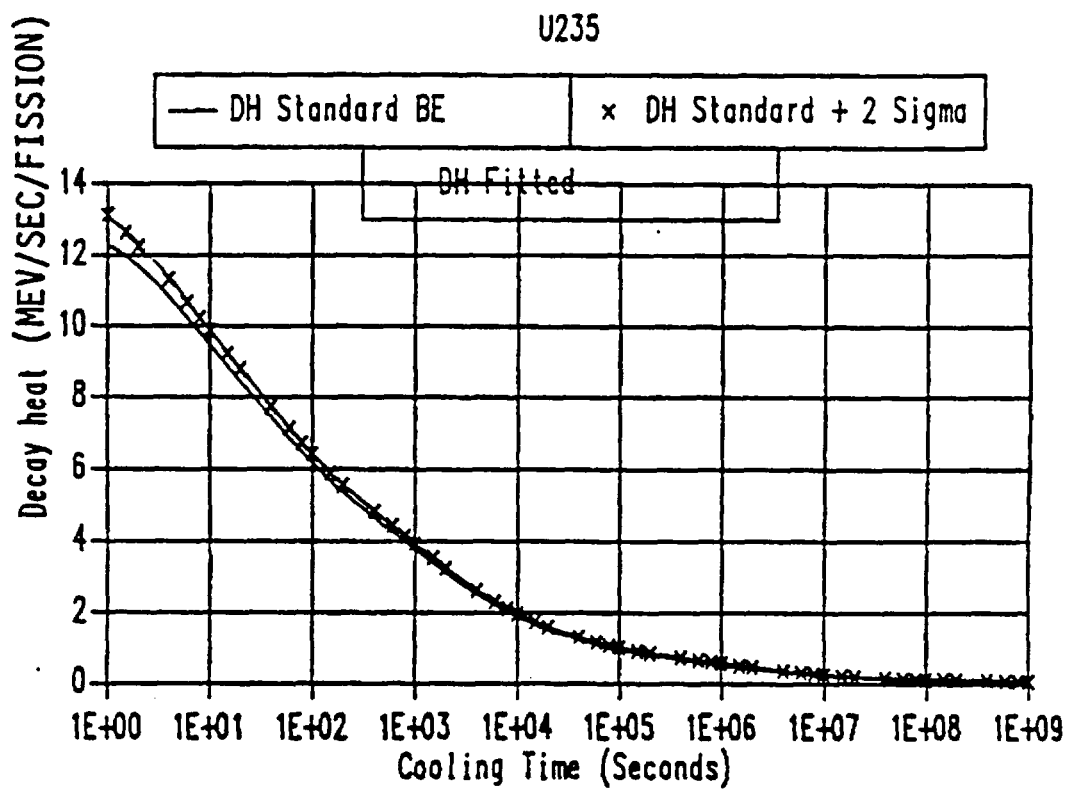


Figure 8-26. U-235 ANSI/ANS 5.1 - 1979 Decay Heat Standard vs. Fitted Results

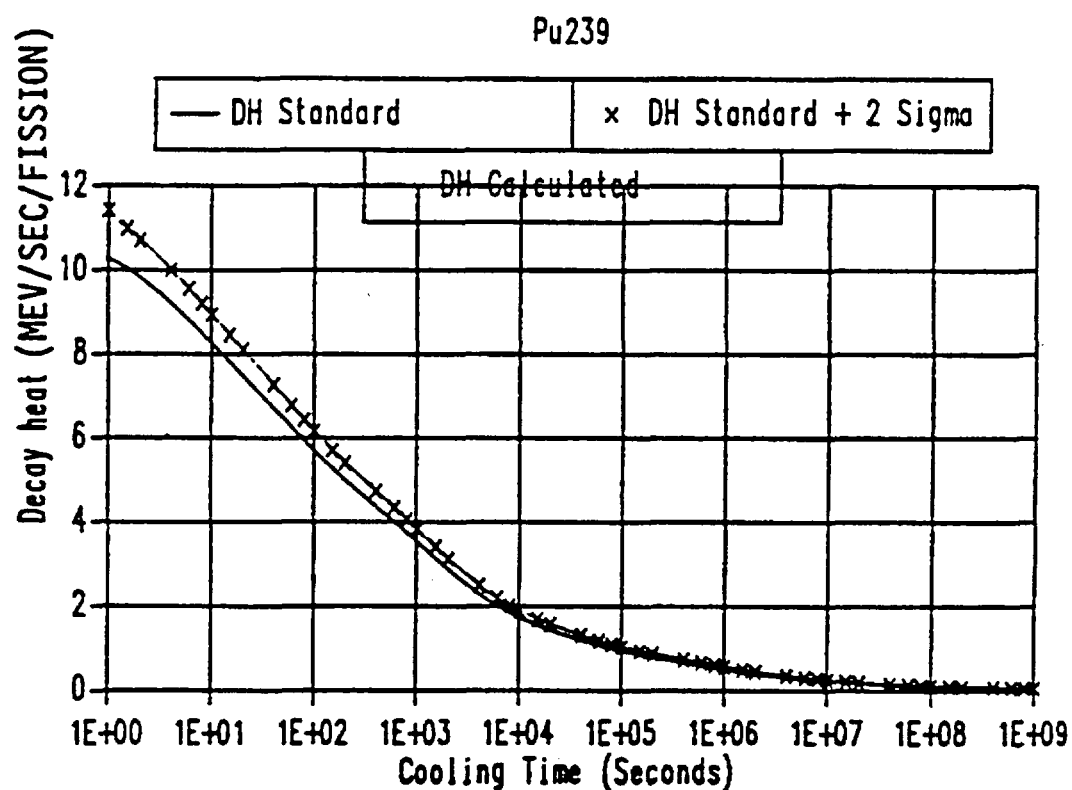


Figure 8-27. Pu-239 ANSI/ANS 5.1 - 1979 Decay Heat Standard vs. Fitted Results

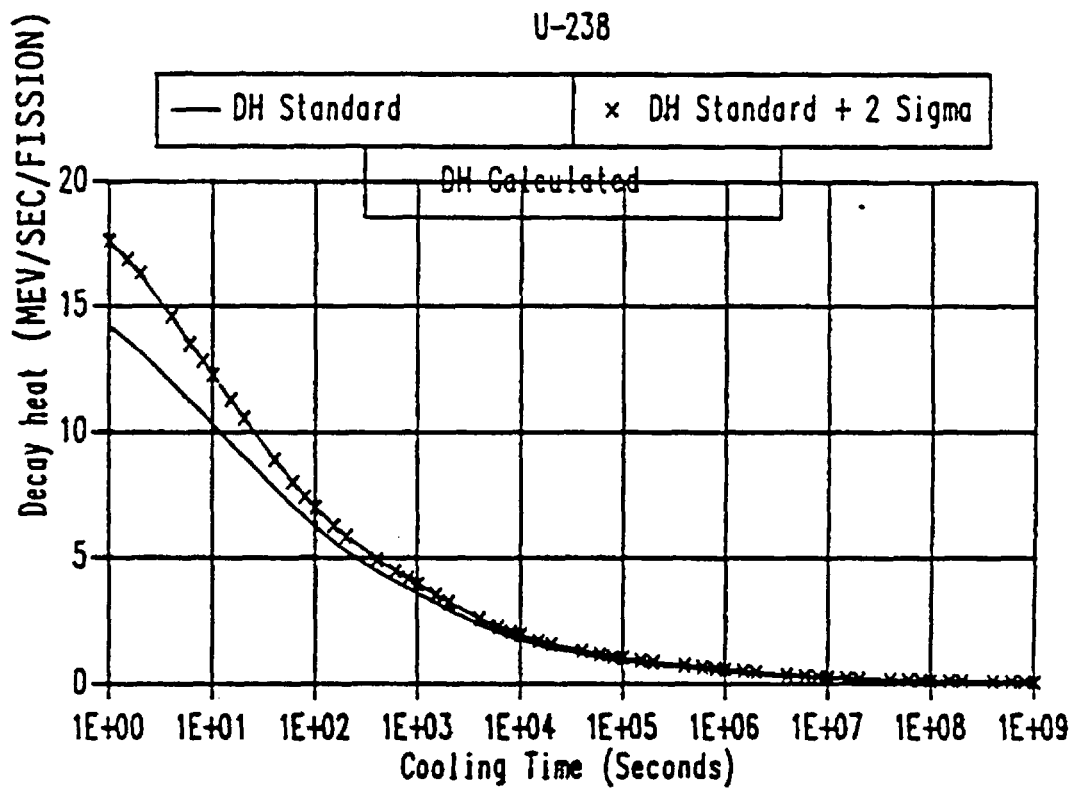


Figure 8-28. U-238 ANSI/ANS 5.1 - 1979 Decay Heat Standard vs. Fitted Results

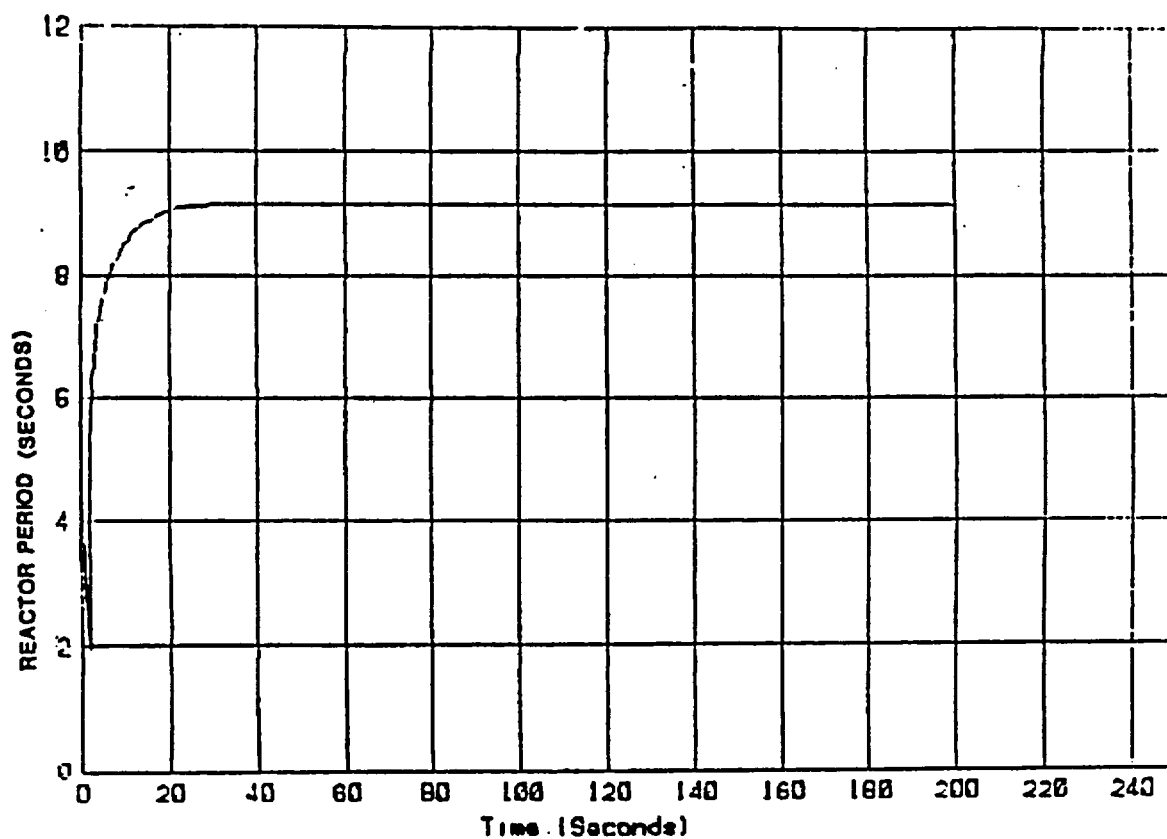


Figure 8-29. Time Dependent Reactor Period for + 0.003 ΔK Reactivity Insertion versus Time After Insertion

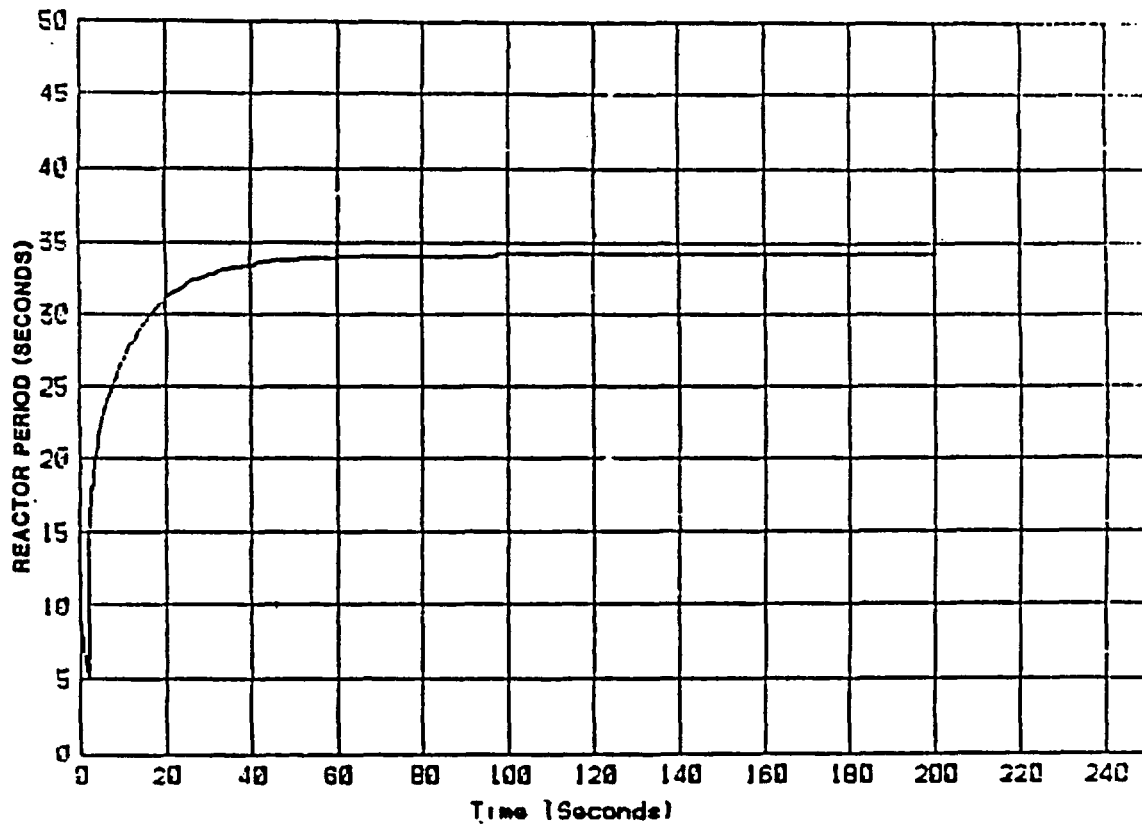


Figure 8-30. Time Dependent Reactor Period for + 0.0015 ΔK Reactivity Insertion versus Time After Insertion

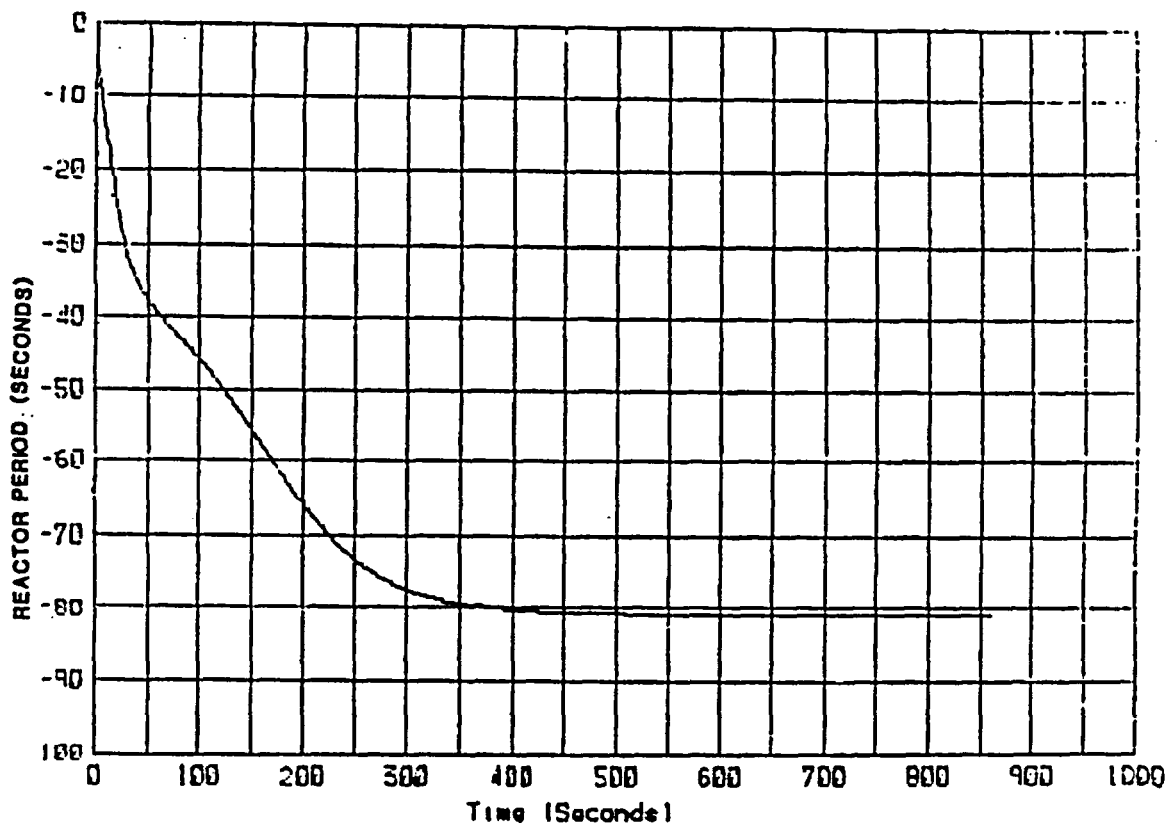


Figure 8-31. Time Dependent Reactor Period for - 0.030 ΔK Reactivity Insertion versus Time After Insertion

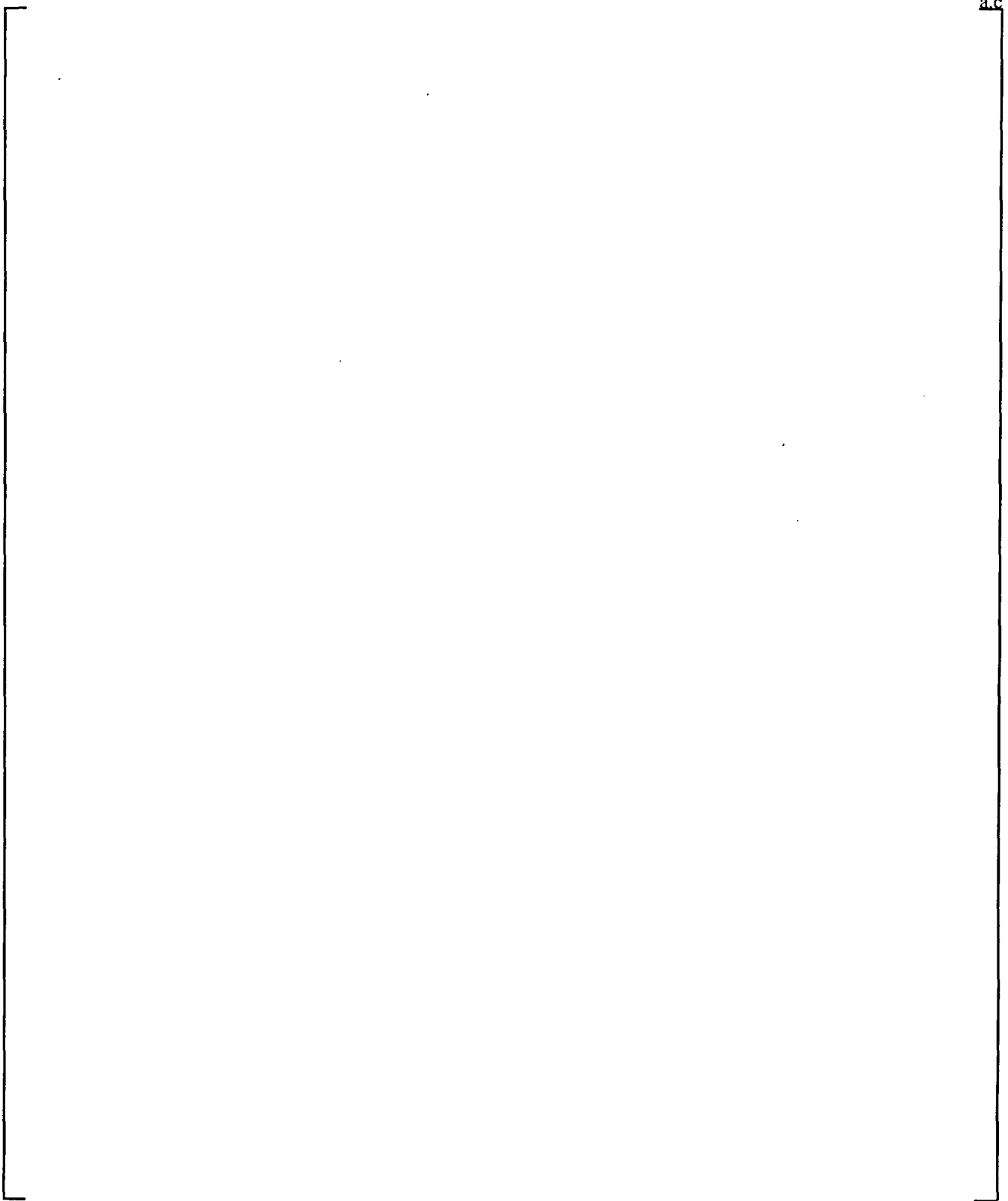


Figure 8-32. Total Actinide Decay Power versus Burnup and Initial Enrichment

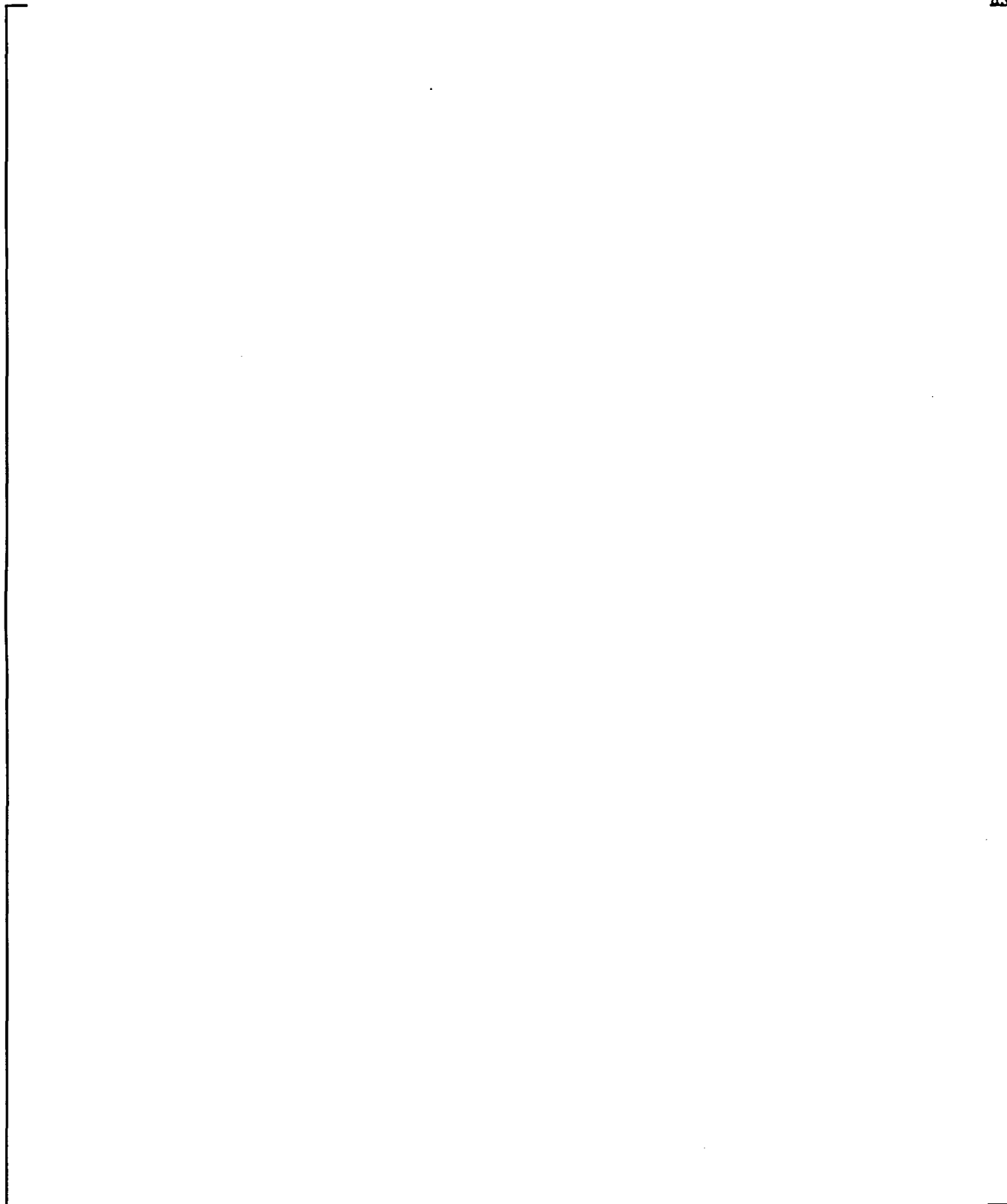


Figure 8-33. Actinide Decay Power versus Burnup and Initial Enrichment

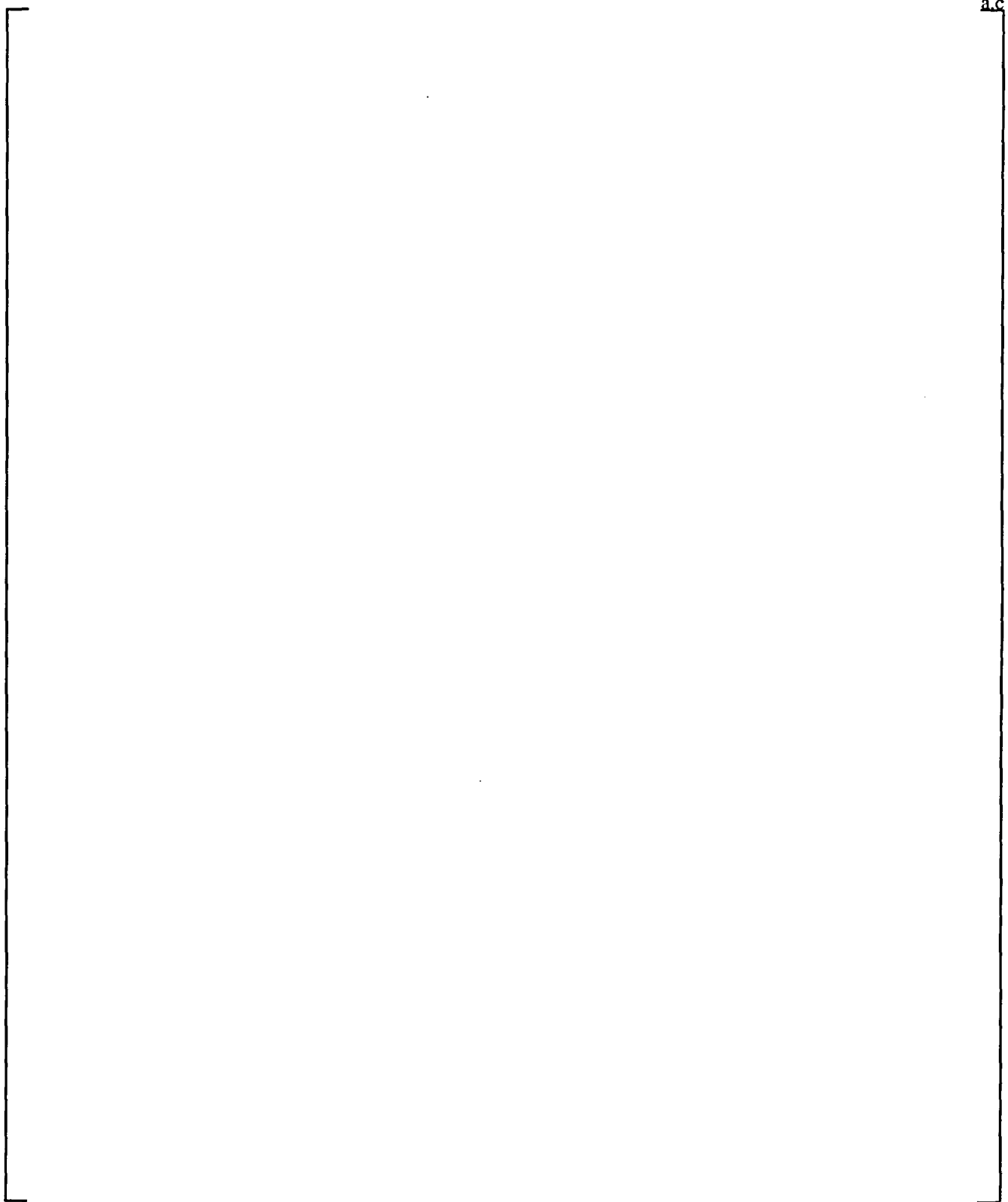


Figure 8-34. Capture Correction versus Burnup and Initial Enrichment

OPTIONS IN WCOBRA/TRAC FOR NEUTRONICS CALCULATIONS

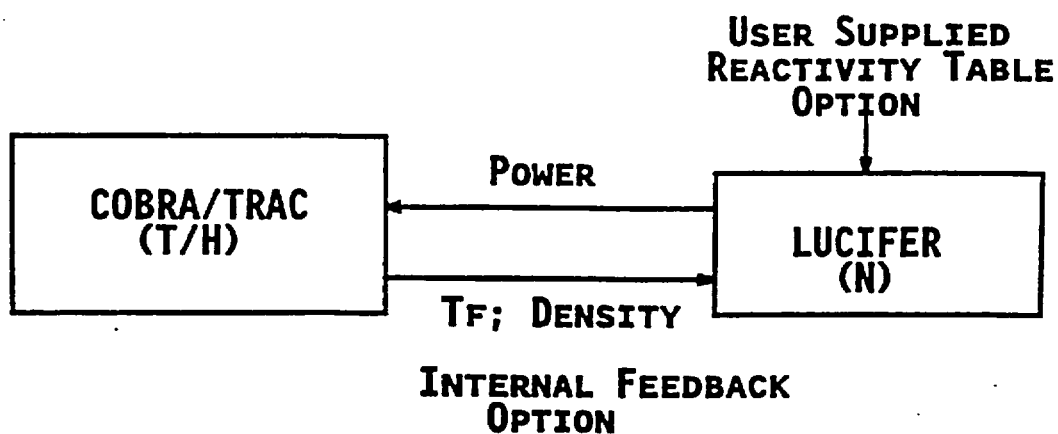


Figure 8-35. WCOBRA/TRAC Calculation Block Diagram